UNIVERSITY OF SOUTHAMPTON
FACULTY OF ENGINEERING
SHIP SCIENCE

PARTIALLY SEPARATED FLOW AROUND MASTS AND SAILS

by

Stuart Wilkinson

A Thesis Submitted for the Degree of
Doctor of Philosophy

- 1984 -

UNIVERSITY OF SOUTHAMPTON

ABSTRACT

FACULTY OF ENGINEERING AND APPLIED SCIENCE

SHIP SCIENCE

Doctor of Philosophy

PARTIALLY SEPARATED FLOW AROUND MASTS AND SAILS

by Stuart Wilkinson

A variable camber aerofoil and a miniature boundary layer traverse unit have been designed and built to investigate the nature of flow around two-dimensional, highly cambered, sail-like aerofoil sections with circular masts. Data has been obtained in the form of static pressure distributions and boundary layer velocity profiles over representative ranges of Reynolds number, camber ratio, incidence angle, mast diameter/chord ratio and mast angle for both NACA a = 0.8 and NACA 63 mean-line camber distributions. All flow regimes present have been identified and related to the salient model and flow parameters.

Using knowledge gained from the experimental results, a new partially separated flow theory was developed based on a discretized vortex/source panel technique. Comparison between experimental and theoretically predicted static pressure distributions showed excellent agreement.

ACKNOWLEDGEMENTS

The Author wishes to express his thanks to Professor G.J. Goodrich (Head of Department), Dr. J.F.Wellicome (Project Supervisor) and all staff and postgraduates, past and present, of the Ship Science Department at Southampton University, for the support,advice and encouragement given during the period of this research.

Special thanks are also given to the technicians and workshop staff of the Engineering Faculty for their patience and craftmanship during the construction and operation of the experimental apparatus.

Finally thanks are due to Mrs Wright-Green who undertook the typing of this thesis, and who did such an excellent job.

This research was sponsored by the Science and Engineering Research Council (SERC).

LIST OF CONTENTS

Page No.

Chapter 1 - Model Aerofoil Design

Chapter 2 - Support Structure Design for Aerofoil and Masts

Page No.

Chapter 6 - Expertimental Procedures

Chapter 7 - Data Acquisition and Reduction Methods

Chapter 8 - Presentation and Discussion of Results

Page No.

Chapter 9 - Development of a New Partially Separated Flow Theory

Chapter 10 - Comparison of Experimental and Theoretical Results

LIST OF FIGURES

Figure No. Page No.

LIST OF PLATES

NOMENCLATURE

FLOW PARAMETERS :

α	aerodynamic incidence angle
$\Delta\alpha$	incidence angle correction for streamline curvature
Re	Reynolds number based on local sail chord length
Re_d	Reynolds number based on mast diameter
ρ	air density
ρ_L	fluid density (manometers)
g	gravitation constant
ν	kinematic viscosity
θ	flow yaw angle

MODEL PARAMETERS :

d	mast diameter
CR	local spanwise camber ratio of the sail
C	local spanwise chord length of the sail
ϕ	mast angle (angle between local sail chordline and the boat ℄, see figure 1)
Ca	local sail camber length

CO-ORDINATES :

X	chordwise co-ordinate (origin at the sail leading edge, see figure 1)
Y	co-ordinate normal to the sail chordline
XX	co-ordinate along boat ℄
x	curvi-linear co-ordinate parallel to the local sail surface
y	curvi-linear co-ordinate normal to the local sail surface
z	spanwise co-ordinate (origin at the 'mouse' centre, see figure 22)
s	sail surface length co-ordinate (origin at sail leading edge, see figure 1)

POSITION PARAMETERS :

X_k	chordwise position co-ordinate of a panel control point (K)
Y_k	position co-ordinate of a panel control point (K) normal to the chordline
X_{j+}	chordwise position co-ordinate of the +ve singularity end of panel (j)
Y_{j+}	position co-ordinate of the +ve singularity end of panel (j) normal to the chordline
X_{j-}	chordwise position co-ordinate of the -ve singularity end of panel (j)
Y_{j-}	position co-ordinate of the -ve singularity end of panel (j) normal to the chordline
Se	separation location
R	reattachment location
T	transition location along the bubble bounding free streamline
T'	transition location projected onto the sail surface
η	reattachment surface angle (angle between the local sail surface and the bubble boundary at reattachment)
Q_{jk}	influence coefficient dependant entirely on mast/sail geometry
A_{jk} B_{jk} E_{jk} F_{jk}	position arrays based on geometric data (see equation 9.9)
y_g	position of the measuring probe geometric centre normal to the sail surface

LENGTH PARAMETERS :

Δs	doublet panel length
ΔL	distance between adjacent control points
Δy	sheet separation distance, or displacement of probe geometric centre

a	casing oval ½ x major diameter
b	casing oval ½ x minor diameter
R+	straight line distance between a +ve singularity and any flow field point
D	probe tubing outer diameter

VELOCITIES :

U	apparent wind velocity (tunnel free stream velocity)
u	local velocity (corrected)
Δu_x	local tangential velocity due to a vortex sheet
Δu_y	local normal velocity due to a source sheet
u_x	total local velocity in the x-direction (tangential to the surface)
u_y	total local velocity in the y-direction (normal to the surface)
u_i^v	local induced velocity due to a vortex doublet panel
u_i^s	local induced velocity due to a source doublet panel
$u_i^{+(-)}$	local velocity induced by a +ve point vortex (or -ve point vortex)
u_δ	local velocity at the boundary layer outer edge
u_τ	friction velocity ($= \sqrt{\tau_\omega / \rho}$)
u_T	local velocity at transition
u_m	measured local velocity
G	free stream velocity vector

PRESSURES, PRESSURE HEADS AND PRESSURE COEFFICIENTS :

$P_{1,2 \text{ or } 3}$	pressures measured by the three tubes of the yaw-probe
P_R	surface pressure at reattachment
P_T	static pressure at transition on the bubble boundary
$P_{T'}$	surface pressure at transition
Δp	local dynamic pressure
ΔP	free stream dynamic pressure
σ	pressure recovery coefficient (see equation 8.1)

Cp	local pressure coefficient = $1 - (u/U)^2$
Cp_R	pressure coefficient at reattachment
Cp_{se}	pressure coefficient at separation
$h_{1,2 \text{ or } 3}$	pressure heads measured by the three tubes of the yaw-probe
h_T	calibration tunnel working section total pressure head
h_S	calibration tunnel working section static pressure head
h_A	wall static pressure head at the calibration tunnel inlet
h_B	wall static pressure head at the end of the calibration tunnel contraction
Δh	dynamic pressure head

FORCES AND FORCE COEFFICIENTS :

ΔD	drag correction due to horizontal buoyancy
C_D	overall drag coefficient
C_L	overall life coefficient

BOUNDARY LAYER THICKNESS AND FRICTION PARAMETERS :

δ	boundary layer thickness
δ^*	boundary layer displacement thickness
δ^{**}	boundary layer momentum thickness
H	shape factor ($= \delta^*/\delta^{**}$)
τ_ω	wall shear stress
C_f	skin friction coefficient

CALIBRATION PARAMETERS :

y^*	Preston tube calibration factor
x^*	Preston tube calibration factor
$K_{1,2 \text{ or } 3}$	yaw-probe calibration factors
K_o	combined calibration factor

PANEL PARAMETERS :

γ	local vorticity
$\Gamma +$	strength of a +ve vortex
$\Gamma -$	strength of a -ve vortex
μ	vortex doublet panel strength
M	source/sink doublet panel strength
k	suffix indicating a particular control point
j	suffix indicating a particular doublet panel
L LL	alternative panel identification suffices
β_K	local panel slope
$\theta +$	flow field angle (see figure 79)

CONSTANTS :

Λ	horizontal buoyancy constant
r	wing orientation constant for solid blocking
N	number of vertical traverse pulses displayed on the control box
H_i	tunnel working section height
ε_{sb}	solid blocking correction
ε_{wb}	wake blocking correction
n	index constant
A_o B_o }	Nikuradse 'law of the wall' constants

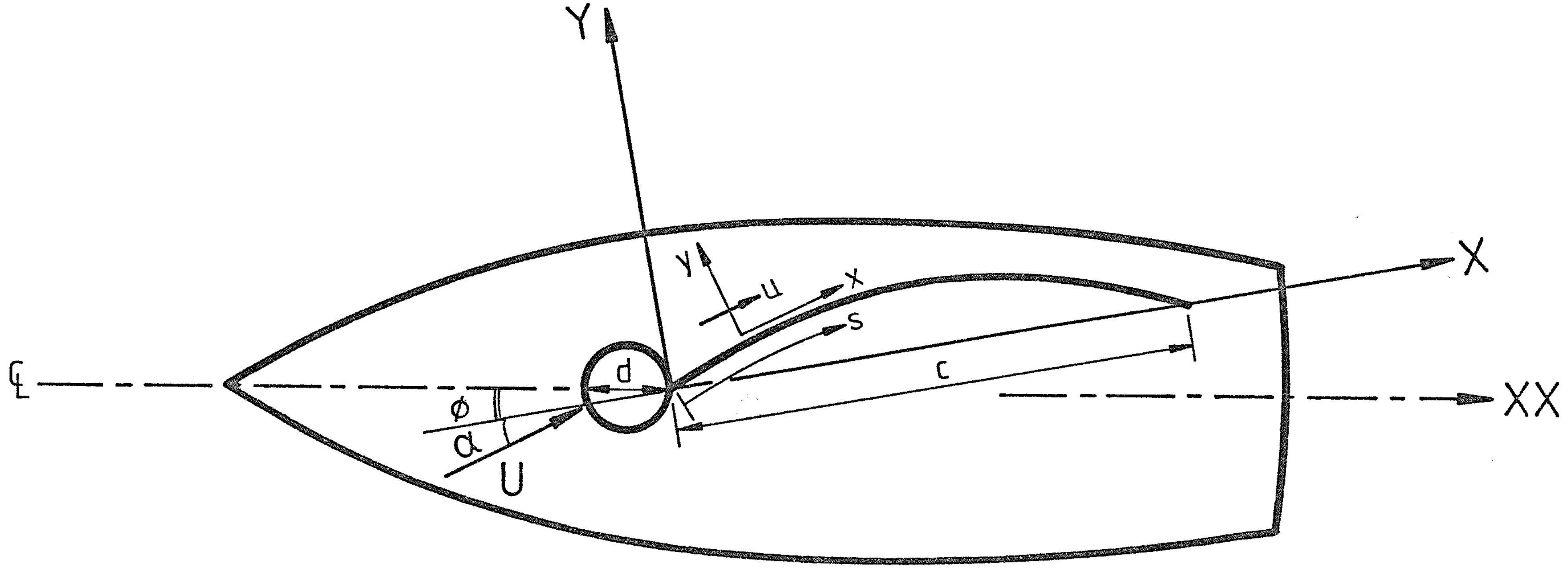

Fig(1) Principal Parameter and Axis Definitions

0.1 Introduction

There has for many years been a constant desire amongst racing yachtsmen to obtain ever more improved performance from both hull and sail rigs, but since the recent rapid increase in fuel prices renewed interest has also begun to be shown in the use of wind power to either assist, or fully replace, conventional engines on commercial vessels.

Previous development in sail rig design has largely been of an empirical nature with changes and improvements being based on a combination of trial and error plus experience.

Such methods, although valuable, are time-consuming, very expensive and provide no guarantee of achieving an overall optimum in design.

The approach most likely to lead to efficient high performance sailing rigs is mathematical modelling, since by employing computation techniques, it would be possible to assess the merits of a large number of design variants in a relatively short time, without it becoming necessary to construct many expensive prototypes.

However to create the necessary comprehensive mathematical model would be a formidable task, since it would require a complete understanding of all the aspects of the problem, such as aero-elastic properties of the cloth sails, rig elastic properties, 3D unsteady flow influences, sail/hull interactions, separated flow effects, atmospheric turbulence and velocity gradient etc.

A complete solution to this overall problem was beyond the scope of the present work, however an attempt has been made to more fully understand just one aspect of the problem, that of mast/sail partially separated flow.

Whenever conventional cloth sails are used, some form of mechanical support is always required to hold them in place and to transmit the aerodynamic forces to the boat hull. This support can take several forms but the most common are masts and forestay/luff groove systems, for mainsails and foresails respectively. Such mechanical supports inevitably act as leading edge obstructions to the incident apparent wind, and result in complex partially separated flows. These flow separations are in addition to the high degree of trailing edge separation that results from the very thin, highly cambered section shapes characteristic of modern sails.

This unique situation of a substantial leading edge obstruction ahead of an unusually thin, highly cambered aerofoil, results in aerodynamics which are quite different to those normally encountered around conventional aircraft wings for which virtually all predictive theories have been developed.

Prior to this study virtually no work had been published concerning the fundamental flows present around typical mast/sail combinations, and certainly insufficient data was available upon which to base any new partially separated flow theory.

In view of the lack of fundamental research in this area the present work considers only 2D flows and masts of circular cross section.

Part A of this report describes the detailed design and calibration of the experimental equipment used to obtain a comprehensive body of data relating to the aerodynamics of typical mast/sail combinations. Some emphasis has been placed on this design aspect of the work because of its complexity and in view of the relatively large amount of project time that had to be devoted to this.

Part B gives details of the experimental procedures adopted together with the analysis of the results obtained.

Finally Part C describes a new partially separated flow theory based on the fundamental knowledge gained from the experimental study.

PART A

EXPERIMENTAL DESIGN AND CALIBRATION

0.2 Previous Experimental Work

Previous investigations of separated flow around typical mast/sail combinations have been largely confined to qualitative observations only. In most of these cases some form of flow visualization technique, principally wool tufts, has been employed which has enabled areas of reversed or disturbed flow to be identified on either model or full size sail rigs.

Although valuable in emphasizing the scale of the separation problem, qualitative observations alone do little to describe the fundamental flow physics involved, nor do they help in the development of a predictive theory, for this the measurement of relevant physical quantities is essential.

The static pressure distribution across a full size sail has been carried out for the yacht 'Papoose' whilst actually at sea as reported by Marchaj (1). However, only one spanwise station was studied in this experiment, whilst the apparent wind speed and direction were both ildefined. In addition the interference caused by the lengths of pressure tubing used might well have been significant in the 'Papoose' results since the shape of any sail is dependent on the pressures acting simultaneously on both surfaces.

As regards reliable scientific data relating to flow around sails, only two papers are known to have been published to date. The first of these due to Milgram (2) provides 2D section data for a range of thin, highly cambered sail-like aerofoil sections, however no mast effects were included in these experimental results. To determine these effects, Milgram (3) has more recently performed a further series of experiments on sail-like aerofoils, but this time various size circular and elliptical masts were included. In carrying out this study Milgram had at his disposal the pressurised water tunnel at MIT, with this facility it was possible to obtain realistic full size Reynolds numbers whilst using a model chord of only 0.229m.

Although Milgram's work was well performed and presented, and supplied data in an area previously untouched, it was apparent that it had a number of short-comings.

Firstly only one type of sail shape was investigated namely the NACA a = 0.8 mean-line (see Abbot and von. Doenhoff (4)). This is not the only shape that is or can be used for sails, nor is it by any means certain that the NACA a = 0.8 represents the optimum sail shape, especially in view of the separated flow regimes thought to be present. It was clear from this that any further test programme would have to include more than one sail shape.

Secondly, having decided to investigate just the NACA a = 0.8 sail shape, Milgram carried out tests at only two different settings of camber ratio (CR = 12% and 15%). Milgram's results show that camber ratio can have a significant effect on mast/sail aerodynamics, but with only two values of camber ratio tested it was impossible to identify any detailed trends or make any firm conclusions.

Again in view of this it was clear that any further study would require a much wider range of camber ratios to be covered.

Finally, the water tunnel models used by Milgram were attached to dynamometers located at the tunnel walls, this arrangement provided data only in the form of force and moment coefficients. Such data, although valuable in performance prediction calculations, provides little information regarding the type and extents of the fundamental flow regimes present, this being essential if a predictive theory is to be developed. Data in the form of static pressure distributions plus boundary layer velocity profiles would have provided the fundamental information required whilst still enabling force and moment coefficients to be readily deduced.

0.3 General Apparatus Form and Dimensions

Following the observations made regarding the previous work in the field it was clear at the commencement of this study that any new experimental programme would have to include more than one sail shape together with a wide range of camber ratios, these being in addition to an appropriate spread of other relevant variables such as mast size, incidence angle, Reynolds number etc. Finally any new experiments would have to produce data of a more fundamental nature such as static pressure distributions plus boundary layer velocity profiles.

With these general requirements in mind a detailed design and development programme was embarked upon to create an experimental apparatus capable of accurately simulating flows over typical mast/sail geometries, and able to supply scientific data in the required form.

The first thing considered when designing this experimental apparatus was the permanent test facilities required. In the present case where a study of fluid dynamics was to be undertaken it was essential to have the use of a wind or water tunnel in order to provide the necessary free stream flow conditions. The basic test facility available for this purpose was the 7' x 5' working section wind tunnel at Southampton University.

The use of this tunnel immediately imposed some basic dimensions on the apparatus to be designed. Since, as mentioned in the 'Introduction', it was intended to concentrate on 2D flow conditions only, it followed that any aerofoil models constructed to simulate various sail forms would each have to be made to fit across the tunnel working section with the minimum gap possible at the walls. This being essential to prevent tip flow migrations between upper and lower surfaces of the aerofoil. Because of this it was clear that any aerofoil models would have to have a span of approx. 7' (2.1 m) or 5' (1.52 m) depending on whether these models were to be mounted in the tunnel horizontally or vertically. In the case of the Southampton University tunnel the balance system was installed directly above the working section, its presence there would have made any model end fixings on the tunnel ceiling difficult. In addition, the boundary layer traverse system discussed later in this report would not have been compatible with operation on a vertical surface. These two considerations together precluded the use of vertically orientated aerofoil models and hence established that any models constructed would have to span the 7' horizontal width of the tunnel.

Full size sails operate at Reynolds numbers based on local chord of between 200 000 and 2000 000. The approximate maximum air velocity attainable in the tunnel working section was 40 m/s, so in order to achieve representative Reynolds numbers in the tunnel it was readily calculated (using the definition given in the nomenclature) that any aerofoil models should have a chord length of around 0.7 m.

Having established the basic dimensions required for the aerofoil models, it then became clear, using data from reference (2) and standard relationships, that the lift generated by such models would far exceed the maximum allowable load that could be handled by the wind tunnel balance system (400 lbf). Reducing the model size would have been impossible if 2D flow and the necessary Reynolds numbers were to have been preserved. As a result the wind tunnel balance could not be used for either force measurement or for model suspension in the working section. This situation reinforced the earlier decision to obtain data in the form of static pressure distributions, since these would in fact provide the only means of establishing force coefficients without the use of the balance system.

As for supporting the aerofoil models in the working section, a choice had to be made between tensioned wires or a rigid slender frame-work. The detailed design chosen for this support system is described in Chapter 2, but as regards general requirements it was clear that any support system would have to hold an aerofoil model stably in the centre of the working section where any blockage effects would be minimized, and provide facilities for readily adjusting such variables as incidence angle, camber ratio etc.

Finally to complete the general apparatus arrangement some means of collecting accurate boundary layer data had to be devised, together with an appropriate system for holding and adjusting a number of different size mast sections at the leading edge of the aerofoil models. These two systems are described in detail in Chapter 3 and section 2.6 respectively.

CHAPTER 1

MODEL AEROFOIL DESIGN

1.1 Concept of the Variable Camber Aerofoil

The most important part of the experimental apparatus was undoubtedly the 2D aerofoil sections required to simulate typical sail flow conditions. A real sail is of course constructed from woven cloth, this however was not a suitable material from which to build the wind tunnel models because of its low rigidity and therefore inability to maintain any given aerofoil shape without distortion across a 7' span when under aerodynamic loading. In addition it would be extremely difficult to obtain pressure distributions across both sides of a single piece of cloth because of the tube or wire accommodation problem.

Milgram (3) constructed his aerofoil models from bronze plate, one aerofoil for each camber ratio tested. However since Milgram had at his disposal the MIT pressurized water tunnel facility, his models were relatively small (0.506 m span x 0.229 m chord), also only two camber ratios were tested in this work with no attempt made to install pressure tappings in these aerofoils.

For the experimental programme presented here it was intended to test more than one aerofoil form each over a large range of camber ratios, further to this, pressure measurement facilities were also necessary for each case. With the model size required in the present test programme being 7' span x 0.7 m (2.3') chord it was clear that a bronze type of aerofoil construction would have been prohibitively expensive. Indeed it would have been very expensive to construct a large number of aerofoils of this size, each with a complex pressure tapping layout, out of any material including wood or GRP. It therefore became clear at this stage in the project that the way ahead was to construct just one aerofoil, but one with the ability to take up any of the required shapes or indeed any that might need to be tested in future. Such a model could be regarded as a 'variable camber' aerofoil.

This 'variable camber' aerofoil had to be sufficiently flexible in a chordwise sense to take up any required shape, but as rigid as possible in the spanwise direction in order to maintain dimensional stability across the tunnel, even at very low cambers when the contribution of curvature to rigidity was at a minimum. In addition the aerofoil had to be as thin as possible in order to closely simulate sail flow conditions, whilst being sufficiently thick to accommodate the necessary pressure tapping tubes.

1.2 Aerofoil Design Evolution

The first and most obvious design considered for the thin, variable camber aerofoil was a single piece of flexible sheet material such as metal, plastic or plywood. Although simple this type of construction was found to be unsuitable for the following reasons. Firstly a single sheet of material would have been equally flexible in all directions, such that at low cambers significant deflections would undoubtedly have occurred across the aerofoil span when under aerodynamic loads. Secondly a single thin sheet of material would not have been able to house the necessary pressure tubes without seriously weakening the aerofoil structure. Increasing the sheet thickness would have relieved both of the previously mentioned problems but only at the cost of increasing the chordwise stiffness which would have made the representation of high curvature aerofoil shapes impossible, as well as creating severe restoring moments at the restraints.

It was clear therefore that some form of laminate construction with unidirectional properties would have to be adopted. One method of obtaining high rigidity in the spanwise direction whilst preserving chordwise flexibility was to use some form of independent spanwise running stiffening elements sandwiched between two surface skins. A simple form of this concept is shown in figure (2a). In this case the stiffening elements have been shown as metal rods, some of which being hollow tubes to carry pressure information. Although this design satisfied the necessary rigidity requirements it can be seen from figure (2b) that the lower compression surface skin would have been prone to buckling if highly cambered aerofoil sections were attempted, whilst the upper surface skin would have had to cope with severe stretching. The final design had therefore to overcome these problems together with other considerations such as choice and availability of materials, ease of construction and maintenance, reliable installation of pressure tappings etc.

1.3 The Spanwise Stiffening Elements

The first refinement that was made to improve the initial laminate design concept was to adopt rectangular section spanwise stiffening elements instead of circular ones. There were a number of benefits in this change, firstly by using rectangular elements it was possible for a given aerofoil thickness to increase the spanwise stiffness, or alteratively the aerofoil thickness could be reduced for the same stiffness. The extent of this thickness reduction was simply estimated to be in the order of 16% by equating the second moment of area expressions for a circular section of diameter d and that for a rectangular section of width d and thickness t. This thickness reduction for the same spanwise stiffness enabled the aerofoil model to more closely simulate the very thin nature of real sails.

Another very important advantage of using rectangular elements is demonstrated in figure (3). With the elements initially packed hard together it can be seen that with the aerofoil deflected into a

(a) Uncambered Form

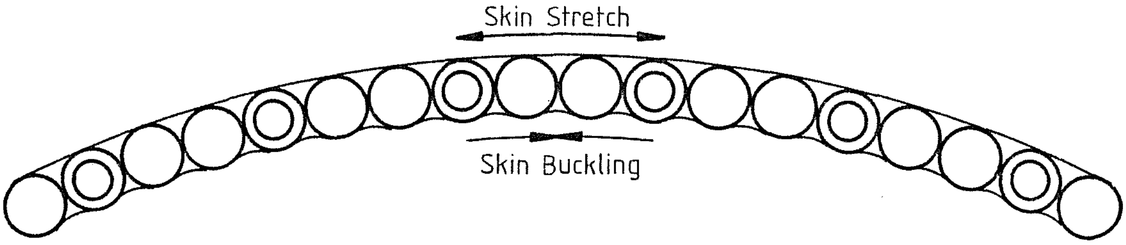

(b) Cambered Form

Fig(2) Simple Variable Camber Aerofoil Concept.

(a) Uncambered Form

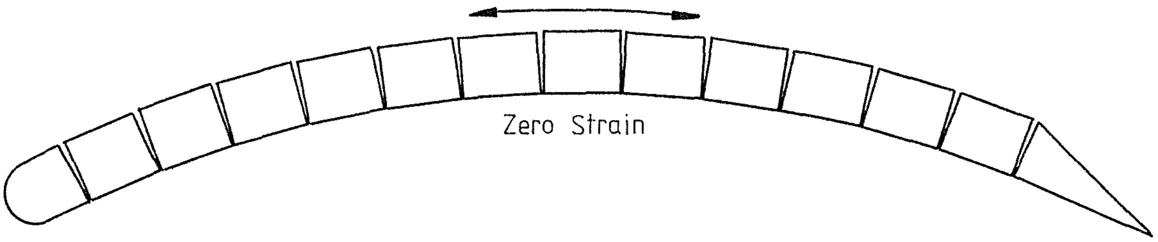

(b) Cambered Form

Fig(3) Aerofoil Using Rectangular Elements cambered form the neutral axis, or plane of zero strain, is forced to occur along the extreme lower surface because of the way in which the lower corners of the elements bear upon each other. This design effectively eliminated the problem of the lower surface compression skin with its tendency to buckle and hence disrupt the essential smooth aerodynamic surface.

Finally a further advantage of using rectangular elements was that they afforded a series of flat surfaces upon which to affix the skin materials. It was felt that adhesive bonding would be the only satisfactory way of attaching the skin materials because screw fastening or riveting would inevitably have left flow disturbing surface irregularities, and would also have interfered with any internal run of tapping tubes.

By performing straightforward design calculations it was quickly demonstrated that it was not possible, with any available element material, for the aerofoil at low or zero camber to maintain its dimensional stability across the entire 7' tunnel width whilst under aerodynamic loading without being of an unacceptable thickness (> 20 mm). It was essential to keep the aerofoil design as thin as possible, not just to closely simulate real sails, but also in order to minimize the length increase that would be suffered by any upper surface skin when in a highly cambered form. In order therefore to adopt a sufficiently thin aerofoil it was necessary to support it at four spanwise positions instead of just at the two tunnel walls. The intermediate case with three support locations was ruled out on the grounds that flow interference would result at the centre of the working section where, because of minimum wall interference at that point, all data would normally be taken. The detailed form of the support structure is described in Chapter 2. By using four support positions it was found that negligible deflections (< 1 mm) could be obtained over the resulting three unsupported minor spans with an aerofoil thickness of only 5 mm.

In the final design the material used for the stiffening elements was aluminium alloy, this was chosen because of its good corrosion resistance, relatively low cost, availability in a variety of extruded cross-sectional shapes and because of its high stiffness to weight ratio, this being important for ease of transportation in and out of the tunnel.

When in the tunnel the aerofoil self-weight and aerodynamic loads were made to some extent self cancelling by ensuring that the convex aerofoil surface faced upwards, this helped in reducing spanwise deflections to the low level previously stated. This technique could not have been used had the option of vertically mounting the aerofoil been adopted.

The cross-sectional shape chosen for the stiffening elements is shown in figure (4a), the central slot in the otherwise essentially rectangular elements was used to carry pressure tapping tubes, the details of which are given in section 1.5. The effect of this slot on the bending stiffness was negligible since the majority of stresses were carried by the extreme upper and lower surfaces of the extrusions. These stiffening elements were available as standard extrusions and were delivered as flat 7' lengths thus avoiding any need for joints.

Forty extruded stiffening elements were used to make up the complete 'variable camber' aerofoil. Although this type of aerofoil construction produced an aerofoil shape that was built up from a series of elemental straight line segments, it was felt that by employing such a large number of elements any difference between the best attainable segmented shape and the required smooth aerofoil form would have been aerodynamically insignificant.

Specially shaped wider stiffening elements were machined for the leading and trailing edges of the aerofoil. Figure (4b and c) shows the cross-sectional shapes of these edge elements. The trailing

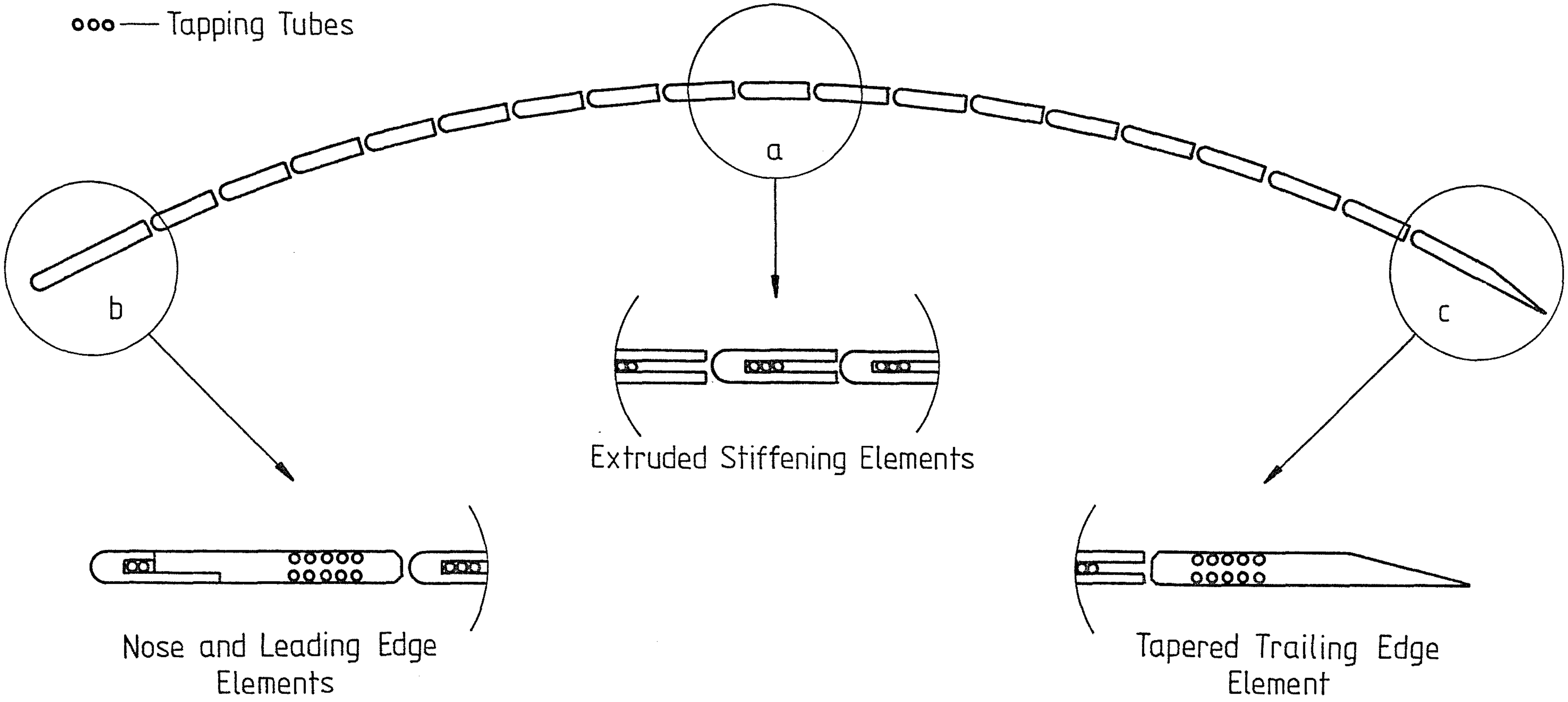

Fig(4) Final Layout and Form of the Aerofoil Stiffening Elements edge element was constructed from aluminium alloy and incorporated a 2 degree taper over ¾ of its 50 mm width. The leading edge element was made from steel to cope with any pressure loading peaks, and was of a stepped form to allow the fitting of a variety of nose shapes or any luff-groove system simulations. For the test programme described in this report the nose form used was semi-circular with a radius of half the aerofoil thickness (2.5 mm).

1.4 The Aerofoil Skin Materials and their Attachment

The choice of lower skin material was crucial because it was through this that all the aerodynamic loads had to be carried before being taken out by the supports.

When bonded to the bottom surfaces of all the stiffening elements, this lower surface skin had to cope with a curious and high stress deflection form. With the aerofoil in a cambered mode the lower skin took the form of a series of straight lines with changes of local slope occurring only along lines corresponding to the boundaries between adjacent elements.

It was clear that no conventional sheet material such as metal or thin plywood could possibly cope with the local stresses that the deflection shape would produce without delaminating, suffering permanent deformation or developing very large restoring moments. Very thin plastic sheet material would probably have been able to overcome these problems, but with the small thickness necessary this type of skin material would have been subject to tearing or stretching when loaded.

The material finally chosen for this skin was woven polyester sail-cloth, this was thin, had good strength and tear resistance properties, provided a good keying surface for bonding, and was resistant to UV light and humidity degradations. Most importantly the woven nature of the material enabled it to cope with the aforementioned sudden local slope changes of the deflection shape without sustaining damage or developing any significant restoring moments.

The requirements of the upper surface skin were quite different to those involved in the lower surface case. Referring back to figure (3b) it can be seen that the extreme upper surfaces of the stiffening elements would tend to move apart if the aerofoil was deflected into a cambered shape. Any skin material bonded to the element upper surfaces therefore had to cope with very extensive stretching. The severity of this stretching was dependent not only on camber, but also on the width of the bonded portion on each element. By using only a short bonded portion, the length of unbonded skin material free to cope with the stretch would have been increased and hence strain values kept low. However with such short bonded portions the tendency for delamination was increased, further, because the upper surface skin was on the 'suction' side of the aerofoil these large lengths of unbonded skin might have tended to be drawn away from the stiffening elements, resulting in the creation of flow disrupting surface irregularities. It was therefore decided for the final design to adopt the opposite case, where the skin was bonded over the maximum width possible, this avoided the problems of skin lifting and delamination. The penalty for this, of course, was very high strains in the skin material when cambered. The only skin material that was capable of coping with such high strains was thin rubber sheet. The material finally chosen was 1/100" thick Neoprene-Latex rubber in a sheet form sufficiently large to cover the aerofoil upper surface without any joins. This very thin sheet was chosen to minimize restoring moments. The latex structure easily handled the high strains involved without suffering permanent deformation, and the Neoprene component protected the latex from UV degradation and perishing.

The adhesive used for both skins was standard epoxy resin. Sample tests showed that the bond strengths obtained with this adhesive were more than adequate. Epoxy was also a well established adhesive with its ageing and chemical resistance properties well known. Some of the more modern adhesive types such as the cyanoacrylates (super glues) have long-term ageing properties, are very dependant on UV light and humidity, and are highly influenced by joint preparation and handling. Such modern adhesives also had an unknown long-term performance with such unique adherends as polyester cloth or rubber onto aluminium.

Prior to bonding, the aluminium stiffening elements were abraded and degreased. The relatively long curing time of epoxy also gave adequate opportunity for even spreading of the adhesive and final positioning of the skins.

A better adhesive might possibly have been that recently produced by Permabond Ltd., this includes rubber particles in suspension that give excellent impact resistance. More importantly, however, is the ability of this adhesive to give exceptionally high strength with little or no joint preparation. The adhesive was not used for the aerofoil because of its cost which was approximately 100 times that of epoxy.

1.5 Static Pressure Tapping Design and Installation

The successful installation of static pressure tappings into the aerofoil was crucial to the whole data acquisition method, since without these only qualitative results in the form of flow visualisation information would have been possible.

Since nothing had been previously published regarding the nature of flows around mast/sail geometries, such as separation locations, reattachment positions or base pressures, it was felt that the maximum possible number of tappings should be installed in order to fully describe any points of interest without ambiguity.

It was decided therefore to place one upper and one lower surface pressure tapping in each stiffening element used to make up the aerofoil chord (i.e. at a 20 mm chordwise pitch), and to repeat this at three spanwise locations. In addition the leading and trailing edge stiffening elements were each fitted with 5 upper and 5 lower surface pressure tappings at a finer pitch of 5 mm, again this was repeated at the same three spanwise locations. These close groups of tappings were installed especially to identify any sudden pressure changes that might have occurred behind the mast or near the extreme trailing edge.

The final pressure tapping layout therefore consisted of 3 upper and 3 lower surface rows, each containing 40 individual tapping points. These chordwise rows of tappings were repeated at the various spanwise locations for three main reasons. Firstly by comparing pressures for the same chordwise position but obtained at different spanwise locations, it could be confirmed that 2D flow conditions were actually being achieved over the model in the tunnel. Secondly when under 2D flow conditions 3 individual tappings were simultaneously measuring the same pressure, this provided a means of ensuring a full set of chordwise data even if some tappings became blocked. Finally, it was felt that in future the aerofoil might be used for 3D flow tests by introducing a spanwise variation of camber or incidence angle, under such conditions pressure measurements would be required in both chordwise and spanwise directions.

At the mid-span position only, additional upper and lower surface pressure tappings were installed into the nose element, this was done to detect any rapid pressure changes that might have occurred on the aerofoil surface directly adjacent to the mast.

Having ruled out alternatives such as electrical pressure sensitive pads on the grounds of expense, the only viable method of extracting pressure information from the aerofoil was by using pressure carrying tubes connected to tapping holes drilled into the aerofoil surfaces.

Two different designs were used on the aerofoil for the installation of the tapping tubes, one method for the majority of tappings which were fitted into the stiffening elements, and another method for those installed into the leading and trailing edge elements.

The use of metal hypodermic tubing was preferred because of its good dimensional stability, bonding properties and resistance to collapse, especially when drilling radial holes through the tube wall. However since approximately 170 m of tubing was required for the complete aerofoil it was found that metal tubing was prohibitively expensive. In view of this the material finally chosen for the pressure tubing was silicone rubber of 1 mm diameter bore. This material was available relatively cheaply in economic lengths (leaving little waste when cut to length) and in a variety of colours, it also had excellent resistance to chemicals including epoxy and good ageing properties. Silicone rubber was adopted rather than plastic tubing because of its good long-term sealing properties when stretched over a metal connector. Many plastics (i.e. P.V.C.) have time-dependant properties that allow a plastic tube to relax its grip on a metal connector over a period of time and thus give rise to pressure leaks.

It was a simple job to feed the pressure tubing into the slots in the stiffening elements and glue and seal them in place with epoxy, provided that this was carried out prior to the attachment of the skins, but problems were encountered when it became necessary to connect these tubes to surface tapping holes. With tubing of such small dimensions it was found to be almost impossible to drill the necessary 0.5 mm diameter tapping holes through the stiffener wall plus the sealing epoxy and then successfully penetrate into the small bore of the pressure tubing, without misalignments resulting in the drill completely missing the tube. On those occasions when the tapping drill was found to be correctly aligned, it failed to cleanly penetrate the rubber walls of the tube, resulting in tube wall collapse and ripping. Fortunately these problems were discovered early in the design process during tests on sample materials. Further tests of this type eventually ensured that a more reliable pressure tapping connection method was perfected before any work began on the final aerofoil.

The final connection method devised had to both prevent tube collapse when drilled, and guarantee a reliable pressure tight joint between the pressure tubes and surface tapping holes despite any small drill misalignments. To solve the aforementioned problems a number of special metal connectors were designed and built, the construction details of these is shown in figure (5). Each connector consisted of a short length of small bore brass tube fitted centrally into one end of a much larger diameter metal tube, this having firstly been compressed down to a thickness equal to that of the central slot in the stiffening elements. By sealing the ends of the compressed tube with epoxy the final design took the form of a flat hollow chamber with a small protruding neck tube, similar in appearance to a miniature bottle. These connectors could be pushed onto the ends of the rubber pressure tubes and sealed in place in the stiffener slots with epoxy. Being brass these connectors did not collapse when drilled, and because of their increased width over that of the tubing alone, they were easily located and penetrated by the tapping drill.

Chue (5) states that the effect of a hollow chamber below a surface pressure tapping is only likely to introduce an error in measured static pressure of approximately 1%, this was considered as negligible.

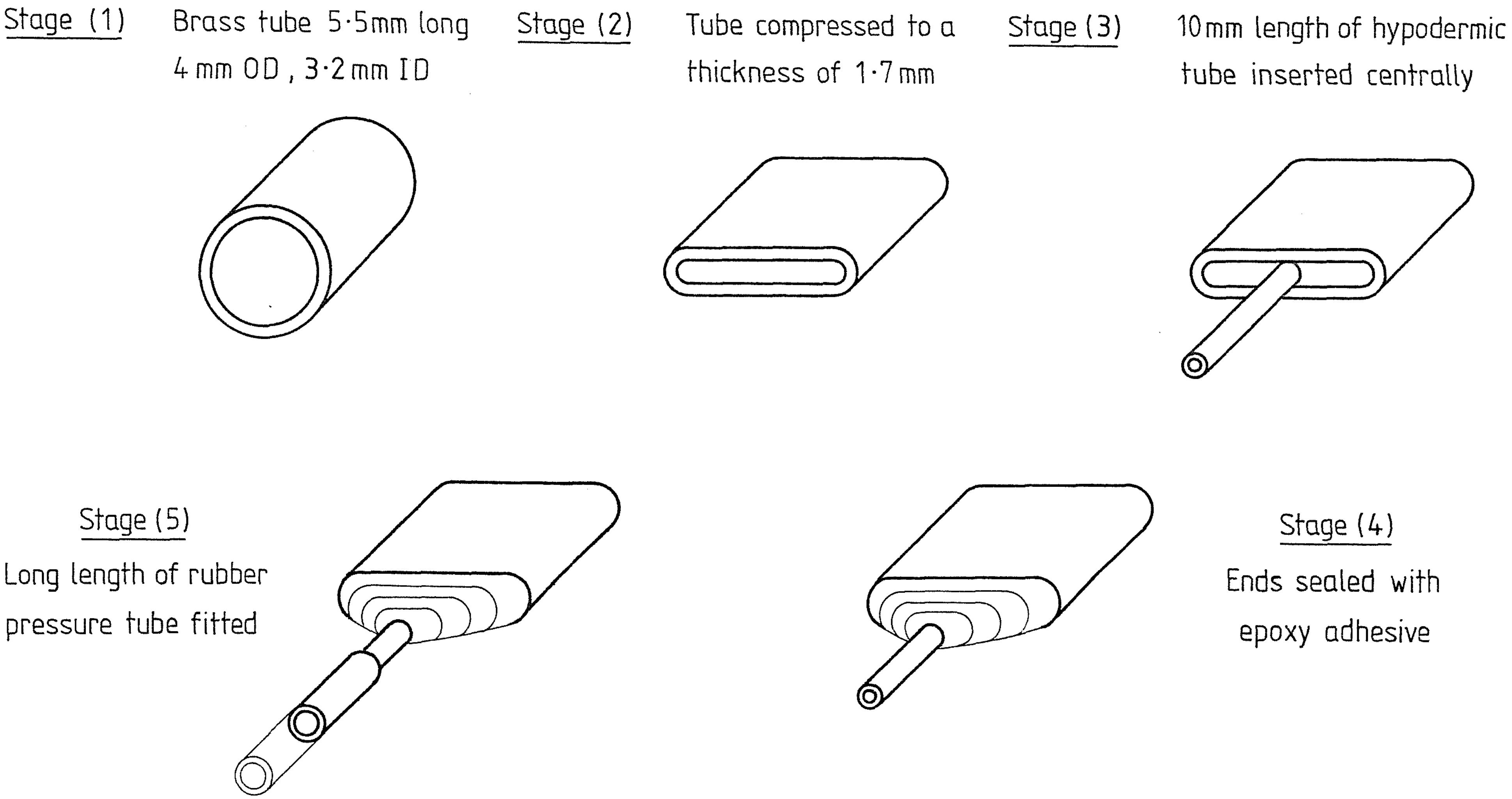

Fig(5) Tapping Connector Construction Details

As stated previously each stiffening element was required to accommodate 3 upper and 3 lower surface tappings at various spanwise locations. It was therefore necessary for the central slot along the length of each extruded element to carry 6 lengths of tubing. Because of the limited space available in these slots it was decided to adopt a layout of tubes whereby a maximum of only 3 tubes would be adjacent to each other at any spanwise position. Simply this meant that 3 tubes would be fed into each central element slot from both extreme spanwise ends. Figure (6a) shows how the pressure tubes with their connectors were placed in each element, sealed and glued in position, and then routed to the surface with the tapping drill. Figure (6b) describes the run of tubes within each element with the identification colours used for each upper and lower surface spanwise station.

It will be noted that the spanwise locations for upper and lower surface rows of tappings were slightly different, this was partly because with the slot width available it would not have been possible to accommodate more than one brass tapping connector at any particular spanwise position, and partly to be compatible with a boundary layer traverse unit which will be discussed in Chapter 3.

The leading and trailing edge elements, unlike the other stiffening elements, were not available as extrusions and therefore they had to be machined from rectangular section stock material into the tapered and stepped cross-sections required. It was not possible with the workshop equipment available to machine accurately these cross-sectional shapes over continuous 7' (2.1 m) lengths, so it was decided to adopt a jointed design for these elements instead. These edge elements were therefore constructed from 3 identical sub-span components placed end to end, plus two short end pieces. The assembly for the trailing edge is shown in figure (7), that for the leading edge was very similar.

(a) Installation Method

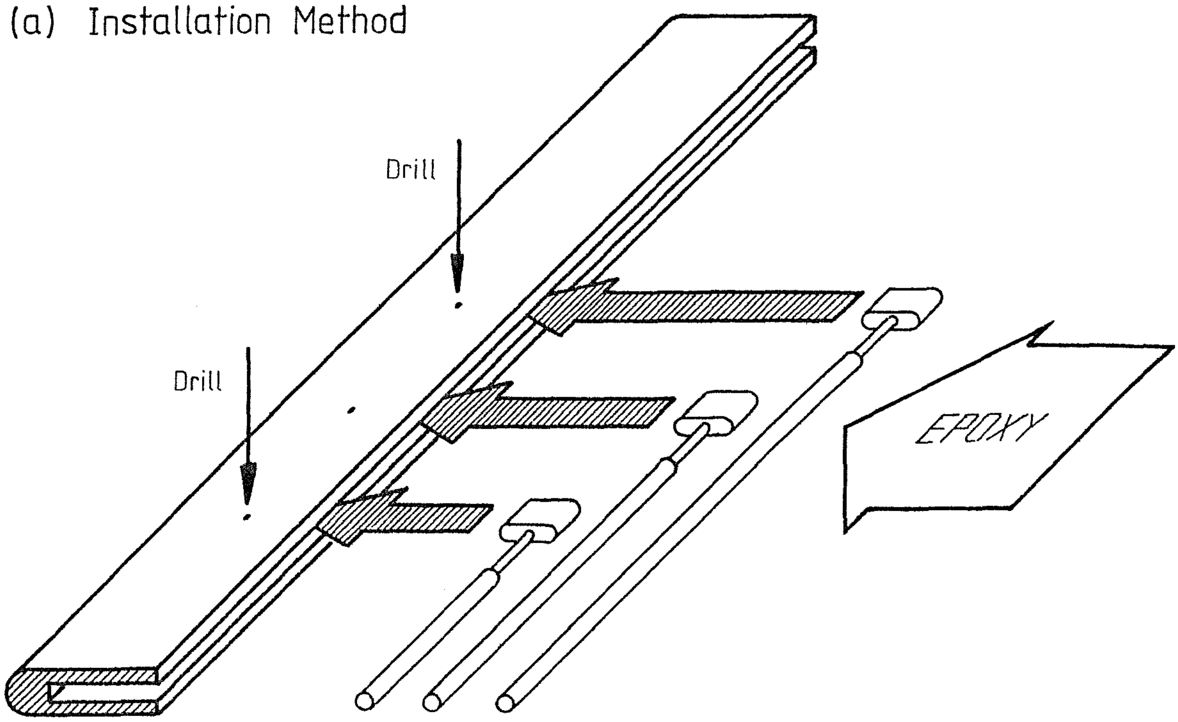

(b) Tube Layout and Tapping Locations

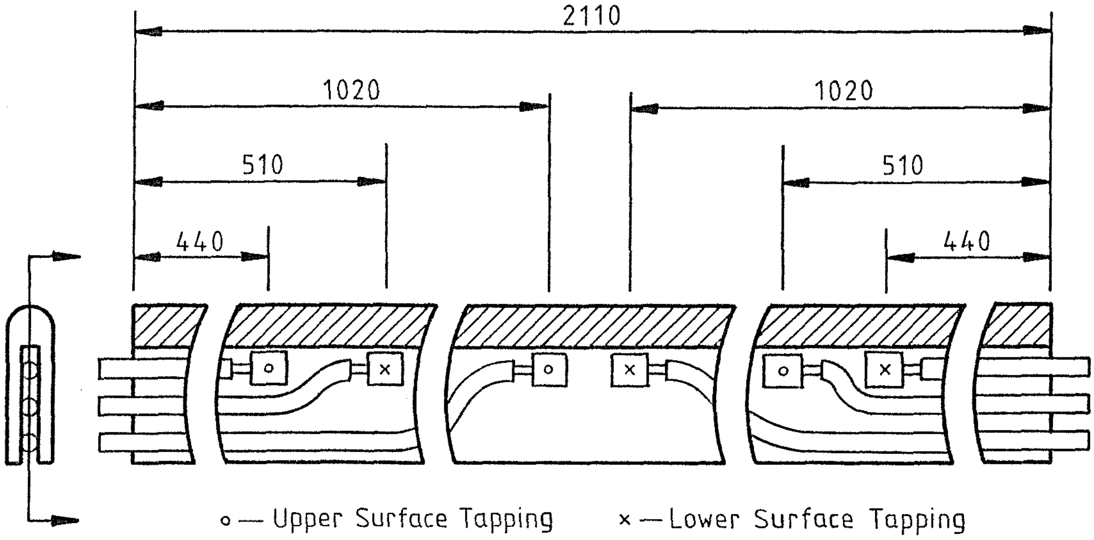

Fig (6) Installation of Pressure Tappings within each of the Aerofoil Stiffening Elements

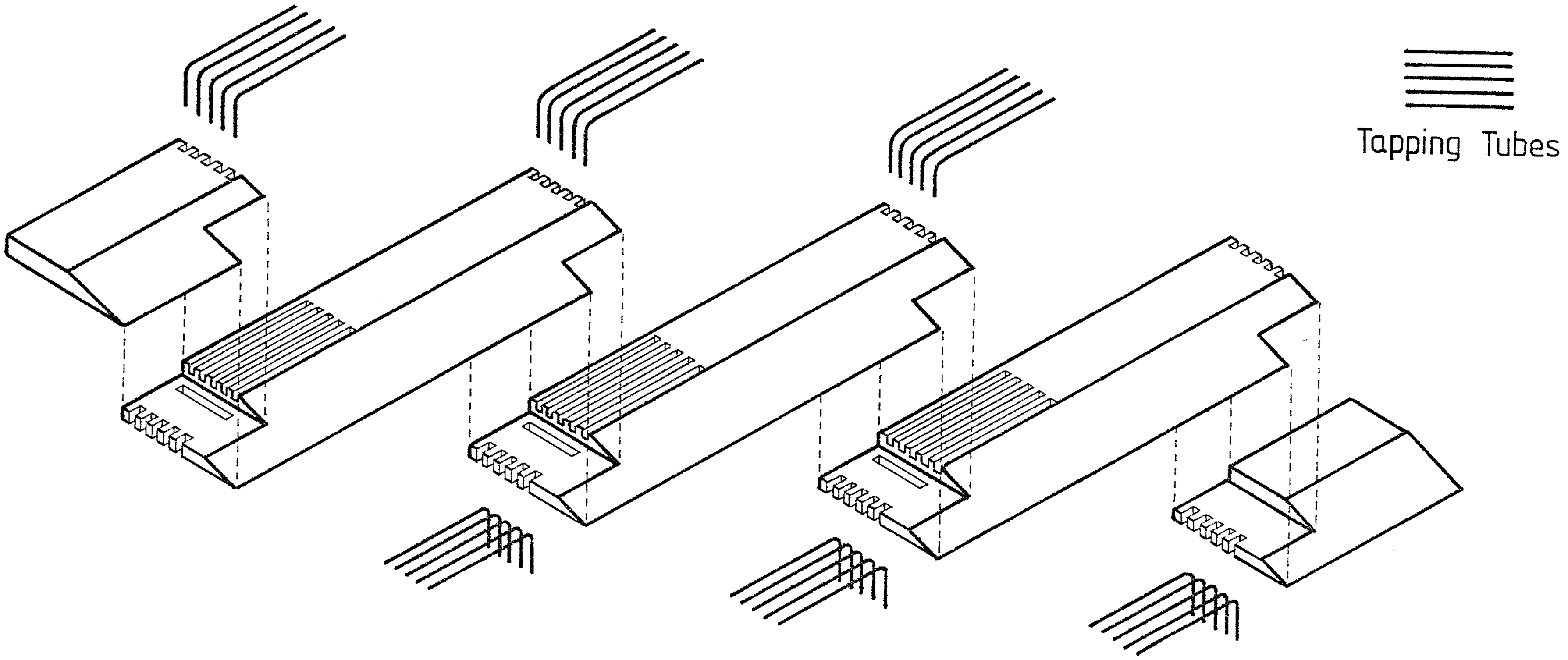

Fig(7) Aerofoil Trailing Edge Stiffener Assembly

Because of the large number of tappings required in each edge element assembly (30), it was felt that the same method of installation as used before would have been unsuitable because of the need to machine a very deep central slot in each element component. Such slots would have seriously weakened the element structure, so as an alternative approach it was decided to install the pressure tapping tubes into shallow 2 mm grooves milled into the upper and lower surfaces of the elements. Having cut these grooves in the required groups of 5 at a 5 mm pitch, the rubber tapping tubes were laid into the grooves and routed out of the lower aerofoil surface through ports at the joints where the leading or trailing edge element components were fixed together. These joint locations were also designed to coincide with the support positions necessary to maintain spanwise dimensional stability of the aerofoil at low cambers. With the rubber pressure tubes in the grooves lying flush with the aerofoil surfaces it was possible to complete the pressure tappings by firstly pushing a short length of small bore brass tube onto the ends of the rubber tubes. These tube ends were then glued and sealed in place in the grooves with epoxy resin. Since the small brass tubes were visible through the epoxy adhesive and only approximately 0.5 mm below the surface, it was a simple job to penetrate the adhesive and enter the bore of the brass tubes with a small tapping drill. Figure (7) also shows the layout of tapping tubes as used on the trailing edge element component assembly. That for the leading edge assembly was very similar.

1.6 Aerofoil Assembly Sequence

In order to successfully build the variable camber aerofoil it was necessary to follow a strict assembly sequence. Special care had to be taken in ensuring that all the pressure tappings were kept clear even when attaching the skin materials with adhesive.

Having installed all the pressure tubes into the stiffening elements as described in the previous section, all the pressure tapping holes were then covered over with small squares of clear adhesive tape to prevent the holes becoming blocked by adhesive when attaching the skins. The skin materials were then cut to the required sizes and all the stiffening elements assembled together on a flat table, lower surface upwards. Epoxy adhesive was then spread evenly over all the elements and the cloth skin manoeuvred into position before being pushed flat to exclude trapped pockets of air.

Once the adhesive had set, the tapping holes, which were easily visible through the white cloth skin and the clear tape, were unblocked using a combination of a small drill and hot pin.

The whole assembly was then carefully turned over and adhesive applied to the upper surface of the elements. The rubber skin was then manoeuvred into position and pressed down as before. This time however due to the highly elastic nature of this upper skin it was found to be impossible to remove all trapped air pockets, those that remained were however sufficiently small to be regarded as aerodynamically insignificant.

Because the upper surface skin material was black, the tapping holes could not be seen underneath but the thin nature of the rubber made it possible to make out the minute surface irregularities made by the squares of clear tape beneath. By probing with a small pin in the general area of these surface irregularities it was possible to find and clear virtually all the upper surface tapping holes. Of a total of 240 tappings installed only 3 were found to be unserviceable due to blockages, and none of these were on the central upper or lower surface rows of tappings.

The laminate construction used for the final variable camber aerofoil design is shown in figure (8).

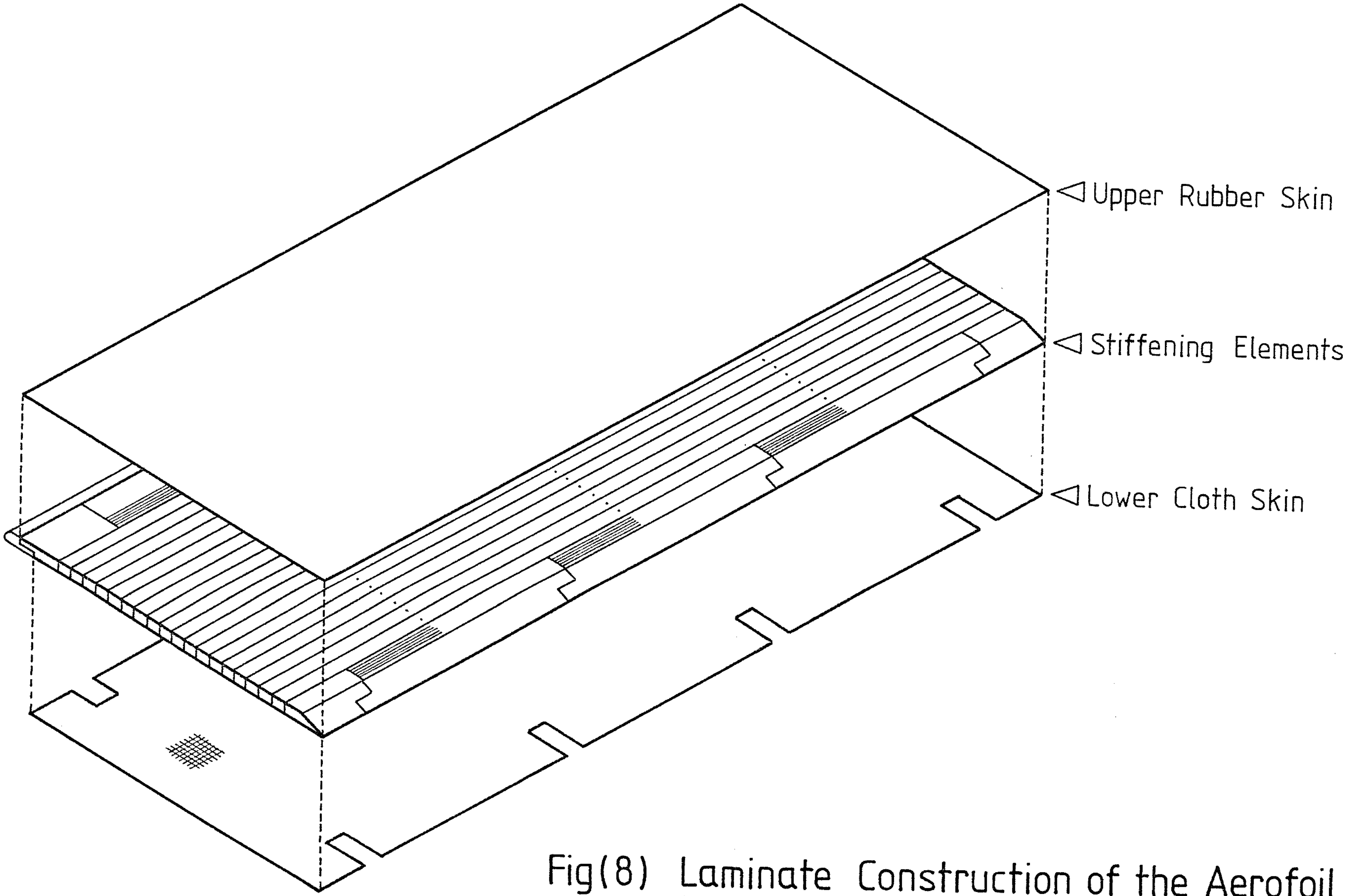

Fig(8) Laminate Construction of the Aerofoil

CHAPTER 2

SUPPORT STRUCTURE DESIGN FOR AEROFOIL AND MASTS

2.1 Introduction

Having designed a variable camber aerofoil it was then necessary to develop some form of structure with which to support it. This structure had to satisfy the following design criteria.

(a) The structure had to hold the aerofoil steady in the centre of the tunnel working section without allowing any bending or torsional vibrations.

(b) The structure had to support the aerofoil sufficiently to ensure dimensional stability across the entire span even at low values of camber ratio.

(c) The structure had to provide some means of adjusting the aerodynamic incidence angle simply and efficiently.

(d) The structure had to afford a rapid method of setting and maintaining the camber distribution and ratio of the aerofoil.

(e) The structure had to produce the minimum possible aerodynamic interference or blockage effects.

(f) The initial installation and setting up time of the support structure had to be minimized to make best use of the limited tunnel time available for testing.

As mentioned previously it was necessary to support the aerofoil at four spanwise locations in order to ensure mid-span deflections of < 1 mm with the 5 mm thick aerofoil set at low camber. The use of wires to support the aerofoil at these positions would certainly have minimized any blockage or flow interference effects, but these would not have been able to provide the necessary rigidity to prevent vibrations. Additional diagonal wires might possibly have improved the support rigidity but only at the expense of increased flow disturbance and greater tunnel set-up time.

It was decided therefore to support the aerofoil with a form of rigid space-frame, made as narrow as possible and bolted to the floor of the tunnel working section.

2.2 Method of Setting and Maintaining the Camber Distribution

It was clear from the nature of its laminate construction that the aerofoil would not remain in any selected cambered shape unless constrained to do so. Therefore before any detailed form of space-frame support could be developed it was necessary to establish some method of setting, resetting and maintaining the camber distribution of the aerofoil.

Another important feature of the aerofoil was that it was a constant camber length device and not one with a constant chord length i.e. when the camber ratio of the aerofoil was increased so the chord length of the aerofoil was reduced. It was necessary therefore, with the aerofoil leading edge held rigidly, for the support structure to cope with a degree of chordwise movement of the trailing edge.

One simple method considered for setting and maintaining the required camber shape employed pre-shaped wooden or plastic pattern plates. By using section data, such as that given in

Abbott (4), the chord length for any camber distribution could be calculated from the known camber length (0.7 m) and required camber ratio. Having obtained by this method the value of chord length that the aerofoil would take up when deflected into any required shape, the section data could then be used to determine the true XY co-ordinates of the aerofoil contour. With such co-ordinates it would have been possible to cut from board material a set of 4 supporting pattern plates each with the required aerofoil shape along the upper edge. When pushed hard against the aerofoil lower surface these pattern plates would have forced the aerofoil to adopt their shape and therefore duplicate the required aerofoil cambered form. This simple technique for setting the aerofoil camber distribution is shown in figure (9).

The disadvantage of this method was that it would have required a large number of individual pattern plates, i.e. for 2 aerofoil shapes each at 5 settings of camber ratio a total of 40 pattern plates would have been necessary. Also if during testing in the wind tunnel it became necessary to investigate an unexpected intermediate setting of camber ratio, a whole new set of pattern plates would have been necessary at short notice. Production of these would have been dependent on the availability of materials, cutting equipment and workshop personnel.

For the final design this concept of pattern plates was used, but instead of cutting from board material many individual plates, it was decided to use infinitely adjustable pattern plates. These adjustable pattern plates were mechanically more complex than the simple idea of shaped board material, but with just one set of 4 adjustable plates it was possible to obtain virtually any aerofoil shape or camber ratio. Two sets of adjustable pattern plates were actually produced since this allowed the aerofoil to be in the tunnel under test at one shape, whilst the second set of patterns was adjusted ready for the next required shape change.

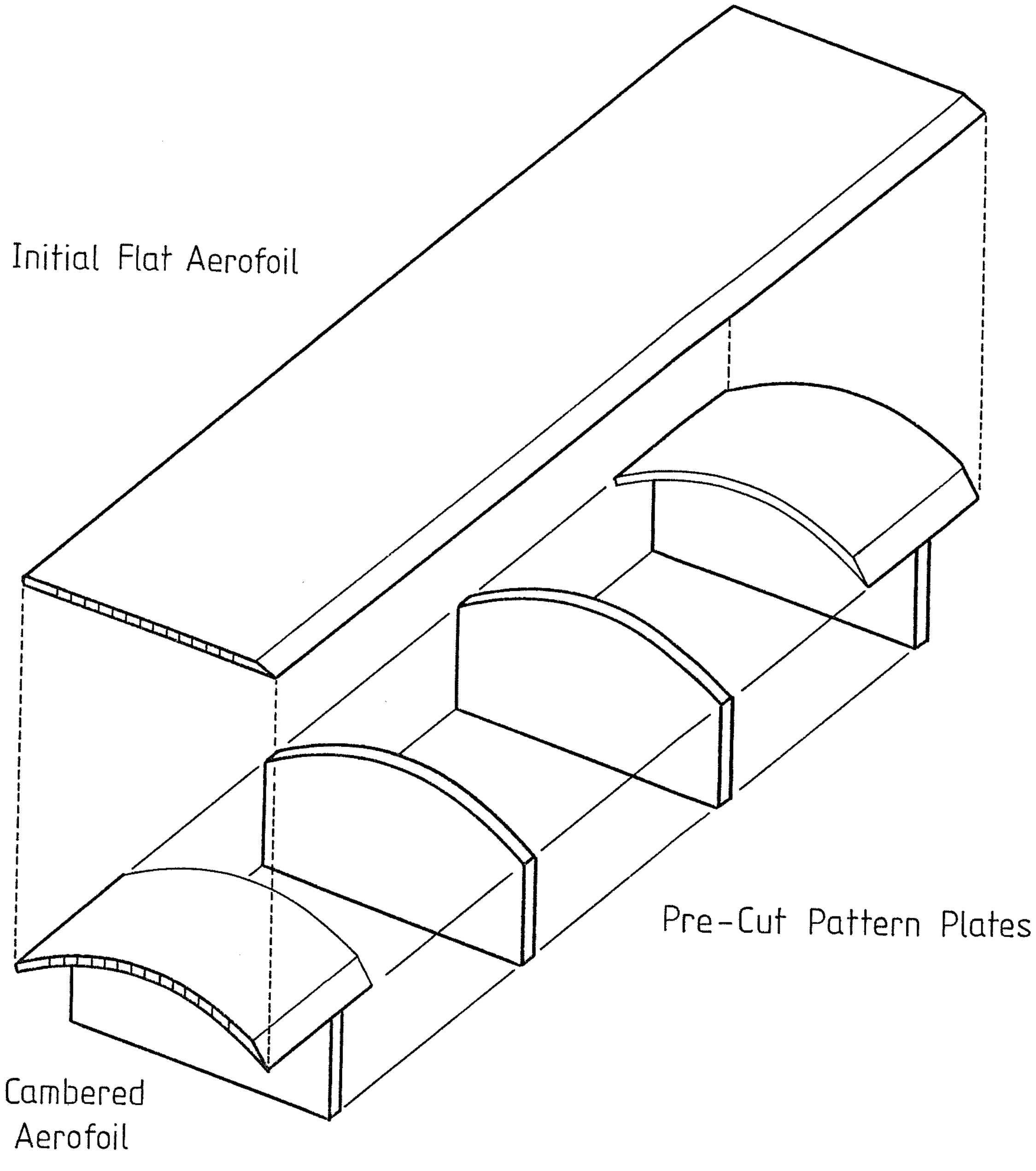

Fig (9) Camber Setting Using Pattern Plates

The final design chosen for the adjustable pattern plates was referred to as a 'camber-cassette', this is shown in figure (10). This design consisted of a length of channel-section steel through the base of which had been machined a central slot. Into this channel could be placed up to 20 close fitting threaded rectangular blocks which could be moved along the channel to any required position. Through each threaded block could be fitted a threaded screw-jack, the central slot in the channel-section allowing any amount of these to protrude through the lower surface. By rotating each screw-jack its length above the upper surface of the threaded block could be varied.

A computer program was written which, by using data obtained from reference (4), could determine the chord length that would be adopted by the aerofoil for any required shape, and then produce a corresponding table of screw-jack height (Y') versus threaded block position (X') for the camber-cassettes. With the screw-jacks adjusted to the correct heights and the threaded blocks moved along the channel section to the required positions as indicated by the computer data, it was then possible to lock each camber-cassette assembly together by fitting nuts onto the protruding parts of the screw-jacks below the channel section.

By machining a number of screw-jacks of various lengths it was possible to assemble a set of camber-cassettes for typical aerofoil shapes with camber ratios ranging from 0 to 20%. In each case the screw-jacks used were selected to produce the required camber distribution with the minimum amount protruding below the channel section. It will be shown in section 2.4 that this was important to ensure compatability with the overall support frame design when at high incidence.

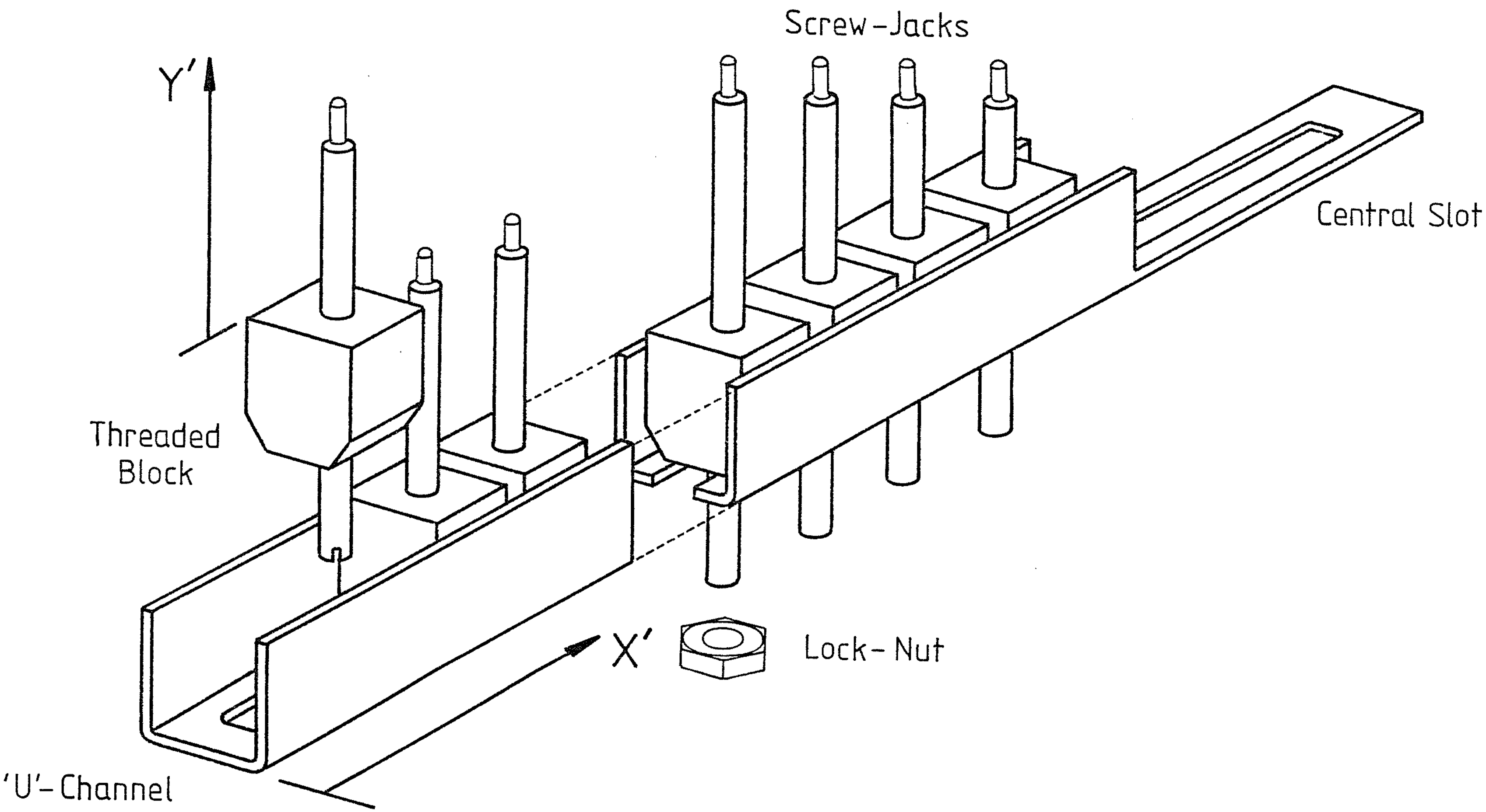

Fig(10) The 'Camber-Cassette' Design

2.3 Method of Aerofoil to Support Frame Attachment

Having developed a camber adjustment system it then became necessary to devise a means of holding the screw-jacks in each camber-cassette securely against the aerofoil lower surface. Figure (11) shows the principle of the system adopted for this. This system basically consisted of 4 inverted steel channel-section members, again each with a central slot machined along the length, but this time with internal dimensions equal to the external size of the camber-cassettes. This meant that a camber-cassette could fit tightly inside each inverted channel-section member.

The aerofoil, pivoted about its extreme edges, was suspended above these inverted channel-section members, with accommodation for trailing edge chordwise movement via a threaded adjuster at the end of each member.

To set the aerofoil shape from an initial zero camber condition as in figure (12a), the threaded adjusters were first used to move the leading and trailing edges of the aerofoil closer together until they were just under the required chord length apart as in figure (12b). The preset camber-cassettes could then be pushed up into the inverted channel-section members from below, with the screw-jacks protruding through the central slots i.e. figure (12c) and (12d). The camber-cassettes could be clamped securely in position using a number of nuts screwed down from the top ends of the screw-jacks, as shown in figure (12e). The required aerofoil shape could finally be achieved simply by using the threaded adjusters to move the leading and trailing edges of the aerofoil apart again. The effect of this was to force the aerofoil down onto the 4 rows of screw-jacks protruding from the camber-cassettes, and hence cause the aerofoil to adopt a corresponding profile, i.e. figure (12f).

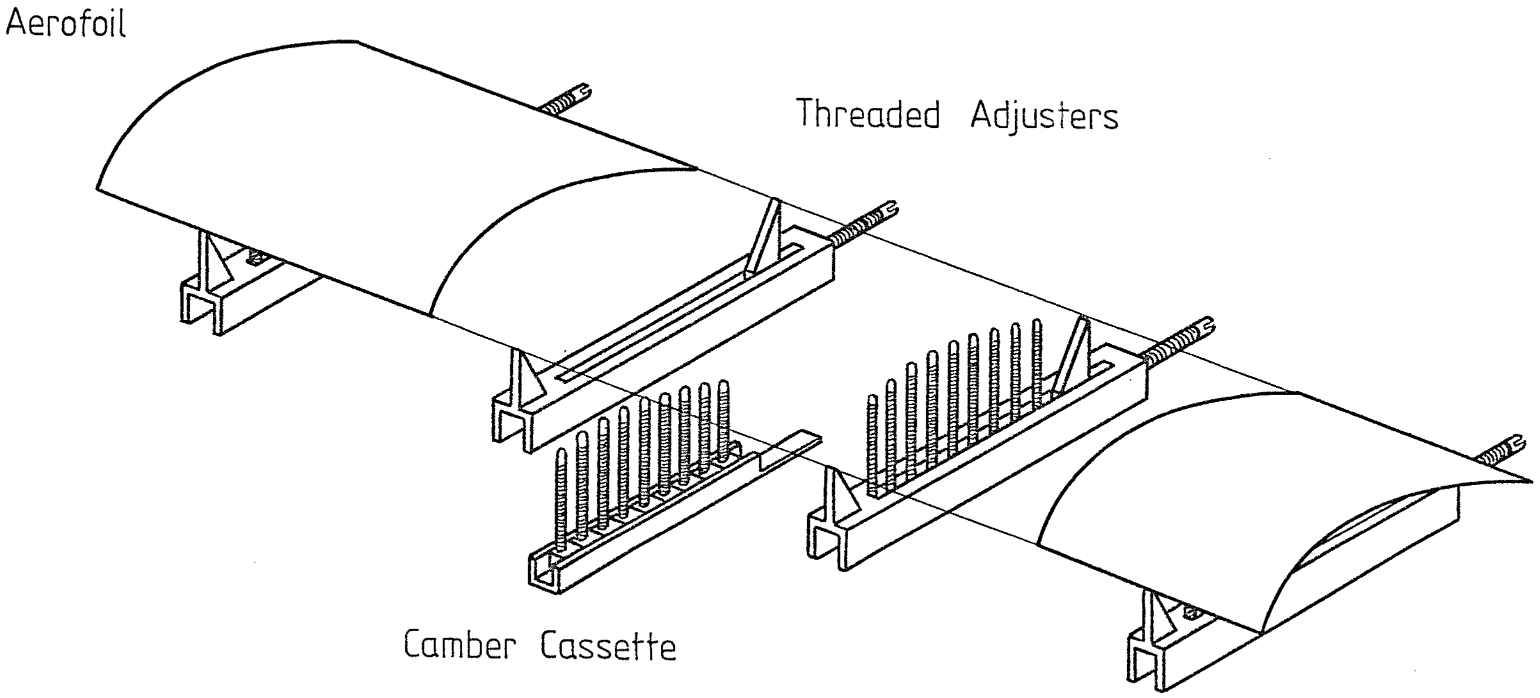

Fig(11) Camber Setting Using 'Camber-Cassettes'

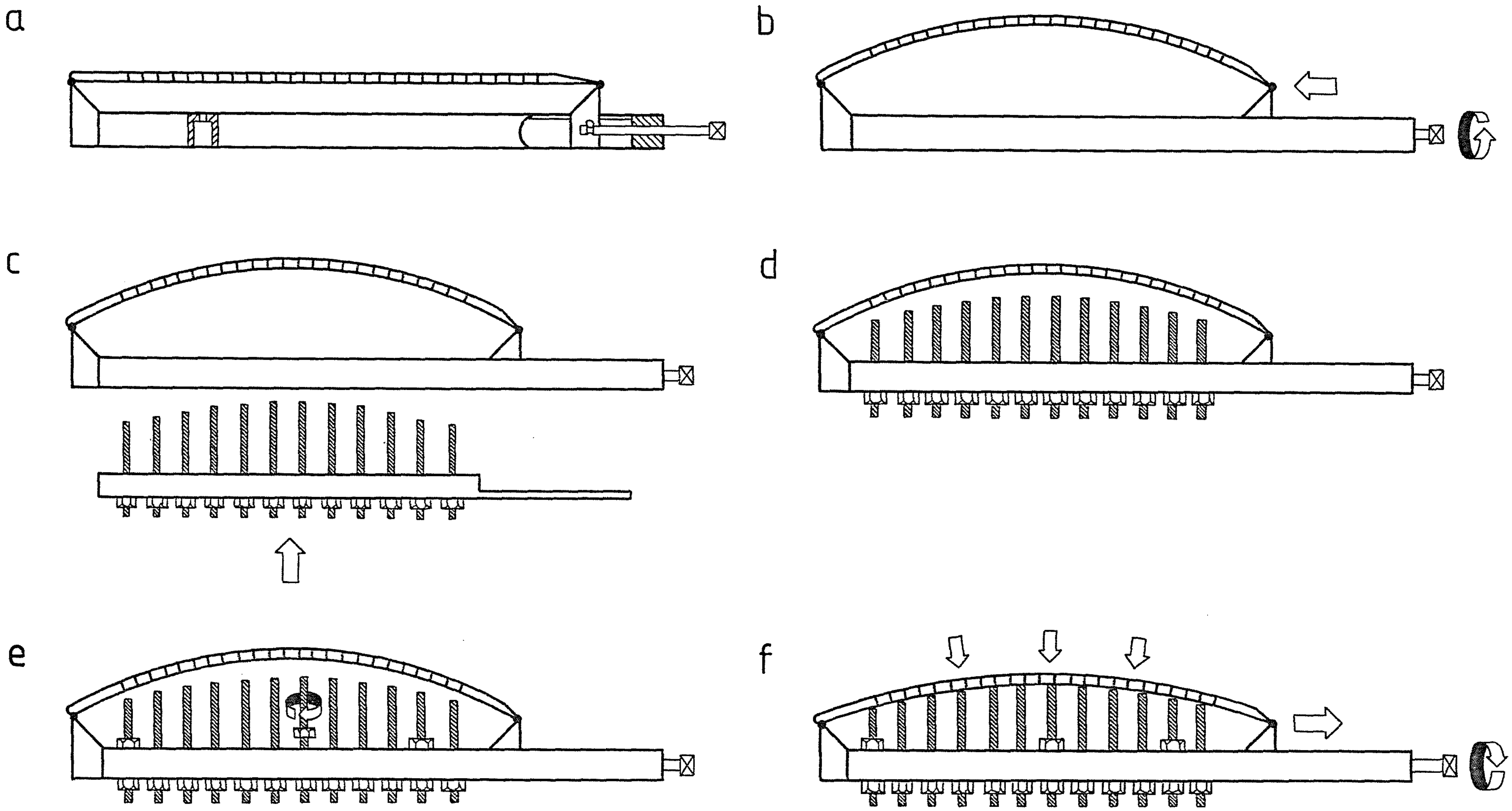

Fig(12) Camber Setting Sequence

A number of refinements to this system were however necessary before the design was finalised and built. The first of these refinements involved the leading and trailing edge pivot designs. Since the aerofoil trailing edge was tapered it was felt that there was insufficient body of solid material in this area to attach a conventional type of pivot. Similarly the presence of a removable nose element at the aerofoil leading edge would have made the installation of a conventional pivot in this area equally difficult.

The method of aerofoil attachment finally chosen as an alternative to conventional pivots involved parallelogram linkages. The geometry of these linkages was arranged so that the extreme leading and trailing edges of the aerofoil remained in exactly the same location in space no matter what aerofoil shape was adopted. These linkages therefore stimulated exactly the effect of the required pivots yet allowed the necessary attachments to be made away from the leading and trailing edges where sufficient anchoring material was available. The linkage details are shown in figure (13) for the aerofoil trailing edge.

A further refinement that was made to the design was to attach a 30 mm wide (32 BG) spring steel strip between the leading and trailing edge linkages. This provided additional support to the aerofoil between adjacent screw-jacks and helped to produce a much smoother aerofoil shape. The spring steel strip also provided a hard surface for the screw-jacks to bear upon, thus preventing damage to the thin aluminium stiffening elements.

When under aerodynamic loading there was a danger that the aerofoil might, by suffering slight stretching, have been sucked away from the screw-jacks, resulting in a small change in aerofoil shape. To prevent this the aerofoil was attached at various chordwise positions to the tensioned spring steel strip by a series of clips fixed to the aerofoil lower surface. Details of these attachment

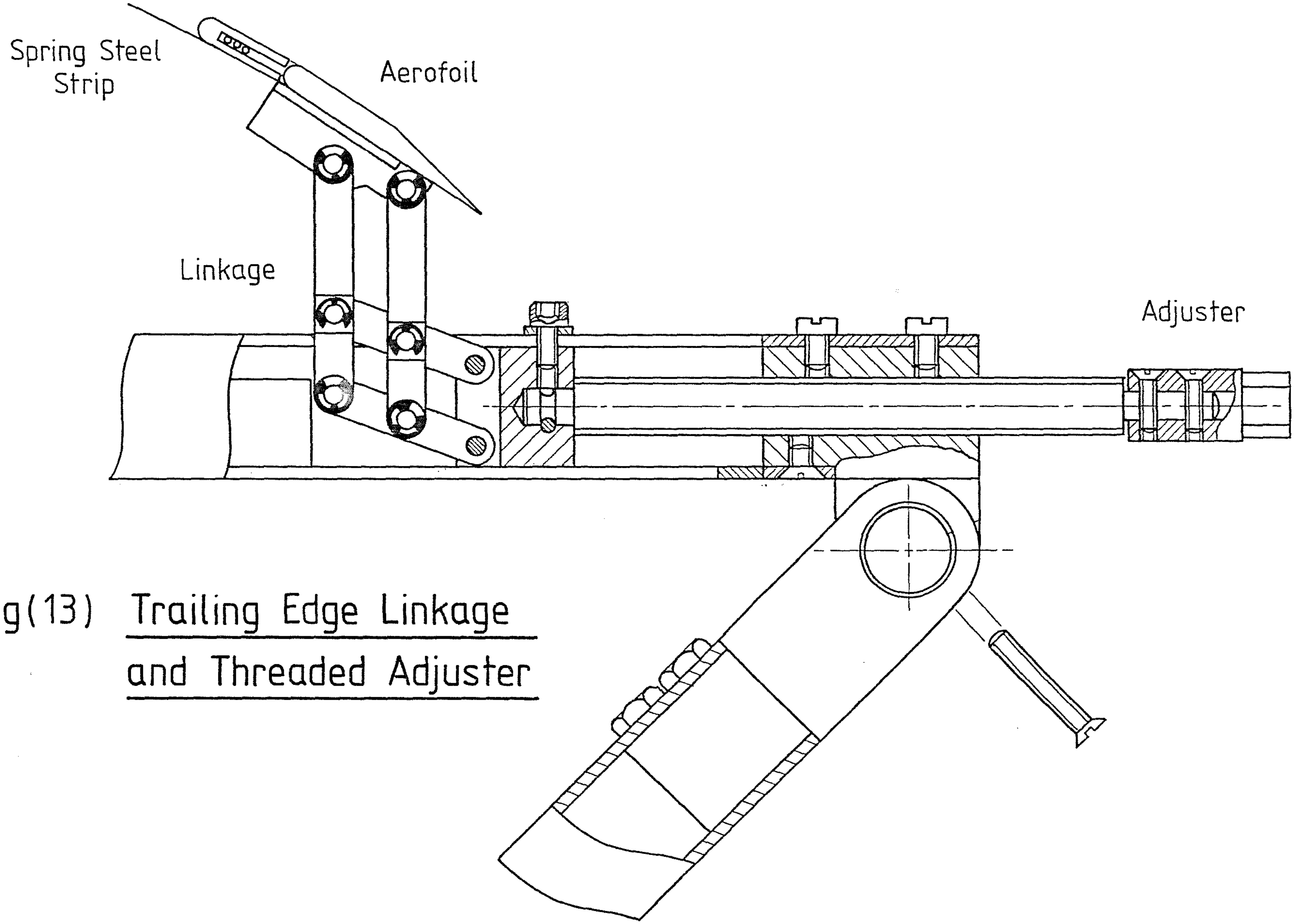

Fig(13) Trailing Edge Linkage and Threaded Adjuster

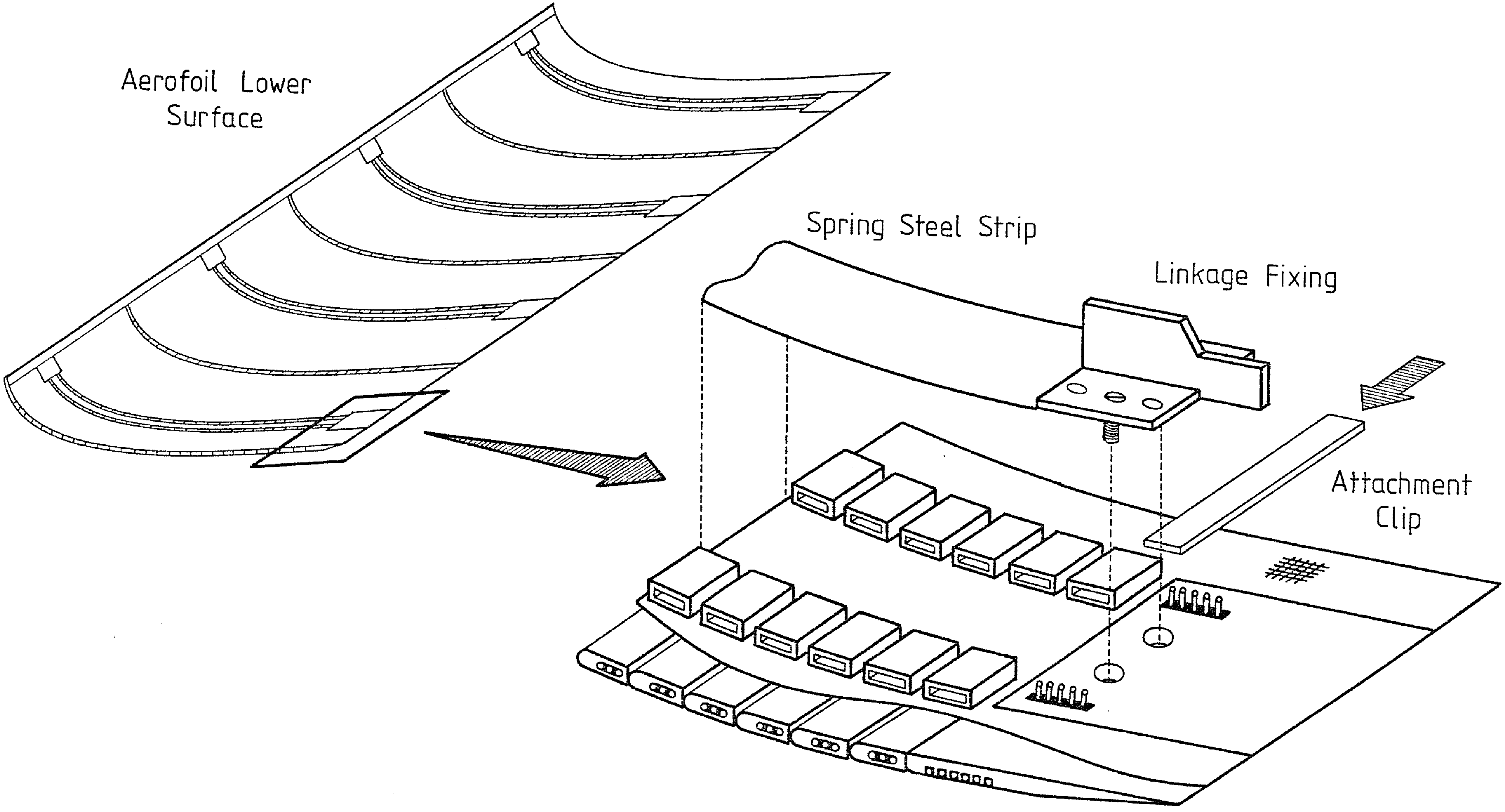

Fig(14) <u>Attachment Clip Design</u>

clips are shown in figure (14). A total of 30 clips were fitted to the aerofoil above each of the 4 support positions. These successfully eliminated all problems of aerofoil shape distortion due to aerodynamic lifting.

2.4 Method of Incidence Angle Variation

Having designed a mechanical assembly for setting and maintaining any required camber distribution, it was then necessary to incorporate this into a further system for adjusting the aerodynamic incidence angle of the aerofoil.

This system had to rotate the whole of the aerofoil and its camber setting assembly relative to the tunnel center-line, preferably without the aid of non-standard engineering components such as curved guide rails or circular arc racking.

After some consideration it was decided to adopt a design which incorporated a single straight lead-screw plus two moving framework members, one of these being the camber setting assembly discussed previously. The line diagram in figure (15) shows the design principle. The component geometry finally chosen enabled the incidence angle of the aerofoil to be varied between -5° and +25°.

It will be discussed later in section 2.6 how the mast sections used in the experiments were attached to the tunnel walls and not in any way to the aerofoil support structure. In order therefore, for the leading edge of the aerofoil to remain butted up against the rear of each mast, no matter what incidence angle was selected, it was essential for the incidence angle variation to take place about a centre of rotation located at the extreme aerofoil leading edge. That is to say that the aerofoil leading edge had to remain at exactly the same location in the wind tunnel at all times.

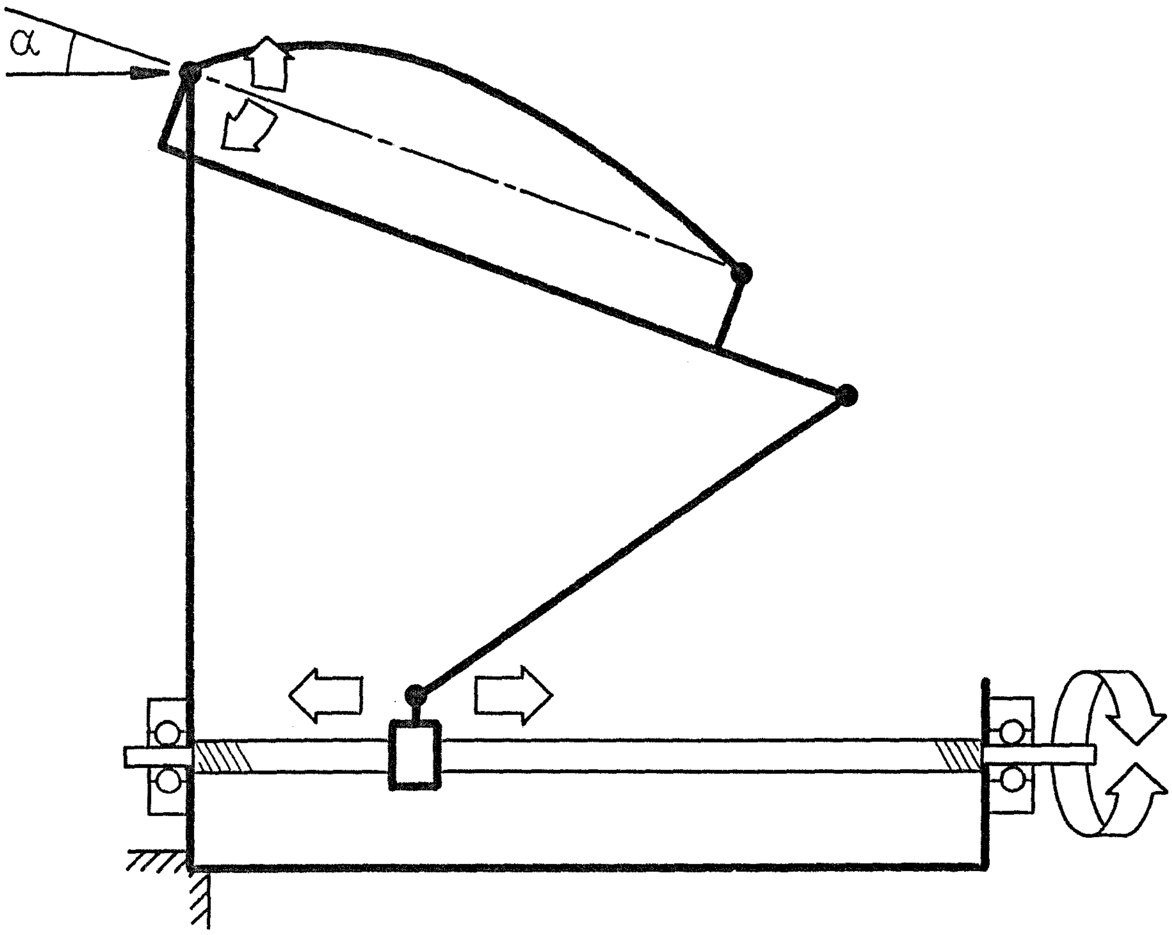

Fig(15) Incidence Variation Principle

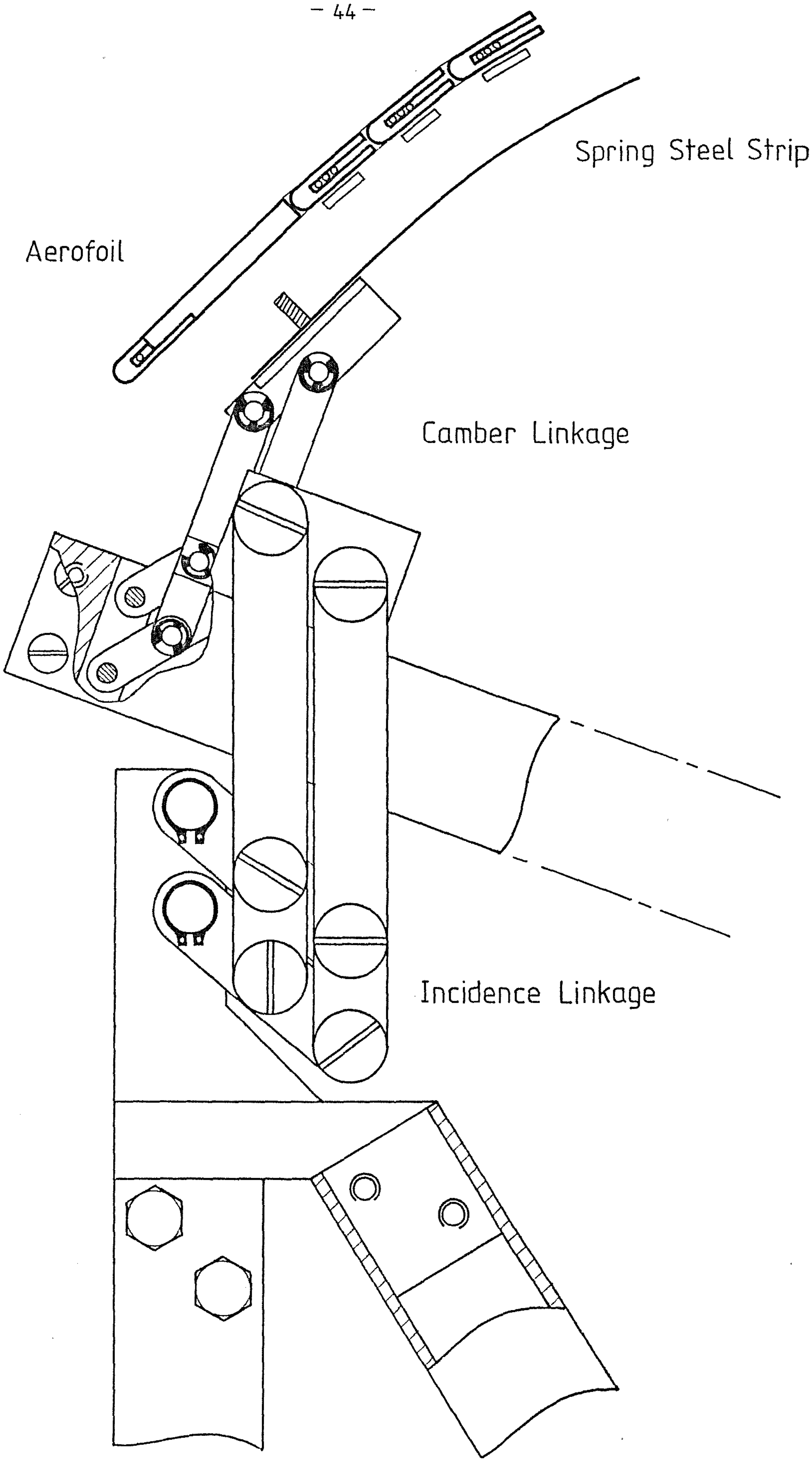

Fig (16) <u>Leading Edge Linkage Assembly</u>

It has already been explained why it was not possible to place a pivot along the aerofoil leading edge, so as before a parallelogram linkage system was adopted.

Two independant parallelogram linkages were therefore required at the aerofoil leading edge at each support position, one to keep the leading edge at the same location during adjustments of camber distribution (or camber ratio), and another to maintain the leading edge position throughout changes in incidence angle. The final leading edge attachment assembly was therefore quite complex, this is shown in figure (16).

The lead-screws used for incidence angle adjustment had ½" BSW threads and were supported at their ends by bearing housings each containing 2, single row, radial, ball race bearings. A locking device was also fitted to each lead-screw so that the entire system could be securely clamped at each required incidence setting.

2.5 Overall Aerofoil Support Frame Structure

Although provision had to be made for adjusting and maintaining both aerofoil shape and incidence angle, the primary function of the support structure was to hold the aerofoil stably in the centre of the tunnel working section when under aerodynamic loading. To achieve this a space-frame of slender structural members was added to the previously described camber setting and incidence variation systems so that they extended down to the tunnel floor.

The inner two of the four supports were extended with space-frames consisting of 30 mm square steel tubing, this was used rather than aluminium alloy so as to provide the maximum possible rigidity with the least member width, this being important to minimize blockage effects. This space-frame design was computer optimised so that it could be assembled from a number of identical

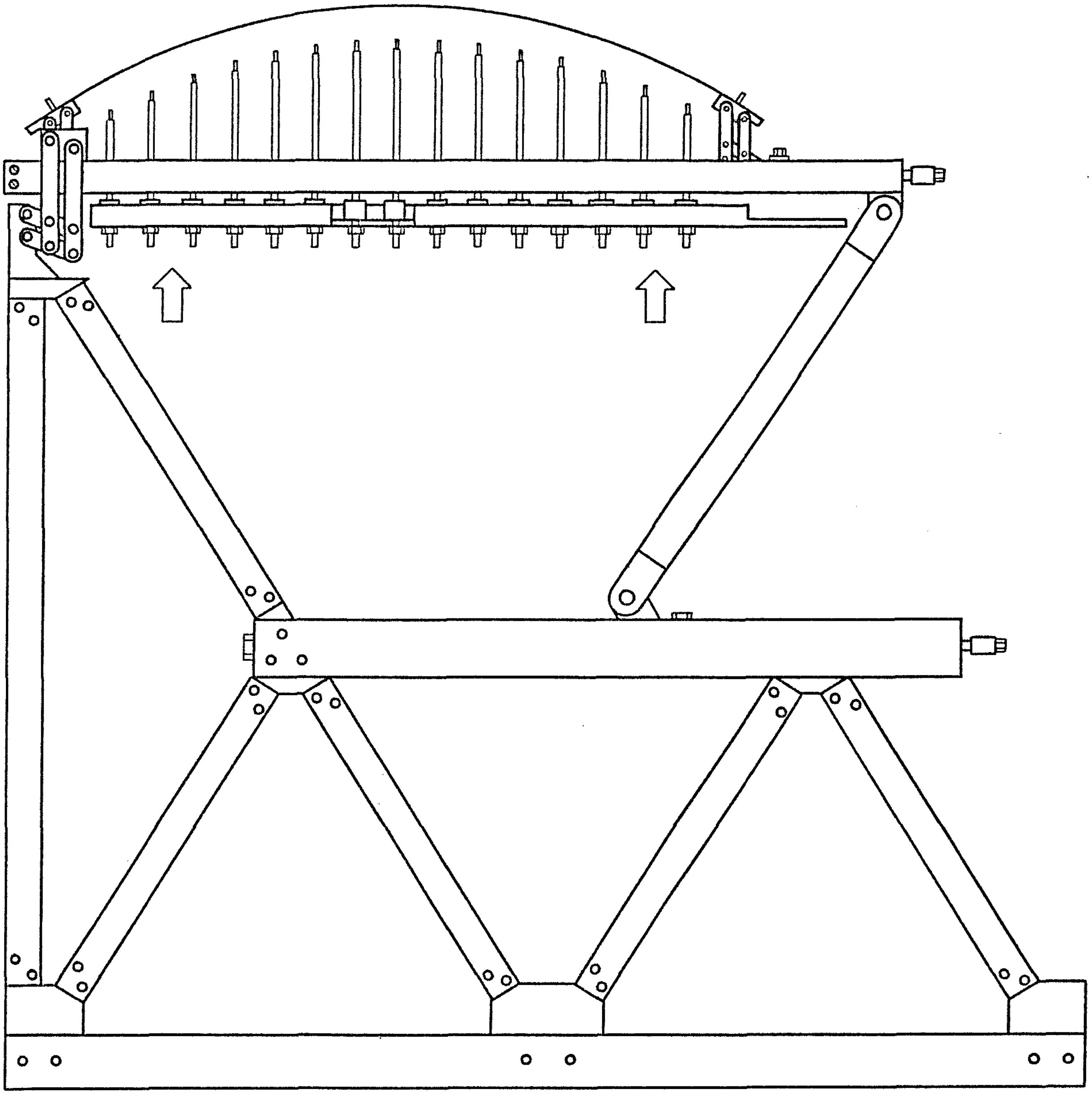

Fig(17) Full Length Support Frame

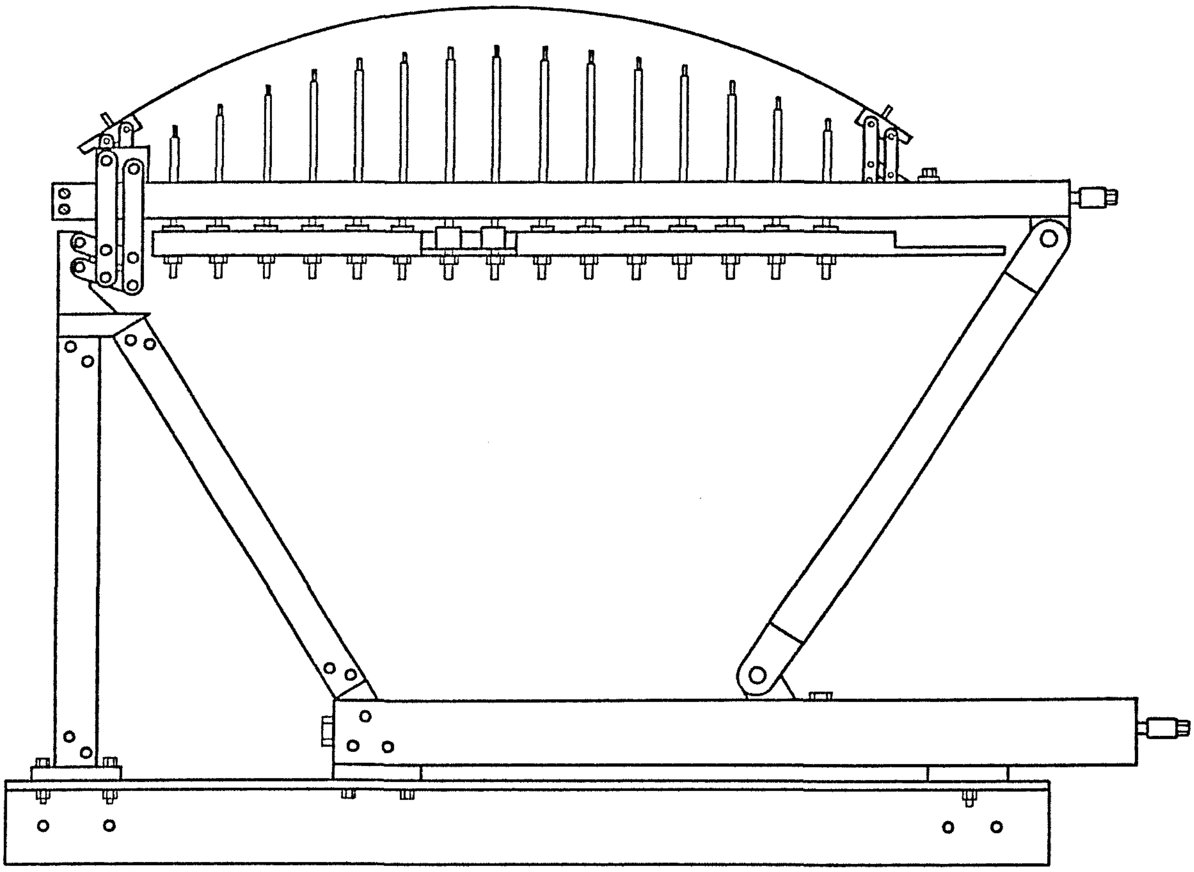

Fig(18) Shortened Support Frame

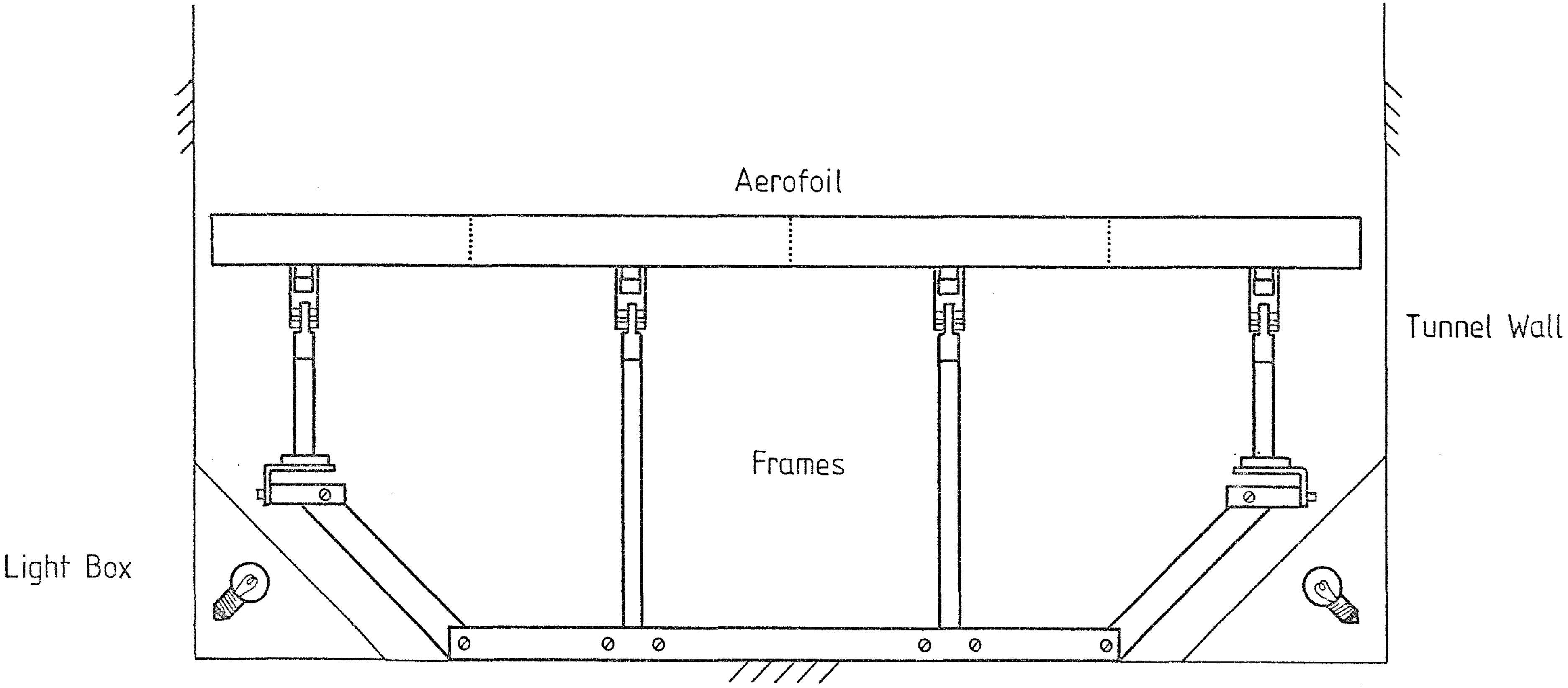

Fig (19) Aerofoil and Support Frame Assembly

PLATE 1 - TRAILING EDGE VIEW OF AEROFOIL

Note :

(i) Rubber Upper Surface Skin with Slight Irregularities due to Trapped Air During Assembly.

(ii) 'Mouse' Traversing Unit.

(iii) Run of 'Mouse' Control Cables through the Tunnel Roof.

(iv) Segmented 'Mouse' Tracks.

(v) Length and Positioning of Probe Arm.

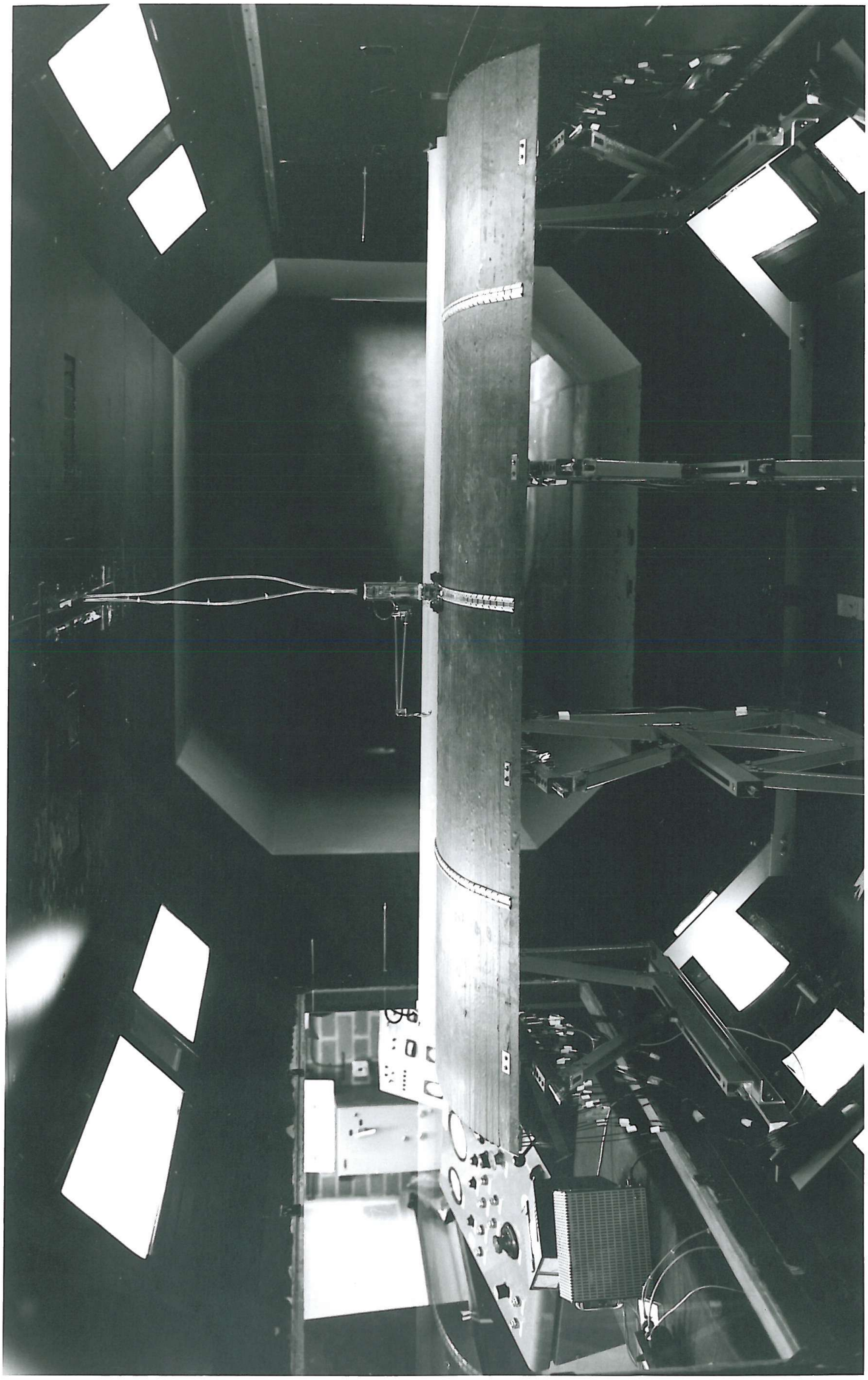

PLATE 2 - COMPLETE SYSTEM VIEWED THROUGH THE TUNNEL WINDOW

Note :

(i) 'mast' Wall Fixing.

(ii) Camber Cassettes.

(iii) Support Frames.

(iv) Stiffening Elements with Emerging Tapping Tubes.

(v) Instrumentation (including Control Box).

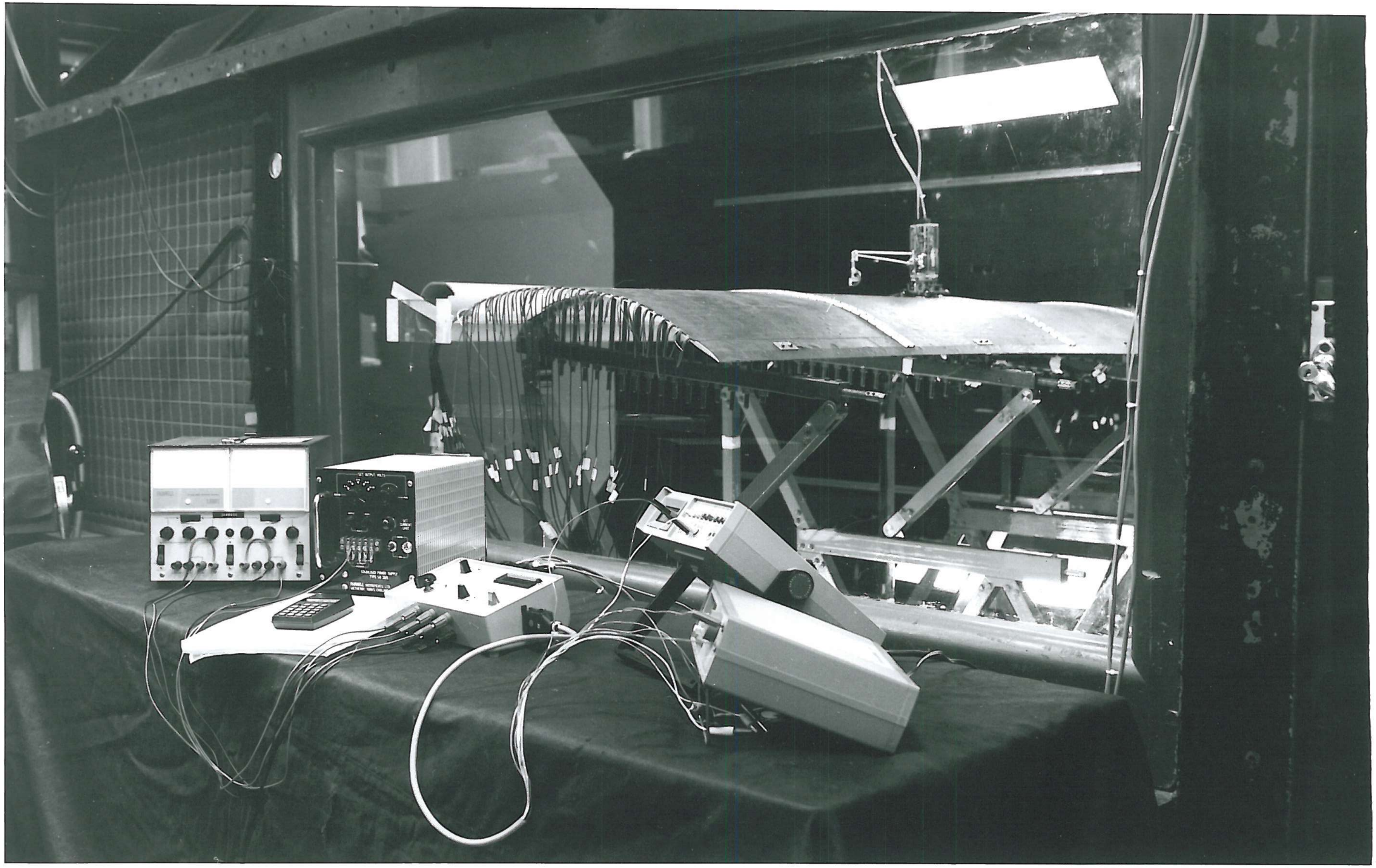

length component tubes, and finally the design was fully 'stressed' to confirm that it could cope with all likely loading cases. The complete design of these inner two support frames is shown in figure (17).

With the outer two support positions it was not possible to extend the space-frames to the tunnel floor directly because of the presence of sloping light housings. It was therefore decided to adopt a shortened version of the previous design for these supports. This is shown in figure (18).

All the 4 support structures were finally held securely in their respective spanwise locations by a frame-work that was designed to fit snugly across the tunnel floor and over the light housings. This made the entire aerofoil and support frame system into one integral assembly, allowing extremely quick installation into the tunnel with excellent positional repeatability.

The overall support frame structure is shown in figure (19) and in Plate (1) and (2).

2.6 Mast Design and Attachment Method

A large variety of mast cross-sectional shapes are currently available, but because of the lack of fundamental research in the area of mast/sail flow separations it was decided to concentrate on circular sections only.

Three different size masts were tested these having diameters of 110.5 mm, 68 mm and 28.5 mm. The larger two of these were commercially available in grey polypropylene material as gutter or drain-piping. The smallest mast was made of aluminium alloy since in plastic this diameter would not have had sufficient rigidity to remain horizontal over the 7' tunnel width when only supported at the walls.

Each mast was fitted with 10 equally spaced pressure tappings around the circumference at the mid-span position.

In order to set each mast to any required angle relative to the aerofoil chord line (ϕ as defined in figure (1)), it was necessary to devise a mast support system. Not only did this support system have to provide the necessary angular movement of the mast about a centre of rotation located at the extreme aerofoil leading edge, but it also had to be capable of securely holding masts of any size or cross-sectional shape. Finally the support system had to permit changes of mast to be made rapidly in order to ensure the most effective use of the limited tunnel time available.

As part of the support system finally adopted, each mast had a 3 mm wide x 25 mm deep slot cut across the diameter at each end. These slots allowed each mast to be easily slipped on or off of specially designed mast support ledges which were fitted to opposite walls of the tunnel working section. The details of these mast support ledge units are shown in figure (20). Air pressure alone kept each mast hard up against the aerofoil leading edge without any other locking mechanism being necessary.

With this support design any mast could be replaced with another in a matter of minutes simply by sliding the masts on or off of the support ledges.

The double pivoted screw adjusters shown in figure (20) allowed any required mast angle to be set easily in conjunction with an inclinometer that could be rested on the protruding forward portion of the ledges.

Note : The aerofoil and support structure were built by the Southampton University Engineering Faculty workshops

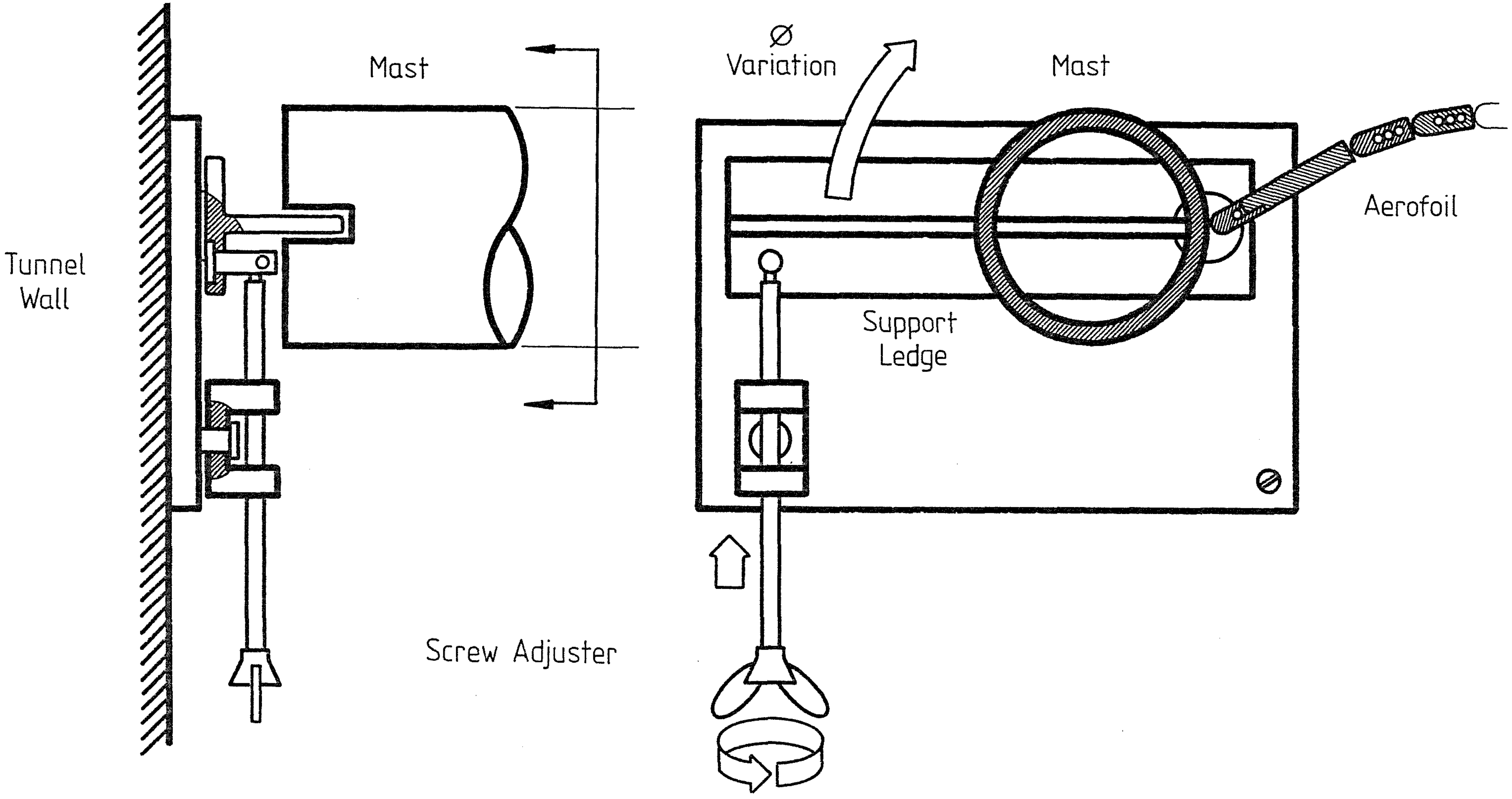

Fig(20) Mast Support Ledge Assembly

from a complete suite of design drawings prepared by the author of this thesis. These drawings are available for reference purposes in a separate volume which can be considered as forming Appendix V of this thesis.

CHAPTER 3

BOUNDARY LAYER TRAVERSE SYSTEM DESIGN

3.1 Introduction

In addition to static pressure distributions, it was felt that experimental data in the form of boundary layer velocity profiles would prove invaluable when attempting to understand the fundamental flow regimes present around typical mast/sail geometries.

Several velocity profiles obtained at various chordwise positions would help identify locations of transition, separation and reattachment, as well as provide surface displacement estimates, skin friction information and thickness parameter variations.

It was however by no means a simple task to obtain this type of boundary layer data, since to define each velocity profile with sufficient accuracy to yield meaningful values of the thickness parameters, it was necessary to obtain a very large number of individual velocity readings. Furthermore the majority of these velocity readings had to be obtained very close to the aerofoil surface where the changes in velocity with height were very rapid.

In the case of the highly cambered aerofoils tested, the region of rapid velocity change took place within approximately the first 3 mm above the local aerofoil surface. At least 10 data points were required to define such a region, which suggested a positional accuracy for any measuring probe used of better than ± 0.05 mm. The total boundary layer thicknesses observed over the highly cambered aerofoils were found to be relatively large at around 5% of the chord length (35 mm approx.). The velocity measuring probe used to collect this data had therefore to be placed above the aerofoil surface with high positional accuracy, but also be capable of operating over a relatively large height range.

Precision boundary layer data of this type is usually provided by some form of traversing mechanism, fitted above the tunnel working section, which is capable of manoeuvring a measuring probe on the end of a slender yet rigid arm to any required location. The linear motions involved are often achieved using motorized carriages (incorporating anti-backlash worm drives, position transducers and feed-back circuits) running on precision tracks. Some systems cater for probe rotations in addition to these linear motions, such systems are however much more complex and expensive.

Unfortunately no traverse system of any description was available for the Southampton University 7' x 5' wind tunnel, and it was clear that the design and installation of a precision system of the type previously described would have involved major work on the tunnel, and incurred equipment costs far beyond the limited resources available for the present work.

An overhead type of traverse system would, in any case, have run into difficulties when used with highly cambered aerofoil sections, unless capable of remotely pitching the probe through large angles.

To accurately measure velocity, the probe used had to be aligned as closely as possible to the local flow, this involved orientating the probe parallel to the local aerofoil surface when measuring within the attached boundary layers. In some cases the angle between the local aerofoil surface and the undisturbed free stream flow was as high as 50°, which would have been beyond the range of most pitchable traverse systems, and would certainly have ruled out the use of a cheaper non-pitchable traverse system in conjunction with the best available pitch insensitive probe.

Another major disadvantage with overhead traverse systems, is that they are only capable of providing boundary layer data over one surface of an aerofoil model unless it is possible to turn the model over in the tunnel.

3.2 Possible Alternative Measuring Systems

Having ruled out the installation of a traverse system above, or indeed anywhere around the outside of the tunnel working section, the only remaining alternative was to affix a measuring device to the aerofoil itself. This concept immediately solved the problem of probe alignment with the flow, since any system attached to the aerofoil surface would automatically stand normal to the local surface at the point where it was located.

One simple device that was considered for measuring boundary layer profiles in this way involved using a miniature comb of total pressure head tubes. A comb of this type would be made up from a large number of small diameter hypodermic tubes, positioned one above the other in a single plane, and held together with silver solder or epoxy. Each tube could then be bent through 90° to form a support stem, and to allow the pressure information to be routed down onto the aerofoil surface from where plastic tubing could run to measuring manometer banks.

To obtain a range of velocity profiles across the aerofoil chord, the comb would be moved to different locations, perhaps even to pre-installed sockets on the aerofoil surface. Alternatively a whole set of such combs could be constructed and fitted across the aerofoil chord, possibly along a diagonal line to avoid mutual downstream interference.

This type of system, despite its obvious merits such as simple robust construction, ease of operation and low flow interference, does however have a number of serious disadvantages. The major problem was that with combs the minimum separation between adjacent measuring points will be equal to the diameter of the tubes used in construction. For a comb to have supplied the necessary 10 data points within a 3 mm distance above the aerofoil surface would therefore have required tubes for its construction of only 0.3 mm O/D. Such tube, even if available, would not have been sufficiently robust, would have suffered from very low pressure response speeds, and would have been dogged by blockages due to airborne dust particles etc.

A further problem with the comb system of velocity profile measurement was that the individual tubes would detect only total pressure, which meant that traverses would only have been possible at locations adjacent to surface static pressure tappings, since both types of pressure are necessary to determine flow velocity.

The method chosen for overcoming these problems was to use just a single measuring probe rather than a comb, but one which was capable of recording both static and total pressure, and fitted with a means of being traversed normal to the local aerofoil surface with the required positional accuracy.

Such a concept is not new, Pankhurst and Bryer (6) describe a device of this type which was developed by the Douglas Aircraft Company (7) in 1955 to obtain boundary layer data over slender bodies. This system which was referred to as a boundary layer 'mouse' is shown in Figure (21).

For the present work it was decided to adopt this 'mouse' concept but to develop it to a much more advanced state, capable of very accurate yet more flexible operation, by incorporating many extra modes of movement plus electronic control systems. Special attention was also paid to both the selection of modern materials and component miniaturization.

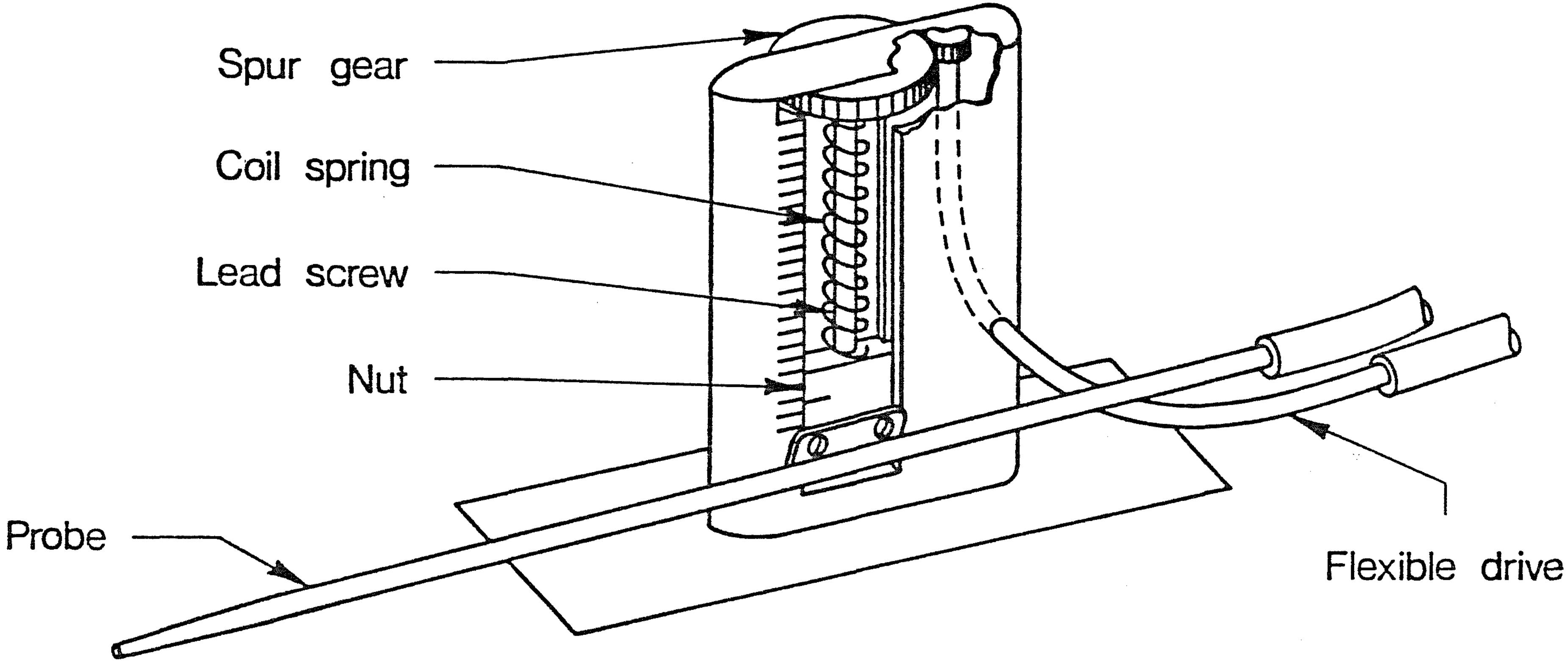

Fig(21) Original 1955 'Mouse' Design as given in Ref.6

3.3 Basic 'Mouse' Design Requirements

Before the 'mouse' could be designed it was necessary to establish all the functions that it would be required to perform.

Most importantly the 'mouse' had to be able to remotely move a measuring probe along a line normal to the local aerofoil surface, over a linear range of at least 35 mm. Obviously related to this motion was the additional requirement for the final 'mouse' design to incorporate a system for both monitoring and instantaneously displaying the measuring probe height above the local aerofoil surface to a positional accuracy of better than ± 0.05 mm.

In order to avoid the need to switch off the wind tunnel and enter the working section each time that a boundary layer traverse was required at a different chordwise location, it was decided to also provide a remotely-controlled chordwise motion system for the 'mouse'. In connection with this was the need to devise systems both for securely attaching the 'mouse' to the aerofoil, and for steering it along the required chordwise path. This attachment system, like all the functions of the 'mouse', had to be made to operate over the aerofoil lower surface as well as on top.

Since measurements were to be made through and near partially separated flow regimes, a system had to be included in the 'mouse' design for remotely turning the probe through 180° so that reversed flow velocities could be accurately measured.

It was also essential to install all the 'mouse' systems inside an aerodynamically shaped casing so as to reduce flow interference effects, but despite this casing it was expected that some small flow disturbance would still result from the presence of the 'mouse' body. The 'mouse' design therefore involved the use of an arm, attached at one end to the vertical motion system and with the measuring probe fitted to the other end. This arm had to be long enough to keep the probe as far away from the 'mouse' body as possible, whilst being sufficiently rigid to maintain probe positional accuracy.

The final system required for inclusion in the 'mouse' was a housing containing pressure transducers with which to convert those pressures observed by the probe into electrical signals. Placing these transducers in the 'mouse', rather than outside the wind tunnel, was intended to reduce the lengths of pressure tubing required, and therefore increase response speeds.

3.4 'Mouse' Individual System Descriptions

3.4.1 General Structure

For the basic 'mouse' structure it was decided to adopt a chassis or skeletal design, onto which could be fitted all the necessary systems. This type of layout was intended to enable essential maintenance or component replacements to be carried out without the need to dismantle the entire 'mouse' assembly. This advantage would have been lost if the alternative approach had been used where individual components also act as structural members, here of course the advantage would have been in weight saving.

The material chosen for this chassis structure was brass. This material was non-magnetic and therefore would not have acted as a path for any magnetic fields created by solenoids or motors. Fields of this kind if carried near to the electronic circuits may well have caused interference problems. Brass also had better corrosion resistance properties than steel, and being a good electrical conductor it was possible to use the 'mouse' chassis as a -ve earth connection. Heat conduction and dissipation properties were also good with brass which reduced temperature drift problems with the electronics and helped prevent solenoid overheating.

Finally brass was chosen for the basic 'mouse' structure because of its good machinability, this made it an excellent material from which to produce the required miniature components, especially those that involved very small screw threads.

In addition to brass, the chassis also incorporated a substantial amount of perspex. This material was used for some of the larger lightly loaded components in order to save weight. Perspex was chosen in preference to other plastic materials because of its excellent machinability and resistance to both UV light and the lubricating oils used on the 'mouses' moving parts. The transparent nature of perspex made it useful from the maintenance point of view, since worn or damaged components could be seen without dismantling the 'mouse'.

3.4.2 Casing Design

In order to minimize any flow disturbances due to the presence of the 'mouse' in the wind tunnel, it was necessary to make the 'mouse' as small as possible, and to enclose all the systems inside a suitable aerodynamically shaped casing.

This casing shape had to be symmetrical since in regions of reversed flow the air-stream approached the 'mouse' from the downstream direction. To simplify the design calculations it was decided to adopt a 'Rankine Oval' casing shape since the potential flow was easily described in 2-dimensions by a source and sink in a uniform stream. A 3-dimensional design calculation was not necessary since the measuring probe was operated well below the top of the 'mouse' where tip effects were insignificant.

The casing design calculations performed were necessary to determine the optimum combination of oval slenderness ratio (major diameter/

minor diameter), and distance away from the casing required for the probe.

Figure (22) shows a chart based on the equations developed in Appendix I from the theory due to Glauert (8) for flow around Rankine Ovals. This chart shows how the ratio of observed velocity in the flow field to the undisturbed velocity, changes with slenderness ratio and distance away from the oval along the line of the minor diameter. In the final design the probe nose was positioned on this minor diameter line so that, when rotated for reversed flow measurement, the probe would maintain its chordwise location. This was not possible with the forward projecting probe design used on the original 1955 'mouse' shown in figure (21).

The rather surprising conclusion arrived at from figure (22) was that for velocity measurements made in the flow field at distances greater than $z/b = 4$, it was better to use an oval of low slenderness (i.e. approaching a circle). In the light of this it was decided to use a 2:1 (70 mm x 35 mm) Rankine Oval casing shape ($a/b = 2$) for the 'mouse', this exploited the low slenderness advantage, yet for a given minor diameter it provided more internal space than a circular casing for the installation of the various 'mouse' systems.

Figure (22) shows that for a 2:1 Rankine Oval casing shape, an error in velocity measurement of only 2% could be expected due to the 'mouse' body, provided that the probe was placed 5 minor diameters ($z/b = 10$) away.

As a simple design method no account was taken of any flow separations from the rear of the oval casings. It was however felt that further mathematical modelling would probably not have provided sufficient additional design information to justify the extra work required.

Flow Field Velocity Ratios at Points Approaching
Various Size Rankine Oval Casing Shapes

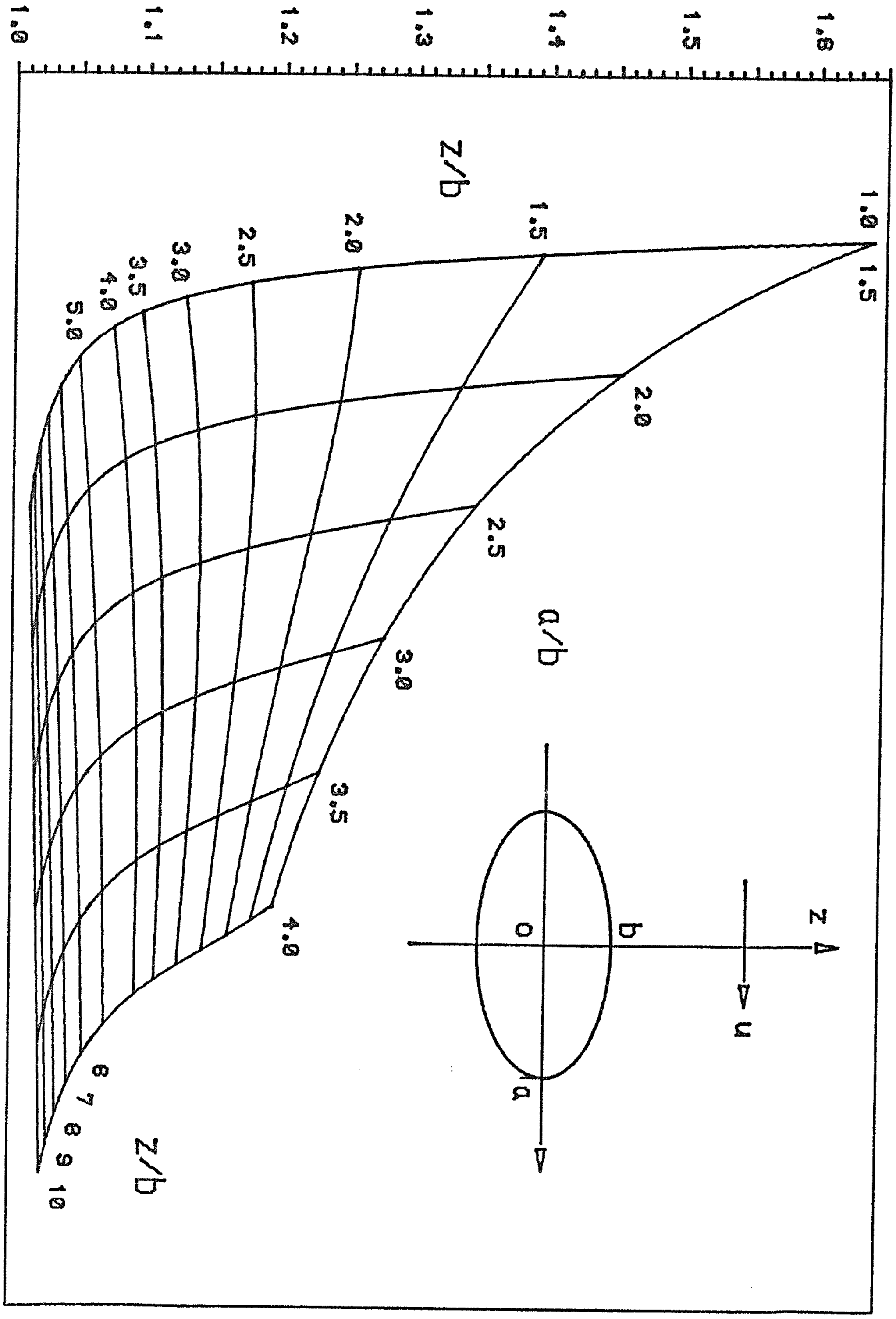

Fig(22) "Mouse" Casing Design Chart

The casing material chosen was transparent plastic card. This was thick enough to protect the 'mouse' systems from minor impacts, and its transparent nature allowed potential faults to be continually monitored without the need to remove any of the casing.

3.4.3 Mouse to Aerofoil Attachment Method

It was necessary to ensure that the 'mouse' was always securely attached to the aerofoil in order to prevent it being swept down the wind tunnel by the force of the oncoming air stream. The attachment method chosen also had to allow for the required chordwise motion of the 'mouse'.

The system finally adopted was of a two part design, this consisted of tracks laid across the aerofoil surfaces, working in conjunction with a track follower device fitted to the underside of the 'mouse' body.

Each of these tracks was made up from a row of short elements cut from a length of extruded aluminium alloy having a dovetail cross-section. One of these track elements was bonded with epoxy adhesive to the aerofoil surfaces directly above (or below for lower surface tracks) each stiffening element.

A clearance was allowed between adjacent track elements to accommodate their relative movement when the aerofoil camber was varied. Three tracks of this type were laid across the upper and lower aerofoil surfaces, their positions and construction are shown in Figure (23).

The track follower had to provide low friction running along these tracks, whilst also being able to cope with the camber related variable clearances between the track elements.

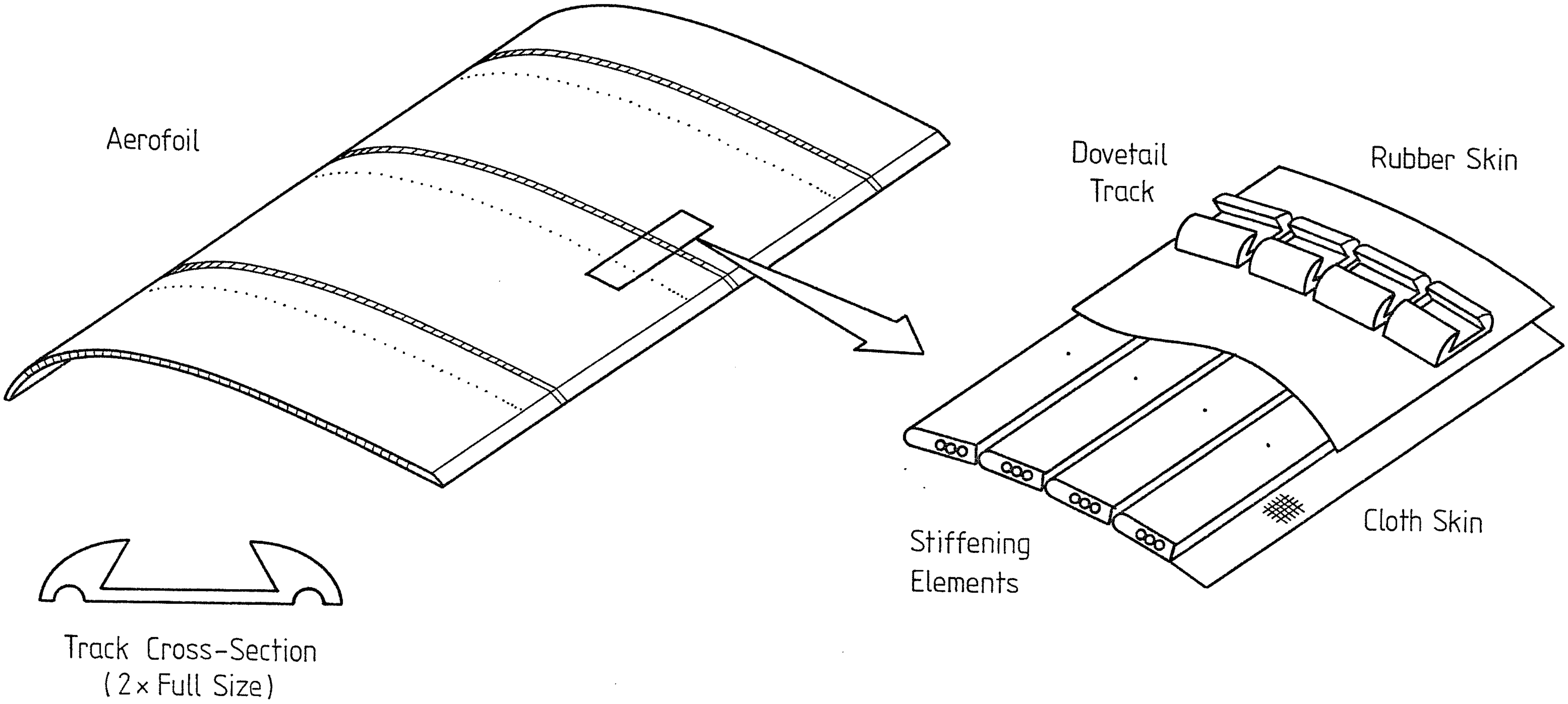

Fig(23) 'Mouse' Track Design and Layout

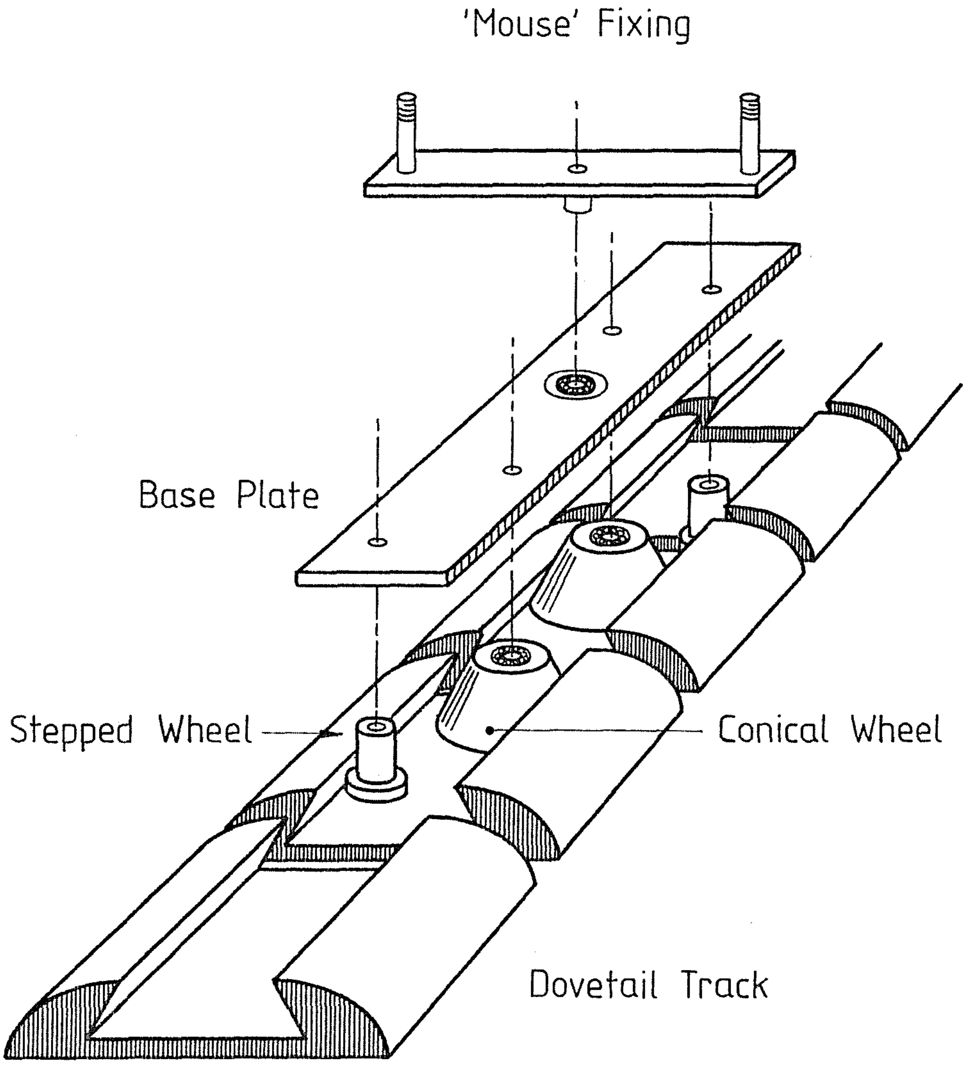

Fig(24) Track Follower Design

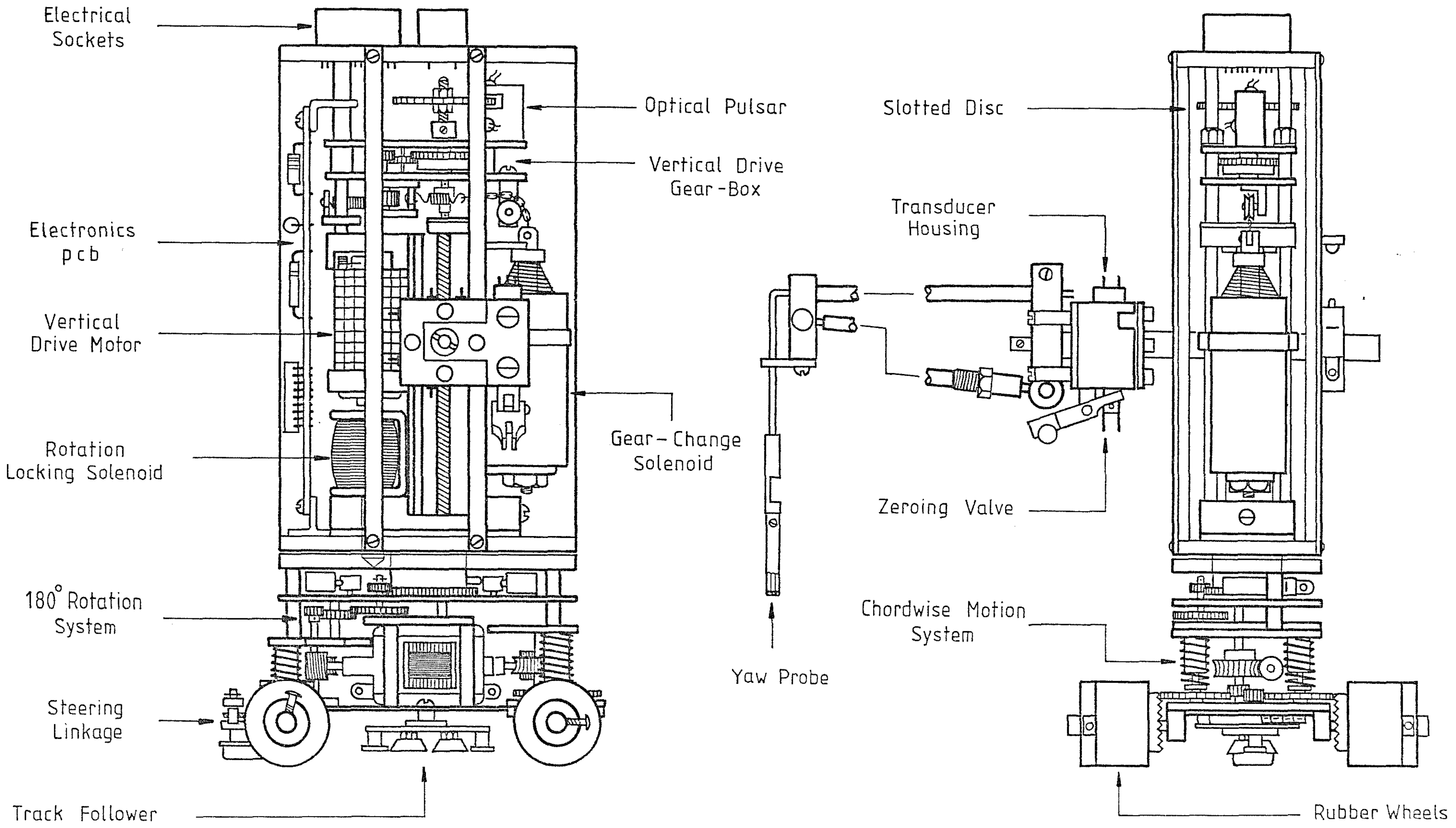

Fig(25) 'Mouse' Systems Layout

The track follower design is shown in figure (24), this consisted of a base-plate onto which was fitted two conical wheels and two stepped wheels, the latter being positioned close to the leading and trailing edges of the base-plate. The function of the stepped wheels was to jump the clearance gaps between adjacent track elements, and also to keep the base-plate aligned with the track whether moving forwards or backwards. The steps on these wheels prevented them from lifting vertically out of the dovetail track. The stepped wheels were designed to deal with alignment side forces only, and not with the high aerodynamic forces on the 'mouse' attempting to pull it away from the surface.

The high aerodynamic forces on the 'mouse' were passed through to the track, and eventually into the support frames, by the two conical wheels on the base-plate. These conical wheels were designed to run along the inside faces of the dovetail slot in the track elements. Low friction running was achieved, even under heavy loading, by the use of miniature ¼" O/D ball-race bearings set inside each conical wheel.

Finally the follower base-plate was attached to the underside of the 'mouse' through a central pivot containing a further ball-race bearing. This arrangement allowed small rotations of the follower relative to the 'mouse' itself, and therefore catered for any slight misalignments between adjacent track elements.

Figure (25) shows the location of the track follower together with all the other systems involved in the final 'mouse' design. The upper surface tracks are also clearly visible in Plate (1).

3.4.4 Chordwise Motion System

To propel the 'mouse' across the aerofoil surfaces it was decided to employ a small electric motor, driving through a reduction gear chain to a set of rubber drive-wheels resting against the upper or lower skin materials.

Including the whole of this propulsion system within the 'mouse' made it completely self-contained, and therefore independent of any periphery equipment apart from a power supply. This would not have been the case with an alternative Bourdon cable/external motor type of drive system, which would also have been subject to cable internal twist and hence problems of poor response speed and positional accuracy.

The electric motor used, like all those installed in the 'mouse', was of a 12v d.c. permanent magnet type manufactured by Scalectrix and fitted with replaceable brushes. These motors and any spare parts were readily available locally, making repairs in the event of a breakdown simple and quick. More powerful motors of similar size were available using advanced selenium/cobalt magnets, however these were about 10 times more expensive and could not be bought locally.

To produce maximum torque it was necessary to operate the chordwise drive motor at between 6000 and 7000 rpm. The gear-chain was therefore necessary to produce low rotational speed at the rubber drive-wheels whilst retaining the maximum motor torque. High output torque was essential since it was necessary for the motor to drive the 'mouse' up the sloping surfaces of highly cambered aerofoils at moderate incidence. In addition this motion had to possible against the air flow in the wind tunnel working section. The low rotational speed at the drive-wheels also helped in accurate positioning of the 'mouse' along the aerofoil surface.

The transmission gear-chain used included a high reduction worm and wheel combination, together with a number of nylon plane gears. The final drive was carried through crown gears fitted to the two rear rubber wheels. The total reduction achieved was 1:180, giving an output speed at the drive wheels of approx. 30 rpm (or

½ rev. per second) for a motor speed of 6000 rpm. Further speed reductions were possible simply by decreasing the supply voltage slightly. The inclusion of a worm and wheel in the gear-chain acted as a brake, since these are non-reversible.

In order to ensure the best possible grip between the rubber drive-wheels and the aerofoil surfaces, the 'mouse' was fitted with a special compression spring on each wheel. These springs forced the wheels down onto the aerofoil, whether operating on the upper or lower surface, by reacting the forces through the track follower and down into the aerofoil via the track. This arrangement meant that there had to be relative movement between the drive wheels and the motor, this was accommodated in the transmission system by permitting axial movement between two of the plane gears.

Figure (26a) shows the chordwise motion system in detail, and figure (25) again shows its position relative to the rest of the 'mouse'.

The two undriven wheels at the front of the 'mouse' were given a simple steering capability, this enabled the 'mouse' to easily cope with any slight curves or misalignments in the tracks. The steering movement was controlled by a low friction PTFE guide arm running along the track, this turned both front wheels via a simple parallelogram linkage arrangement. Figure (26b) shows this steering mechanism together with the previously described compression spring system.

To minimize losses due to friction in the transmission system, a total of 14 miniature ball race bearings were used, this included 2 in each of the 4 alloy wheel hubs. In one location a special ball race bearing was used which measured only 4 mm OD x 1 mm Bore.

All the drive wheels were fitted onto independent stub axles, since space had to be left underneath the 'mouse' for clearance over the tracks.

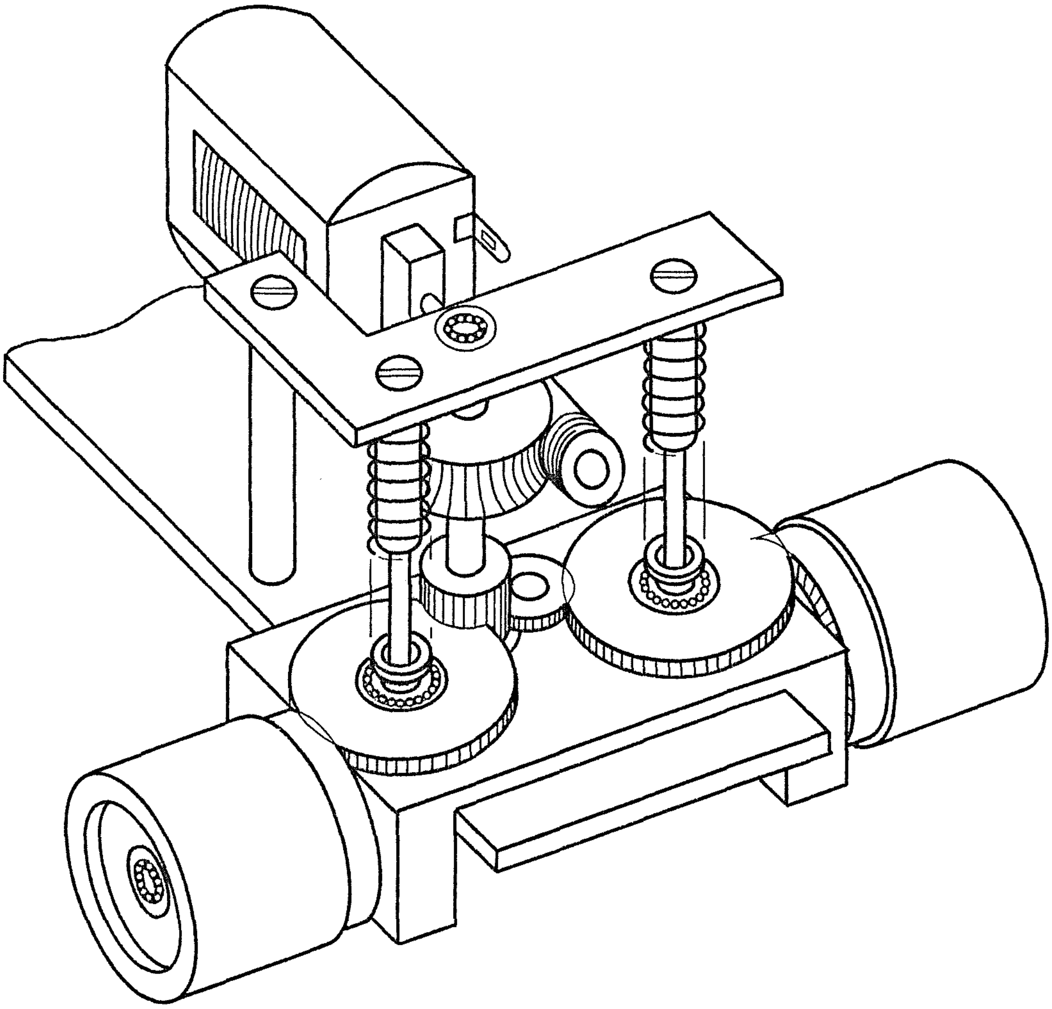

Fig(26a) 'Mouse' Chordwise Motion System

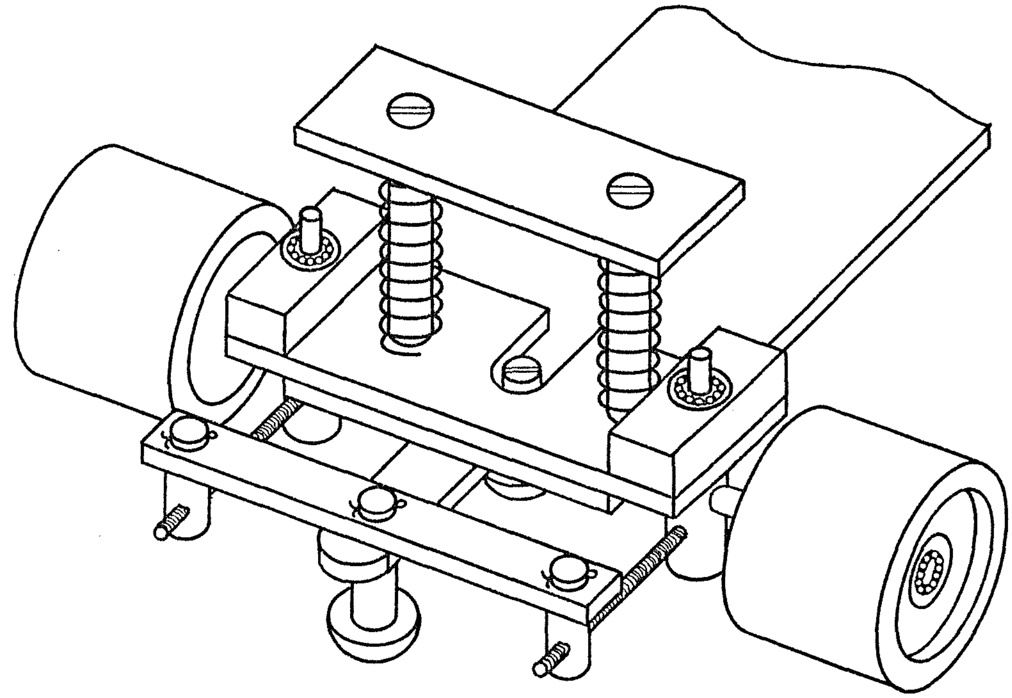

Fig(26b) 'Mouse' Steering Mechanism

3.4.5 Vertical Traverse Motion System

This was arguably the most important system in the entire 'mouse'. As well as being able to move a measuring probe to any required location above the aerofoil surface with a positional accuracy of better than ± 0.05 mm, it also had to cope with being the most used of all the 'mouse' systems.

It was vital that this system function perfectly over extended periods, with reliability and repeatability, despite frequent direction changes and the need to stop and restart at each measuring position. The system had to achieve this reliability despite the buffeting caused by the turbulent flow behind the masts, and also be capable of working satisfactorily upside down on the aerofoil lower surface.

In principle the design adopted was similar to that used in the 1955 system, in that the drive was supplied via a reduction gear-box to a leadscrew. This leadscrew rotation then produced linear motion of a threaded carriage running in a precision guide.

In the present design the main drive was again supplied by a 12v dc motor inside the 'mouse' casing. The Bourdon cable/external motor system employed in the 1955 system was not used because of cable twist, high power absorption in the cable, and the need for frequent cable lubrication and maintenance.

The gear-box required had to transmit power from the motor to the leadscrew, whilst also producing a significant speed reduction. 9 gears were used in the gear-box, arranged in a planetary form between two brass plates. Like all the 'mouse' systems, this gear-box had to be extremely small (20 mm x 40 mm x 8 mm) to reduce the overall 'mouse' dimensions and therefore minimize flow interference effects. the gears used were obtained from several sources including an old clock and a food mixer.

The final speed reduction achieved with the gear-box was 1000:1. The resulting low output speed at the leadscrew, although excellent for accurate probe positioning, did however mean waiting a long time after the completion of a vertical traverse for the probe to be returned to its start position at the aerofoil surface. It was therefore decided to include a remote gear-change capability into the vertical motion transmission system.

This gear-change capability was achieved by allowing one of the drive pinions to be swung between two different spur gears. One of these gears was at the beginning of the gear-chain, whilst the other was much nearer to the output end of the gear-chain. Swinging the drive pinion between these two gears resulted in a number of the reduction gears being excluded from the chain and the output speed was thereby increased.

This 'crash' gear-box design required no clutch since special springs were fitted to absorb the impact loads and promote rapid meshing without damage. The reduction obtained when in the high speed mode was 13:1.

The remote gear-change activation within the 'mouse' was provided by a miniature 12v (5W) solenoid. This activation system was deliberately designed so that the high output speed was selected with the solenoid energised, springs then returned the gear-box to its low speed mode when the solenoid was switched off. This ensured that most time was spent during operation with the solenoid switched off, the use of a high-power/small size/intermittent operation solenoid was therefore possible, and overheating problems were minimized. The high current passing through the solenoid was handled with specially requested polyester winding insulation and PTFE covered power leads.

The final drive between the gear-box and leadscrew included a sub-miniature universal joint of only 4 mm diameter x 10 mm length,

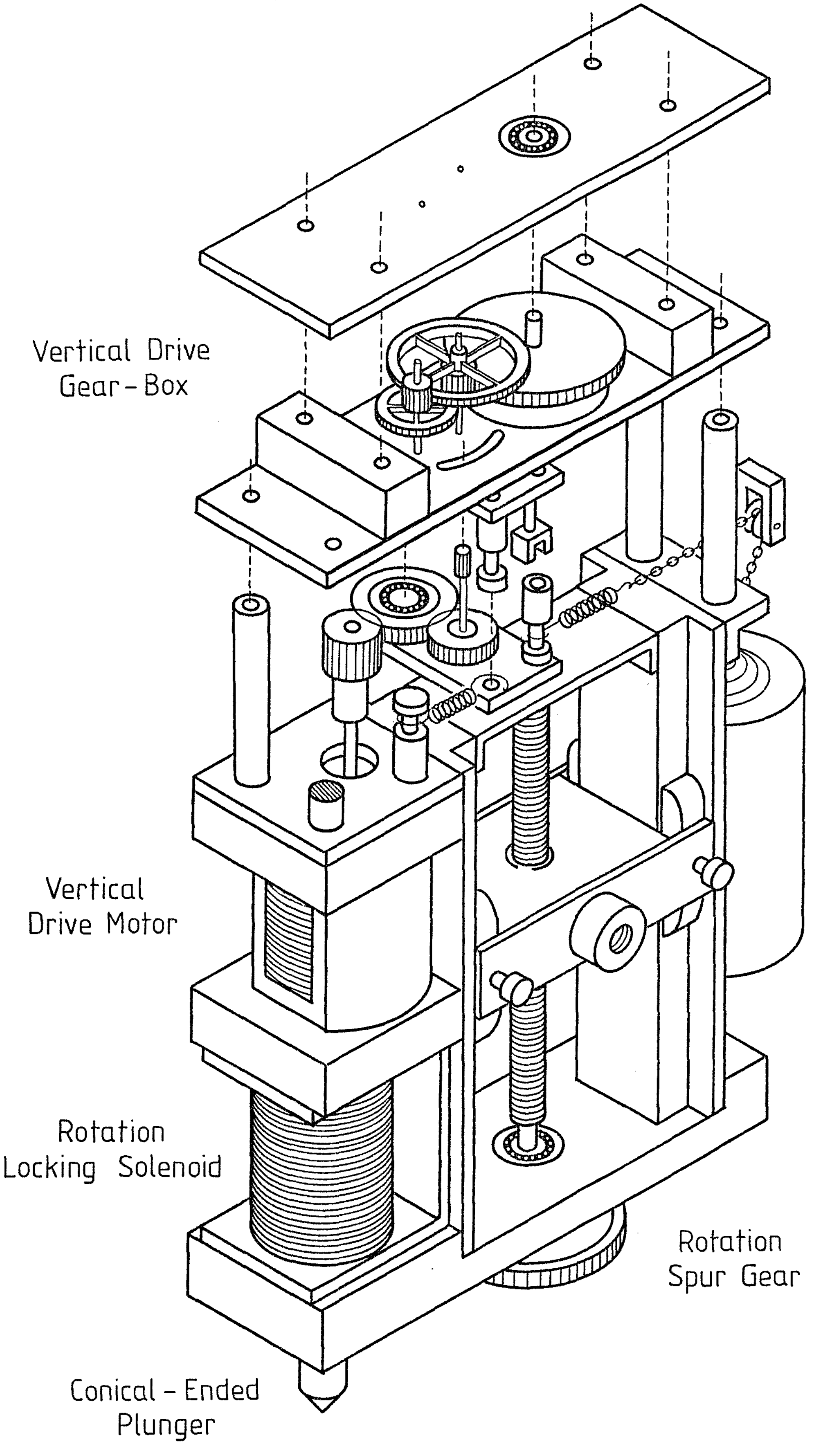

Fig(27) Vertical Traverse Motion System

this was intended to deal with any slight misalignments in the transmission layout. The leadscrew was constructed from a 65 mm length of 4 BA brass studding, and was mounted between 2 miniature ball race bearings.

The carriage was made from lightweight aluminium alloy and was driven by the leadscrew between 2 precision guide rails. Backlash was eliminated, and sliding contact maintained with the guides, by using adjustable low friction PTFE runners.

Finally a small micro-switch was installed to automatically switch off the drive motor when the carriage reached the end of the leadscrew.

Figure (27) shows the vertical traverse motion system, and figure (25) again shows its location within the 'mouse'.

3.4.6 Arm Design for Measuring Probe Support

As mentioned previously, it was necessary for the measuring probe to be held at a suitable distance away from the 'mouse' body, in order to avoid errors in velocity readings due to interference from the 'mouse' casing. The measuring probe was therefore fitted to the end of an arm, which was in turn attached to the carriage of the vertical traverse motion system.

The arm was made 220 mm long (approx. 12 x casing minor radius) and assembled from light-weight aluminium alloy tube. The design was carefully chosen so as to maximize the bending stiffness in the vertical plane, this ensured probe positional accuracy above the aerofoil surface despite the relatively large unsupported length involved.

The arm structural members, being hollow, were able to carry the pressure tubes from the probe to the 'mouse' body internally, this minimized aerodynamic drag forces on the arm and protected the fine tubes from accidental damage.

A universal type of fitting was placed at the end of the arm so that a variety of different probes could be used. This fitting was however designed to be more than just a means of securely holding a measuring probe, it also included two very sensitive electrical switches. One of these switches was designed to disconnect the vertical drive motor when the probe touched the aerofoil surface, whilst the other had to both zero the height monitoring system (discussed in Section 3.4.7) and indicate the precise moment of the probe leaving the surface at the beginning of a vertical traverse.

The arm attached to the 'mouse' can be seen in Plate (1), and the details of the probe fixing and electrical switches can be seen in Plate (3).

The sequence of switching that took place, just prior to a vertical traverse is shown in Figure (28). When a vertical traverse was required the probe and arm were firstly lifted clear of the aerofoil surface, and then the 'mouse' was driven to the necessary chordwise location. The probe was then driven at low speed down towards the aerofoil surface, Figure (28a). On reaching the surface the probe was forced to rotate about a pivot as the arm continued to decend. As a consequence of this rotation the contact switch 'A' was disconnected, this acted as an instruction to a height monitoring system (Section 3.4.7) telling it to reset to zero, Figure (28b). Continued arm descent resulted in further rotation until finally switch 'B' was opened, this disconnected the drive motor from the power supply and prevented further arm motion, Figure (28c).

To commence the vertical traverse, the power supply polarity to the motor was reversed, switch 'B' in this case was overridden by a diode which allowed the arm to ascend. Despite this upward motion

PLATE 3 - PROBE FIXING AND ELECTRICAL SWITCHES

Note : (i) Yaw Probe Design.

(ii) Run of Pressure Tubes.

(iii) Electrical Switches.

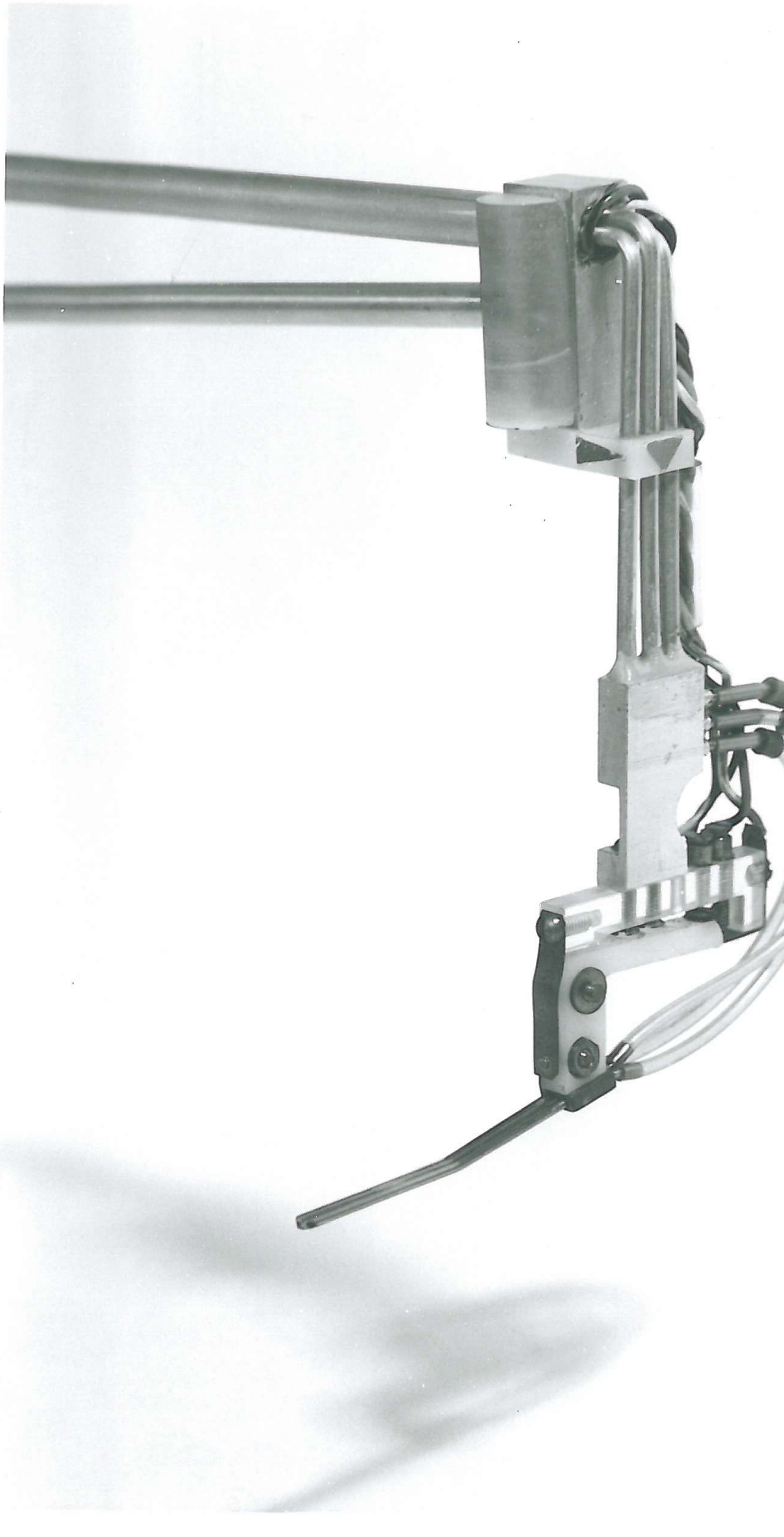

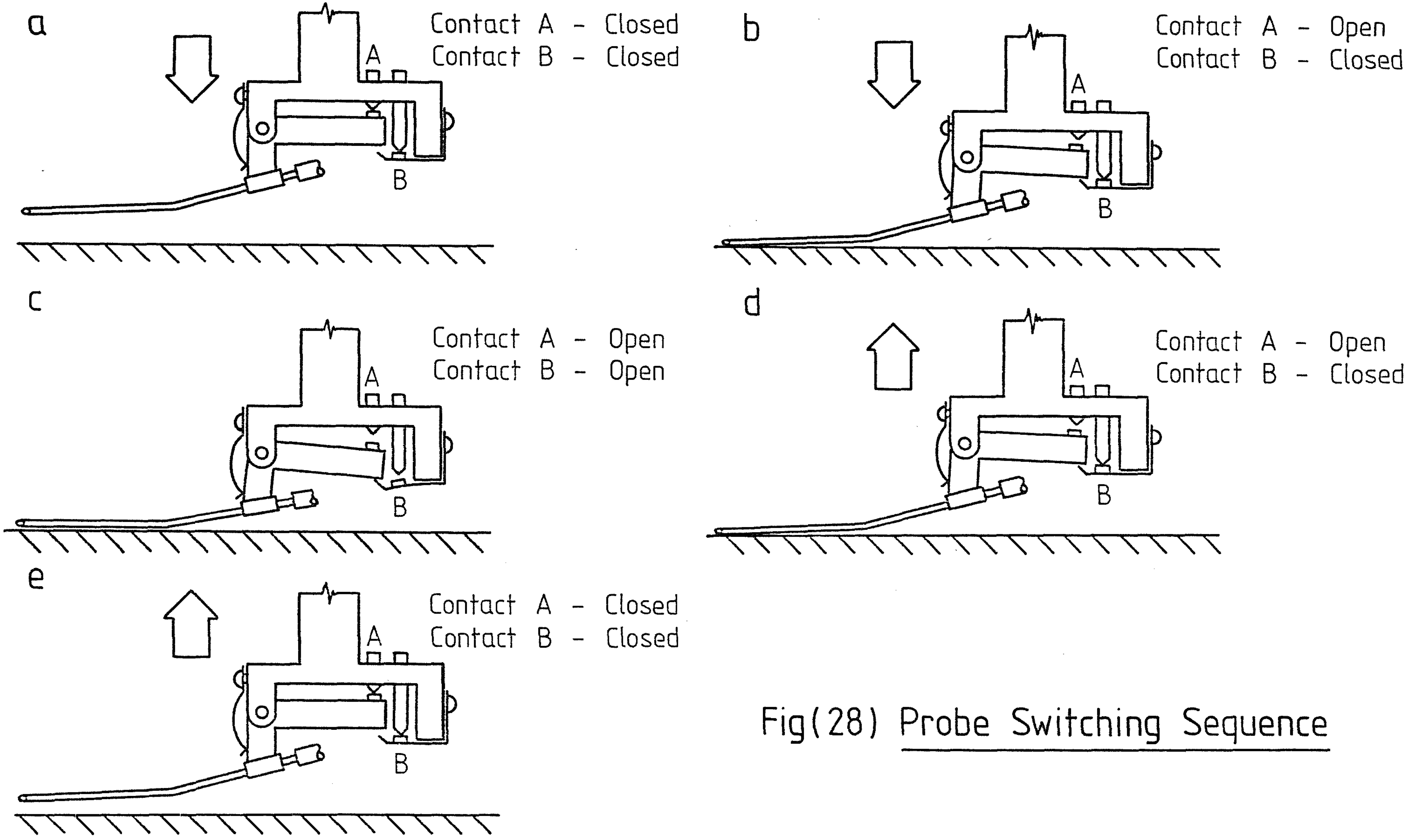

Fig(28) Probe Switching Sequence

of the arm, the probe nose remained in contact with the aerofoil surface by rotating back under the action of a small return spring. After a certain amount of return rotation, the switch 'B' became restored to its closed position, this of course had no effect when in this ascending mode, (Figure 28d). Following further arm ascent, with the probe nose still remaining in contact with the aerofoil surface, the switch 'A' finally became closed. The physical act of this switch contact prevented any further rotation, and immediately allowed the probe nose to lift away from the surface, Figure (28e). With the closing of switch 'A' an instruction was instantaneously sent to the height monitoring system to commence operation from its zeroed state.

This probe fixing design, with its built-in switches, therefore automatically enabled accurate zero probe height conditions to be established at the beginning of any required traverse.

3.4.7 Probe Height Measuring System (Optical Pulser)

To accurately measure the height of the measuring probe above the aerofoil surface, use was made of the known pitch of the leadscrew. The leadscrew used had a 4 BA thread which gave a vertical carriage movement of 0.66 mm per revolution. To obtain the required accurate height information it was therefore necessary to monitor the angular displacement of the leadscrew. this was achieved by placing a 20 mm diameter slotted circular disc on top of the leadscrew above the gear-box. The slots, numbering 30 in all, were cut 3 mm deep radially into the disc circumference. When rotating with the leadscrew, the disc edge was made to pass between a matched infra-red light source and phototransistor, placed in an ambient light excluding housing.

An electrical pulse was produced by the phototransistor each time that infra-red light was able to reach it from the light source.

30 of these pulses were therefore produced during every full revolution of the leadscrew, since the leadscrew pitch was 0.66 mm each electrical pulse represented 0.022 mm of probe vertical movement.

The electrical pulses produced by the phototransistor were fed into a 'Schmitt trigger' circuit which converted the raw pulses into a clear 5v square wave form. These were then suitable to be transmitted away from the 'mouse' via screened cable to an electronic control box where they were counted and displayed (all the electronic circuits involved are described in section 3.5).

An integrated circuit was available containing six inverting Schmitt triggers in a package size of only 19 mm x 6 mm. In addition to the use previously described, a Schmitt trigger circuit was also employed in producing a 5v square pulse to reset the counter when the arm switch 'A' was opened.

The Schmitt trigger package, plus additional resistors and electrical noise absorptive capacitors, were soldered into a specially etched printed circuit board (pcb) to save space in the 'mouse' and avoid loose wiring.

To avoid the production of erroneous pulses within the circuits due to the alternating magnetic field around the nearby vertical traverse motor, special screening was provided. This involved encasing the motor with an alloy of high magnetic permeability. For cooling purposes a mesh form of this material was used so as to permit normal air circulation around the motor.

3.4.8 180° Probe Rotation System

Since the 'mouse' was to be used in the presence of partially separated flows, it was thought likely that measurements within reversed flow regions would be required. Because the measuring probe had always to be aligned with the local flow, a 180° rotation of the probe was necessary when within these reversed flow regions.

The lower part of the 'mouse' had to remain in secure contact with the aerofoil surface and track, so the 'mouse' was designed so that just its upper section was free to rotate. this rotatable 'mouse' upper section contained the vertical traverse motion system, including the leadscrew, carriage and arm. The probe nose was initially positioned on the casing minor center-line, so by rotating the 'mouse' upper section relative to its base, the probe could be reversed in direction whilst maintaining its chordwise location.

The remote drive for the rotation system was again a 12v dc permanent magnet motor, this was placed in the lower section of the 'mouse' adjacent to the chordwise drive motor. As with the other systems, the transmission was via a reduction gear-chain, in this case containing a 60:1 worm and wheel together with 5 nylon plane gears. The last gear in the transmission chain was fixed to the 'mouse' upper body which was in turn attached to the lower section via a low friction pivot. Incorporated within the system were two sub-miniature micro-switches, these switched off the drive motor once the required 180° rotation had been completed.

Fitted into the 'mouse' upper section was an additional very small solenoid with a sprung, conical-ended plunger. Normally this solenoid was de-energised with the plunger resting in a conical seating hole in the 'mouse' lower section. On activation of the rotation drive motor, the solenoid was automatically energised and the conical-ended plunger withdrawn from the seating. Once the required rotation had been achieved, one of the micro-switches was operated which, as well as stopping the drive motor, also disconnected the solenoid. With the solenoid de-energised the plunger was forced down, by the return spring, into the conical seating again. The effect of the plunger entering the conical seating after each 180° rotation, was to pull the 'mouse' upper section accurately in

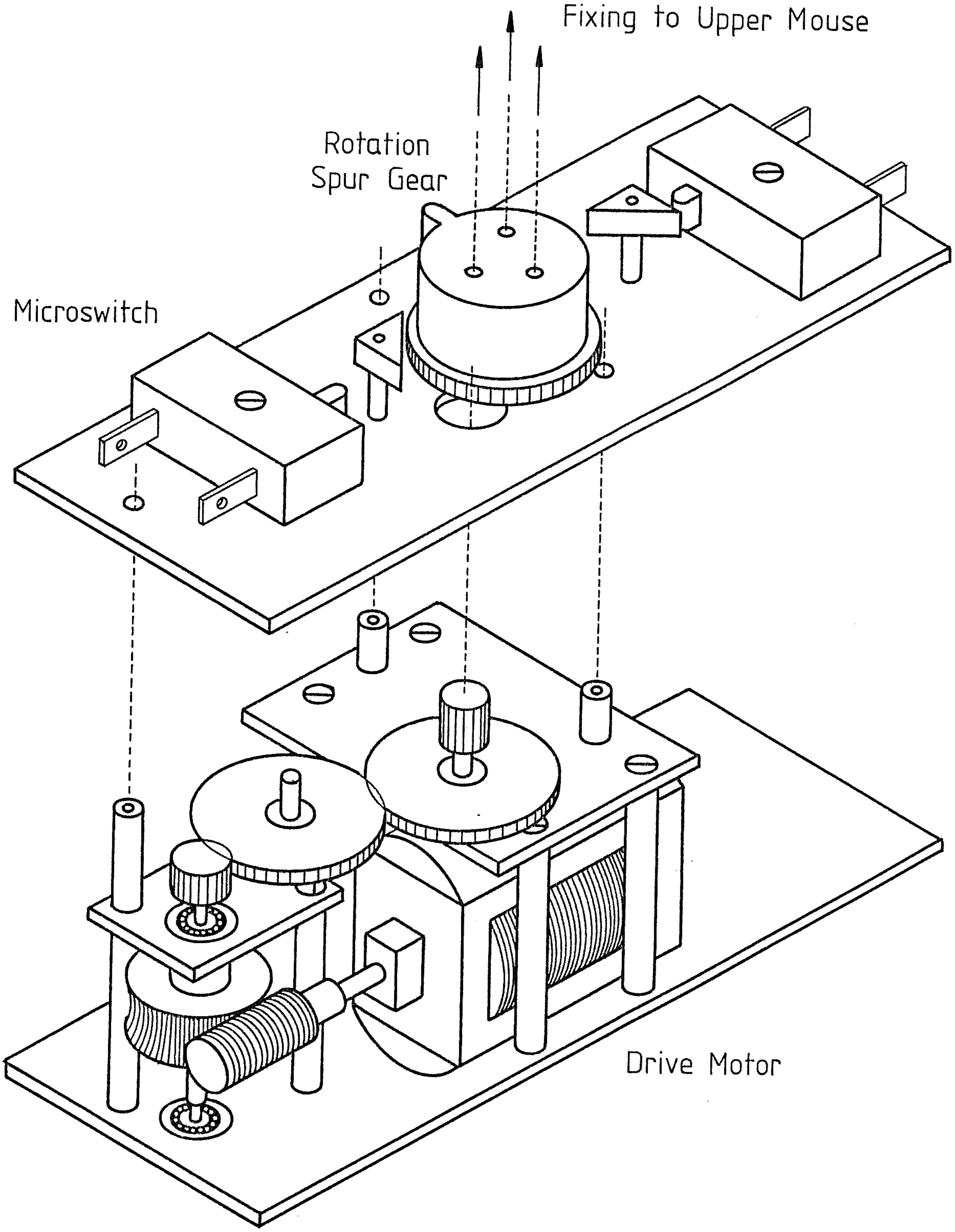

Fig (29) 180° Rotation System

line with its non-rotatable lower section, this then guaranteed correct probe positioning. Once correctly aligned in this way, the plunger acted as a locking pin by preventing any further unwanted rotations.

Figure (29) shows details of the 180° rotation system, and figure (25) shows its relative position in the 'mouse'.

3.5 'Mouse' Electronic Circuits

Excluding the power supplies, the electronics involved were housed in just two locations, these being the 'mouse' itself and within a specially constructed control-box which was kept outside the wind tunnel. See Plate (4).

All connecting wires between the two sets of circuits were incorporated within lengths of miniature, screened, multicore cable. These entered the 'mouse' through two independent sets of sockets, one was placed on top of the 'mouse' and accepted cables entering through the tunnel roof, and the other was fitted to the 'mouse' underside and took a cable fed from the aerofoil trailing edge. This cable arrangement minimized flow interference whilst completing all the necessary connections without the need to have wires running through the rotation pivot.

All the electronic circuits used are given in the series of diagrams that make up figure (30). These circuits could be placed under the following general headings :

(a) Regulators - Circuits for providing very stable supply voltages for the logic systems.

(b) Motor Stops - Circuits for switching off the drive motors when the required motion extremities were reached, whilst still permitting reverse movement.

PLATE 4 - 'MOUSE' CONTROL BOX

Note : (i) Layout of Control Switches

(ii) Digital Probe Position Display

(iii) Internal p.c.b.'s and Wiring Loom

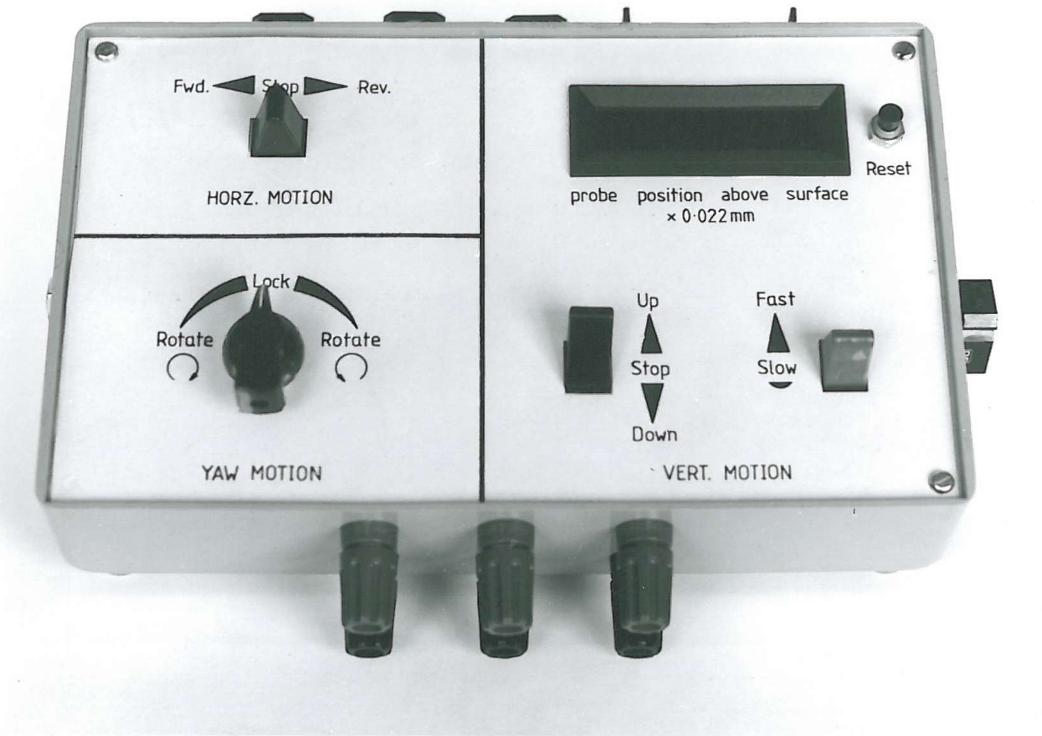
Fwd.
Stop
Rev.
HORZ. MOTION
Reset
probe position above surface
× 0·022 mm
Lock
Rotate
Rotate
YAW MOTION
Up
Stop
Down
Fast
Slow
VERT. MOTION

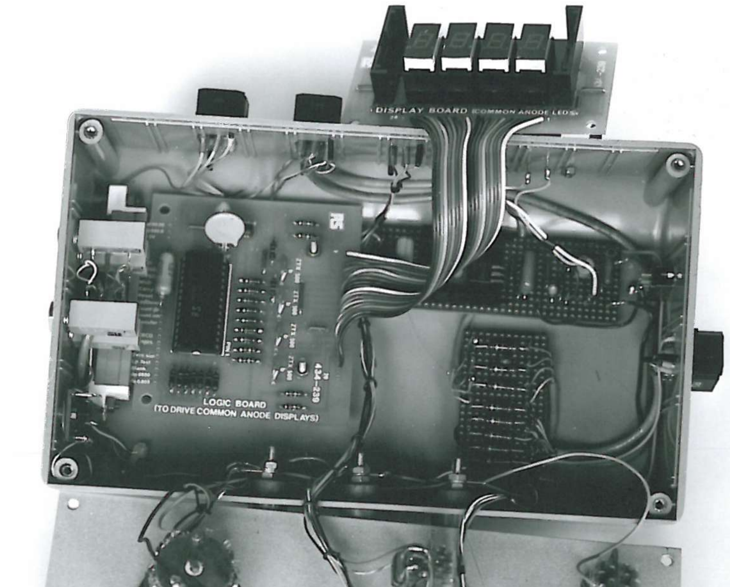
DISPLAY BOARD COMMON ANODE LEDS
434-239
LOGIC BOARD
(TO DRIVE COMMON ANODE DISPLAYS)

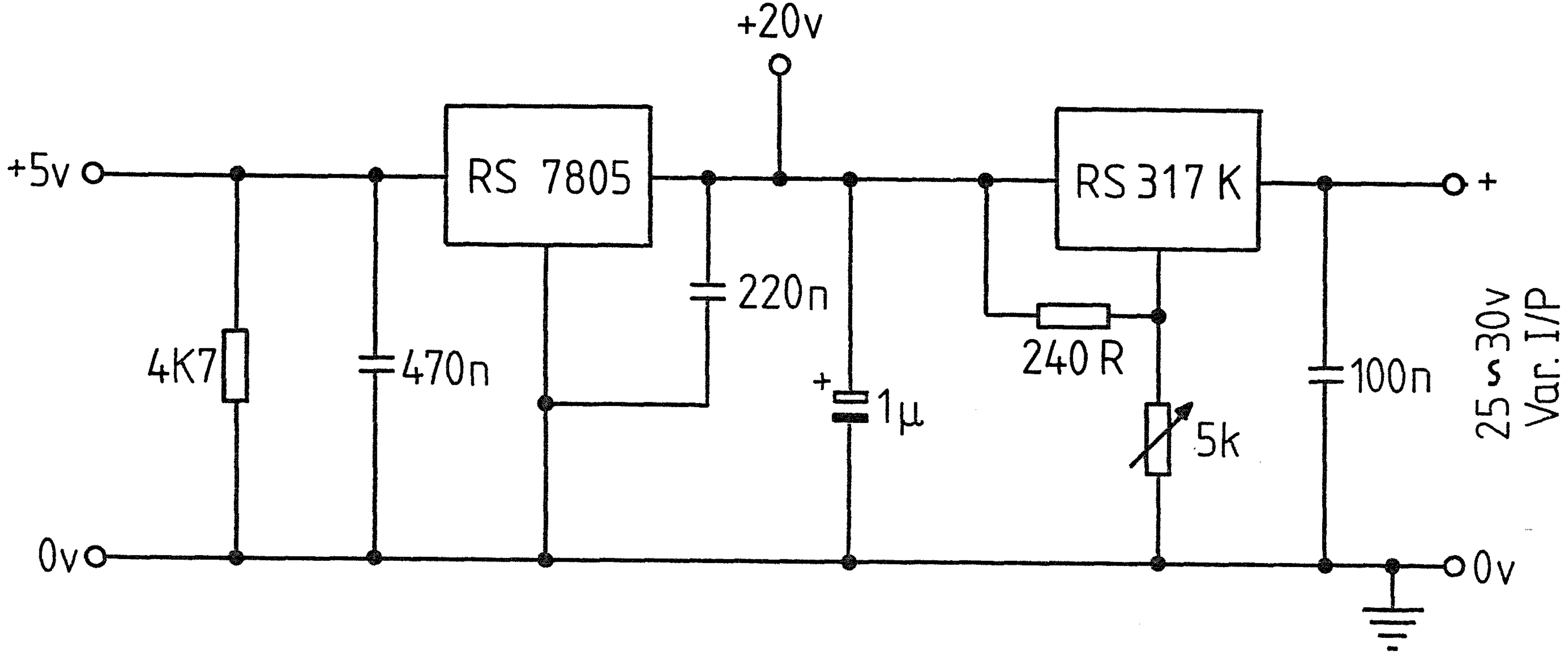

Fig (30a) Two-Stage Voltage Regulator

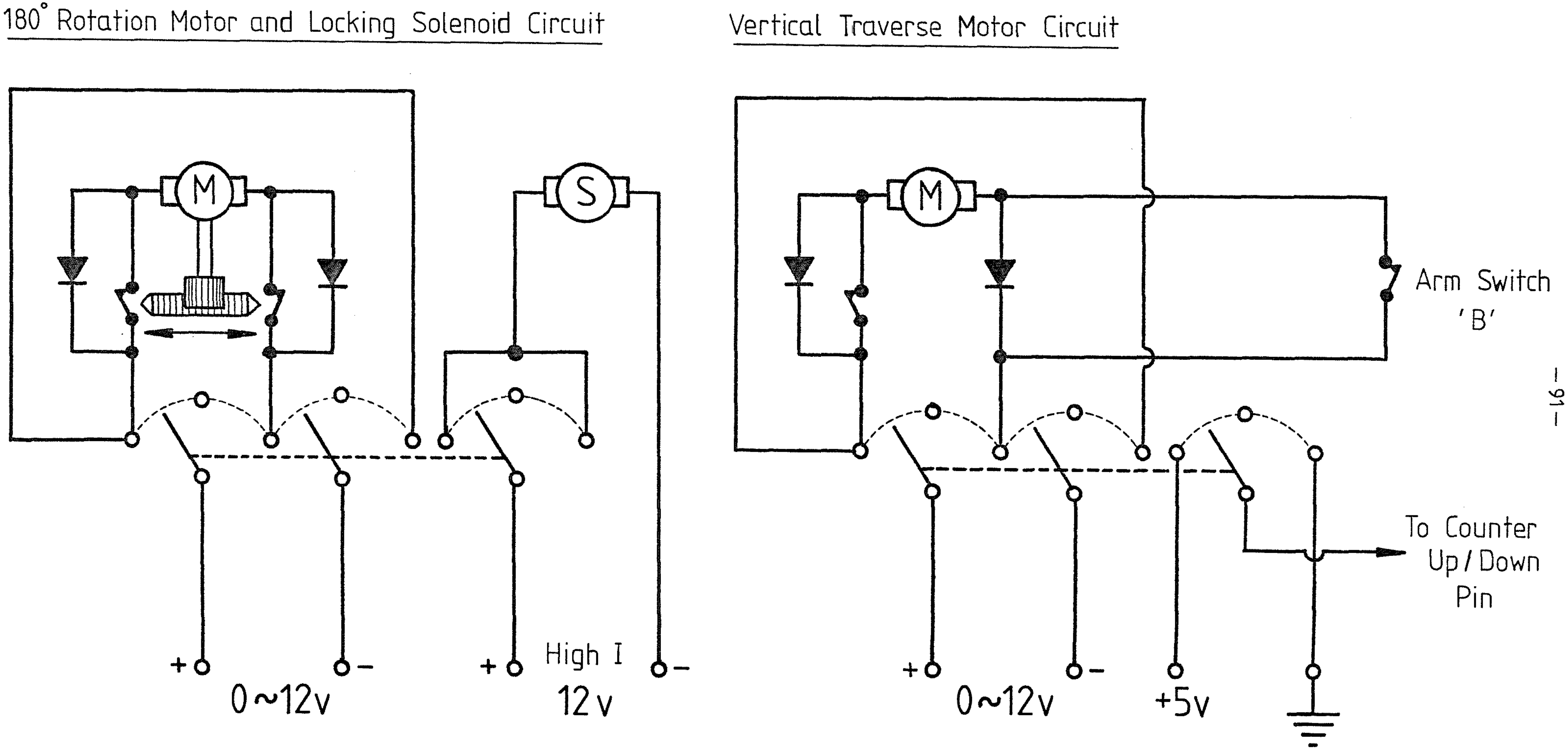

180° Rotation Motor and Locking Solenoid Circuit

Vertical Traverse Motor Circuit

Fig(30b) Motor Stop Circuits

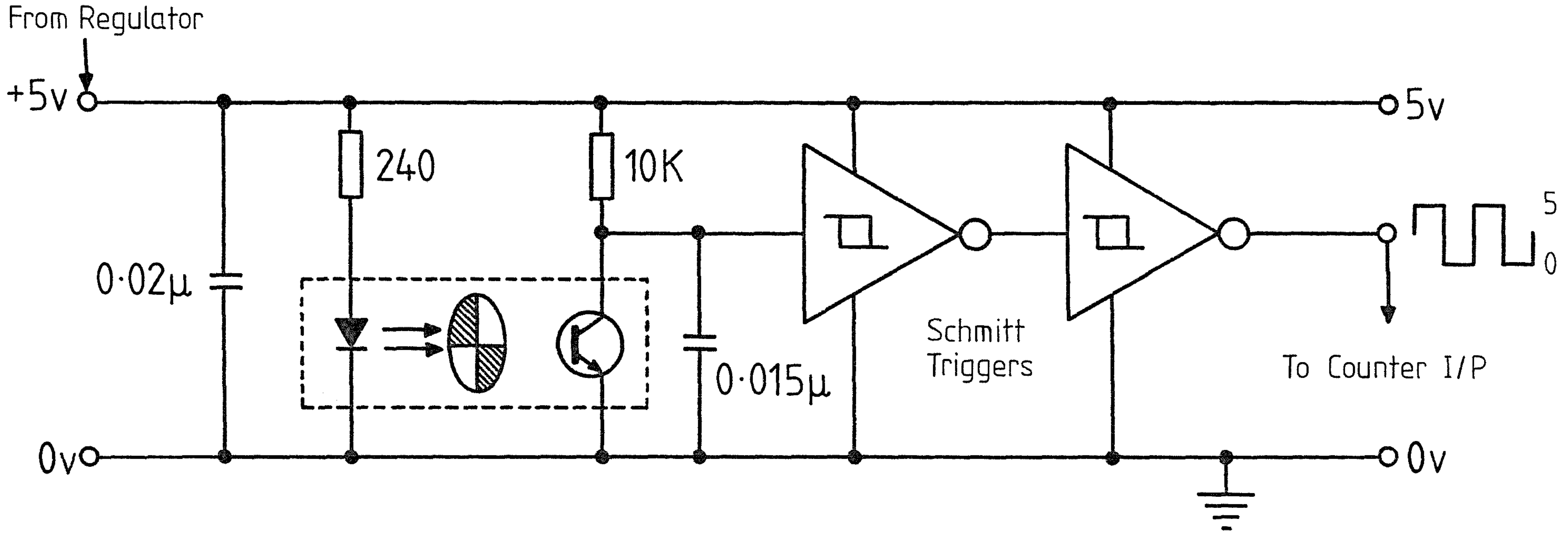

Fig (30c) Optical Pulser Circuit

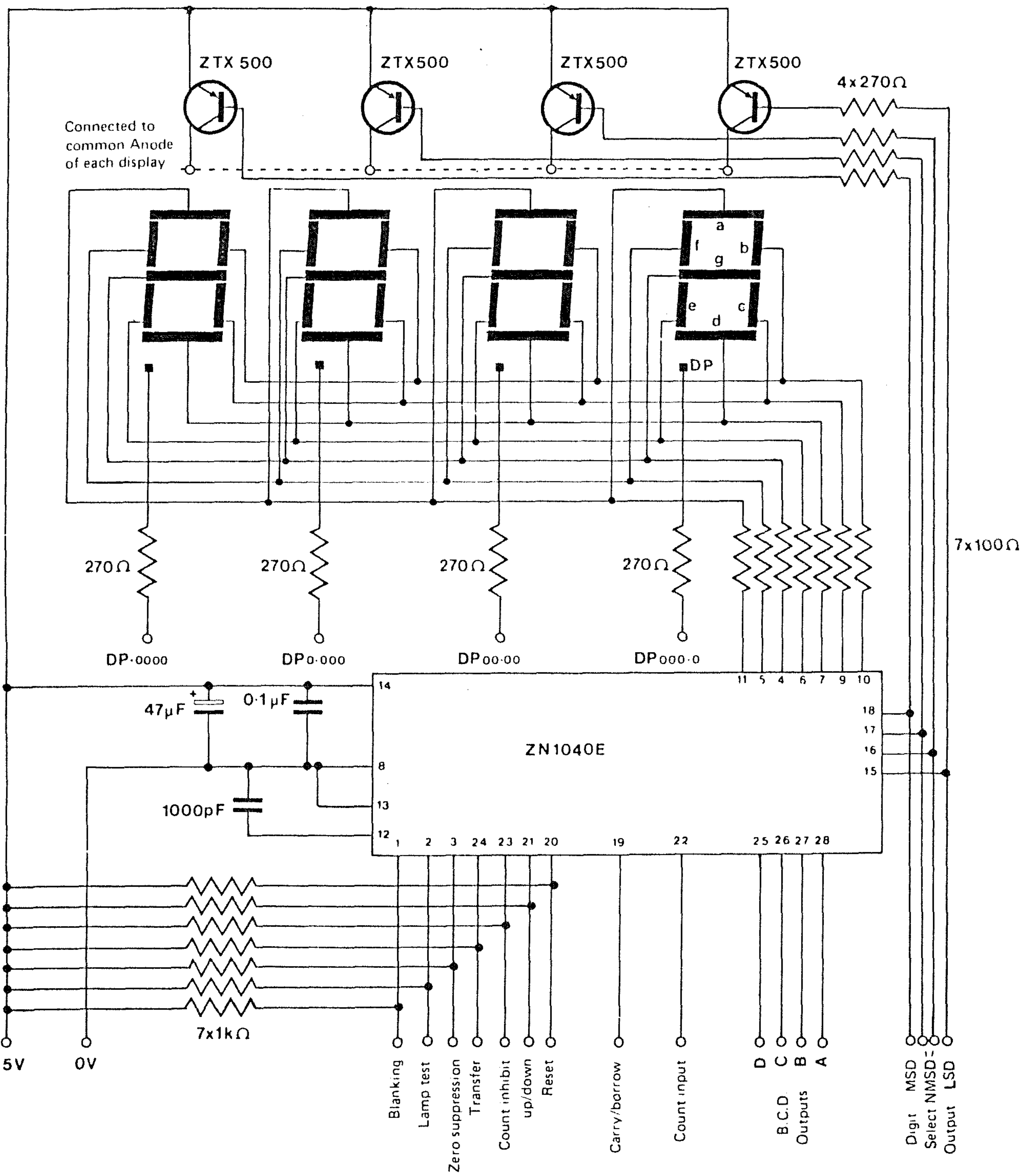

Fig(30d) <u>4 - Decade Pulse Counter</u>

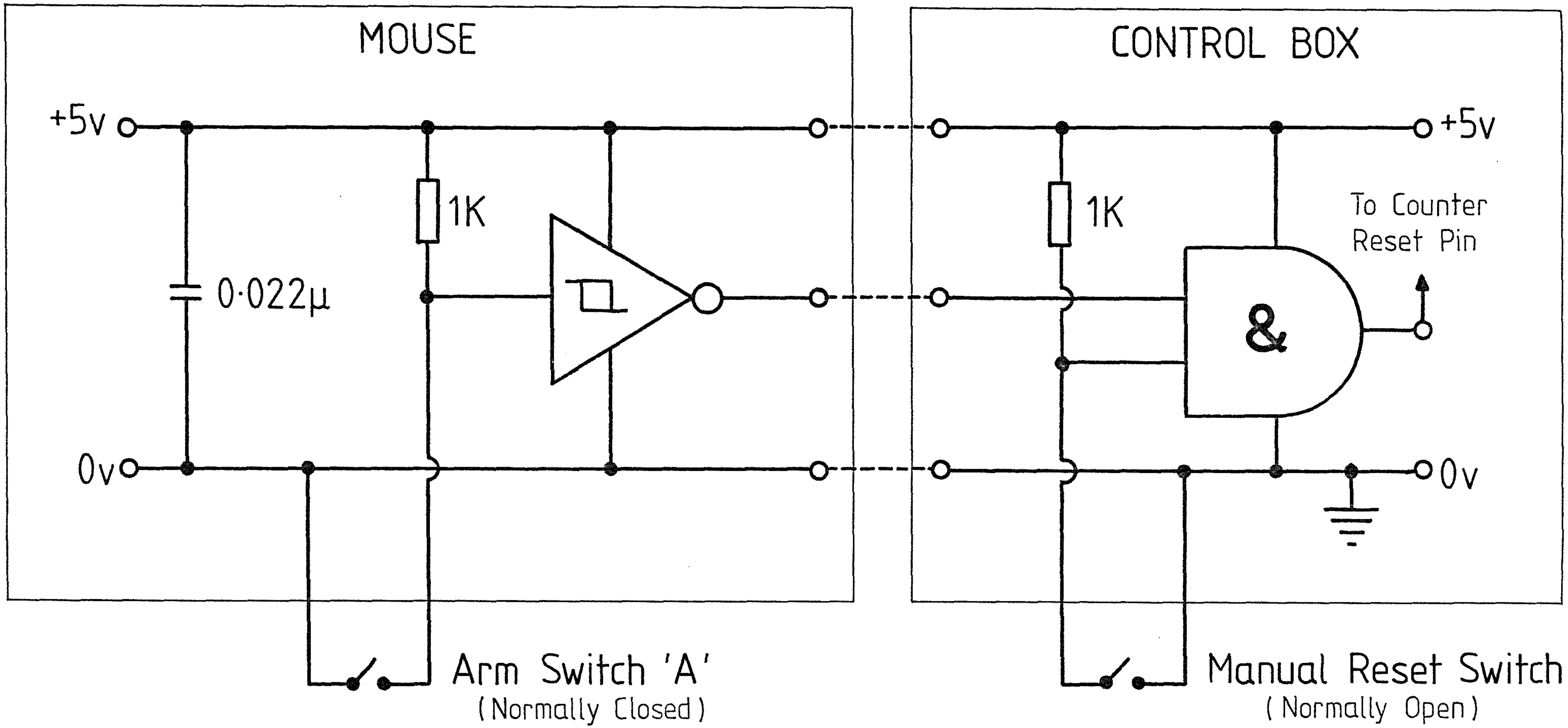

Fig(30e) Reset Logic Circuit

(c) Optical Pulser	- Circuit for producing clean square pulses from the interruption of a light beam.
(d) Counter	- Circuits for counting and displaying pulses, either up or down depending on the drive motor direction.
(e) Reset logic	- Circuits for zeroing the counter, either manually at any time, or automatically when the probe touched the aerofoil surface.

3.6 Summary of Mouse Capabilities and Dimensions

The final 'mouse' design was capable of remotely moving a measuring probe to any desired point above the local aerofoil surface within a 0-35 mm range, and with a positional accuracy of ± 0.022 mm. Two general speed ranges could be selected for this vertical motion system, with finer speed settings possible within each range by varying the supply voltage.

The exact position of the probe above the aerofoil surface was measured and then displayed in LED's on a control box, this gave the correct position information whether the probe was ascending or descending. This height monitoring system was designed to establish its own datum by automatically zeroing at the aerofoil surface.

Chordwise motion was also possible over both the aerofoil upper and lower surfaces, with the 'mouse' always securely held down by a dovetail track. A steering capability was also included to cope with track misalignments.

The 'mouse' was also capable of correctly aligning the probe with the local air-stream when within reversed flow regions, this was possible by incorporating a 180° probe rotation system.

The 'mouse' overall dimensions were only 150mm tall x 70 mm wide, yet it contained a leadscrew and carriage assembly, 3 motors, 2 solenoids, 3 miniature gear-boxes and an optical pulser unit with its associated electronics. All this was in addition to the main chassis, motor magnetic screening material, a complete wiring loom, various electrical sockets, 3 micro-switches, a track follower assembly, 4 wheels and a number of linkages.

To reduce friction, and hence make best use of the limited output powers from the motors, a total of 26 individual miniature ball-race bearings were used throughout the 'mouse'.

The 'mouse' was assembled using a large number of small brass screws, all between 8 and 12 BA. These enabled all or any part of the 'mouse' to be dismantled for maintenance purposes, no permanent joints were used in the 'mouse' construction.

Plates (5) and (6) show details of the fully assembled 'mouse'.
Note : The entire 'mouse' was designed and built personally by the author of this report using his own EMCO UNIMAT 3 modellers machine center, which was purchased specifically for the purpose. In addition, the electronic circuits were also assembled personally by the author without workshop assistance.

PLATE 5 - FRONT VIEW OF 'MOUSE'

Note :

(i) Electronics p.c.b.

(ii) Front Steering Linkage

(iii) Pressure Transducer Housing

(iv) Zeroing Valve

(v) Rubber Wheels

(vi) 180° Rotation System Drive Motor

(vii) Locking Solenoid

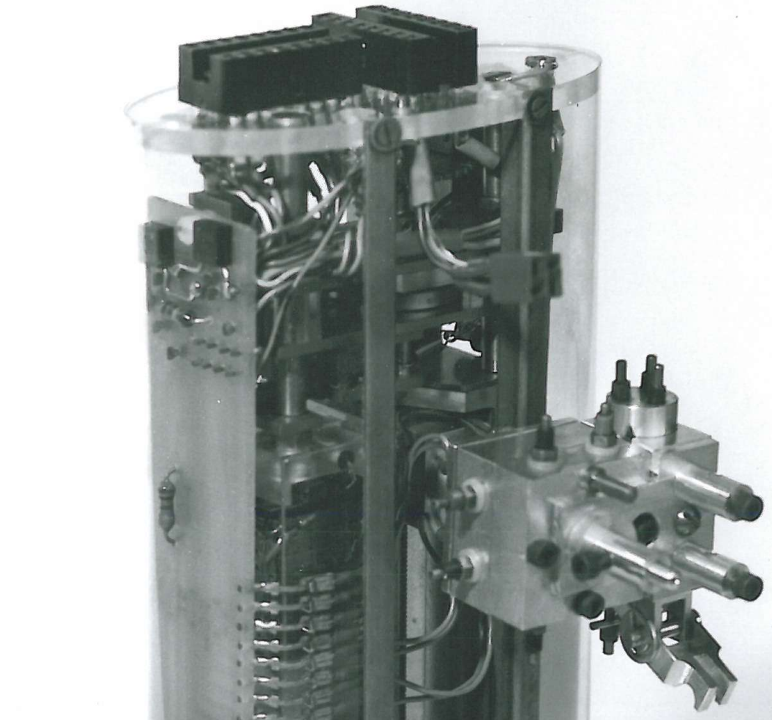
RS 401068 W

PLATE 6 - REAR VIEW OF 'MOUSE'

Note : (i) Gear Change Solenoid

(ii) Upper Electrical Connectors

(iii) Chordwise Motion Drive Gearing

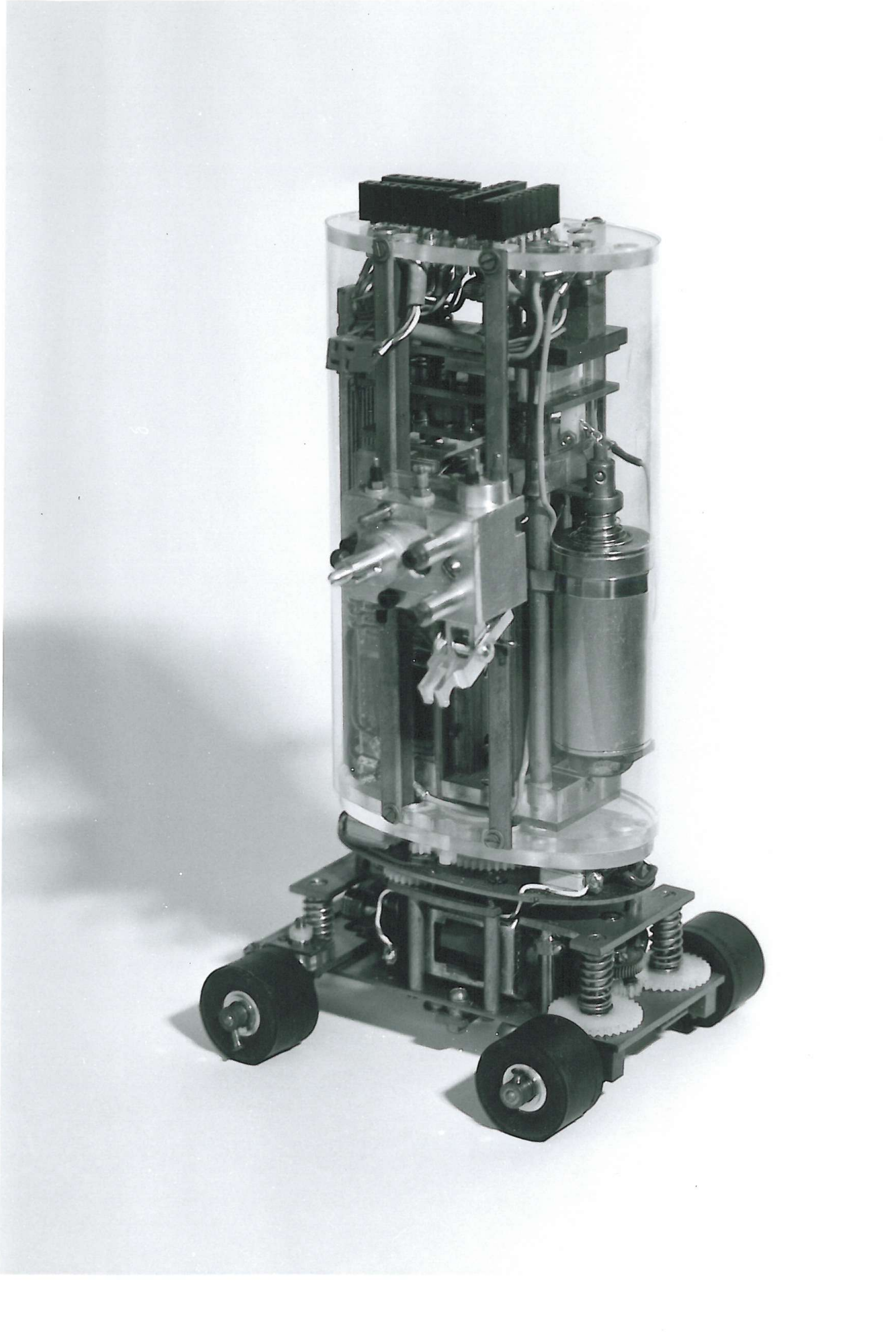

CHAPTER 4

PROBE AND PRESSURE TRANSDUCER SELECTION AND CALIBRATION

4.1 Probe Selection

The design of measuring probe chosen for determining the velocity profiles was of vital importance since it was this that governed the overall extent and quality of data obtained, not the 'mouse' which was only present to ensure accurate positioning.

Since it was necessary to determine values of velocity at very precise points above the aerofoil surface, a pressure probe had to be used. Other devices, such as hot-wires or miniature flexure probes, cannot generally be made as small as hypodermic tubing and so tend to measure over regions of the flow rather than at specific points. Hot-wires record velocity directly and are therefore unable to supply valuable total and static pressure information.

There were however a bewildering number of pressure measuring probe designs available, each developed for a specific set of requirements. Such types included spherical, hemi-spherical, conical, pyramid and wedge probes as well as those assembled from combinations of open-ended tube. Construction details of these various probe types, together with their applications, are given by Chue (5) and Bryer and Pankhurst (6).

In order to obtain data of the highest possible accuracy it was essential that the probe chosen for the present work had characteristics best suited to the flow conditions it was to encounter. Seetharam (9), in his experimental investigation of partially stalled aerofoils, used

3 separate probes. These included a 5-tube pitot probe for use in the outer flow field where the flow orientation and static pressures were unknown; a flattened probe for use close to the aerofoil where the flow orientation was parallel to the surface, where the static pressure could be obtained from a surface tapping, and where the probe dimensions normal to the surface had to be small; and a cylindrical probe for use in reversed flow regions where stem interference had to be minimized.

To avoid time-consuming probe changes it was decided for the present test programme to use just a single probe, but one capable of operating successfully in all the flow regimes encountered.

Because of the limited traverse capabilities of the 'mouse', all measurements were confined to within a relatively small region above the aerofoil surfaces. For this region, the local flow was always approximately parallel to the aerofoil surface. The flow did tend to lose this parallelism when close to separation regions, but since the boundary layers always separated tangentially, the angle between the local flow and the aerofoil surface remained relatively small for some distance downstream of the separation point. Therefore since the 'mouse' ensured that all traverses were performed normal to the local surface, any probe chosen did not require any pitch measuring capability, provided that it was relatively insensitive to pitch over a range of approximately ± 12°.

It was decided that any probe type chosen would have to be able to measure static pressure as well as total pressure. This would then allow traverses to be performed at locations with no adjacent surface pressure tapping. In any case it was by no means certain that the static pressure remained constant through the entire boundary layer, especially when measuring velocity profiles close to separation points.

Since measurements were required very close to the aerofoil surface it was obviously necessary to choose a probe with very small dimensions normal to the surface.

The final requirement for the probe was that it should be relatively easy to construct and calibrate so that replacement probes could be produced at short notice if required.

Having identified all the necessary requirements for the measuring probe, it was possible to choose a suitable design.

After much consideration the probe form finally adopted was a modified 3-tube version of the 'Conrad probe'. This consisted basically of 3 small hypodermic tubes arranged such that they were unidirectional and coplanar. The end of the center tube was then cut square whilst the outer two tubes were chamfered off at an angle.

Several types of probes could be constructed in this manner simply by orientating the outer tubes differently about their polar axes. One such probe developed by Yajnik (10), had the outer tubes arranged so that one chamfered end faced upwards and the other downwards Figure (31a). This probe was ideally suited to pitch measurements as well as for determining total and static pressure. Similarly Raghava (11) designed a probe where the outer tube chamfers were arranged in a curious 45° axial orientation as shown in Figure (31b). This probe type was capable of measuring both yaw and pitch angles in the flow field, as well as total and static pressures.

These two probe designs were however both asymetric, and as such were much more suited to applications where a 'null' technique could be used, as opposed to an alternative 'calibration' method. The 'null' technique involves mechanically orientating the probe

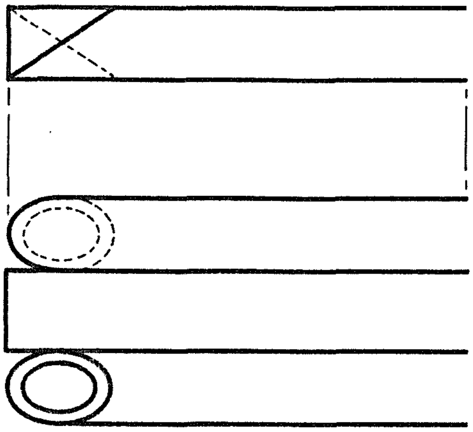

(a) Pitch Probe

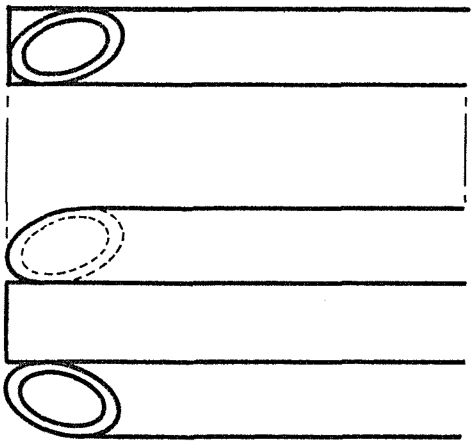

(b) Combination Probe

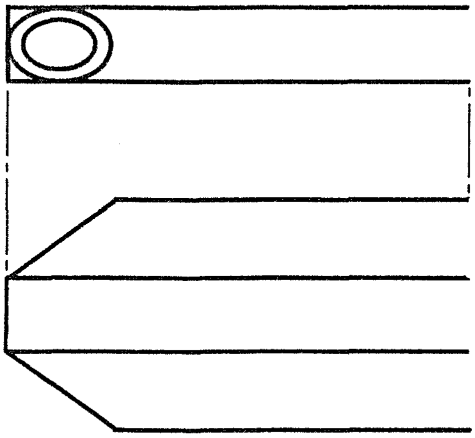

(c) Yaw Probe

Fig(31) 3-Tube Conrad Probe Nose Forms until the outer two tubes read the same pressure. When this is achieved the probe is assumed to be aligned with the local flow. Total pressure can then be read directly from the centre tube, and the flow angles can be deduced from the mechanical movement required in the nulling process. Alternatively the 'calibration' method works by keeping the probe fixed in just one direction, and deduces the required flow parameters from the pressure differences between the 3 tubes used in conjunction with a set of pre-determined calibration graphs.

Obviously the 'null' technique could not be used with the 'mouse' since no facilities were included that could remotely orientate the probe to the required alignment position. Therefore the chosen probe design had to be compatible with the 'calibration' method of usage.

The final probe design adopted was that shown in Figure (31c). This is known as a 'yaw-probe' because of its ability to accurately determine flow yaw angle in addition to total and static pressures. The symmetrical form of this probe made it ideally suited to the required 'calibration' method. As described by Rajaratnam (12), this type of probe can also be used as a 'Preston tube' to measure skin friction, and even for obtaining turbulence data as detailed by Jezdinsky (13).

4.2 Probe Construction and Dimensions

To create a probe that could gather data as close as possible to the aerofoil surface, it was decided to use very small diameter tubing in construction. The probe was therefore built from 3 lengths of 0.8 mm OD/0.5 mm bore stainless steel hypodermic tubing. The 3 tubes were attached together in the required form using silver solder. Using a precision grinding jig, specially produced for the purpose, the necessary chamfers were machined across the ends of the outer two tubes whilst the centre tube was cut square. The final probe nose-form had to be perfectly symmetrical, without either of the chamfers encroaching on the center tube. It was felt that this requirement could not easily have been met if smaller tube had been used.

The chamfer angle chosen was 45°, and the silver solder was hand finished to produce smooth surfaces. These two features were essential for producing the necessary pitch insensitivity without any serious loss of total and static pressure measuring capability. The merits of various chamfer angles and the effect of having smooth probe surfaces are discussed in Bryer and Pankhurst (6).

Following the work of Dudziniski (14) consideration was also given to including internal bevels on the tube ends to further extend the range of pitch insensitivity, however this was not done for fear of also reducing the pressure reading sensitivity.

Thought was also given to flattening the nose of the probe so that it could operate even lower in the boundary layers. However, no reference to a flat nosed yaw-probe could be found in the literature, so it was by no means certain that the flattened probe would have retained the known useful features of the standard version. It will be shown later, by the results obtained, that the standard version of the probe proved to be quite adequate for the boundary layers encountered. Possibly a flattened yaw-probe would be necessary if operating within very thin boundary layers. The probe details can be clearly seen in Plate (3).

4.3 Probe Calibration

Since the yaw-probe was not to be used in conjunction with a 'null' technique, it was necessary to produce a series of calibration graphs, these were obtained by exposing the probe to known flow velocities with the probe set at precise angles relative to the free-stream.

These calibration velocities were supplied by a small 6" x 6" working section wind tunnel, but before this could be used to calibrate the yaw-probe it was necessary to devise a means of accurately measuring the air velocity at the center of the working section where the yaw-probe was to be placed.

To achieve this, the tunnel was calibrated by comparing readings from a pitot-static tube placed at the center of the working section, with the static pressure head difference produced across the tunnel entry contraction. The results of this tunnel calibration are shown in Figure (32).

With this calibration graph it was possible to remove the pitot-static tube from the working section, and replace it with the yaw-probe. The velocity (or dynamic pressure head) seen by the yaw-probe could then be deduced from the entry contraction static pressure head difference.

The yaw-probe calibration procedure used was that described by Rajaratnam (12) and Abdul Khader (15).

Based on the tube numbering system shown, the pressure seen by each of the 3 tubes comprising the probe could be described by the following equations.

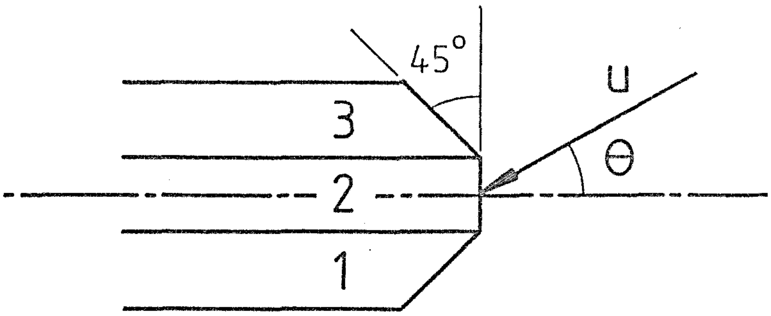

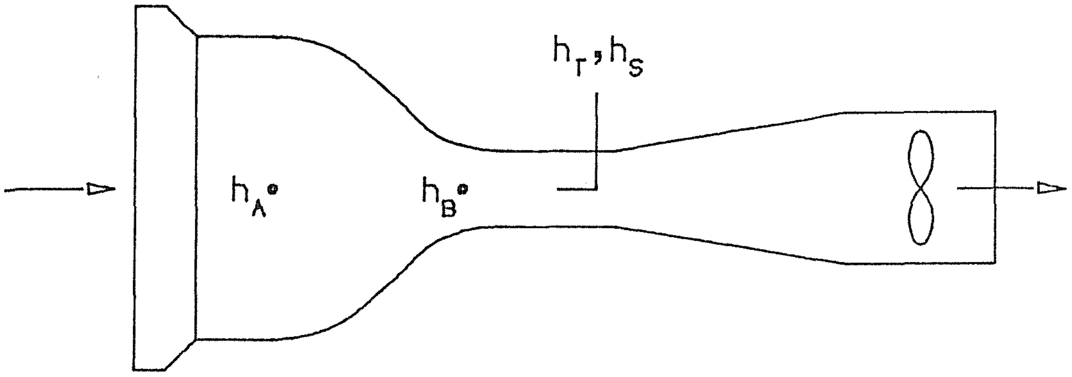

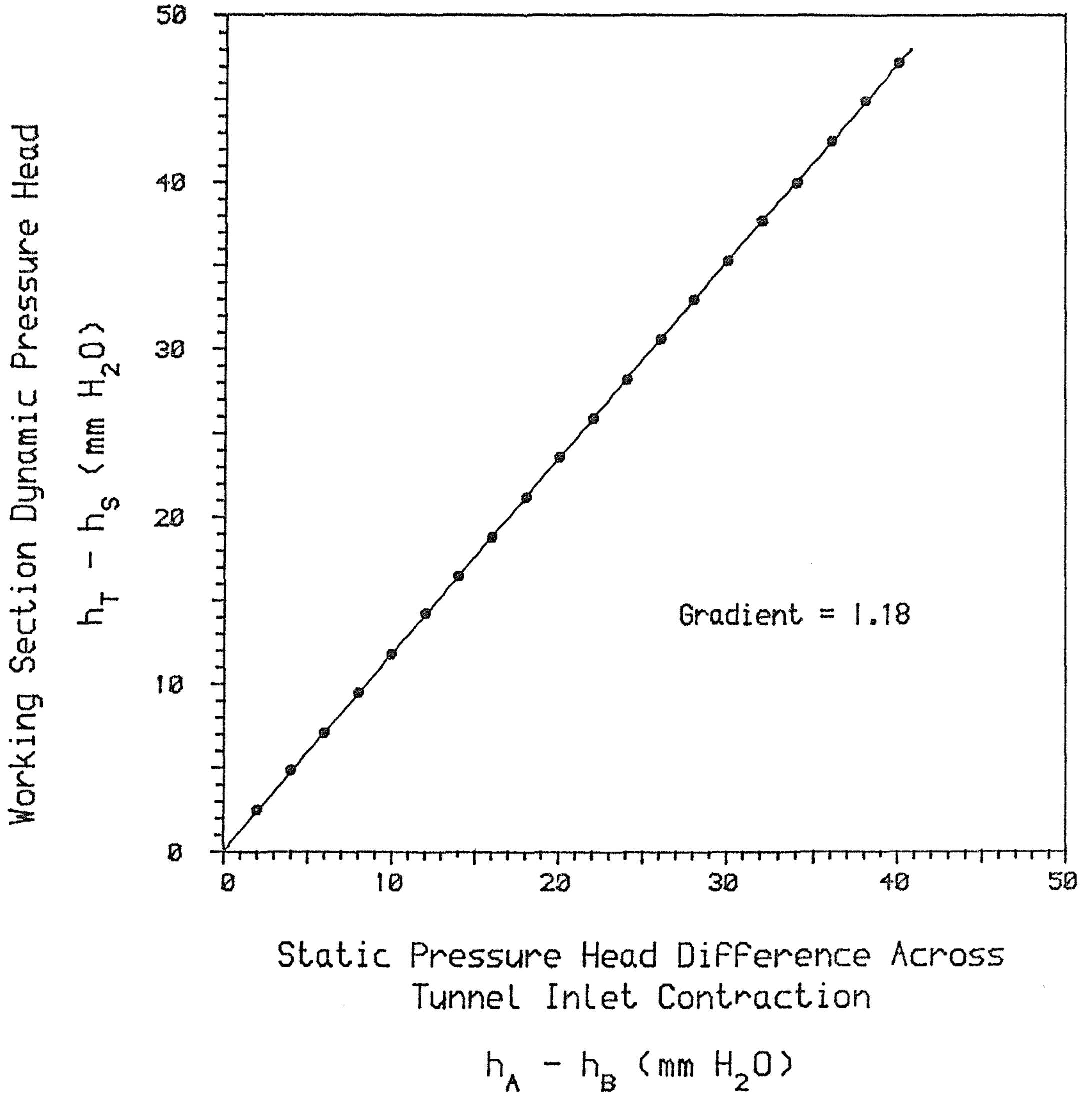

Fig(32) 6″x6″ Wind Tunnel Calibration Graph

$$P_1 = P_s + K_1 \Delta p \qquad \text{———} \qquad 4.1$$

$$P_2 = P_s + K_2 \Delta p \qquad \text{———} \qquad 4.2$$

$$P_3 = P_s + K_3 \Delta p \qquad \text{———} \qquad 4.3$$

where K_1, K_2 and K_3 are calibration factors.
P_s is the static pressure
and Δp is the dynamic pressure.

The calibration factors K_1, K_2 and K_3 are functions of yaw angle (θ) only. To determine the nature of these relationships the equations 4.1, 4.2 and 4.3 can be re-written in terms of pressure heads $h = P/\rho_L g$

$$K_1 = \frac{h_1 - h_s}{\Delta h} \qquad \text{———} \qquad 4.4$$

$$K_2 = \frac{h_2 - h_s}{\Delta h} \qquad \text{———} \qquad 4.5$$

$$K_3 = \frac{h_3 - h_s}{\Delta h} \qquad \text{———} \qquad 4.6$$

Equations 4.4, 4.5 and 4.6 are general in form, however for the specific calibration tunnel used they could be further re-written using the relationship derived in Figure (32), i.e.

$$\Delta h = h_T - h_s = 1.18 \, (h_A - h_B)$$

$$K_1 = \frac{h_1 - h_s}{1.18(h_A - h_B)} \qquad 4.7$$

$$K_2 = \frac{h_2 - h_s}{1.18(h_A - h_B)} \qquad 4.8$$

$$K_3 = \frac{h_3 - h_s}{1.18(h_A - h_B)} \qquad 4.9$$

where $(h_A - h_B)$ is the static pressure head difference across the tunnel inlet contraction.

By placing a sensitive tilting-tube-manometer across the tunnel inlet contraction, the head difference $(h_A - h_B)$ was obtained directly. Similarly, a further tilting-tube-manometer was placed between a wall static pressure tapping fitted to the working section opposite the probe nose, and any one of the 3 tubes comprising the probe. This enabled the quantities $(h_1 - h_s)$, $(h_2 - h_s)$ and $(h_3 - h_s)$ to be read directly. By combining these pressure differences in the manner suggested by equations 4.7, 4.8 and 4.9, values of K_1, K_2 and K_3 were obtained with the probe set at various yaw angles relative to the free-stream. The zero yaw angle condition was identified by $(h_1 - h_3) = 0$.

To guarantee accurate settings of yaw angle, a special jig was built. This was designed to hold, not only the probe, but also the entire support arm so that any interference effects from this arm were included in the calibration process. The jig also made sure that the probe was positioned at the center of the tunnel, and that the center of rotation in yaw took place about the probe nose. Figure (33) shows details of the jig design, and Plate (7) shows it in place around the calibration tunnel.

Figure (34) presents the values of K_1, K_2 and K_3 obtained by the calibration method over a range of yaw angles 0 to 40°. Each set of readings was repeated at 3 different tunnel speeds in order to demonstrate the independence of the calibration factors on air velocity. The calibration graphs show this velocity independence will except possibly with K_1 at yaw angles greater than 20°, here the data produced at the 3 tunnel speeds can be seen to diverge slightly. Fortunately the probe in practice was operated at yaw angles well below this angle.

The final stage in the calibration process was to determine the relationship between a 'combined calibration factor' K_0, and the flow yaw angle.

From equations 4.2 and 4.3

$$P_3 - P_2 = (K_3 - K_2)\,\Delta p \qquad \text{———————} \qquad 4.10$$

Similarly from 4.1 and 4.2

$$P_1 - P_2 = (K_1 - K_2)\,\Delta p \qquad \text{———————} \qquad 4.11$$

The 'combined calibration factor' was defined as :

$$K_0 = \frac{P_3 - P_2}{P_1 - P_2} = \frac{K_3 - K_2}{K_1 - K_2} \qquad \text{———————} \qquad 4.12$$

Using the values of K_1, K_2 and K_3 obtained from Figure (34) at various settings of yaw angle, a final graph of K_0 vs θ could be produced. This is shown in Figure (35).

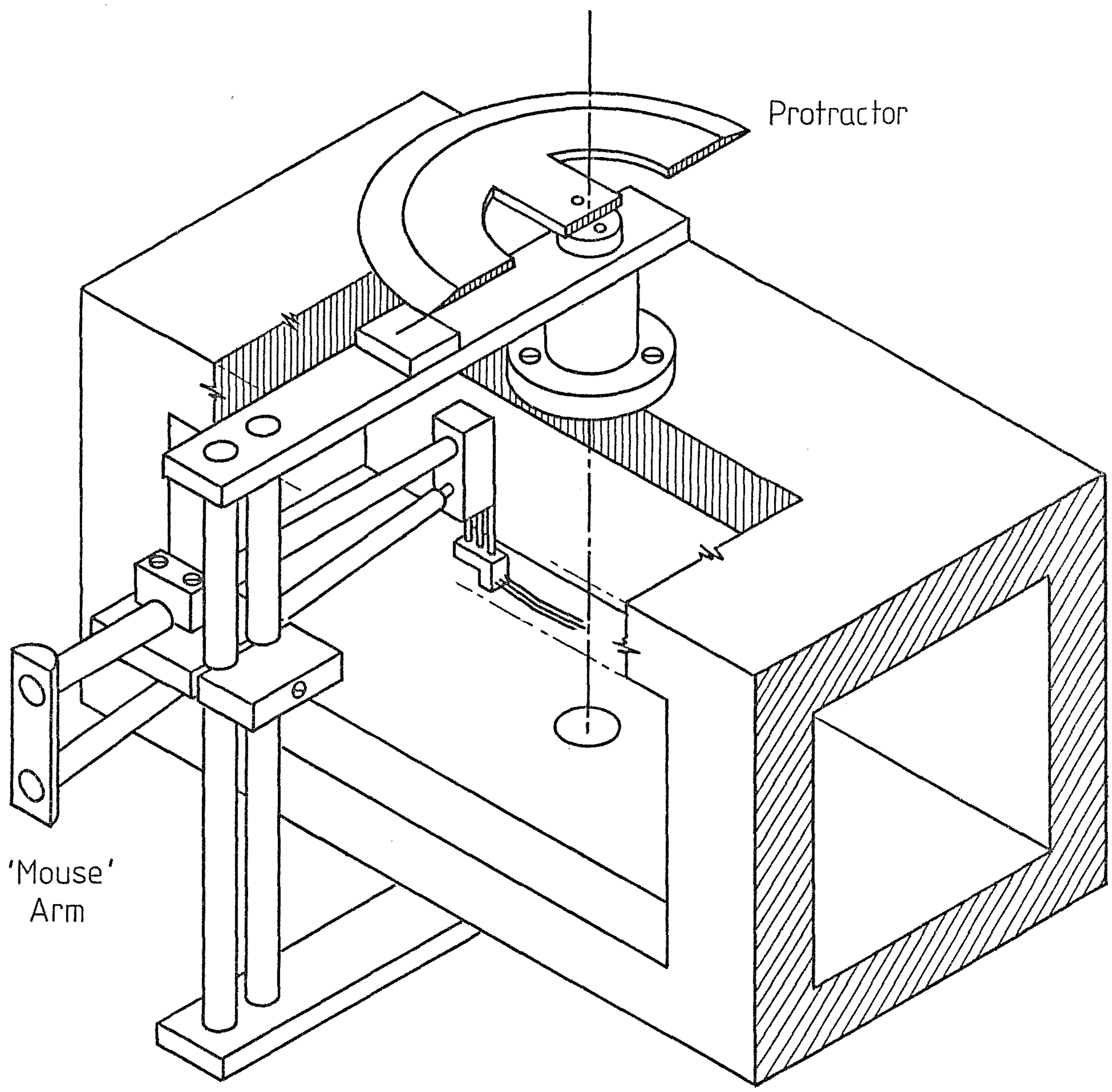

Fig(33) Probe Calibration Jig

PLATE 7 - PROBE CALIBRATION SET-UP

Note : (i) Tilting-Tube Manometers

(ii) Tunnel Contraction

(iii) Probe Calibration Jig


2
2

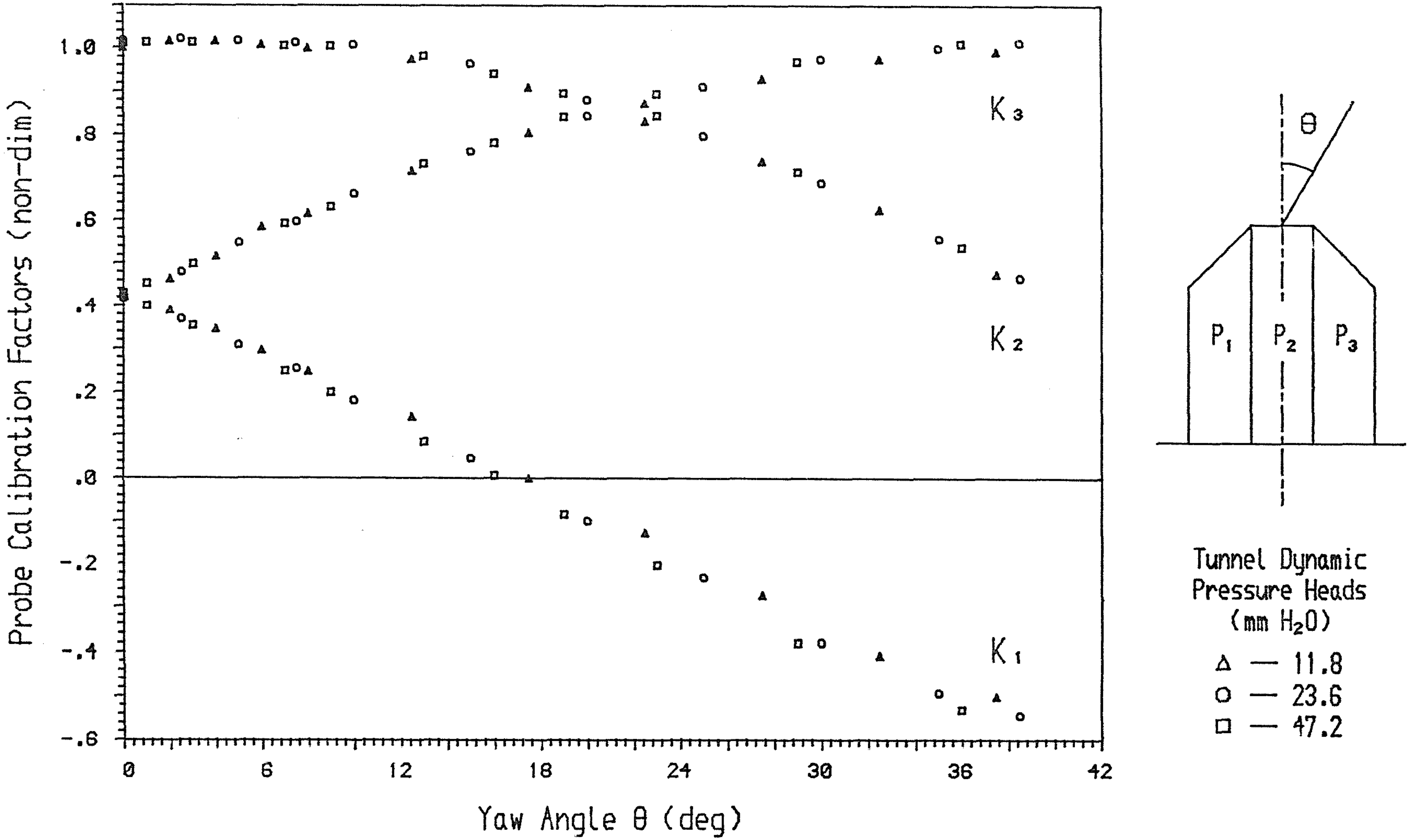

Fig(34) Variation of Probe Calibration Factors K_1 K_2 and K_3 with Flow Yaw Angle

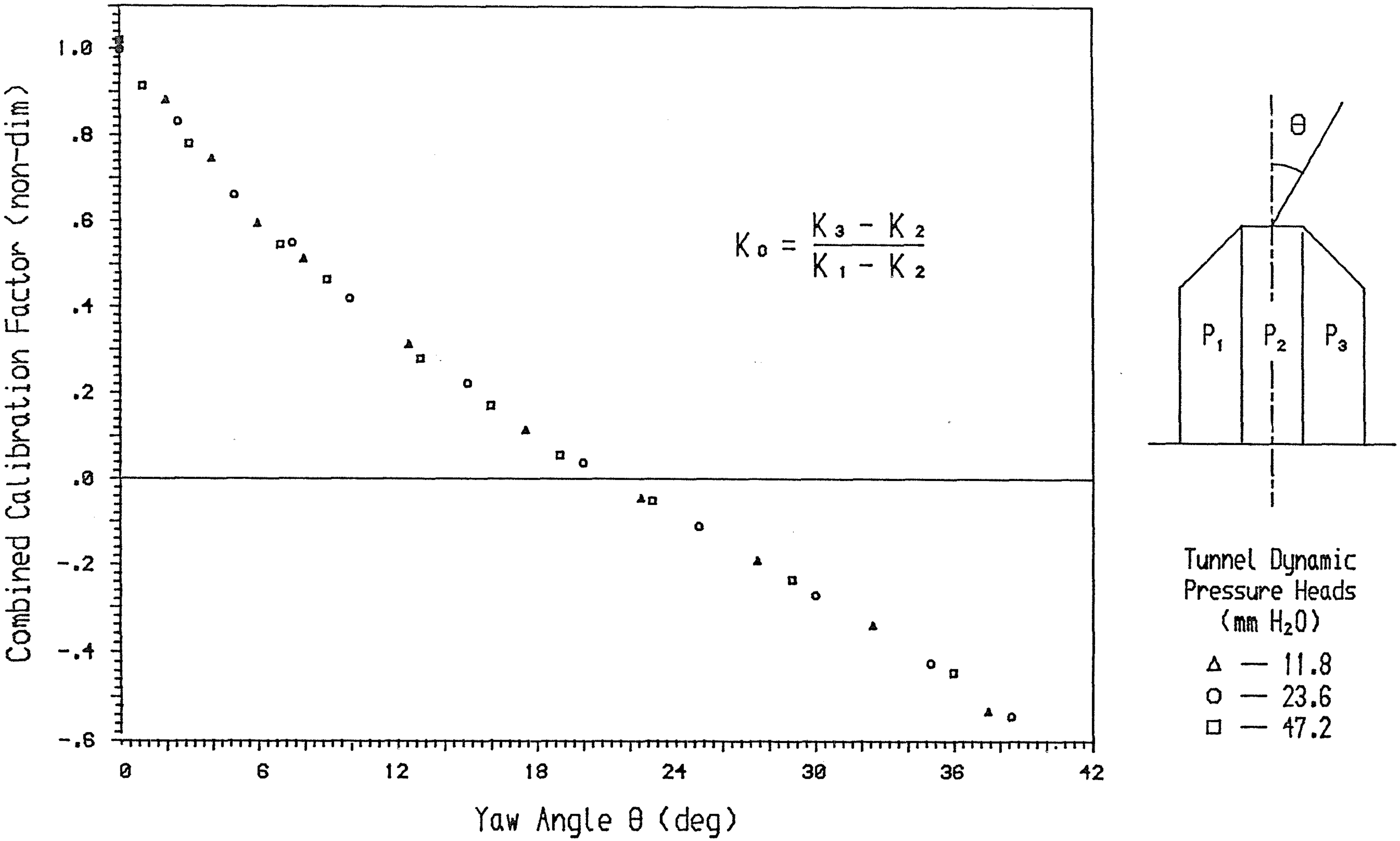

Fig(35) Variation of Probe Combined Calibration Factor K_0 with Flow Yaw Angle

With the aid of these calibration graphs it was a simple task to deduce values of velocity from the yaw probe, and hence build up accurate velocity profiles. This was done by initially measuring the pressure head differences between tubes 3 and 2, and between 1 and 2 of the yaw probe. These were then divided into each other to produce the combined calibration factor K_0, as defined in equation 4.12. With Figure (35) a unique value of flow yaw angle could be obtained using K_0. Knowing the yaw angle, Figure (34) was then used to determine the corresponding values of K_1, K_2 and K_3. Finally with the pressure head differences known across the tubes comprising the yaw probe, together with all the calibration factors, equations 4.10 or 4.11 could be employed to find the dynamic pressure and hence the velocity.

Although the calibration curves were produced in the tunnel free-stream, Rajaratnam (12) has demonstrated that for yaw angles up to 15° there is virtually no difference between the free-stream curves and those obtained when the probe is close to a solid surface such as an aerofoil.

4.4 Pressure Transducer Selection

To provide the maximum amount of boundary layer data possible during the limited time available for testing, it was important to maximize the pressure response speed of the measuring system.

Since the yaw-probe was constructed from tube of only 0.5 mm bore, it was expected that its pressure response speed would be unalterably low. Bradfield (16) confirmed this by showing that fast response speeds with small probes can only be achieved if the probe nose is an orifice rather than a parallel passageway, and if the probe body consists of tubing with a tapered, steadily increasing, bore leading away from the nose. Both these features were absent from the probe design used (essentially because of the manufacturing complexity that would have been involved).

In addition to the probe itself, further influence on response speed came from the connecting tubing used to link the yaw-probe to the pressure measuring system. Since the probe response speed was already low, it was important not to further worsen the situation by using long lengths of such connecting tubing with their associated large volumeric capacity and therefore sluggish response.

To minimize the lengths of connecting tubing it was decided to place the pressure measuring system as close as possible to the yaw-probe. Taking this to its logical conclusion meant that the best position for the pressure measuring system was within the 'mouse' itself. It was therefore necessary to find or develop a pressure measuring system which was both small enough to fit in the 'mouse', and sensitive enough to accurately measure the pressures detected by the yaw-probe.

A whole variety of novel pressure measuring system ideas were considered, ranging from miniature coil manometers with automatic fluid level detection, to devices using optical methods, such as fringes, frequency shift or attenuation. Despite some of these ideas looking very promising, they would all have required a substantial amount of development time before they could have been used successfully. It was therefore decided to look for a commercially available device that possessed the necessary small size and low pressure operating range. This however proved to be quite difficult.

Most small pressure transducers currently available have been produced for use in hydraulic and pneumatic systems, and are therefore suited to much higher pressures than those encountered during wind tunnel testing. These devices use piezoelectric crystal technology, and are even available with dimensions small enough for the entire transducer to fit into the 2 mm diameter bore of a pitot-tube. However because these devices have high stiffness diaphragms they are typically manufactured to respond to differential pressures over the range 0-25 psi (0 - 17500 mm H_2O). A few more sensitive transducers with a working range of 0 to 5 psi (0-3500 mm H_2O) were discovered after a substantial search of manufacturers literature, and one with a 0-1 psi (0-700 mm H_2O) range was eventually found. All of these devices were also quoted with linearity and hysteresis errors of around $\pm$ 1% of the full scale pressure rating. This implied that with a 0-1 psi device, the deviation of the indicated pressure from the actual pressure could be as high as $\pm$ 7 mm H_2O.

For the variable-camber-aerofoil operating at a moderate Reynolds number (Re) of 700000, the free-stream dynamic pressure head was around 12 mm H_2O. The pressure difference between the tubes comprising the yaw-probe could, as a first approximation, be considered as half of the dynamic pressure, i.e. 6 mm H_2O for the case considered. Obviously pressures measured low down in the boundary layer would be less than this free-stream value. From this it was clear that the 0-1 psi (0-700 mm H_2O) transducer would have been totally unsuitable for the present application, since its linearity and hysteresis error of $\pm$ 7 mm H_2O was as large as the entire pressure operating range required.

Pressure transducers were available with the necessary very low operating range, but these used a vibration isolated diaphragm in combination with a network of unbonded strain-gauges instead of piezoelectric crystals, and so were extremely large and robust.

By extending the search to the USA, a pressure transducer was eventually found which had the combined requirements of both high sensitivity and small size. This device was called a 'PITRAN' and used an operating method totally different to any other device available. The transducer consisted basically of a silicon NPN planar transistor that had its emitter-base junction mechanically coupled to a diaphragm. This transducer was housed in a standard TO-46 transistor can, which had had a special stylus attached to the underside of the can lid. This can lid then acted as a diaphragm by deflecting under the action of an applied differential pressure, this then applied a mechanical load to the junction via the stylus which in turn produced a reversible change in the transistor gain.

The TO-46 housing had a diameter of only 5 mm and a depth of 2 mm, yet the PITRAN was designed to have a differential pressure operating range of 0-0.1 psi (0-70 mm H_2O). With linearity and hysteresis errors quoted at ± 0.5% of full scale, the possible difference between indicated and actual pressures was ± 0.35 mm H_2O. This still represented 6% of the estimated measuring range required, but since the PITRAN represented the 'state of the art' in small size/high sensitivity transducers it was decided to purchase a number of these devices and test them.

Five PITRAN transducers (Model PT-L2) were obtained directly from the USA (they were not advertised or marketed in the UK) at £70 each. It was felt that even if these eventually proved to be too insensitive for boundary layer measurements, they would undoubtedly still be of use with faster air or water flows.

4.5 Pressure Transducer Housing Design

Because of the uncertainty concerning the suitability of the transducers for boundary layer work, it was decided not to instal the transducers within the 'mouse' body, but instead to place them within a separate housing fitted externally to the vertical motion carriage. In this way it would be a simple task to replace the PITRAN housing with a different one containing more suitable transducers, should these become available in future. This would be possible without the need to dismantle the 'mouse', or rearrange its internal systems to accommodate the new, and undoubtedly differently shaped, transducers. External mounting of the PITRAN housing also exposed it to the tunnel air stream, this had the advantage of keeping the housing at a much more stable temperature than would have been possible amongst the motors and solenoids inside the 'mouse'.

For the present study the pressure transducer housing was designed to contain 4 PITRANs, these were arranged so that they measured the pressure differences $(P_1 - P_2)$, $(P_2 - P_3)$, $(P_1 - P_3)$ and $(P_2 - P_2)$ based on the yaw probe numbering system previously shown. The pressure differences $(P_1 - P_2)$ and $(P_3 - P_2)$ were required to obtain the local dynamic pressure as described in Section 4.3, $(P_1 - P_3)$ was included to identify the zero yaw angle condition should the transducers in future ever be used in conjunction with a 'null technique', and finally the transducer installed to measure $(P_2 - P_2)$ was intended to act as a 'dummy' by responding to temperature effects alone.

Figure (36) shows the PITRAN housing design, this measured only 20 mm x 20 mm x 14 mm. The housing material used was aluminium alloy, this was chosen because of its good heat dissipation properties and low weight.

All the seals were achieved using miniature (7 mm OD) 'O' rings, and the electrical connections were made through the special fittings shown in Figure (36a). All 4 fittings incorporated 3 gold plated turned pin connectors which had been carefully removed from a d.i.l. (dual in line) integrated circuit socket. Using this method, good contact was made between the 3 leads on each PITRAN and the external flying leads, without loss of seal and with no soldering being necessary. This made the replacement of any defective PITRAN very simple, and avoided the possibility of heat damage during soldering.

Once all the components had been assembled into their correct positions, the seals were completed by clamping the 3 main body elements together with a set of socket-head cap-screws. Pressures

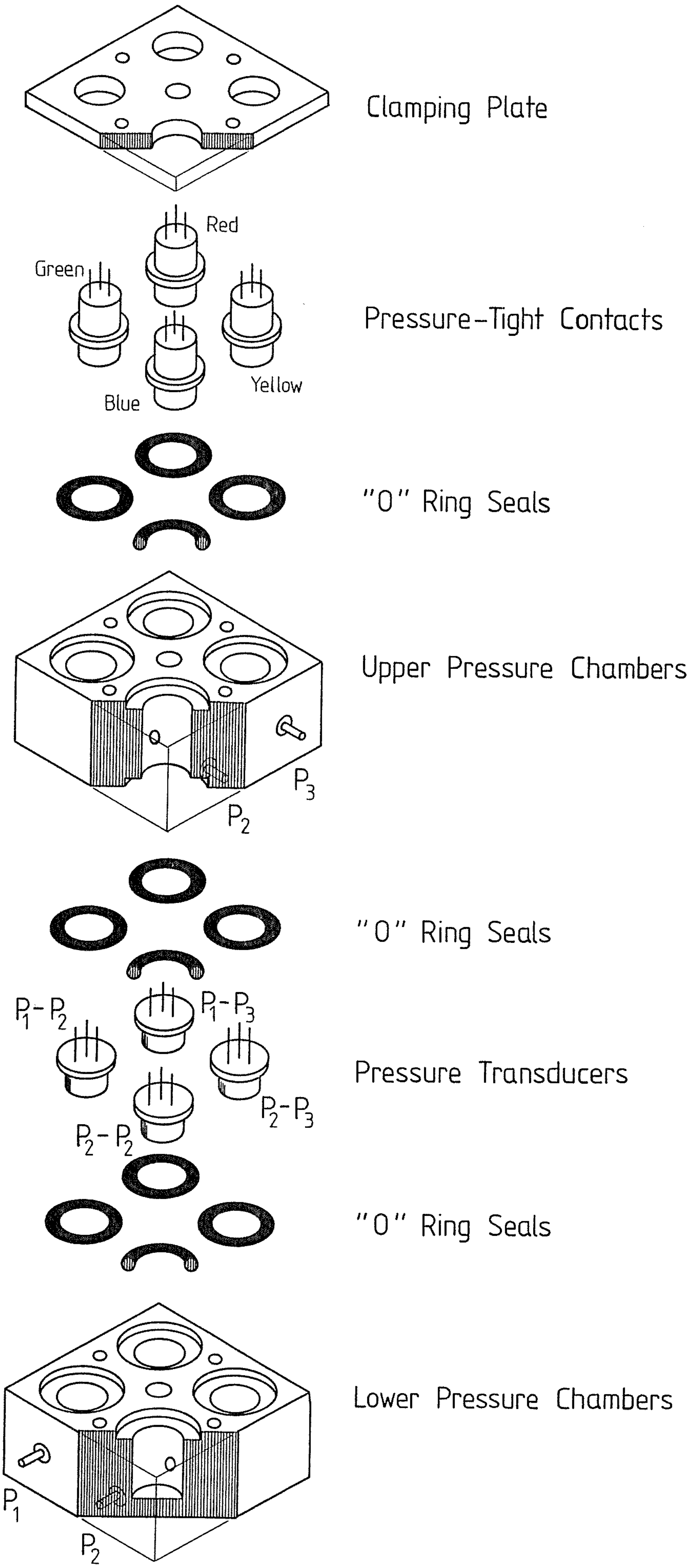

Fig(36) Pressure Transducer Housing (exploded view)

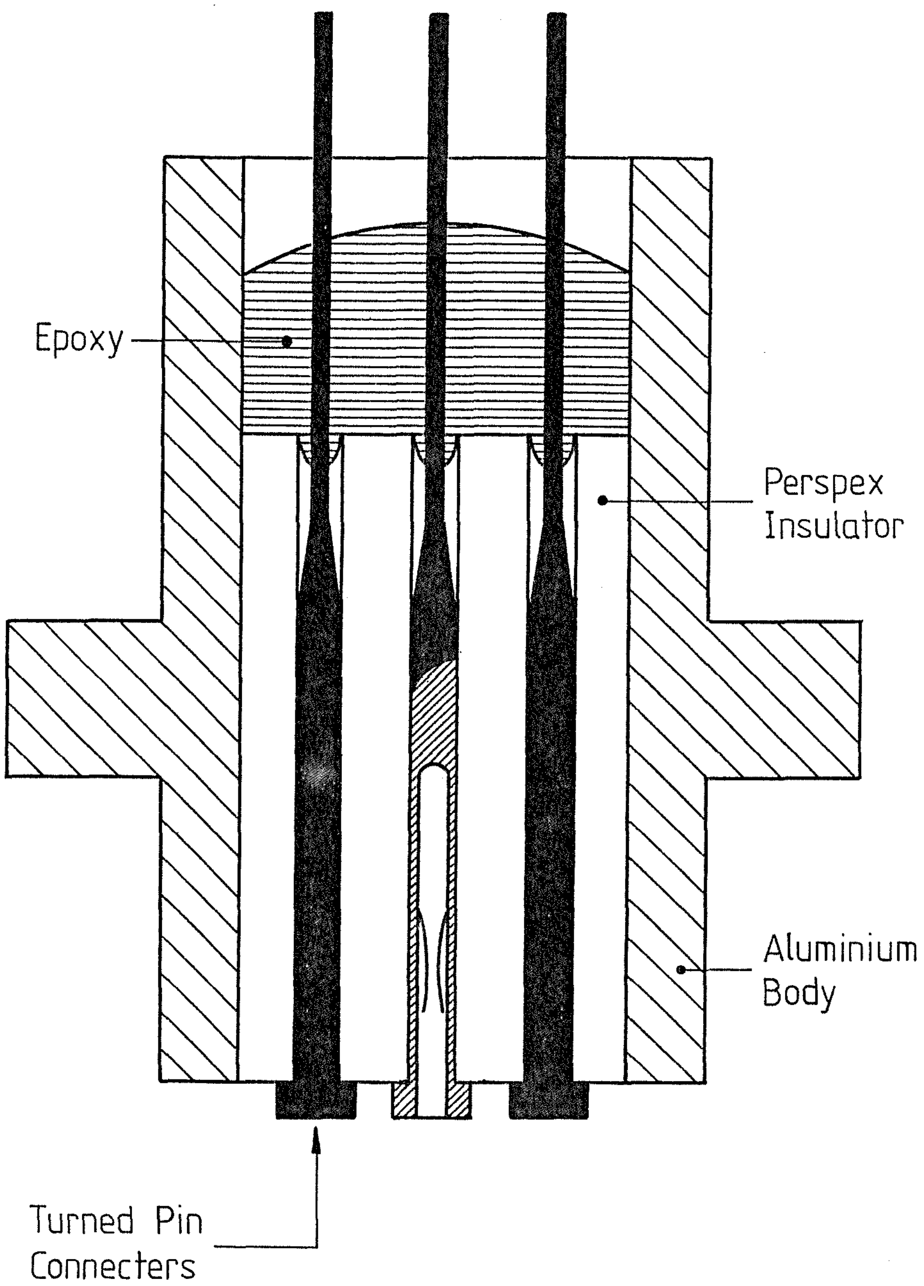

Fig(36a) Pressure-Tight Contact Construction could then be applied to the PITRANs by using the small protruding pressure ports.

The 4 PITRANs included in the housing were identified by the insulation colours used for their flying leads, i.e. Transducer measuring $(P_2 - P_2)$ = Blue, Transducer measuring $(P_1 - P_2)$ = Green, Transducer measuring $(P_2 - P_3)$ = Yellow, and Transducer measuring $(P_1 - P_3)$ = Red.

The entire housing was fitted to the carriage using an attachment hole drilled through its center. Because of the internal layout of chambers and pressure passages, this central hole was possible without any loss of seal.

The pressure transducer housing was again designed, machined and assembled personally by the author of this report. The completed housing can clearly be seen in Plates (5) and (6).

4.6 Pressure Transducer Calibration

Having placed the transducers inside a suitable housing it was necessary to calibrate them so that their output voltages could be related to any applied differential pressure. Since the PITRANs were basically just transistors it was necessary for them to be incorporated into an electrical circuit before they could be used to produce a suitable output voltage. The circuit used is shown in Figure (37), this operated on a 20v supply voltage and employed 20 kΩ resistors throughout. With this circuit it was possible to obtain a linear output voltage of up to ± 2v, at the maximum pressure level of 0.1 psi (70 mm H_2O), for each PITRAN.

To produce the required calibration curves, a range of known pressures had to be applied across each PITRAN and the corresponding output voltages recorded. To provide the known pressures the 6" x 6"

All Resistors 20 KΩ

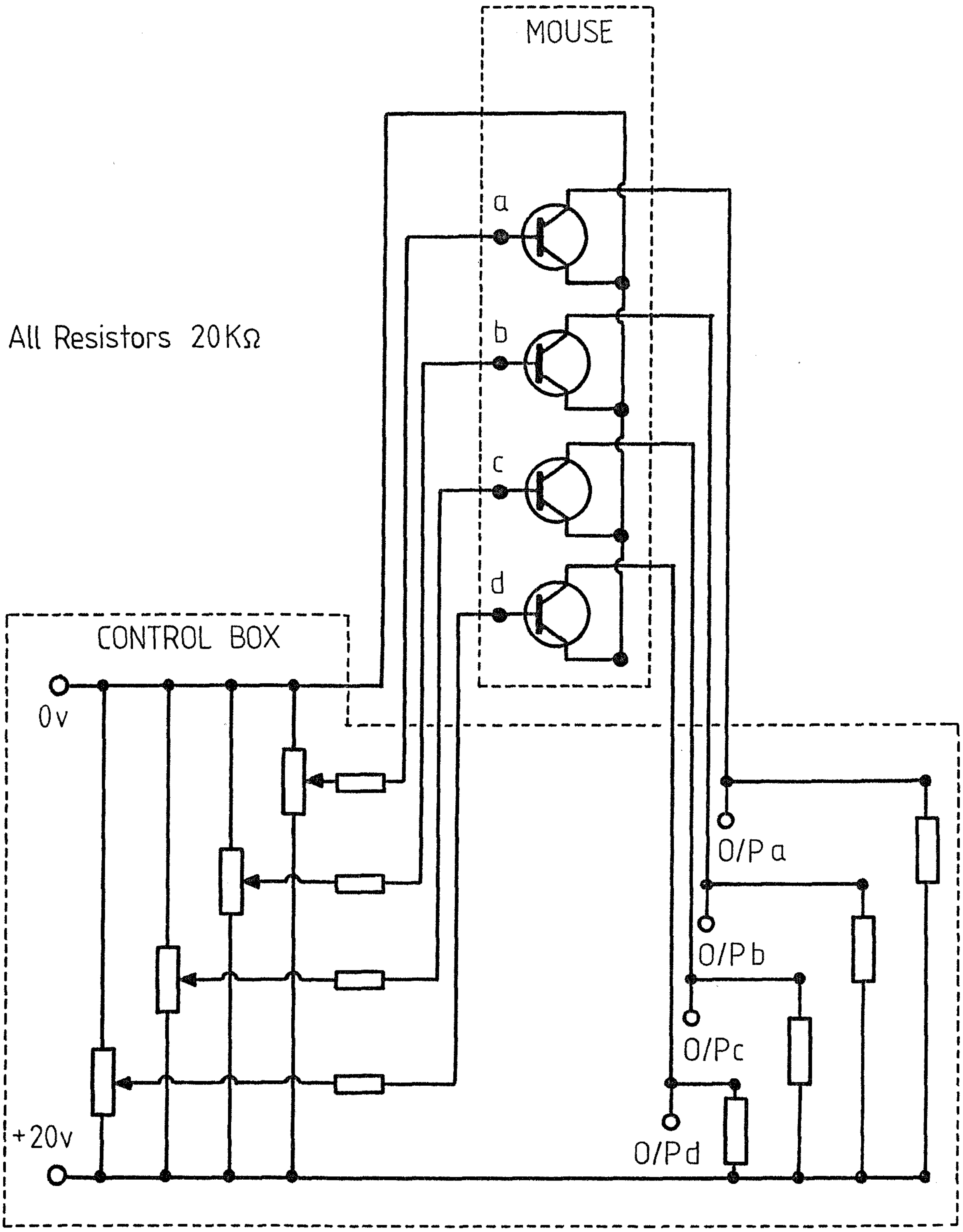

Fig (37) Pressure Transducer Circuit

calibration tunnel was again used. One side of an accurate tilting-tube manometer was connected to a wall static pressure tapping at the tunnel working section, whilst the other side of the manometer was left open to the atmosphere. The pressure difference, indicated by the manometer fluid level, could be set to any desired value simply by varying the tunnel speed. Having obtained, by this method, a particular value of pressure difference, the tube connected to the wall static tapping was removed from the manometer and applied to one side of the PITRAN requiring calibration, whilst the opposite side was left open to the atmosphere. In this way the PITRAN was subjected to the same pressure difference as had been indicated on the manometer. The corresponding output voltage from the PITRAN was then measured by using a digital volt meter.

As well as being very sensitive to pressure, the PITRANs were unfortunately also sensitive to temperature, both ambient and that generated internally by resistance effects. This temperature sensitivity was very acute with these transducers, as much as 15% of the maximum rated output voltage per °C. The 'dummy' transducer installed within the housing especially to act as a temperature compensating device, proved not to be successful. There were two reasons for this, firstly all 4 PITRANs were not electrically matched and so each had a different sensitivity to temperature, and secondly much of the temperature drift was due to internal resistive heating within each device. The latter of these was related to the current flow through each device, and was therefore dependant on the unknown pressure measuring history since switch on. With the heat being generated internally within each PITRAN, it was not possible to monitor the relevant temperatures with a thermometer and calibrate out the effects in this way.

Fortunately the effect of temperature was almost entirely a zero off-set and not a sensitivity change. This meant that the PITRANs could still be used successfully provided that the output voltage for zero pressure difference could be continually monitored.

The 4 PITRANs were each calibrated in the manner previously described, but to compensate for temperature the tube running from the tunnel wall static tapping was applied to one side of a transducer, not just once, but several times by removing and then reconnecting it again in quick succession. Recording the output voltages from the transducer, both when the tube was connected and when it was disconnected, produced a series of voltage values in pairs. The first voltage value of each pair was obtained when the tube was connected, and so it corresponded to the applied pressure difference plus any temperature off-set. The second voltage value of each pair was obtained when the tube was disconnected, and so it corresponded to the zero off-set due to temperature alone. Subtracting the voltage pairs produced the true output voltage corresponding to just the applied pressure difference.

At each pressure difference level tested, approximately 10 pairs of output voltage values were taken. Each of the 10 voltage pairs were substracted, and then an average value of these differences was calculated. This average voltage difference was then plotted against the corresponding applied pressure difference, the resulting calibration graph obtained is shown in Figure (38). This demonstrates the linear nature of the PITRAN output voltages with applied pressure difference, once compensated for temperature. Also clearly shown is the large spread of sensitivities obtained from the 4 PITRANs tested, this being indicated by the various graph slopes.

To remotely perform the continuous zero monitoring required for temperature compensation when the 'mouse' and pressure transducers were within the 7' x 5' wind tunnel, a special valve was designed and built. This was attached to the transducer housing and was controlled by a very fine tensional Bourdon-cable. When operated, the valve automatically put the same pressure across both sides of each PITRAN,

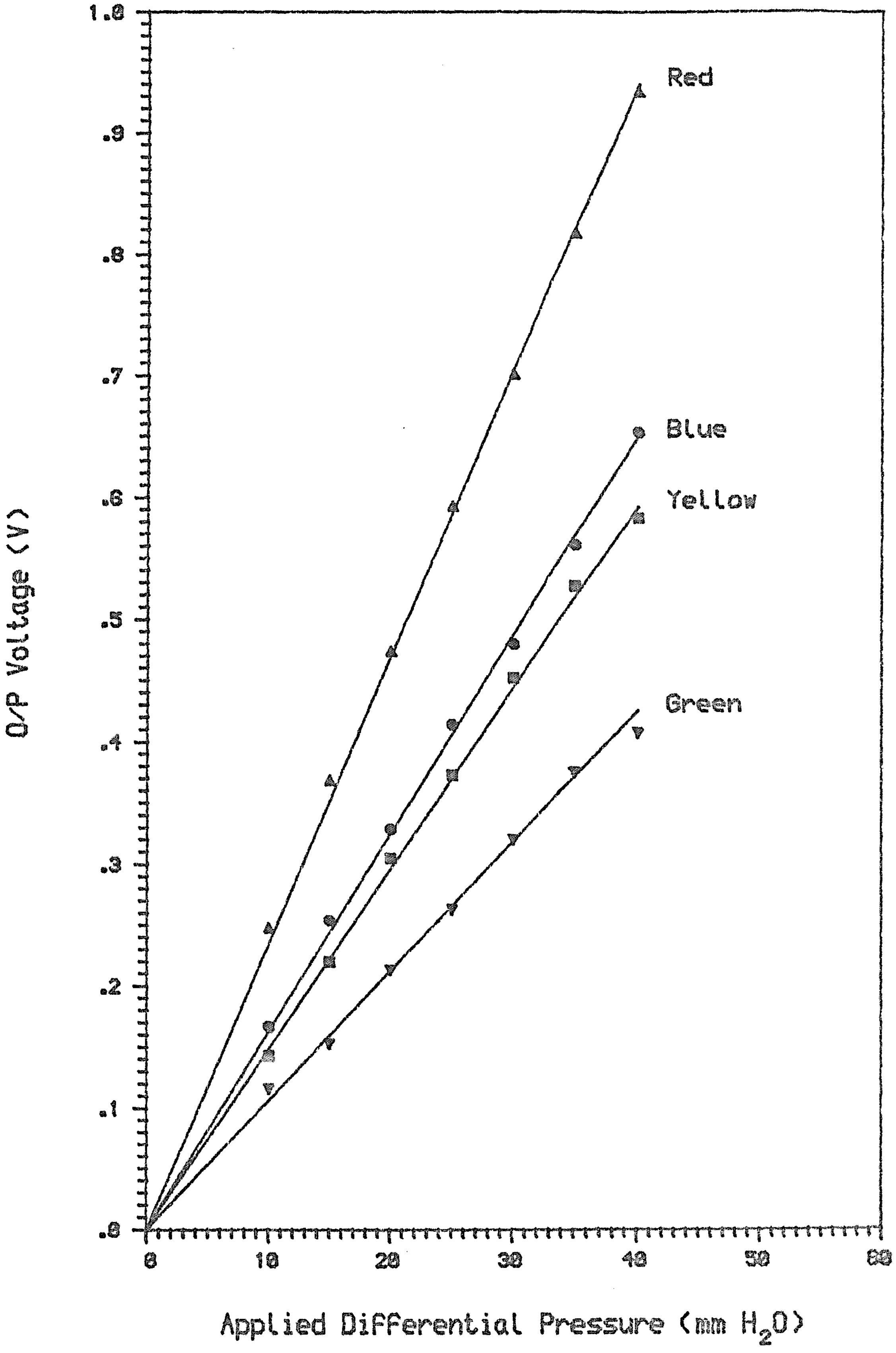

Fig(38) "PITRAN" Pressure Transducer Calibration Curves therefore producing the zero pressure difference condition. On being released the valve reconnected the housing pressure ports to the yaw-probe tubes using a return spring. The miniature valve design is shown in Figure (39).

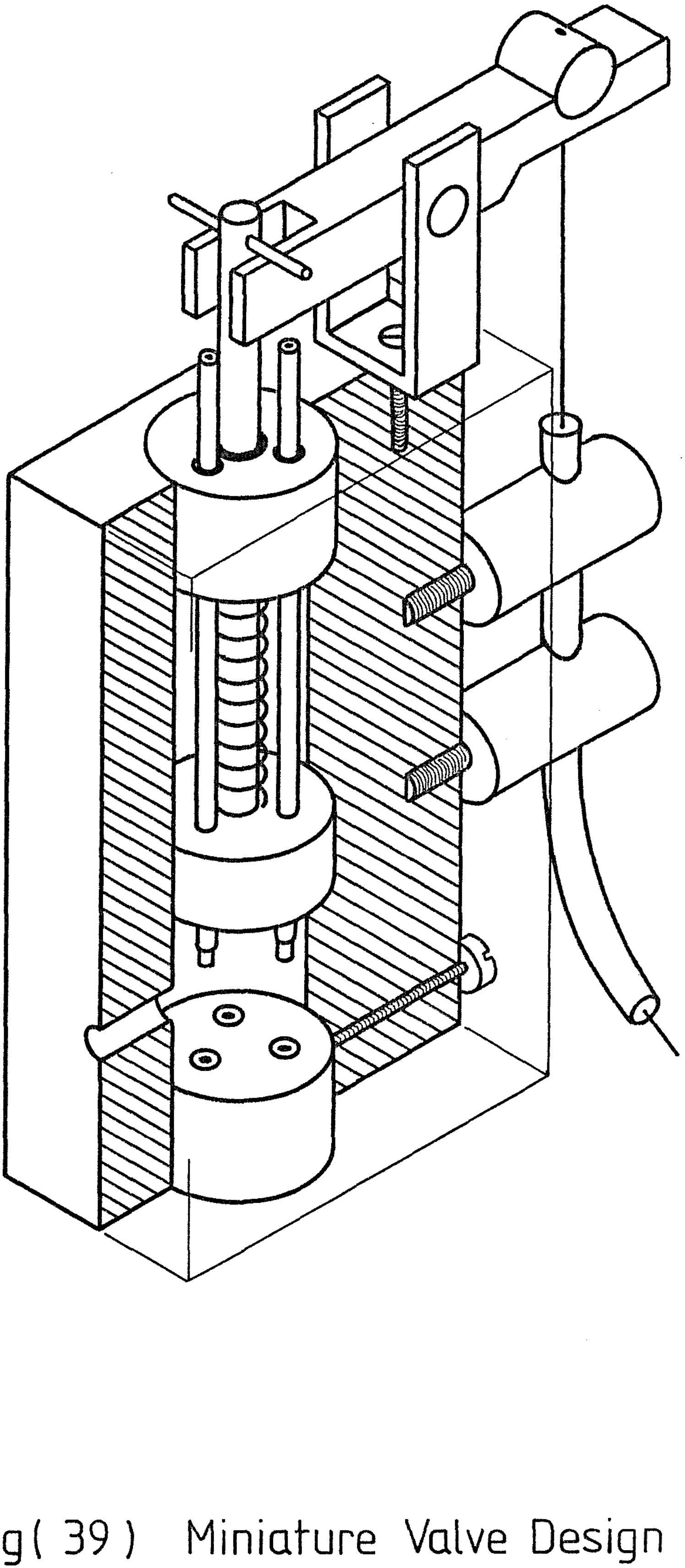

Fig(39) Miniature Valve Design

PART B

EXPERIMENTAL PROGRAMME, PROCEDURES AND DISCUSSION OF RESULTS

CHAPTER 5

EXTENT OF EXPERIMENTAL TESTING PROGRAMME

5.1 Introduction

Part A of this report has described in detail the design and development of an apparatus for simulating air-flows over masts and sails. The final form of this apparatus had a number of capabilities such as the means to vary the aerofoil shape (camber distribution), camber ratio (CR), incidence angle (α), mast diameter (d), mast angle (ϕ) and Reynolds number (Re). In addition to these, boundary layer velocity profiles could be obtained using the 'mouse' traverse unit.

With such a large number of variables involved, it was not possible, in the time available, to obtain static pressure distributions for every possible combination of these variables. Therefore it was necessary to devise a programme for testing only those variable combinations which were considered to be representative of full size sail conditions.

5.2 Test Programme for Static Pressure Distribution

To aid the selection of representative variable combinations figure (40) was compiled from the information given by Milgram (3) and Marchaj (1 & 17), for close-hauled sailing conditions. Figure (40) shows how certain variable combinations would not be met in practice, and so did not have to be included in the test programme.

Because of the near triangular planform of conventional sails, the local chord length (c) tends to decrease towards the sail head. This decreasing chord length with height above the sail foot results

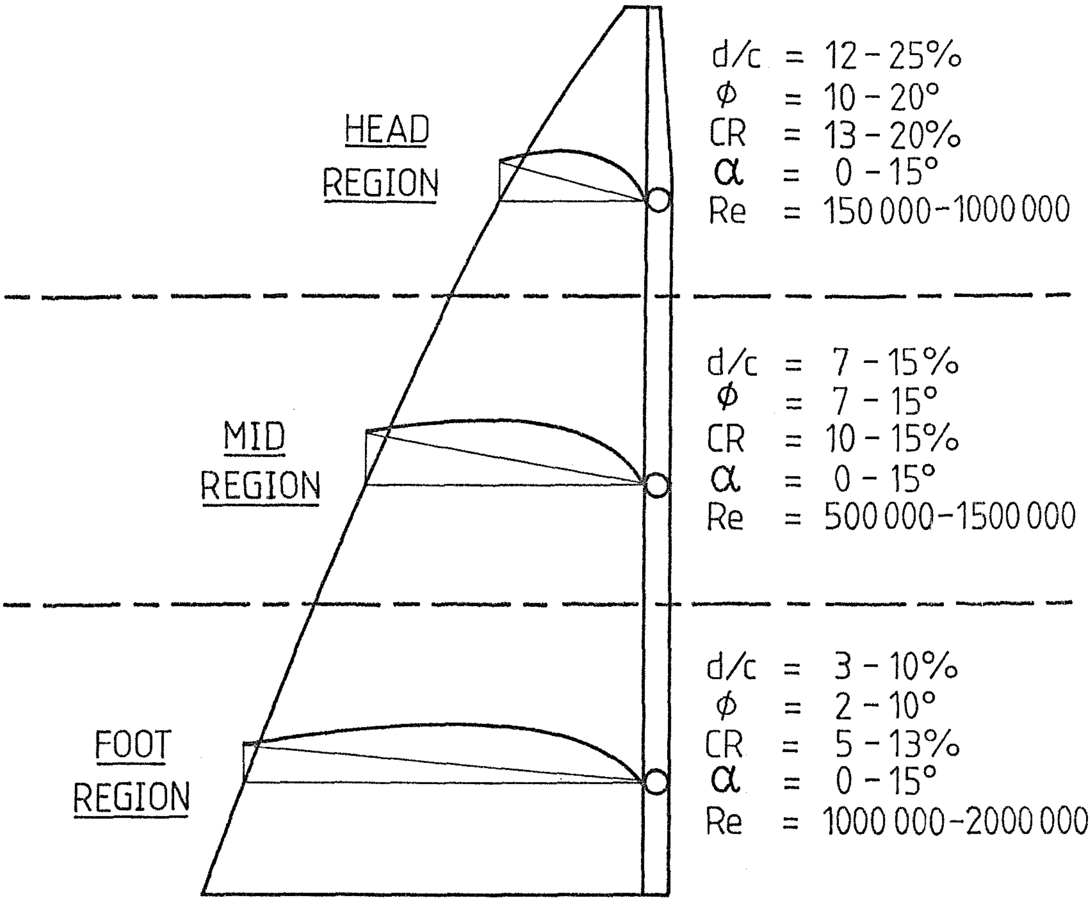

Fig(40) Typical Parameter Ranges Across a Mainsail

<table>
<tr><th></th><th colspan="12">HEAD REGION</th><th colspan="12">MID REGION</th><th colspan="12">FOOT REGION</th></tr>
<tr><td>d/c (%)</td><td colspan="12">17</td><td colspan="12">10</td><td colspan="12">4</td></tr>
<tr><td>ϕ (°)</td><td colspan="12">15</td><td colspan="12">10</td><td colspan="12">5</td></tr>
<tr><td>CR (%)</td><td colspan="4">12·5</td><td colspan="4">15·0</td><td colspan="4">17·5</td><td colspan="4">10·0</td><td colspan="4">12·5</td><td colspan="4">15·0</td><td colspan="4">7·5</td><td colspan="4">10·0</td><td colspan="4">12·5</td></tr>
<tr><td>Re x 10⁵</td><td colspan="4">3·5</td><td colspan="4">6</td><td colspan="4">10</td><td colspan="4">6</td><td colspan="4">10</td><td colspan="4">14</td><td colspan="4">10</td><td colspan="4">14</td><td colspan="4">16</td></tr>
<tr><td>α (°)</td><td colspan="3">2·5</td><td colspan="3">5</td><td colspan="3">7·5</td><td colspan="3">10</td><td colspan="3">2·5</td><td colspan="3">5</td><td colspan="3">7·5</td><td colspan="3">10</td><td colspan="3">2·5</td><td colspan="3">5</td><td colspan="3">7·5</td><td colspan="3">10</td></tr>
</table>

Table(1) Parameter Values Tested

in a drop in the local Reynolds number, together with a rise in the mast diameter/chord ratio (d/c). In addition, the mast angle also tends to increase towards the sail head due to growing twist.

These variable trends over sails meant that such combinations as high d/c with low ϕ or high d/c with high Re etc. are never met in practice. So by excluding such unrepresentative variable combinations Table (1) was compiled, this shows the variable values decided upon for testing within each of the 3 sail regions shown. The chosen variable values were also selected so that they overlapped, this enabled data trends to be established across all 3 regions.

With one value of d/c, one value of ϕ , three values of CR, three values of Re, and four values of α required in each sail region, 36 individual test runs were necessary to represent all the variable combinations in that region. A total of 108 test runs were therefore necessary to cover all the relevant variable combinations over all regions.

This whole series of tests had to be repeated each time that a different aerofoil shape was investigated. For this reason only two aerofoil shapes were used in the experimental programme, these were the NACA a = 0.8 and the NACA 63 mean-lines as defined by Abbott (4). The NACA a = 0.8 shape was investigated since it was representative of actual sails, it was also the shape tested by Milgram (3). The NACA 63 shape was tested to help ascertain the effect of moving the point of maximum camber forward towards the mast at the leading edge.

The Tables in Appendices II and III show the variable settings during each test performed, these individual tests were identified by a number ranging between 1 and 108 for the NACA a = 0.8 shape, and 109 and 192 for the NACA 63. With the latter shape no tests were performed with CR = 17.5% or 7.5% since these extreme cases had been shown, when testing the NACA a = 0.8, to be of limited value.

For each of the 192 tests performed, the static pressure distribution was recorded around the mast and over the two aerofoil surfaces.

5.3 Boundary Layer Test Programme

Because the measurement of boundary layer velocity profiles was time-consuming, no attempt was made to obtain this form of data during the 192 individual static pressure distribution tests. Instead it was intended to gather boundary layer data over just 3 special mast/sail geometries. The variable values chosen for these boundary layer tests were Re = 1 000 000, CR = 12% and $\alpha = 5°$, these occurred in each of the sail regions shown in figure (40), and so simply by changing the mast diameter it was possible to represent different spanwise locations on a full size sail. It was hoped that this boundary layer data would provide fundamental information about the nature of the flows present, and enable identification of particular features on the static pressure distributions to be made.

Because of the demand for wind tunnel time, only 6 days were available for the completion of all the traverses required, this also had to include the apparatus installation and removal times. With the 'mouse' designed for fast and efficient data acquisition this time-scale seemed adequate.

Unfortunately although the 'mouse' worked perfectly without any breakdowns, the pressure transducers, as had been feared were not sufficiently sensitive to distinguish between the pressure levels at adjacent heights in the boundary layers. It was subsequently established that in order to define a sufficiently accurate velocity profile, it was necessary to measure pressure differences between adjacent heights in the boundary layer of as low as 0.05 mm H_2O. This can be compared with the PITRAN reading error due to linearity and hystesis of $\pm$ 0.35 mm H_2O. Since the PITRANs represented the current 'state of the art' as regards high sensitivity/small size pressure transducers, it will require some technical advance in the field of pressure transducer technology before the 'mouse' can be made to realize its true potential.

Without the fast response of pressure transducers placed close to the yaw probe, the time required to obtain the velocity profiles was drastically increased. Tubes had to be run all the way from the yaw probe to a micromanometer situated outside the tunnel, the disadvantages of such lengths of tubing were discussed in section 4.4. The micromanometer used was a NPL, null-reading, tilting-tube design called a 'Combist', this instrument was capable of a reading accuracy of ± 0.002 mm H_2O over a 0-38 mm H_2O range when using low viscosity silicone fluid.

The results obtained using the micromanometer were of very high quality, but unfortunately few in number because of the time required for each reading. As well as allowing for the response speed of the connecting tubing, time was also taken in adjusting the tilting tube to its null reading position, and in ensuring that the fluid had fully settled in the small-bore glass manometer passages.

Over the period of 6 days available for boundary layer testing, only one complete set of 5 traverses was successfully completed, this was over the upper surface of the aerofoil when in the presence of the smallest mast (d/c = 4.03%). No traverses were obtained over the lower aerofoil surface, nor were any tests performed with the larger masts. In the limited time available, the small mast was investigated in preference to the others, since a particular interesting feature observed on the pressure distributions, and requiring clarification, was much more pronounced with this set-up. This feature known as the 'upper bubble reattachment region' is discussed in section 8.2.3.

The final Reynolds number of the flow used when performing the traverses was Re = 709 000, and not the preferred value of Re = 1000 000. This lower Reynolds number was selected in order to minimize the risk of the 'mouse' becoming detached from the aerofoil surface. There was no evidence at the time that such an event was imminent, but since the static pressure distributions, and therefore probably the velocity profiles, were virtually independent of Reynolds number (see section 8.3.1), it seemed wise not to increase the danger by increasing the tunnel speed unnecessarily.

Since the 'mouse' could only operate on the surfaces of the aerofoil, and no overhead traversing system was available, it was not possible to perform any wake traverses.

CHAPTER 6

EXPERIMENTAL PROCEDURES

6.1 Procedures for Obtaining Pressure Distributions

Before any testing could begin, the experimental apparatus had to be installed in the wind tunnel. Firstly the support frames were correctly aligned in the working section with the aid of a special wooden jig, and then the aerofoil was manoeuvred into position through a removable observation window in the tunnel wall. The aerofoil was attached to the support frames using the method described in section 2.3.

Only the central rows of upper and lower surface tappings were used in the present test programme. These were each blown through with a small hand pump to remove any blockages before being connected to longer lengths of tubing which were routed away through the tunnel floor to a 'Scani-Valve' system.

The initial aerofoil shape and camber ratio was achieved using the cassette method described in section 2.2, with the screw-jack co-ordinates being supplied by a computer programme.

The incidence angle could then be set by adjusting the four leadscrews on the support frames as described in section 2.4. These leadscrews were rotated in synchronism to avoid producing excessive twist in the aerofoil. The incidence adjustment system was locked in place once the correct angle had been achieved, as indicated by placing an inclinometer onto each of the 4 chordwise members of the support frames.

The required mast was slipped onto the support ledges as described in section 2.6, and set to the required mast angle using the available adjustment facilities and an inclinometer. Because of the rig geometry the angle required for the support ledges was equal to the mast angle plus the incidence angle ($\phi+\alpha$), this meant that the support ledge angle had to be readjusted each time that the incidence angle was changed in order to maintain a constant value of mast angle. Any small gap between the mast and the aerofoil leading edge was sealed with adhesive tape. Finally the mast pressure tappings were connected to the scani-valve system in the same manner as with the aerofoil.

With all the parameters set to their required values, in the manner described, all that remained was to turn on the wind tunnel and allow air to flow over the mast/sail simulation. To produce the correct Reynolds number of the flow, the necessary free-stream dynamic head was calculated using the true value of chord length (as given by the computer program), plus values of air density and viscosity corrected for the free-stream temperature. This free-stream dynamic head was set using an illuminated manometer attached to a pitot-static probe situated in the working section some distance ahead of the model.

Having in this way created all of the parameter settings required for the first test, enough time was allowed for the pressures in the connecting tubing to stabilize. The scani-valve system was then activated, which automatically measured and recorded all of the static pressures over the mast and aerofoil surfaces at the mid-span location.

To create the correct geometry conditions required for each of the tests, it was necessary to frequently change the apparatus parameters. Some of these parameters were however more time-consuming to change than others, i.e. ranging from the most to the least time-consuming the parameters could be ranked as follows: aerofoil shape (NACA a = 0.8 or 63), camber ratio, mast size, mast angle, incidence

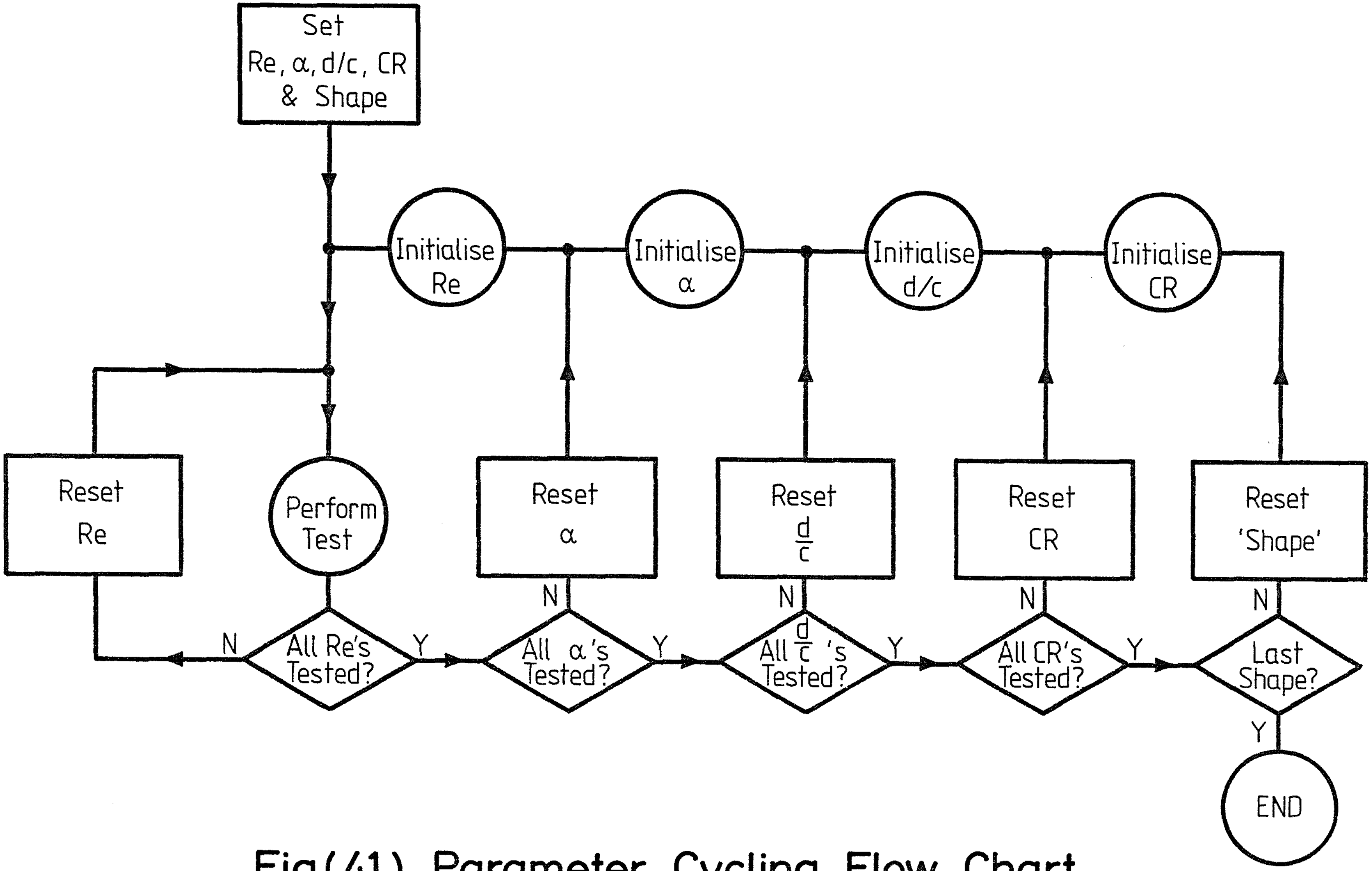

Fig(41) Parameter Cycling Flow Chart

angle, Reynolds number. Therefore to perform all of the required 192 tests in the minimum time, a procedure was adopted to ensure that the most lengthy parameter changes were carried out the least possible number of times.

Using this economic procedure for cycling the parameter combinations, as shown in figure (41), the entire 192 test runs were completed in just 12 days of tunnel testing, including installation and removal times. Several test runs were performed twice to check for repeatability in the results, this was found to be very good with repeat values generally within 1% of the initial test results.

6.2 Procedures for Obtaining Boundary Layer Traverse Data

To carry out the boundary layer traverses, the test parameters required were all set as before, but in addition to these a row of wood tufts was attached to the aerofoil surfaces using masking tape. These tufts aided in locating the points of flow separation and reattachment present, so that traverses could be performed at the most interesting chordwise positions.

The 'mouse' traversing unit was attached to the central upper surface track, and all the necessary cables were connected to it before being routed out of the tunnel working section. Outside the tunnel these cables were connected to the electronic control box together with all the necessary power supplies.

3 tubes were run between the yaw-probe at the 'mouse', and the micromanometer outside the tunnel. Since the micromanometer could only measure one differential pressure at a time, only 2 of these 3 tubes could be connected across the manometer at once. The tube running from the central yaw-probe tube was connected to the micromanometer permanently, whilst the other 2 tubes had to be connected in turn in order to produce the necessary readings of $(P_1 - P_2)$ and $(P_3 - P_2)$. Care was taken to ensure that the sensitive

micromanometer was always levelled correctly using bubble gauges before any readings were taken.

Before the tunnel was switched on, the 'mouse' was remotely moved to the extreme leading edge of the aerofoil behind the mast using the chordwise motion system described in section 3.4.4, this was done to ensure that most chordwise motions during the testing period would be air-flow assisted. The 'mouse' was shown to be capable of moving against the oncoming air-stream, but in order to minimize the load on the drive motor, this motion direction was avoided whenever possible.

To perform the boundary layer traverses, the 'mouse' was remotely driven to the required chordwise position using the chordwise motion system. The vertical traverse motion system was then used to drive the yaw-probe down towards the aerofoil, where, on touching the surface, further downward motion was automatically prevented and the probe height measuring system zeroed. The supply voltage polarity to the vertical drive motor was then reversed to allow the probe to move slowly away from the surface. The L.E.D.s on the control box constantly displayed the vertical height attained by the probe. On reaching a required height above the surface, the drive motor was switched off, this allowed time for the yaw-probe pressure differences to be measured by the micromanometer. In this way pressure differences were obtained at steadily increasing heights above the aerofoil surface.

Having completed a traverse, the chordwise motion system was again used to move the 'mouse' along the track to the next required chordwise location. Since, following a previous traverse , the probe was usually near to its maximum height above the surface, the fast traverse speed mode was selected by remotely operating the gear-change solenoid so that the probe could be driven quickly back towards the aerofoil surface. Near to the surface the vertical motion system was restored to the low speed mode, this motion then continued until the probe came to contact with the surface as before. The traverse procedure was then repeated.

When traversing through regions of separated flows, as indicated by the wool tufts, the 180° rotation system was remotely activated if pressure readings could not be obtained with the probe at its normal orientation.

Approximately 20 data points were obtained during each traverse, over half of these being measured in the lower part of the boundary layers where the velocity changes were rapid.

Two of the boundary layer traverses were re-run on a different day to test for repeatability in the results. This proved to be good with repeat values within 5% of the initial test results.

CHAPTER 7

DATA ACQUISITION AND REDUCTION METHODS

7.1 Introduction

The variable-camber-aerofoil and all 3 masts were each fitted with a large number of static pressure tappings. In order to measure all of these pressures accurately, but quickly, during the 192 tests performed, a scani-valve and data logging system was used. The data obtained in this way could then be reduced to a graphical form, suitable for report presentation, by using a series of machine steps.

7.2 Data Processing Sequence for the Pressure Distributions

The data reduction sequence employed is shown in figure (42). Having set all the parameters to the values required for a test run, the tunnel was allowed to run for a while to ensure pressure equalisation in the connecting tubes. When a suitable time had elapsed (approximately 2 minutes), the PET computer was given the identifying test number via the keyboard, and instructed to commence a scan of the static pressure tappings. The 128 port scani-valve system then automatically exposed one side of an internal differential pressure transducer to each of the static pressure tubes and to the tunnel total pressure in an alternating fashion. The other side of the pressure transducer was permanently connected to the tunnel static pressure. The pressure transducer therefore alternately produced analogue voltages corresponding to the values of local minus free-stream static pressure, and the tunnel dynamic pressure. These voltages were measured and digitized by a SOLARTRON 7055 microprocessor voltmeter, before being placed into the PET computer memory.

On completion of a scan, the PET computer proceeded to calculate

Fig(42) Data Processing Sequence

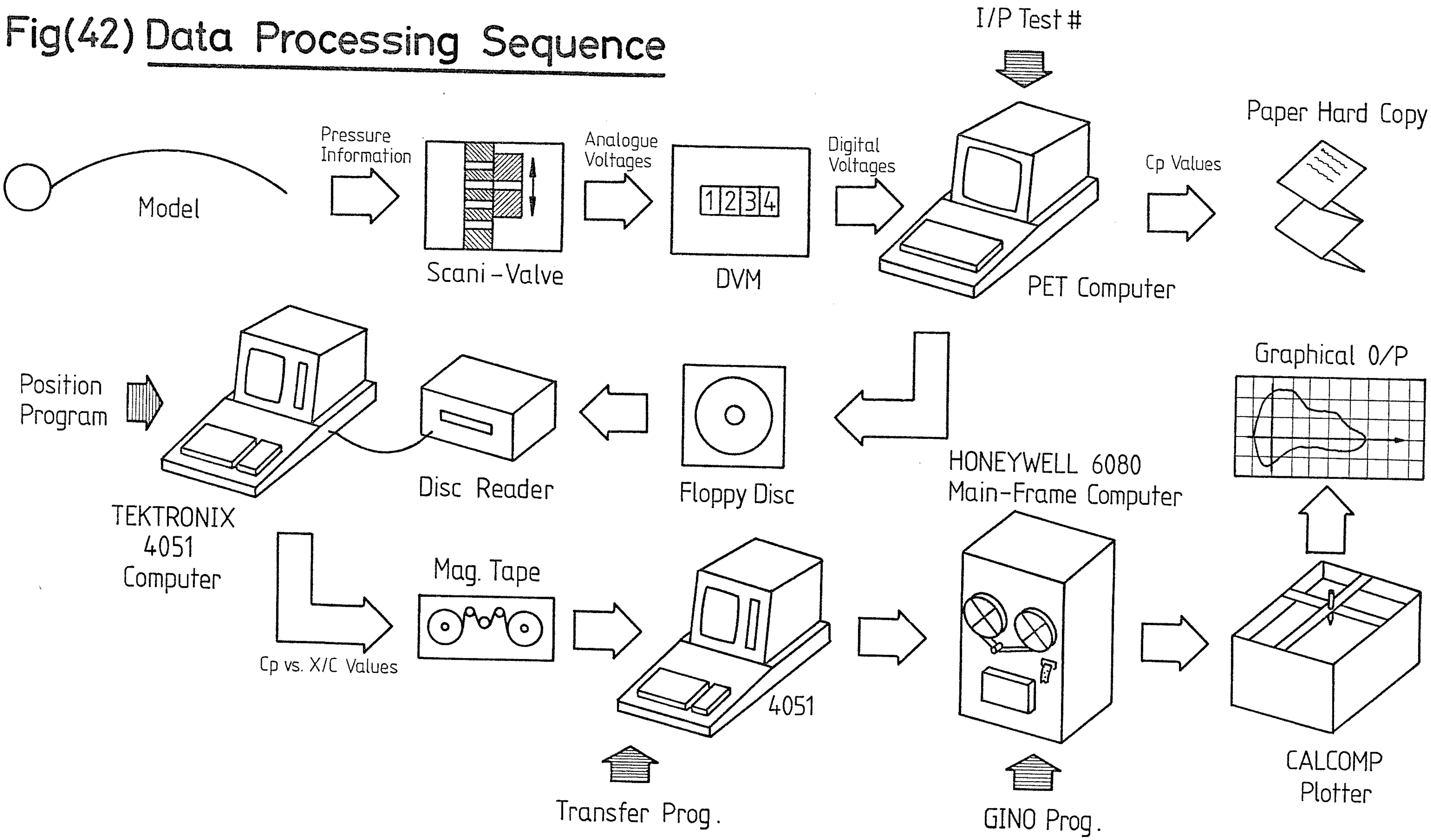

values of local static pressure coefficient (Cp) by dividing the voltage pairs in the computer memory, according to the definition for Cp given in the nomenclature.

The pressure coefficient results were output from the PET in two ways, firstly via a line-printer onto paper, and secondly directly onto a magnetic 'floppy' disc. If after checking the paper hard-copy the pressure coefficients looked correct, the rig parameters were reset to those required for the next test, and the whole scanning sequence restarted.

The data from the 192 tests filled 3 'floppy' discs, converting this information into graphical form suitable for report presentation required a number of further machine steps. The first of these was to provide corresponding position data to go with the values of pressure coefficient.

Pressure coefficient data is conventionally presented with respect to non-dimensionalized position projected onto the chord line (X/c). With the variable-camber-aerofoil the chordwise positions of the pressure tappings were dependant on both shape and camber ratio, similarly the projected chordwise locations of the mast tappings were dependant on diameter and mast angle. This is shown in figure (43).

A computer program was therefore written for a TEKTRONIX 4051 to calculate the required chordwise tapping locations. Built into this program was shape information for the NACA a = 0.8 and 63 aerofoils, plus the position of each tapping along the aerofoil camber (S/Ca), these positions were independant of the mast/sail geometry. Pressure coefficient data for any test was accessed by the TEKTRONIX from the 'floppy' discs by using a disc-reader facility, following this, all information relevant to the test under consideration was input via the keyboard i.e. aerofoil·type, camber ratio, mast diameter/chord ratio, mast angle etc. The TEKTRONIX computer then calculated all

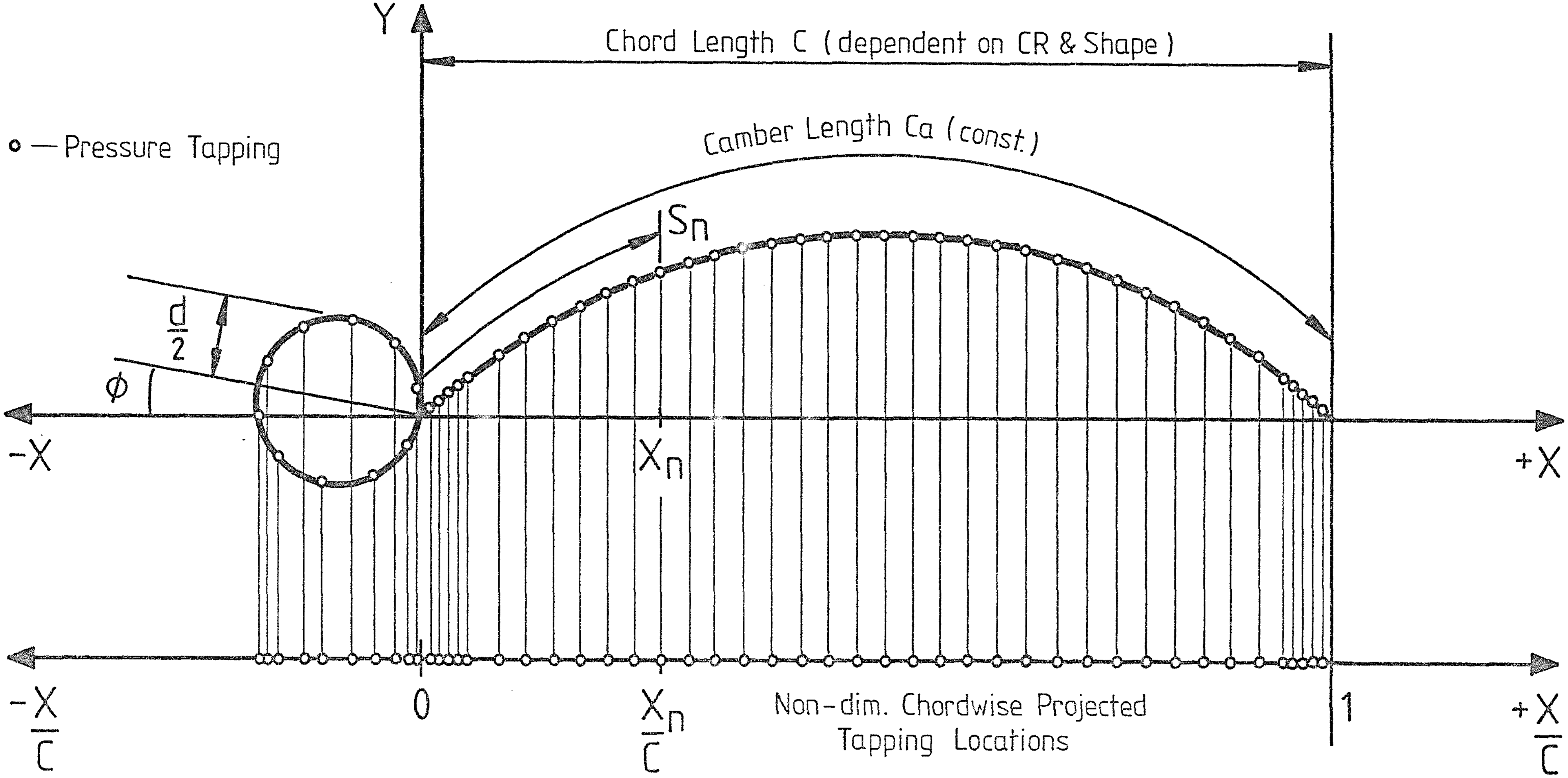

Fig(43) Chordwise Projection of Tapping Locations of the required X/c locations, and formatted these with the corresponding Cp values. These formatted results were output onto a magnetic tape cassette.

The magnetic tape was then used to transfer the experimental data from the TEKTRONIX 4051 to a HONEYWELL 6080 main-frame computer. A GINOGRAF/GINO-F graphics program was written to run on the HONEYWELL using the formatted data. This program enabled the experimental data to be drawn out by a CALCOMP plotter in the form of graphs of Cp against X/c for all 192 test runs.

7.3 Wind Tunnel Boundary Corrections

It is well known that the conditions under which a model is tested in a wind tunnel are not the same as those in free air. Pope (18) states nine quite distinct errors that can be caused by the presence of tunnel lateral boundaries, however only four of these are relevant to 2D testing. These errors are known as : Horizontal Buoyancy, Solid Blocking, Wake Blocking, Stream line Curvature.

The usual way of correcting for such wind tunnel boundary effects is to use the 'method of images'. This involves simulating the aerofoil under test with a combination of mathematical singularities such as sources, vortices or doublets. A second identical model is then placed behind the boundary to be represented. In this way the solid tunnel boundary is simulated by the 'zero' streamline created halfway between the two mathematical models. The effect of the second, or image, model on the aerofoil mathematical model then describes the influence of the tunnel boundary on the real aerofoil under test.

For 2D testing, only the tunnel floor and ceiling have to be represented in this way. Theoretically however, each image model used requires its own image model of opposite sign, such that to represent the tunnel floor and ceiling an infinite number of image models are necessary. Fortunately in practice 3 or 5 models are usually sufficient to produce satisfactory results.

For conventional aerofoils, with little or no separation, the mathematical models necessary to simulate them are relatively simple, but with the present mast/sail combinations the separation regions were found to be very extensive (as will be shown later). Such highly separated conditions are not easy to model mathematically, one attempt at this is described in PART C of the present report, however even this is not entirely accurate and further work is still required.

Because sufficient accuracy from a mathematical model could not be guaranteed, it was decided not to adopt an image technique, but rather to leave the experimental results uncorrected for tunnel boundary effects. It was felt that by presenting the data in its 'raw' state it would be easier for future researchers to apply any new, more accurate correction techniques, without firstly having to remove a previous less precise attempt.

It was however possible to get some idea of the likely error in the present experimental data due to the tunnel boundaries, by applying the approximate methods of Allen and Vincenti.

7.3.1 Horizontal Buoyancy

Almost all wind tunnels with closed throats exhibit a reduction in static pressure along the axis of the test section, this results from the thickening of the wall boundary layers as they progress towards the exit cone.

This pressure variation results in a tendency for the model to be 'drawn' downstream, this in turn produces measured drag values which are slightly too high.

The difference between true and measured drag due to horizontal buoyancy can be expressed as :

$$\Delta D = \Lambda . (\frac{-c^2 \pi}{8}). \frac{dP}{dXX}$$

where c = aerofoil chord length

$\frac{dP}{dXX}$ = static pressure gradient along the tunnel working section center-line.

and Λ is a quantity that depends on aerofoil shape and camber ratio (typically $\Lambda = 0.2 - 0.3$ for CR = 11% - 16% for most aerofoils).

The effect of horizontal buoyancy is usually insignificant for wings, and only becomes important when considering fuselages and nacelles.

i.e. typically : $\frac{\Delta D}{\text{(measured drag)}} \simeq 0.1\%$

for most aerofoils and wind tunnels.

In the light of this, horizontal buoyancy was considered to be negligible in the present series of tests.

7.3.2 Solid Blocking

The presence of a model in a tunnel working section reduces the area through which the air must flow, which by continuity increases the air velocity over the model. This velocity increase, which is usually considered as uniform over most models, is called 'solid blocking'. Its effect is a function of model thickness, camber distribution and overall dimensions.

Thorn (19) presents a simple solid blocking correction as :

$$\varepsilon_{sb} = \frac{r.(\text{Model Volume})}{(\text{Tunnel Working Section Area})^{3/2}}$$

where r = 0.74 for a wing spanning the tunnel breadth
or r = 0.52 for a wing spanning the tunnel height

and

$$\varepsilon_{sb} = \frac{(\text{local velocity corrected for solid blocking})-(\text{measured local velocity})}{(\text{measured local velocity})}$$

The previous equation has been derived with conventionally shaped aerofoils in mind, because of this it was uncertain how to calculate the 'model volume' for the very thin, highly cambered aerofoil shape used in the present experimental programme.

Two alternative approaches were tried, the first of these assumed that the 'model volume' was given by the true volume of material used in construction i.e. aerofoil thickness (0.05 m) x camber length (0.7 m) x span (2.11 m). The second approach assumed that the 'model volume' was given by the volume contained between the camber line and chord line, for an average setting of camber ratio (12.5%) this was given by 0.7 (for a circular arc aerofoil form) x chord length (0.68 m) x maximum Y co-ordinate (0.085 m) x span (2.11 m).

Fortunately both these alternative approaches gave almost identical results i.e.

$$\text{model volume} = 0.08 \text{ m}^3$$

The tunnel working section dimensions were 1.51m (height) x 2.13 m (width).

PLATE 8 - LEADING EDGE VIEW OF AEROFOIL AND SUPPORT FRAME

Note :

(i) Blockage Effect of Aerofoil and Frames.

(ii) Mast Section.

(iii) Working Section cross-sectional Shape

(iv) Light Boxes.

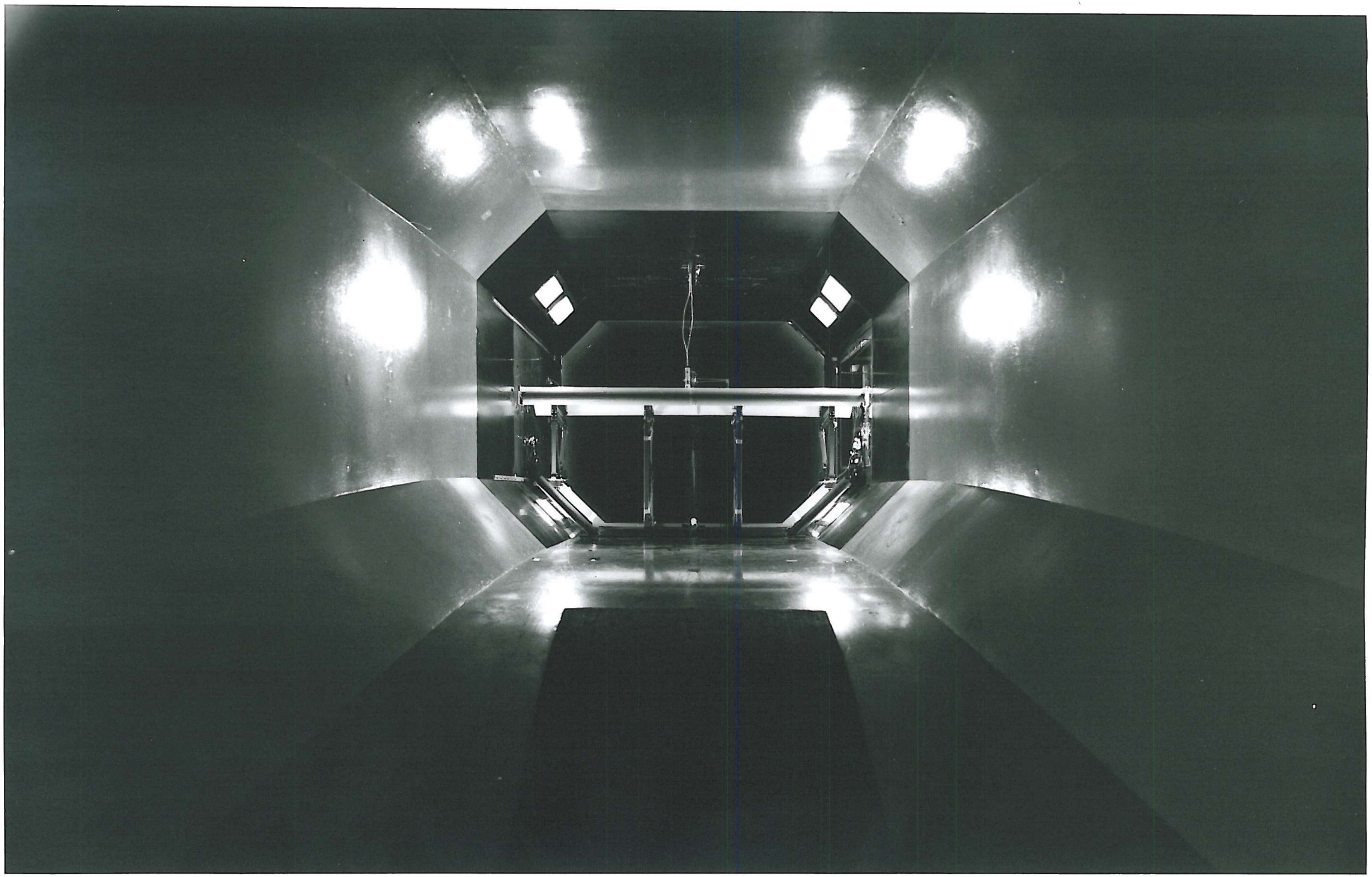

$$\therefore \quad \varepsilon_{sb} = \frac{0.74 \times 0.08}{(2.13 \times 1.51)^{3/2}} \simeq 0.01$$

This implied that, due to solid blocking, the uncorrected local velocities measured in the tunnel around the model were approximately 1% higher than those that would be obtained in an uncontained air-stream.

7.3.3 Wake Blocking

Any body in an air-stream will have a wake behind it which has a mean velocity lower than that in the free-stream. From the law of continuity, the velocity outside the wake in a closed tunnel must be higher than that outside the wake in an unconstrained air-stream in order to preserve a constant volume flow through the working section. This results in a velocity increment over the model.

For wake blocking $\varepsilon_{wb} = \left(\frac{c}{4\,H_i}\right) . \, C_D$

where C = aerofoil chord length
H_i = tunnel working section height
C_D = uncorrected overall drag coefficient

and $\varepsilon_{wb} = \dfrac{\text{(local velocity corrected for wake blocking)} - \text{(measured local velocity)}}{\text{(measured local velocity)}}$

The drag coefficient was not directly measured in the present series of tests, however Milgram (3) has obtained both lift and drag coefficients for typical mast/sail geometries. These results indicate that although the drag coefficient varies with the model and flow parameters, a value of $C_D = 0.3$ is representative for much of the data.

$$\therefore \quad \varepsilon_{wb} = \left(\frac{0.68}{4 \times 1.51}\right) .\ 0.3 \simeq 0.035$$

This implies that due to wake blocking, the local velocities measured in the tunnel around the model were approximately 3.5% higher than those that would have been obtained in an unconstrained air-stream.

7.3.4 Streamline Curvature

The presence of a tunnel ceiling and floor prevents the normal curvature of the free-air that occurs around any lifting body. Because of this, relative to the unconstrained flow case, an aerofoil in a closed wind tunnel appears to have too much lift and pitching moment at a given incidence angle, and indeed, the incidence angle itself is modified.

Lift and pitching moment coefficients were not directly measured in the present test programme, the principal data obtained being static pressure distributions. Fortunately where $(c/H_i) < 0.7$ the effect of streamline curvature on the distribution of lift (and hence pressure) may be neglected ($c/H_i = 0.5$ in the present work).

The error in incidence angle due to streamline curvature is given by :

$$\Delta\alpha \text{ (in degrees)} = \frac{1}{8} . \left(\frac{c}{H_i}\right)^2 . C_L$$

typically from Milgram (3), $C_L = 1.5$

$$\therefore \quad \Delta\alpha = \frac{1}{8} \cdot \left(\frac{0.68}{1.51}\right)^2 .1.5 = 0.04°$$

7.3.5 Combined Effect of Tunnel Boundaries

The complete low-speed wall effects for the wind tunnel tests could be obtained by summing together all of the previously mentioned individual error sources.

For local velocity, the principal errors were due to solid and wake blocking, such that :

$$u = u_m(1 + \varepsilon_{sb} + \varepsilon_{wb})$$

where u = corrected local velocity
u_m = measured local velocity
and ε_{sb} and ε_{wb} are as previously defined.

For the present series of tests, the appropriate total percentage error in local velocity due to the closed tunnel working section was :

$$\left(\frac{u-u_m}{u_m}\right) \text{x } 100 = (\varepsilon_{sb} + \varepsilon_{wb})\text{x}100 = (0.01+0.035)\text{x}100 = 4.5\%$$

Since the effect of solid and wake blocking was basically to speed up the flow over the mast/sail model by approximately 4.5%, then for a given free-stream Reynolds number, the static pressure at any point on the model surface was slightly too low.

Streamline curvature had no effect on local velocity, but did modify the aerodynamic incidence angle. In section 7.3.4 it was shown that the incidence angles quoted in the present results are likely to be approximately 0.04° too low. This represents a 1.6% error with $\alpha = 2.5°$, and a 0.4% error for $\alpha = 10°$ (this, of course, assumes an average lift coefficient of 1.5 in each case).

7.4 Boundary Layer Data Analysis and Presentation Method

When performing boundary layer traverses, the data was initially obtained, via the micromanometer, in the form of two pressure differences $(P_1 - P_2)$ and $(P_2 - P_3)$. These differences were then converted by hand into values of local dynamic pressure Δp, using the calibration graphs and procedures described in section 4.3. It was however felt that automated processing, using polynomial curves fitted to the calibration graphs, would be preferable in future if large amounts of data had to be handled in this way.

For each height in the boundary layer, the ratio of local to free-stream velocity was determined using the following relationship:

Local dynamic pressure (as measured by the yaw probe) $= \Delta p = \frac{1}{2}\rho u^2$

Tunnel free stream dynamic pressure $= \Delta P = \frac{1}{2}\rho U^2$

$$\therefore \frac{u}{U} = \left(\frac{\Delta p}{\Delta P}\right)^{\frac{1}{2}} \qquad 7.1$$

where u = local velocity and U = free-stream velocity.

Each value of local velocity ratio (u/U) obtained while traversing the boundary layer, corresponded to a particular normal distance (y) above the aerofoil surface. The 'mouse' vertical height monitoring system produced an electrical pulse for every 0.022 mm of motion between the aerofoil surface and the underside of the yaw probe. Therefore for any velocity measuring location in the boundary layer, the distance between the aerofoil surface and the probe geometric center (y_g) was simply obtained by multiplying the number of pulses displayed on the control box by 0.022 mm, and then adding to this the tube radius used to construct the probe (0.4 mm)

$$\text{i.e.} \quad y_g = 0.022\ N + 0.4 \qquad \text{———} \qquad 7.2$$

where N is the number of displayed pulses.

When taking measurements in the neighbourhood of a solid surface, where a transverse velocity gradient exists, the velocity observed by the probe is not necessarily located at the probe geometric centre, but is in general displaced slightly from this by an amount Δy.

Therefore for any particular velocity ratio observed in the boundary layer, the corresponding normal height above the surface was given by :

$$y = y_g + \Delta y \qquad \text{———} \qquad 7.3$$

7.4.1 Boundary Layer Height Corrections

Chue (5) states that the error caused by the presence of a shear flow across the mouth of a pitot probe may be due to the following two effects :

(a) the stagnation pressure is proportional to the square of the velocity and when this is integrated over the orifice, it will have a higher value than the stagnation pressure calculated from the square of the velocity at the geometric centre of the orifice.

(b) the presence of the probe in a velocity gradient causes deflection of the stream lines towards the region of lower velocity. This deflection causes the probe to indicate an impact pressure in excess of that existing at the same location in the absence of the probe.

Both these effects cause the probe to read high, or the displacement of the effective from the geometric centre is towards the region of higher velocity.

The error contribution described in (a), known as the 'velocity head displacement effect', has been quantified by Chue by integrating a velocity profile, linearized in the neighbourhood of the probe nose. The result of this integration gave the displacement correction necessary as .021 times the bore diameter (0.5 mm). For the present probe this correction would only have been 0.01 mm, which was considered as negligible.

The error contribution described in (b), known as the 'total pressure gradient displacement effect', has been tackled by a number of researchers.

Young and Maas (20) studied this displacement effect in the wake close to a symmetrical aerofoil. Their results showed that the distance between the geometric and effective centres for a round pitot with its end cut square, and with the inner and outer diameters in the ratio 0.6 (similar to the tubing used for the present yaw probe) was given by :

$$\Delta y = 0.18\ D \qquad \text{———————} \qquad 7.4$$

where D is the outside diameter of the probe tubing.

MacMillan (21), also using square cut, round pitots with diameter ratios of 0.6, looked at the displacement effects in both turbulent pipe and boundary layer flows. His results indicated a relationship:

$$\Delta y = 0.15\ D \qquad \text{———————} \qquad 7.5$$

Finally Livesey (22) investigated the displacement effect in a turbulent boundary layer artificially thickened by a wire screen. Again with square-cut, round pitots with 0.6 diameter ratios, the conclusion reached was :

$$\Delta y = 0.16\ D \qquad \text{———————} \qquad 7.6$$

Equations 7.4, 7.5 and 7.6 have all been obtained using square-cut, round pitot probes, no data could be found for the displacement effects when yaw probes are employed. Quarmby and Das (23) have produced results for a set of rectangular mouthed pitot probes, which gave the displacement effect as 0.19 times the probe minor dimension. This was very similar to the previously stated round probe results, provided that the representative length chosen was always that normal to the surface, and implied that the probe head form has only a minor effect on the displacement correction required.

For very small probes, such as that used in the present test programme, all of the previously quoted equations for the displacement correction Δy, give virtually identical results, and so any of these relationships could have been employed for the present work. However, as pointed out by MacMillan (21), the equations 7.4, 7.5 and 7.6 are only valid when the probe is at a distance from the solid surface of greater than 2D. Within this 2D region above the surface a further correction becomes necessary.

The extra correction was required because of what is known as the 'wall proximity effect', this occurs when the stream lines near the solid surface as displaced outwards as they approach the effective step produced by the presence of the probe. In this way the presence of the wall tends to reduce the displacement of the effective probe centre, i.e. in the opposite sense to that produced by the shear flow.

There would appear to be considerable confusion in the literature concerning the level of influence that the wall proximity actually has. MacMillan describes the wall proximity effect in terms of a velocity correction at various heights above the surface. When this was combined with the influence of shear, MacMillan showed that the total displacement correction necessary within 2D of the wall was not constant, but a function of both Reynolds number and distance above the surface. This is shown in figure (44). The corrections necessary in this region, were less than those required further away from the wall as the shear and proximity displacements tended to cancel each other out.

Davies (24) tested a number of geometrically similar pitot tubes, with the largest almost 16 times the diameter of the smallest. His results, unlike those of MacMillan, indicated no appreciable displacement error, even when the probe was resting on the surface. Possibly for the conditions met in Davies's experiments, the shear and wall proximity effects cancelled each other out completely at each height. this however does seem unlikely.

In contrast, Patel (25) carried out experiments that seem to indicate, beyond any doubt, the existence of a finite value of displacement error for pitot probes close to solid surfaces.

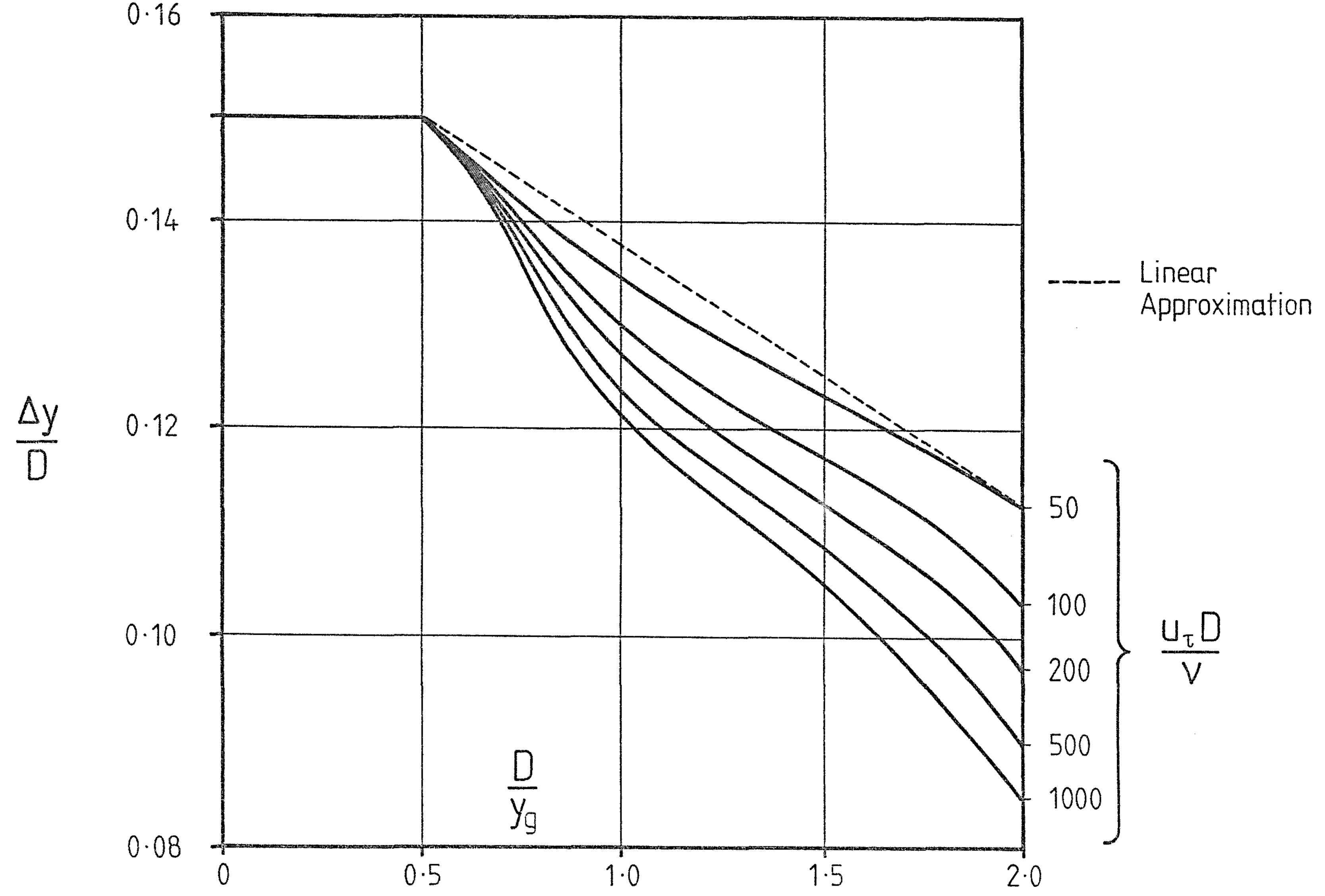

Fig (44) Total Displacement Effect (MacMillan Ref. 21)

For the present series of experiments it was decided to use MacMillan's correction method, since his results formed the most comprehensive data available. To simplify the corrections, the relationship between Δy and y_g shown in figure (44) was fitted with an approximate straight line for the case where $u_\tau D/\nu = 50$ (since, as will be shown later $44 < u_\tau D/\nu < 55$ for the present results). This linearized displacement correction graph is shown in figure (44) also.

The equations of the linearized graph was :

$$\frac{\Delta y}{D} = 0.1625 - 0.025 \left(\frac{D}{y_g}\right) \qquad 7.7$$

For $y_g < 2D$

and
$$\frac{\Delta y}{D} = 0.15 \qquad 7.5$$

For $y_g > 2D$

It was then possible to substitute equations 7.7 and 7.5 into 7.3 to give the corrected probe heights above the aerofoil surface :

$$y = y_g + 0.1625D - \left(\frac{0.025\ D^2}{y_g}\right) \qquad 7.8$$

For $y_g < 2D$

and
$$y = y_g + 0.15D \qquad 7.9$$

For $y_g > 2D$

By using equation 7.2 for y_g and D = 0.8 mm, the above equations 7.8 and 7.9 were used to find the true probe heights corresponding to the velocity ratios obtained.

With these corrected heights, the boundary layer data were initially presented as profiles of u/U against y/c.

Although the flow involved in the turbulent boundary layers tested was basically unsteady, the large lengths of tubing and the micromanometer used caused heavy damping and therefore recorded average quantities. These were however subject to an error arising from the local turbulence intensity. Only fast response instrumentation, such as hot-wire or laser anemometry could have determined the turbulence intensity accurately, thus it was not possible to correct the present data for unsteady flow effects. The readings obtained were however generally very repeatable, as stated in section 6.2.

7.4.2 Boundary Layer Thickness Parameter Determination

Before the thickness parameters could be determined it was necessary to redefine the axes against which the boundary layer profiles had been originally plotted.

Firstly the value of corrected height y corresponding to the point where the velocity ratio reached 99% of its maximum value, had to be determined by 'eye'. This height was known as the 'boundary layer thickness', and was given the symbol δ . The local velocity corresponding to the thickness δ was given the symbol u_δ i.e. the local velocity at the outer edge of the boundary layer.

The boundary layers were then replotted as values of u/u_δ against y/δ. This analysis was also performed for the profiles obtained through the separation regions, although it is arguable whether these results were meaningful. For these separated cases, $y = 0$ was taken at the bounding separation streamline, rather than at the solid surface.

The thickness parameters were defined as :

$$\text{Displacement Thickness } \delta^* = \delta \int_0^1 \left(1 - \frac{u}{u_\delta}\right) d\left(\frac{y}{\delta}\right) \text{———} 7.10$$

Momentum Thickness $$\delta^{**} = \delta \int_0^1 \left(\frac{u}{u_\delta}\right).\left(1 - \frac{u}{u_\delta}\right) d\left(\frac{y}{\delta}\right) \qquad 7.11$$

Shape Factor $$H = \delta^{*}/\delta^{**} \qquad 7.12$$

These thickness parameters were obtained by plotting graphs of $(1 - u/u_\delta)$ against (y/δ), and $(u/u_\delta).(1-u/u_\delta)$ against (y/δ), and mechanically determining the areas beneath these for $0 < y/\delta < 1$ with a planimeter.

As a means of comparison the thickness parameters were also obtained using the approximate equations developed by Garner (26) :

$$\frac{\delta^*}{\delta} = 0.8769 - 0.3370 \left(\frac{u_1}{u_\delta}\right) - 0.5289 \left(\frac{u_2}{u_\delta}\right) \qquad 7.13$$

$$\frac{\delta^{**}}{\delta} = 0.8774 - 0.3302 \left(\frac{u_1}{u_\delta}\right)^2 - 0.5310 \left(\frac{u_2}{u_\delta}\right)^2 - \frac{\delta^*}{\delta} \qquad 7.14$$

where u_1 and u_2 are the local velocities at $(y/\delta) = 0.1468$ and 0.6195 respectively.

These equations were relatively insensitive to errors in the estimate of δ, but were intended for use on fully developed turbulent profiles only.

7.4.3 Determination of the Local Wall Shear Stress

To determine values of local wall shear stress (τ_w), the method described by Rajaratnam (12) was used. He showed that a yaw probe can be used to measure shear stress in the same manner as that demonstrated by Preston (27) with circular pitot tubes. This involved resting the probe against the solid surface at the point where the shear stress was required, and then measuring the local dynamic pressure Δp. Preston identified a unique relationship between two non-dimensional quantities based on the dynamic pressure and the shear stress. i.e.

$$\frac{\Delta p\, D^2}{4\,\rho\nu^2} = f\left(\frac{\tau_w D^2}{4\rho\nu^2}\right) \qquad\text{———— 7.15}$$

Using the governing equations for the yaw probe as given in section 4.3, it can be shown that :

$$\frac{\Delta p\, D^2}{4\,\rho\nu^2} = \frac{(P_2-P_1)D^2}{4\rho\nu^2}\cdot\frac{1}{(K_2-K_1)} = f\left(\frac{\tau_w\, D^2}{4\rho\nu^2}\right) \qquad\text{—— 7.16}$$

Rajaratnam showed that the calibration factors K_1, K_2 and K_3 are the same whether the probe is calibrated in the free stream or close to a solid surface provided that the yaw angle (θ) is less than 10°. Fortunately this condition was always met in the present tests when the probe was resting on the aerofoil surface.

The shear stress was therefore obtained by measuring the pressure difference ($P_2 - P_1$) between the probe tubes, when the probe was touching the aerofoil surface. Using the corresponding values of the calibration factors K_1 and K_2, obtained in the way described in section 4.3, the non-dimensional quantity in the centre of equation 7.16 was calculated. Using this value, the right hand side of equation 7.16 was then obtained from the calibration relationships presented by Patel (25) and Head (28 and 29). Patel describes the functional relationship of equation 7.15 in three distinct regions such that :

$$y^* = \tfrac{1}{2}x^* + 0.037 \text{ for } 0 < x^* < 2.9 \qquad\text{———— 7.17}$$

$$y^* = 0.8287 - 0.1381x^* + 0.1437(x^*)^2 - 0.006(x^*)^3 \text{ for } 2.9 < x^* < 5.6 \qquad\text{———— 7.18}$$

$$x^* = y^* + 2\log_{10}(1.95y^* + 4.10) \text{ for } 5.6 < x^* < 7.6 \qquad\text{———— 7.19}$$

where $y^* = \log_{10} \left(\frac{\tau_w D^2}{4\rho\nu^2} \right)$ and $x^* = \log_{10} \left(\frac{\Delta p D^2}{4\rho\nu^2} \right)$

Quarmby (30) showed that there is very little change in these functional relationships when a rectangular mouthed Preston tube is used instead of a circular type. This suggests that the probe head form is unimportant, and this therefore supports the use of Patel's circular probe relationships for the present yaw probe.

The shear stress obtained by this method was presented as a skin friction coefficient, i.e.

$$Cf = \frac{2\tau_w}{\rho u_\delta^2} \qquad 7.20$$

The Preston tube method of determining the local wall shear stress assumes the existence of a universal inner law or 'law of the wall' common to fully developed boundary layers. Having obtained values of shear stress, the 'law of the wall' was investigated for the attached boundary layers by plotting (u/u_τ) against corresponding values of $\log_{10} (u_\tau y/\nu)$, where u_τ is the friction velocity defined by :

$$u_\tau = \left(\frac{\tau_w}{\rho}\right)^{\frac{1}{2}} \qquad 7.21$$

CHAPTER 8

PRESENTATION AND DISCUSSION OF RESULTS

8.1 General

In addition to areas of attached flow, the experimental results presented in this report confirmed the presence of a number of separation regions around the mast/sail geometries tested. Firstly, a certain amount of trailing edge separation was observed, due to the adverse pressure gradient towards the rear of the aerofoil upper surface. In addition the bluff-body type of wake behind the mast at the leading edge, resulted in the formation of further separation regions over the forward portion of both aerofoil surfaces.

The experimental results obtained, enabled the chordwise extents of these separation regions, and their internal base pressures, to be related to the various model and flow parameters.

8.2 Form of the Static Pressure Distributions

The static pressure distribution results obtained for the NACA $a = 0.8$ and NACA 63 mean-line aerofoils are given in Appendix II and Appendix III respectively.

After studying these, it was found to be possible to describe all of the results obtained by reference to just one universal form of pressure distribution. This could be subdivided into a number of regions, where each indicated the presence of particular flow regimes. In this way it could be shown that all of the apparently different pressure distribution shapes observed during testing, were in fact just forms of this universal distribution, where the model and flow parameters had merely modified the relative lengths and

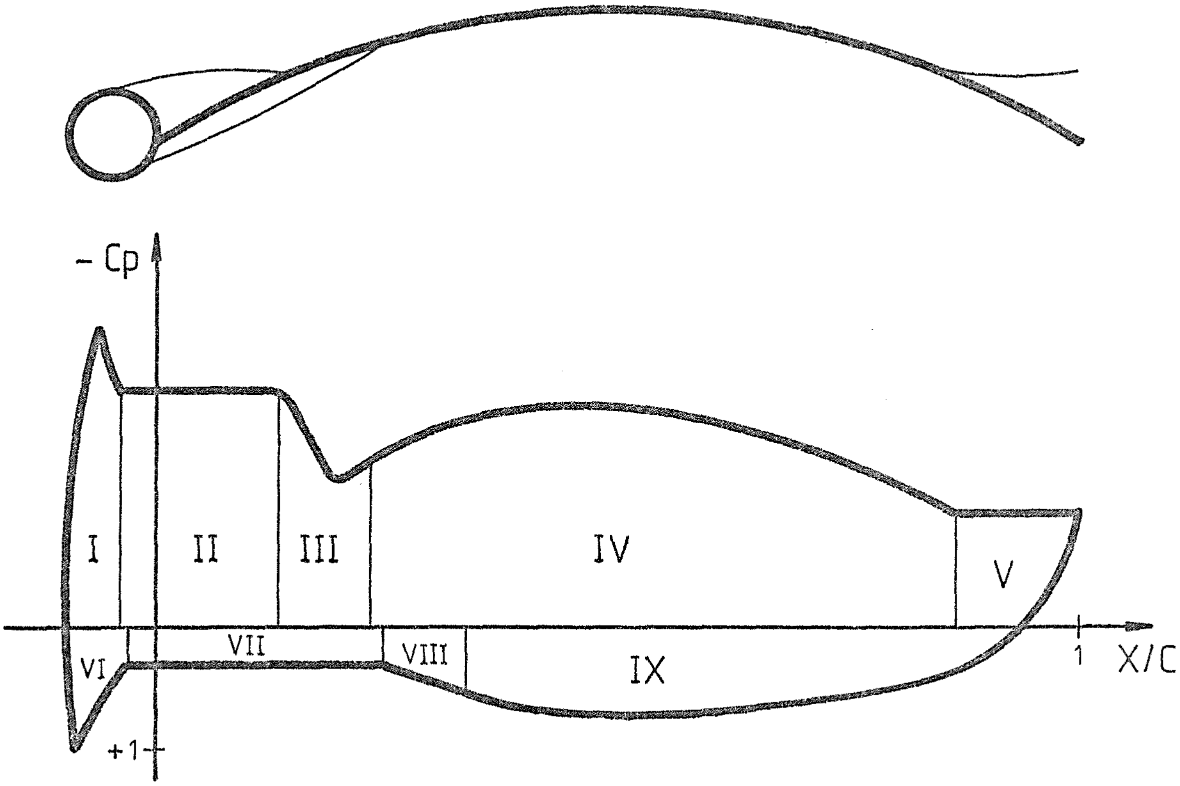

REGION	DESCRIPTION
I	Upper Mast Attached Flow Region
II	Upper Separation Bubble
III	Upper Reattachment Region
IV	Upper Aerofoil Attached Flow Region
V	Trailing Edge Separation Region
VI	Lower Mast Attached Flow Region
VII	Lower Separation Bubble
VIII	Lower Reattachment Region
IX	Lower Aerofoil Attached Flow Region

Fig(45) Universal Pressure Distribution

magnitudes of each region.

The universal pressure distribution form is shown in figure (45), together with the various flow regions involved.

8.2.1 Region I - Upper Mast Attached Flow Region

When the mast/sail model was exposed to a uniform air stream, the flow was initially deflected around the solid contour of the mast, situated at the aerofoil leading edge. In moving around the upper part of the mast in this way, the flow underwent an initial acceleration followed by a retardation. This was reflected on the pressure distributions by the presence of a pressure peak. This feature was not seen on all the test results, but this was put down to a lack of pressure tappings at the precise location of the peak each time, rather than some physical reason why the peak should occur under some conditions whilst being absent on other occasions.

As the flow was accelerated around the mast, the fluid in contact with the solid surface was always at rest due to viscous effects, this resulted in the formation of a steadily thickening boundary layer around the mast upper surface, starting from the forward stagnation point. The surface geometry towards the rear of the mast produced an adverse (positive) pressure gradient acting along the surface contour, in all tests performed, this pressure gradient eventually caused the upper mast boundary layer to detach from the surface and become a 'free shear layer'. This boundary layer detachment or 'separation' point, at the rear of the mast upper surface, marked the end of the attached flow in Region I, and the start of the upper surface bubble, identified by Region II on the universal pressure distribution of figure (45).

8.2.2 Region II - Upper Separation Bubble

On separating from the rear of the mast upper surface, the boundary layer took the form of a free shear layer. This shear layer was then swept away from the mast in the down-stream direction by the general flow. Eventually, due to the combination of the model geometry and flow parameters, a point was reached where the local pressure gradient conditions were again conducive to attached flow. At this point, known as 'reattachment', the free shear layer reverted back to the form of an attached boundary layer, but this time on the upper aerofoil surface rather than the mast.

A line of zero velocity, or 'separation stream line', could then be considered to run between the upper mast separation point and the upper aerofoil reattachment point, following along the lower extremity of the shear layer. A region of fluid was therefore effectively isolated from the rest of the flow by this separation stream line and the mast/sail solid surfaces. This isolated body of fluid was referred to as a 'separation bubble'. The flow inside this upper surface separation bubble was turbulent and highly disturbed, but in terms of time-averaged quantities it was extremely slow moving. Reversed flow was suspected in the bubble, but this could not be confirmed because of the very low mean velocities involved, this is discussed in section 8.4.1.

The extent of the upper surface bubble was observed in each test by the use of wool tufts, when this information was compared with the corresponding static pressure distributions it was revealed that the bubble was always made up of two distinct parts. Over approximately the first 75% of the bubble length, all mast and aerofoil surface pressure tappings under the separation stream line recorded the same pressure. This forward part of the upper surface separation bubble was therefore indicated on the static pressure distributions by a horizontal straight line at the level of this constant 'base-pressure'.

In all cases tested the value of this base-pressure was equal to the static pressure existing on the mast at the point of separation.

The constant base-pressure part of the upper surface separation bubble is shown as Region II on the universal pressure distribution shown in figure (45).

8.2.3 Region III - Upper Reattachment Region

The last 25% of the upper surface bubble was highly influenced by the mechanism of reattachment, this being characterized by a pressure recovery, rather than the constant base-pressure observed over the majority of the bubble length.

This reattachment region was arguably the most interesting, yet most difficult to explain, of all the features observed on the static pressure distributions. Although the reattachment region has been shown on the universal pressure distribution in figure (45) as a sharp pressure rise, the actual shapes observed in this region during testing were extremely variable, ranging from a very severe recovery in test no. 62 to no visible pressure change at all in test no.11.

Although the bubble internal flow was highly complex and dominated by viscous effects, it was found that the influence of the bubble on the surface static pressure, including the recovery at reattachment, could be quite adequately explained by reference to the external flow alone. However, before the external flow around the bubble could be considered in any detail, it was necessary to have some idea of the typical bubble shape.

Although no bubble shapes were measured in the present test programme, some valuable information could be obtained from the work of Gault (31) who has presented shape data for bubbles on a

NACA 663-018 aerofoil. This is shown in figure (46). The bubble observed in Gault's experiments was caused by high leading edge curvature, whilst in the present tests the upper separation bubble was stimulated by the presence of a mast (bluff leading edge obstruction), however it was assumed that the essential features of the bubble shape would be the same in each case. These features were :

(a) Initial separation took place smoothly along a line tangential to the local surface.

(b) A relatively sudden reduction in bubble thickness occurred over approximately the last 25% of its length, with the separation stream line boundary making a large angle to the local surface at the reattachment point ($\simeq$ 70°).

Figure (47) shows this typical bubble shape applied to the present situation of a sail and circular mast combination, this is also compared with the local pressure distribution.

It would seem then that the pressure recovery observed on the pressure distributions for the last 25% of the bubble length, also corresponded to an extremely rapid reduction in bubble thickness over that region. A possible explanation for this is again given by Gault who has shown, using hot wire techniques, that if laminar separation has occurred at Se (in figure 47), the free shear layer around the bubble remains laminar up to the point T (in figure 47). At this point transition begins which results in the development of a spreading fan of turbulence, this re-energises the shear layer and promotes a very rapid reattachment at the highest tolerable level of adverse pressure gradient. Gaster (32) confirms the importance of transition on the mechanism of reattachment, in his work on the structure and behaviour of bubbles.

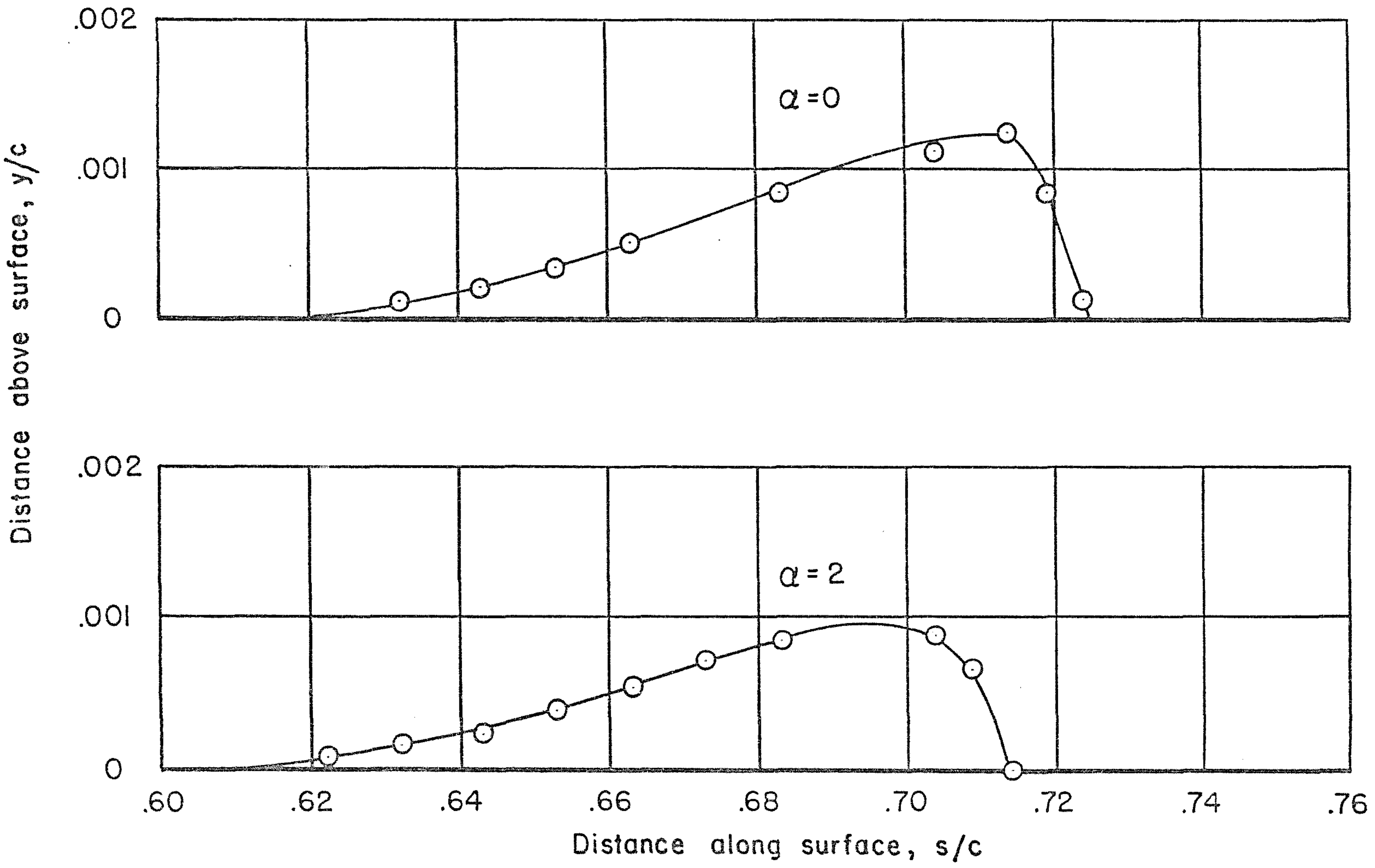

Fig(46) Bubble Shapes Measured on a NACA 66_3-018 Aerofoil (Gault Ref. 31)

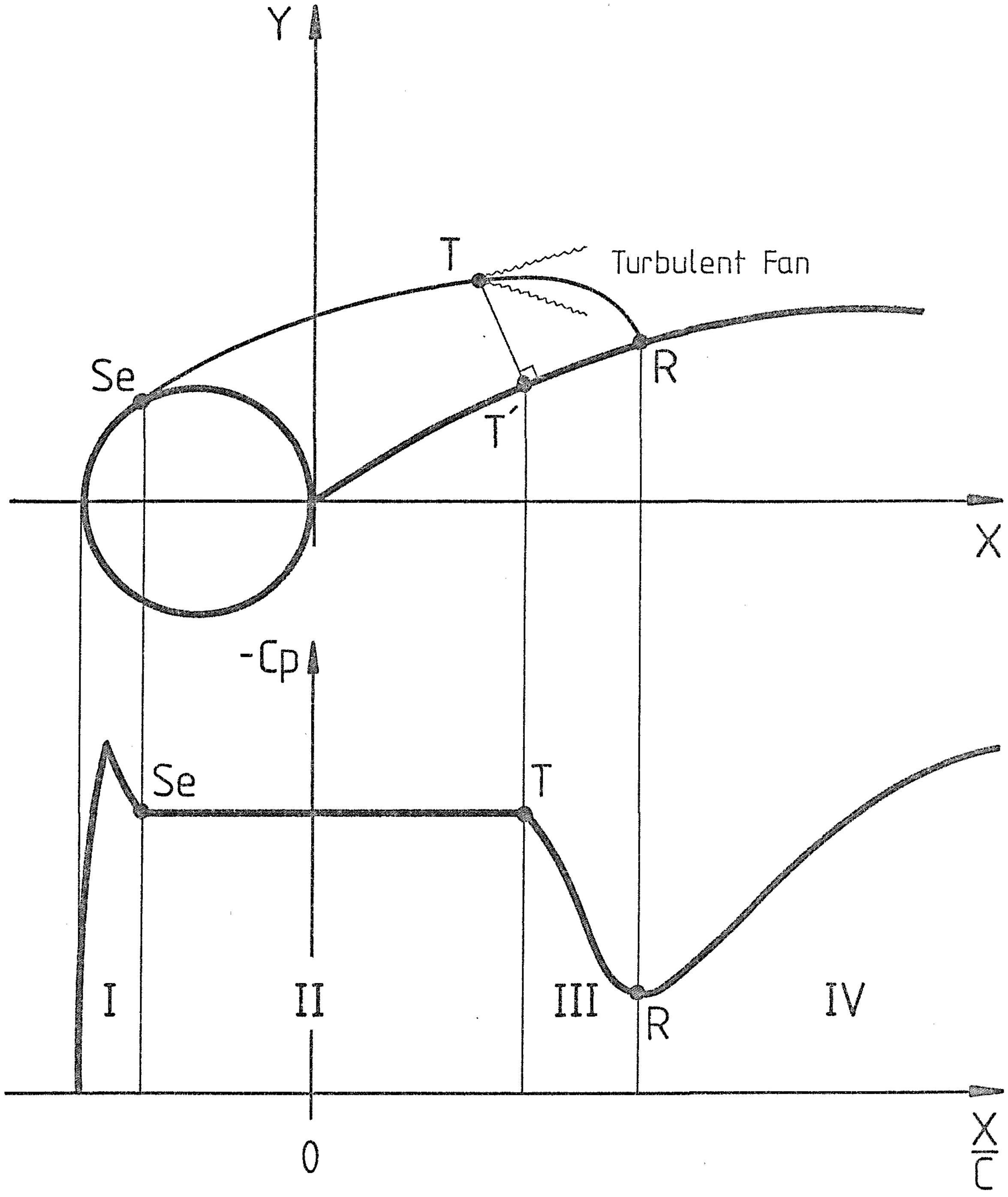

Fig(47) Bubble Geometry and Pressure Comparisons

It was this transition and turbulent mixing process, taking place over approximately the last 25% of the bubble length, that produced the rapid reduction in bubble thickness and the associated pressure recovery in Region III of the pressure distributions. Further evidence to support this transition theory was obtained from the boundary layer data measured, this is discussed fully in section 8.4.2.

Why a pressure recovery should occur over this transition dominated region can be explained in very simple terms by considering the pressures to either side of the region. The pressure just prior to transition at T, and hence the pressure at the surface point T', was equal to the base-pressure in Region II, which as stated in section 8.2.2 was equal to the pressure at the separation point Se i.e. $P_T = P_{T'} = P_{Se}$. The pressure at the surface just following reattachment at R (i.e. P_R) was determined by the local tangential flow velocity. A pressure recovery was therefore expected over Region III equal to the pressure difference $P_R - P_{T'}$ (or $P_R - P_{Se}$).

The magnitude of the pressure recovery varied greatly between tests because of the relative differences between the pressures existing at separation and reattachment in each case. These pressures were influenced by many factors such as surface roughness and free stream turbulence, as well as by the particular model and flow parameter settings.

Crabtree (33) devised a non-dimensional parameter to describe the degree of pressure recovery at the end of separation bubbles, by considering the outer flow around the bubble from T to R as similar to a divergent nozzle flow. This parameter, called the 'pressure recovery coefficient' was defined as :

$$\sigma = \frac{(P_R - P_T)}{\frac{1}{2}\rho u_T^2} = \frac{(Cp_R - Cp_{se})}{(1-Cp_{se})} \qquad \text{———————} \quad 8.1$$

This parameter can vary between 0 and 0.5, increasing with the severity of the pressure rise, a typical value being 0.35. The tables in Appendix IV present data obtained from all the tests performed, including separation, transition and reattachment locations together with the corresponding values of σ.

As pointed out by Roshko (34), it is difficult to predict values of σ for given model and flow parameters because of its likely dependence on many unknown factors, however it was possible to predict general trends in the maximum reattachment pressure P_R. The maximum reattachment pressure was to a large extent governed by the local tangential flow velocity, which itself was related in a crude way to the angle between the local surface and the bubble boundary at reattachment. this angle was called the 'reattachment surface angle' (η).

Consider a highly simplified case where the separation stream line around the bubble is a straight line parallel to the free-stream as shown in figure (48). If in this case the incidence angle is increased, whilst leaving all other model parameters unchanged, it can be seen in figure (48a) that the angle η is reduced (and the reattachment point moves downstream slightly). This implies a reduction in the value of P_R with increasing incidence angle. Despite the simple form of this bubble model, the trend of falling P_R with increasing incidence angle was confirmed in the present experimental programme by test nos. 62, 63, 68 and 71. Similarly, as shown in figure (48b), the effect of increasing camber ratio alone on the simple model was to increase the angle η, and hence increase P_R. Again this trend was shown to be correct by test nos. 62, 86 and 98. Finally, decreasing the mast size should increase the angle η, as shown in figure (48c), and produce a rise in P_R. Test nos 38, 50 and 62 demonstrate that this was also the trend in the experimental data obtained.

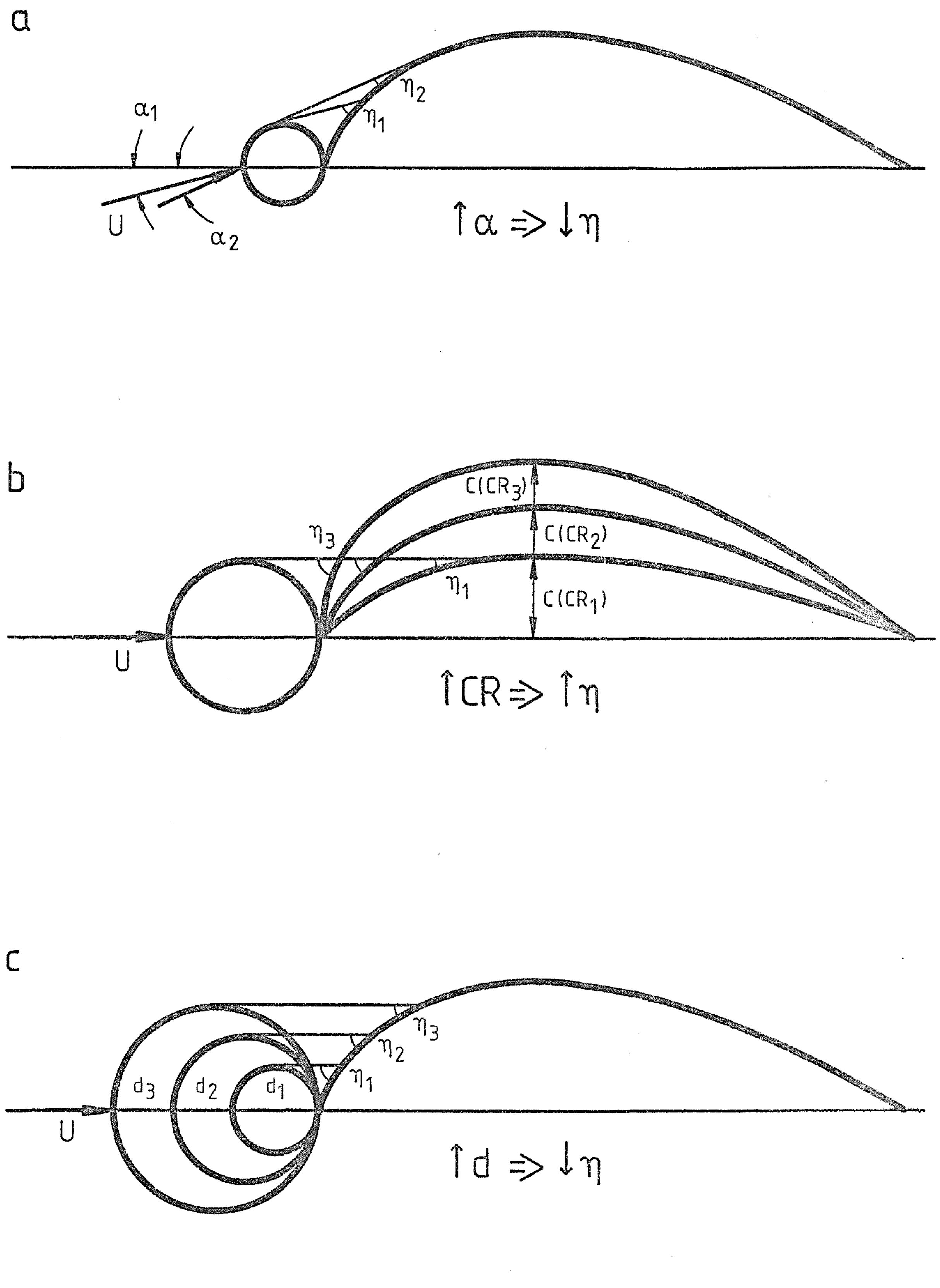

Fig(48) Effect of Parameter Changes on "η"

It would seem then, that it is possible to predict trends in the value of the reattachment pressure P_R by considering the effect of a parameter change on the reattachment angle η .

8.2.4 Region IV - Upper Aerofoil Attached Flow Region

Following reattachment in Region III, the flow was accelerated around the upper surface of the aerofoil, this is shown on the universal pressure distribution in figure (45) as a characteristic domed shape representing the lift producing low pressure in this Region IV.

The flow over the aerofoil remained attached to the surface, with a steadily growing turbulent boundary layer, until the adverse pressure gradient conditions existing towards the aerofoil trailing edge finally produced separation once again.

8.2.5 Region V - Trailing Edge Separation Region

As the attached flow moved over the aerofoil upper surface it came under the influence of an external pressure which increased with distance along the surface. The effect of this adverse pressure gradient was to produce a compensating loss of kinetic energy, and therefore velocity, in the boundary layer. Eventually a stage was reached where the fluid adjacent to the surface was on the point of reversing its flow direction. This was called the point of trailing edge separation, and marked the beginning of Region V on the universal pressure distribution.

At separation the boundary layer became detached from the surface to become a free shear layer, in the same manner as observed on the mast. A line of zero velocity or 'separation stream line' could again be considered to run along the lower extremity of this shear layer. All the fluid flow in between the separation stream line and the aerofoil surface was highly disturbed and possibly reversed, although no reversed flow could be detected by the yaw probe.

The static pressures observed along the aerofoil surface after separation were all the same, and equal to that at the point of separation. This 'base pressure' was represented by a horizontal straight line in Region V of the universal pressure distribution in figure (45).

8.2.6 Region VI - Lower Mast Attached Flow Region

The regions observed over the lower surface of the mast and aerofoil were very similar to those encountered on the upper surfaces.

In a similar way to Region I, some of the oncoming air stream was initially deflected around the lower surface contour of the mast. In contrast to the upper surface flow, the fluid taking this lower route, was firstly decelerated before gaining velocity again towards the rear of the mast. This velocity variation was reflected on all of the static pressure distribution results by a sharp peak extending into the positive side of the coefficient axis, thus indicating static pressures higher than that in the undisturbed free-stream.

As can be seen quite clearly on virtually all the experimental pressure distributions, the maximum value of pressure coefficient obtained under these lower mast peak conditions was Cp = 1, this represented the forward stagnation point. A pressure coefficient of unity implied a local surface pressure equal to the total pressure of the flow, or alternatively, at this stagnation point the impinging flow was brought to rest.

8.2.7 Region VII - Lower Separation Bubble

In an identical way to that described in Region II, the flow over the mast lower surface was forced to separate from the rear of the mast due to the large adverse pressure gradient in that area. Again conditions downstream eventually became conducive to reattachment, the separation stream line then enclosed another bubble flow region behind the mast, but this time on the lower aerofoil surface.

Just like the upper surface bubble, all pressure tappings within approximately the first 75% of the lower bubble length recorded an identical base pressure. This is represented by the horizontal straight line in Region VII of the universal pressure distribution.

The relative lengths of the upper and lower surface bubbles varied with the model and flow parameters, but all three length combinations were encountered i.e. upper bubble length >, < or = lower bubble length.

8.2.8 Region VIII - Lower Reattachment Region

It was concluded in section 8.2.3 that the surface pressure could rise quite steeply at the bubble reattachment point due to the deceleration and turbulent mixing suffered by the flow following transition and boundary layer reenergisation. The maximum reattachment pressure P_R, was also shown to be related to the reattachment surface angle η.

This pressure recovery could be easily seen on the upper surface pressure distributions, since the deceleration at reattachment was immediately followed by an acceleration around the convex aerofoil surface, thus producing a characteristic dip in the pressure distributions. The pressure recovery at reattachment was not as obvious for the lower surface for two main reasons. Firstly, because of the aerofoil geometry and the positive nature of the mast angle (ϕ), the reattachment surface angle η was always relatively small, thus minimizing the flow deceleration. Secondly, the reattachment deceleration on the lower surface was followed by a further deceleration of the attached flow over the concave lower aerofoil surface. The net effect of these two conditions was that the reattachment region was indicated on the static pressure distributions by just a steady rise in pressure which linked the bubble base-pressure to the developed attached flow pressure. This is shown as Region VIII in figure (45).

8.2.9 Region IX - Lower Aerofoil Attached Flow Region

Following reattachment the flow remained attached over the whole of the remaining lower aerofoil surface. There was no trailing edge separation present since the pressure gradient was always favourable. The pressure distribution in this Region IX was of a characteristic domed shape which projected into the positive part of the Cp axis. This represented a general retardation of the flow.

At the extreme point of the trailing edge, the upper and lower surface flows met. Since it was not possible for a fluid to support an instantaneous pressure change, the pressure on the lower surface tended to decrease as the trailing edge was approached. This steady reduction of the lower surface pressure towards the rear of the aerofoil, finally resulted in the upper and lower surface pressures being identical at the point of the trailing edge, and equal to the base-pressure within the trailing edge separation region, i.e. Region V.

8.3 Effect of Model and Flow Parameters on the Static Pressure Distributions

Having identified each of the fundamental regions that comprised all the pressure distributions, it was then possible to look at the way in which these regions were influenced by the various model and flow parameters.

8.3.1 Effect of Reynolds Number

Generally the shapes of the pressure distributions were independent of Reynolds number over the ranges tested. There were however two exceptions to this.

Firstly, the Reynolds number test range chosen to represent flows over the head region of sails, was from 200 000 to 1000 000, however when the tunnel was run to simulate the lower limit of this, the results obtained were highly scattered, this can be seen in test nos 13, 16, 19 and 22. The reason for this scatter was not clear, one possible explanation was that to achieve this low Reynolds number the tunnel had to be run at an extremely low speed, in fact very close to its lower limit. This may have resulted in a non-uniform air-stream through the tunnel working section, involving the presence of large scale gusts. Alternatively, a Reynolds number of 200 000 might well have involved unusual flow physics, where very large, slow moving eddies were shed from the mast.

In order to obtain more usable results, the Reynolds number test range for the sail head region was raised to 350 000 - 1000 000 after test no.22. The results obtained with the new lower limit of this range no longer showed any appreciable scatter, and the pressure distribution shapes observed were similar to the universal form shown in figure (45). It was felt that a Reynolds number of 350 000 was still a reasonably representative value for simulating low speed flows over the head region of sails.

The only other Reynolds number effect present was noticed during those experiments which involved the largest mast, the lowest values of camber ratio, and the highest settings of incidence angle, all acting together i.e. test nos. 46, 47 and 48, test nos. 139, 140, 141, and test nos. 142, 143, 144. It will be seen from these that with Reynolds numbers of 350 000 and 600 000 the separated flow from the mast did not reattach, such that the whole of the aerofoil surface remained entirely separated. However when the Reynolds number was increased to 1000000 the higher energy of the flow enabled reattachment to be completed successfully. The precise mechanism involved in this reattachment only at high Reynolds number remains in question. Possibly the higher flow velocity might have aided the turbulent mixing process, and hence entrainment of energy from the free-stream into the reattaching shear layer. This might then have allowed reattachment at a higher level of adverse pressure gradient than was possible at lower values of Reynolds number.

8.3.2 Effect of Incidence Angle

To help visualize the effect of incidence angle without it being necessary to refer to a number of different results pages, several NACA a = 0.8 upper surface pressure distributions have been correlated together into the form of 3-dimensional surface plots.

The effect of incidence angle is therefore clearly described in figures (49), (50) and (51), one plot being presented for each of the three mast sizes tested. The case of Re = 1000 000 and C_R = 12.5% was chosen for these plots, since this parameter combination was common to all three parts of the sail shown in figure (40).

It was found that changes in incidence angle affected all of the pressure distribution regions to some extent, but that the general effect on any particular region was independant of mast size.

Within the upper surface bubble (Region II), the base-pressure fell with increasing incidence angle for all three masts, the rate of this decrease did however appear to be reduced with a growth in mast size. The length of Region II only increased slightly with a rise in incidence angle.

The maximum pressure at reattachment (P_R) in Region III fell with increasing incidence angle, this was consistent with a decreasing reattachment surface angle (η) as described in section 8.2.3.

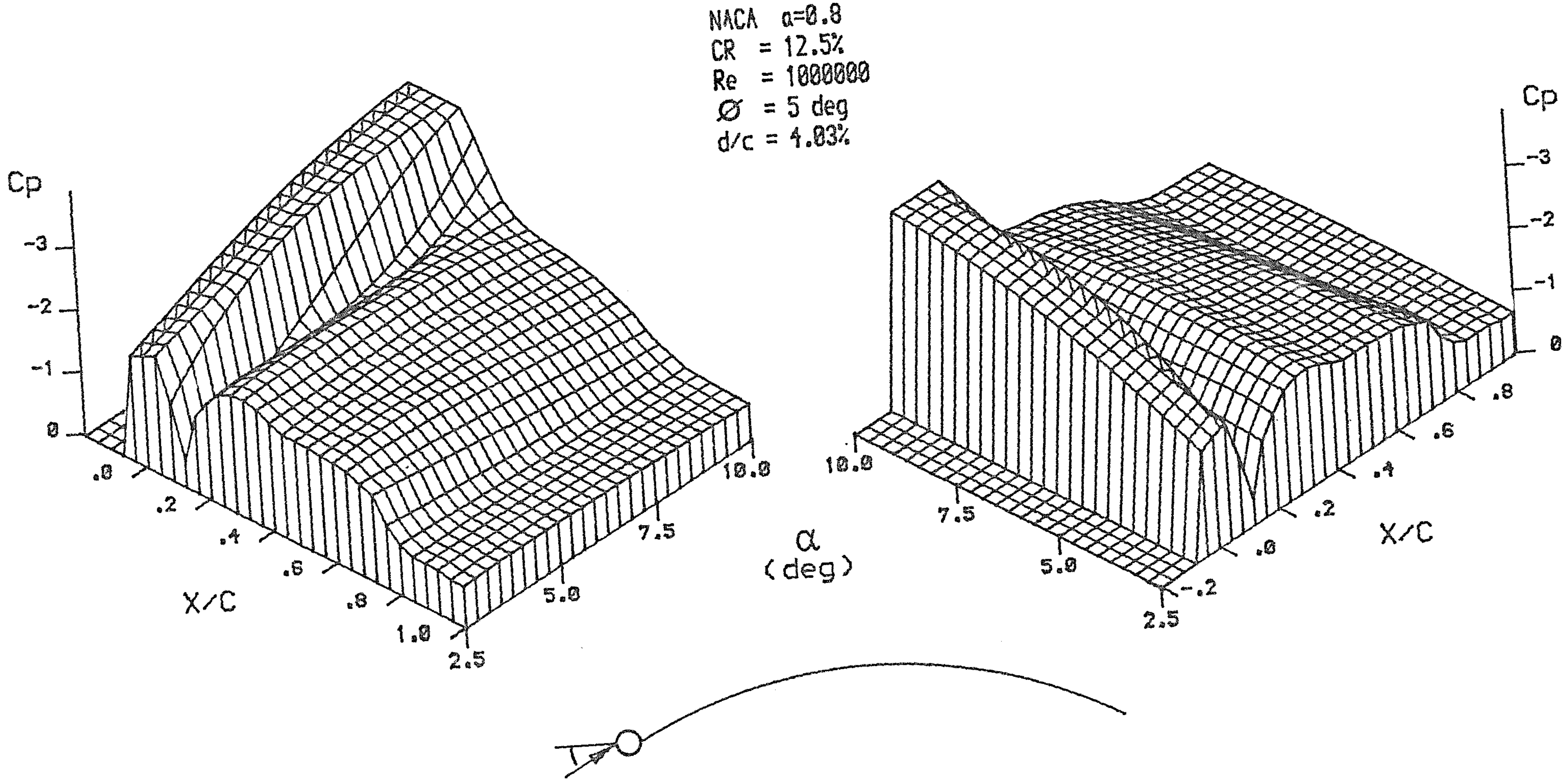

Fig(49) Evolution of Static Pressure Distribution with Changing Incidence Angle

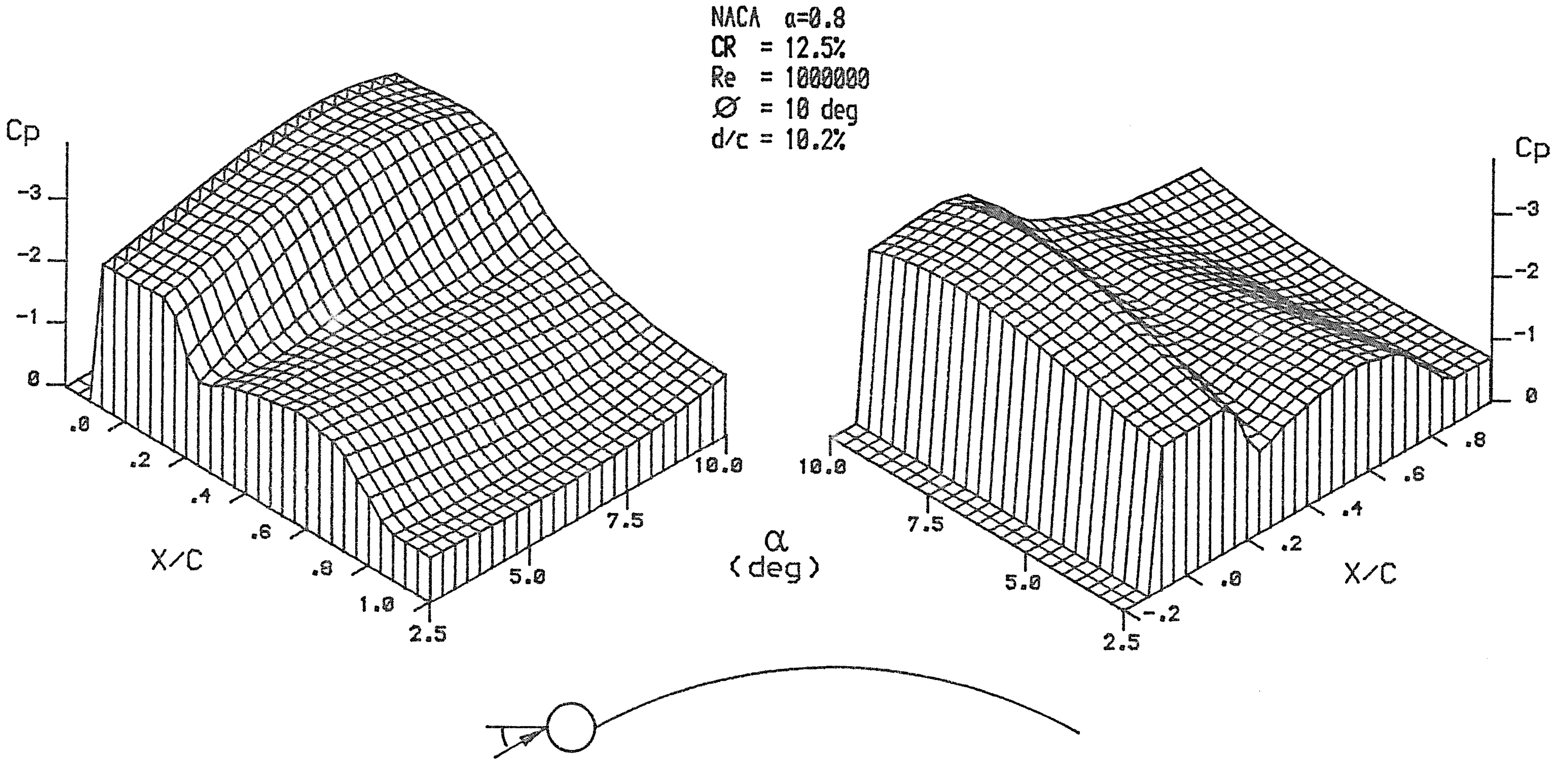

Fig(50) Evolution of Static Pressure Distribution with Changing Incidence Angle

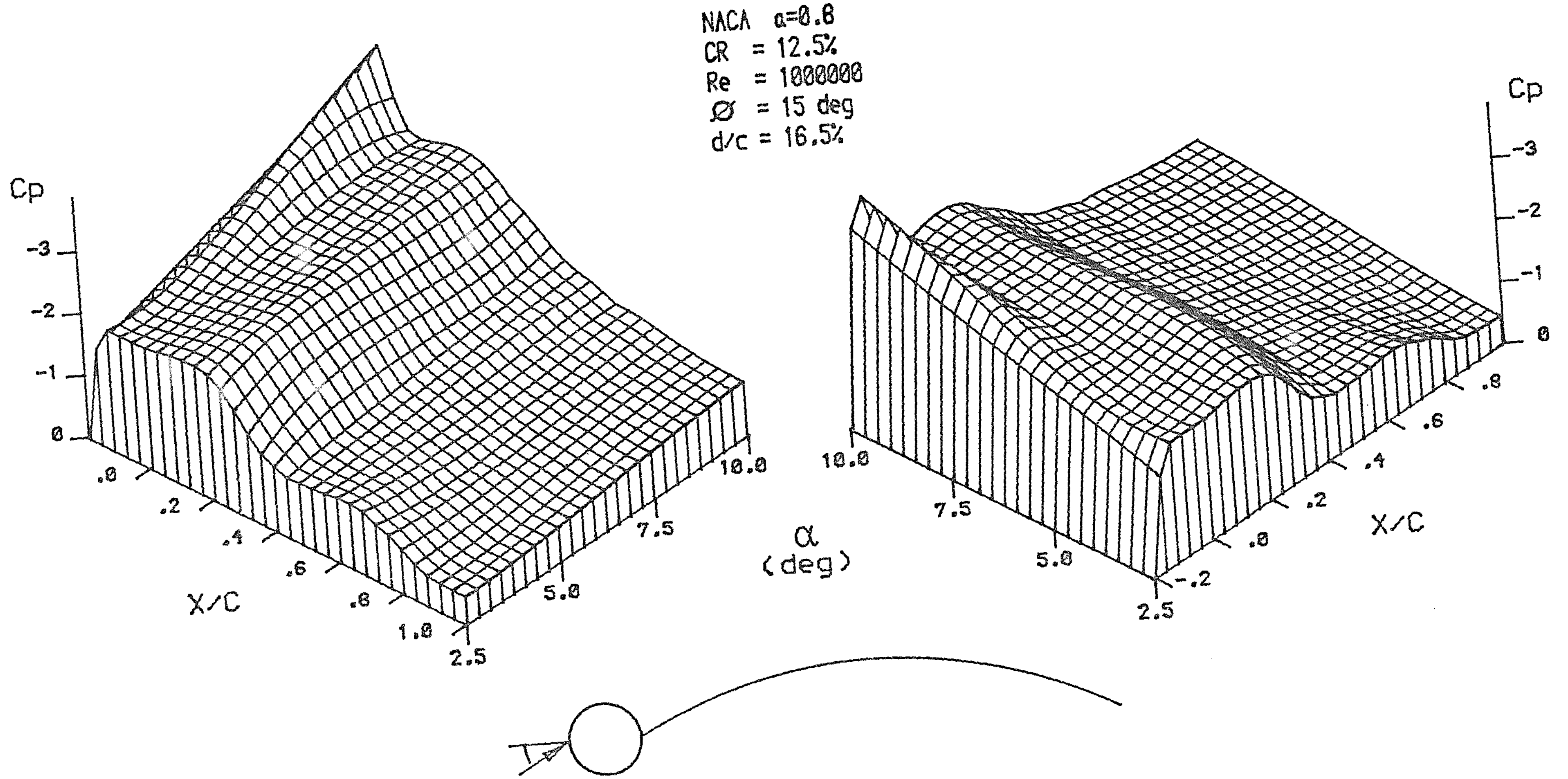

Fig(51) Evolution of Static Pressure Distribution with Changing Incidence Angle

The characteristic suction dome of the upper attached flow region (Region IV) became flatter with an increase in incidence angle. This was to be expected since at higher incidence angles the forward portion of the aerofoil became more aligned with the oncoming free-stream, and thus less acceleration resulted over the upper surface.

The trailing edge separation region (Region V) became more extensive with increasing incidence angle as the separation point advanced towards the leading edge. The base-pressure within this region fell slightly with a rise in incidence angle, this being more obvious with the medium and large size masts.

Although not shown on the surface plots, it was also found that the lower surface bubble (Region VII) was reduced in length with increasing incidence angle i.e. test nos. 61, 64, 67 and 70.

8.3.3 Effect of Mast Size

By considering corresponding planes of constant incidence angle from each of the figures (49), (50) and (51), the effect of mast size can be seen. The changes shown are, of course, not just as a consequence of mast size, but also of mast angle (ϕ) since this was reset for each mast tested. These mast size and angle combinations were, however, representative of those encountered on real sails, it would be unusual in practice to have an increasing mast diameter/chord ratio up a mainsail without an associated increase in mast angle due to sail twist.

Increasing the mast size and angle produced a growth in length of the upper surface constant pressure bubble (Region II), not only over the now larger chordwise expanse of the mast, but also over the forward portion of the sail.

As a consequence of this increase in bubble length, the location of the reattachment pressure rise (Region III) tended to move towards the trailing edge with increasing mast size and angle. In addition the maximum reattachment pressure (P_R) became significantly less with increasing mast size, again this was consistent with a reduction in reattachment surface angle (η) as described in section 8.2.3.

Finally a rise in mast size and angle tended to suppress the attached flow suction dome (Region IV), and reduce the length of the trailing edge separation region (Region V).

8.3.4 Effect of Camber Ratio

Again a number of the pressure distribution results have been presented together in the form of surface plots, but this time with camber ratio as the varying parameter, these are shown in figures (52) and (53).

With the small mast ($d/c = 4.01\%$), the range of camber ratios tested was from $C_R = 7.5\%$ to 12.5%, this increase in camber ratio caused a slight rise in base-pressure within Region II, and produced a small reduction in the bubble length.

With the medium mast ($d/c = 10.2\%$), where the camber ratio was increased from $C_R = 10\%$ to 15%, no change in base-pressure or length was observed for the constant pressure upper surface bubble (Region II) over this camber ratio range.

All other pressure distribution regions were similarly affected by increases in camber ratio, despite the range of values tested or the mast size involved. With increasing camber ratio the maximum reattachment pressure (P_R) in Region III became greater, and the attached flow suction dome in Region IV increased in fullness. Finally, the extent of the trailing edge separation region (Region V) grew with

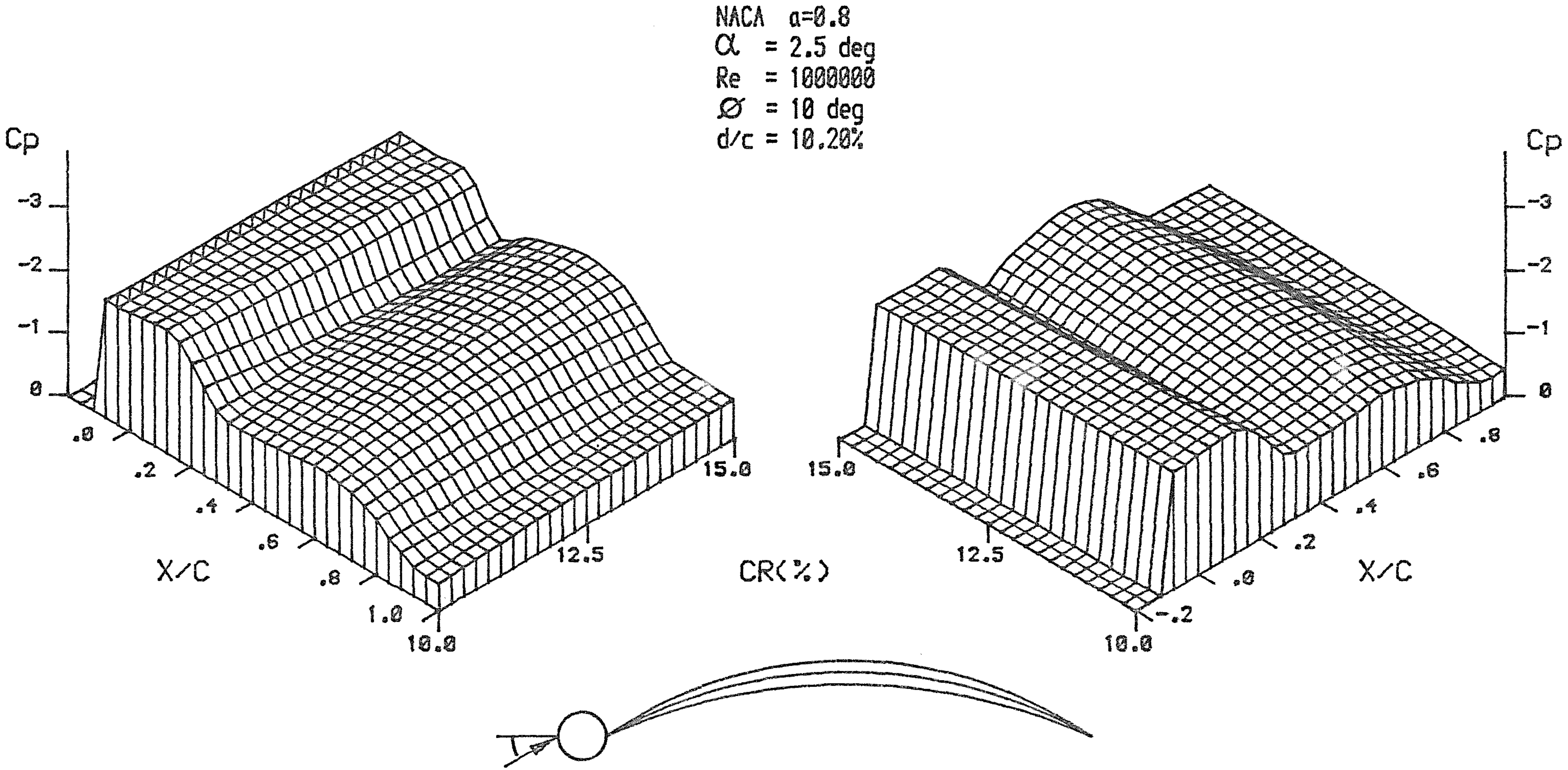

Fig(52) Evolution of Static Pressure Distribution with Changing Camber Ratio

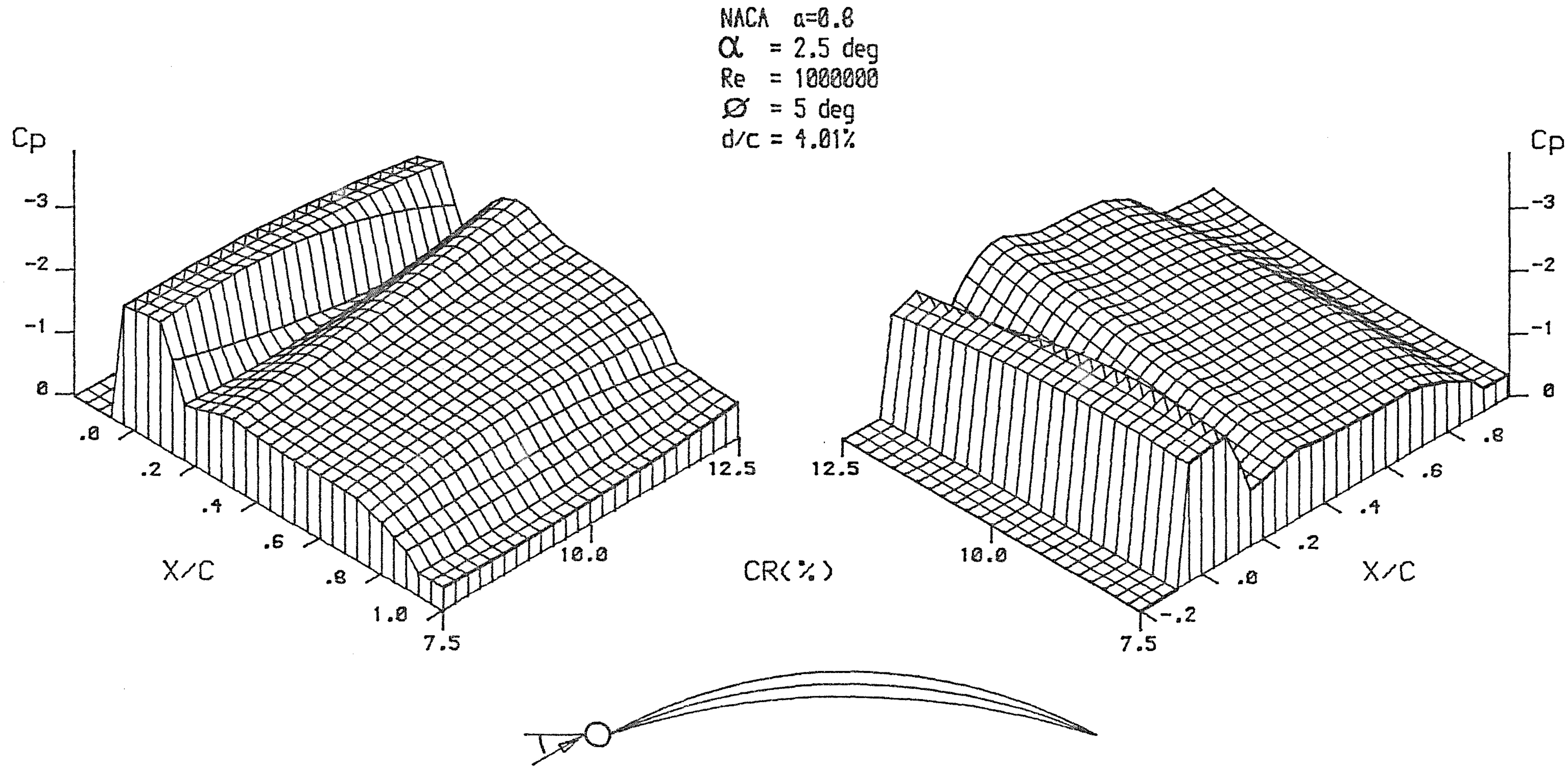

Fig(53) Evolution of Static Pressure Distribution with Changing Camber Ratio increasing camber ratio, whilst the base-pressure was reduced.

8.3.5 Effect of Aerofoil Shape

The results of tests on the NACA 63 mean-line aerofoil are presented in Appendix III. No 3-dimensional surface plots have been compiled from this data, but generally the NACA 63 and NACA a = 0.8 aerofoil shapes responded in a similar way to changes in the various model and flow parameters.

With the NACA 63 aerofoil, the point of minimum pressure within the upper attached flow dome of Region IV always occurred further forward than with the NACA a = 0.8 shape. The length and base-pressure of the upper surface bubble (Region II), however, remained unaltered by the change in aerofoil shape, i.e. test nos. (50) and (146).

Finally the lower surface bubble (Region VII) was generally slightly larger with the NACA 63 aerofoil, whilst its base-pressure was largely unaffected by aerofoil shape. This result was to be expected since the base-pressure was dependent on the mast pressure at separation, whilst the bubble length was determined by aerofoil geometry for any given set of flow parameters.

8.3.6 Pressure Distributions of Special Interest

Amongst the 192 pressure distribution results were several cases of special interest. These essentially involved examples showing extreme conditions within the various flow regions.

Consider the upper surface constant pressure bubble (Region II), the shortest example of this was obtained in test no. 62, i.e. with the smallest mast (d/c = 4%), at the lowest incidence angle (α = 2.5 deg), and with the maximum camber ratio (CR = 12.5%). The longest example of Region II was obtained in test no. 47 when all of the parameters were set to their opposite extreme values. In this latter case the separated flow from the mast upper surface failed to reattach, such that the bubble extended over the entire upper aerofoil surface. An equally valid interpretation in this case was that the trailing edge separation point had advanced forward to be coincident with the mast separation point.

Test nos. 142 and 179 are also examples of the aerofoil upper surface seeming to be entirely separated, but in these two cases the base-pressures corresponding to the upper surface bubble (Region II) and the trailing edge separation region (Region V) were different. Since the base-pressure in any separation region was always equal to the pressure at the point of separation, it is clear that some reattachment of the upper surface bubble must have occurred in test no. 179. It is likely that in test no. 179 this bubble reattachment was immediately followed by further separation. Because of the slight deceleration suffered by the flow at this reattachment, the pressure at separation, and hence that in the trailing edge separation region, was slightly higher than that in the upper surface bubble.

Test no. 142, however, showed a pressure decrease between the two base-pressures, this change being extremely sudden. No set of flow conditions could be envisaged that would result in such an instantaneous pressure drop between Regions II and V, so this feature, which was unique to test no. 142, was attributed to some form of measuring system malfunction.

The length of the lower surface bubble (Region VII) also varied greatly which changes in the various model and flow parameters. In test no. 2 the lower surface bubble failed to reattach, leaving the whole of the aerofoil lower surface separated. This fully separated case occurred with the maximum size mast (d/c = 17%), the largest camber ratio (17.5%), and at the lowest incidence angle (2.5°).

With these parameters set to their opposite extreme values, in test no. 107, the lower surface bubble was virtually non-existent.

8.4 Boundary Layer Traverse Results - General Descriptions

The results of the boundary layer traverses performed, together with their corresponding spanwise locations are shown in figure (54). Five velocity profiles were obtained in all, each will be discussed in the following sections.

The spanwise locations of the traverses are also shown relative to the static pressure distribution in figure (55).

8.4.1 Traverse Location ① - (Upper Surface Bubble)

This first traverse was performed close behind the mast at a location within the upper bubble region as indicated at the time of testing by the wool tufts. It can be seen from figure (55) that this traverse passed through the constant base-pressure region (Region II) on the corresponding pressure distribution.

Although the wool tufts quite clearly indicated the presence of reversed flow by pointing towards the mast (in an agitated manner), the yaw probe was unable to detect any velocities in either the upstream or downstream directions. This result was surprising since the micromanometer was capable of measuring differences between the tubes of the yaw probe as low as 0.002 mm H_2O. Despite this reading accuracy, zero pressure differences were obtained between the yaw probe tubes when within the upper bubble region whatever the probe orientation. This result was confirmed by a repeat traverse on a different day.

Seetharam (9) has carried out a detailed experimental investigation of flows around separated aerofoils, using both wool tufts and boundary

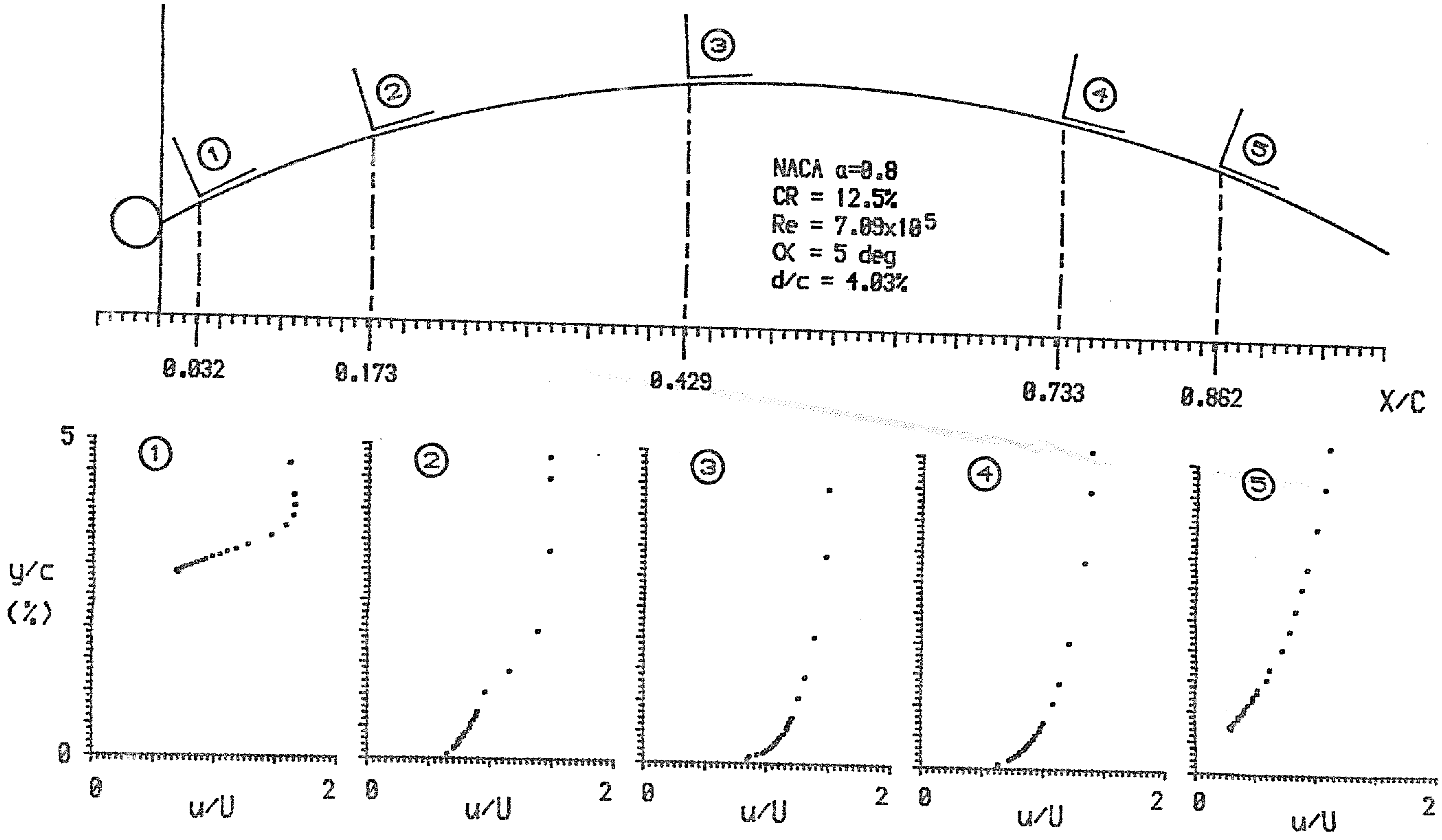

Fig(54) Boundary Layer Velocity Profiles

NACA a=0.8
CR = 12.5%
Re = 709000
α = 5 deg
d/c = 4.03%

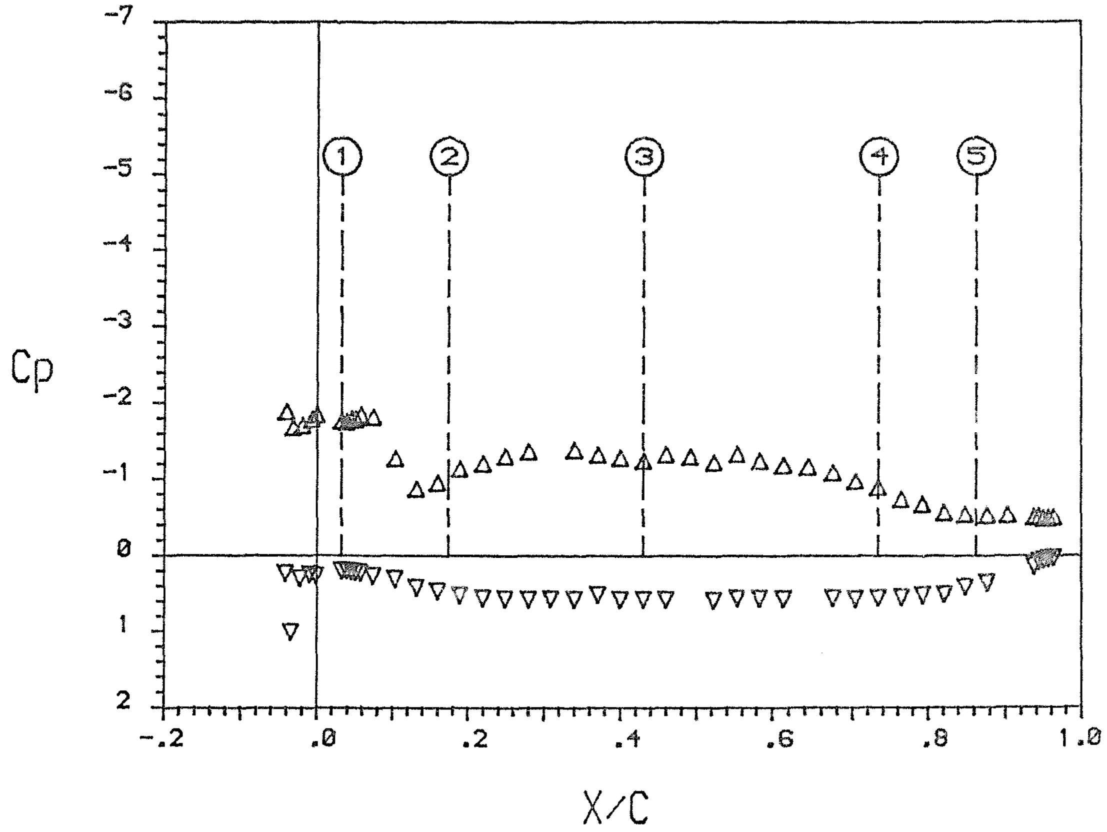

Fig(55) Boundary Layer Traverse Positions Relative to the Corresponding Pressure Distribution layer probes. He too found that no velocity readings could be detected by the probes when within separation regions, despite the wool tufts clearly indicating significant reversed flow conditions. Seetharam concluded that the flow within separation regions probably involved only very low mean velocities but with very strong fluctuations around the zero velocity point. This meant that the inertia of the wool tufts enabled them to respond to the mean reversed flow, whilst the probes were too insensitive to detect the low velocities involved. This was probably the situation within the upper surface bubble in the present test programme, however, further investigations using hot wire probes would be required to confirm this.

By steadily moving the yaw probe away from the local aerofoil surface, a point was eventually reached where the local downstream flow velocity could be measured. This indicated the lower extremity of the free shear layer that enclosed the bubble, as described in section 8.2.2.

Further vertical traversing of the yaw probe eventually revealed the entire velocity profile across the free shear layer, this is shown in figure (54). The shape of this profile was characteristic of a laminar shear layer, or alternatively the boundary layer on the mast was laminar when it separated.

The criteria for laminar to turbulent transition over an isolated circular cylinder is well established at between Re_d = 250 000 and 380 000 (where Re_d is the Reynolds number based on diameter), depending on the extent of free-stream turbulence and surface roughness, see figure (56). Figure (40) includes the typical ranges of Re_d across a mainsail (from $Re \times \frac{d}{c}$), this demonstrates that the mast flow is always below transition (i.e. laminar), except possibly at the extreme head of the sail where conditions are of the lower limit of the transition range. For this reason no turbulence simulators were applied to the mast sections, the use of such simulators would

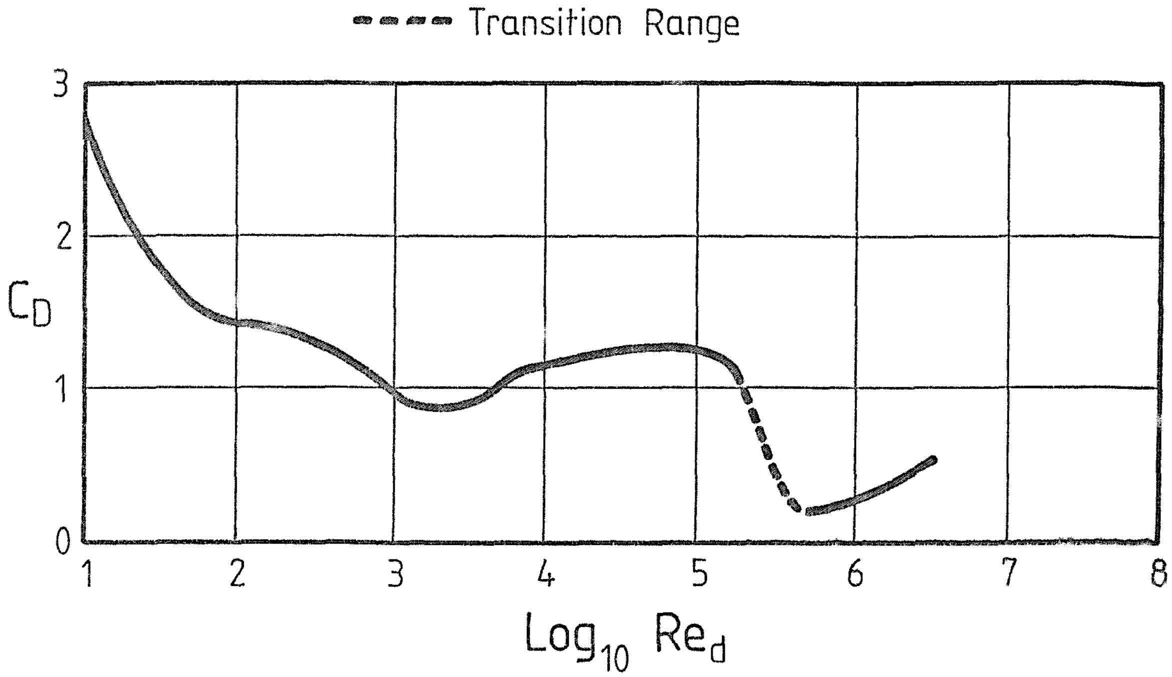

Fig (56) C_D vs. Re_d for an Infinite Circular Cylinder

	HEAD REGION			MID REGION			FOOT REGION		
$\frac{d}{c}$ (%)	17			10			4		
$Re \times 10^5$	3·5	6	10	6	10	14	10	14	16
$Re_d \times 10^4$	6	10	17	6	10	14	4	5·6	6·4

Table (2) Values of Reynolds Number Tested also have introduced another variable into the already large test programme.

The values of Re_d involved in the test programme are given in Table (2). Most commercially produced masts do not incorporate stimulators and therefore separation from them, in practice, would be laminar. For those few masts that do have stimulators, Milgram (3) has shown the effect on drag to be Reynolds number dependant.

8.4.2 Traverse Location ② - (Reattaching Flow)

Using the wool tufts as a guide, this traverse was performed as close as possible to the reattachment point of the upper surface bubble. It can be seen from figure (55) that the traverse actually took place just abaft of the reattachment point, as indicated by the maximum pressure peak in Region III.

From figure (54) it can be seen that the flow at this point was fully attached and no longer completely laminar, the rapid velocity increase very close to the surface being characteristic of turbulent flow conditions. It would seem therefore that transition did indeed take place within the last 25% of the bubble length (Region III), as suspected in section 8.2.3.

The boundary layer just following reattachment, although turbulent, was not however of a characteristic shape over its entire thickness, instead it clearly exhibited a curious double curvature profile. This shape was confirmed by a repeat test.

Both Gault (31) and Burnsall (35) in their investigations of the flows around bubbles on thin wings, observed the detailed evolution of velocity profile shape around a bubble contour. The double curvature profile at reattachment was also obtained in their results, although neither author mentioned the phenomenon in the written text of their reports.

Based on the detailed velocity profile data obtained by the previous two authors for thin wings, plus the information gained from the two profiles observed around the bubble in the present test programme, it was possible to build up a picture of the likely evolution of velocity profile shape around a mast induced bubble. This is shown in figure (57).

Since a sub-critical Re_d existed, the boundary layer on the mast was laminar, this progressed around the mast upper surface from the forward stagnation point to the separation point, accompanied by a slight increase in boundary layer thickness.

At separation the fluid close to the surface was halted by the adverse pressure gradient, this resulted in a vertical profile slope at the surface and zero wall shear stress. Seetharam (9) shows that this vertical profile slope often exists only very close to the surface ($<$ 0.05%C), making its experimental detection extremely difficult, and leaving the remainder of the characteristic velocity profile shape unchanged.

Following separation the laminar shear layer left the surface of the mast along a line of zero velocity, or separation streamline, that was initially tangential to the surface. As confirmed by the present work, and that by Gault (31), Burnsall (35) and Seetharam (9), the velocity in the separation region below the separation stream line was normally zero, but with strong fluctuations about this zero level. As described in section 8.4.1, the shear layer outside the bubble boundary remained stable and exhibited a characteristic laminar profile shape.

The laminar shear layer existed up to the point of transition as described in section 8.2.3. At this point a steadily spreading fan of turbulence developed which promoted turbulent mixing between the free-stream and the separated shear layer. The result of this was to

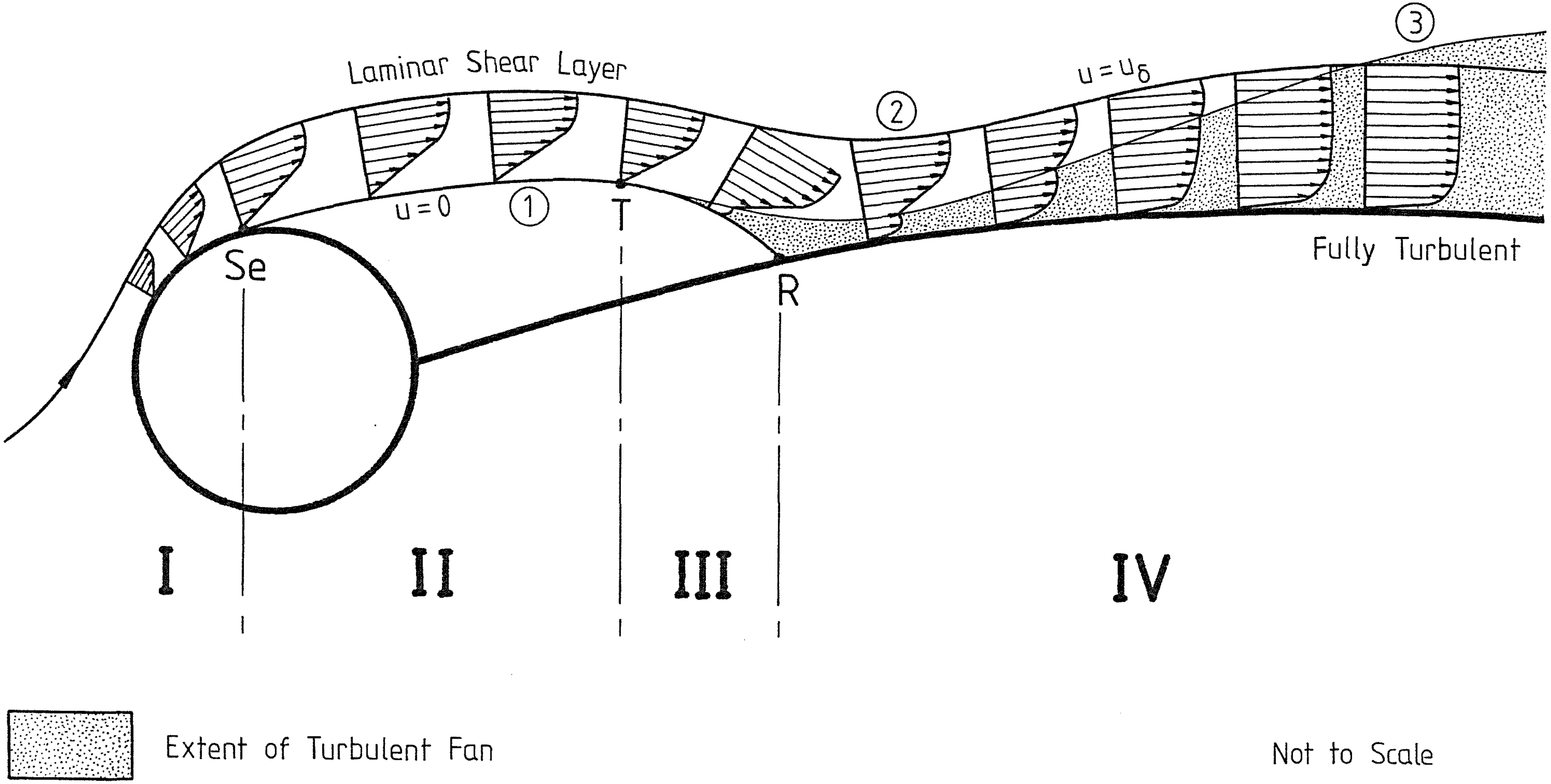

Fig (57) Velocity Profile Evolution Around an Upper Surface Bubble re-energise the shear layer, starting with the slowest moving fluid close to the bubble boundary. The velocity profile above the bubble following transition began to increasingly exhibit a double curvature shape, as the fluid low down in the shear layer gained kinetic energy whilst that towards the top of the profile remained essentially laminar.

The turbulent mixing following transition resulted in a rapid loss in bubble thickness, followed by reattachment. However even at reattachment the evolution from a laminar to a turbulent profile was still not complete. Following reattachment the lower portion of the now attached boundary layer continued to fill out as more energy was entrained from the outer flow by turbulent mixing. Eventually the boundary layer velocity profile ceased to exhibit the double curvature, finally culminating in the establishment of a conventional fully developed turbulent boundary layer profile.

8.4.3 Traverse Location ③ - (Fully Attached Turbulent Flow

This traverse, which was performed in the centre of the fully attached flow region (Region IV), revealed a boundary layer profile that was characteristic of fully developed turbulent flow.

Rapid changes in velocity occurred very close to the surface followed by a more steady increase over the remaining thickness of the layer, this was quite different to the previously mentioned laminar and double curvature profiles.

8.4.4. Traverse Location ④ - (Flow Approaching Separation)

Again using wool tufts as a guide, an attempt was made to perform a traverse as close as possible to the trailing edge separation point. It was very difficult, using this technique, to judge accurately the location of the required separation point because of the irregular behaviour exhibited by the tufts when nearing separation regions.

Because of this, as shown in figure (55), the actual traverse was unfortunately performed some distance ahead of the separation point as indicated by the onset of constant base-pressure.

The velocity profile obtained at this location was very similar to that described in section 8.4.3, however the profile this time was thicker and less full, as a consequence of the loss of kinetic energy experienced in overcoming the adverse pressure gradient.

If the traverse had been performed closer to the separation point it is likely that this would have revealed a profile that was even more retarded, with the lower part of the layer showing a significantly higher proportion of the energy loss than the rest.

8.4.5 Traverse Location ⑤ - (Trailing Edge Separation)

This final traverse was carried out through the trailing edge separation region (Region V), as indicated both by the wool tufts and the corresponding pressure distribution in figure (55).

As with the bubble, no flow velocities could be detected at any orientation during the initial part of the traverse above the aerofoil surface. By continuing with the vertical traverse, a point was eventually reached where a downstream flow velocity could be measured, this indicated the location of the bounding stream line for the separation region as described in section 8.2.5.

Although this traverse took place approximately 1/3 of the way through Region V, the distance from the surface to the separation stream line was relatively small, this suggested a tangential flow separation similar to that in figure (46) for a typical bubble.

Figure (54) shows that above the separation stream line, the free shear layer was basically turbulent, but extremely thick, so much so that the 'mouses' total traverse range of 40 mm was unable to detect the upper limit. Although thick, the profile of the shear layer was also quite narrow, indicating a severe loss of energy in overcoming the adverse pressure gradient.

8.5 Results of Boundary Layer Analysis

As described in section 7.3.2 the boundary layer profiles obtained were analysed to determine their thickness and friction parameters. The results of this analysis is shown in figure (58) for the attached profiles, and in figure (59) for the separated profiles. No friction parameters have been presented for the separated cases, since the wall shear stress for these was found to be zero.

8.5.1 The 'Law of the Wall' and Effect of Pressure Gradient

It is well established that turbulent boundary layers can be divided into three distinct parts, and that the form of these can be related to the friction velocity (u_τ) as follows :

(a) Laminar Sublayer - this occurs close to the solid surface and is described by

$$\frac{u}{u_\tau} = \left(\frac{u_\tau y}{\nu}\right) \qquad \text{———} \quad 8.2$$

(b) Inner Velocity Region - this exists directly above the laminar sublayer, and is governed by the logarithmic 'law of the wall' i.e. :

$$\frac{u}{u_\tau} = A_0 \log_{10}\left(\frac{u_\tau y}{\nu}\right) + B_0 \qquad \text{———} \quad 8.3$$

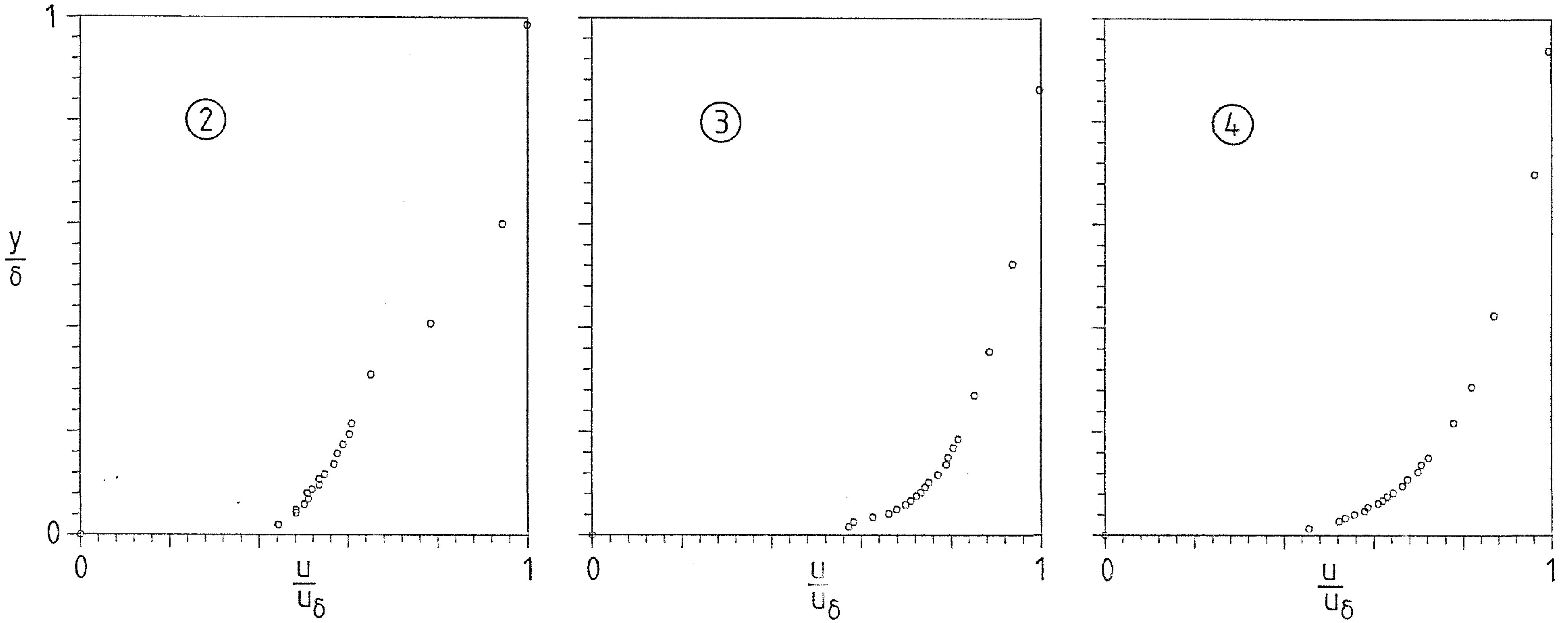

$\frac{\delta}{c}$	= 0·034	$\frac{Du_\tau}{\nu}$	= 44·8	$\frac{\delta}{c}$	= 0·039	$\frac{Du_\tau}{\nu}$	= 55·6	$\frac{\delta}{c}$	= 0·048	$\frac{Du_\tau}{\nu}$	= 43·8
$\frac{\delta^*}{\delta}$	= 0·204	$\frac{\delta^{**}}{\delta}$	= 0·124	$\frac{\delta^*}{\delta}$	= 0·108	$\frac{\delta^{**}}{\delta}$	= 0·080	$\frac{\delta^*}{\delta}$	= 0·143	$\frac{\delta^{**}}{\delta}$	= 0·101
$\frac{u_\tau}{U}$	= 0·048	$\frac{u_\delta}{U}$	= 1·471	$\frac{u_\tau}{U}$	= 0·060	$\frac{u_\delta}{U}$	= 1·480	$\frac{u_\tau}{U}$	= 0·047	$\frac{u_\delta}{U}$	= 1·390
H	= 1·652	C_f	= 0·00213	H	= 1·358	C_f	= 0·00329	H	= 1·417	C_f	= 0·00229

Fig (58) Normalized Attached Profiles

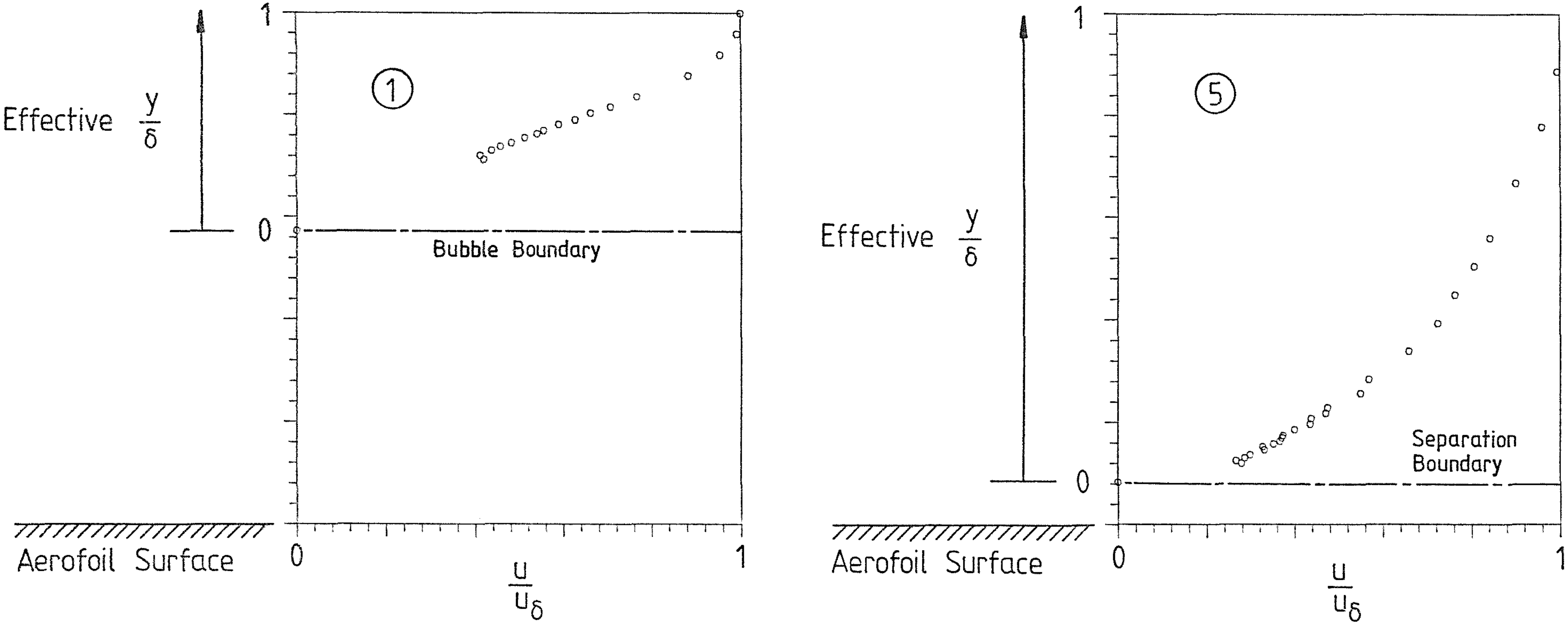

$\frac{\delta}{c} = 0{\cdot}0171 \quad \frac{\delta^*}{\delta} = 0{\cdot}1743$

$\frac{\delta^{**}}{\delta} = 0{\cdot}0555 \quad H = 3{\cdot}1370$

$\frac{\delta}{c} = 0{\cdot}0550 \quad \frac{\delta^*}{\delta} = 0{\cdot}2238$

$\frac{\delta^{**}}{\delta} = 0{\cdot}1168 \quad H = 1{\cdot}9159$

Fig(59) Normalized Separated Profiles

This region includes most of the boundary layer thickness, and has been shown by Nikuradse (36) to be almost universally applicable when $A_0 = 5.75$ and $B_0 = 5.5$.

(c) Outer Velocity Region - Although the 'law of the wall' equation 8.3 was originally derived on the basis of conditions that hold in the inner region of fully developed turbulent boundary layers, where the shear stress is constant, it has been found in practice to approximate reasonably well to the mean velocity distribution over most of the boundary layer above the laminar sublayer. However when a more accurate description is required for the outer part of the boundary layer, Duncan (37) has shown that the following expression best fits experimental data for zero pressure gradient :

$$\left(\frac{u_\delta - u}{u_\tau}\right) = 2.8\ [1 - \mathrm{Sin}^3(\frac{\pi y}{2\delta})] - 5.75 \log_{10}\left(\frac{y}{\delta}\right) \qquad 8.4$$

Alternatively Nikuradse (36) has also proposed a power law form for this part of the boundary layer i.e.

$$\left(\frac{u}{u_\tau}\right) = \mathrm{Const.}\left(\frac{u_\tau y}{\nu}\right)^{1/n} \qquad 8.5$$

Pressure gradient does of course have an effect on the form of turbulent layers, although as shown by Nikuradse it is an adverse pressure gradient that has by far the greatest influence, with favourable gradients appearing to modify the profile shapes only slightly.

Duncan presents a graph showing the typical effect of increasing adverse pressure gradient on a turbulent boundary layer when plotted as u/u_τ against $\log_{10}(yu_\tau/\nu)$. This graph has been reproduced in figure (60), with dotted lines representing the equations 8.2 and 8.3.

This graph demonstrates that adverse pressure gradient has a profound effect on the outer part of a boundary layer, but leaves a

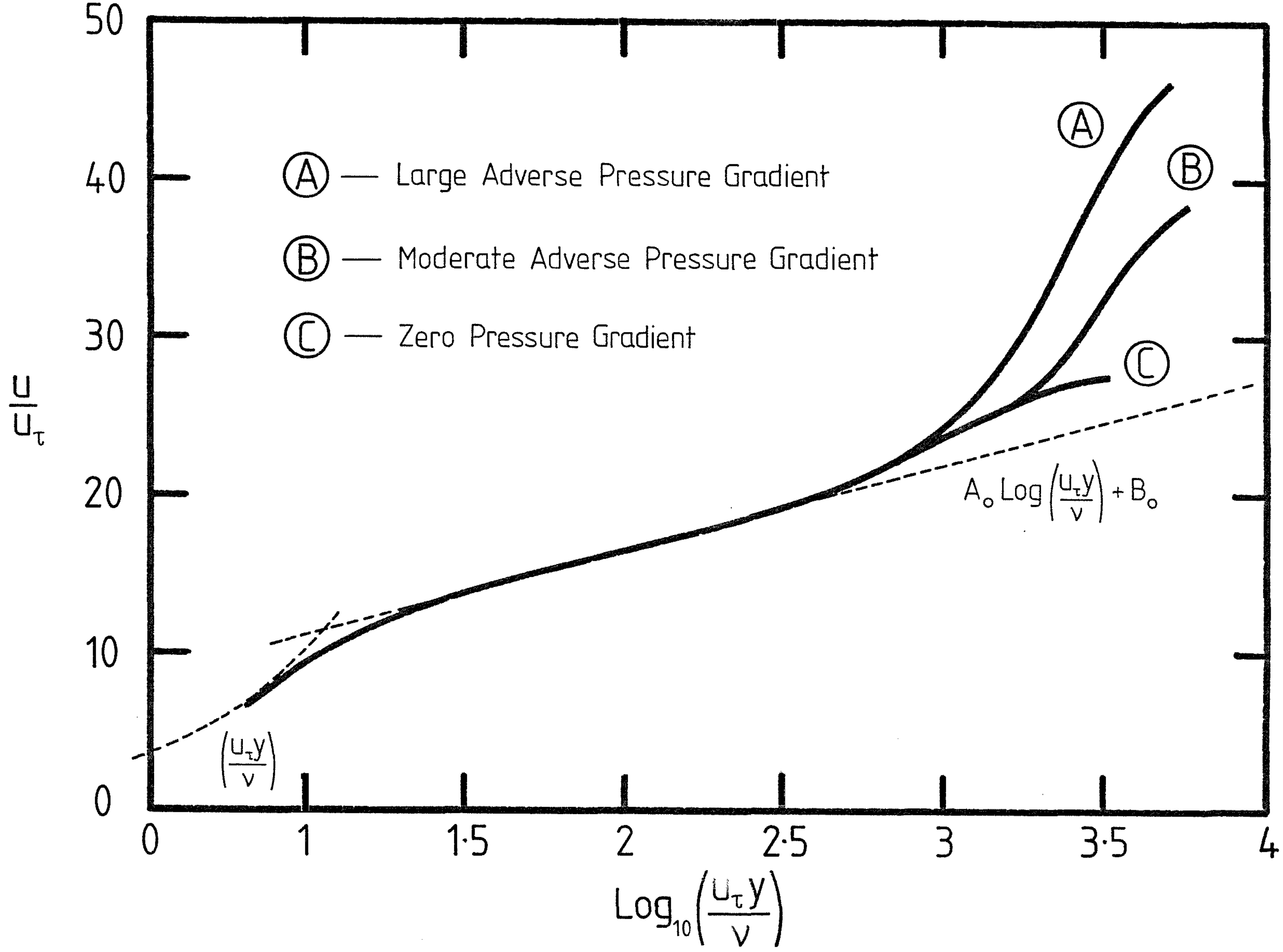

Fig (60) Effect of Pressure Gradient

narrow region above the sublayer where the 'law of the wall' of equation 8.3 still holds. It was this fact that led Preston (27) to suggest the application of his pitot tube technique for measuring skin friction, this being the method used in the present test programme.

The three attached boundary layer profiles obtained in the present test programme have each been plotted in the same logarithmic form as in figure (60), and compared with equations 8.2 and 8.3, these are shown in figures (61), (62) and (63).

All three graphs confirmed the presence of the logarithmic 'law of the wall' low down in the boundary layers, this demonstrated the turbulent nature of these attached profiles.

In each case the reading corresponding to the probe resting on the aerofoil surface fell almost exactly on the line representing equation 8.3. This confirmed that the probe used was small enough for accurate skin friction measurement using Preston's technique, although it was too large to operate within the laminar sublayer.

By comparing figure (61) with figure (60), it can be seen that a large adverse pressure gradient existed around the bubble reattachment point. This was consistent with the assumption that reattachment took place after transition at the end of a separation bubble, at the highest level of adverse pressure gradient that could be tolerated by turbulent mixing.

Figure (62) shows that at the centre of the attached flow region (Region IV) the pressure gradient was virtually zero, and the height of boundary layer over which the 'law of the wall' acted was relatively large.

Finally for the profile approaching trailing edge separation as shown in figure (63), a moderate to large adverse pressure gradient was again present as suspected.

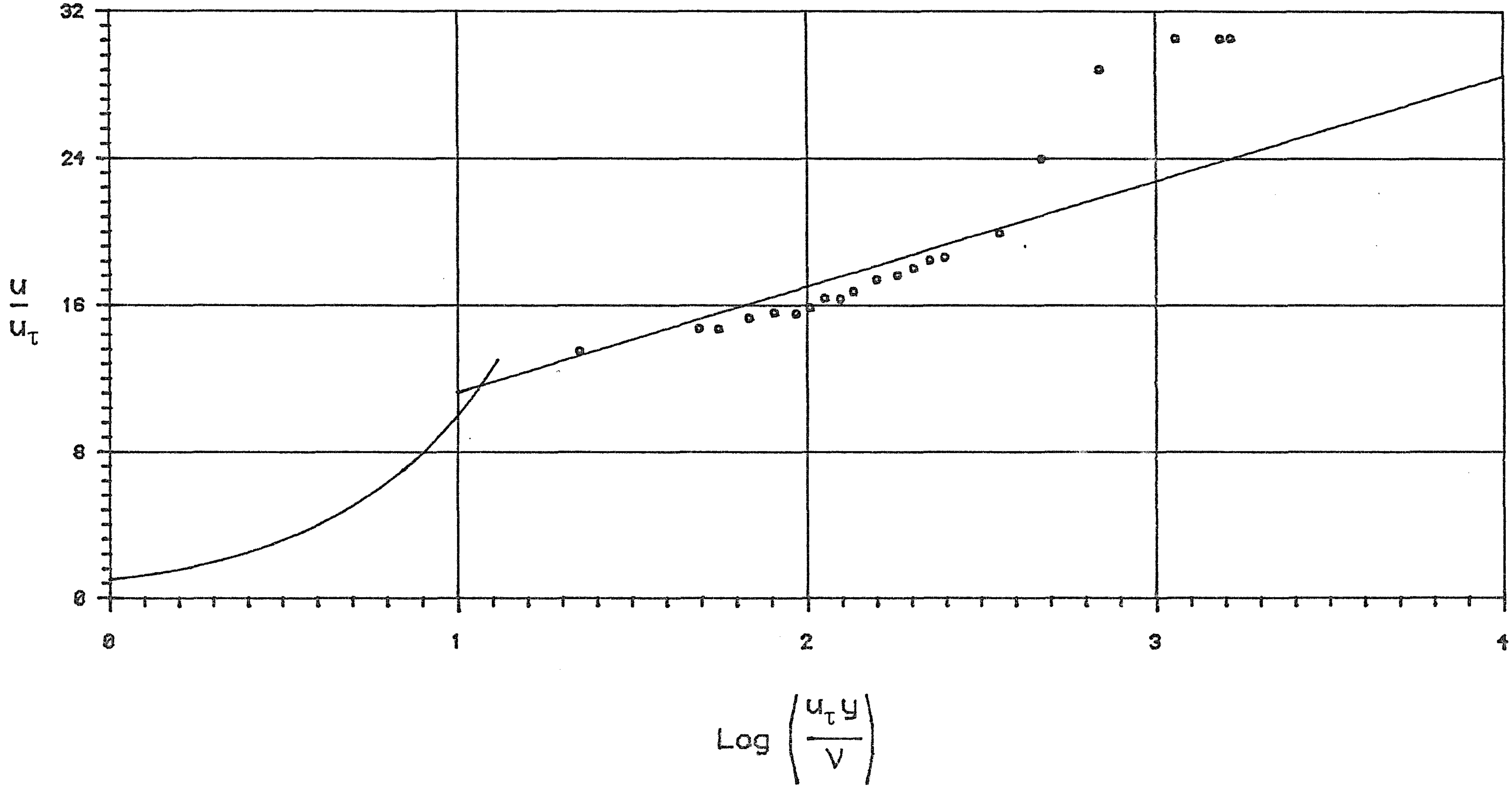

Fig(61) Comparison of Boundary Layer Profile ② with the Logarithmic "Law of the Wall"

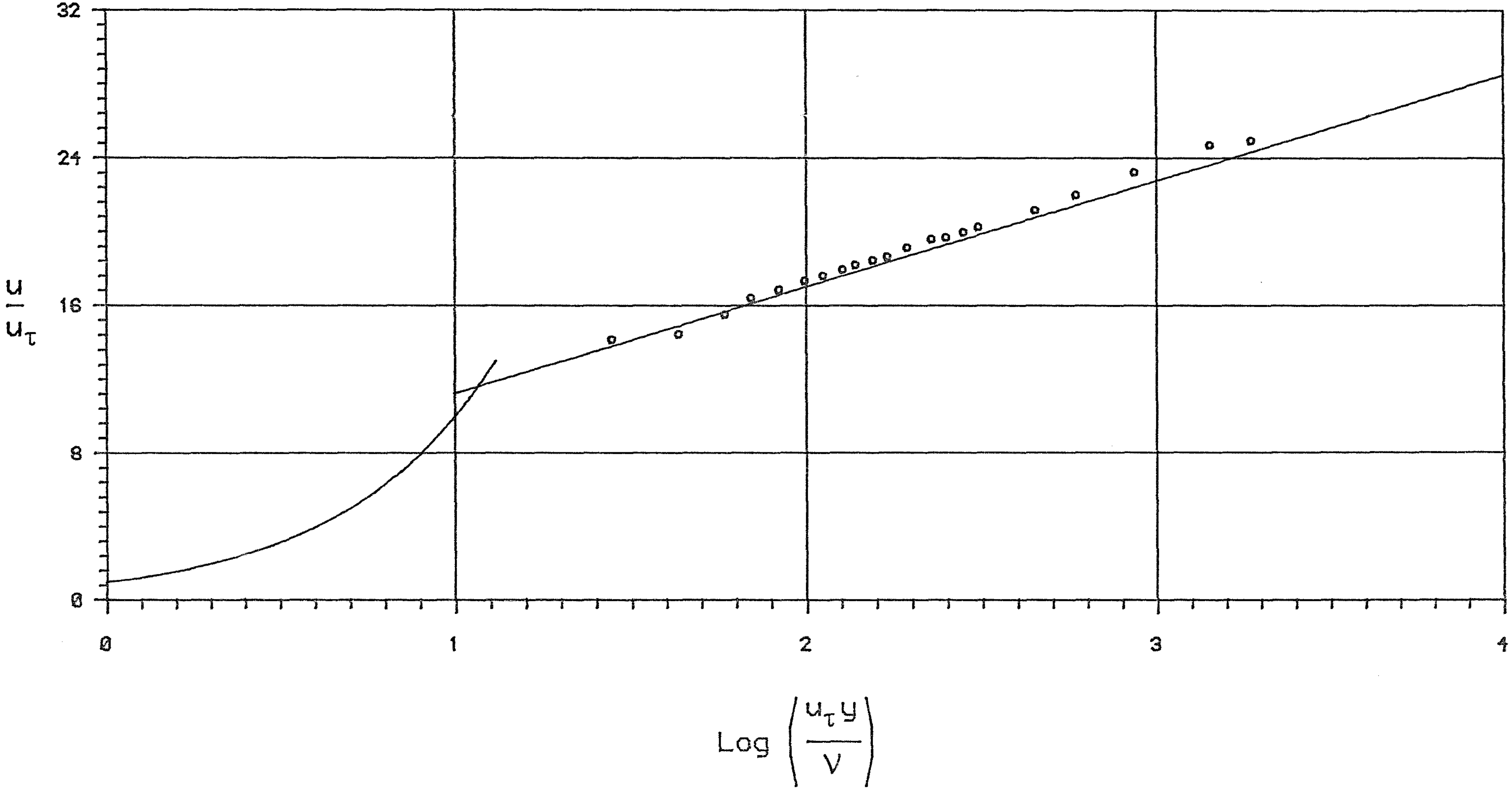

Fig(62) Comparison of Boundary Layer Profile ③ with the Logarithmic "Law of the Wall"

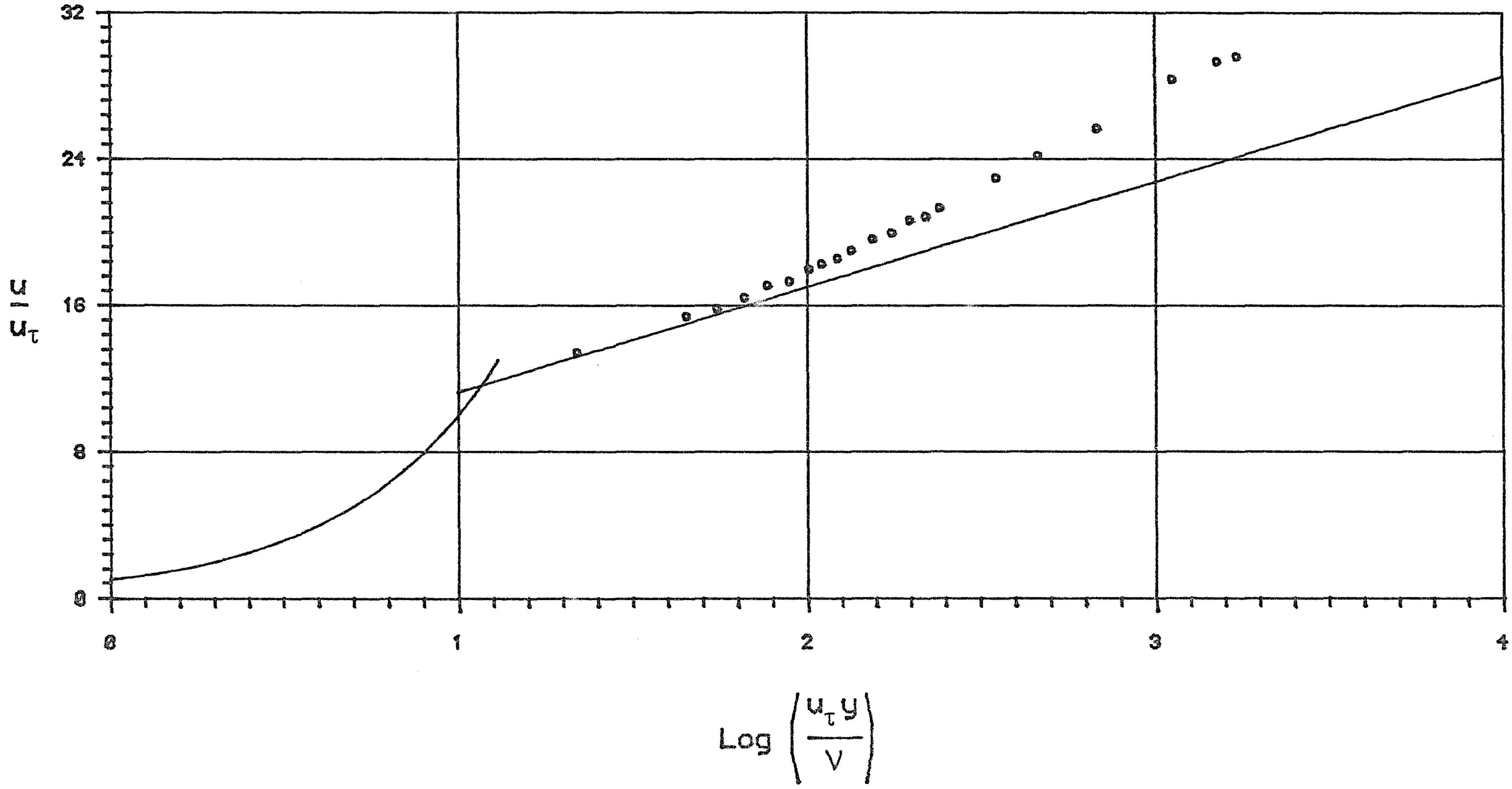

Fig(63) Comparison of Boundary Layer Profile ④ with the Logarithmic "Law of the Wall"

8.5.2 Thickness Parameter Variation

All the various thickness parameters for the boundary layer profiles obtained have been presented in figures (58) and (59), those relating to the separated cases have been calculated by considering the separation stream line as a solid surface where $y = 0$.

The simplest of these parameters was the boundary layer (or shear layer) thickness, the variation of this with chordwise position is shown in figure (64). It can be seen that the shear layer above the upper surface bubble started off relatively thin, but a rapid thickening took place around the point of reattachment. Following reattachment the boundary layer growth was fairly slow, eventually however, a more rapid increase in thickness started to occur again as the trailing edge separation point was approached.

The variation of displacement and momentum thickness with chordwise position is shown in figure (65). With a conventional aerofoil, without any leading edge obstruction or bubble of any kind, these thickness parameters would normally follow the same trends across the chord as exhibited by the boundary layer thickness, i.e. steadily rising with chordwise position away from the leading edge, followed by a more rapid increase as trailing edge separation is approached. However, with the present results, a peak was observed in both thickness parameters around the point of reattachment. Since these parameters were directly related to the area under the velocity profiles, it seems clear that the double curvature profile shape obtained due to transition near the reattachment point was the cause of these peaks. This was the case since the area under such a double profile curvature will always be higher than that for a conventional fully developed turbulent layer of the same thickness.

The shape factor H ($= \delta^{*}/\delta^{**}$) is often used in boundary layer

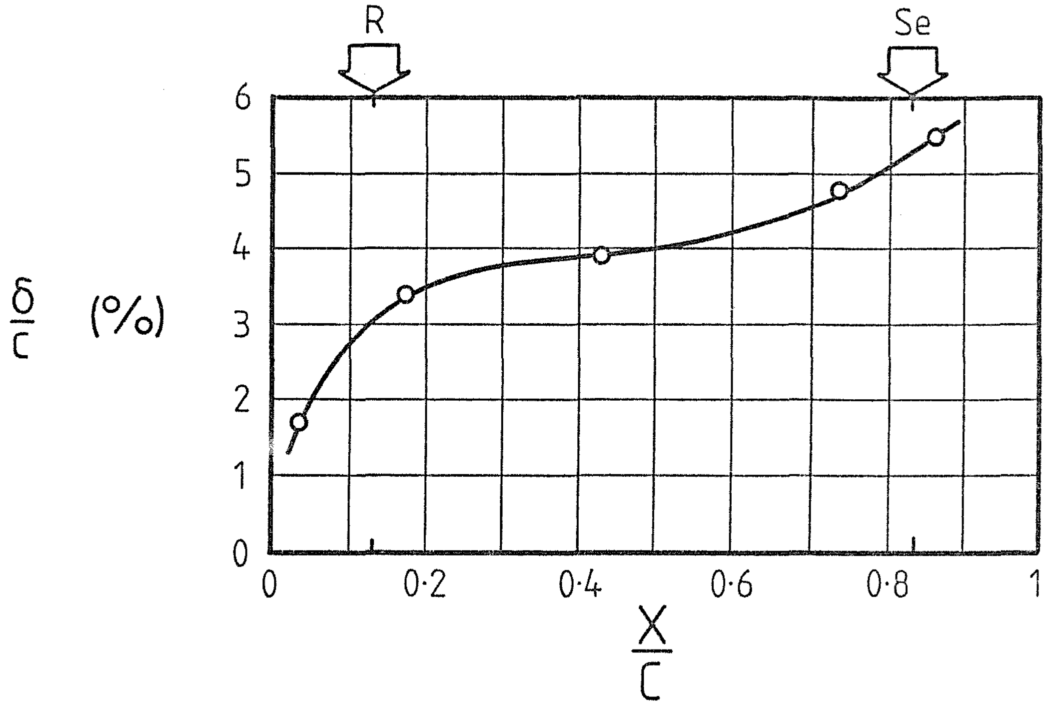

Fig(64) Boundary Layer Thickness Variation

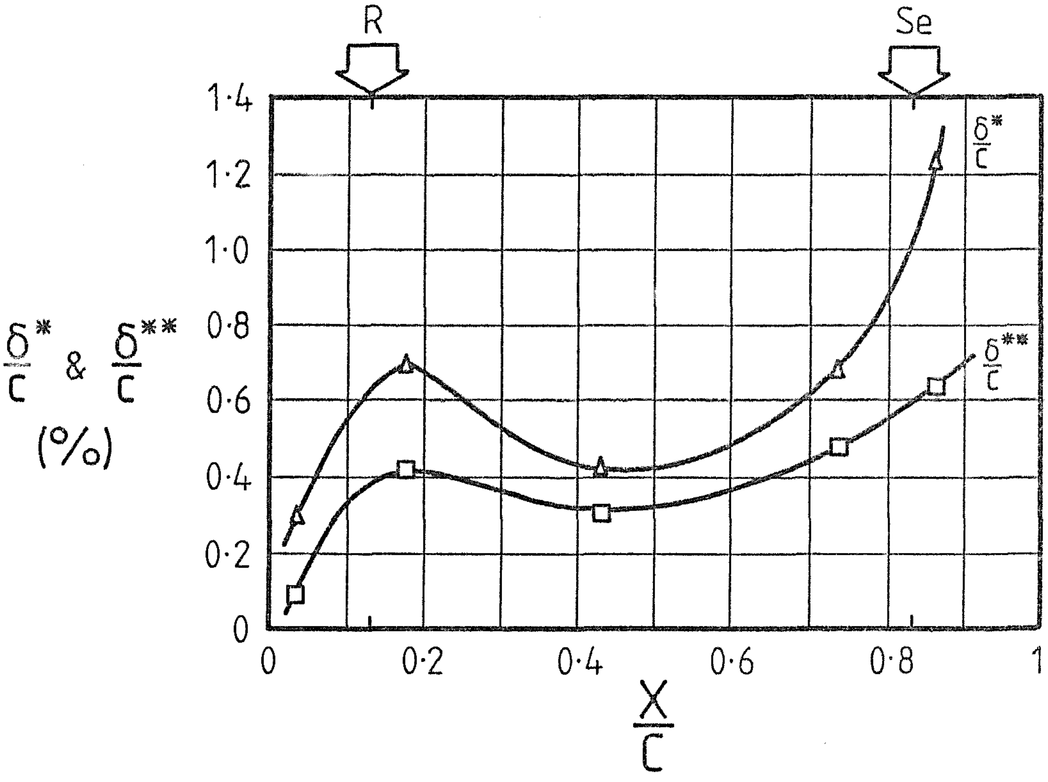

Fig(65) Thickness Parameter Variation

calculation methods to predict the location of trailing edge separation, with conventional aerofoil forms this is normally expected to occur when H reaches a value somewhere in the range 1.8 - 2.2, see Schlichting (38).

Seetharam (9) has measured the variation in H over a GA(W)-1 aerofoil, with trailing edge separation but no leading edge bubble flow. This is shown in figure (66). In this case the shape factor remained essentially constant at around 1.4 over most of the aerofoil, but as separation was approached, H began to rise very rapidly reaching a value of 1.9 at the separation point, before attaining a level of 3.5 at the trailing edge.

Burnsall (35) has measured the variation of H over a NACA 663-018 aerofoil following reattachment of a leading edge bubble. His results, given in figure (67), show a relatively high shape factor of 2.6 at reattachment, followed by a very rapid drop to a near constant value of 1.3.

The variation of shape factor with chordwise position for the present mast/sail combination is shown in figure (68). Since this model involved both a leading edge bubble and a trailing edge separation region, it was not surprising to find that the shape factor acted in a way that combined the essential features of both figures (66) and (67). Those parts of the curves prior to reattachment and following trailing edge separation have been shown dotted, since, with the limited data obtained in these areas, it was by no means certain that the interpolations given were representative.

It is worth noting at this point that had boundary layer traverses been made in the reattachment region (Region III), the results obtained would not have been meaningful. The reason for this is that the flow in this region would have been parallel to the separation stream line, and not to the aerofoil surface. Since there

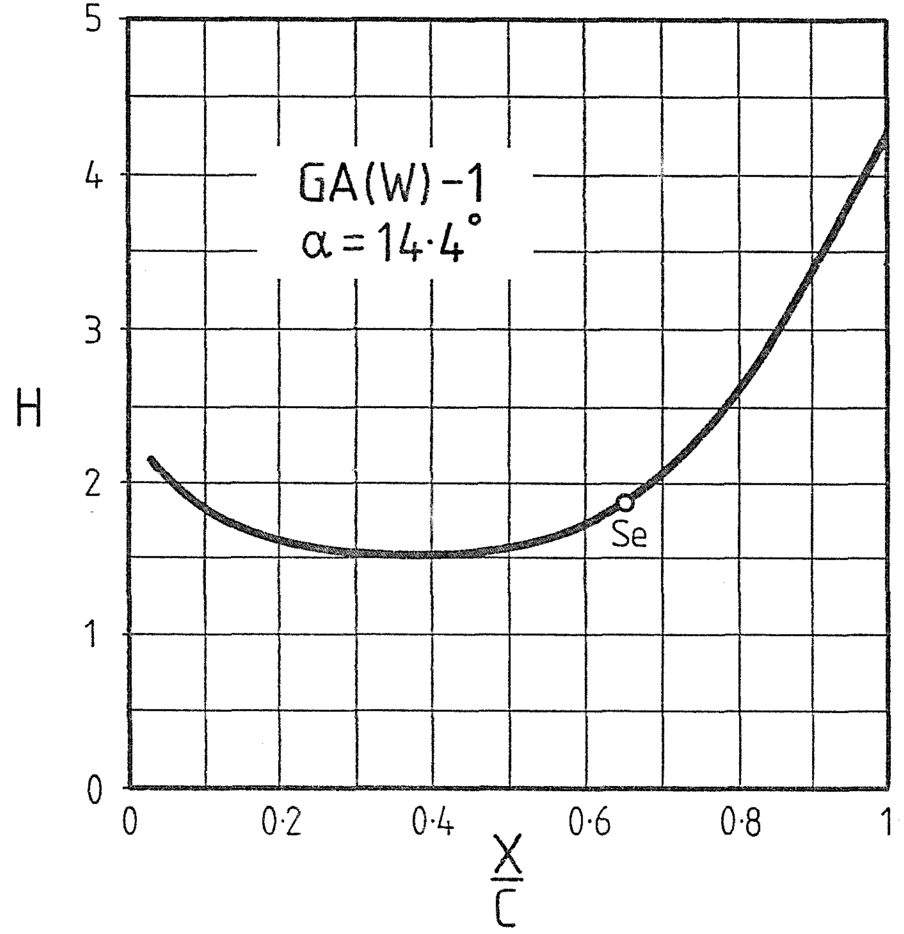

Fig(66) Effect of Trailing Edge Separation on Shape Factor (Seetharam Ref. 9)

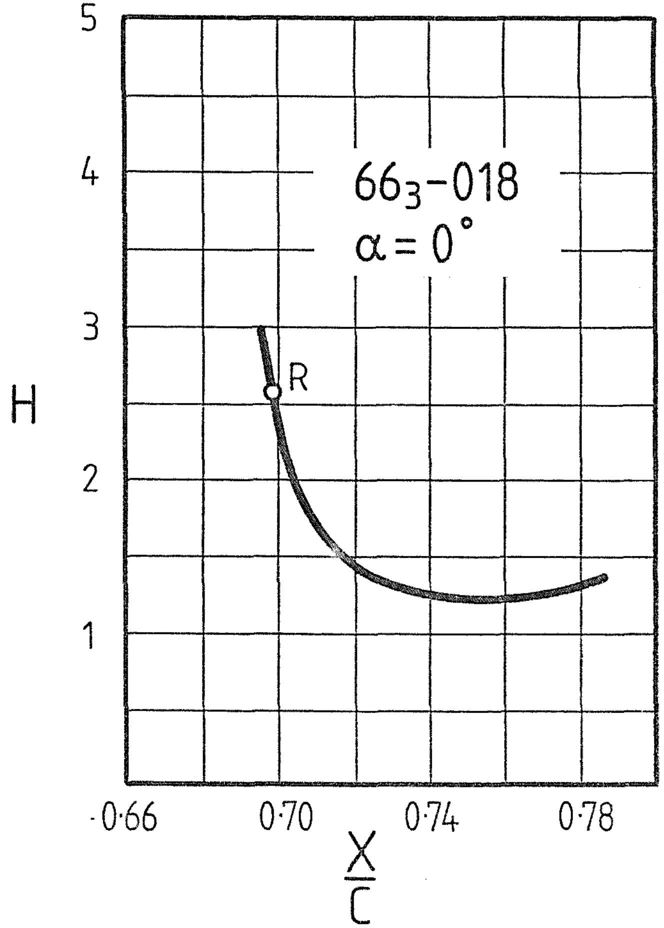

Fig(67) H Variation Across a Bubble Reattachment Point (Bursnall Ref. 35)

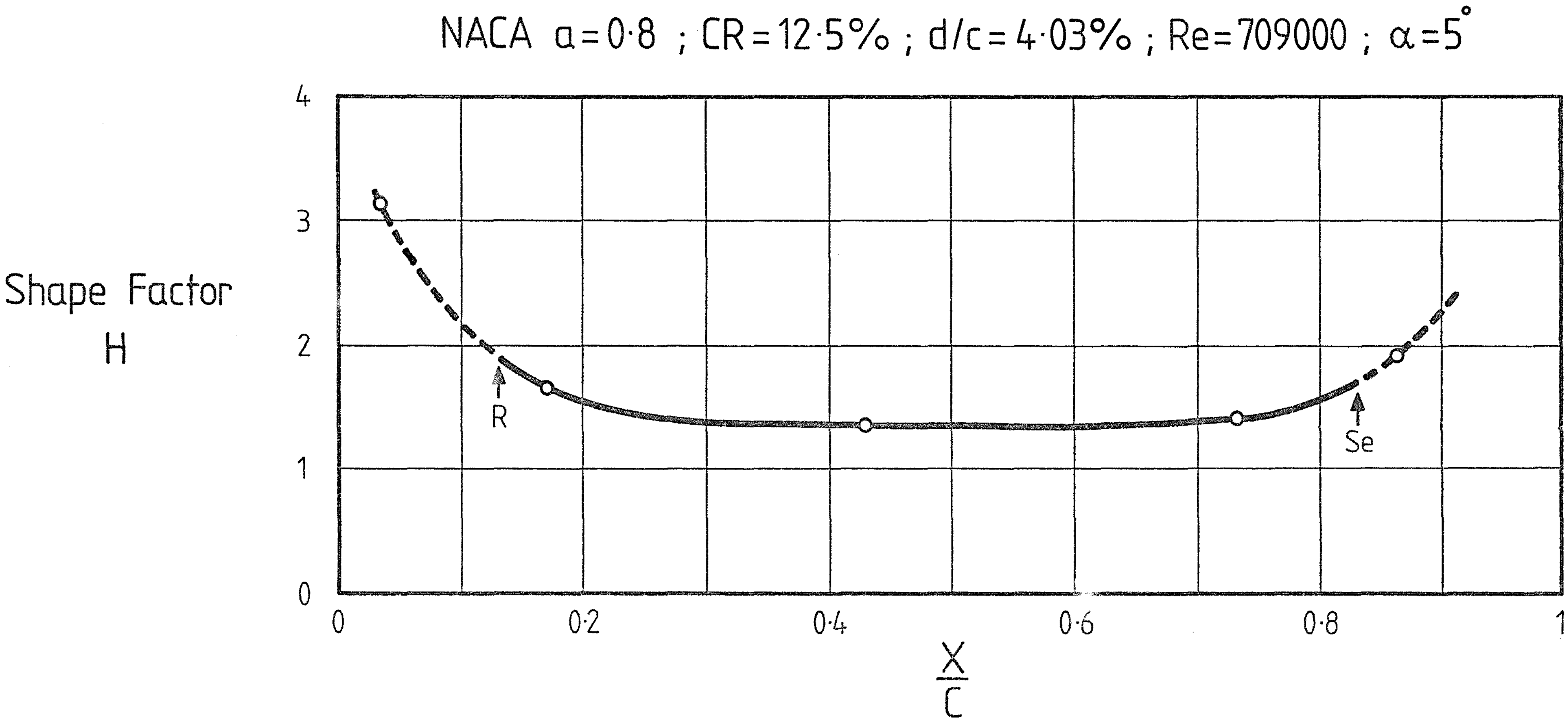

Fig (68) Shape Factor Variation Across Sail Upper Surface was a rapid fall in bubble thickness associated with this region, the difference in angle between the flow and the surface would have been very high (approximately 70° at reattachment). This fact was not appreciated at the time of probe selection, so that the yaw-probe used, with its pitch insensitivity of ± 12°, would obviously have given inaccurate results when traversed parallel to the local surface in this reattachment region. It was therefore fortunate that no traverses were performed through Region III, to successfully complete a meaningful traverse through this region in future would probably require a 5-hole pitot probe. In all other regions including Region II and Region V, the pitch angle of the flow relative to the local surface was small, as anticipated in section 4.1.

8.6 Conclusions and Recommendations for Future Work

The large number of parameter combinations tested in the complete experimental programme, provided a substantial body of previously unavailable 2D pressure distribution data representing typical mast/mainsail geometries under close-hauled (low incidence angle) conditions.

Although the detailed physics of the air flows around the mast/sail geometries was undoubtedly complex, the resulting form of the static pressure distributions was found to be remarkably ordered. The distributions were in each case built up from 9 fundamental regions which were identified as being representative of particular flow regimes. The magnitudes and extents of these regions were found to be related to the various model and flow parameters.

The boundary layer velocity profiles obtained using the 'mouse' system, also helped to confirm the nature of the flows within some of the regions on the sail upper surface. One interesting feature observed was that within bubble and separation regions below the separation stream line, any reversed flow present must have been extremely slight since it was undetectable with the probe and measuring system used.

The upper surface bubble investigated exhibited similar characteristics to laminar separation bubbles observed on thin aerofoils without leading edge obstructions, however in the present case the bubble thickness was determined by the mast size, and was thus very large in comparison with conventional bubbles.

Bubble reattachment appeared to be governed by transition of the shear layer accompanied by subsequent turbulent mixing within a rapidly spreading turbulence fan. This interpretation was reinforced by the double curvature profile obtained near reattachment, since the lower part of this profile was turbulent in appearance whilst the upper section still exhibited laminar features.

A detailed experimental investigation still needs to be carried out on behind mast bubbles where the mast separation is initially turbulent (i.e. using stimulators), since the mechanism of reattachment is likely to be significantly different in such cases.

The boundary layer profiles obtained, enabled variations in the thickness and friction parameters to be determined over the aerofoil upper surface. Further investigations are required into the growth of boundary layers over the lower sail surface, and especially around the lower bubble, since the occurrence of a lower surface bubble at +ve incidence, and the simultaneous existence of bubbles on both aerofoil surfaces, are both rarely witnessed with conventional aerofoils.

Further work is also required in testing non-circular mast forms, and sail shapes other than the NACA a = 0.8 and NACA 63 mean-lines.

No wake traverses were performed since the original intention at the commencement of the test programme was to deduce skin friction drag from boundary layer profile data. However, because of problems with the speed of data acquisition possible using the micromanometer, only a small number of upper surface traverses were possible in the time available. Without measurements of skin friction drag for each individual test, it was not possible to obtain force coefficient data entirely from the static pressure distributions. The main aim of the present work was to obtain a more fundamental understanding of the flows around mast/sail geometries, and in this respect the tests performed were sufficient.

The flow over real sails is of course 3-dimensional, and influenced by many factors such as wind gradient, rig/hull aerodynamic interaction, free-stream turbulence, sail elastic properties etc. these effects were beyond the scope of the present test programme but it was felt that the new understanding gained concerning the effect of 2D mast/sail geometry on pressure distribution, boundary layer development, and on separation and reattachment, constitutes a further step towards an eventual solution to the overall problem of sail aerodynamics.

PART C

THEORETICAL PREDICTIONS AND COMPARISON WITH EXPERIMENTAL RESULTS

CHAPTER 9

DEVELOPMENT OF A NEW PARTIALLY SEPARATED FLOW THEORY

9.1 Previous Theoretical Methods

Only one method for predicting flows around 2D mast/sail combinations is known to have been published to date, this was developed by Vaussy (39). This method does not however take into account any separation regions, and is therefore only applicable to cases with a small camber ratio, at low incidence, and with streamlined masts at -ve mast angles.

It has been shown by experiment in the present work that the separation regions involved around typical mast/sail geometries have a profound effect on the pressure distributions, therefore any predictive theory must accurately model these regions.

Although no work has been published regarding separated flows over masts and sails, a number of researchers have dealt theoretically with the problem of separation around more conventional aerofoil forms. Most of these have considered trailing edge separation only, and have approached the problem from the point of view of the outer flow, using experimental data for separation location and in some cases base-pressure as well. Such methods are useful since they can be coupled iteratively with boundary layer calculations to include viscous effects and to obtain true separation location from an initial estimate.

These outer flow methods can be divided into three main types depending on the modelling technique employed i.e. mappings, complex variable techniques and panel methods.

9.1.1 Mapping Methods

A number of authors such as Hayashi (40), Kumar (41), Wu (42) and Milgram (43) have used mapping methods to obtain a solution to the problem of aerofoils with significant trailing edge separation. Although these attempts differ in terms of detail they all basically adopt the same broad principle. The trailing edge separation region was in each case assumed to be bounded by two free stream lines in the manner described by Roshko (44), one leaving the upper surface at separation and the other leaving the lower surface at the trailing edge. The pressure (or tangential velocity) along these streamlines was initially constant in keeping with experimental base-pressure observations. Eventually these streamlines became parallel to the free-stream, and from this point on the pressure was allowed to relax back to free-stream conditions.

Analytical calculations were made easier by using conformal transformations which allowed the aerofoil and free stream-line boundaries to be mapped onto some more simple geometric shape, such as a circle or straight line.

Such techniques can be very successful provided that a suitable mapping function can be found. This approach was not however adopted for the present case of a mast and sail, partly because a mapping function was not readily available to represent the mast, sail, bubbles and wake, but mainly because this method leaves little prospect of extension into 3-dimensions. Such an extension would certainly be necessary if the theory were to eventually be made applicable to real sails, with account taken of rig/hull interaction etc.

9.1.2 Complex Variable Techniques

The mapping methods described previously involved complex variables as part of the mathematical mapping process, however there are examples of the use of complex variables without any need for mapping at all.

One such method for separated aerofoils has been published by White (45). Again the trailing edge separation region and wake were bounded by two free streamlines, these being iteratively located to give the stream line condition of flow tangency, together with constant velocity to represent the base-pressure up to the point where the streamlines became parallel to the free-stream. Unlike the mapping cases described, the base-pressure was obtained as part of the solution such that only the separation location was required as an empirical input.

The potential flow was calculated numerically using a Cauchy principal value integral equation over 100 grid points, with the iterative streamline location procedure completed after three computations.

Although the results obtained by this method were reasonably good, there was again some doubt about its application to bubbles as well as trailing edge separation. Extension to 3-dimensions also looked unlikely.

9.1.3 Panel Methods

Since the invention of fast powerful computers, panel methods, with their reliance on numerical solution, have become widely used.

Mathematical models involving flow singularities such as vortices, sources and sinks, can be applied to both 2D and 3D problems, and it is also possible to link two or more individual models together to observe interaction effects.

Panel methods have been applied to 2D aerofoil trailing edge separation, with the pioneering work in the field having been done by Jacob (46). This method, which has also been adopted by Abbott (47) and Hahn (48), involved placing a source distribution over an aerofoil upper surface downstream of the separation point, figure (69). The source strengths were then estimated using empirical data in an attempt to simulate the effect of separation streamline displacement on the attached pressure distribution. The tangential velocity (and hence pressure) downstream of separation was assumed to be constant and equal to that at separation, but no attempt was actually made to model this condition.

Farn (49) however, pointed out that the computed velocity along the separation streamline in Jacob's model was far from being constant. Since it was essential for this constant pressure streamline condition to be met in order to obtain an accurate blockage correction, the empirical source strength distribution used by Jacob must have been unrepresentative.

With this in mind, Farn (49) went on to present a similar method using surface sources downstream of separation, but in this case their strengths were mathematically determined to produce constant pressure conditions along an iteratively located free streamline, figure (70). This free streamline was regarded as the new aerofoil surface contour, and the aerofoil pressure distribution downstream of separation was therefore taken as that along this new contour. The pressure on the actual aerofoil surface downstream of separation in this theoretical model was, of course, not constant. This method only worked by using empirical charts of base-pressure versus separation location.

Henderson (50) has taken this type of model one step further by iteratively locating not only the upper surface separation streamline, but also free streamlines bounding a closed wake. This was achieved by placing singularity panels on these streamlines rather than just on the aerofoil surface downstream of separation. Boundary

Source Strengths Estimated to Approximately Model the Effect of Separation Streamline Displacement on the Attached Flow.

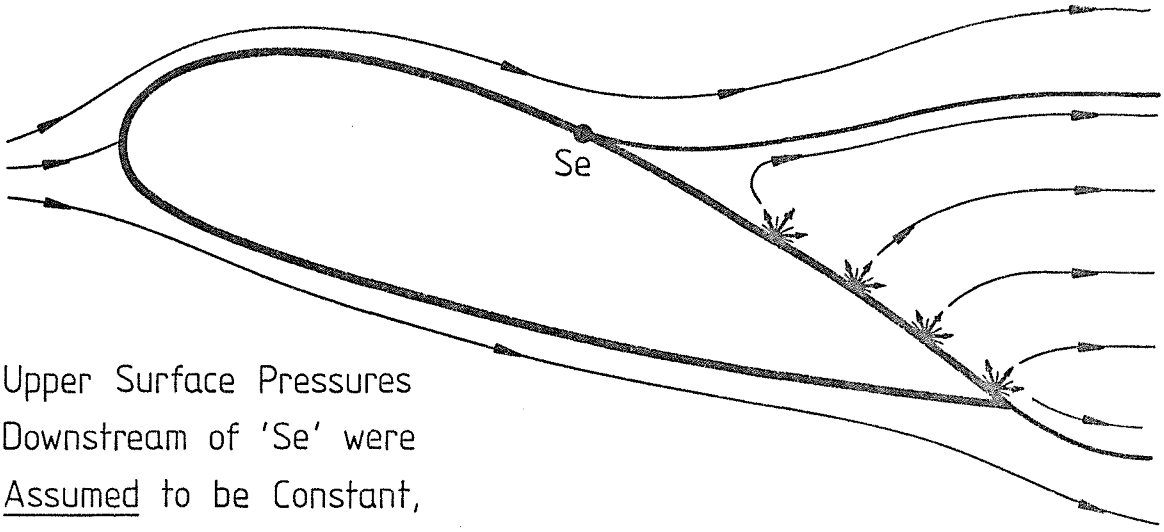

Upper Surface Pressures Downstream of 'Se' were Assumed to be Constant, but not Enforced.

Fig(69) Jacob's Theoretical Model (Ref. 46)

Source Strengths Mathematically Determined to Produce an Empirically Based Constant Pressure Along an Iteratively Located Separation Streamline

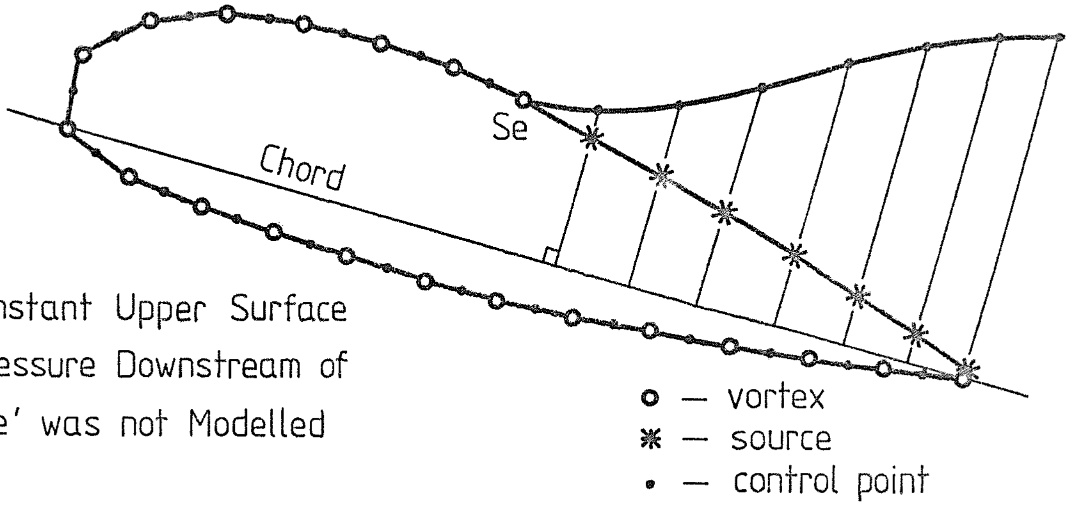

Constant Upper Surface Pressure Downstream of 'Se' was not Modelled

Fig(70) Farn's Theoretical Model (Ref. 49) conditions were specified to enable the position of these streamlines to be found, these were :

(a) Flow tangency to the aerofoil surface prior to separation, and to all the free streamlines bounding the separation region and wake.

(b) Constant tangential velocity (and hence pressure) along the separation streamline up to the trailing edge, and equal to that at the trailing edge.

(c) No net force across the wake by ensuring equal tangential velocity on opposite sides of the wake at any point.

(d) Tangential separation of the separation streamline from the upper aerofoil surface.

Once iteratively located, these separation and wake streamlines formed a closed displacement body attached to the rear of the original aerofoil, figure (71). It was then argued that potential flow analysis of this combined shape would provide the correct pressure distribution for the aerofoil with trailing edge separation. Comparison of this method with experimental results proved to be good.

Other similar panel methods have been presented by Barnwell (51), Gross (52) and Zumwalt (53).

9.2 Mast/Sail Modelling Difficulties

In order to provide for future extension to 3-dimensions, it was clear that any theory for masts and sails would have to be based on panel methods. There were however, a number of features unique to the mast/sail case that made the existing aerofoil theories

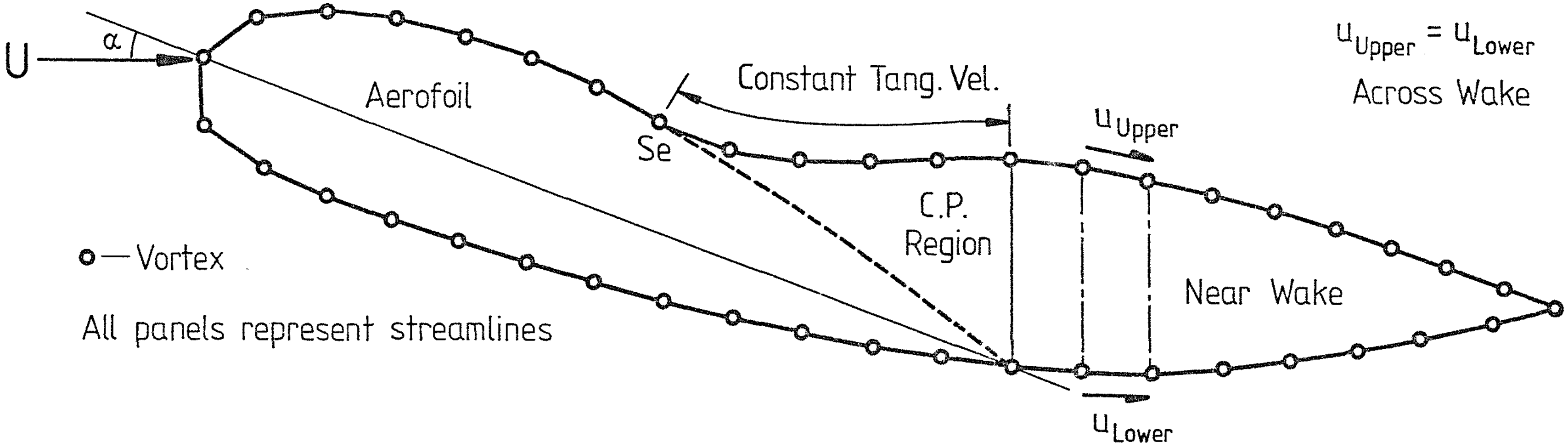

Fig(71) Henderson's Theoretical Model (Ref. 50)

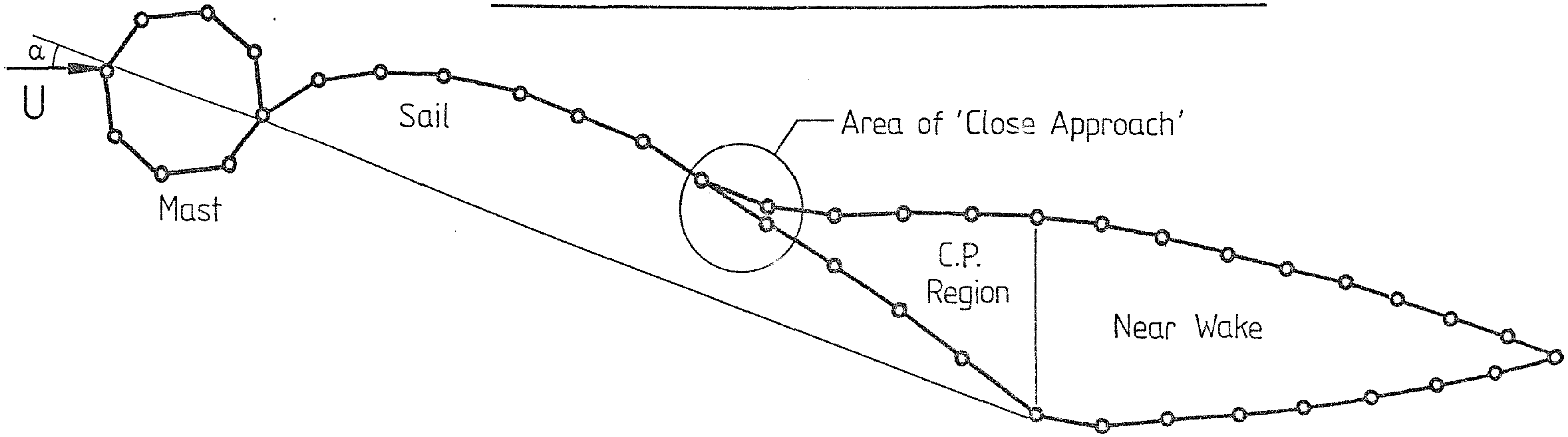

Fig(72) Henderson's Method Applied to a Mast/Sail Geometry difficult to adopt. These were : (a) the simultaneous presence of upper and lower surface bubbles, and (b) essentially zero sail thickness.

Virtually all of the panel methods previously described, involved an iterative procedure to produce and locate a constant pressure free streamline bounding the trailing edge separation region, and in some cases this procedure was extended to model the near wake as well. In Henderson's method the panels were actually placed along these off-body free streamlines, this fact alone ruled out this theoretical approach, because of the zero sail thickness with the present situation, the nature of this problem is shown in figure (72). Because the camber line of the sail effectively had zero thickness, any panels along this line had to represent both upper and lower surface flow conditions. The singularity panels placed along the tangentially detaching upper surface free streamline, therefore became perilously close to the downstream panels following separation representing the lower surface flow. It is well known that discrete singularity methods break down when two or more distinct singularity sheets became too close to each other, this is known as the 'close approach' problem.

An attempt was nevertheless made to describe mast/sail trailing edge separation using Henderson's method, by incorporating Maskew's (54) system for coping with 'close approach'. The tangential nature of the approach, however, was too severe for this method to be successful.

To avoid 'close approach' problems it was clear that panels could only be placed along the contours of the mast/sail model that represented the solid surfaces. Farn's model fell into this category, but certain difficulties were apparent with this method :

(a) Farn's results lacked the displacement effect of the wake, and the placing of sufficient source panels onto the sail surface downstream of separation to model this wake accurately, would have been difficult.

(b) The technique was essentially an iterative one which would have required long computing times if applied, not only to the trailing edge separation streamline, but also to those bounding the bubbles and wake.

(c) An empirical value of base-pressure was required as well as separation location. Minimum empirical input was thought desirable.

At this stage a fundamental reversal in approach was made to the problem. In none of the previously described methods were the actual conditions on the aerofoil surface downstream of separation modelled, instead the required constant base-pressure was either assumed (Jacob), or imposed along a separation streamline (Farn, Henderson). The assumption in the latter case was that if the constant pressure free streamline was modelled correctly, then correct conditions on the aerofoil surfaces would inevitably result. The implication of this must therefore be that if conditions on all the solid surfaces are modelled correctly, then the resulting separation and wake streamline boundaries will automatically be correct as well. If the previous statement were true (and subsequent results show this to be likely), then it is possible to accurately model separation regions without paying attention to conditions along, or positions of, any off-body streamlines. This, of course, immediately removed any necessity for iteration, provided that conditions at the solid surfaces could be accurately modelled. This formed the basis of the mast/sail theoretical model developed in the present work.

9.3 Basic Description of the Mast/Sail Model (Boundary Conditions)

Before any detailed mathematical model could be formulated it was necessary to review the known surface boundary conditions that would make a solution possible. These boundary conditions are shown in figure (73) and listed in the following :

(a) No fluid could cross the solid mast or sail boundaries (i.e. flow tangency).

(b) Bubble and trailing edge separation had to occur tangentially (including fluid leaving the lower surface at the trailing edge).

(c) Surface tangential velocities had to be constant within separated base-pressure regions, and equal to that at the point of separation in each case. This avoided any need for an empirical base-pressure input.

There are two basic types of mathematical singularity that can be used for flow modelling, these are vortices and sources. It was decided to distribute these over the mast and sail surfaces, and solve for their strengths by using known boundary conditions. Each singularity used required a unique boundary condition to solve for its' strength, and conversely, each required boundary condition needed one signularity to model it.

The mast and aerofoil contour was represented by a sheet of vorticity, since the sail, which was considered in the model to be infinitely thin, had to support a pressure difference across it (DE in figure (73)). Such a pressure discontinuity, or lifting surface, could only be represented by vortices, since a sheet of sources would simply exhibit an identical tangential velocity (and hence pressure) on both sides of the sheet. The strength of this vortex could be solved using the flow tangency condition (a).

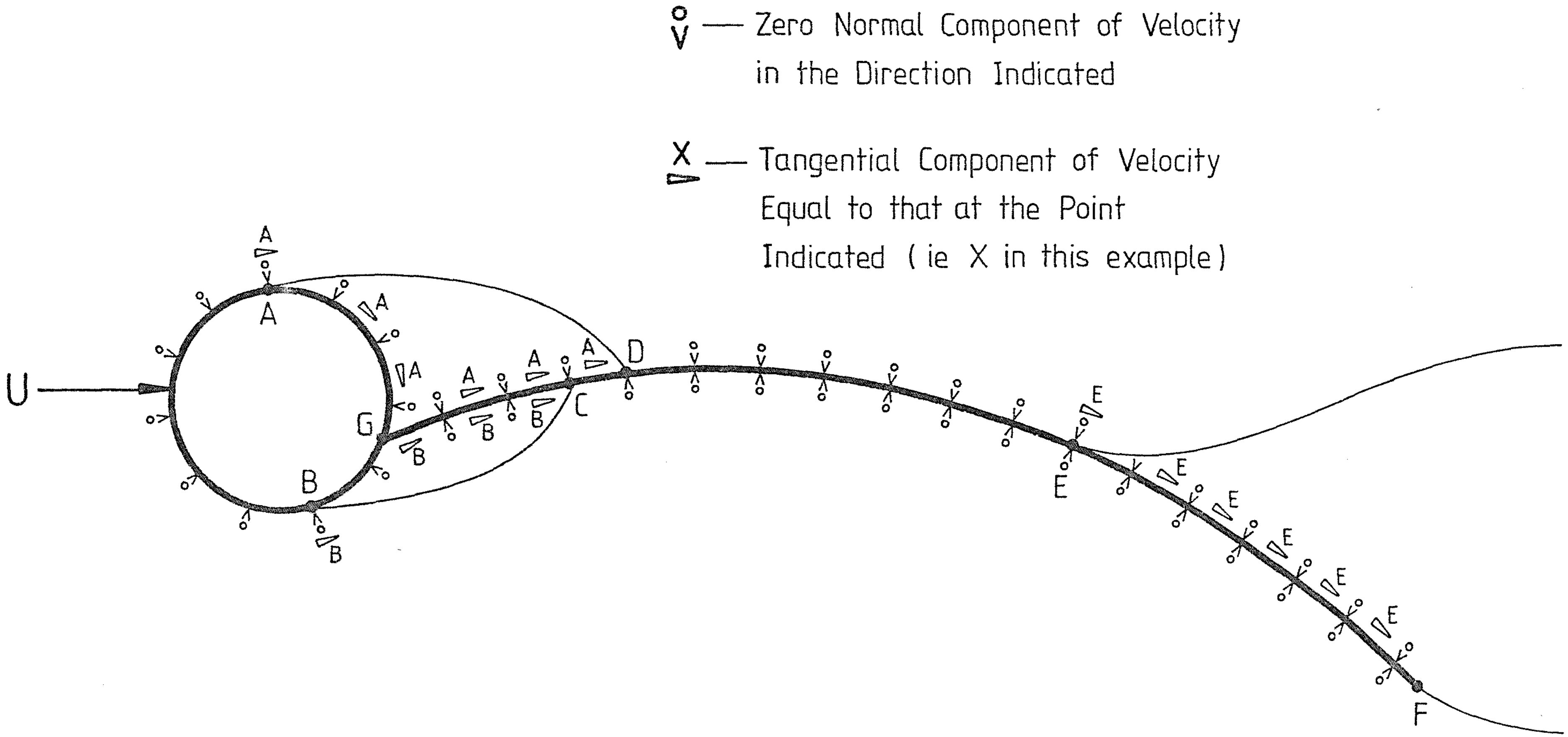

Fig(73) Boundary Conditions for Mast/Sail Model

For those parts of the model surface, AG, BG, CD and EF in figure (73), two boundary conditions had to be represented, i.e. no flow through the mast or sail surfaces and constant tangential velocity on one side of these surfaces. Two singularities were required to represent these two boundary conditions, so to model these regions source sheets were placed on top of the basic vortex sheet. Sources were well suited to this role, since they represented surface thickness which was basically what existed when the streamlines were deflected around the 'dead air' within separation regions.

Finally for the surface region GC in figure (73), three boundary conditions were necessary i.e. no flow through the sail surface, constant tangential velocity on one side of the sail surface, and another different constant tangential velocity on the other side. In this case two source sheets were placed on top of the basic vortex sheet. Normally this would be unsolvable, since two similar types of singularity occupying the same space would only produce one independent equation instead of the necessary two. This was not a problem with the present model, however, since the sources representing the upper and lower surface flow were regarded as independant sheets, and solved using different boundary conditions.

The layout of vortex and source sheets for the mast/sail model is shown in figure (74), the source sheets are shown slightly displaced from the vortex sheet for clarity, however in the actual model all sheets occupied the same space along the mast/sail contours, any other positioning would again have run into 'close approach' problems.

9.4 Sheet Discretization and Doublet Panels

To make a numerical solution possible, the continuous sheets of varying vorticity and source density had to be discretized into point vortices and sources. This process is described in figure (75) where a sheet of vorticity is shown with an arbitrary continuous

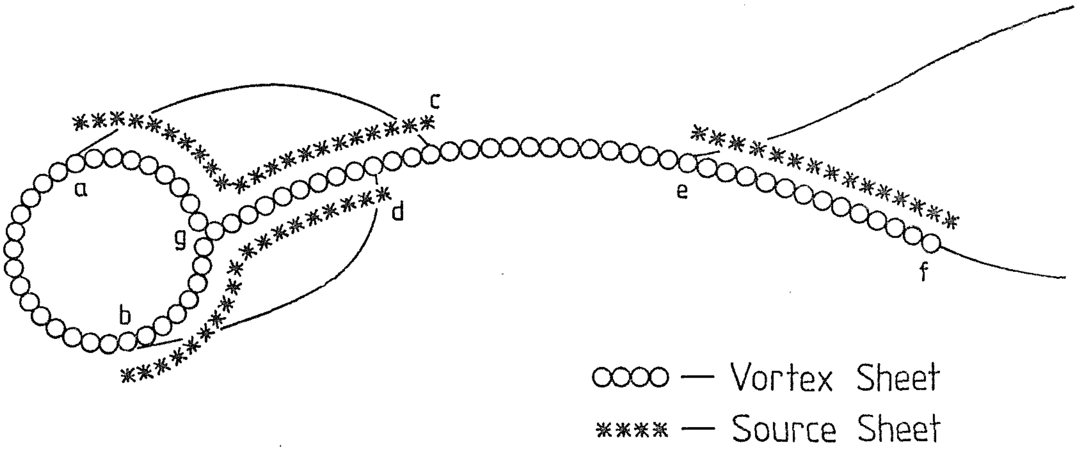

Fig (74) Sheet Layout for Mast / Sail Model

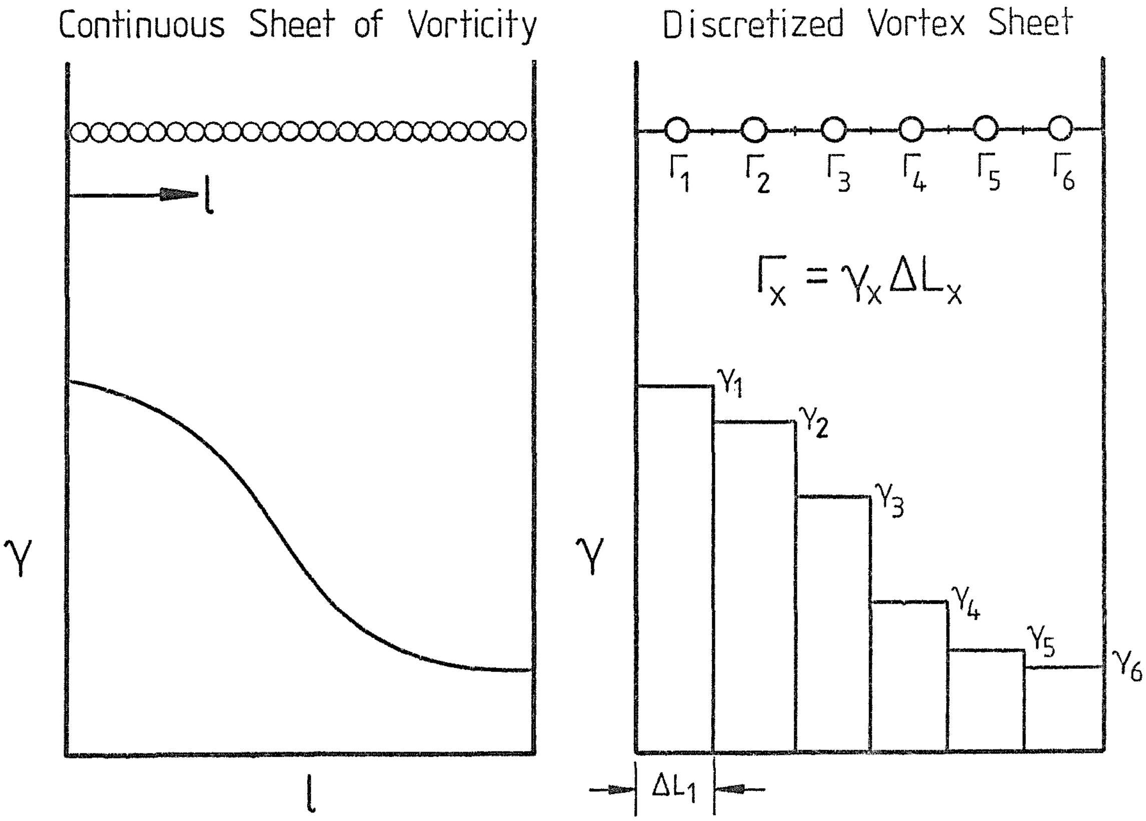

Fig (75) Discretization Process

variation in local vortex strength along its length. This continuous variation has been approximated by a discretized histogram , made up of a number of short lengths of constant vorticity. Based on this histogram distribution it was possible to replace the continuous vorticity sheet by a line of discrete vortices placed centrally over the histogram columns. The strength of each discrete point vortex (Γ) was determined by the constant level of vorticity across the histogram column (γ), multiplied by the column width (ΔL).

The point vortices and sources used in the discretized model to represent continuous sheets, were basically mathematical singularities since velocities became infinite at their centres. To avoid any inaccuracies due to these singularities, it was decided to model the required boundary conditions only at 'control points' placed mid-way between the singularities.

Unfortunately, as shown in figure (76a), a row of point vortices or sources with control points between them will always produce one too few control points, and hence equations, to solve for all the unknown vortex or source strengths. This difficulty led to the adoption of doublet panels.

Figure (76b) shows how a row of 6 point vortices of unknown strength can be reformulated into only 5 unknowns by considering the vortices in pairs. The fundamental element, or building block, from which all sheets could be represented was therefore changed from a single singularity, to a pair of singularities of equal strength but opposite sign, separated by a straight line distance Δs, and with a control point placed at the mid point. these panels could be represented mathematically by a single variable known as the 'panel strength', this was given the symbol (μ) for vortex panels. The vortex strength at the +ve end of a panel was simply given by $\Gamma + = \mu$, and the vortex strength at the -ve end was expressed by $\Gamma - = -\mu$. Figure (76c) shows a typical vortex panel element.

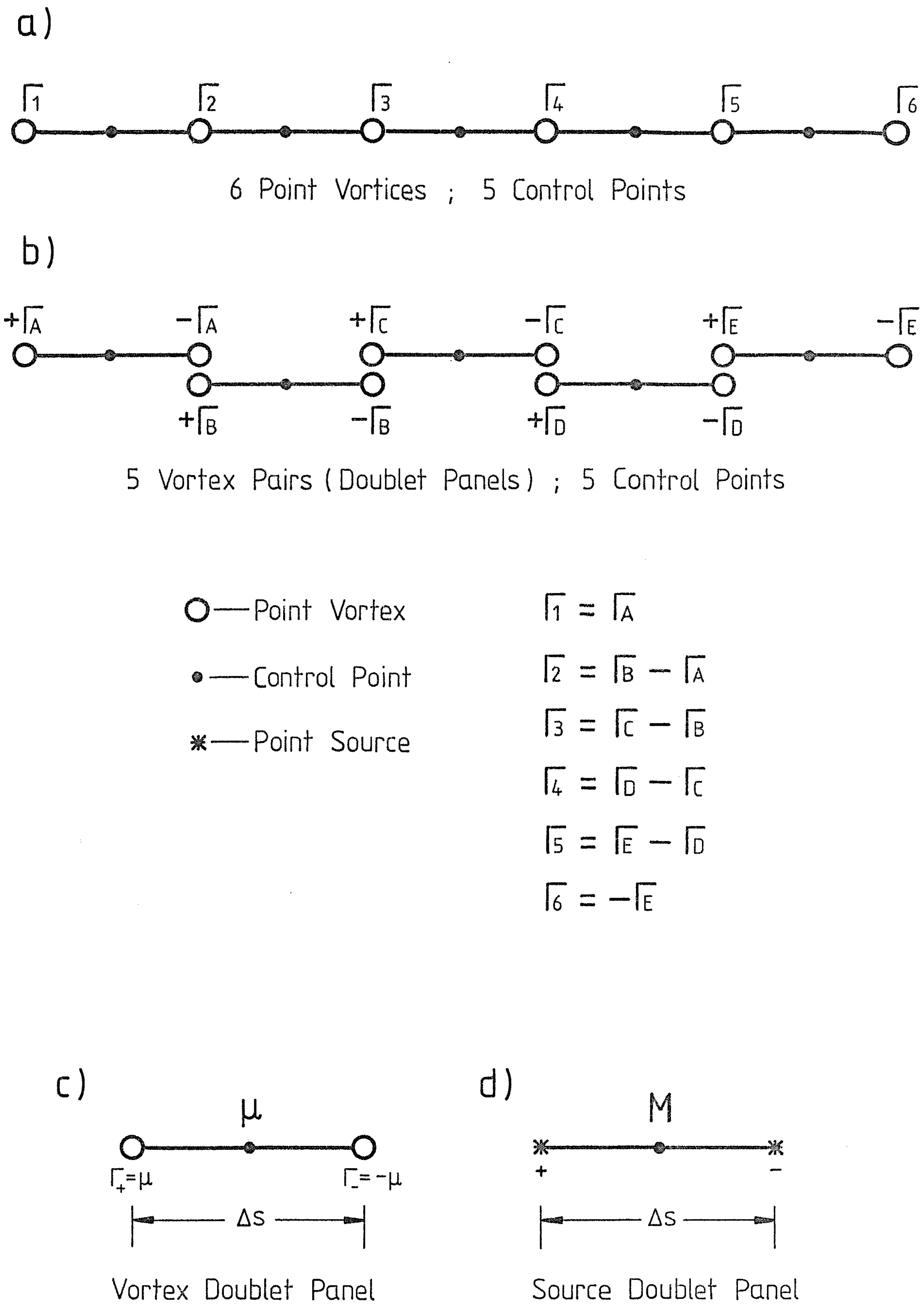

Fig (76) Panel Definitions

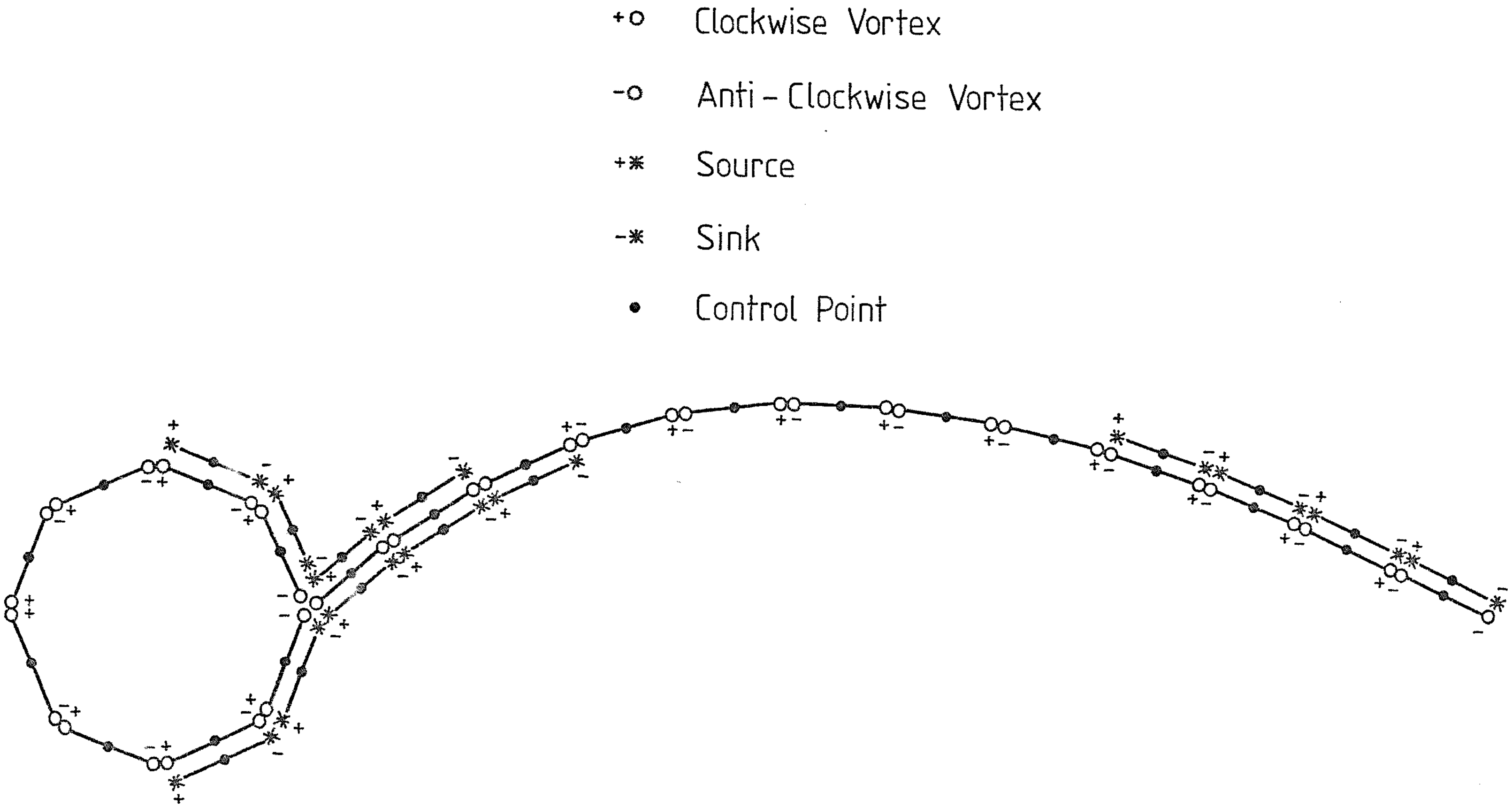

Fig(77) Doublet Panels Applied to the Mast / Sail Model

Such an element can be shown to be representative of a row of constant strength doublets, i.e. a constant doublet panel. By using this type of panel, an equality between unknown panel strengths and the number of control points (and hence equations), was always assured whatever the form of geometry to be modelled.

Doublet panels could be constructed not only with vortices of opposite sign, but also with sources of opposite sign (source and sink). In this case the source doublet panel strength was given the symbol (M), this is shown in figure (76d). Source doublet panels had the advantage of mass conservation, since for any source there was always a sink of equal strength. This was ideal for modelling bubbles where a region of fluid was enclosed by a separation streamline across which there could be no flow.

The continuous sheet model of figure (74) was then discretized using vortex doublet and source doublet panel elements, this is shown in figure (77). Singularities at the panel boundaries are shown separately for clarity, however all singularities at the ends of adjacent panels actually occupied the same space, similarly the source doublet panels occupied the same space on the model contours as the vortex doublet panels.

9.5 Formulation of Mathematical Equations

All the vortex and source doublet panels used in the mast/sail model were initially of unknown strength, it was therefore necessary, using the known boundary conditions, to formulate an independant equation at each control point. Since there existed a control point for every panel of unknown strength, the resulting set of simultaneous equations enabled all unknowns to be found.

By placing the double panel model in a uniform stream at an incidence angle, the resulting velocities normal and tangential to the local surface at each control point, could be attributed to three fundamental mechanisms.

9.5.1 Free-Stream Velocity Components

The first of these contributions to velocity came directly from the free-stream velocity resolved into components normal and tangential to the local surface at each control point.

Consider the mast/sail model within a flow field, defined by an XY axis system as originally shown in figure (1). Using a further curvilinear xy axis system following the surface contour, it was possible to compare free-stream velocity components with local surface geometry, this is shown below in figure (78).

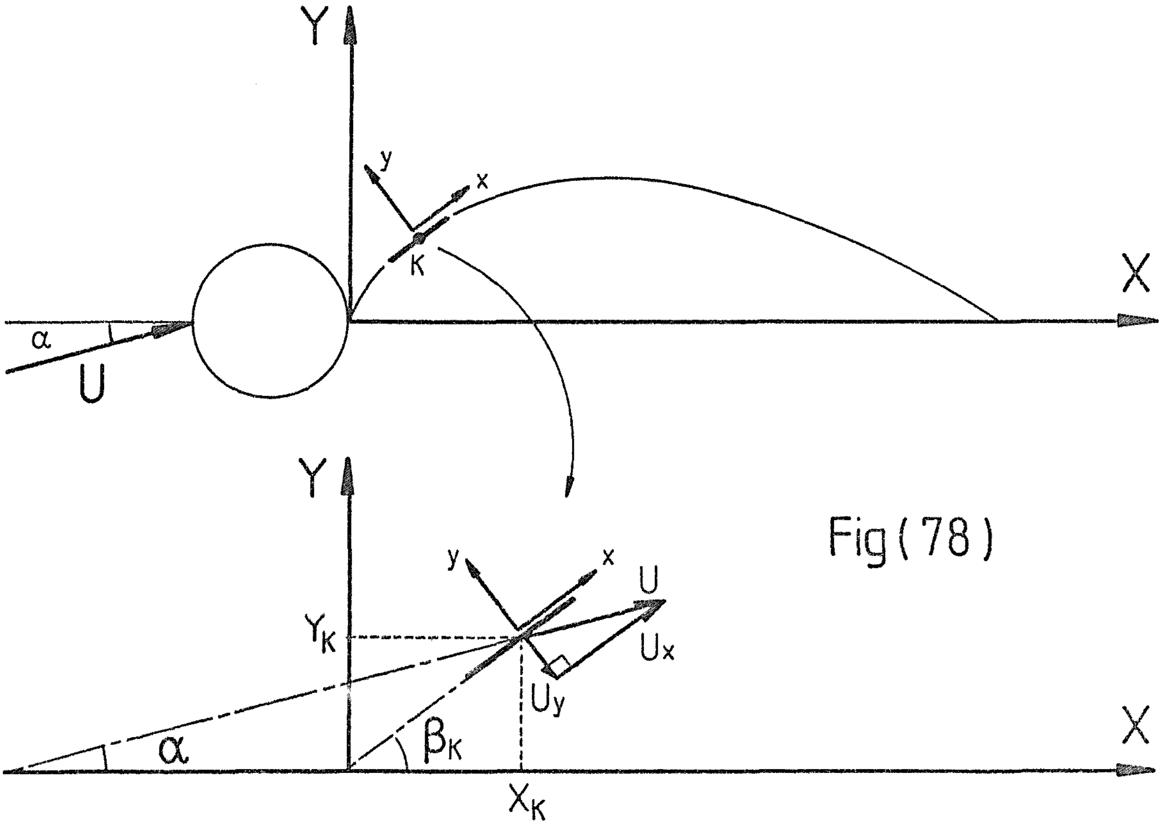

Fig(78)

By considering any panel (k) comprising the model, with its control point at (X_k, Y_k), the component of free-stream velocity normal to the panel (U_y) and that tangential to the panel (U_x), could be expressed in terms of the panel slope (Tan β_k) relative to the XY axes, the free-stream velocity (U) and the aerodynamic incidence angle (α) :

$$U_y = -U \sin(\beta_k - \alpha)$$

and

$$U_x = U \cos(\beta_k - \alpha)$$

In terms of local panel slope, these reduce to :

$$U_y = \frac{-U}{(1 + \tan^2\beta_k)^{0\cdot5}} (\tan\beta_k \cos\alpha - \sin\alpha) \qquad \text{———} \quad 9\cdot1$$

$$U_x = \frac{U}{(1 + \tan^2\beta_k)^{0\cdot5}} (\tan\beta_k \sin\alpha + \cos\alpha) \qquad \text{———} \quad 9\cdot2$$

9.5.2 Velocity Components due to Flow Field Singularities

The second contribution to velocity stemmed from the fact that each doublet panel (vortex or source) placed on the contour of the mast/sail model affected every point in the flow field.

Consider first the effect of the +ve end of a vortex doublet panel (j) placed at an arbitrary point (X_{j+}, Y_{j+}), on a control point at (X_k, Y_k) with panel slope $(\tan \beta_k)$. The basic geometry of this situation is shown in figure (79).

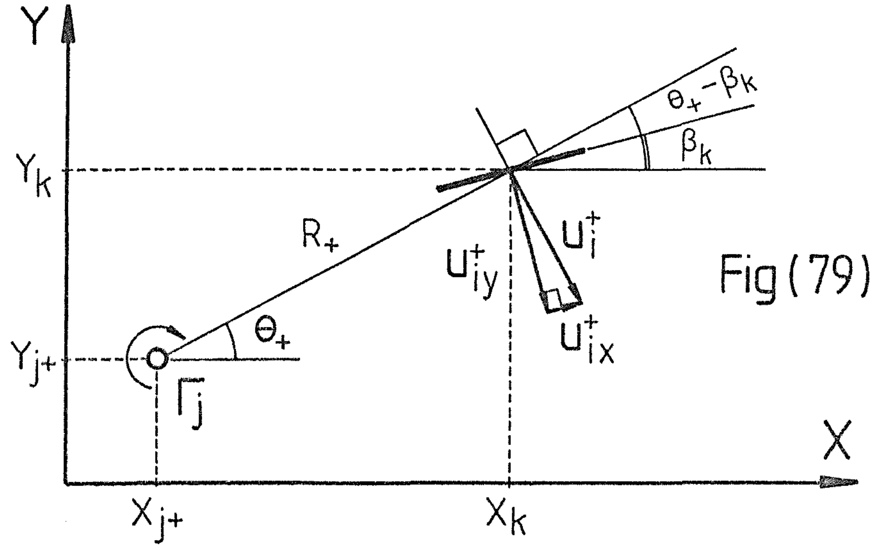

Fig (79)

The velocity induced at a point by a +ve vortex at some other point is given by :

$$u_i^+ = \frac{\Gamma_{j+}}{2\pi R_+} = \frac{\mu_j}{2\pi R_+}$$ in terms of the panel strength

Where the induced velocity (u_i^+) acts normally to the straight line, of length R+, joining the vortex to the point considered.

This relationship combined with the geometry shown in figure (79), led to the following equations for the induced velocity components normal and tangential to the panel (k).

$$u_{iy}^+ = -u_i^+ . \cos(\theta_+ - \beta_k) = \frac{-\mu_j}{2\pi R_+} . \cos(\theta_+ - \beta_k)$$

$$u_{ix}^+ = u_i^+ . \sin(\theta_+ - \beta_k) = \frac{\mu_j}{2\pi R_+} . \sin(\theta_+ - \beta_k)$$

These can be further re-written as follows :

$$u_{iy}^{+} = \frac{-\mu_j}{2\pi R_+}(\cos\theta_+\cos\beta_k+\sin\theta_+\sin\beta_k) = \frac{-\mu_j}{2\pi R_+}(\cos\theta_+ + \tan\beta_k\sin\theta_+).\cos\beta_k$$

$$u_{ix}^{+} = \frac{\mu_j}{2\pi R_+}(\sin\theta_+\cos\beta_k-\cos\theta_+\sin\beta_k) = \frac{\mu_j}{2\pi R_+}(\sin\theta_+ - \tan\beta_k\cos\theta_+).\cos\beta_k$$

Finally by substituting $\sin\theta_+ = (\frac{Y_k - Y_{j+}}{R_+})$, $\cos\theta_+ = (\frac{X_k - X_{j+}}{R_+})$ $\cos\beta_k = (1 + \tan^2\beta_k)^{-\frac{1}{2}}$ and $R_+^2 = (X_k - X_{j+})^2 + (Y_k - Y_{j+})^2$ the induced velocity components became :

$$u_{iy}^{+} = \frac{-\mu_j}{2\pi(1+\tan^2\beta_k)^{0.5}} \cdot \left[\frac{(X_k-X_{j+})+(Y_k-Y_{j+})\tan\beta_k}{(X_k-X_{j+})^2+(Y_k-Y_{j+})^2}\right] \text{———} 9.3$$

$$u_{ix}^{+} = \frac{\mu_j}{2\pi(1+\tan^2\beta_k)^{0.5}} \cdot \left[\frac{(Y_k-Y_{j+})-(X_k-X_{j+})\tan\beta_k}{(X_k-X_{j+})^2+(Y_k-Y_{j+})^2}\right] \text{———} 9.4$$

If now, a similar process is carried out for the -ve end of the vortex panel at the point (X_{j-}, Y_{j-}), the normal and tangential velocity components induced at (X_k, Y_k) become :

$$u_{iy}^{-} = \frac{\mu_j}{2\pi(1+\tan^2\beta_k)^{0.5}} \cdot \left[\frac{(X_k-X_{j-})+(Y_k-Y_{j-})\tan\beta_k}{(X_k-X_{j-})^2+(Y_k-Y_{j-})^2}\right] \text{———} 9.5$$

$$u_{ix}^{-} = \frac{-\mu_j}{2\pi(1+\tan^2\beta_k)^{0.5}} \cdot \left[\frac{(Y_k-Y_{j-})-(X_k-X_{j-})\tan\beta_k}{(X_k-X_{j-})^2+(Y_k-Y_{j-})^2}\right] \text{———} 9.6$$

The total effect of both +ve and -ve ends of a vortex doublet panel (j) on a control point (K), in terms of induced velocity components normal and tangential to the local surface at (K) therefore becomes :

$$u_{iy}^{v} = u_{iy}^{+} + u_{iy}^{-} = \frac{\mu_j}{2\pi(1+\tan^2\beta_k)^{0\cdot5}}(A_{jk}+B_{jk}\tan\beta_k - E_{jk} - F_{jk}\tan\beta_k) \qquad \text{———— } 9\cdot7$$

$$u_{ix}^{v} = u_{ix}^{+} + u_{ix}^{-} = \frac{\mu_j}{2\pi(1+\tan^2\beta_k)^{0\cdot5}}(F_{jk} - E_{jk}\tan\beta_k - B_{jk} + A_{jk}\tan\beta_k) \qquad \text{———— } 9\cdot8$$

where

$$A_{jk} = \frac{(X_k - X_{j-})}{(X_k - X_{j-})^2 + (Y_k - Y_{j-})^2}$$

$$B_{jk} = \frac{(Y_k - Y_{j-})}{(X_k - X_{j-})^2 + (Y_k - Y_{j-})^2}$$

$$E_{jk} = \frac{(X_k - X_{j+})}{(X_k - X_{j+})^2 + (Y_k - Y_{j+})^2} \qquad \text{———— } 9\cdot9$$

$$F_{jk} = \frac{(Y_k - Y_{j+})}{(X_k - X_{j+})^2 + (Y_k - Y_{j+})^2}$$

A_{jk}, B_{jk}, E_{jk} and F_{jk} formed the elements of 4 square matrices of size (j_{max} x k_{max}). These matrices could be created from just the geometric positions of all the control points (K) and panel ends (j+ and j-) in the flow field.

The equations 9.7 and 9.8 were formulated for vortex doublet panels, however a similar set of equations has also been derived for source doublet panels, by considering all flows from sources and sinks to be radial.

The total effect of both +ve and -ve ends of a source doublet panel (j) on a control point (K), in terms of the induced velocity components normal and tangential to the local surface at (K) was found to be :

$$u^s_{iy} = \frac{M_j}{2\pi(1+\tan^2\beta_k)^{0\cdot5}}(F_{jk} - E_{jk}\tan\beta_k - B_{jk} + A_{jk}\tan\beta_k) \qquad \text{———} \; 9\cdot10$$

$$u^s_{ix} = \frac{M_j}{2\pi(1+\tan^2\beta_k)^{0\cdot5}}(E_{jk} + F_{jk}\tan\beta_k - A_{jk} - B_{jk}\tan\beta_k) \qquad \text{———} \; 9\cdot11$$

where M_j is the strength of the source doublet panel (j) (i.e. the sink strength at the -ve end of panel (j) is given by $-M_j$ and the source strength at the +ve end of panel (j) is given by M_j).

9.5.3 Local Velocity Components Close to Sheet Discontinuities

It can be shown that equation 9.8 gives the tangential component of velocity induced at a control point (k) by a vortex doublet panel at (j) as zero when j = k, i.e. when the control point considered is at the centre of the vortex doublet panel. In reality this cannot be so, the error in this case being directly attributable to the descretization process.

A special equation had therefore to be derived for the tangential velocity at a control point due to the adjacent vortices when j = k.

Consider the continuous sheet of vorticity of constant strength γ/unit length shown in figure (80).

Fig(80)

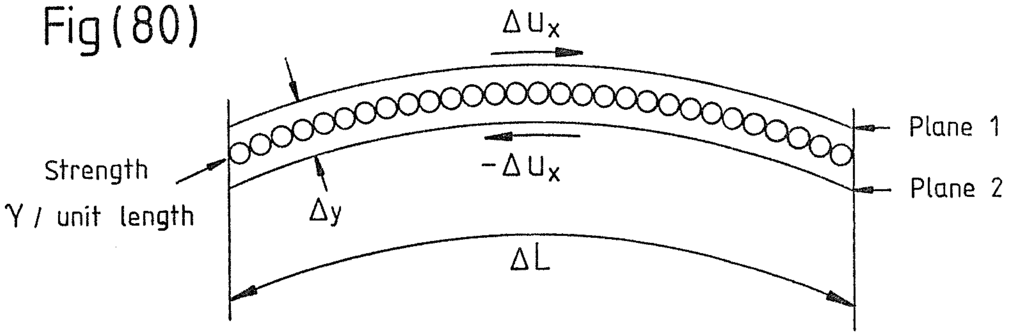

If the planes 1 and 2 are considered running above and below the sheet respectively, at an infinitely small distance from the sheet i.e. $\Delta y \to 0$, then a tangential velocity Δu_x will exist along these planes in opposite directions.

Circulation along plane 1 $= \Delta u_x \cdot \Delta L$ (+ clockwise)

Circulation along plane 2 $= \Delta u_x \cdot \Delta L$ (+ clockwise)

$\therefore$ Total circulation around the sheet $= 2\,\Delta u_x\,\Delta L$

However the circulation due to the sheet vorticity $= \gamma \Delta L$

$\therefore$ By conservation of circulation $\gamma \Delta L = 2 \Delta u_x \Delta L$
or

$$\boxed{\Delta u_x = \frac{\gamma}{2} \qquad 9\cdot 12}$$

This demonstrates that the local tangential velocity is equal to ½ of the local vorticity.

Consider now not a sheet of constant vorticity, but one of continuously varying vorticity. If the rate of variation is small, then this can be approximated by two adjacent sheets of different but constant vorticity γ_1 and γ_2. This is shown in figure (81).

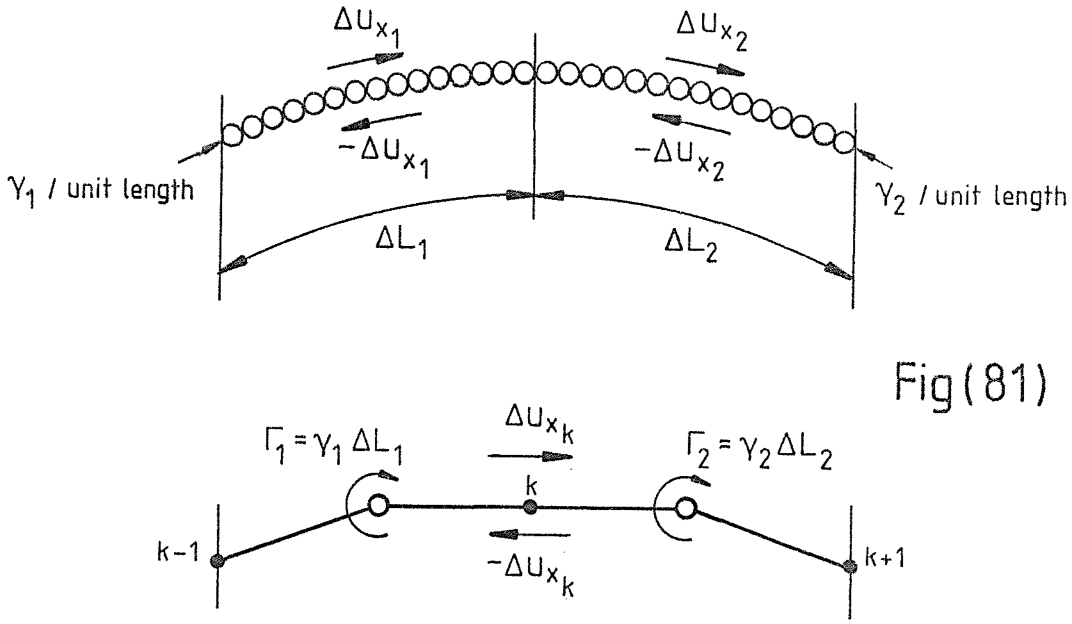

Fig(81)

The continuously varying vorticity sheet in figure (81) is also shown discretized by lumping together the lengths of constant vorticity into centrally placed concentrated point vortices, with control points positioned mid-way between them.

To find the local tangential velocity at the control point (k) using equation 9.12, it was necessary to estimate the local value of vorticity at the control point. This was taken as the average vorticity of the two adjacent point vortices, i.e.

$$\gamma_K = \frac{\gamma_1 + \gamma_2}{2} = \left[\frac{\Gamma_1}{\Delta L_1} + \frac{\Gamma_2}{\Delta L_2}\right] \cdot \frac{1}{2}$$

Then by using equation 9.12

$$\Delta u_{x_k} = \left[\frac{\Gamma_1}{\Delta L_1} + \frac{\Gamma_2}{\Delta L_2}\right] \cdot \frac{1}{4} \qquad 9{\cdot}13$$

Equation 9.13 has been expressed in terms of the adjacent vortex strengths Γ_1 and Γ_2 and the distances between control points ΔL_1 and ΔL_2. It was more meaningful, however, to express equation 9.13 in terms of panel strengths μ_k, μ_{k+1}, and μ_{k-1} and panel widths ΔS_k, ΔS_{k+1} and ΔS_{k-1}, i.e.

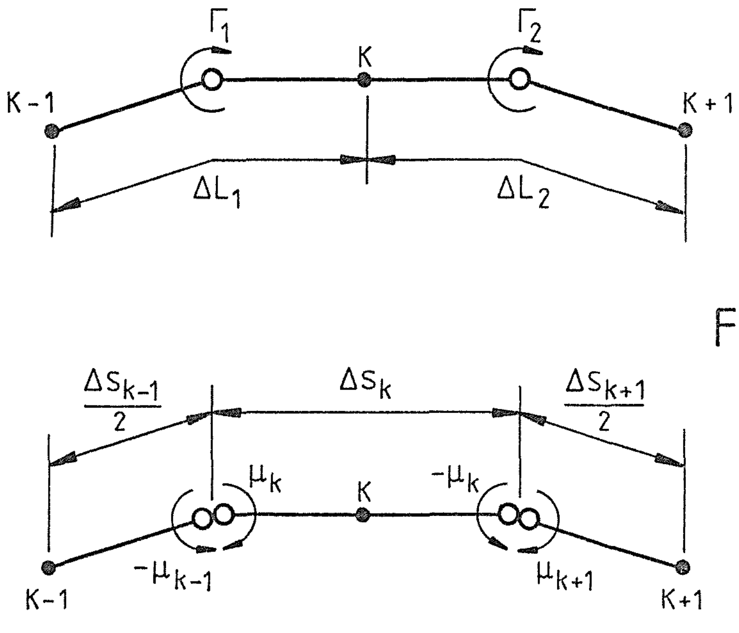

Fig (82)

From the two equivalent diagrams shown in figure (82), it can be seen that :

$$\Gamma_1 = \mu_K - \mu_{K-1} \quad ; \quad \Gamma_2 = \mu_{K+1} - \mu_K$$

$$\Delta L_1 = \frac{(\Delta s_K + \Delta s_{K-1})}{2} \quad ; \quad \Delta L_2 = \frac{(\Delta s_K + \Delta s_{K+1})}{2}$$

Substituting these in equation 9.13 gives :

$$\boxed{\Delta u_{x_k} = \frac{1}{2} \cdot \left[\frac{(\mu_k - \mu_{k-1})}{(\Delta s_k + \Delta s_{k-1})} + \frac{(\mu_{k+1} - \mu_k)}{(\Delta s_k + \Delta s_{k+1})} \right] \text{———} 9{\cdot}14}$$

Equation 9.14 provided the tangential velocity at a control point (k) due to the adjacent panel strengths. This velocity acted in the +ve x direction above the vorticity sheet, and in the -ve x direction below the vorticity sheet.

When considering a panel at the beginning of a sheet, $\mu_{k-1} = 0$ and $\Delta S_{k-1} = 0$ were substituted into equation 9.14, similarly for the last panel on a sheet, $\mu_{k+1} = 0$ and $\Delta S_{k+1} = 0$ were substituted.

In a similar way, equation 9.10 implied that zero normal velocity was induced by a source doublet panel at its own control point i.e. at j = k. Using a mass flow balance instead of circulation conservation, a similar equation to 9.14 has been derived for the local normal velocity at a control point (k) due to adjacent source panels.

$$\boxed{\Delta u_{y_k} = \frac{1}{2} \cdot \left[\frac{(M_k - M_{k-1})}{(\Delta s_k + \Delta s_{k-1})} + \frac{(M_{k+1} - M_k)}{(\Delta s_k + \Delta s_{k+1})} \right] \text{———} 9{\cdot}15}$$

In this case the normal velocity was in the +ve y direction above the source sheet, and in the -ve y direction below the sheet. As before, when considering a panel at the beginning of a sheet M_{k-1} and ΔS_{k-1} were both zero, similarly for the last panel representing a sheet M_{k+1} and ΔS_{k+1} were both zero in equation 9.15.

9.6 Mathematical Representation of Boundary Conditions

A typical layout of panels for the mast/sail mathematical model adopted is shown in figure (83). Panels 1 to 28 represents vortex doublet panels placed along the mast and sail surface contours, whilst panels 29 to 45 are source doublet panels representing the various separation regions.

The locations of the vortex doublet panels in the flow field were determined in each case by the particular mast/sail geometry to be simulated, and were therefore dependant on sail shape, camber ratio, mast diameter/chord ratio and mast angle.

The curious numbering system shown for panels around the mast contour, ensured that the +ve panel ends were always at a lower X location than the -ve ends, this meant that the square root in equations 9.1, 9.2, 9.7, 9.8, 9.10 and 9.11 was always +ve.

To simulate the separation regions, empirical data was required to ensure correct positioning of the source doublet panels. The experimentally obtained information required was the trailing edge separation location, plus the start and end positions of the two bubble constant base-pressure regions. These locations could be expressed to the nearest panel number, i.e. for the example shown in figure (83) the empirical information necessary was :

Upper bubble separation point	NUBS	at panel 6
End of upper bubble Region II	NUBE	at panel 11

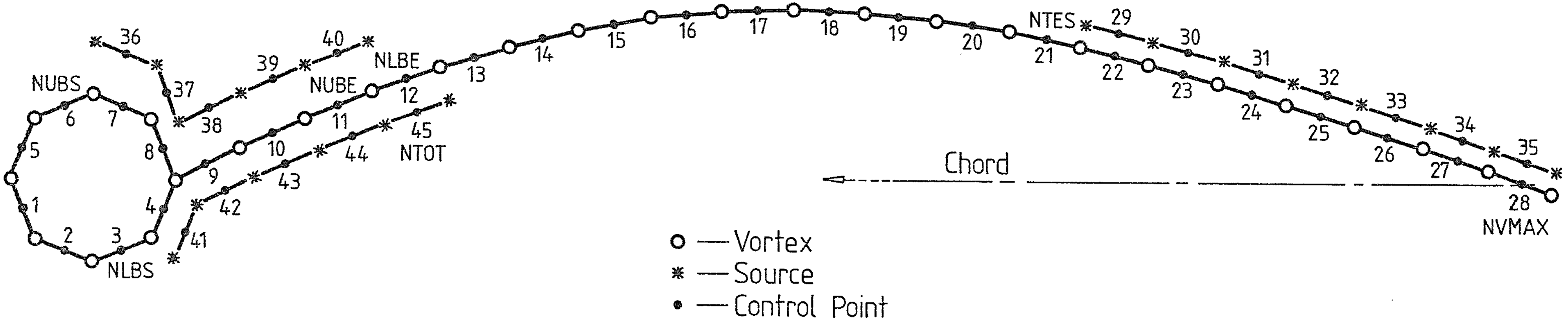

Fig (83) Typical Panel Numbering for the Final Mast / Sail Model

Lower bubble separation point	NLBS	at panel 3
End of lower bubble Region VII	NLBE	at panel 12
Trailing edge separation point	NTES	at panel 21

To avoid any danger of numerical instabilities occurring during the solution of singularity models, panel lengths are usually kept as uniform as possible. It was found in the present model that a maximum of only 8 panels could be used for mast representation, otherwise their size in comparison to those on the sail would have become too small when considering very low mast diameter/chord ratios.

This problem could be avoided in future by regulating the number of sail panels used, depending on the mast size involved. This however would inevitably lead to longer solution times, because of the large increase in flow field panels that would result when considering low (d/c) cases.

With just 8 mast panels, control points were only available at every 45° of arc, this made it difficult to precisely model the true bubble separation points in each case. For this reason it was found that panels 6 and 3 were universally applicable as regards mast separation locations.

With the start and finish locations of the separation regions found empirically, source doublet panels could be placed directly on top of the vortex doublet panels within each defined separation region. A source doublet panel was not placed on the separation panel in each case, the reason for this will be explained later.

Having defined all the panel locations, it was then possible to use the known boundary conditions to formulate independent equations for each control point.

The simplest case was for panels k = 1 to NLBS, k = 5 to NUBS and k = (NLBE + 1)* to NTES in figure (83). For these, only vortex doublet panels were present on the surfaces, and the boundary condition was flow tangency alone (or zero normal component velocity at each control point).

At these control points the normal velocity component was produced by the free stream flow, plus the effect of all vortex and source panels in the flow field, i.e.

$$u_{y_k} = U_y + \sum_{j=1}^{NVMAX\,(=\varkappa)} u_{iy}^{v} + \sum_{j=\varkappa+1}^{NTOT} u_{iy}^{s} = 0$$

Using equations 9.1, 9.7 and 9.18 this could be written as :

$$\boxed{\begin{aligned} 2\pi U(\tan\beta_k\cos\alpha-\sin\alpha) &= \sum_{j=1}^{NVMAX\,(=\varkappa)} \mu_j(A+B\tan\beta_k-E-F\tan\beta_k)_{jk} \\ &+ \sum_{j=\varkappa+1}^{NTOT} M_j(F-E\tan\beta_k-B+A\tan\beta_k)_{jk} \\ \text{For } 1\leqslant K\leqslant NLBS\ ;\ 5 &\leqslant K\leqslant NUBS\ ;\ (NLBE+1)^{*}\leqslant K\leqslant NTES \\ &\text{———— } 9{\cdot}16 \end{aligned}}$$

---

* This could equally well be (NUBE + 1) if the upper bubble was longer than the lower bubble.

In this way an independant equation in terms of all the unknown source and vortex panel strengths could be produced, using equation 9.16, for all the control points (k) in the ranges stated.

Equation 9.16 was, however, incomplete when considering the vortex doublet panels (NTES + 1), $\leqslant k \leqslant$ NVMAX, since in this case source doublet panels were superimposed on top of the vortex doublet panels. The flow tangency condition in this case was only relevant to the sail lower surface, since above the upper surface, a normal component of velocity would inevitably exist due to the source flow representing the separation and wake flow.

Although the source doublet panels in this trailing edge separation region were actually positioned directly on top of the vortex doublet panels, for the purposes of summing the velocity contributions, the source doublet panels were regarded as being at an infinitely small distance above the surface vortex panels.

To ensure flow tangency over the lower surface, the sum of the following normal components of velocity had to be zero, i.e. the free stream velocity, the velocity induced by all source and vortex panels in the flow field, and the -ve local velocity produced by the source sheet.

$$u_{y_k} = U_y + \sum_{j=1}^{NVMAX(=\varkappa)} u^{v}_{jy} + \sum_{j=\varkappa+1}^{NTOT} u^{s}_{jy} - \Delta u_y = 0 \quad \text{------------} \quad 9{\cdot}17$$

With equations 9.1, 9.7, 9.10, 9.15 and using the symbol (L) to identify the number of the source doublet panel placed on top of a vortex doublet panel (K), equation 9.17 could be rewritten as :

Pages 254 is
missing from
this Thesis

Pages 255 is missing from this Thesis

$$2\pi U(\tan\beta_k\cos\alpha-\sin\alpha) =$$

$$\sum_{j=1}^{\mathrm{NVMAX}\,(=\varkappa)} \mu_j(A+B\tan\beta_k-E-F\tan\beta_k)_{jk} + \sum_{j=\varkappa+1}^{\mathrm{NTOT}} M_j(F-E\tan\beta_k-B+A\tan\beta_k)_{jk}$$

$$-\ \pi(1+\tan^2\beta_k)^{0\cdot5}\left[\frac{M_L-M_{L-1}}{(\Delta s_k+\Delta s_{k-1})}+\frac{M_{L+1}-M_L}{(\Delta s_k+\Delta s_{k+1})}\right] \qquad \text{———} \quad 9\cdot18$$

For $(\mathrm{NTES}+1) \leqslant K \leqslant \mathrm{NVMAX}$ Where $L = K-\mathrm{NTES}+\mathrm{NVMAX}$

$(\mathrm{NUBS}+1) \leqslant K \leqslant 8$ Where $L = K-\mathrm{NUBS}+2(\mathrm{NVMAX})-\mathrm{NTES}$

& $(\mathrm{NLBS}+1) \leqslant K \leqslant 4$ Where $L = K-\mathrm{NLBS}+2(\mathrm{NVMAX})-\mathrm{NTES}+\mathrm{NUBE}-\mathrm{NUBS}$

For the latter case of $(\mathrm{NLBS} + 1) \leqslant K \leqslant 4$, the source sheet was regarded as being at an infinitely small distance below the vortex sheet, this meant that the local velocity contribution Δu_y was +ve rather than -ve in equation 9.17.

Equation 9.18 was also applied to control points $(\mathrm{NUBE} + 1) \leqslant K \leqslant \mathrm{NLBE}$, the definition of L in this case was dependent on the relative bubble lengths, as was the sign of the local velocity contribution Δu_y.

Using the flow tangency boundary condition, equations 9.16 and 9.18 enabled independent equations to be developed for all the vortex doublet panel control points, except those in the range

$9 \leqslant K \leqslant$ NUBE (or NLBE if the lower bubble was the shortest). For this part of the model, three panels were placed on top of each other, two source doublet panels and one vortex doublet panel.

When considering the control points on the vortex doublet panels in this three-panel region, the source doublet panels representing the upper surface bubble were regarded as being at an infinitely small distance above the surface vortices, whilst those representing the lower surface bubble were regarded as being at an infinitely small distance below the surface vortices.

The normal velocity contributions at the vortex doublet panel control points came from the free stream, all vortex and source doublet panels in the flow field, the local normal velocity in the -ve y direction from the upper bubble source sheet, and the local normal velocity in the +ve y direction from the lower bubble source sheet, i.e.

$$U_{y_K} = U_y + \sum_{j=1}^{NVMAX(=\varkappa)} U_{iy}^{v} + \sum_{j=\varkappa+1}^{NTOT} U_{iy}^{s} - \Delta U_{y\,(\text{Upper Sheet})} + \Delta U_{y\,(\text{Lower Sheet})} = 0 \qquad \text{——— } 9{\cdot}19$$

For any control point (K) of a vortex doublet panel, the number of the source doublet panel placed on top to represent the upper surface bubble was given the symbol (L), and the number of the source doublet panel representing the lower surface bubble was given the symbol (LL).

By using equations 9.1, 9.7, 9.10 and 9.15, it was possible to rewrite equation 9.19 as :

$$2\pi U(\tan\beta_k \cos\alpha - \sin\alpha) =$$

$$\sum_{j=1}^{NVMAX(=\varkappa)} \mu_j(A + B\tan\beta_k - E - F\tan\beta_k)_{jk} + \sum_{j=\varkappa+1}^{NTOT} M_j(F - E\tan\beta_k - B + A\tan\beta_k)_{jk}$$

$$+ \pi(1+\tan^2\beta_k)^{0\cdot 5}\left[\frac{(M_{LL}-M_{LL-1})-(M_L-M_{L-1})}{(\Delta s_k + \Delta s_{k-1})} + \frac{(M_{LL+1}-M_{LL})-(M_{L+1}-M_L)}{(\Delta s_k + \Delta s_{k+1})}\right] \qquad \text{——— } 9\cdot 20$$

For $9 \leqslant K \leqslant NUBE$ Where $L = K - NUBS + 2(NVMAX) - NTES$

& $LL = L + NUBE - NLBS - 4$

Equations 9.16, 9.18 and 9.20 enabled the flow tangency boundary condition to be satisfied at all the vortex doublet panel control points. It was then necessary to satisfy the boundary conditions at the source doublet panel control points.

Consider any source doublet panel control point (K), the surface tangential velocity at (K) was contributed to by the free stream, all vortex and source doublet panels in the flow field, and the local tangential velocity due to the presence of the vortex sheet. (L was this time used to identify the vortex doublet panel directly above or below the source doublet panel considered at K).

$$u_{x_k} = \left(U_x + \sum_{j=1}^{NVMAX(=\varkappa)} u_{ix}^{v} + \sum_{j=\varkappa+1}^{NTOT} u_{ix}^{s}\right)_k \pm \Delta u_{x_L} \qquad \text{——— } 9\cdot 21$$

The sign of Δux_L was +ve when considering upper surface source panels, and -ve for those on the lower surface.

A similar equation to 9.21 could be derived for the tangential velocity at a separation point SEP, where SEP = NTES, NUBS or NLBS depending on which separation point was under consideration, i.e.

$$u_{x_{SEP}} = \left(U_x + \sum_{j=1}^{NVMAX(=\varkappa)} u_{ix}^{v} + \sum_{j=\varkappa+1}^{NTOT} u_{ix}^{s} \pm \Delta u_x \right)_{SEP}$$

The boundary condition within any separation region was that the base-pressure or tangential velocity at the surface was constant, and equal to that at separation i.e.

$ux_k = ux_{SEP}$ where K is a source panel control point within a separation region and SEP is the vortex panel at the separation point for the region.

Using equations 9.2, 9.8, 9.11 and 9.14* the above equation could be re-written as :

---

* Equations 9.23, 9.24 or 9.25 were used for Δux_L instead of 9.14, when considering panels L = 9, 8 or 4 respectively. See section 9.8.

$$2\pi U\left[\left(\frac{\tan\beta\ \sin\alpha+\cos\alpha}{[1+\tan^{2}\beta]^{0\cdot5}}\right)_{SEP}-\left(\frac{\tan\beta\ \sin\alpha+\cos\alpha}{[1+\tan^{2}\beta]^{0\cdot5}}\right)_{k}\right]=$$

$$\sum_{j=1}^{NVMAX(=\varkappa)}\mu_{j}\left[\left(\frac{F-E\tan\beta-B+A\tan\beta}{[1+\tan^{2}\beta]^{0\cdot5}}\right)_{jk}-\left(\frac{F-E\tan\beta-B+A\tan\beta}{[1+\tan^{2}\beta]^{0\cdot5}}\right)_{jSEP}\right]$$

$$+\sum_{j=\varkappa+1}^{NTOT}M_{j}\left[\left(\frac{E+F\tan\beta-A-B\tan\beta}{[1+\tan^{2}\beta]^{0\cdot5}}\right)_{jk}-\left(\frac{E+F\tan\beta-A-B\tan\beta}{[1+\tan^{2}\beta]^{0\cdot5}}\right)_{jSEP}\right]$$

$$\pm\pi\left[\frac{\mu_{L}-\mu_{L-1}}{(\Delta s_{L}+\Delta s_{L-1})}+\frac{\mu_{L+1}-\mu_{L}}{(\Delta s_{L}+\Delta s_{L+1})}-\frac{\mu_{SEP}-\mu_{SEP-1}}{(\Delta s_{SEP}+\Delta s_{SEP-1})}-\frac{\mu_{SEP+1}-\mu_{SEP}}{(\Delta s_{SEP}+\Delta s_{SEP+1})}\right]$$

$$\text{——————} \quad 9{\cdot}22$$

For $(NVMAX+1)\leqslant K\leqslant NTOT$

This equation mathematically ensured that the tangential velocity and hence pressure in each separation region was constant, and equal to that at the separation point. Further, since the control point on the vortex doublet panel at the separation point, had already had the flow tangency boundary condition guaranteed by application of equation 9.16, the requirement for tangential separation was also satisfied.

9.7 The Kutta Condition

It is a condition with real aerofoils, that flow leaves the trailing edge smoothly (tangentially) from the attached side, this is known as the 'Kutta' condition. Also the upper and lower surface static pressures must be equal at the extreme point of the trailing edge where the two surfaces are coincident, since an instantaneous pressure change cannot be supported in nature.

To guarantee these features on the present model, the panels were arranged, as shown in figure (83), so that the control point on the last vortex doublet panel (K = NVMAX) was precisely on the point of the trailing edge. The now off-body negative vortex at the end of this panel, was then forced to be of zero strength by using $A_{jk} = B_{jk} = 0$ for j = NVMAX. Similarly the last sink at the end of the trailing edge separation region was forced to have zero strength by using $A_{jk} = B_{jk} = 0$ for j = (2. NVMAX-NTES).

Finally by assuming that the strengths of the vortex and source sheets tapered to zero over the trailing edge half-panels, the local vorticity and sourcivity at the trailing edge control points (K = NVMAX and 2.NVMAX-NTES) were regarded as being zero.

With no local velocity components produced at the trailing edge by the vortex or source sheets, the tangential velocity (and hence pressure) at the trailing edge control points was contributed to only by the free-stream and all the flow field singularities, and was therefore the same whether the upper or lower surface of the sail was considered.

Since the flow tangency boundary condition was satisfied at the trailing edge control point (K = NVMAX) by using equation 9.18, and no further singularities existed in the flow field downstream of this point, the required smooth, tangential trailing edge separation was assured.

9.8 The Problem of 3-Way Panel Joints

As can be seen from the discretized model in figure (83), behind the mast the +ve end of vortex doublet panel no. 9, and the -ve ends of vortex doublet panels nos 8 and 4, all shared the same location. This situation of three adjacent panels of similar type, all meeting at a common point, was named a '3-way panel joint'.

The difficulty produced by the presence of a '3-way panel joint' became apparent when attempting to deduce the local vorticity at any of the three adjacent control points at the rear of the mast, for use in equation 9.14.

Conventionally shaped aerofoils can be represented by a continuous vorticity sheet around the upper and lower surface contours i.e.

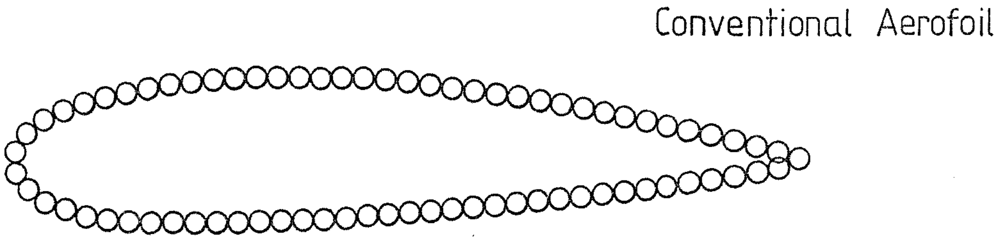

The same is true for the present mast/sail model, except that aft of the mast, the upper and lower vortex sheets are coincident i.e.

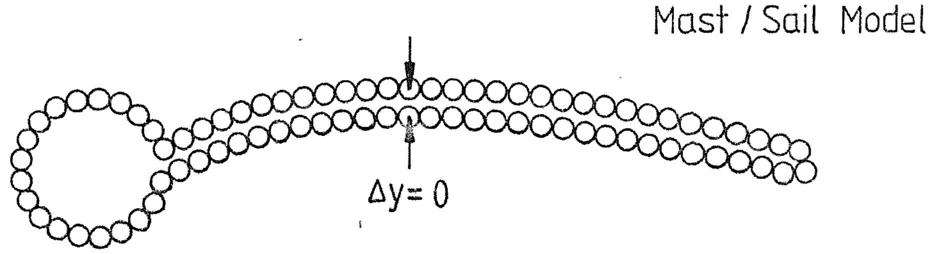

In reality then, the discretized vortex doublet panels used to model the sail contour (K = 9 to NVMAX) shown in figure (83), were in fact representing two distinct, but coincident sheets of vorticity. These panels could therefore be split into component panels, representing the upper (suffix UP) and lower (suffix LO) surface sheets. This is shown for the mast and sail leading edge panels, in figure (84).

It was not possible to actually use these split panels in the mathematical model used, since panels of the same type (vortex or source), occupying exactly the same position, and used with the same boundary condition (flow tangency), would not provide independant equations at the control points, and would therefore be unsolvable.

By splitting the vortex doublet panels in this way, it was clear from figure (84), that the panel strengths are related through :

$$\mu_k \text{ (for model used)} = \mu_{k_{UP}} + \mu_{k_{LO}} \text{ (for split model)}$$

$$\text{where } 9 \leqslant K \leqslant \text{NVMAX}$$

As described in section 9.5.3, the local vorticity at any control point (K) along a discretized sheet, can be expressed in terms of the adjacent panel strengths (μ_{k-1}, μ_k, μ_{k+1}) and lengths (ΔS_{k-1}, ΔS_k, ΔS_{k+1}), as given in equation 9.14 i.e.

$$\gamma_k = \frac{\mu_k - \mu_{k-1}}{(\Delta s_k + \Delta s_{k-1})} + \frac{\mu_{k+1} - \mu_k}{(\Delta s_k + \Delta s_{k+1})}$$

Consider then, the local vorticity at K = 9 using the split sheet model in figure (84). In this case both upper and lower sheets

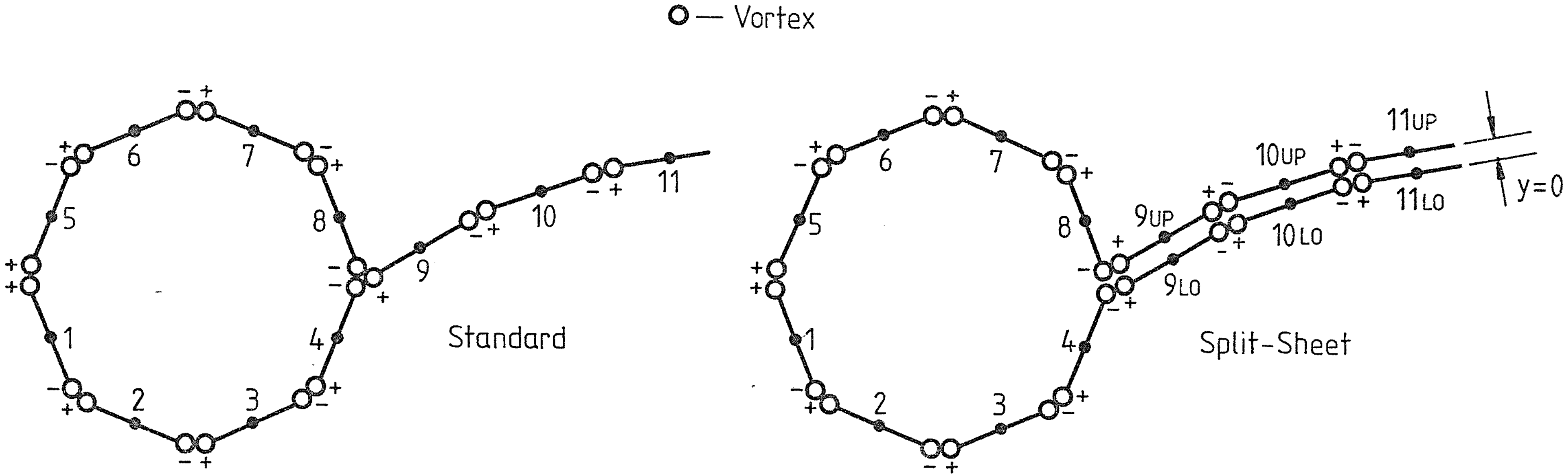

Fig(84) Standard and Split-Sheet Model Comparisons contributed to the local vorticity, since both occupied the same physical space.

$$\gamma_{9up} \text{ (due to upper sheet only)} = \frac{\mu_{9up} - \mu_8}{(\Delta s_9 + \Delta s_8)} + \frac{\mu_{10up} - \mu_{9up}}{(\Delta s_{10} + \Delta s_9)}$$

$$\& \quad \gamma_{9LO} \text{ (due to lower sheet only)} = \frac{\mu_{9LO} - \mu_4}{(\Delta s_9 + \Delta s_4)} + \frac{\mu_{10LO} - \mu_{9LO}}{(\Delta s_{10} + \Delta s_9)}$$

$$\text{Total } \gamma_9 = \gamma_{9up} + \gamma_{9LO} = \frac{\mu_{9up} - \mu_8}{(\Delta s_9 + \Delta s_8)} + \frac{\mu_{10up} - \mu_{9up}}{(\Delta s_{10} + \Delta s_9)} + \frac{\mu_{9LO} - \mu_4}{(\Delta s_9 + \Delta s_4)} + \frac{\mu_{10LO} - \mu_{9LO}}{(\Delta s_{10} + \Delta s_9)}$$

But $\mu_{9UP} + \mu_{9LO} = \mu_9$ and $\mu_{10UP} + \mu_{10LO} = \mu_{10}$, finally if all panels around the mast were of equal length (as they were in the present model), then $\Delta s_8 = \Delta s_4$

$$\therefore \text{ Total } \gamma_9 = \frac{\mu_9 - \mu_8 - \mu_4}{(\Delta s_9 + \Delta s_8)} + \frac{\mu_{10} - \mu_9}{(\Delta s_{10} + \Delta s_9)}$$

$$\& \quad \text{since} \quad \Delta u_{x_k} = \frac{\gamma_k}{2}$$

$$\boxed{\Delta u_{x_9} = \frac{1}{2}\left[\frac{\mu_9 - \mu_8 - \mu_4}{(\Delta s_9 + \Delta s_8)} + \frac{\mu_{10} - \mu_9}{(\Delta s_{10} + \Delta s_9)}\right] \text{ ——— } 9{\cdot}23}$$

This equation implied that the vorticity at the '3-way joint' panel K = 9, could not be determined by assuming the point vortex strength at the joint ($\mu_9 - \mu_8 - \mu_4$) was uniformly distributed over the 3 adjoining half panels, but rather, that it was only spread over two of these.

Consider now the last of the upper surface mast panels i.e. K = 8. It can be seen from the split panel model in figure (84), that in this case the panel strengths μ_4 and μ_{9LO} played no part in contributing to the vorticity at the K = 8 control point, since these two panels were part of a totally separate vorticity sheet.

$$\gamma_8 = \left[\frac{\mu_8 - \mu_7}{(\Delta s_8 + \Delta s_7)} + \frac{\mu_{9up} - \mu_8}{(\Delta s_9 + \Delta s_8)} \right]$$

$$\boxed{\Delta u_{x_8} = \frac{1}{2} \left[\frac{\mu_8 - \mu_7}{(\Delta s_8 + \Delta s_7)} + \frac{\mu_{9up} - \mu_8}{(\Delta s_9 + \Delta s_8)} \right] \text{———} 9{\cdot}24}$$

Similarly for K = 4

$$\boxed{\Delta u_{x_4} = \frac{1}{2} \left[\frac{\mu_4 - \mu_3}{(\Delta s_4 + \Delta s_3)} + \frac{\mu_{9Lo} - \mu_4}{(\Delta s_9 + \Delta s_4)} \right] \text{———} 9{\cdot}25}$$

Equations 9.24 and 9.25 demonstrate the problem caused by '3-way panel joints'. The two coincident vortex sheets over the sail contour could only be modelled by a single row of discretized panels in order to ensure sufficient independent equations. However, to determine the local tangential velocities at the last two mast control points (K = 8 and 4), knowledge was required of the individual split sheet panel strengths for the first sail panel, μ_{9UP} and μ_{9LO}.

It was known that $\mu_9 = \mu_{9UP} + \mu_{9LO}$, but a further equation was required to enable μ_{9UP} and μ_{9LO} to be expressed in terms of the combined sheet panel strength μ_9. Despite an extensive review of the flow physics in the area of the '3-way joint', no independent equation could be found to express μ_{9UP} and μ_{9LO} in terms of μ_9 or other known quantities.

In the light of this, the simplest possible relationship was assumed i.e.

$$\mu_{9_{UP}} = \mu_{9_{LO}}$$

$$\mu_9 = 2\mu_{9_{UP}} = 2\mu_{9_{LO}}$$

There was no justification for this assumption except that the final results given by the theory closely resembled those obtained by experiment (see section 10.2). It seems likely that the overall accuracy of the theoretical model was insensitive to the way in which the vorticity at panel K = 9 was apportioned between upper and lower sheets, such that the relatively crude relationship chosen had little effect on the final pressure predictions. This tolerance may well have been due to the bubble source sheets which enforced constant pressure over the '3-way joint' panels, equal to that at the separation panels, which were not themselves involved in the joint.

Despite the sail contour being comprised of two distinct sheets, it is shown in the following, that equation 9.14 for determining local tangential velocity (derived using only a single sheet model) was still applicable everywhere except at panels 9, 8 and 4, where equations 9.23, 9.24 and 9.25 respectively had to be used instead.

Consider any vortex doublet panel where K > 9 from the split model in figure (84) :

$$\gamma_{k_{up}} = \frac{\mu_{k_{up}} - \mu_{k-1_{up}}}{(\Delta s_k + \Delta s_{k-1})} + \frac{\mu_{k+1_{up}} - \mu_{k_{up}}}{(\Delta s_k + \Delta s_{k+1})}$$

$$\gamma_{k_{LO}} = \frac{\mu_{k_{LO}} - \mu_{k-1_{LO}}}{(\Delta s_k + \Delta s_{k-1})} + \frac{\mu_{k+1_{LO}} - \mu_{k_{LO}}}{(\Delta s_k + \Delta s_{k+1})}$$

Total Vorticity $\gamma_k = \gamma_{k_{up}} + \gamma_{k_{LO}}$

$$\gamma_k = \frac{\mu_{k_{up}} - \mu_{k-1_{up}} + \mu_{k_{LO}} - \mu_{k-1_{LO}}}{(\Delta s_k + \Delta s_{k-1})} + \frac{\mu_{k+1_{up}} - \mu_{k_{up}} + \mu_{k+1_{LO}} - \mu_{k_{LO}}}{(\Delta s_k + \Delta s_{k+1})}$$

but $\mu_k = \mu_{k_{up}} + \mu_{k_{LO}}$; $\mu_{k-1} = \mu_{k-1_{up}} + \mu_{k-1_{LO}}$; $\mu_{k+1} = \mu_{k+1_{up}} + \mu_{k+1_{LO}}$

$$\therefore \gamma_k = \frac{\mu_k - \mu_{k-1}}{(\Delta s_k + \Delta s_{k-1})} + \frac{\mu_{k+1} - \mu_k}{(\Delta s_k + \Delta s_{k+1})} = 2.\Delta u_{x_k}$$

which is identical to equation 9.14.

9.9 Computerised Model Construction and Equation Solving

The previous sections have described a typical layout of panels, together with the various equations necessary to mathematically represent the boundary conditions around a mast/sail model. Based on this modelling technique, a FORTRAN computer program was written for a HONEYWELL 6080 machine, to automate both mathematical model construction and equation solving.

The flow chart in figure (85) shows the sequence of steps used by the program, finally culminating in a surface static pressure distribution prediction, for any given combination of flow parameters and model geometry.

The first step in the automated solution process was the input of sail geometry data. This involved the provision of a suitable number of XY co-ordinates, and associated surface slopes (Tanβ),

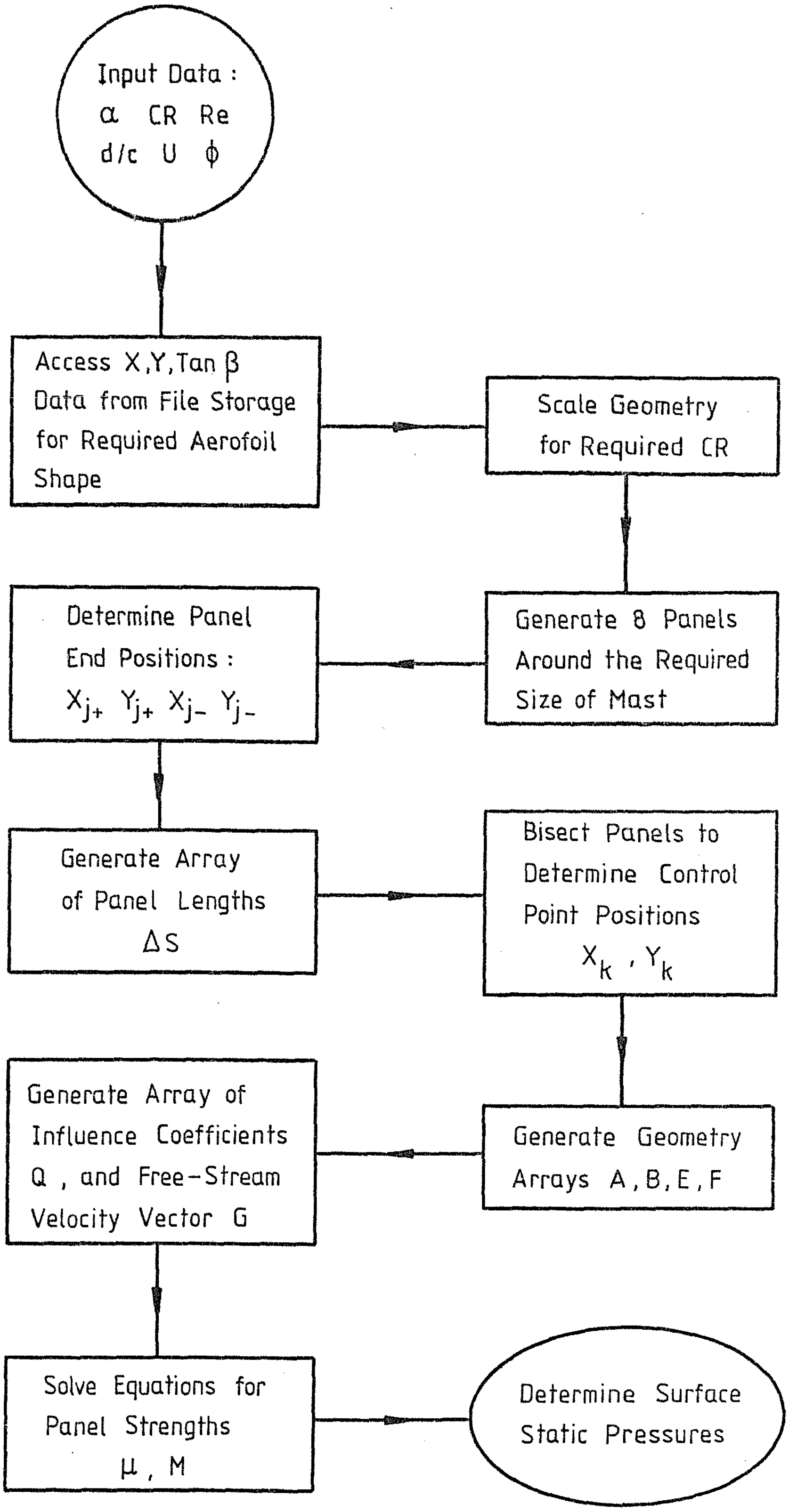

Fig(85) Flow Chart for Computerised Solution Method to adequately describe the required aerofoil shape. This data was obtained directly from Abbott (4), and kept on file storage for various sail shapes. The program carried out scaling on this data to cater for the particular value of camber ratio selected.

By inputting the required values of mast diameter/chord ratio (d/c), and mast angle (ϕ), the computer generated the XY co-ordinates and surface slopes (Tan β) for 8 equally spaced points around the mast circumference.

The slope at each mast or sail co-ordinate was mathematically extended until it intersected with the similarly extended slopes from the two adjacent points. These slope intersection points were regarded by the computer as the panel boundaries, and the corresponding co-ordinates X_{j+}, Y_{j+}, X_{j-} and Y_{j-} where stored in arrays.

Having located all the panel boundaries in this way, the computer then determined the co-ordinates of the panel centres (X_k, Y_k) and placed these in store as control point locations.

The final input data required was that regarding the empirical separation and reattachment points. These were input as a percentage of chord, but the computer converted these to the closest available control point location. Source panel end and control point co-ordinates were then generated within the defined separation regions.

Having deduced the co-ordinates and slopes of all the panel ends and control points in the flow field, it was then a simple task for the computer to generate the arrays A, B, E and F as defined in equation 9.9, plus an array of panel lengths ΔS_k.

It can be seen from equations 9.16, 9.18, 9.20 and 9.22, that the boundary conditions at each control point could be expressed in the form:

$$G_k = \sum_{j=1}^{NVMAX\,(=\varkappa)} Q_{jk}\mu_j + \sum_{j=\varkappa+1}^{NTOT} Q_{jk} M_j \quad \text{———} \quad 9\cdot 26$$

where Q_{jk} is some influence coefficient dependent entirely on mast/sail geometry

G_k is a constant for any control point (K) and is dependent on geometry and free stream velocity (U)

and μ_j and M_j are unknown vortex and source doublet panel strengths respectively.

Since an equation in this form could be produced for every panel in the flow field, the resulting set of simultaneous equations could be represented in matrix form by :

$$\begin{array}{cc} & j \\ k & \begin{bmatrix} \quad Q \quad \end{bmatrix} \end{array} \mathrm{X} \begin{array}{cc} 1 & \\ \begin{bmatrix} \mu_1 \\ \mu_2 \\ \vdots \\ M_j \\ \vdots \\ M_{NTOT} \end{bmatrix} & j \end{array} = \begin{array}{cc} 1 & \\ \begin{bmatrix} G \end{bmatrix} & k \end{array}$$

The unknown panel strengths could therefore be found using :

$$\begin{array}{cc} 1 & \\ \begin{bmatrix} \mu_1 \\ \mu_2 \\ \vdots \\ M_j \\ \vdots \\ M_{NTOT} \end{bmatrix} & j \end{array} = \begin{array}{cc} & j \\ k & \begin{bmatrix} \quad Q \quad \end{bmatrix}^{-1} \end{array} \mathrm{X} \begin{array}{cc} 1 & \\ \begin{bmatrix} G \end{bmatrix} & k \end{array}$$

To obtain a solution by this method the computer applied equations 9.16, 9.18, 9.20 and 9.22 to the control points where each was valid, this enabled the matrix of influence coefficients (Q), and the free stream velocity vector (G) to be determined using the arrays A, B, E, F, ΔS_k and Tan β_k, plus the given free stream velocity U.

The unknown panel strengths were then found by applying a NAG library equation solving routine.

Having found all the unknown panel strengths, the upper and lower surface tangential velocities were easily calculated using equation 9.21, these were then expressed in pressure coefficient form using :

$$Cp_k = 1 - \left(\frac{u_{x_k}}{U}\right)^2$$

The entire program was only 500 lines long, required no iteration procedures, and for an average number of about 45 panels the run time was around 10 seconds. No base-pressure input was required as this was produced as part of the solution, however an empirical input was necessary for separation and reattachment locations.

CHAPTER 10

COMPARISON OF EXPERIMENTAL AND THEORETICAL RESULTS

10.1 Differences between Attached and Partially Separated Pressure Distributions

To demonstrate the need to accurately model the separated flow regions around typical mast/sail geometries, the results obtained using the present theory were compared with those produced by considering all flow to be attached. This comparison is shown in figure (86) for a case with high camber (CR = 15%), high incidence angle ($\alpha = 10°$) and a medium mast size (d/c = 10%).

It can be seen that the attached and partially separated pressure distributions are radically different, such that accurate design predictions would be quite impossible if only fully attached flow information were available.

The presence of an upper surface separation bubble tended to suppress the attached flow pressure peak at the leading edge, whilst reducing the pressure across the attached flow pressure recovery behind the mast. These two effects seemed to approximately cancel each other out when considering the useful lift produced over the forward portion of the mast and sail.

Over the remaining upper sail surface, the characteristic 'roof-top' pressure distribution produced by attached flow over an NACA a = 0.8 mean-line form, was severely modified by the trailing edge separation region. This partially separated pressure distribution represented about a 40% reduction in lift over that produced with completely attached flow.

Incidence Angle = 10.00
Mast/Chord Ratio = .100
Mast Angle = 10.00
Camber Ratio = .150
Reynolds Number = 1000000.0

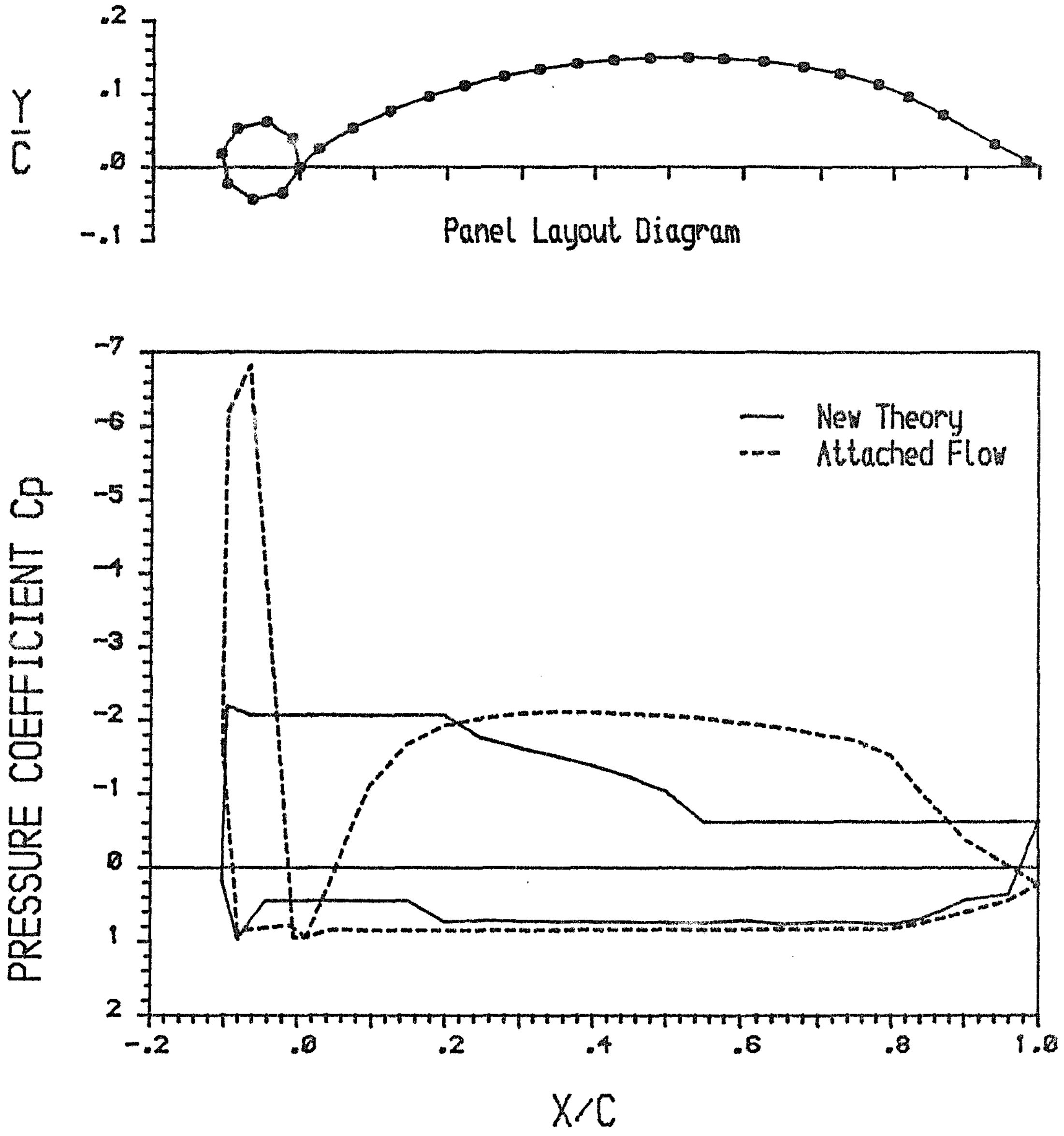

Fig(86) Comparison of Attached and Partially Separated Flow Theories for a NACA a=0.8 Mean Line with a Circular Section Mast

Finally, the lower surface pressure distributions for the attached and partially separated cases were identical except within the lower bubble region. This bubble resulted in a further small loss of lift when compared with the entirely attached case.

10.2 Example Experimental/Theoretical Comparisons

To establish the accuracy of the present theory, it was necessary to compare the predicted results with corresponding experimental data. It was possible to apply the present theory to any of the 192 tests performed during the experimental programme, however just three of these were chosen such that reasonable ranges of incidence angle, mast size, camber ratio and Reynolds number were all represented.

The first of these comparisons between the present theory and the experimental results is shown in figure (87). This was for a case with high camber (CR = 15%), high incidence angle ($\alpha = 10°$), medium mast size (d/c = 10%), and moderate Reynolds number ($Re = 1 \times 10^6$). The theoretical prediction in this case was in excellent agreement with the experimental results (test no. 35), with all the theoretical base-pressures for bubble and trailing edge regions, very close to those measured.

When the corresponding case with low incidence angle ($\alpha = 2.5°$) was predicted and compared with the experimental results (test no. 26), as shown in figure (88), the agreement was not quite as good as before. The base-pressures were all predicted reasonably well, as were the attached flow regions, however the theoretical and experimental results showed significant differences around both upper and lower surface reattachment regions. This effect was not noticeable in figure (87) because the pressure recovery coefficient (σ) in this case was very small.

Incidence Angle = 10.00
Mast/Chord Ratio = .100
Mast Angle = 10.00
Camber Ratio = .150
Reynolds Number = 1000000.0

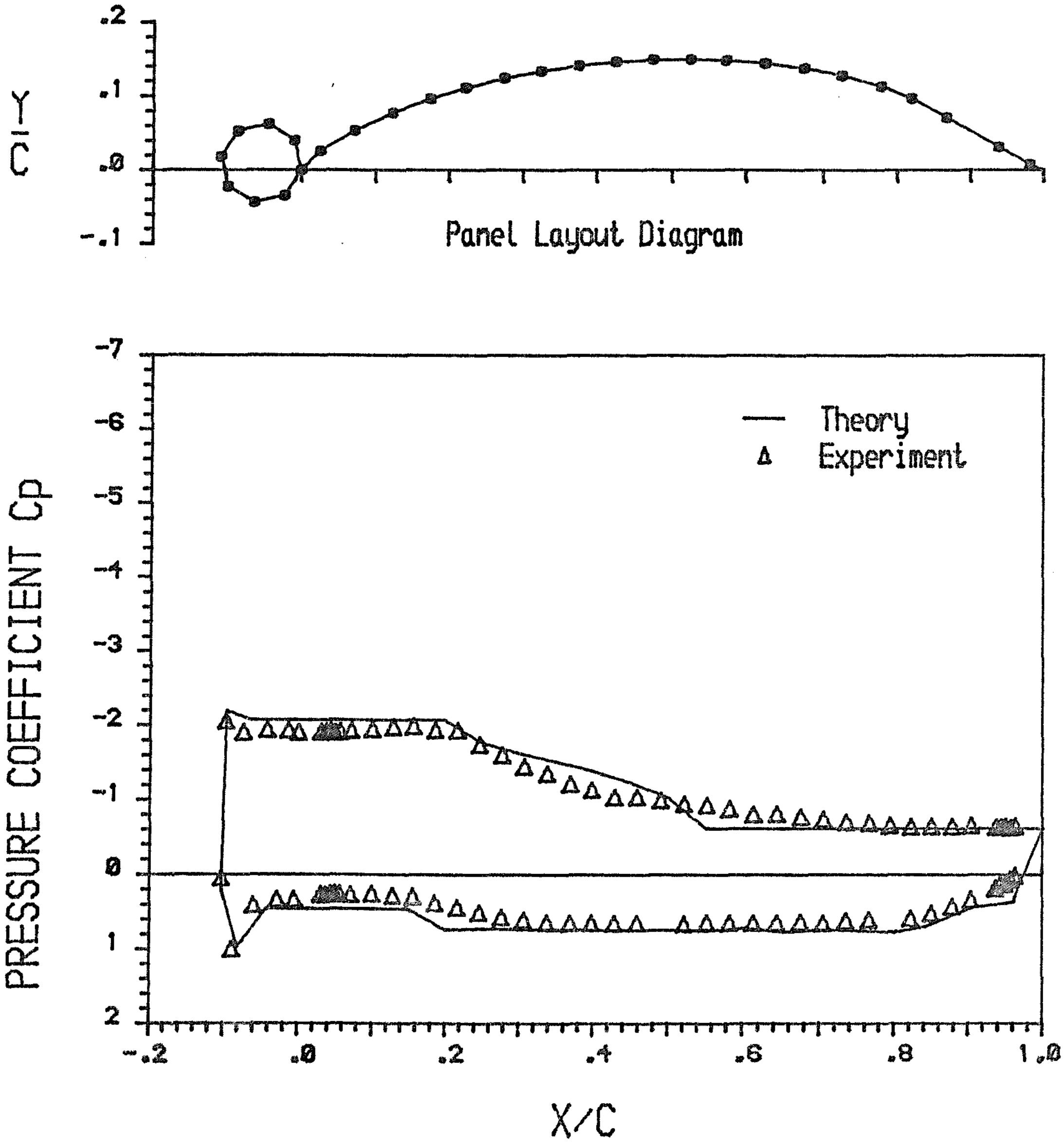

Fig(87) Comparison of Experimental and Computed Pressure Distributions for a NACA a=0.8 Mean Line with a Circular Section Mast

Incidence Angle = 2.50
Mast/Chord Ratio = .100
Mast Angle = 10.00
Camber Ratio = .150
Reynolds Number = 1000000.0

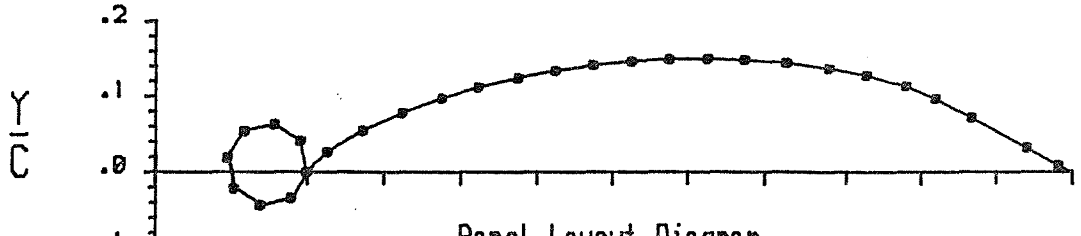

Panel Layout Diagram

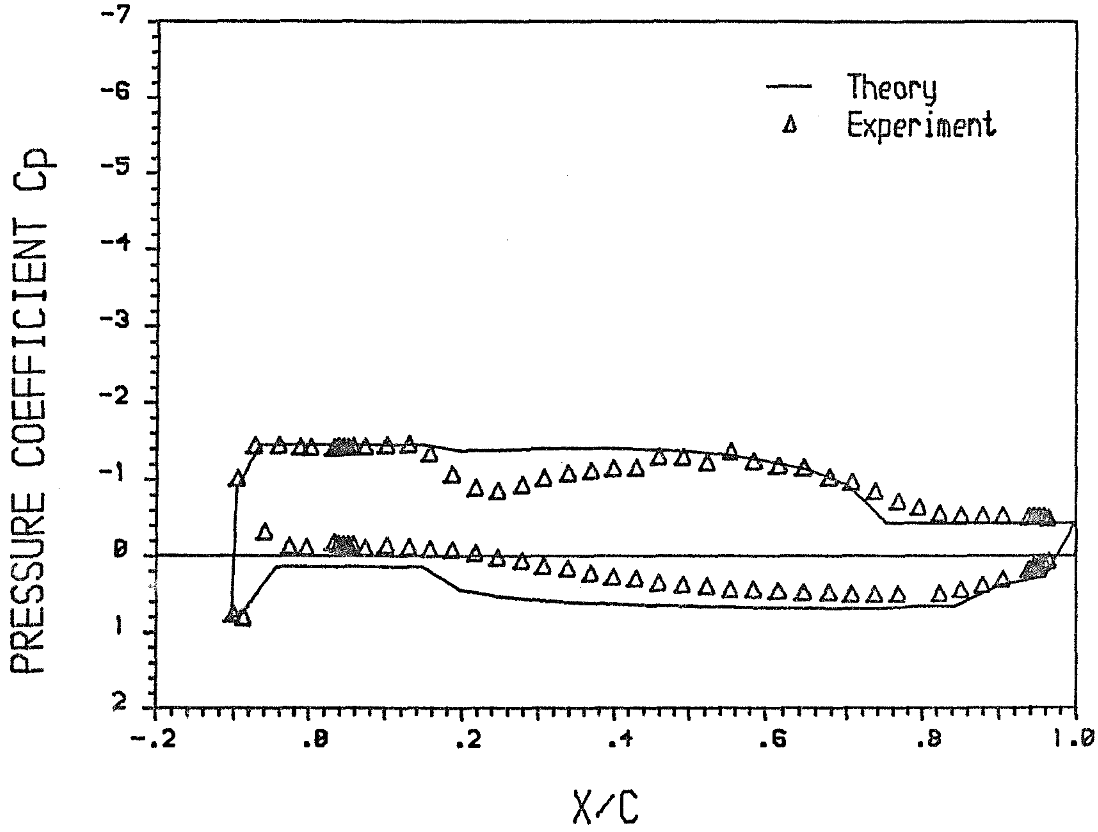

Fig(88) Comparison of Experimental and Computed Pressure Distributions for a NACA a=0.8 Mean Line with a Circular Section Mast

Incidence Angle = 7.50
Mast/Chord Ratio = .040
Mast Angle = 5.00
Camber Ratio = .125
Reynolds Number = 1400000.0

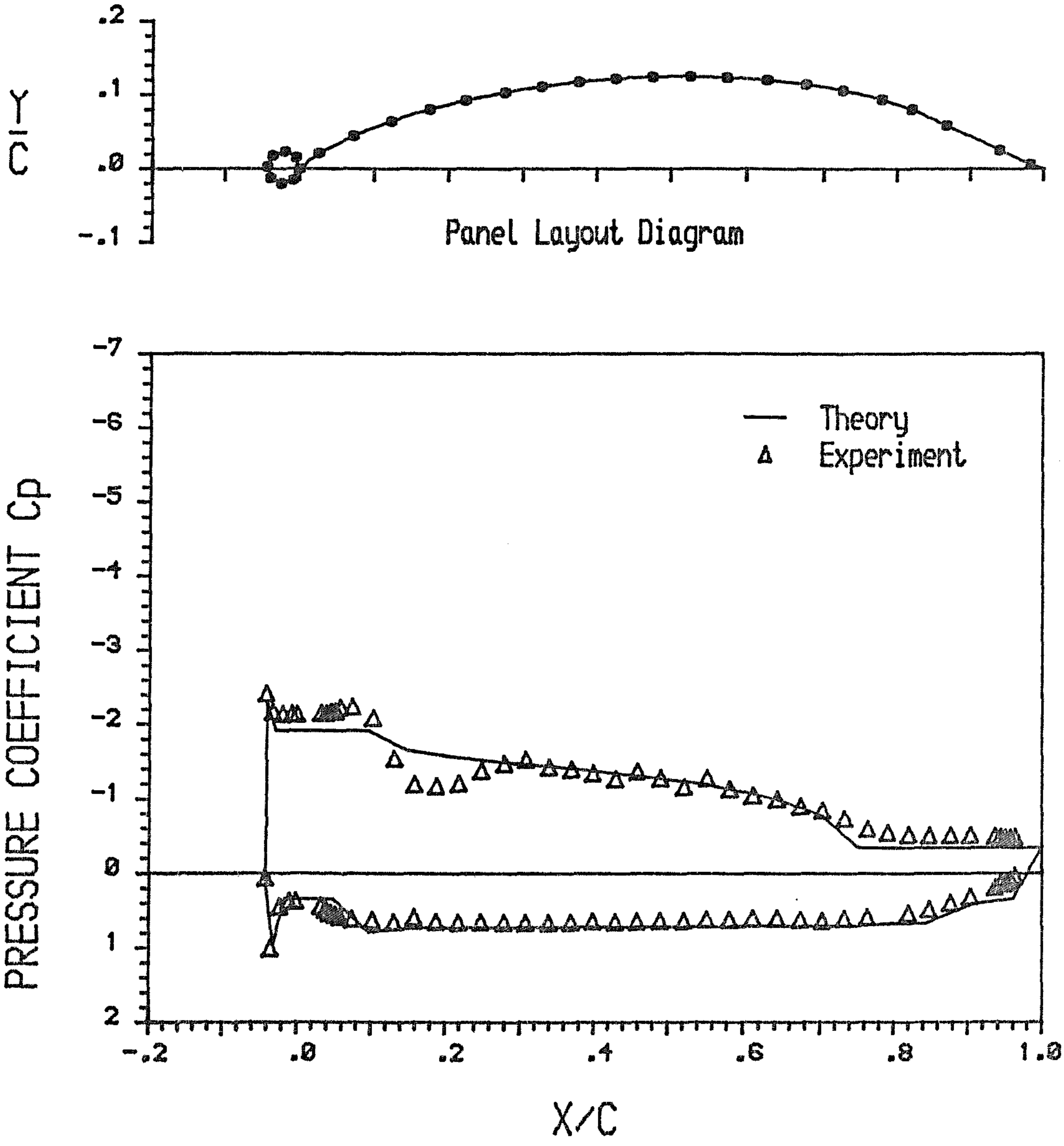

Fig(89) Comparison of Experimental and Computed Pressure Distributions for a NACA a=0.8 Mean Line with a Circular Section Mast

The inability of the present theory to predict the pressure recoveries within the two reattachment regions was not particularly surprising, since at the time when the theoretical model was developed, analysis of all the experimental results had not been completed, and the physics of the reattachment regions had not been fully appreciated. Only two types of surface boundary condition were used in the present theory, these were constant tangential velocity within base-pressure regions, and flow tangency elsewhere. It is clear now, however, that within the reattachment regions the flow was neither tangential to the surface or of constant pressure. A possible way of modifying the present theory to cope with reattachment is given in the next section (10.3).

Having shown that the present theory could provide reasonable predictions at both extremes of incidence angle, the final comparison, shown in figure (89), was chosen to demonstrate the ability of the theory to cope with conditions of lower camber ratio (CR = 12.5%), small masts (d/c = 4%) and high Reynolds number ($Re = 14 \times 10^5$). As before the agreement between theory and experiment was very good except within the upper reattachment region. The panel layout diagram in figure (89) shows how short the 8 mast panels were in comparison to those over the sail. The slightly high base-pressure prediction for the upper separation bubble could be attributed to the inaccurate upper bubble separation location possible with only 8 mast control points.

10.3 Further Theoretical Work

Despite the excellent agreement obtained between theoretical and experimental results, further work is still necessary to obtain a more mathematically correct representation of the '3-way joint' problem, or possibly a method devised for avoiding the problem altogether.

More importantly, however, is the inclusion of an accurate theoretical model for conditions at bubble reattachment. Reattachment as a phenomenon is still only understood in a qualitative way, the actual physical mechanisms involved being transition, turbulent mixing, eddy formation, energy entrainment, viscous dissipation etc., all of which make precise mathematical modelling highly complex.

Attempts at mathematically representing separation bubbles have nevertheless been made by Korst (55) and Chow (56) using a momentum balance technique, and by Horton (57) assuming a given rate of shear layer expansion between transition and reattachment. However for design purposes a relatively crude model of the pressure recovery at reattachment would probably suffice. One such model which could be readily included into the present theory is described in the following :

The basic assumption upon which this reattachment pressure recovery model is based, is that the pressure within the reattachment region (upper or lower) varies linearly from that in the constant base-pressure region to that at reattachment, where the flow is again tangential to the aerofoil surface. This is similar to that suggested by Vincent de Paul (58).

In the existing model, the start and end locations of the base-pressure regions were specified (i.e. K = NUBS, NUBE, NLBS and NLBE), and source doublet panels laid over the surface vortex doublet panels within these regions. The boundary condition applied to these source doublet panels was constant tangential velocity, equal to that at separation, whilst the boundary condition used on all other panels was flow tangency (zero normal velocity component) i.e.

For the present model (upper bubble only) :

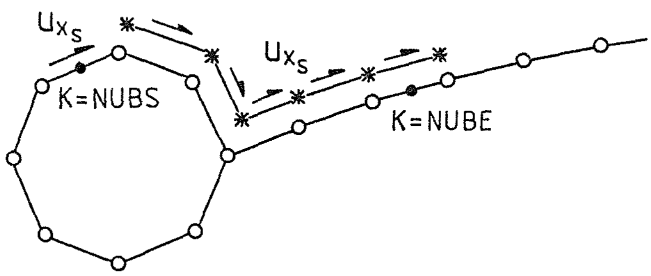

where ux$_s$ is the tangential velocity at separation (K = NUBS)

This implied that the flow was tangential to the surface throughout the reattachment region, which is now known to be untrue.

To model this reattachment region approximately using an assumed linear pressure variation, the location of reattachment (as indicated by the position of maximum pressure in Region III of the pressure distributions) would have to be given as an additional empirical input to the program (i.e. K = NUBR).

The source sheet would then have to be extended up to (but not including) this reattachment location i.e. upper bubble only :

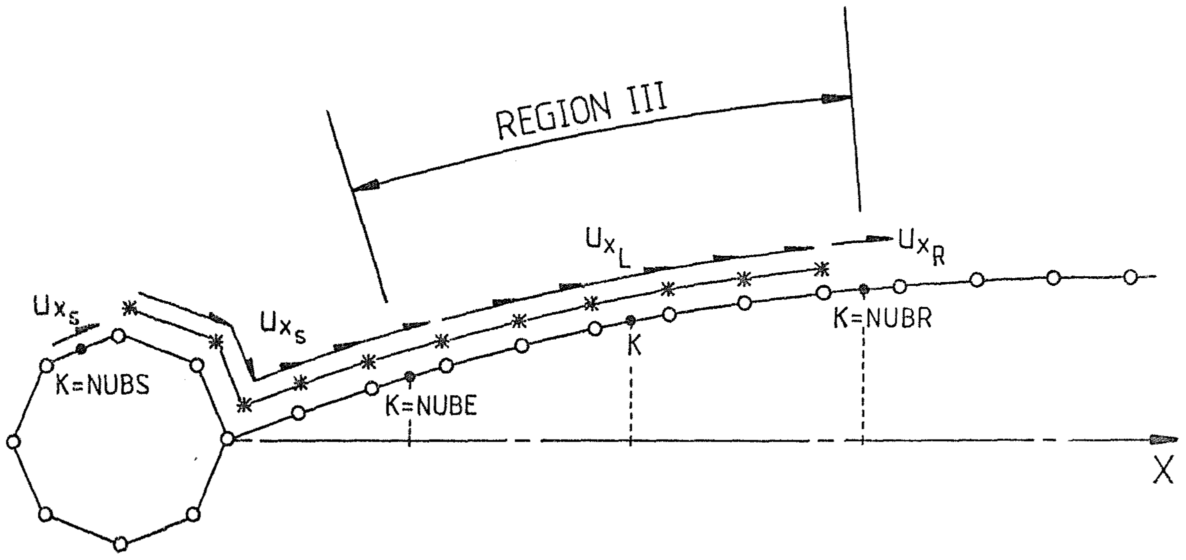

If then the source panel placed on vortex panel (K) is given the symbol (L), the tangential velocity at (L) within the reattachment region can be described by :

$$U_{X_L} = U_{X_S} + \left[\frac{X_K - X_{NUBE}}{X_{NUBR} - X_{NUBE}} \right] . \left(U_{X_R} - U_{X_S} \right)$$

Relationships of the form described in equation 9.21, could then be formulated for Ux_L, Ux_s and Ux_R , which when substituted in the above, would result in governing equations for all control points in the reattachment region with the essential form necessary for inclusion into the existing theoretical model (i.e. as given in equation 9.26).

The present theory involved only potential flow considerations and was therefore unable to produce pressure predictions without an empirical input of separation and reattachment locations. Further work is therefore required to extend the present theory to include viscous effects, this would then avoid any empirical input by producing all separation and reattachment positions as part of the solution, as well as taking account of surface displacement effects due to boundary layer growth.

In broad principle the inclusion of viscous effects seems relatively straightforward as shown by the flow chart in figure (90). However difficulty might well arise at the stage where separation and reattachment positions have to be predicted from the pressure distribution.

Around the mast a laminar boundary layer growth criteria, such as that due to Pohlhausen or Bhatia (59) would probably give results of sufficient accuracy, followed by a laminar separation prediction of the Pohlhausen-Goradia type.

Given an initial estimate of pressure distribution, the prediction of bubble transition and reattachment is a more difficult problem. Possibly shear layer transition could be predicted using

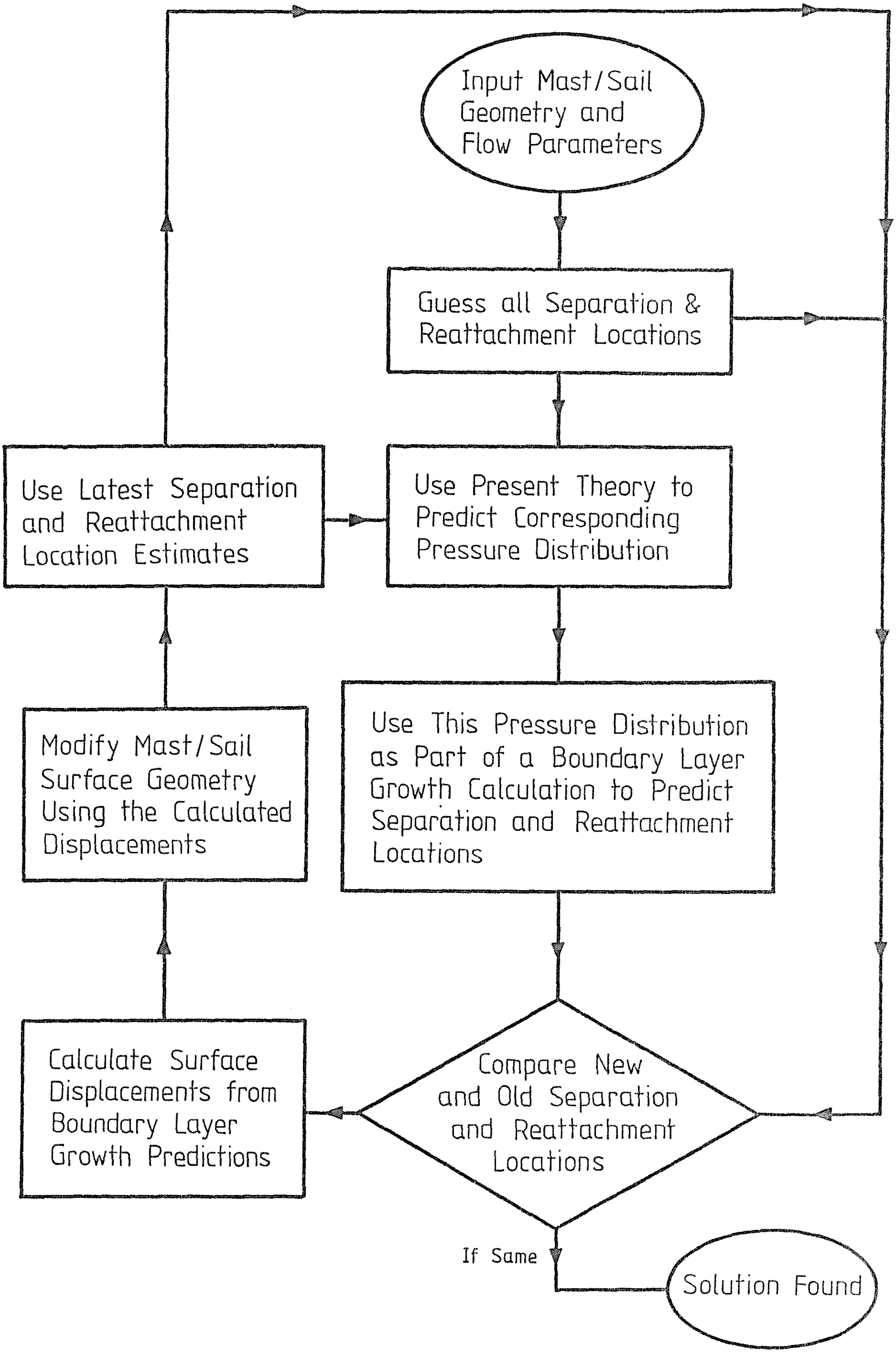

Fig(90) Possible Means of Including Viscous Effects

Granvilles (60) classical method, or by the method of Michel as described by Tani (61). The successful prediction of reattachment location is somewhat less certain, however the previously mentioned methods due to Korst (55), Chow (56) or Horton (57) might possibly suffice.

Finally a turbulent boundary layer growth criteria is required for the flow following bubble reattachment. A simple 'Momentum Integral' technique using a power law velocity profile, or possibly an entrainment method such as that due to Head, would be relatively easy to apply. However some doubt is cast on the accuracy of such methods by Bursnall (35) who states :

> 'The nature of the flow in the turbulent boundary layer immediately after reattachment, was such that the usual methods of predicting the rate of growth and change in shape of the turbulent boundary layer, did not give satisfactory results'.

Possibly one of the more recent boundary layer computation techniques, such as multilevel integral or finite difference solutions, might give sufficiently accurate results, even with the double curvature velocity profiles following reattachment.

10.4 Conclusions (Theoretical Work)

A potential flow singularity technique, using vortex and source doublet panels, has been developed to model the partially separated flows found around typical 2D mast/sail geometries.

The theory is thought to be the first of its kind to tackle the problem of both upper and lower surface separation bubbles acting simultaneously, together with the added difficulties of trailing edge separation and zero aerofoil thickness.

Only conditions on the mast and sail surfaces were modelled, and no iterations or empirical base-pressure inputs were required. The only inputs necessary were mast/sail geometry, incidence angle, free stream Reynolds number, and empirically obtained separation and reattachment locations.

Comparison of theoretical and empirical results showed excellent agreement, except in the region of bubble reattachment. An extension to the theory has been proposed to enable the pressure recovery at reattachment to be more closely modelled.

REFERENCES

(1) MARCHAJ, C.A. Sailing Theory and Practice (Book) Granada Publishing Inc., 1st pub. 1964.

(2) MILGRAM, J.H. Section Data for Thin Highly Cambered Aerofoils in Incompressible Flow. NACA CR-1767, July 1973.

(3) MILGRAM, J.H. Effects of Masts on the Aerodynamics of Sail Sections. Marine Technology. Vol. 15, No.1, p.35-42, January 1976.

(4) ABBOTT, I.H. and Von DOENHOFF, A.E. Theory of Wing Sections (Book). Dover Publications Inc. 1949.

(5) CHUE, S.H. Pressure Probes for Fluid Measurement. Progress in Aerospace Sciences. Vol. 16, No.2, p.147-223, 1975.

(6) BRYER, D. and PANKHURST, R.C. Pressure-Probe Methods for Determining Wind Speed and Flow Direction. (Book). Her Majesty's Stationery Office, 1971.

(7) MURPHY, J.S. The Separation of Axially Symmetric Turbulent Boundary Layers, Part II ; Detailed Measurements in the Boundary Layers on Several Slender Bodies in Incompressible Flow. Douglas Aircraft Co. Inc., Report No. E.S. 17513. Contract No. 52-066, 1955.

(8) GLAUERT, H. The Elements of Aerofoil and Airscrew Theory. (Book). Cambridge University Press.

(9) SEETHARAM, H.C., and WENTZ, W.H. Experimental Investigation of Subsonic Turbulent Separated Boundary Layers on an Airfoil. Journal of Aircraft, Vol. 14, No.1, p. 51-55, January 1977.

(10) YAJNIK, K.S. and GUPTA, R.P. A New Probe for Measurement of Velocity and Flow Direction in Separated Flows. J.Phys. E. : Sci. Instrum., 6, 1, p. 82-86, January 1973.

(11) RAGHAVA, A.K., KUMAR, K.L., MALHOTRA, R.C. and AGRAWAL, D.P. A Novel Arrangement for the Measurement of the Velocity Vector. J.Phys.E., 10, 8, p.884, August 1977.

(12) RAJARATNAM, N. and MURALIDHAR, D. Yaw Probe Used as a Preston Tube. The Aeronautical Jnl. of the Royal Aero. Soc. Vol. 72, p. 1059-1060. 1968.

(13) JEZDINSKY, V. Measurement of Turbulence by Pressure Probes. AIAA Journal, Vol. 4, p. 2072-3. November 1966.

(14) DUDZINSKI, T.J., and KRAUSE, L.N. Effect of Inlet Geometry on Flow-Angle Characteristics of Miniature Total-Pressure Tubes. NASA-TN-D-6406, July 1971.

(15) ABDUL KHADER, M.H., and SURESH, RAO, H. Yaw Probe Measurements in a Helical Flow. Wat. Pwr., 26, 3, p.99-101, March 1974.

(16) BRADFIELD, W.S. and YALE, G.E. Small Pitot Tubes with Fast Pressure Response Time. J. Aero. Sci. p. 697-698. October 1951.

(17) MARCHAJ, C.A. Aero-Hydrodynamics of Sailing (Book). Granada Publishing Inc. 1979.

(18) POPE, A.Y. and HARPER, J.J. Low Speed Wind Tunnel Testing (Book) London, Wiley, 1966.

(19) THOM, A. Blockage Corrections in a High Speed Wind Tunnel. R & M 2033 1949.

(20) YOUNG, A.D. and MAAS, J.N. The Behaviour of a Pitot Tube in a Transverse Total-Pressure Gradient. R & M No. 1770, September 1936.

(21) MacMILLAN, F.A. Experiments on Pitot-Tubes in Shear Flow. R & M No. 3028, February 1956.

(22) LIVESEY, J.L. The Behaviour of Transverse Cylindrical and Forward Facing Total Pressure Probes in Transverse Total Pressure Gradient. J. Aeronautical Sci., Vol. 23, p. 949-955, 1956.

(23) QUARMBY, A. and DAS, H.K. Displacement Effects on Pitot Tubes with Rectangular Mouths. Aeronautical Quarterly, May 1969.

(24) DAVIES, P.O.A.L. The Behaviour of a Pitot Tube in Transverse Shear. J. Fluid, Mech., Vol. 3, p 441-456, 1958.

(25) PATEL, V.C. Calibration of the Preston Tube and Limitations on its Use in Pressure Gradients. J. Fluid Mech. Vol. 23, Part 1, p. 185-208.

(26) GARNER, H.C. Thickness Parameters by Rapid Integration of Turbulent Boundary Layer Profiles. J. Royal Aeronautical Soc., Vol. 61, p. 278-281, April 1957.

(27) PRESTON, J.H. The Determination of Turbulent Skin Friction by Means of Pitot Tubes. J. Royal Aeronautical Soc., Vol. 58, p. 109-121, February 1954.

(28) HEAD, M.R. and RECHENBERG, I. The Preston Tube as a Means of Measuring Skin Friction. J. Fluid. Mech., Vol. 14, p 1-17, 1962.

(29) HEAD, M.R., and VASANTA RAM, V. Simplified Presentation of Preston Tube Calibration. Aeronautical Quarterly, Vol. 22, Part 3, p. 295-300, August 1971.

(30) QUARMBY, A. and DAS, H.K. Measurement of Skin Friction Using a Rectangular Mouthed Preston Tube. The Aeronautical Journal of the Royal Aeronautical Society, Vol. 73, p. 228-230, March 1969.

(31) GAULT, D.E. An Experimental Investigation of Regions of Separated Laminar Flow. NACA TN 3505, September 1955.

(32) GASTER, M. The Structure and Behaviour of Separation Bubbles. R & M 3595, March 1967.

(33) CRABTREE, L.F. Effects of Leading Edge Separation on Thin Wings in 2D Incompressible Flow. Journal of the Aeronautical Sciences, p. 597-604, August 1957.

(34) ROSHKO, A. and LAU, J.C. Some Observations on Transition and Reattachment of a Shear Layer in Incompressible Flow. Proceeding of the Heat Transfer and Fluid Mechanics Institute, Stanford 1965.

(35) BURSNALL, W.J. and LOFTIN, K.L. Experimental Investigation of Localized Regions of Laminar Boundary Layer Separation. NACA TN 2338, April 1951.

(36) NIKURADSE, J. Forschungs-Arb.Ing.-Wesen, Heft 356 (1936).

(37) DUNCAN, W.J., THOM, A.S. and YOUNG, A.D. Mechanics of Fluids (Book) Published by Edward Arnold Ltd., 1970.

(38) SCHLICHTING, H. Boundary Layer Theory (Book), Pergamon, 1955.

(39) VAUSSY, P. Etude D'Une Voile Bidimensionnelle Inextensible en Presence D'Un Mat. International Shipbuilding Progress Vol. 19, No. 219, November 1972.

(40) HAYASHI, M., and ENDO, E. A Method for Calculating the Flow Around Airfoil Sections with Separation. Trans. Japan Soc. Aero. Space Sci. Vol. 20, No. 49, p. 113-124.

(41) KUMAR, A. and SHANKAR, P.N. A Potential Flow Model for Lifting Separated Flows. ASME 80-FE-4, 1979.

(42) WU, T.Y. A Free Streamline Theory for Two-Dimensional Fully Cavitated Hydrofoils. J. Math. Phys., Vol. 35, p.236-65, 1956.

(43) MILGRAM, J.H. Calculation of Attached or Partially Separated Flow Around Airfoil Sections. J. of Ship Research, Vol. 21, No.2, June 1977, p. 69-81.

(44) ROSHKO, A. A New Hodograph for Free-Streamline Theory. NACA TN 3168, July 1954.

(45) WHITE, J.W. A Zone-Interaction Method for the Outer Flow Analysis of a Separated Airfoil. J. Ship Research, Vol. 24, No.2, p. 123-127, June 1980.

(46) JACOB, K. Berechnung de abgelosten inkompressiblen Stromung um Tragflugeprofile und Bestimmung des maximalen Auftriebs. Z. Flugwiss, Vol. 17, p. 221-230, 1969.

(47) ABBOTT, D.E. Prediction of Flows with and without Partial Separation. Purdue Univ., Lafayette, Ind., Fluid Mechanics Group Report, 1972.

(48) HAHN, M., RUBBERT, P.E. and MAHAL, A.S. Evaluation of Separation Criteria and their Application to Separated Flow Analysis. Tech. Report AFFDL-TR-72-145, Air Force Systems Command, January 1973.

(49) FARN, C.L.S., GOLDSCHMIED, F.R. and WHIRLOW, D.K. Pressure Distribution Prediction for Two-Dimensional Hydrofoils with Massive Turbulent Separation. J. Hydronautics, Vol. 10,. No.3, p. 95-101, July 1976.

(50) HENDERSON, M.L. A Solution to the 2-D Separated Wake Modeling Problem and Its Use to Predict CLmax of Arbitrary Airfoil Sections. AIAA 78-156, January 1978.

(51) BARNWELL, R.W. Two Inviscid Computational Simulations of Separated Flow About Airfoils. AIAA 9th Fluid and Plasma Dynamics Conference, AIAA Paper No. 76-379, July 1976.

(52) GROSS, L.W. The Prediction of Two-Dimensional Airfoil Stall Progression. AIAA 16th Aerospace Sciences Meeting. Paper 78-155, January 1978.

(53) ZUMWALT, G.W. and NAIK, S.N. An Analytical Model for Highly Separated Flow on Airfoils at Low Speeds. Wichita State Univ. Aeronautical Report 77-2, May 1977.

(54) MASKEW, B. Subvortex Technique for the Close Approach to a Discretized Vortex Sheet. J. Aircraft, Vol. 14, No. 2, p. 188-193, 1976.

(55) KORST, H.H. A Theory for Base Pressures in Transonic and Supersonic Flow. J. Applied Mechanics, Vol. 23, Trans. ASME, Vol. 78, p. 593-600, 1956.

(56) CHOW, W.L. and SPRING, D.J. Viscid-Inviscid Interaction of Incompressible Separated Flows. J. Applied Mechanics, p. 387-395, September 1976.

(57) HORTON, H.P. A Semi-Empirical Theory for the Growth and Bursting of Laminar Separation Bubbles. British ARC Report CP-1073, 1969.

(58) VINCENT DE PAUL, M. Prevision du Decrochage d'un Profile d'Aile en Encoulement Incompressible. AGARD CP-102, November 1972.

(59) BHATIA, J.C. Computation of Two-Dimensional and Axisymmetric Steady Laminar Boundary Layers by Quadrature. J. Applied Mechanics, September 1974.

(60) GRANVILLE, P.S. The Calculation of Viscous Drag on Bodies of Revolution. The David W. Tayler Model Basic Report No. 849.

(61) TANI, J. Boundary Layer Transition. Annual Review of Fluid Mechanics, Vol. 1, Annual Reviews Inc., Palo Alto, 1969.

APPENDIX I

'MOUSE' CASING DESIGN EQUATIONS

In order to simplify the necessary mathematical analysis it was decided to adopt an 'aerodynamic' casing for the mouse with a geometric shape known as a 'Rankine Oval'.

Such a streamline shape is generated when a 2-dimensional potential flow uniform stream, is combined with a source and sink of equal magnitude placed along the principal flow axis, with a separation distance of 2s.

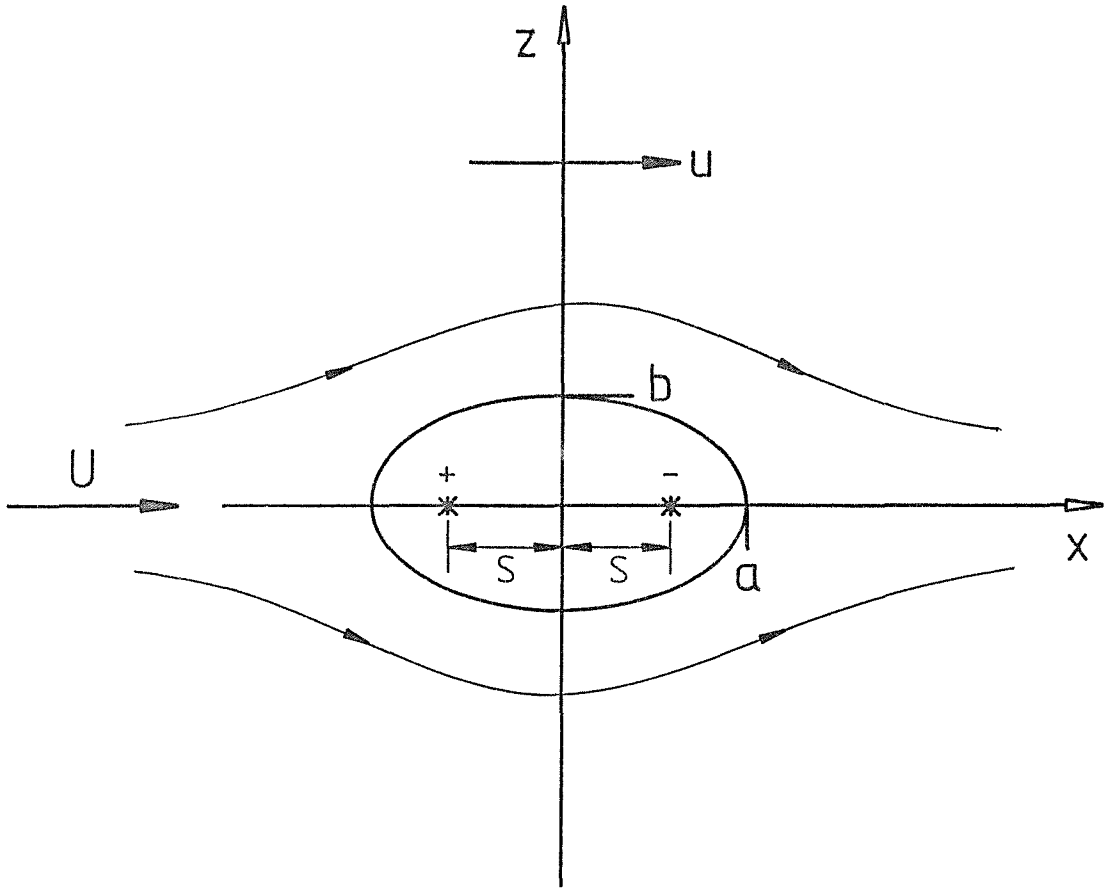

A whole geometric family of such 'Rankine Ovals', as characterised by the ratio of radii (i.e. $\frac{a}{b}$), can be obtained simply by varying the source (and sink) strength or the separation distance.

Glauert (8) has described the shape of the 'Rankine Oval' in terms of the stream function (ψ) as :

$$\psi = -U + \frac{M}{2\pi} \tan^{-1}\left(\frac{2zs}{x^2+z^2-s^2}\right) \text{ ——— A1}$$

The perturbation velocity around this shape can be obtained from :

$$u = \frac{d\psi}{dz} \text{ ——— A2}$$

$$u = -U + \frac{M}{2\pi}\frac{d}{dz}\left[\tan^{-1}\left(\frac{2zs}{x^2+z^2-s^2}\right)\right] \text{ ——— A3}$$

For the mouse casing application, the perturbation velocity was to be measured by a probe and arm arrangement only along the minor axis i.e. x = 0.

$$u_{x=0} = -U + \frac{M}{2\pi}\frac{d}{dz}\left[\tan^{-1}\left(\frac{2zs}{z^2-s^2}\right)\right] \text{ ——— A4}$$

The differential part of this equation can be evaluated by using the substitution :

$$t = \frac{2zs}{z^2-s^2} \text{ ——— A5}$$

$$\therefore\ u_{x=0} = -U + \frac{M}{2\pi}\frac{d}{dz}\left(\tan^{-1} t\right) \text{ ——— A6}$$

Now $$\frac{d}{dz}\left(\tan^{-1} t\right) = \frac{d}{dt}\left(\tan^{-1} t\right)\cdot\frac{dt}{dz} \qquad\text{———— A7}$$

It can be shown that :

$$\frac{d}{dt}\left(\tan^{-1} t\right) = \frac{1}{1+t^2} = \frac{1}{1+\left(\dfrac{2zs}{z^2-s^2}\right)^2} \qquad\text{———— A8}$$

$$\frac{dt}{dz} = \frac{-4z^2s}{(z^2-s^2)^2} + \frac{2s}{z^2-s^2} \qquad\text{———— A9}$$

Substituting (A8) and (A9) in (A7) and then in (A6)

$$u_{x=o} = -U + \frac{Ms}{2\pi}\left[\frac{-4z^2+2(z^2-s^2)}{(z^2-s^2)^2+4z^2s^2}\right] \qquad\text{———— A10}$$

In non-dimensional form this can be rewritten as :

$$\frac{u_{x=o}}{U} = -1 - \frac{M}{2\pi Us}\cdot\left(\frac{1+\left(\frac{z}{s}\right)^2}{\left[\left(\frac{z}{s}\right)^2-1\right]^2+4\left(\frac{z}{s}\right)^2}\right) \qquad\text{———— A11}$$

Glauert (8) has also deduced a further relationship for a 'Rankine Oval' :

$$\frac{M}{\pi Us} = \left(\frac{a}{s}\right)^2 - 1 = \left(\frac{a}{b}\cdot\frac{b}{s}\right)^2 - 1 \qquad\text{———— A12}$$

By substituting (A12) in (A11), and with further manipulation, the following equation can be produced :

$$\boxed{\frac{u_{x=0}}{U} = -1 + \left[1 - \left(\frac{a}{b}\cdot\frac{b}{s}\right)^2\right]\cdot\left(\frac{1+\left(\frac{z}{b}\cdot\frac{b}{s}\right)^2}{\left[\left(\frac{z}{b}\cdot\frac{b}{s}\right)^2-1\right]^2+4\left(\frac{z}{b}\cdot\frac{b}{s}\right)^2}\right) \text{———} A13}$$

Glauert has obtained one additional 'Rankine Oval' relationship:

$$\left(\frac{b}{s}\right) = \cot\left[\frac{\pi U s}{M}\left(\frac{b}{s}\right)\right] \text{————} A14$$

By combining equations (A12) and (A14) the following relationship was formed:

$$\boxed{\left(\frac{b}{s}\right) = \cot\left[\frac{\left(\frac{b}{s}\right)}{\left(\frac{a}{b}\cdot\frac{b}{s}\right)^2-1}\right] \text{————} A15}$$

This equation could be solved iteratively to obtain values of $(\frac{b}{s})$ for various settings of $(\frac{a}{b})$.

Equation (A13) therefore effectively related the velocity ratio $(\frac{u}{U})$ at a point along the minor axis (z-axis) of the oval, to the slenderness of the oval $(\frac{a}{b})$, and the distance of the point from the oval centre $(\frac{z}{b})$.

A carpet plot showing the relationship between these variables is given in figure (22).

APPENDIX II

NACA a = 0.8 STATIC PRESSURE DISTRIBUTION RESULTS

NACA a = 0.8

CR (%)	d/c (%)	α (deg)	Re x 10^5	Test #
17.5	17 (17.1)	2.5	3.5	1
			6	2
			10	3
		5.0	3.5	4
			6	5
			10	6
		7.5	3.5	7
			6	8
			10	9
		10.0	3.5	10
			6	11
			10	12
15.0	17 (16.8)	2.5	2	13
			6	14
			10	15
		5.0	2	16
			6	17
			10	18
		7.5	2	19
			6	20
			10	21
		10.0	2	22
			6	23
			10	24
	10 (10.3)	2.5	6	25
			10	26
			14	27
		5.0	6	28
			10	29
			14	30
		7.5	6	31
			10	32
			14	33
		10.0	6	34
			10	35
			14	36

NACA a = 0.8

CR (%)	d/c (%)	α (deg)	Re x 10^5	Test #
12.5	17 (16.5)	2.5	3.5	37
			6	38
			10	39
		5.0	3.5	40
			6	41
			10	42
		7.5	3.5	43
			6	44
			10	45
		10.0	3.5	46
			6	47
			10	48
	10 (10.2)	2.5	6	49
			10	50
			14	51
		5.0	6	52
			10	53
			14	54
		7.5	6	55
			10	56
			14	57
		10.0	6	58
			10	59
			14	60
	4 (4.3)	2.5	10	61
			14	62
			16	63
		5.0	10	64
			14	65
			16	66
		7.5	10	67
			14	68
			16	69
		10.0	10	70
			14	71
			16	72

NACA a = 0.8

CR (%)	d/c (%)	α (deg)	Re x 10^5	Test #
10.0	10 (10.0)	2.5	6	73
			10	74
			14	75
		5.0	6	76
			10	77
			14	78
		7.5	6	79
			10	80
			14	81
		10.0	6	82
			10	83
			14	84
	4 (4.2)	2.5	10	85
			14	86
			16	87
		5.0	10	88
			14	89
			16	90
		7.5	10	91
			14	92
			16	93
		10.0	10	94
			14	95
			16	96
7.5	4 (4.1)	2.5	10	97
			14	98
			16	99
		5.0	10	100
			14	101
			16	102
		7.5	10	103
			14	104
			16	105
		10.0	10	106
			14	107
			16	108

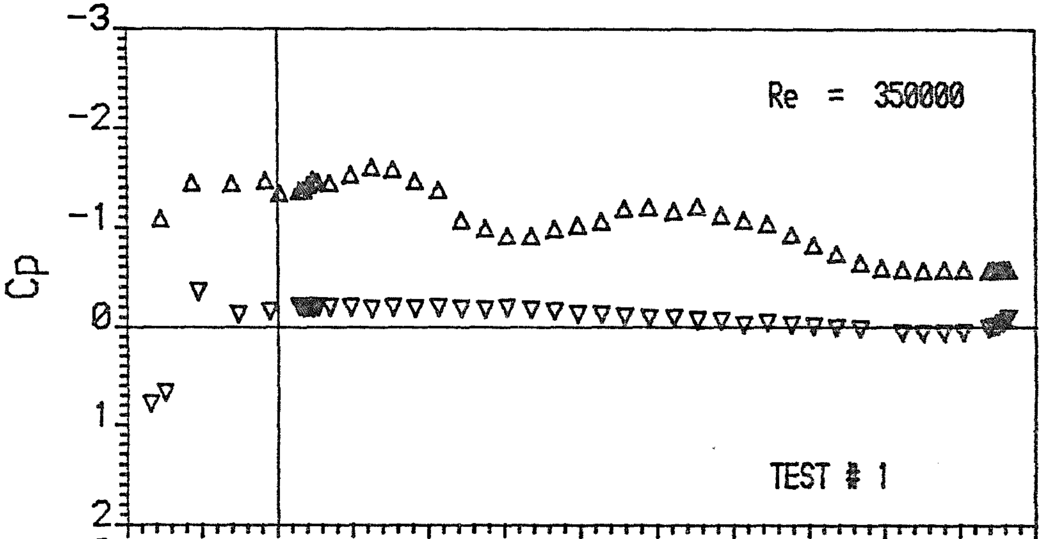

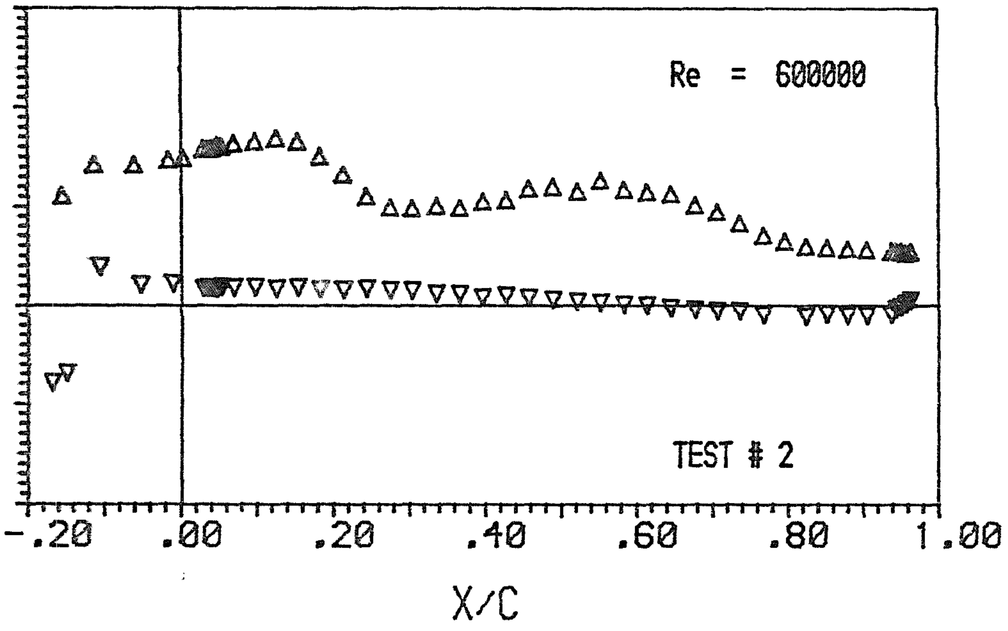

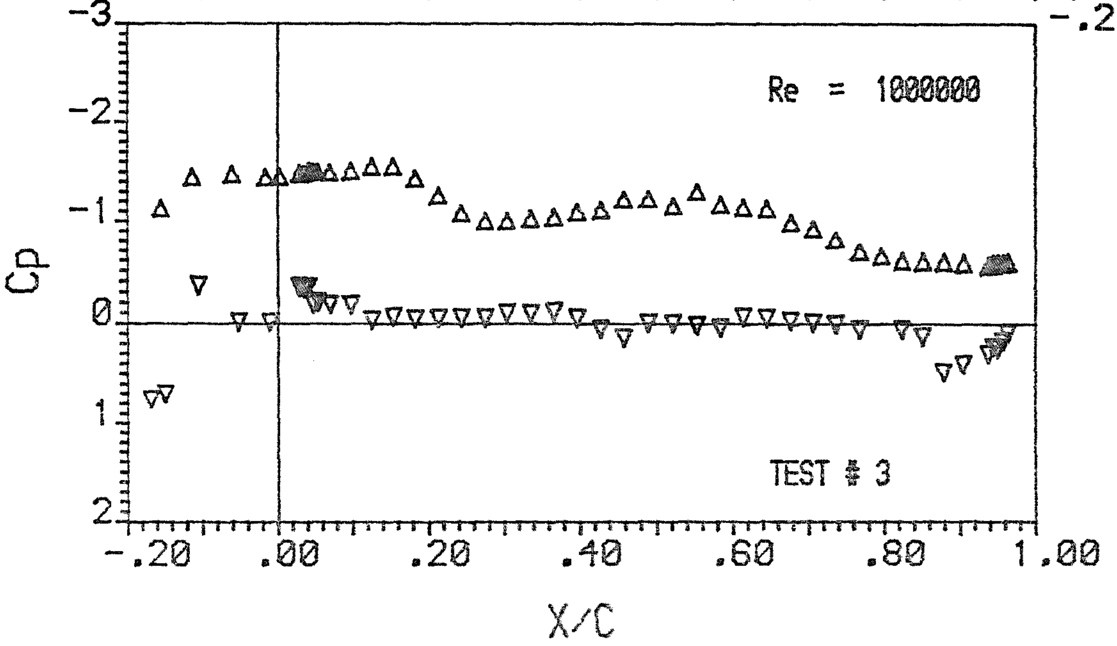

NACA a=0.8

Incidence Angle = 2.50
Mast/Chord Ratio = .171
Mast Angle = 15.00
Camber Ratio = .175

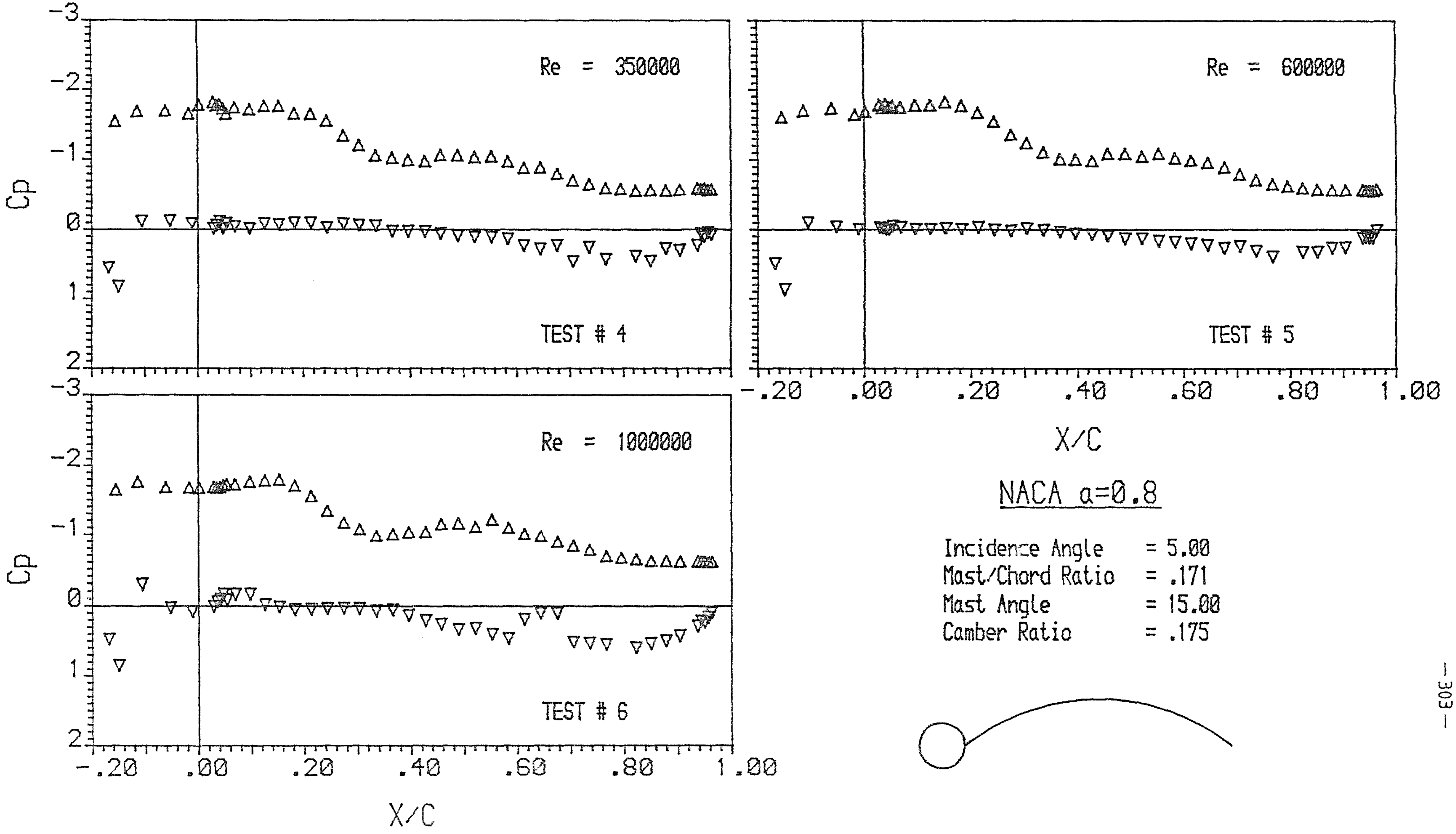

NACA a=0.8

Incidence Angle = 5.00
Mast/Chord Ratio = .171
Mast Angle = 15.00
Camber Ratio = .175

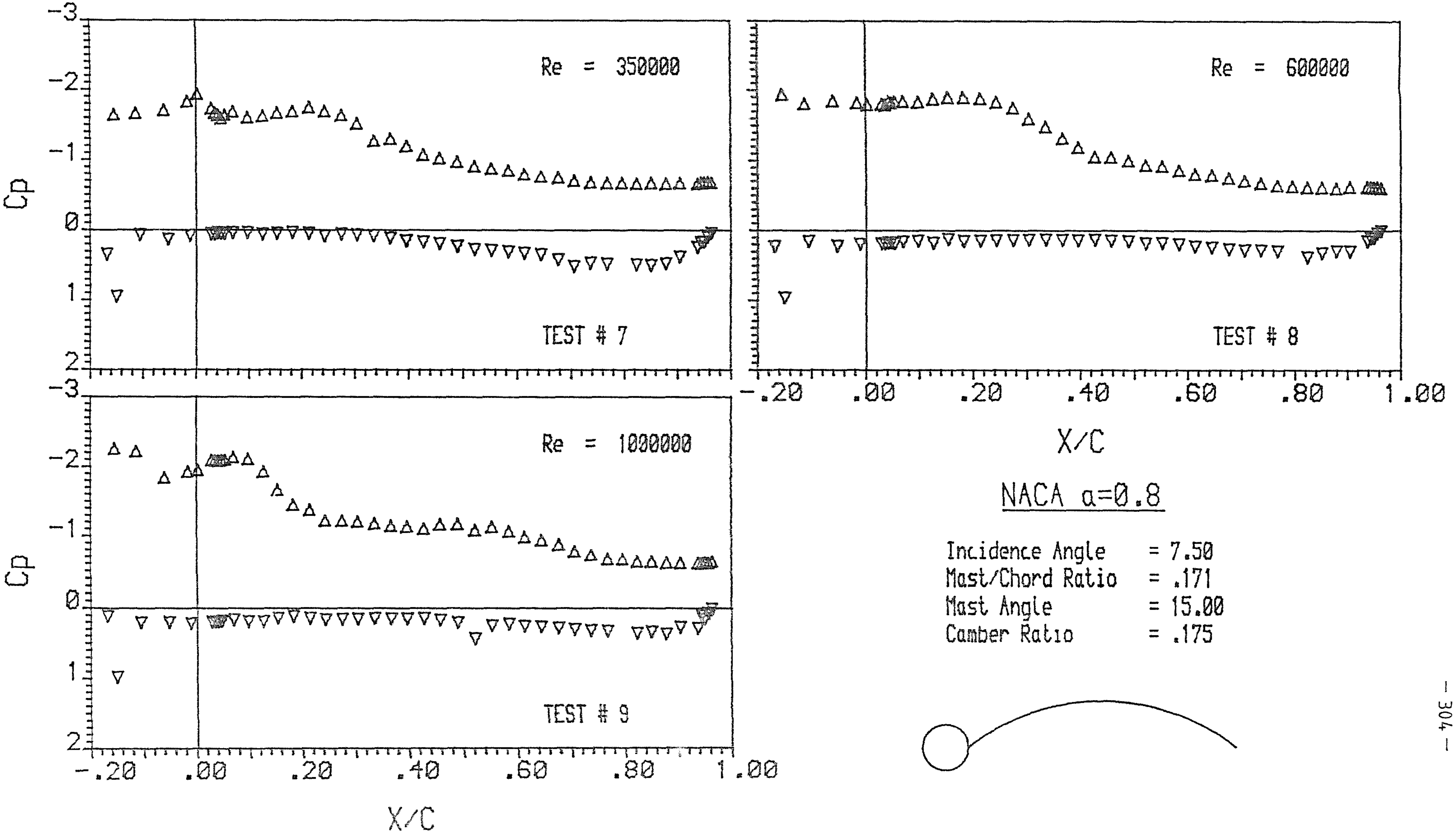

NACA a=0.8

Incidence Angle = 7.50
Mast/Chord Ratio = .171
Mast Angle = 15.00
Camber Ratio = .175

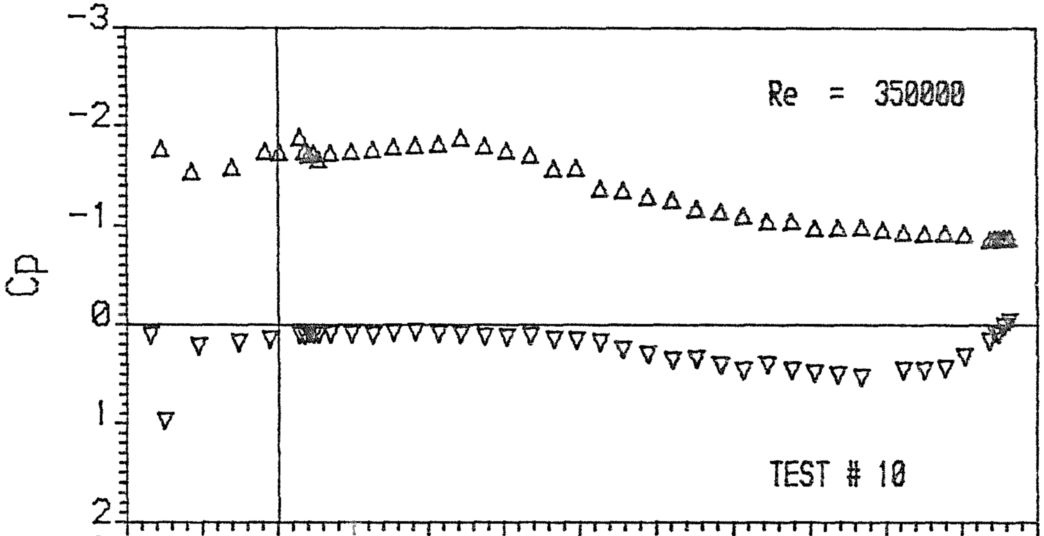

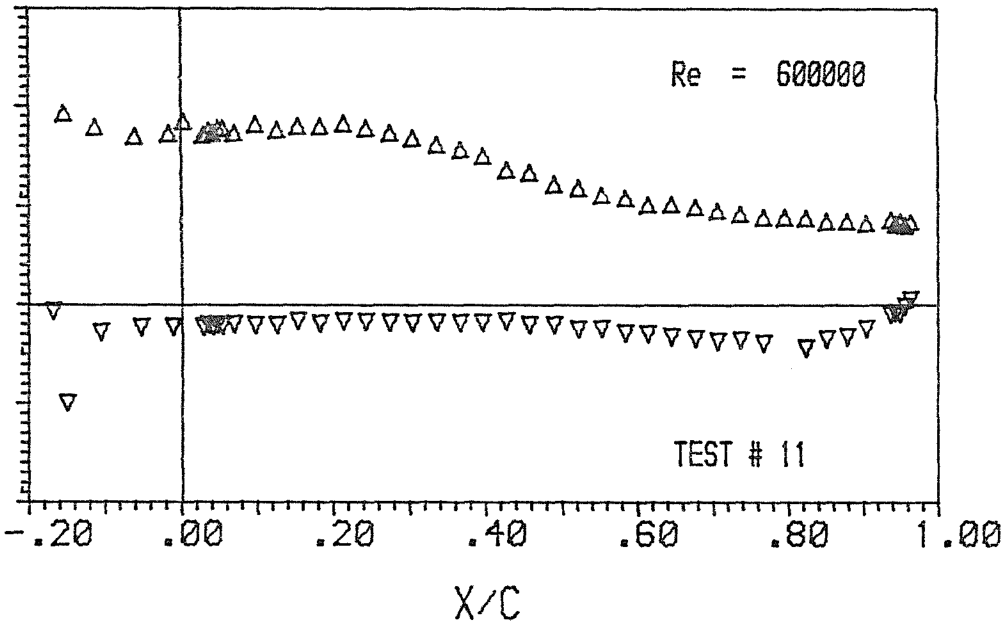

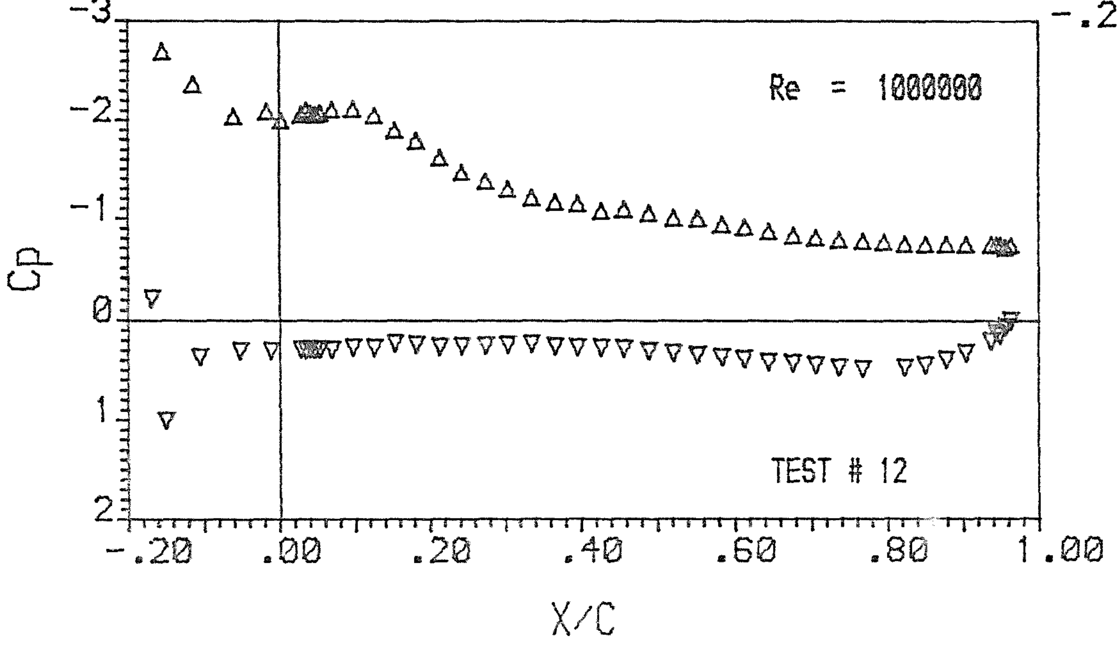

NACA a=0.8

Incidence Angle = 10.00
Mast/Chord Ratio = .171
Mast Angle = 15.00
Camber Ratio = .175

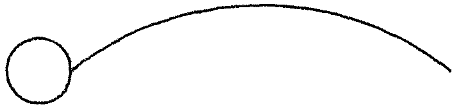

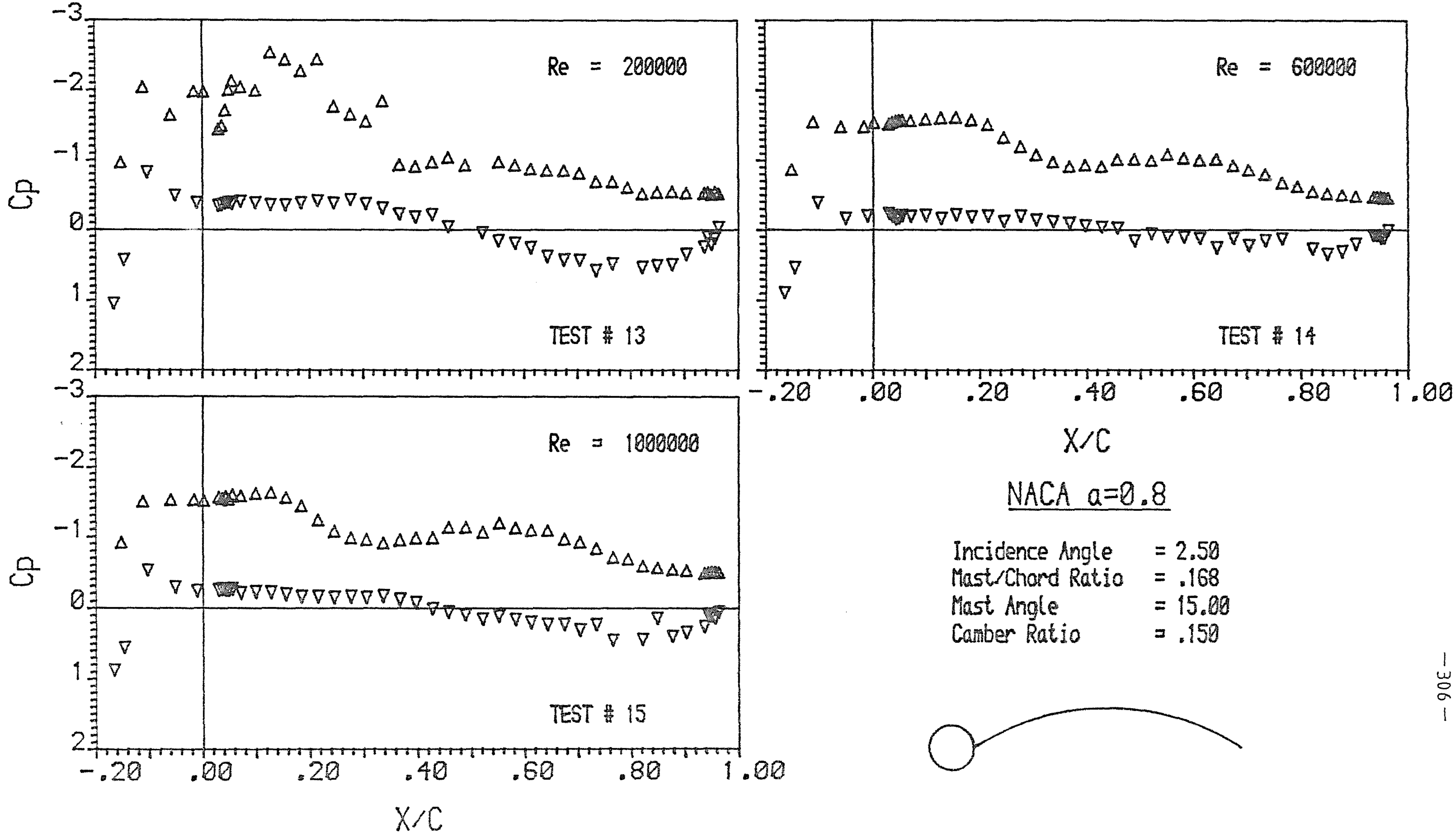

NACA a=0.8

Incidence Angle = 2.50
Mast/Chord Ratio = .168
Mast Angle = 15.00
Camber Ratio = .150

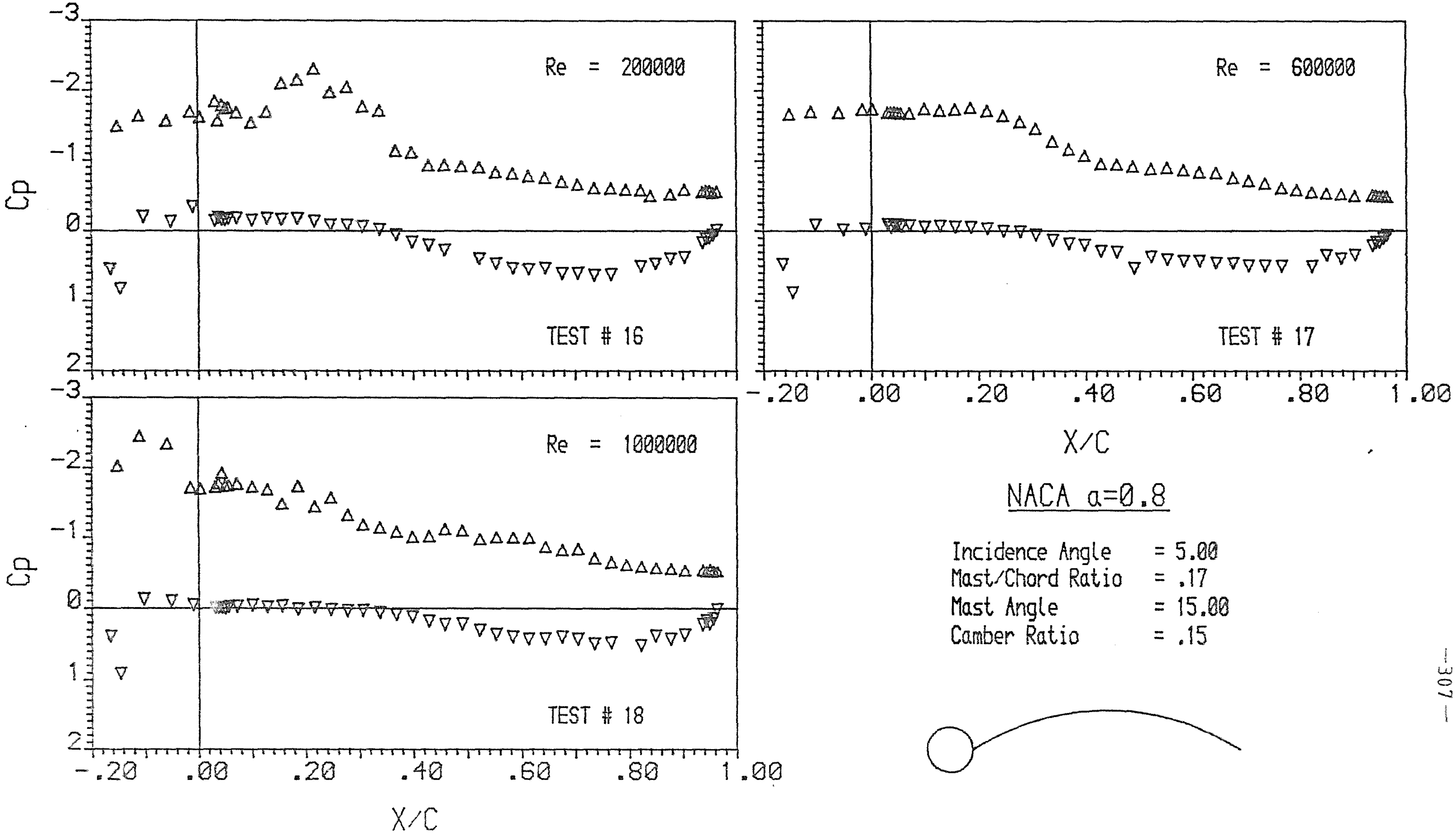

NACA a=0.8

Incidence Angle = 5.00
Mast/Chord Ratio = .17
Mast Angle = 15.00
Camber Ratio = .15

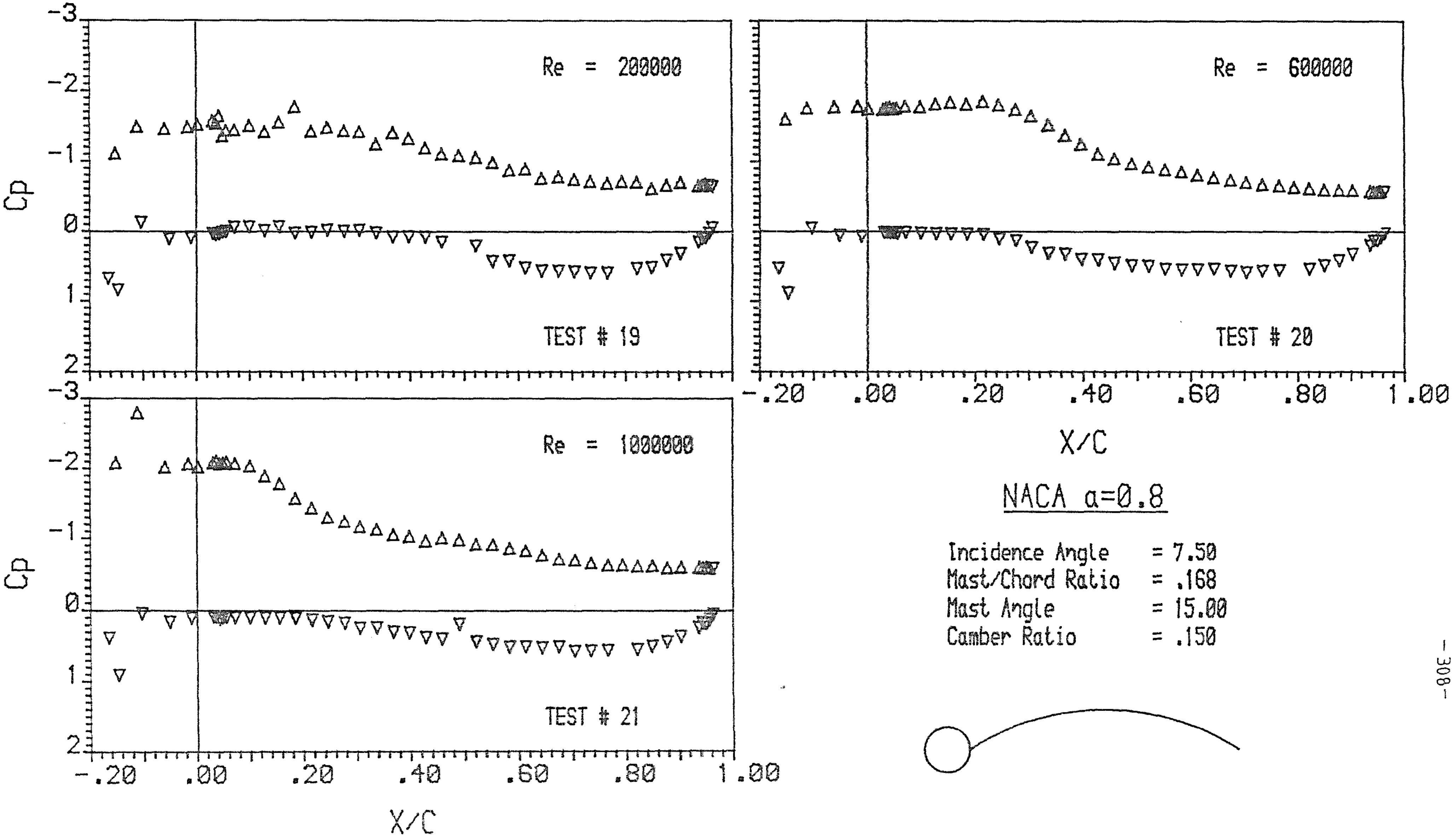

NACA a=0.8

Incidence Angle = 7.50
Mast/Chord Ratio = .168
Mast Angle = 15.00
Camber Ratio = .150

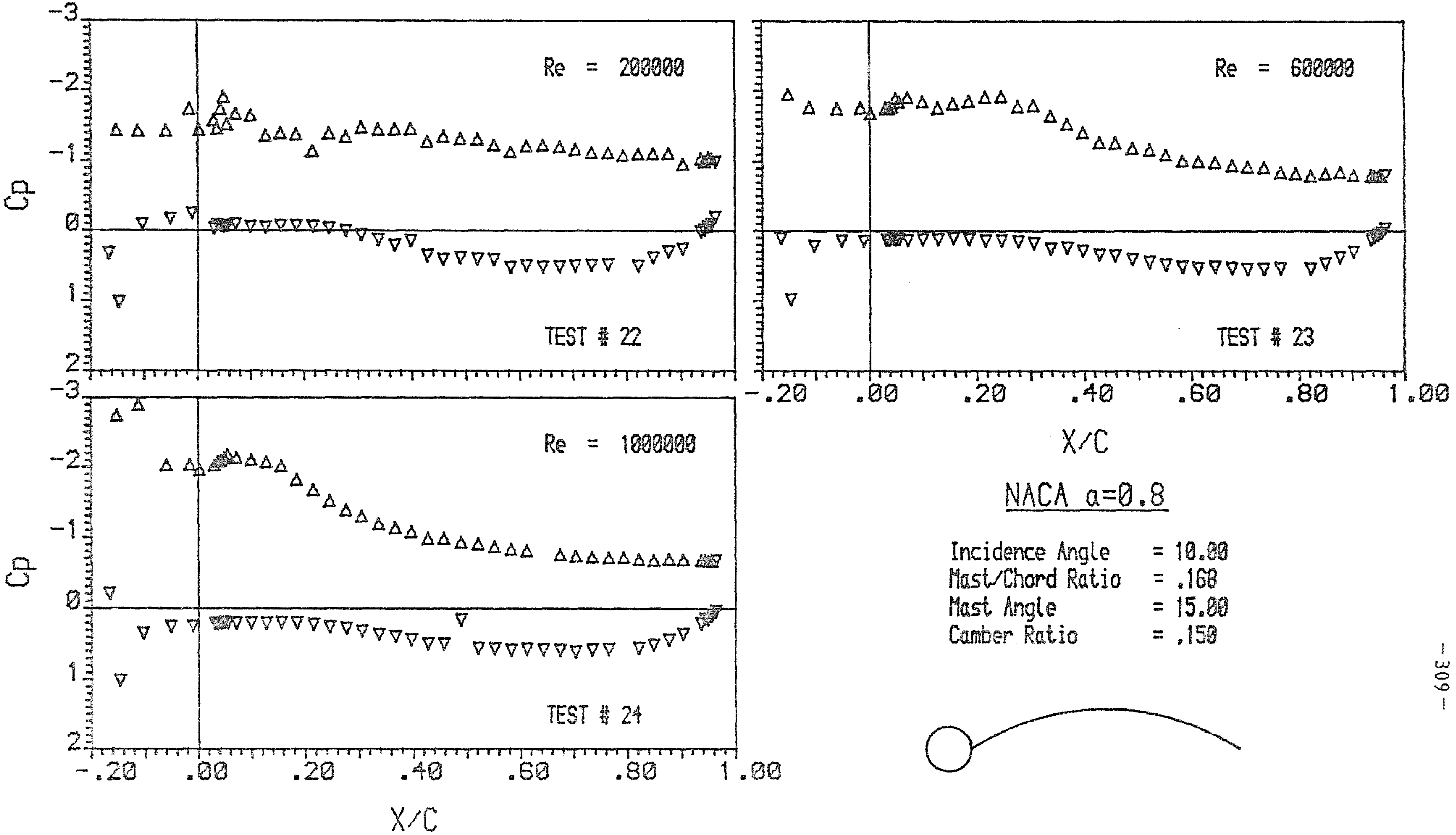

NACA a=0.8

Incidence Angle = 10.00
Mast/Chord Ratio = .160
Mast Angle = 15.00
Camber Ratio = .150

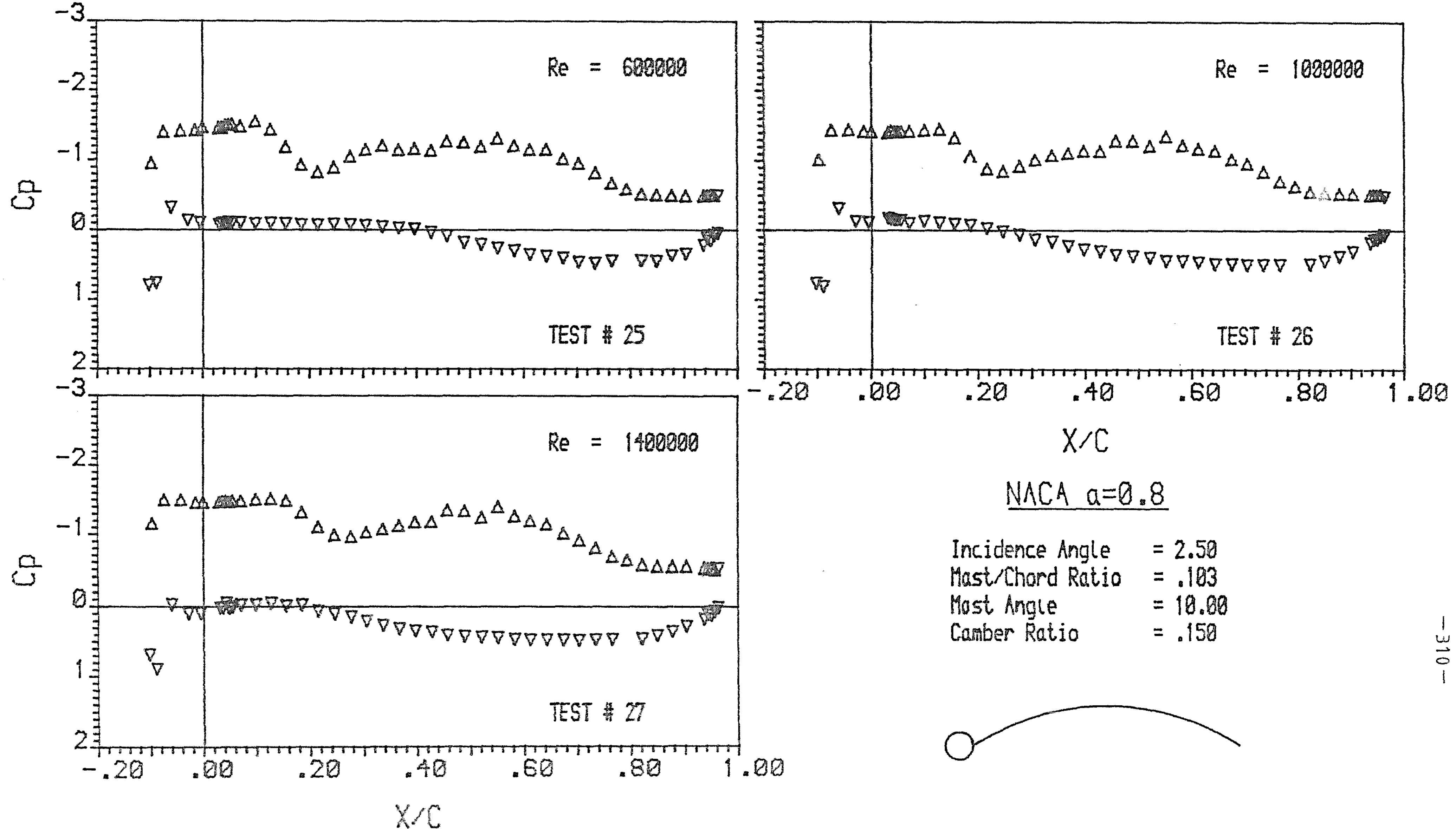

NACA a=0.8

Incidence Angle = 2.50
Mast/Chord Ratio = .103
Mast Angle = 10.00
Camber Ratio = .150

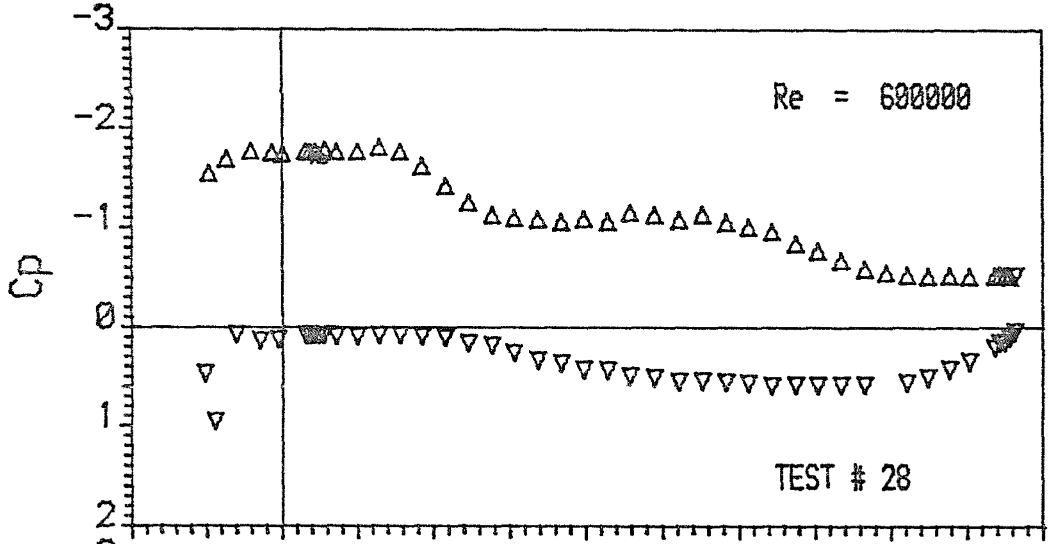

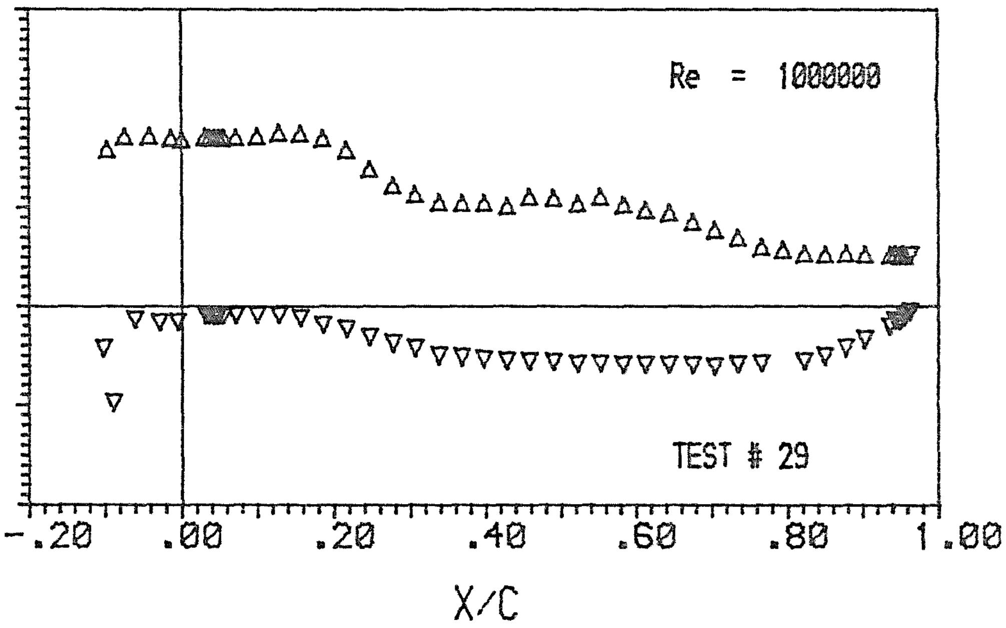

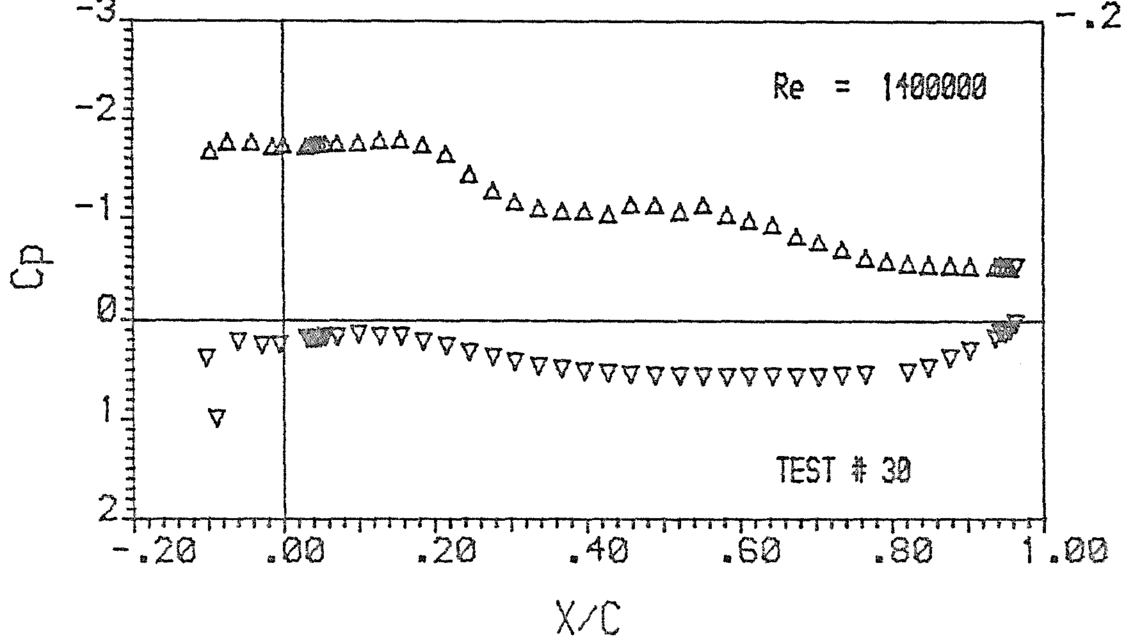

NACA a=0.8

Incidence Angle = 5.00
Mast/Chord Ratio = .103
Mast Angle = 10.00
Camber Ratio = .150

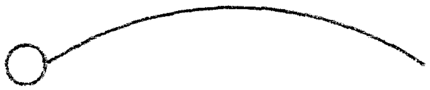

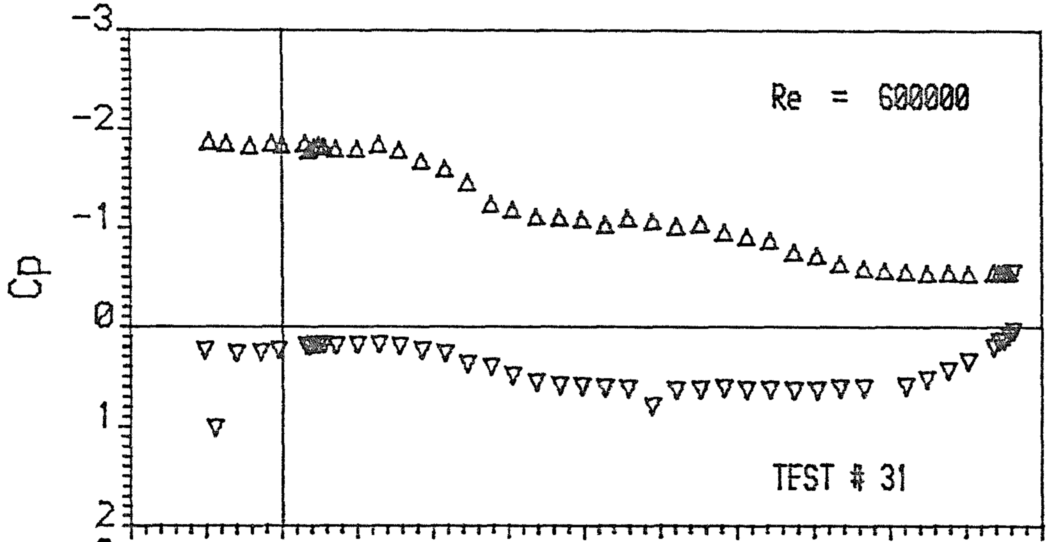

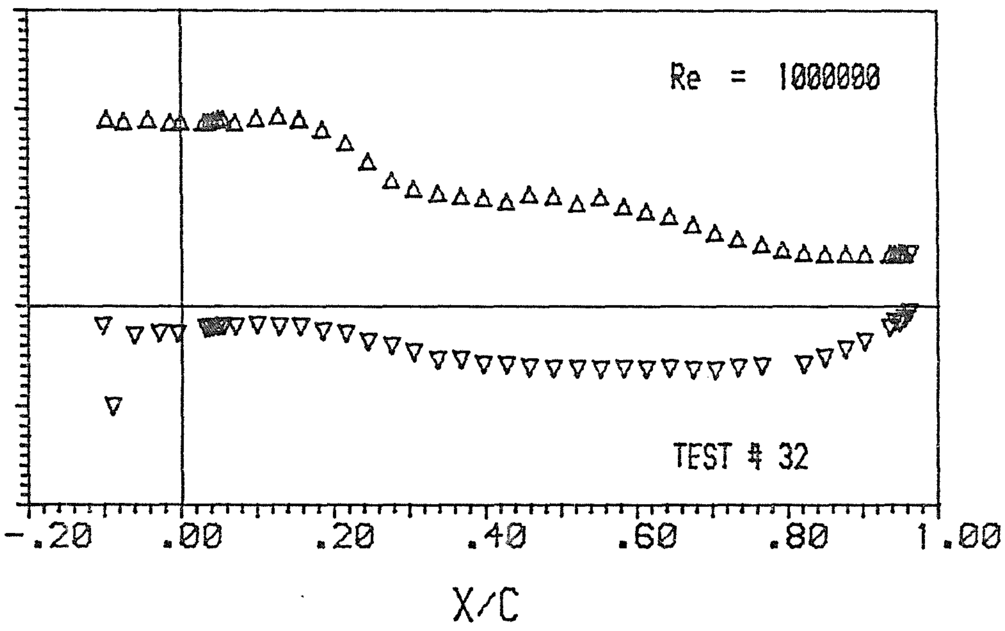

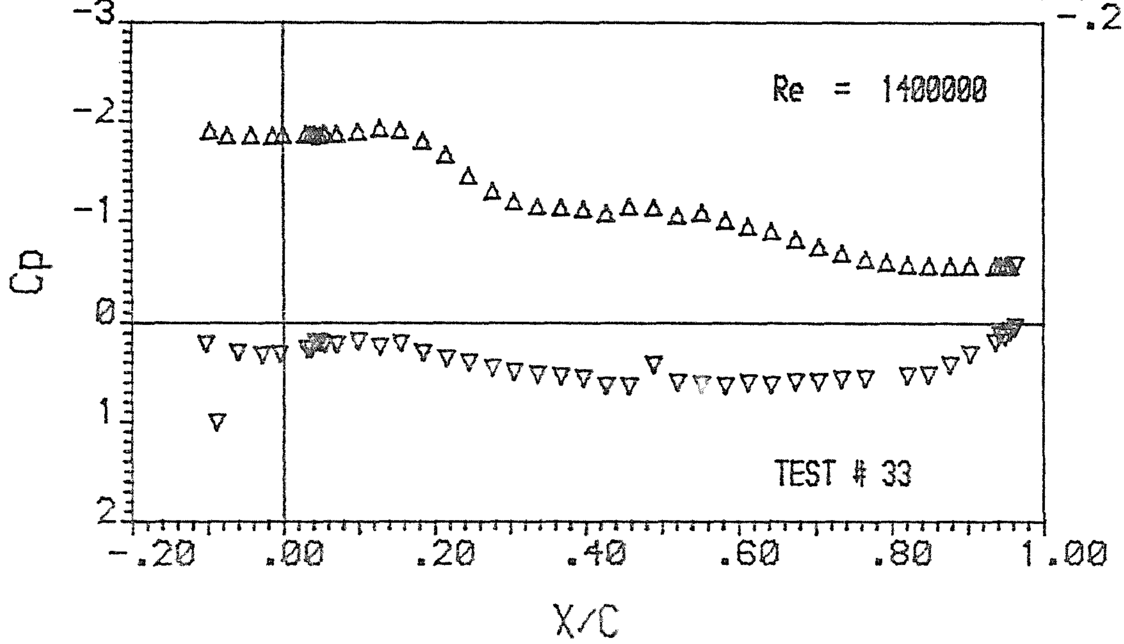

NACA a=0.8

Incidence Angle = 7.50
Mast/Chord Ratio = .103
Mast Angle = 10.00
Camber Ratio = .150

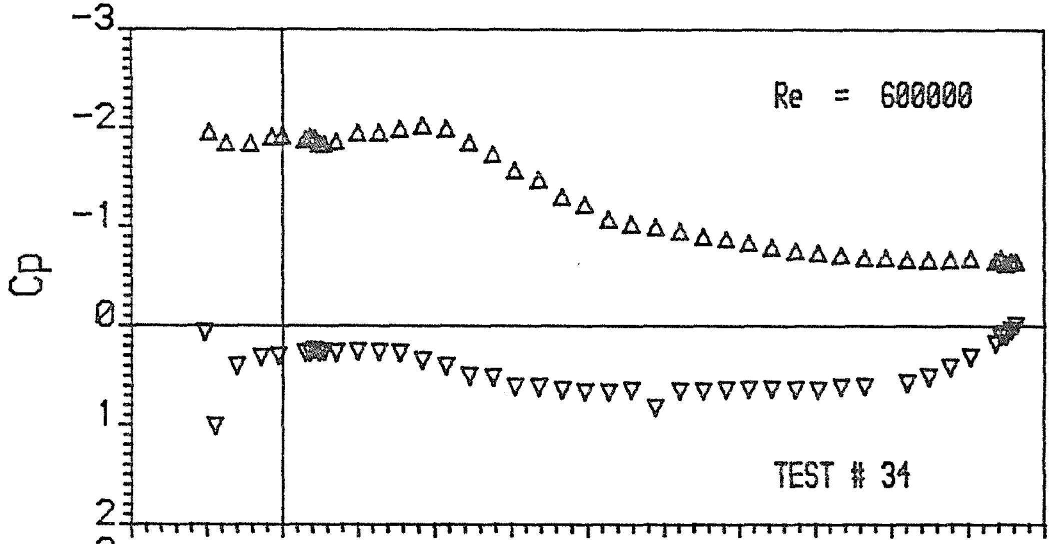

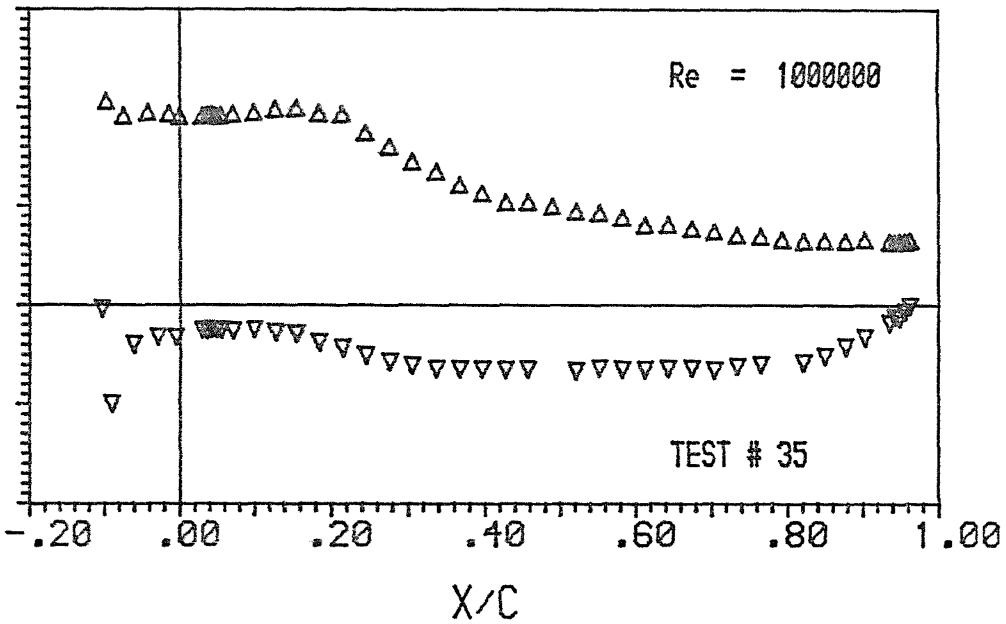

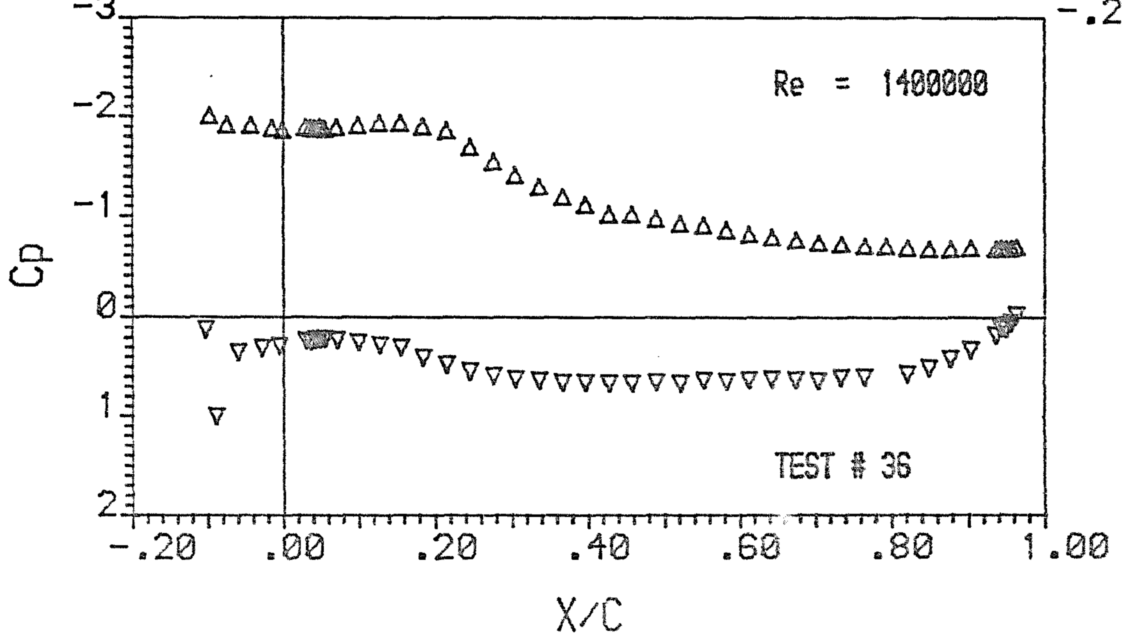

NACA a=0.8

Incidence Angle = 10.00
Mast/Chord Ratio = .103
Mast Angle = 10.00
Camber Ratio = .150

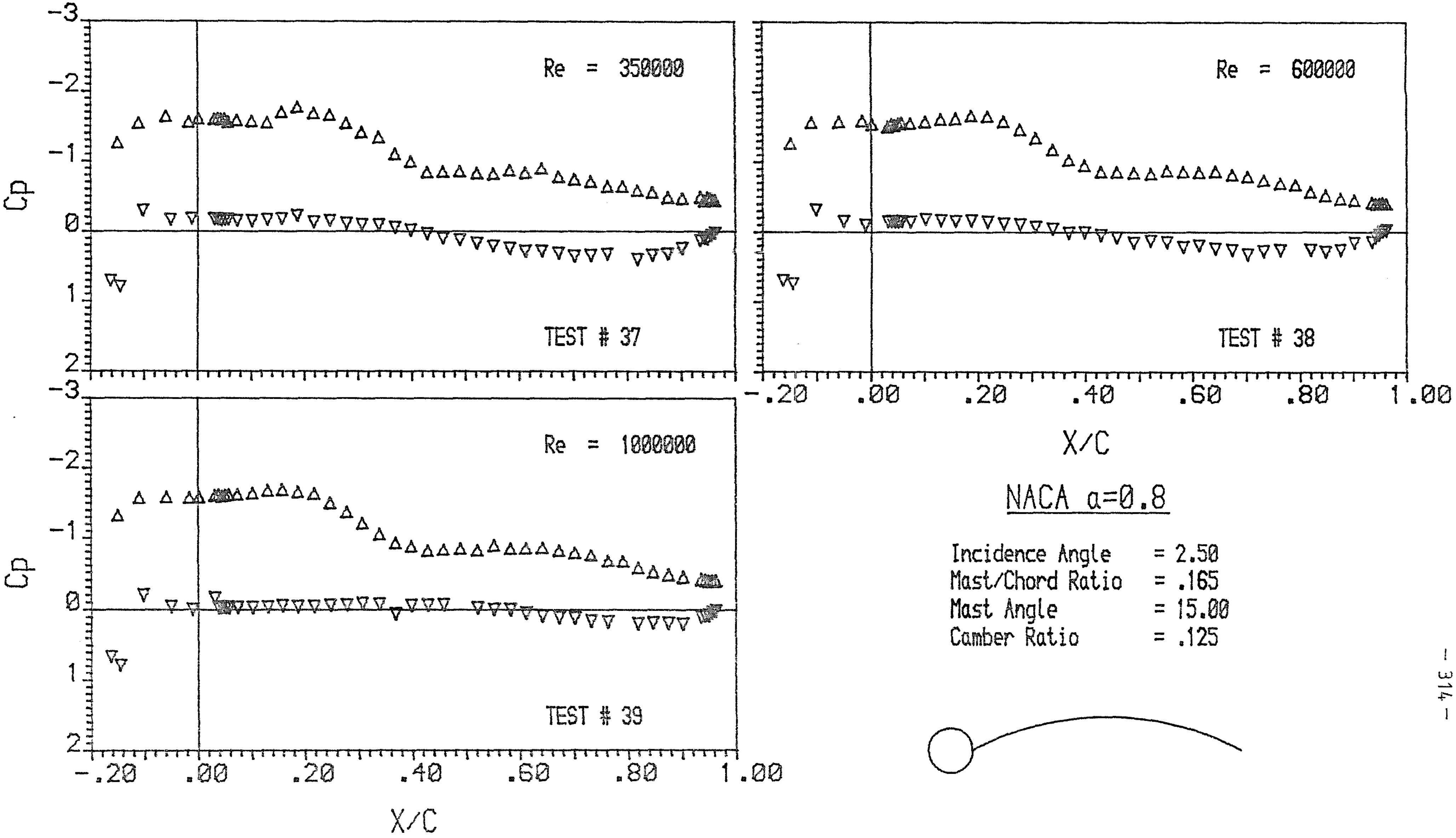

NACA a=0.8

Incidence Angle = 2.50
Mast/Chord Ratio = .165
Mast Angle = 15.00
Camber Ratio = .125

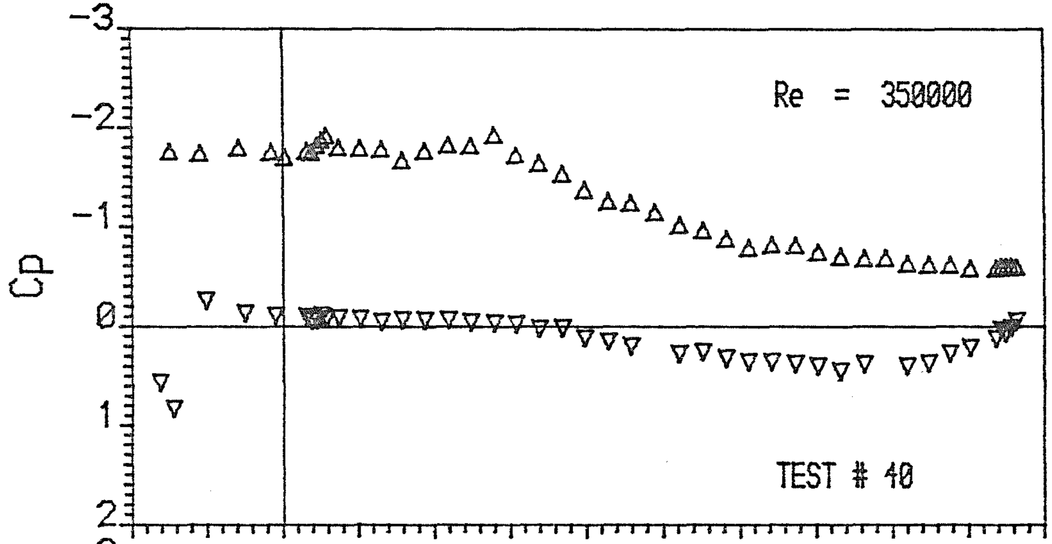

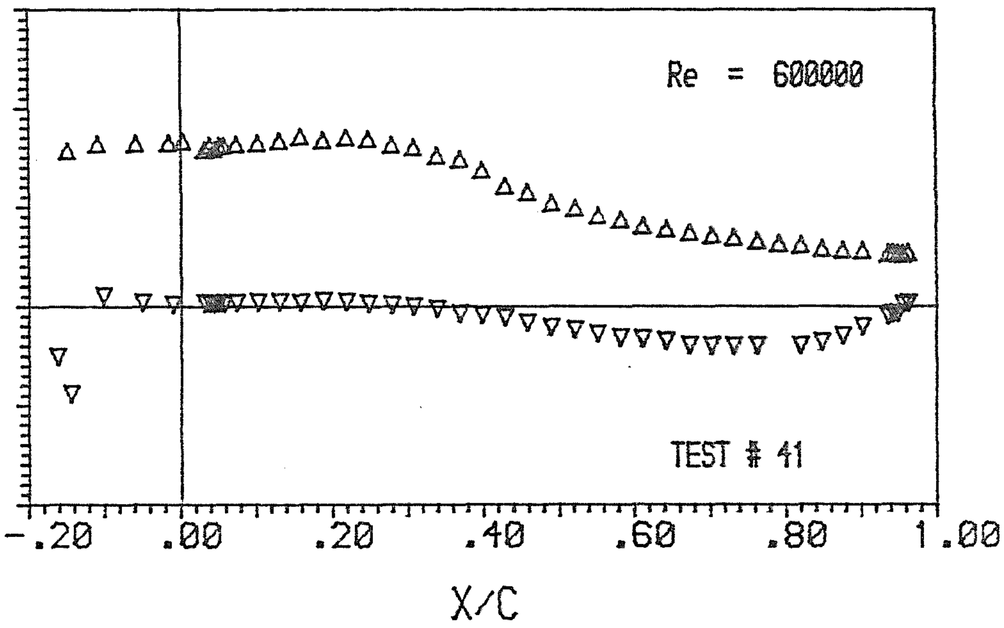

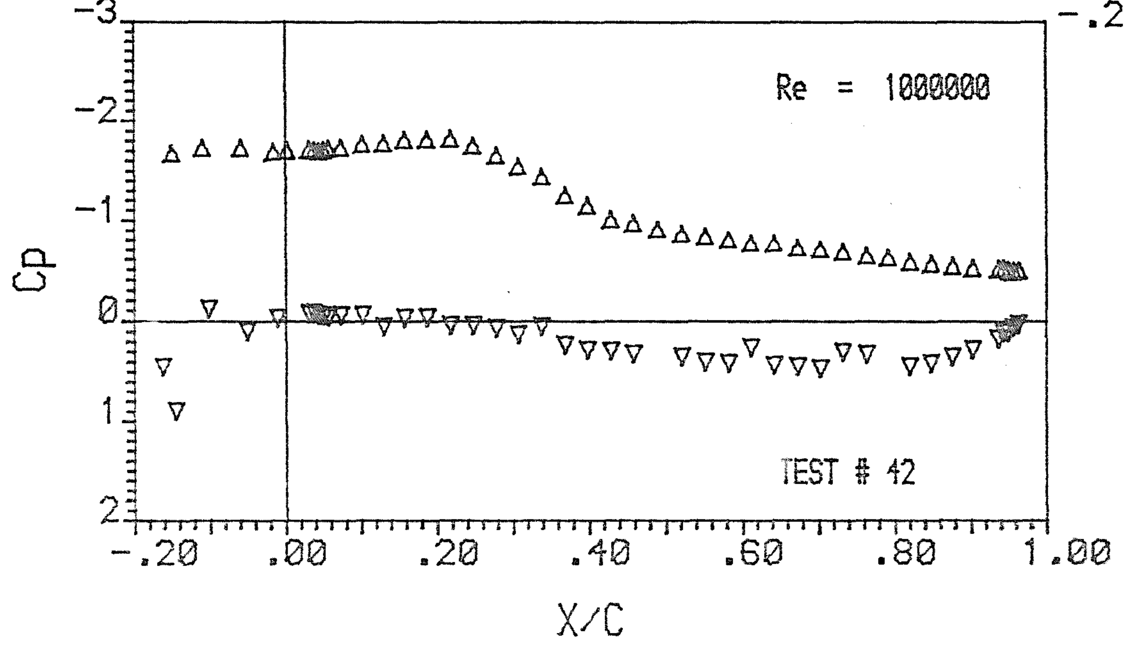

NACA a=0.8

Incidence Angle = 5.00
Mast/Chord Ratio = .165
Mast Angle = 15.00
Camber Ratio = .125

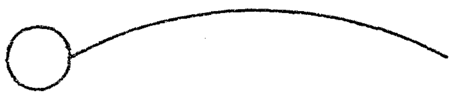

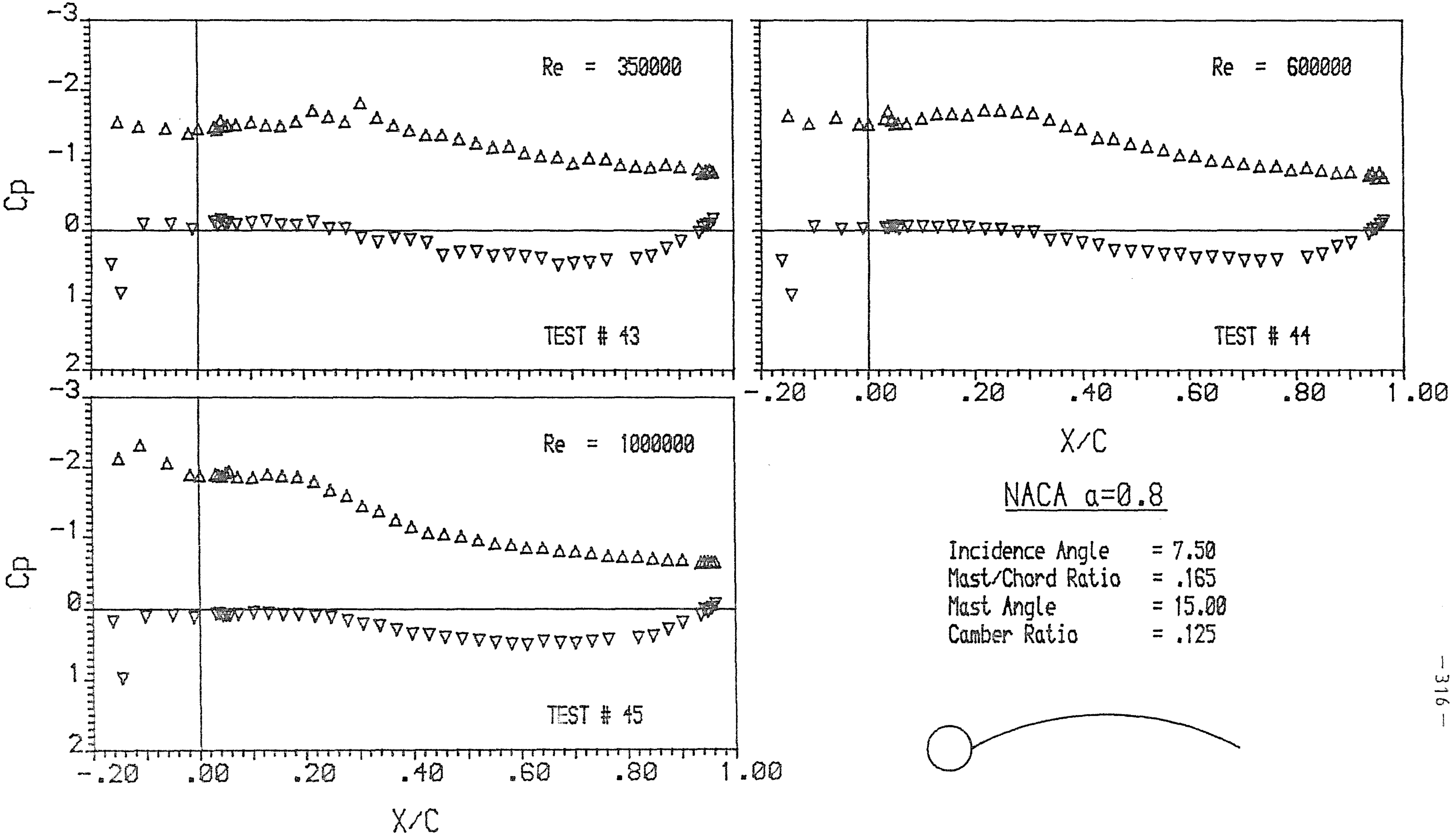

NACA a=0.8

Incidence Angle = 7.50
Mast/Chord Ratio = .165
Mast Angle = 15.00
Camber Ratio = .125

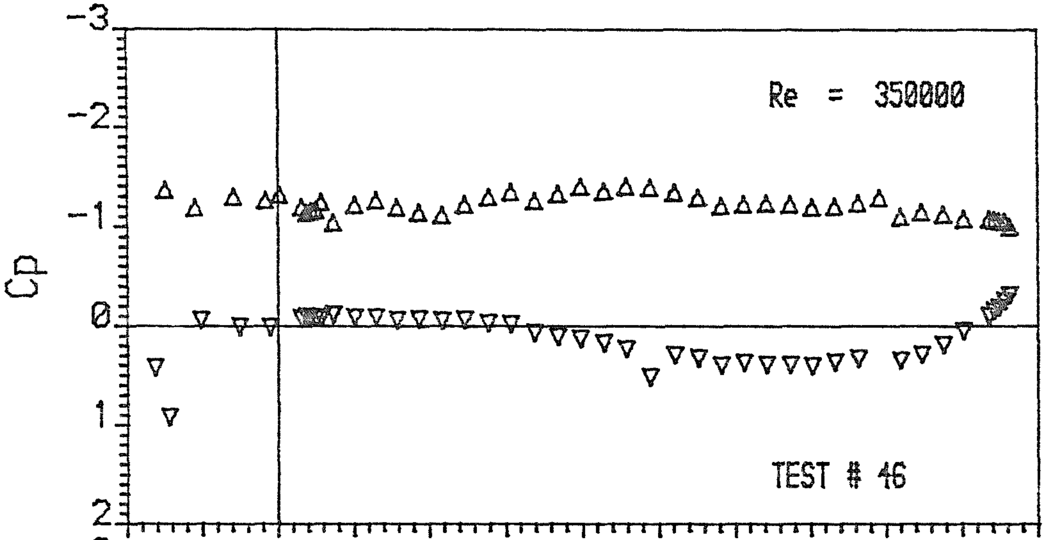

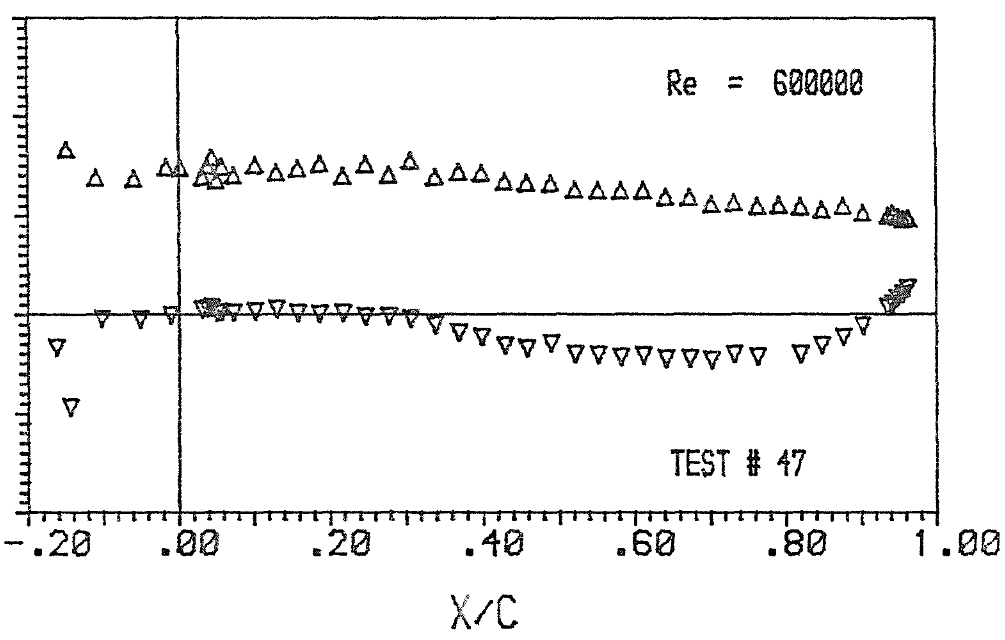

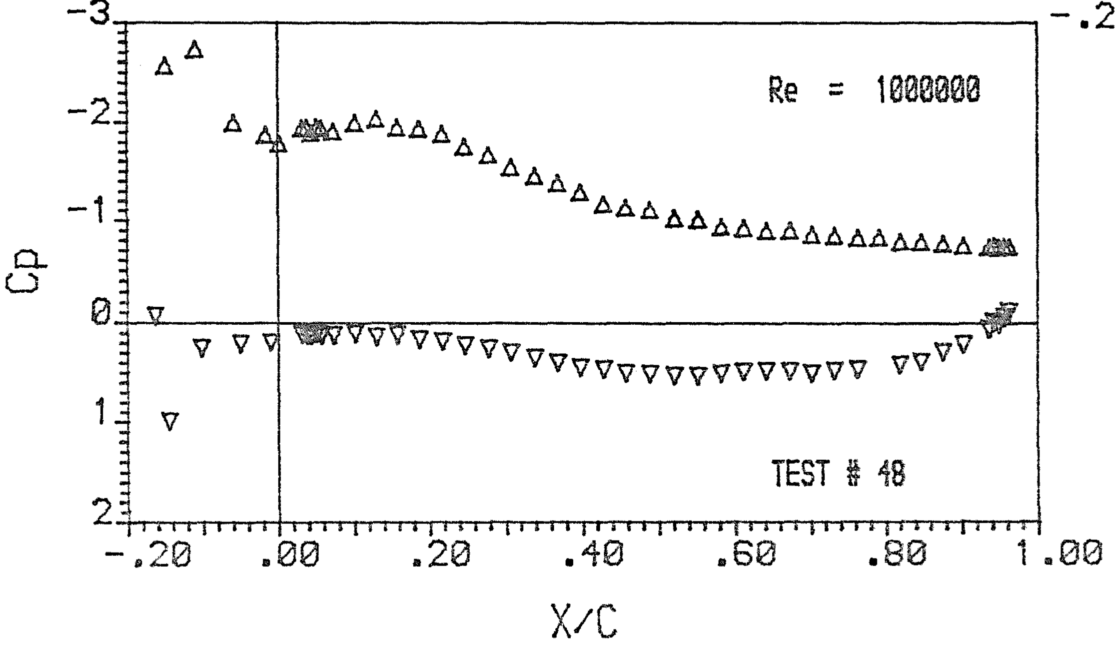

NACA a=0.8

Incidence Angle = 10.00
Mast/Chord Ratio = .165
Mast Angle = 15.00
Camber Ratio = .125

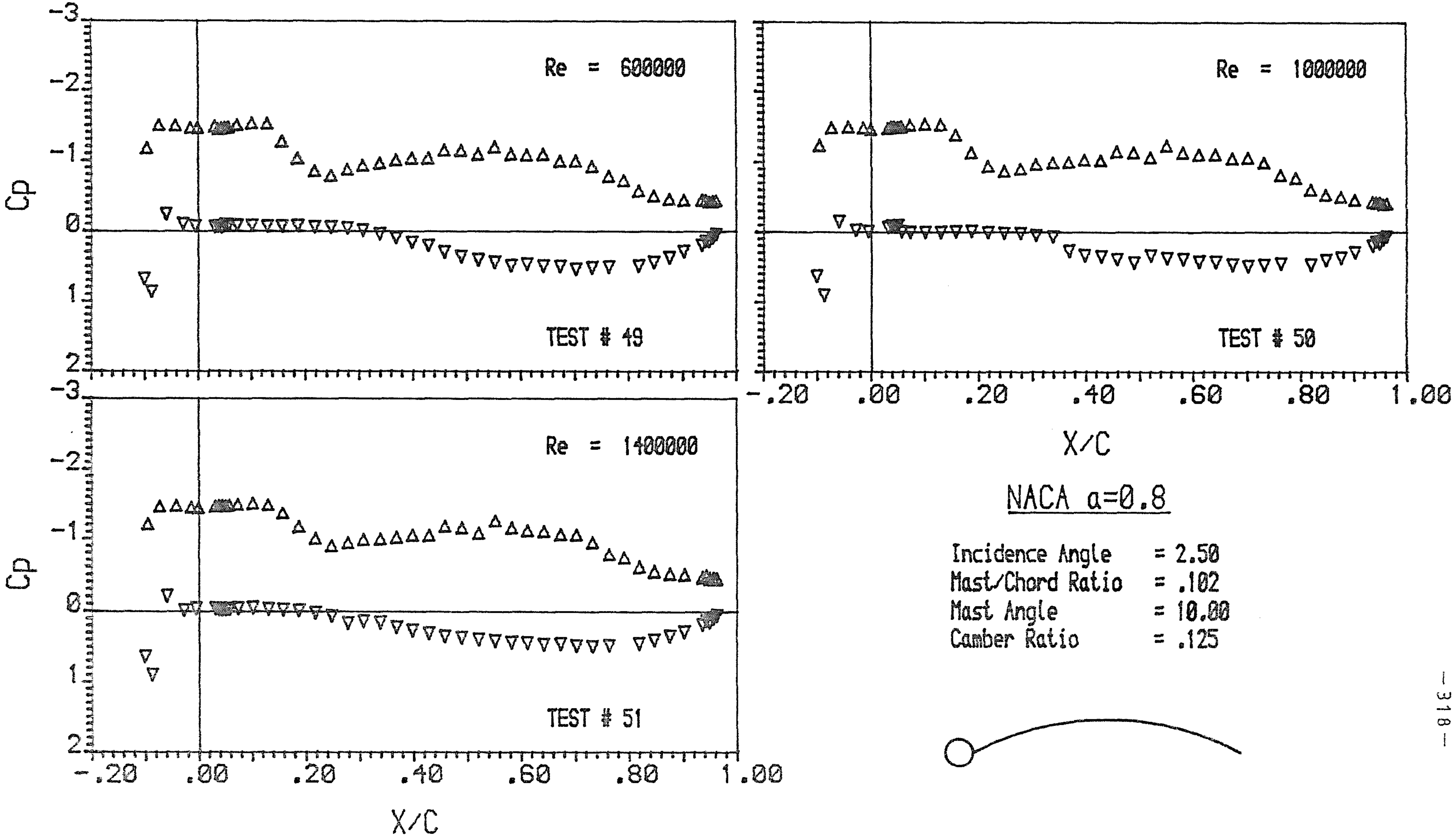

NACA a=0.8

Incidence Angle = 2.50
Mast/Chord Ratio = .102
Mast Angle = 10.00
Camber Ratio = .125

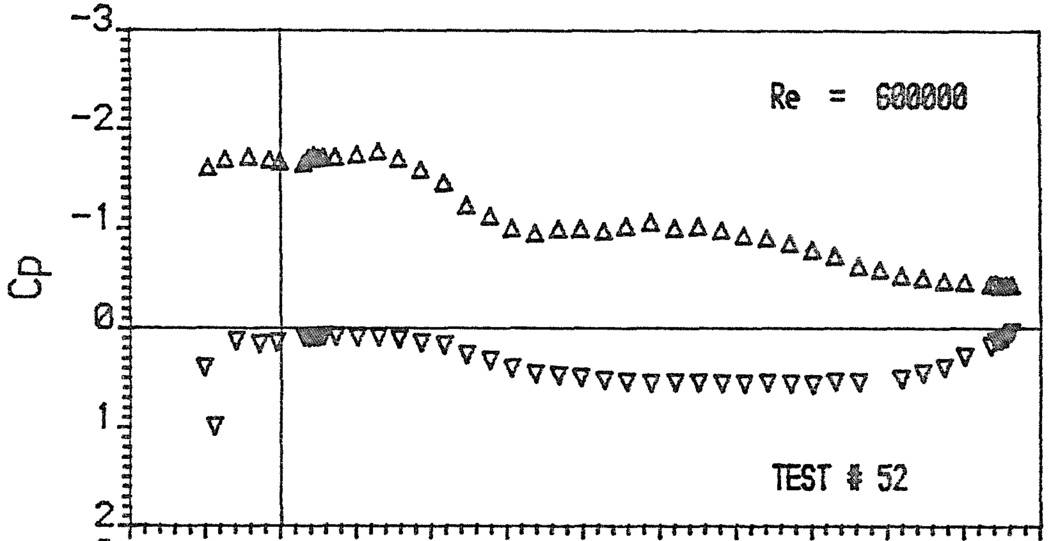
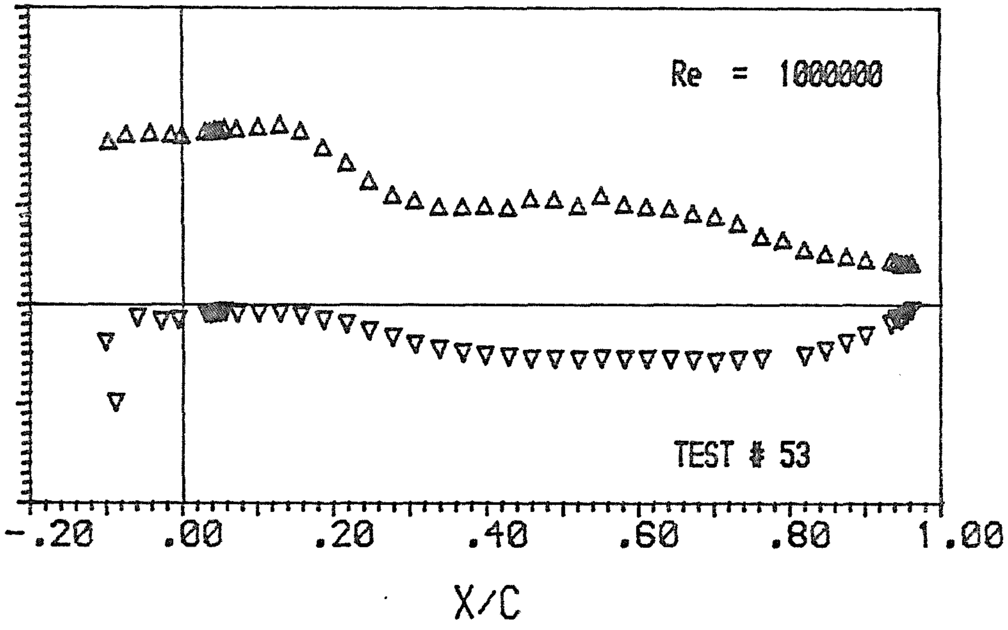
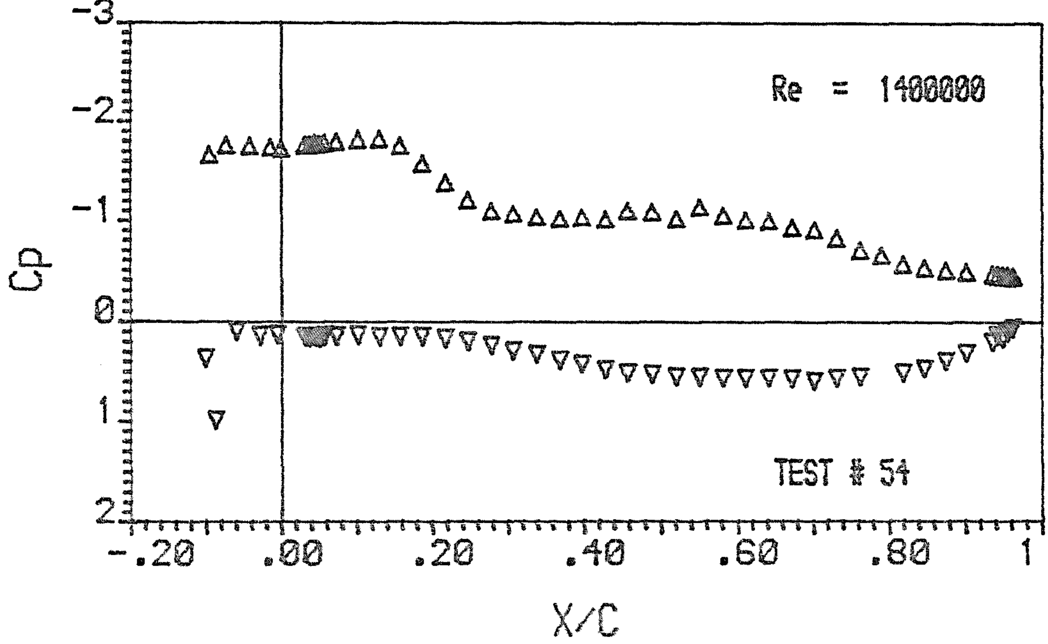

NACA a=0.8

Incidence Angle = 5.00
Mast/Chord Ratio = .102
Mast Angle = 10.00
Camber Ratio = .125

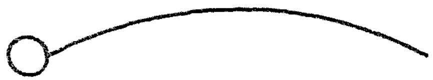

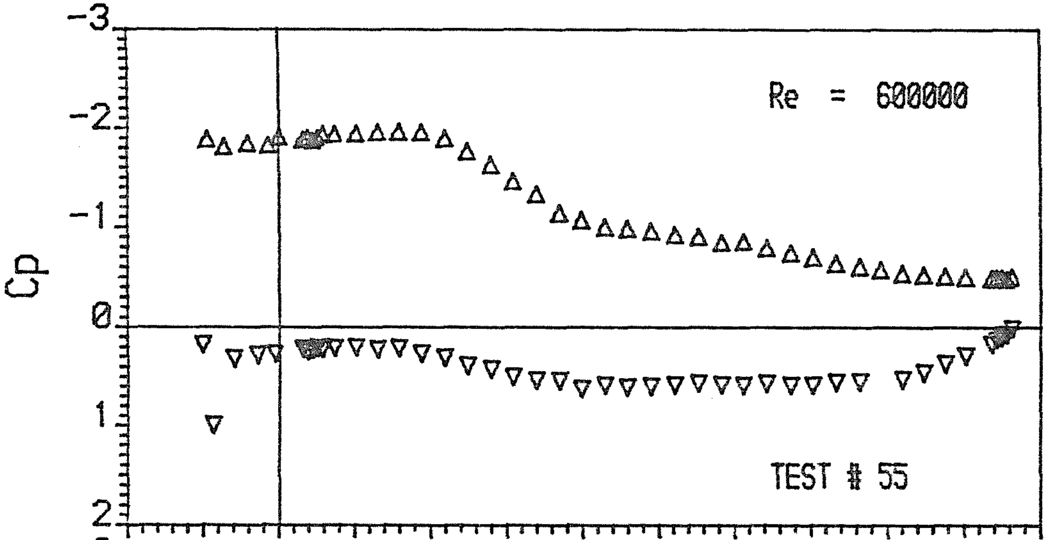

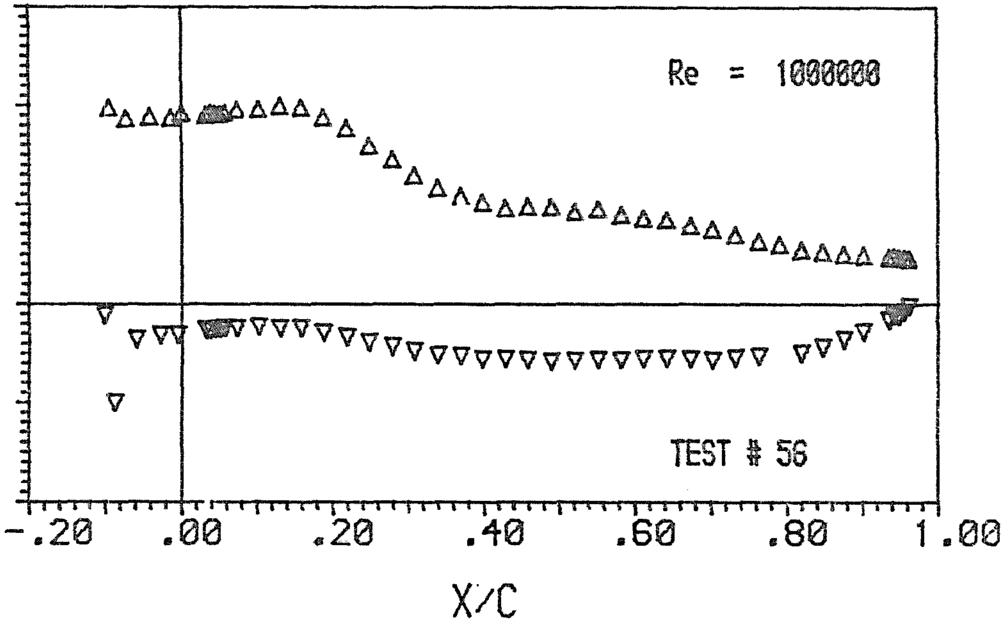

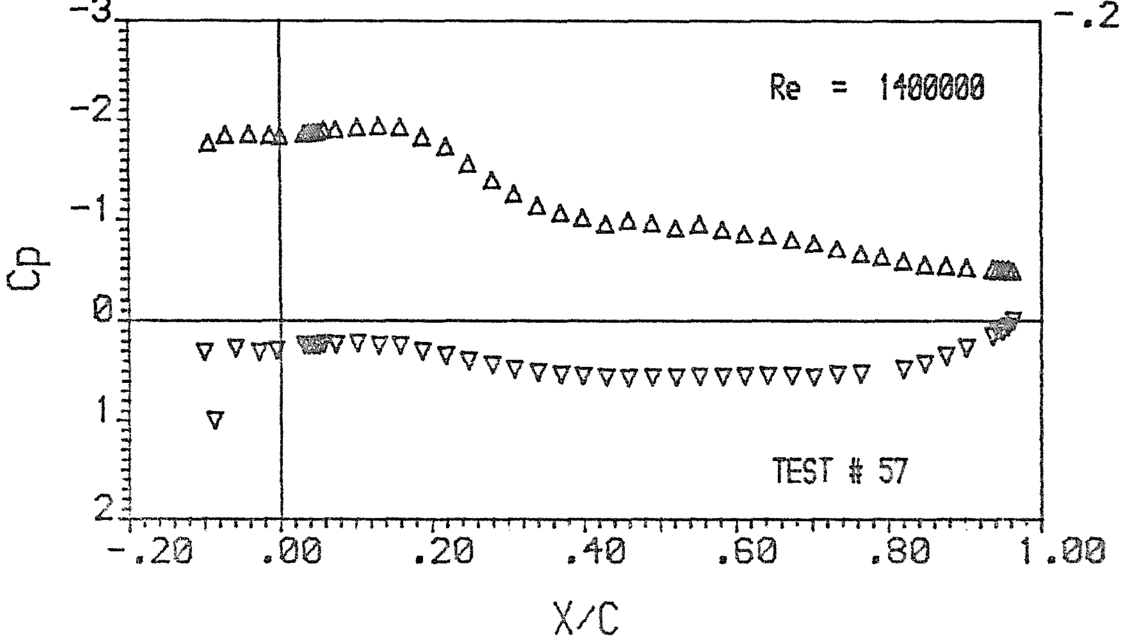

NACA a=0.8

Incidence Angle = 7.50
Mast/Chord Ratio = .102
Mast Angle = 10.00
Camber Ratio = .125

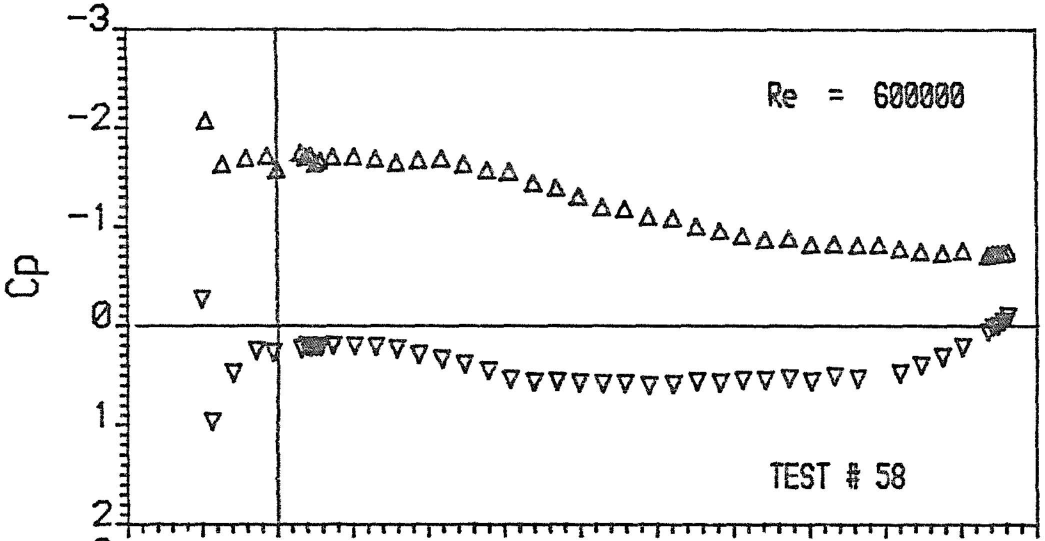

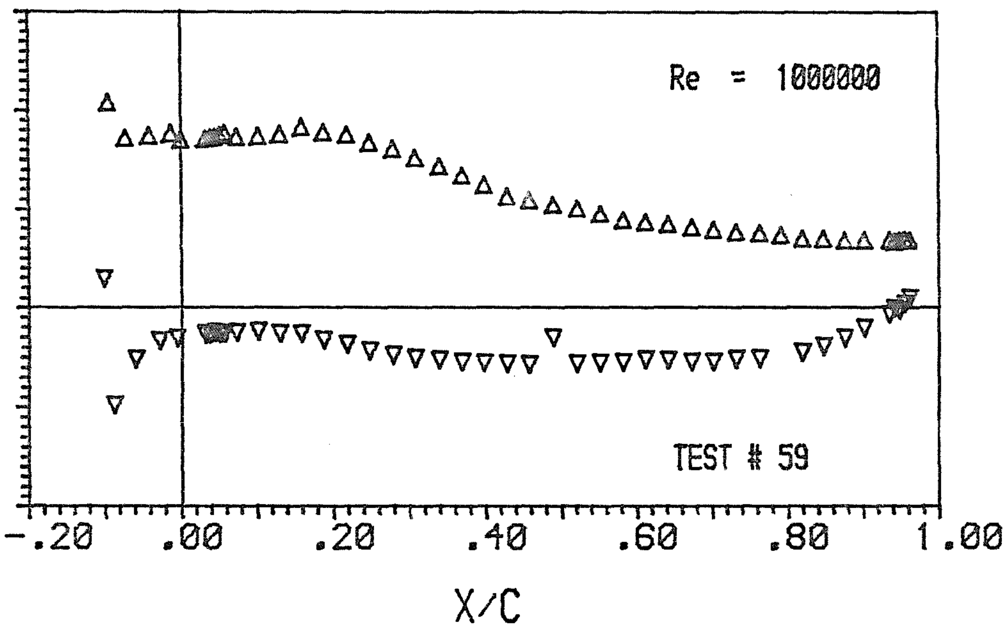

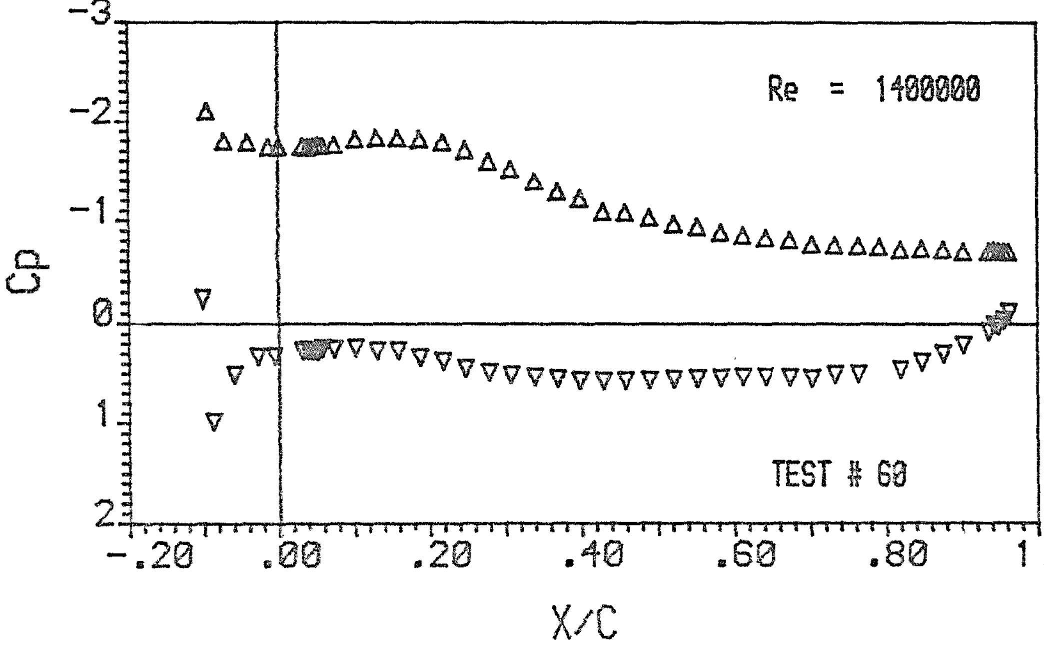

NACA a=0.8

Incidence Angle = 10.00
Mast/Chord Ratio = .102
Mast Angle = 10.00
Camber Ratio = .125

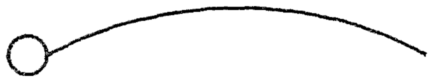

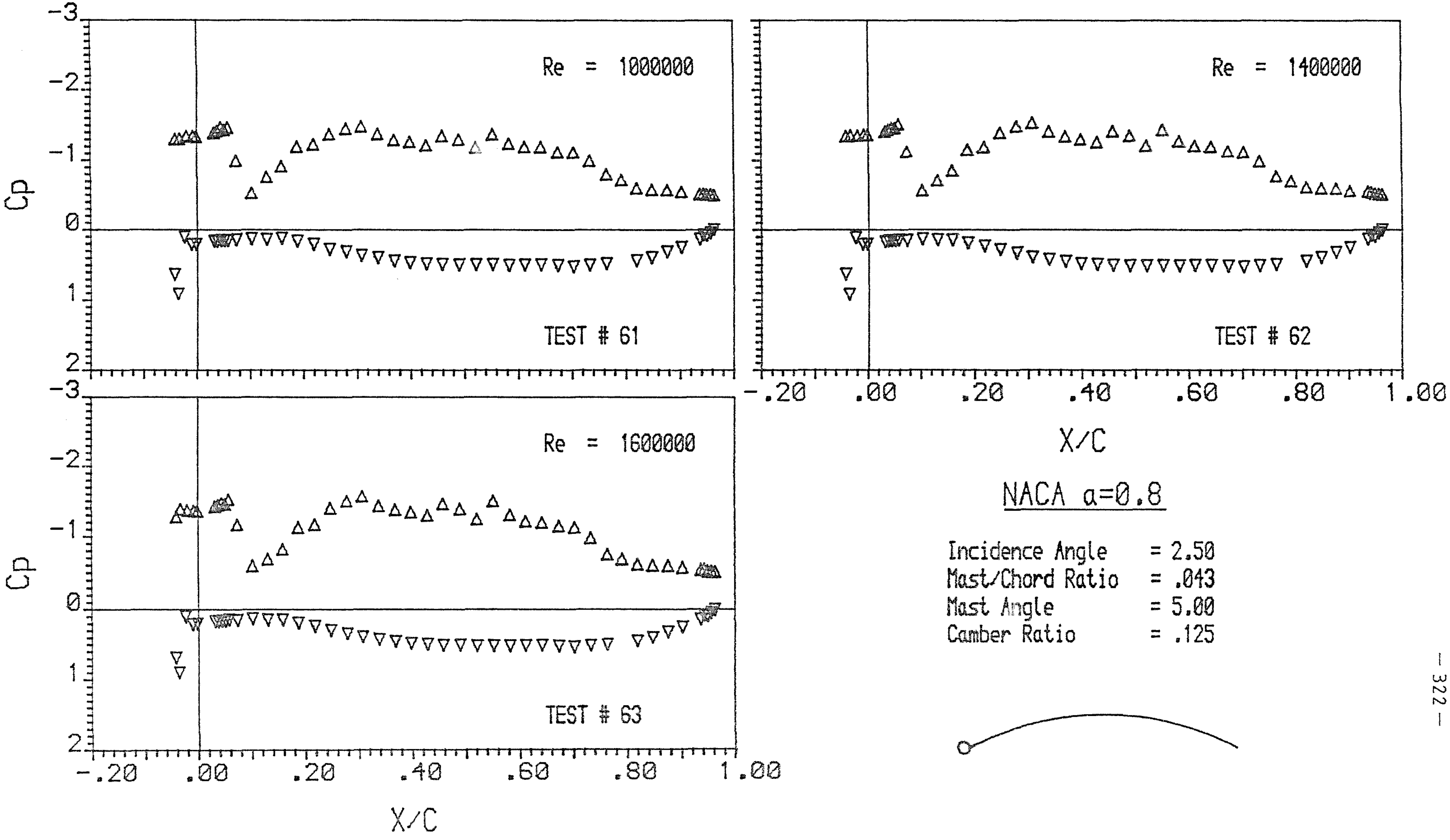

NACA a=0.8

Incidence Angle = 2.50
Mast/Chord Ratio = .043
Mast Angle = 5.00
Camber Ratio = .125

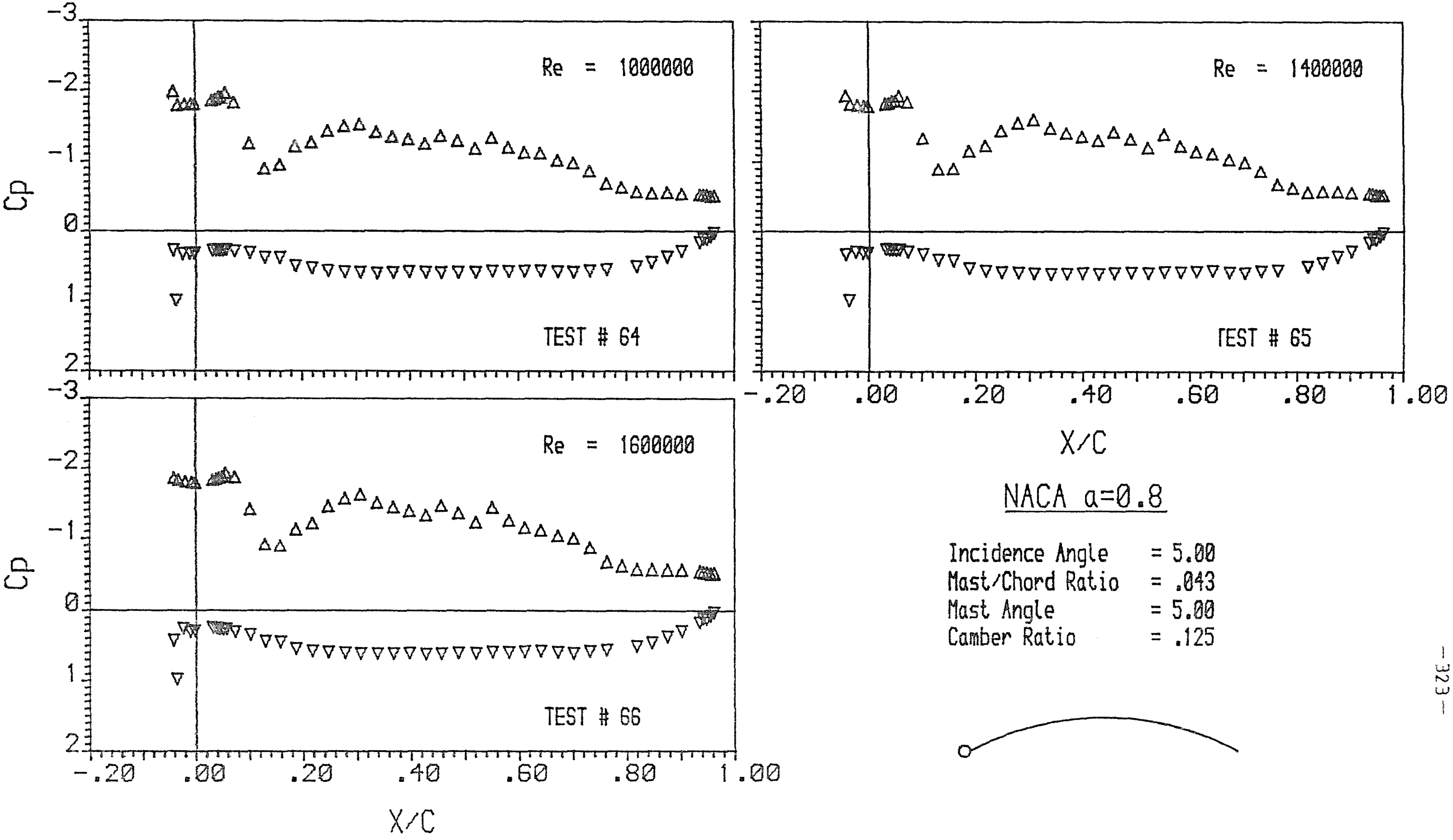

NACA a=0.8

Incidence Angle = 5.00
Mast/Chord Ratio = .043
Mast Angle = 5.00
Camber Ratio = .125

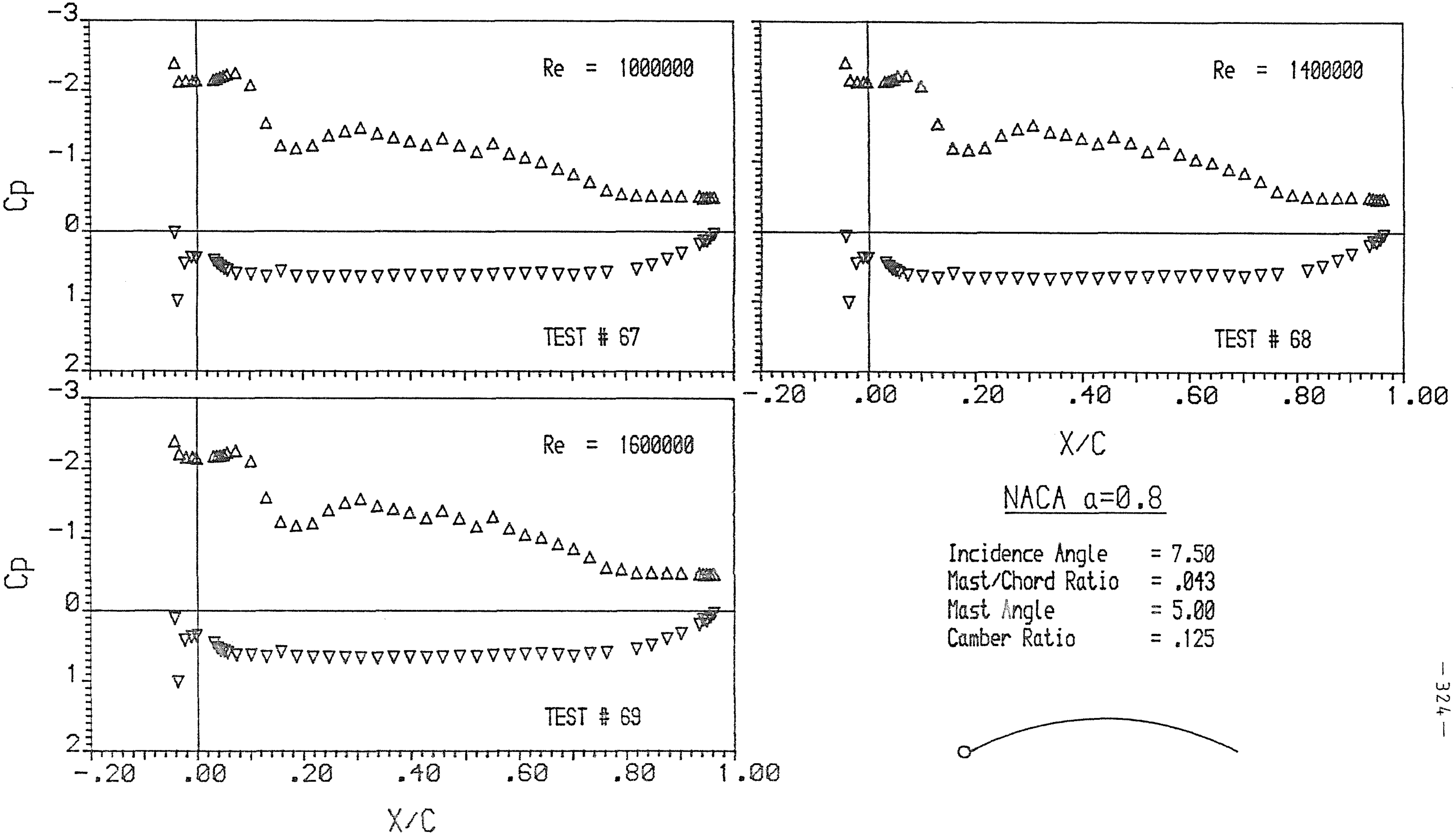

NACA a=0.8

Incidence Angle = 7.50
Mast/Chord Ratio = .043
Mast Angle = 5.00
Camber Ratio = .125

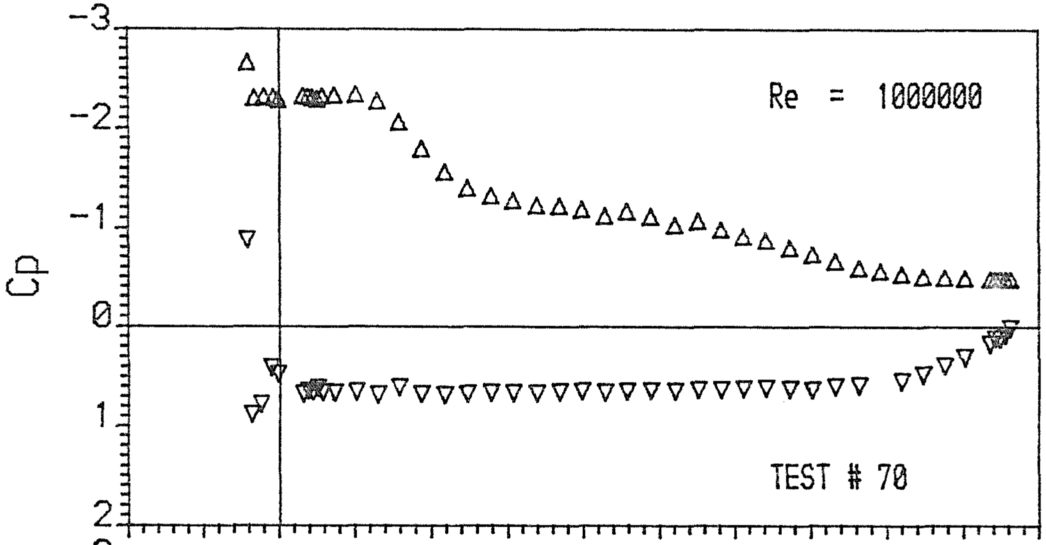

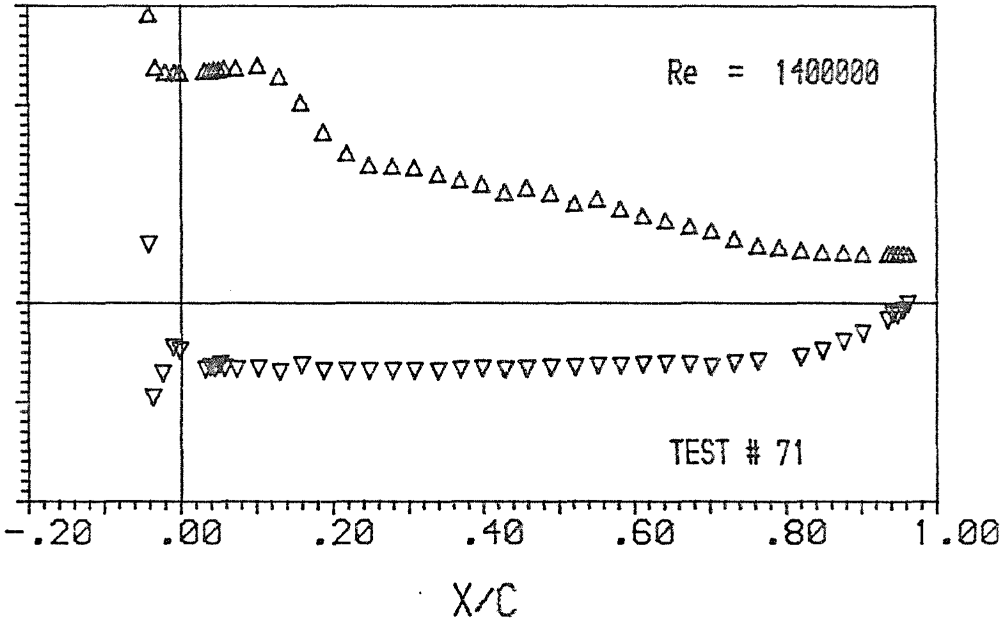

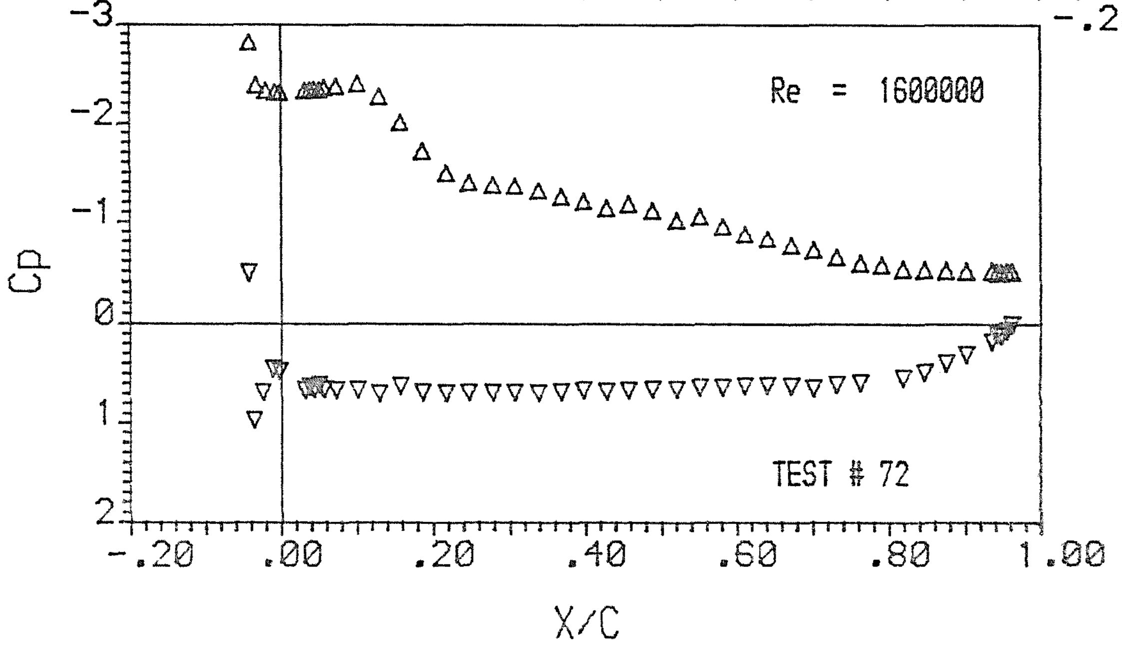

NACA a=0.8

Incidence Angle = 10.00
Mast/Chord Ratio = .043
Mast Angle = 5.00
Camber Ratio = .125

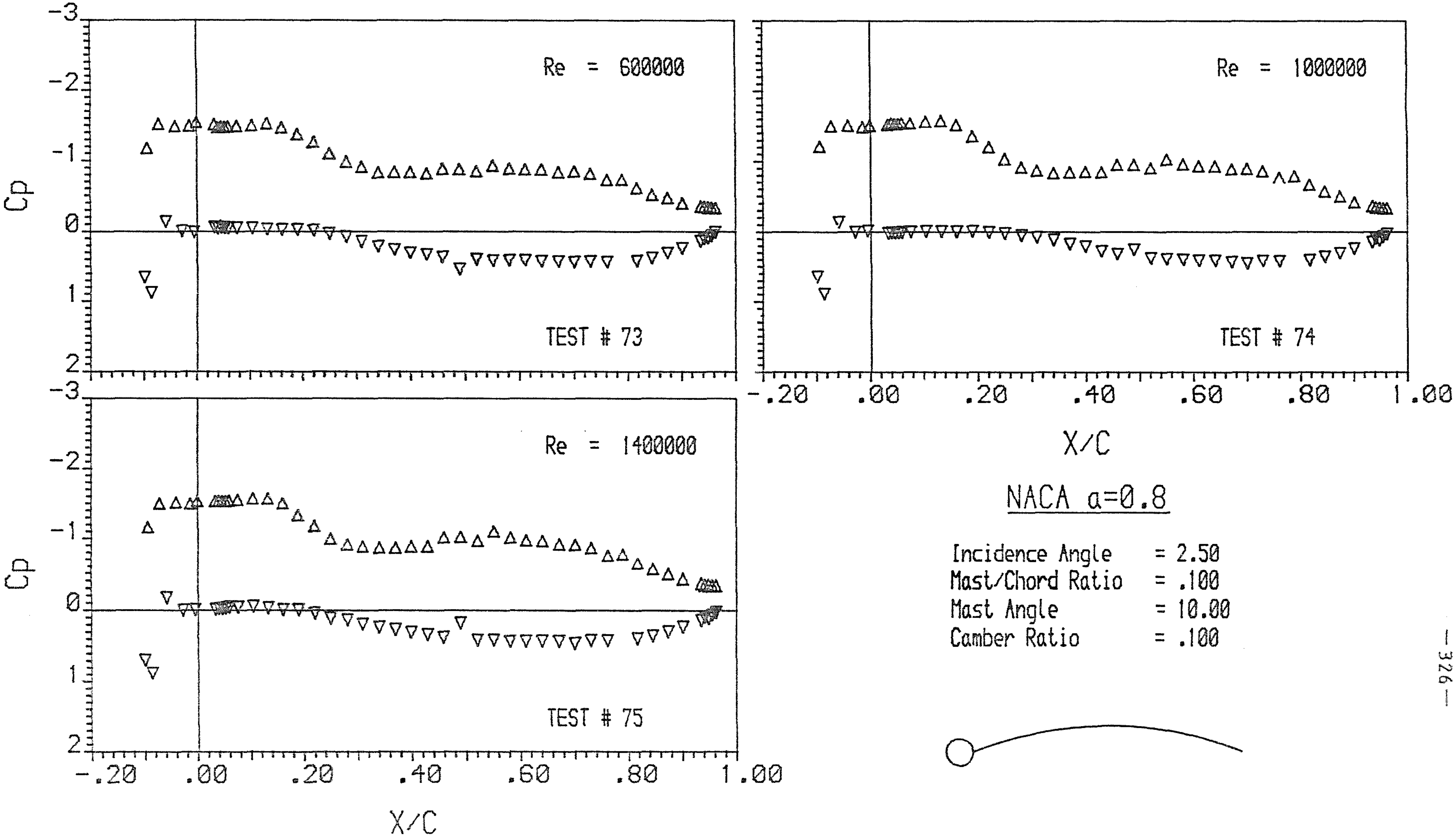

NACA a=0.8

Incidence Angle = 2.50
Mast/Chord Ratio = .100
Mast Angle = 10.00
Camber Ratio = .100

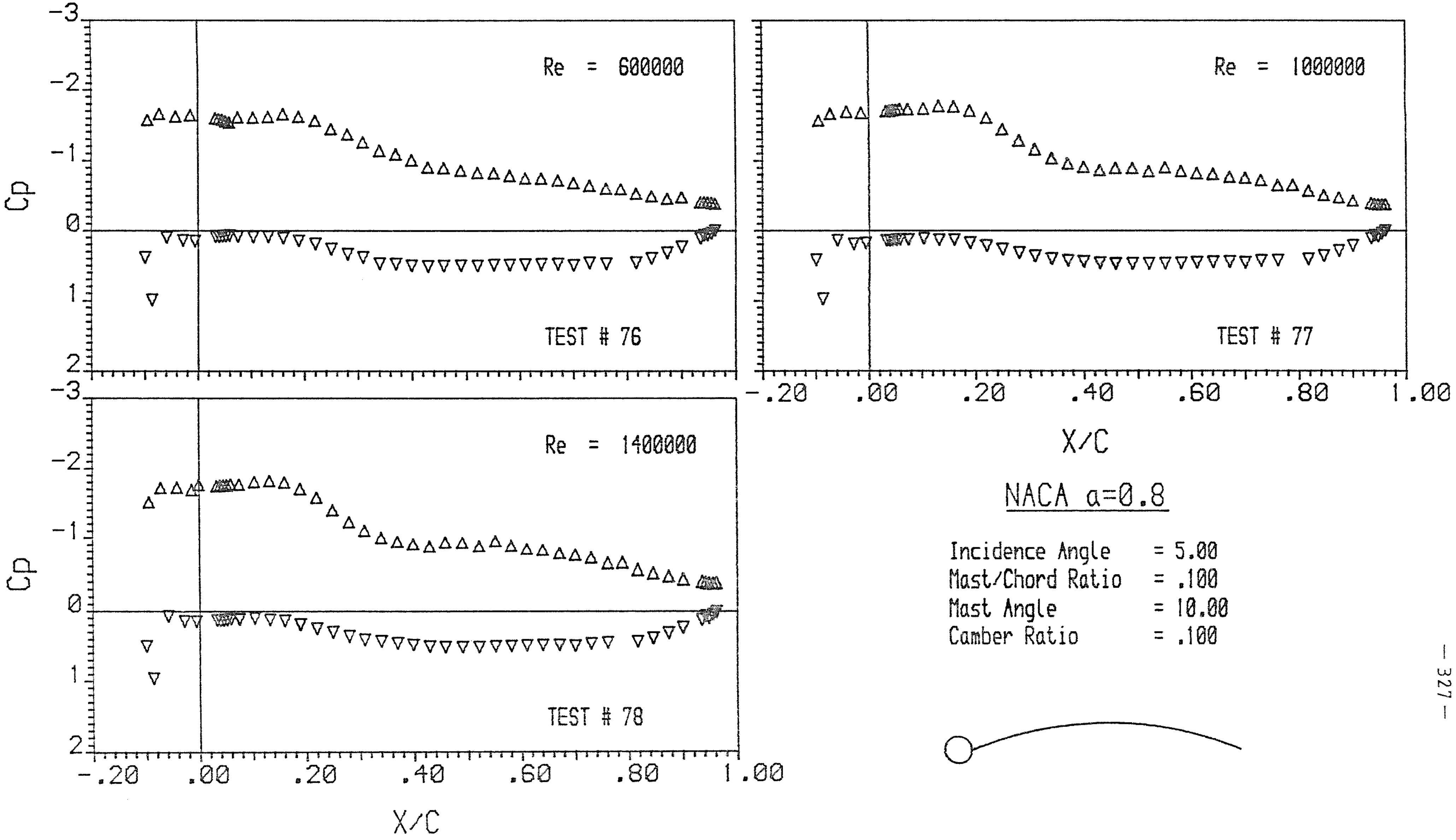

NACA a=0.8

Incidence Angle = 5.00
Mast/Chord Ratio = .100
Mast Angle = 10.00
Camber Ratio = .100

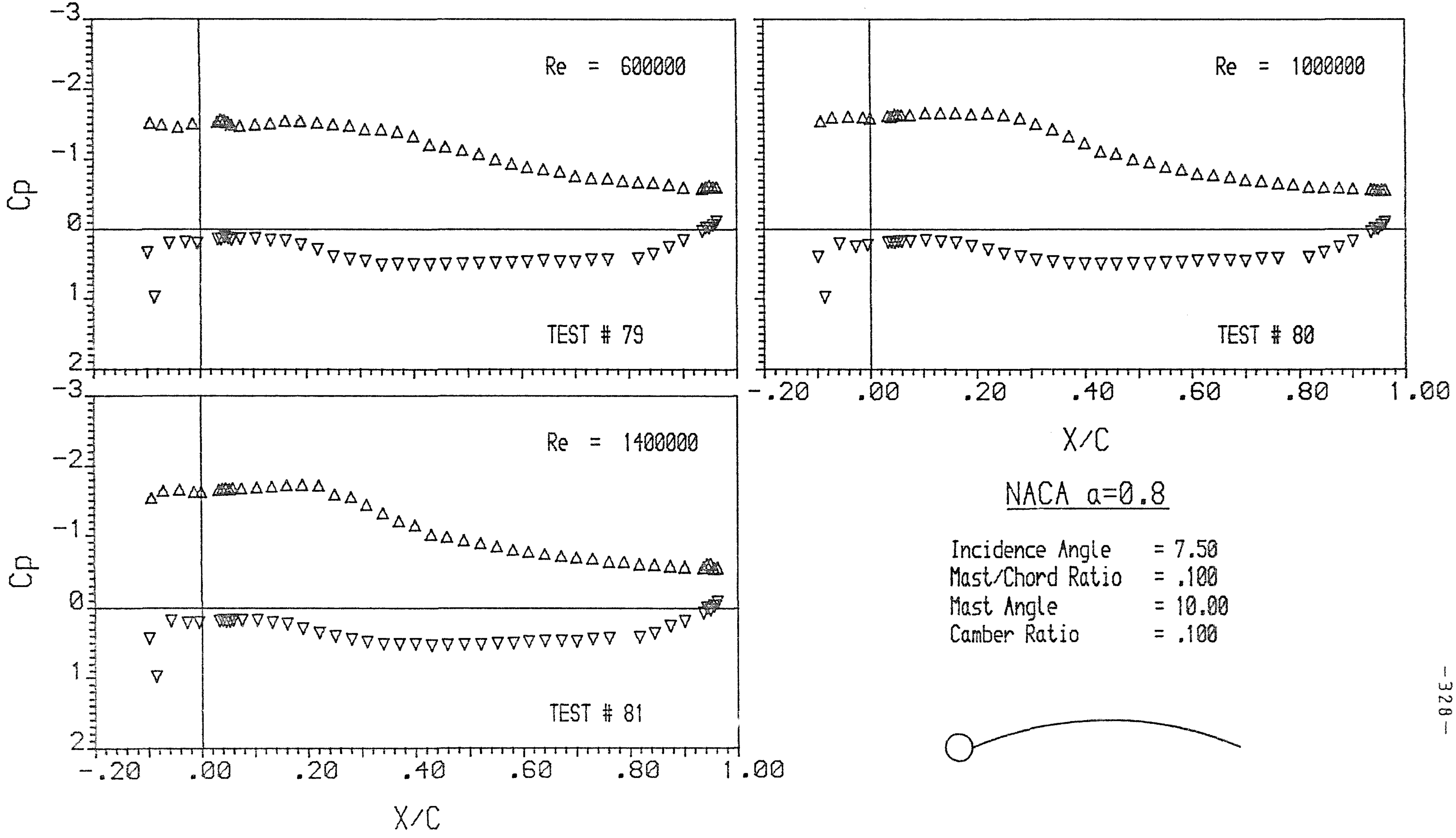

NACA a=0.8

Incidence Angle = 7.50
Mast/Chord Ratio = .100
Mast Angle = 10.00
Camber Ratio = .100

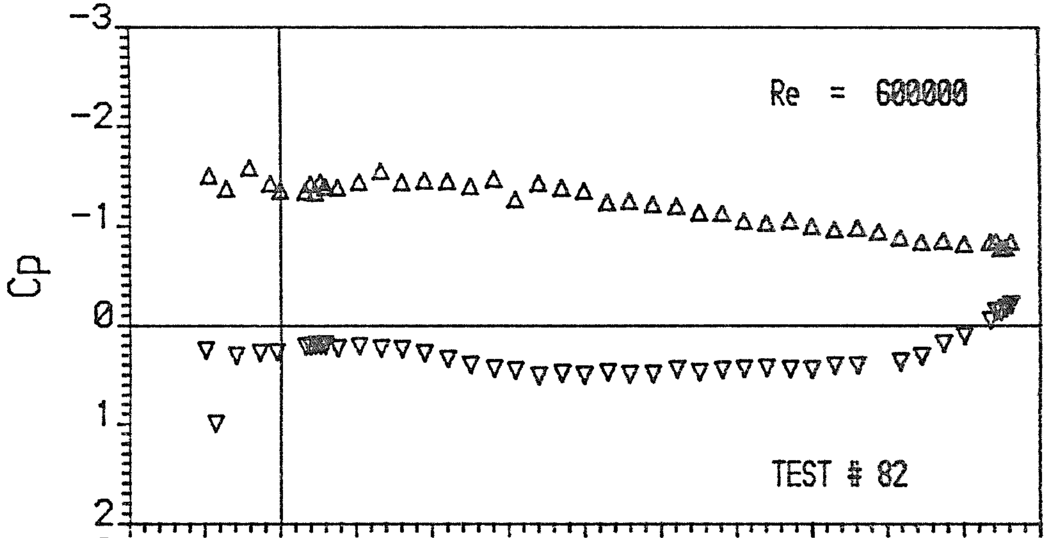

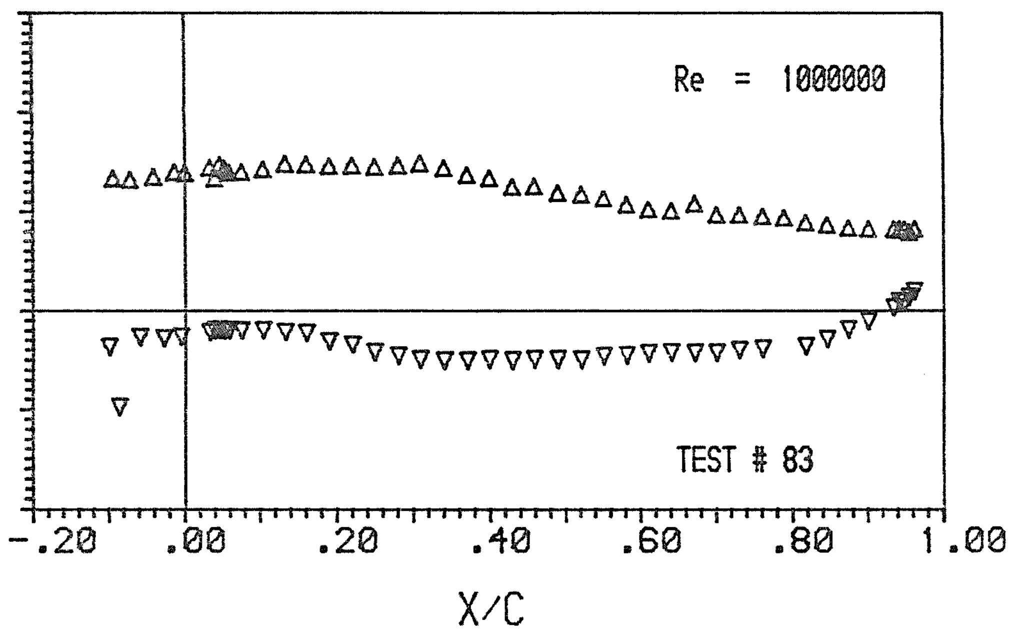

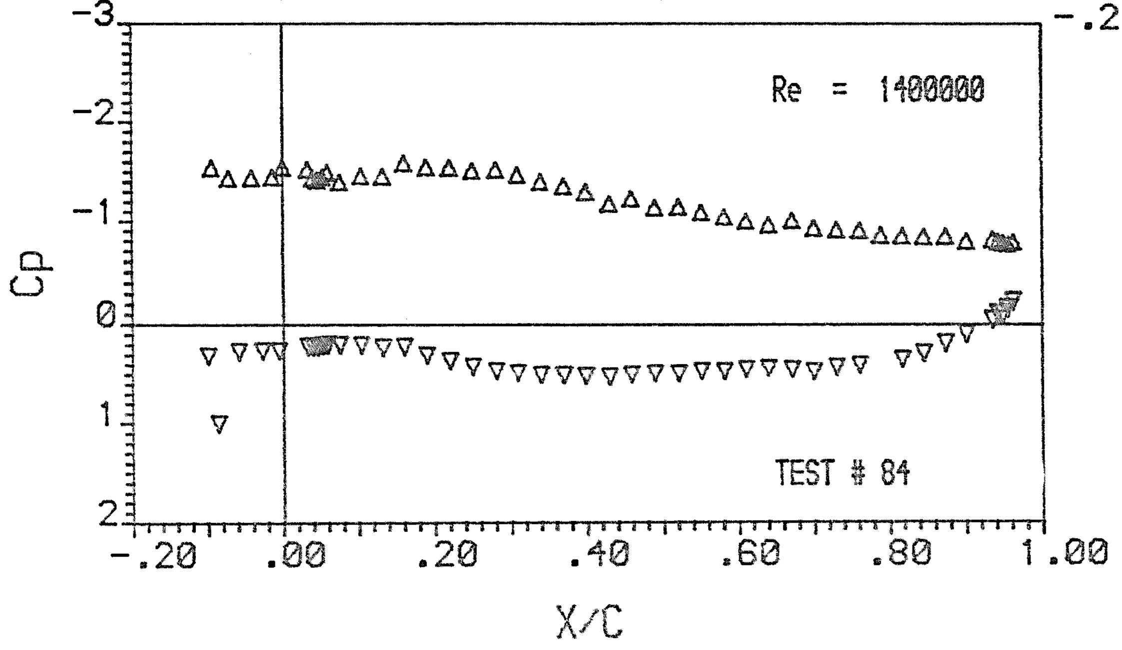

NACA a=0.8

Incidence Angle = 10.00
Mast/Chord Ratio = .100
Mast Angle = 10.00
Camber Ratio = .100

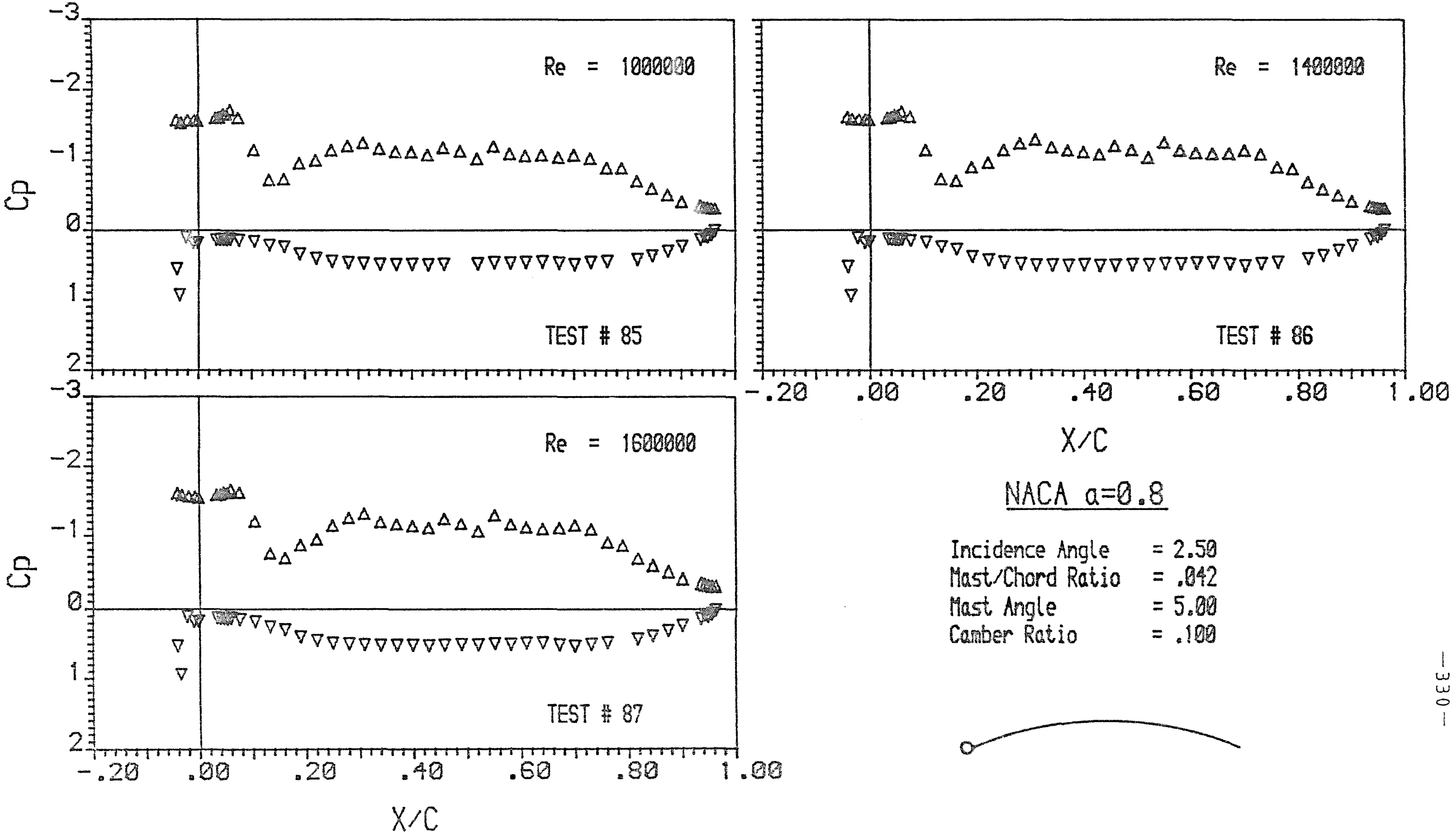

NACA a=0.8

Incidence Angle = 2.50
Mast/Chord Ratio = .042
Mast Angle = 5.00
Camber Ratio = .100

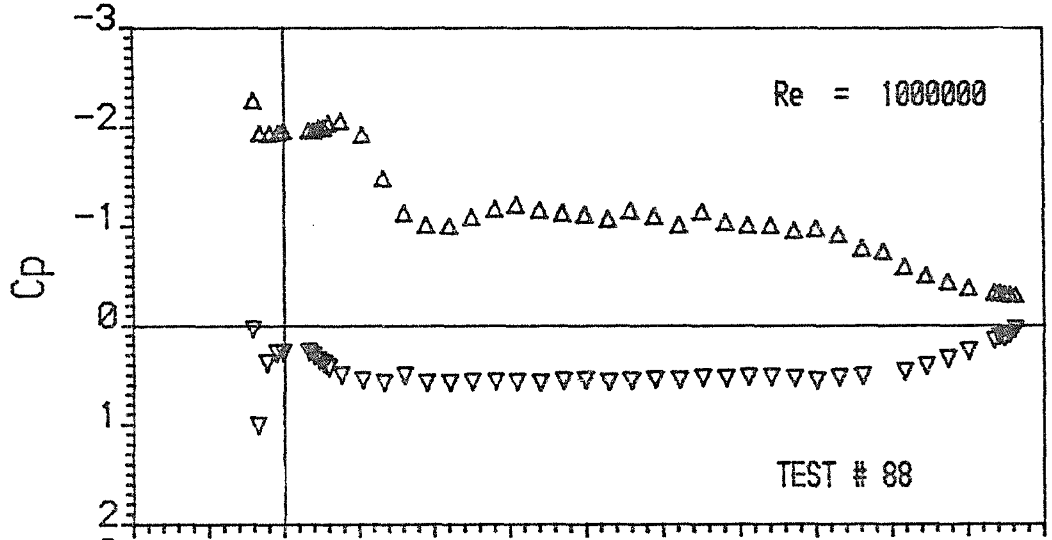

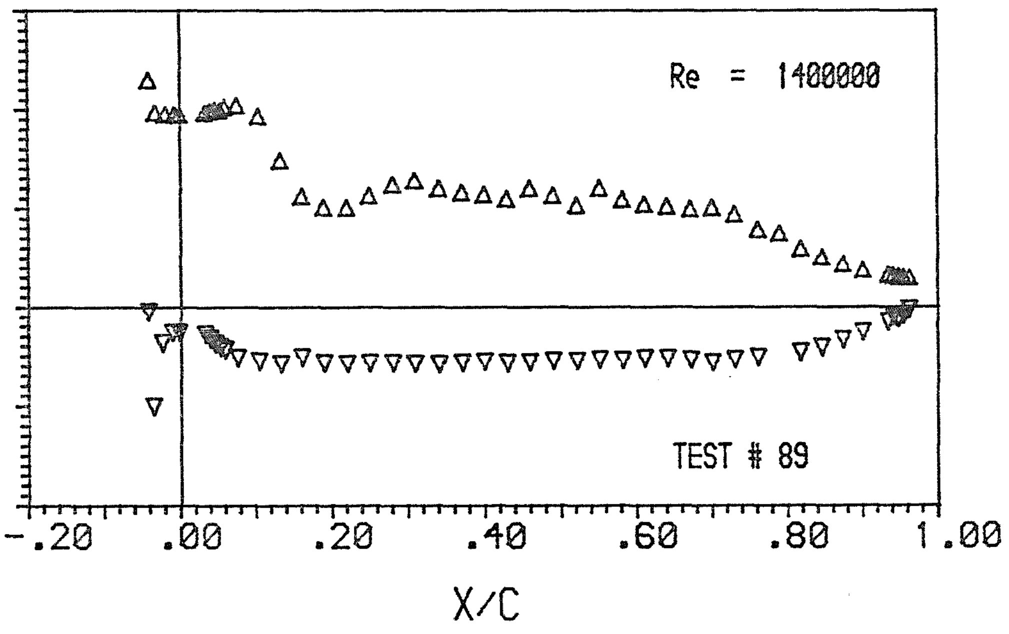

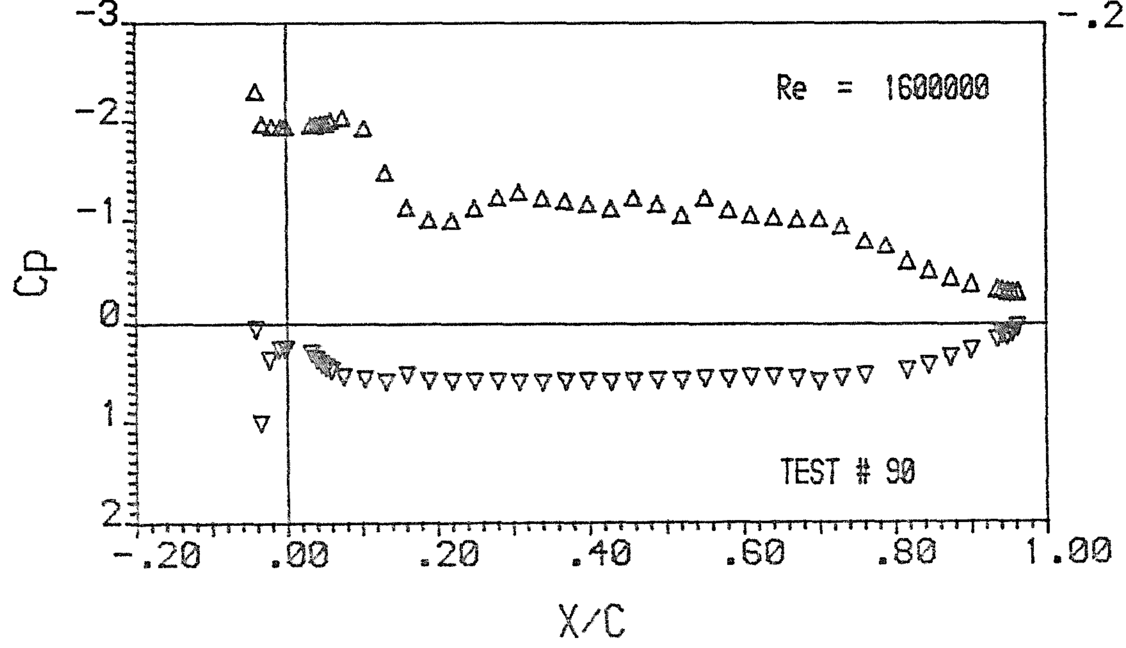

NACA a=0.8

Incidence Angle = 5.00
Mast/Chord Ratio = .042
Mast Angle = 5.00
Camber Ratio = .100

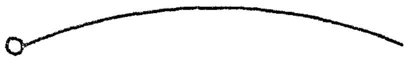

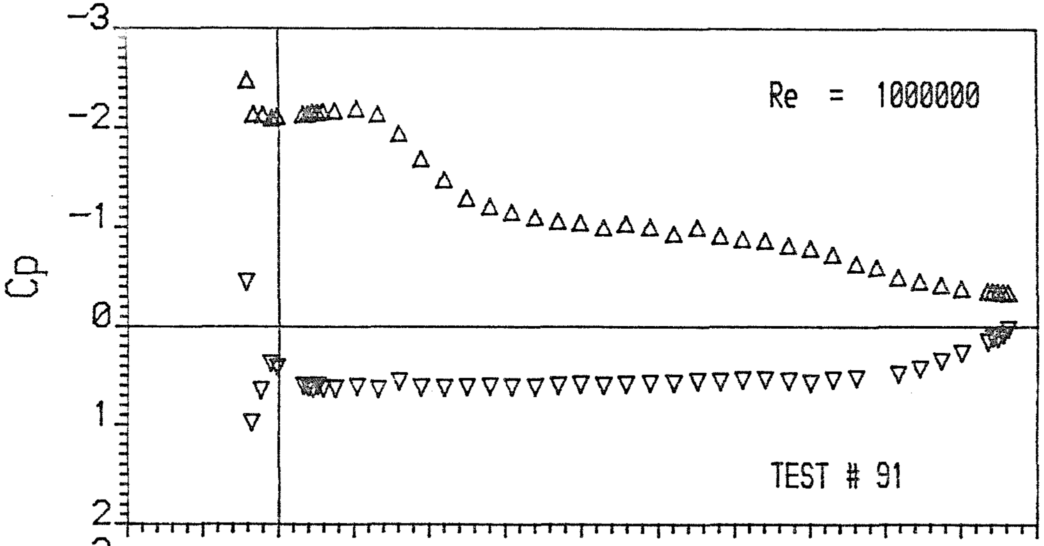

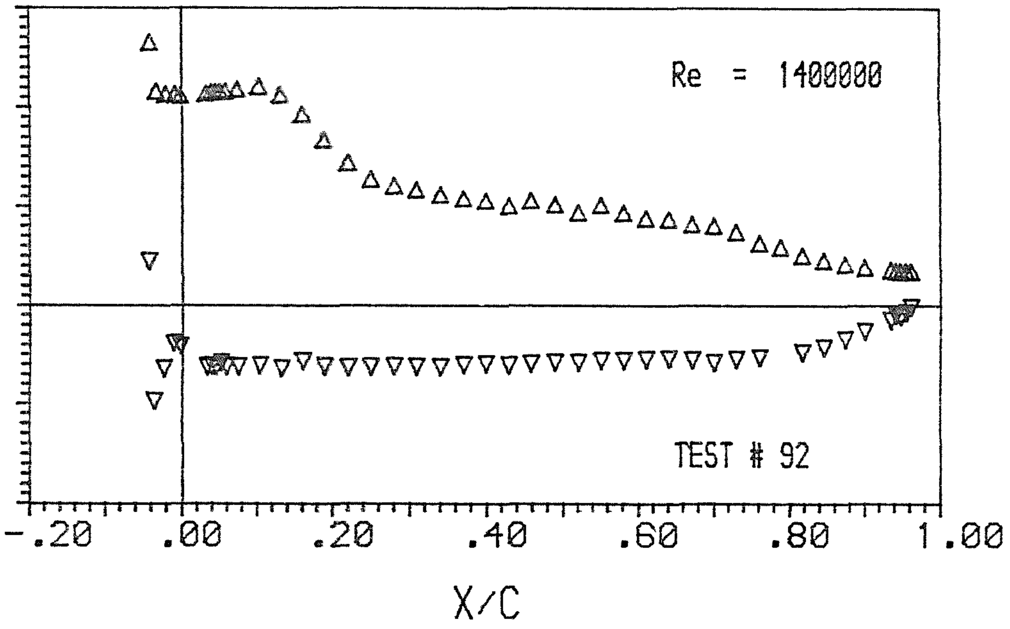

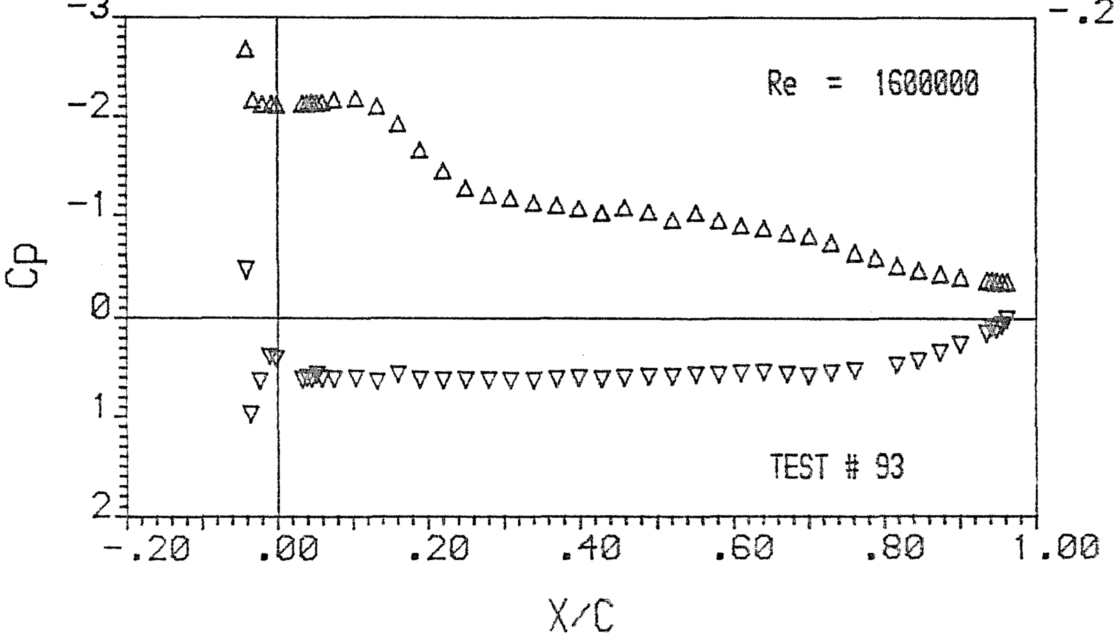

NACA a=0.8

Incidence Angle = 7.50
Mast/Chord Ratio = .042
Mast Angle = 5.00
Camber Ratio = .100

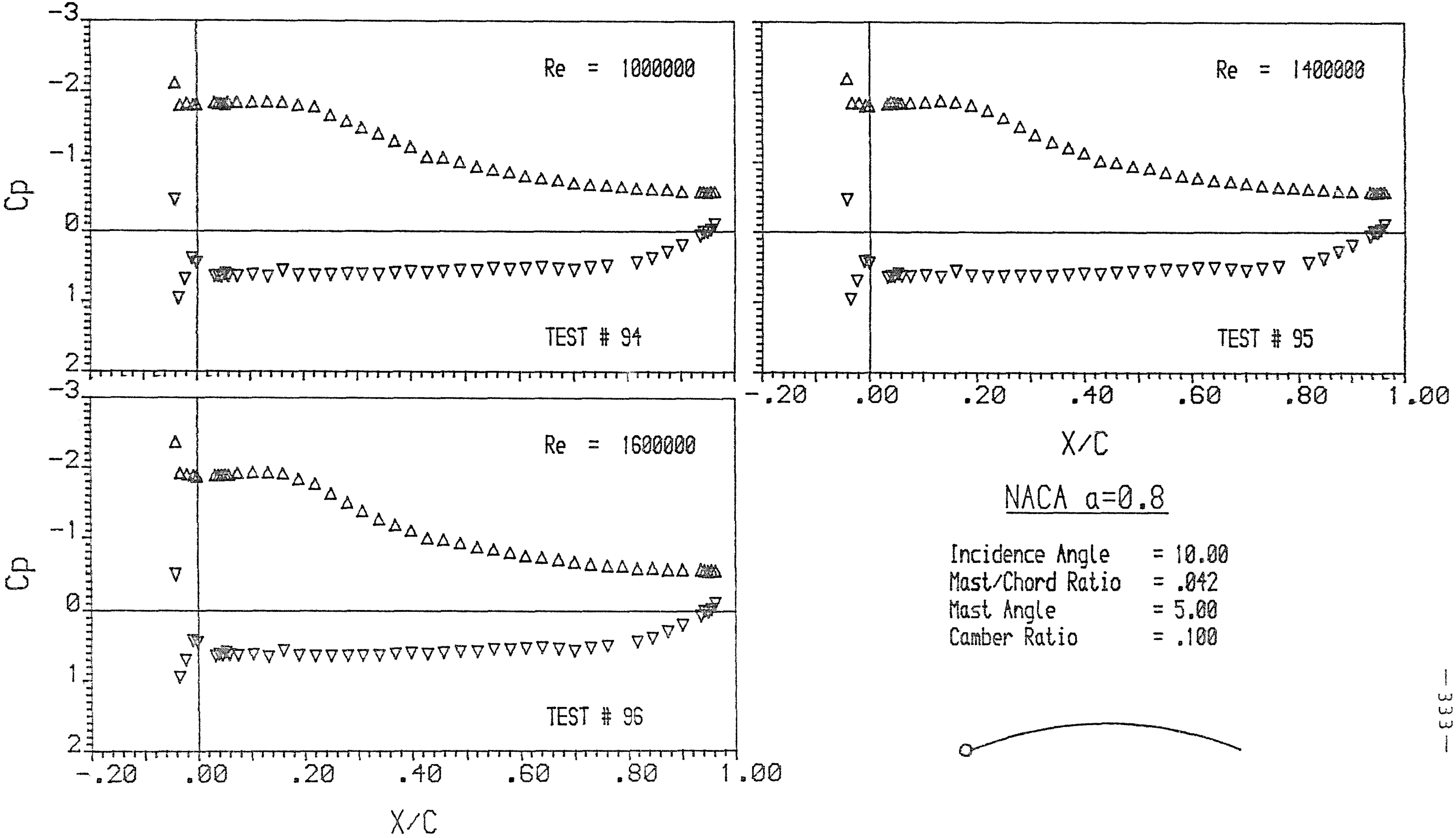

NACA a=0.8

Incidence Angle = 10.00
Mast/Chord Ratio = .042
Mast Angle = 5.00
Camber Ratio = .100

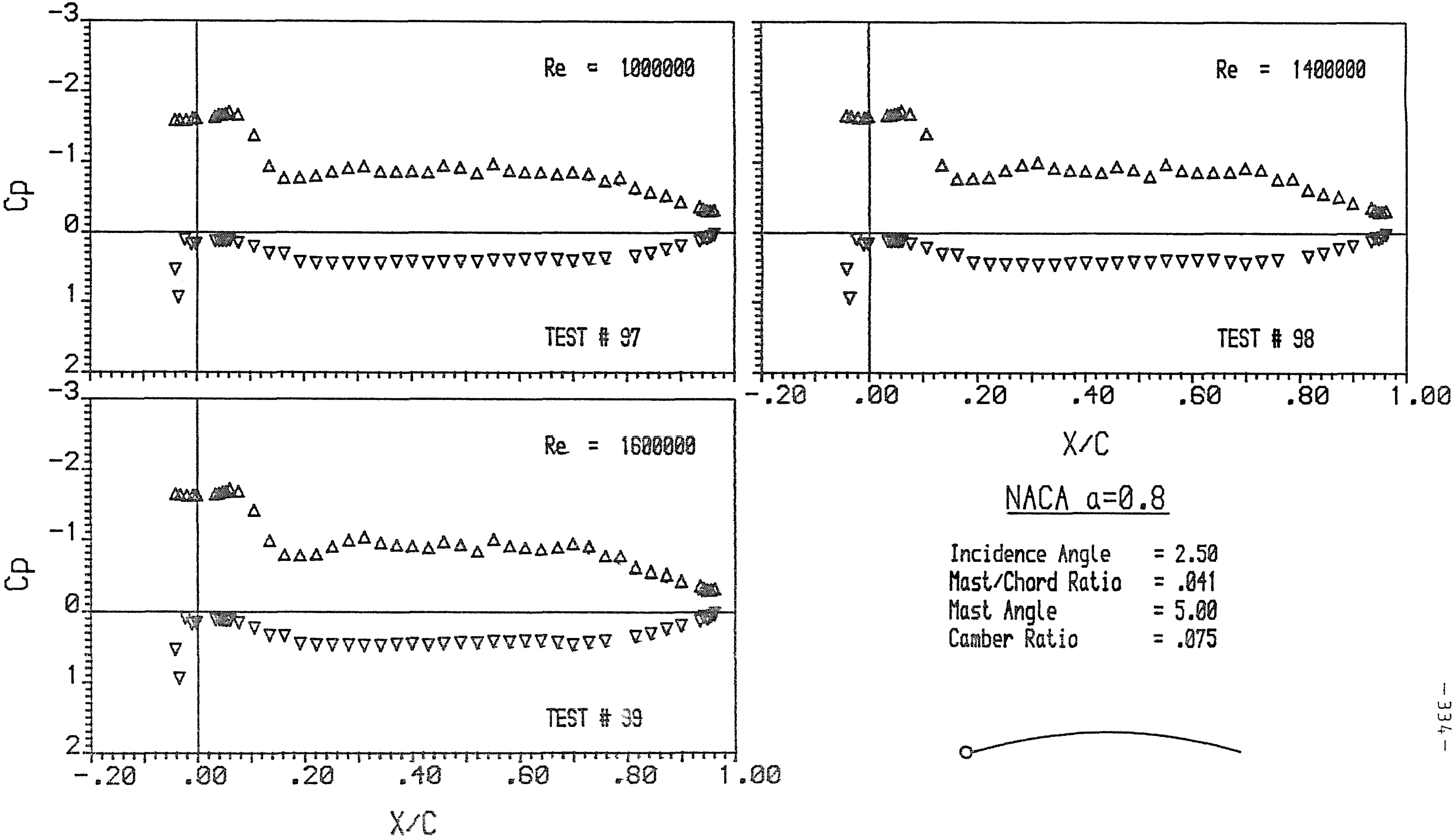

NACA a=0.8

Incidence Angle = 2.50
Mast/Chord Ratio = .041
Mast Angle = 5.00
Camber Ratio = .075

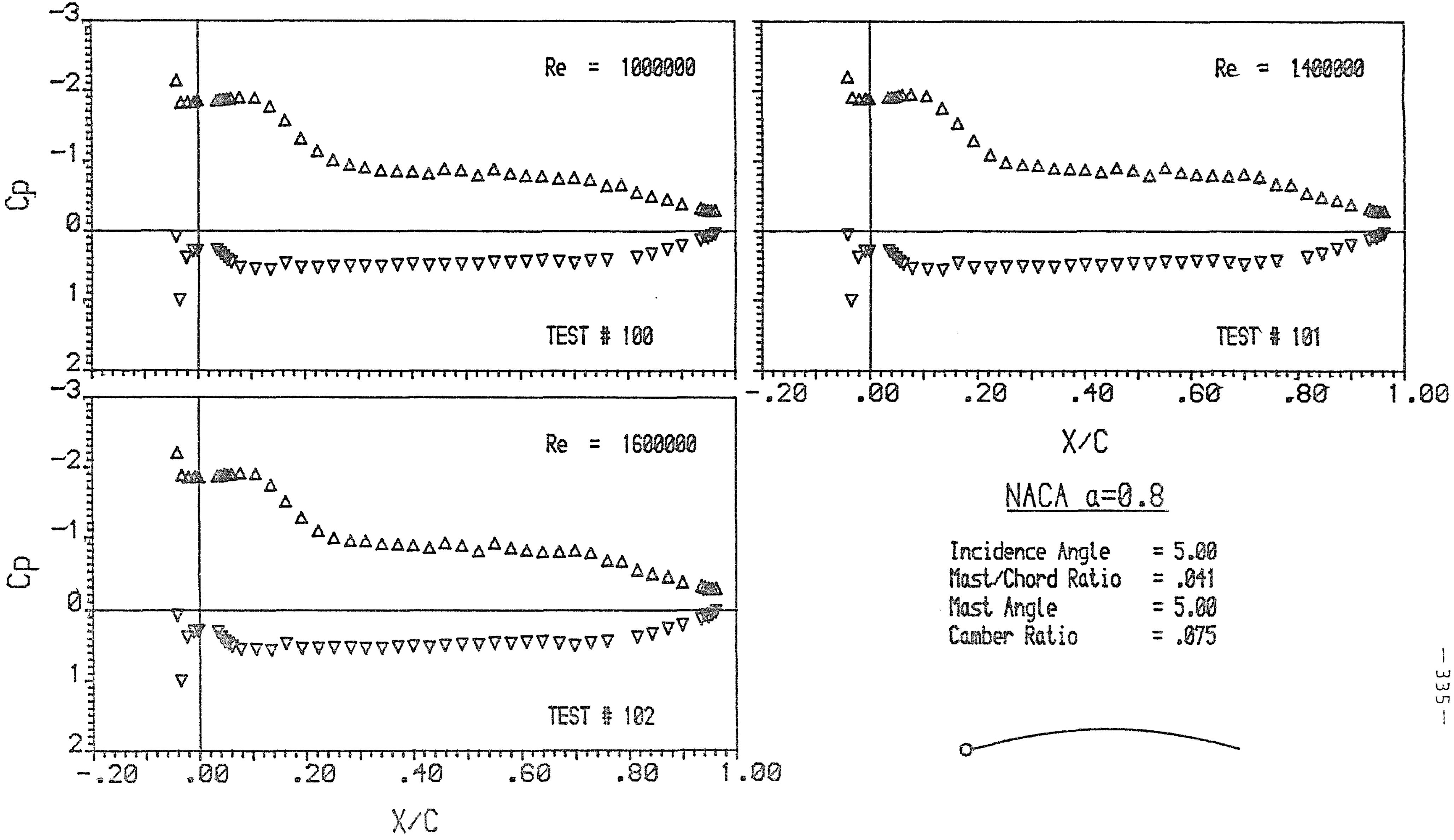

NACA a=0.8

Incidence Angle = 5.00
Mast/Chord Ratio = .041
Mast Angle = 5.00
Camber Ratio = .075

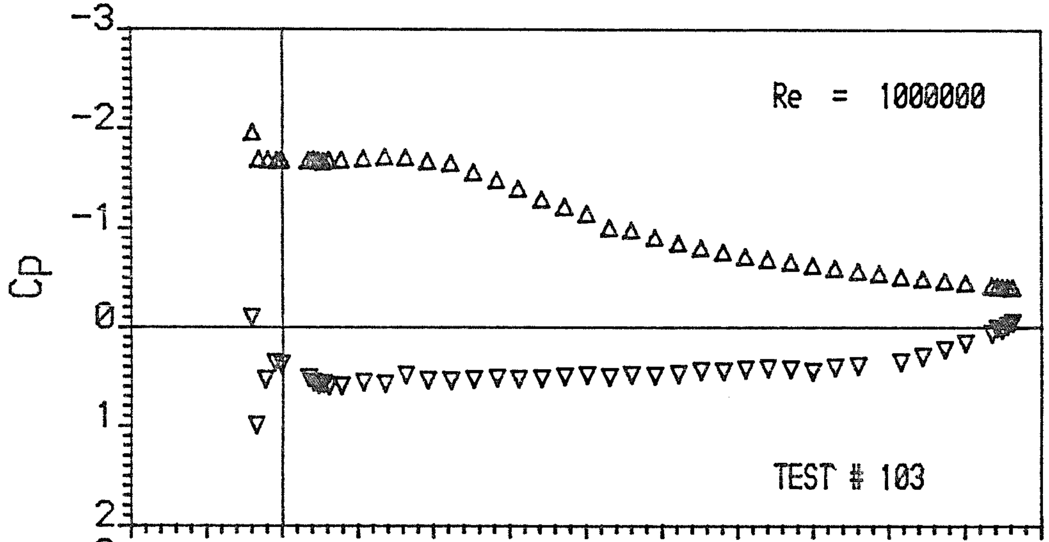

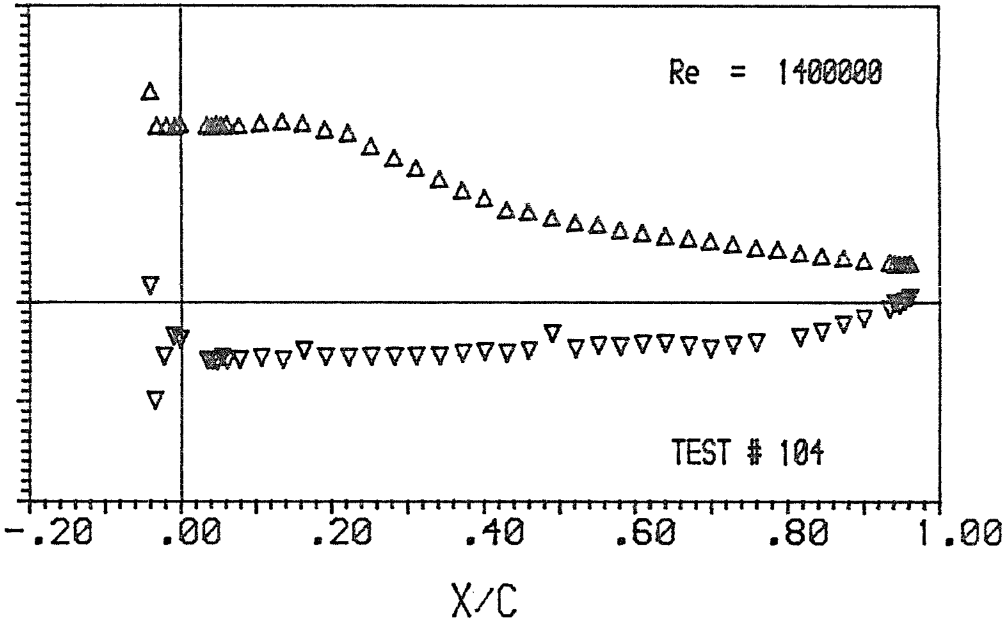

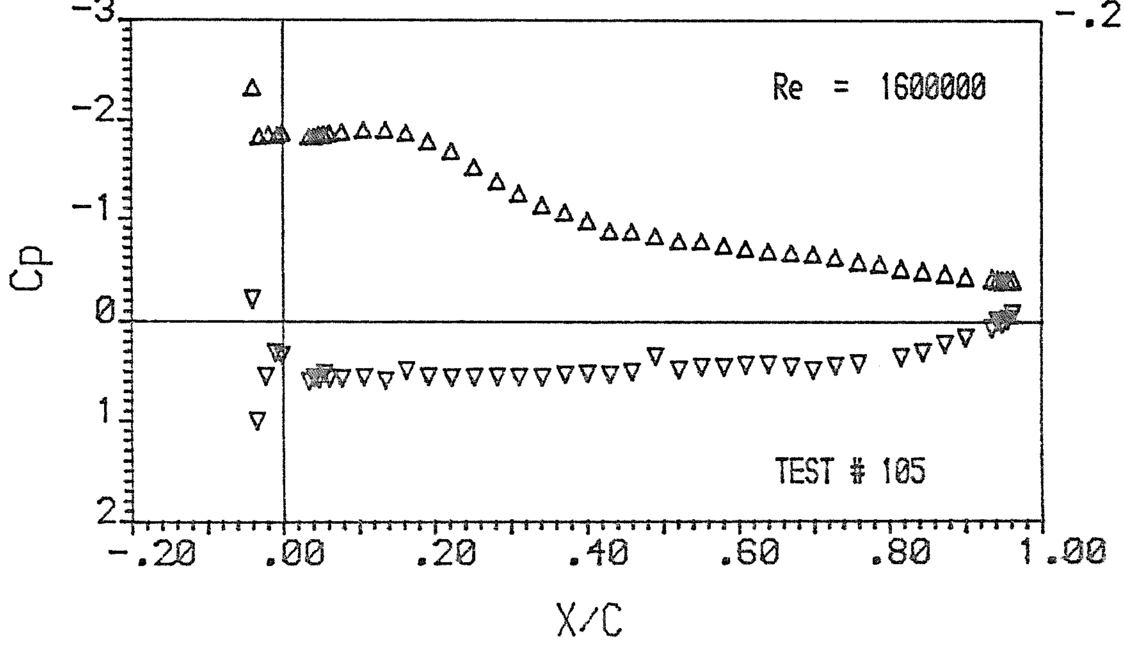

NACA a=0.8

Incidence Angle = 7.50
Mast/Chord Ratio = .041
Mast Angle = 5.00
Camber Ratio = .075

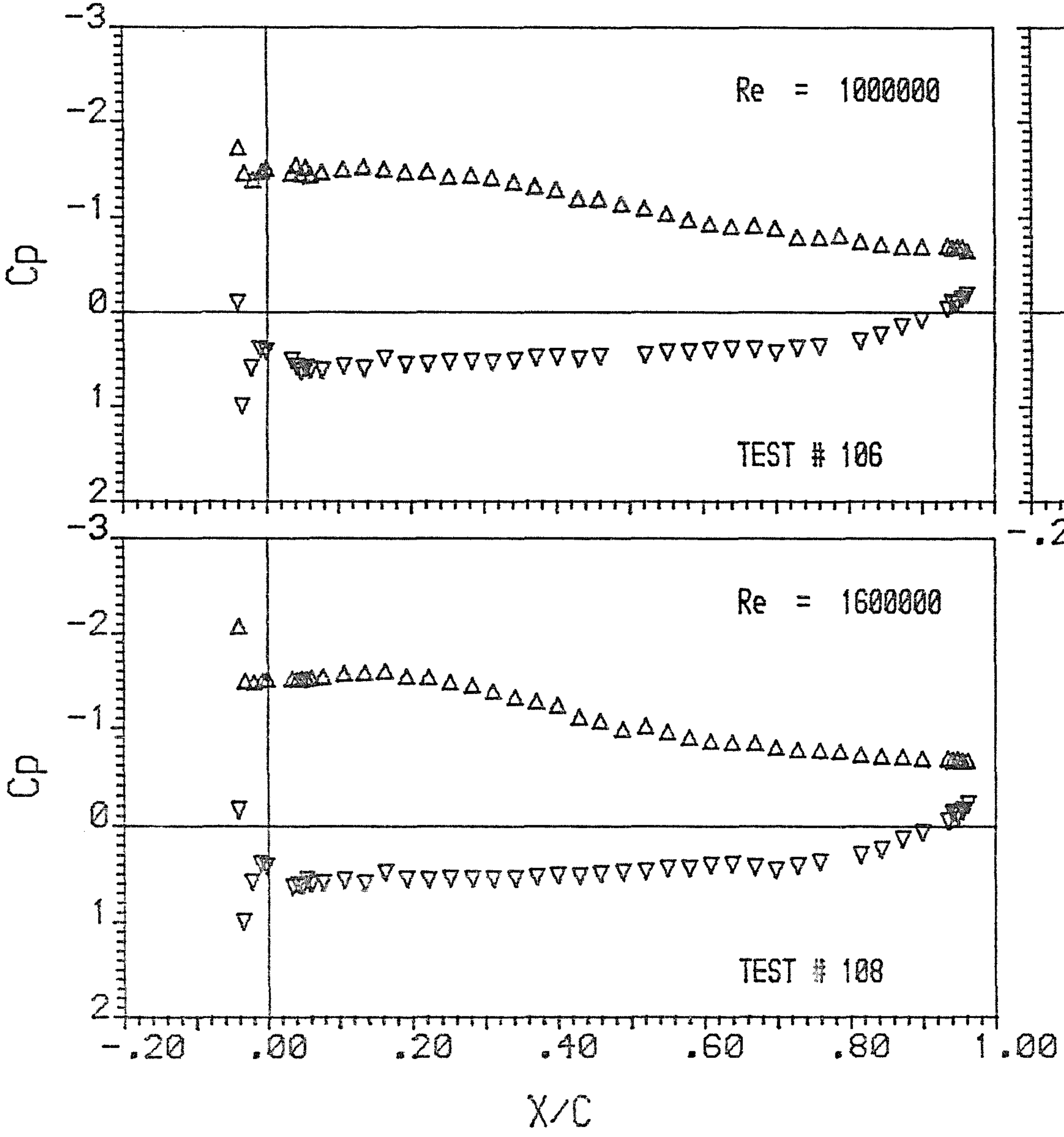

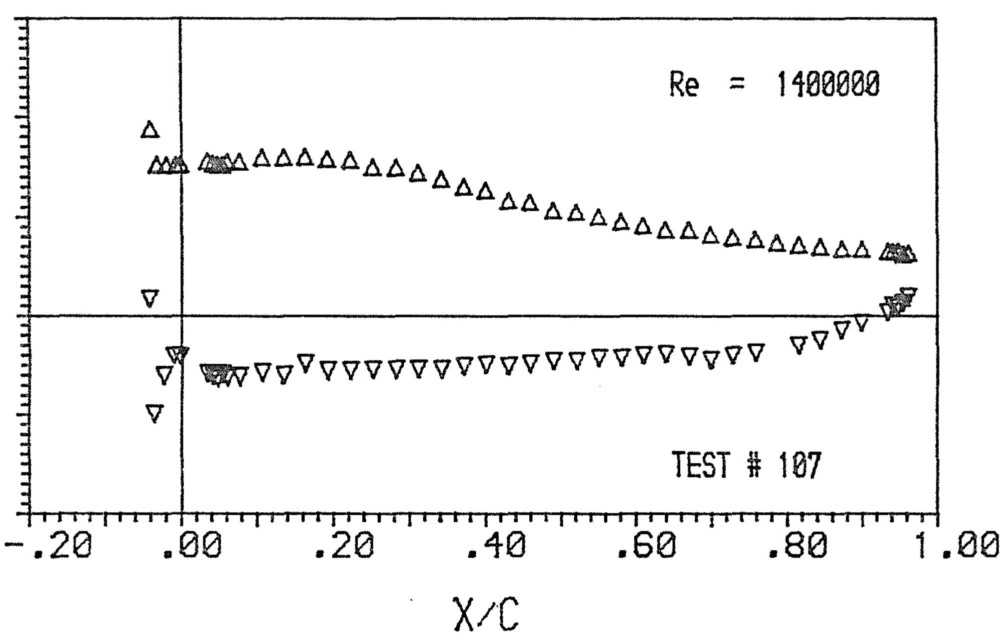

NACA a=0.8

Incidence Angle = 10.00
Mast/Chord Ratio = .041
Mast Angle = 5.00
Camber Ratio = .075

APPENDIX III

NACA 63 STATIC PRESSURE DISTRIBUTION RESULTS

NACA 63

CR (%)	d/c (%)	α (deg)	Re x 10^5	Test #
10.0	10 (10.1)	2.5	6	109
			10	110
			14	111
		5.0	6	112
			10	113
			14	114
		7.5	6	115
			10	116
			14	117
		10.0	6	118
			10	119
			14	120
	4 (4.20)	2.5	10	121
			14	122
			16	123
		5.0	10	124
			14	125
			16	126
		7.5	10	127
			14	128
			16	129
		10.0	10	130
			14	131
			16	132

NACA 63

CR (%)	d/c (%)	α (deg)	Re x 10^5	Test #
12.5	17 (16.52)	2.5	3.5	133
			6	134
			10	135
		5.0	3.5	136
			6	137
			10	138
		7.5	3.5	139
			6	140
			10	141
		10.0	3.5	142
			6	143
			10	144
	10 (10.17)	2.5	6	145
			10	146
			14	147
		5.0	6	148
			10	149
			14	150
		7.5	6	151
			10	152
			14	153
		10.0	6	154
			10	155
			14	156
	4 (4.26)	2.5	10	157
			14	158
			16	159
		5.0	10	160
			14	161
			16	162
		7.5	10	163
			14	164
			16	165
		10.0	10	166
			14	167
			16	168

NACA 63

CR (%)	d/c (%)	α (deg)	Re x 10^5	Test #
15.0	17 (16.82)	2.5	3.5	169
			6	170
			10	171
		5.0	3.5	172
			6	173
			10	174
		7.5	3.5	175
			6	176
			10	177
		10.0	3.5	178
			6	179
			10	180
	10 (10.35)	2.5	6	181
			10	182
			14	183
		5.0	6	184
			10	185
			14	186
		7.5	6	187
			10	188
			14	189
		10.0	6	190
			10	191
			14	192

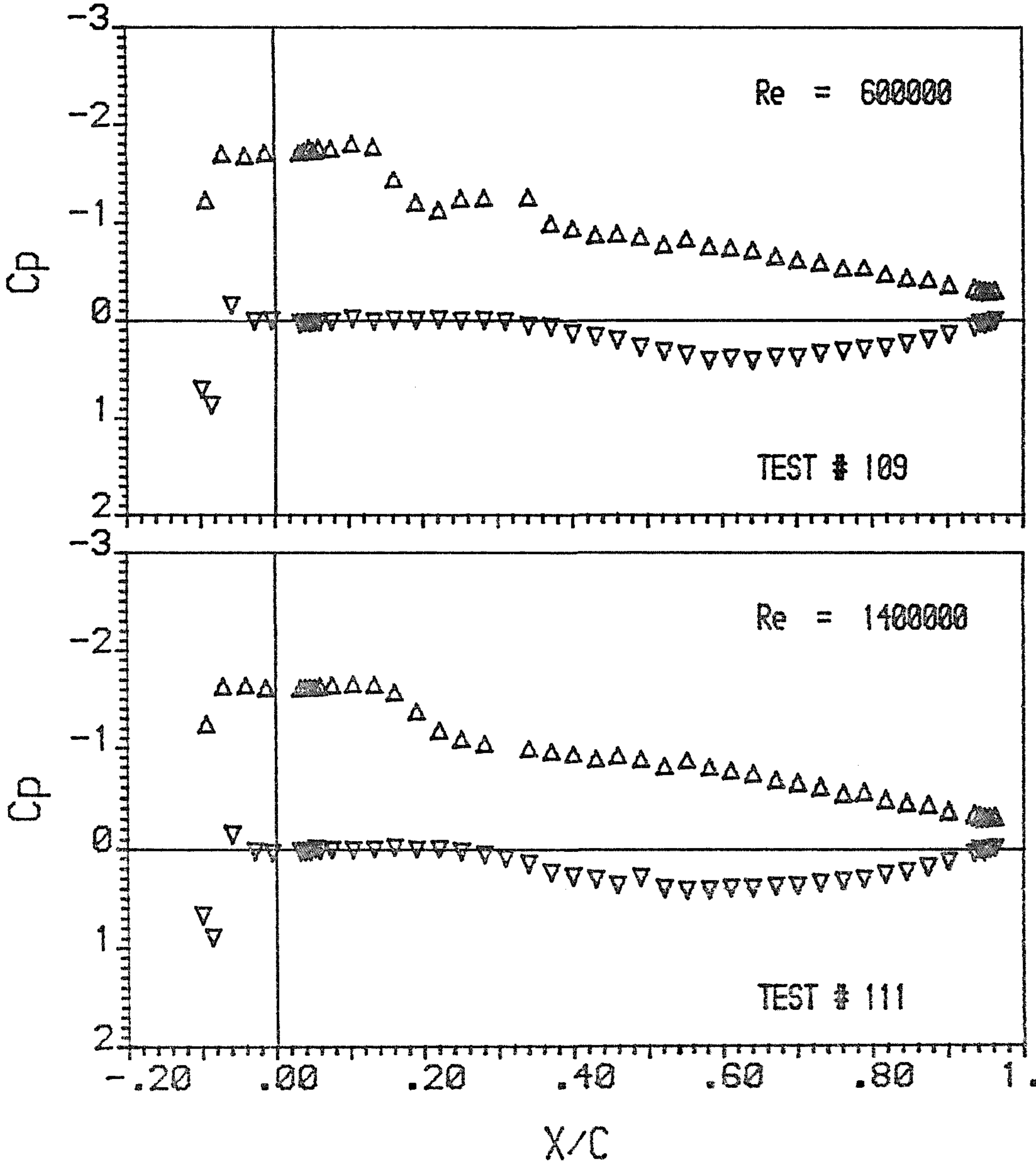
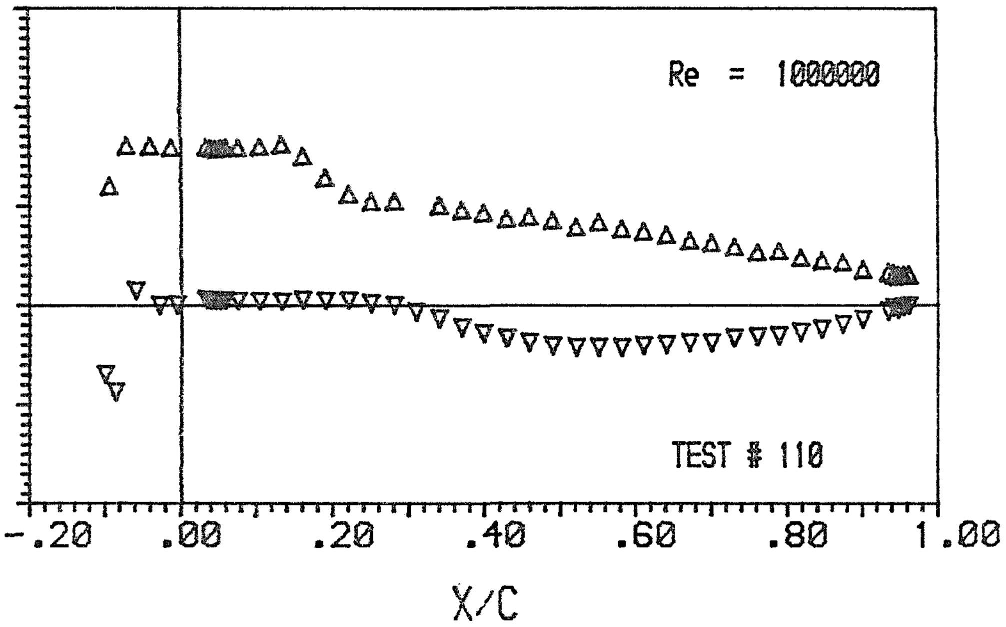

NACA 63

Incidence Angle = 2.50
Mast/Chord Ratio = .100
Mast Angle = 10.00
Camber Ratio = .100

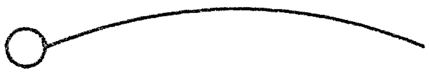

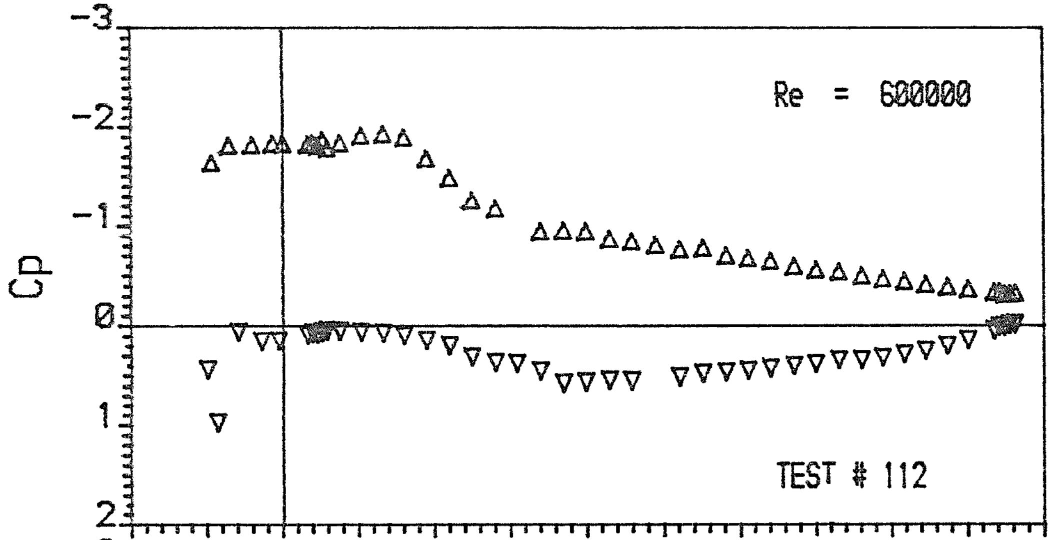

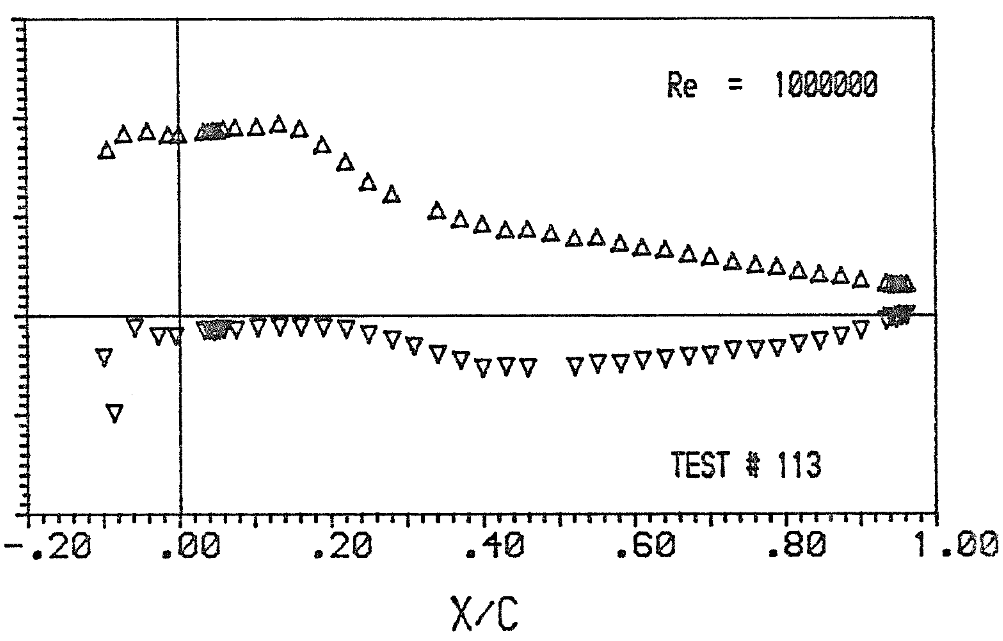

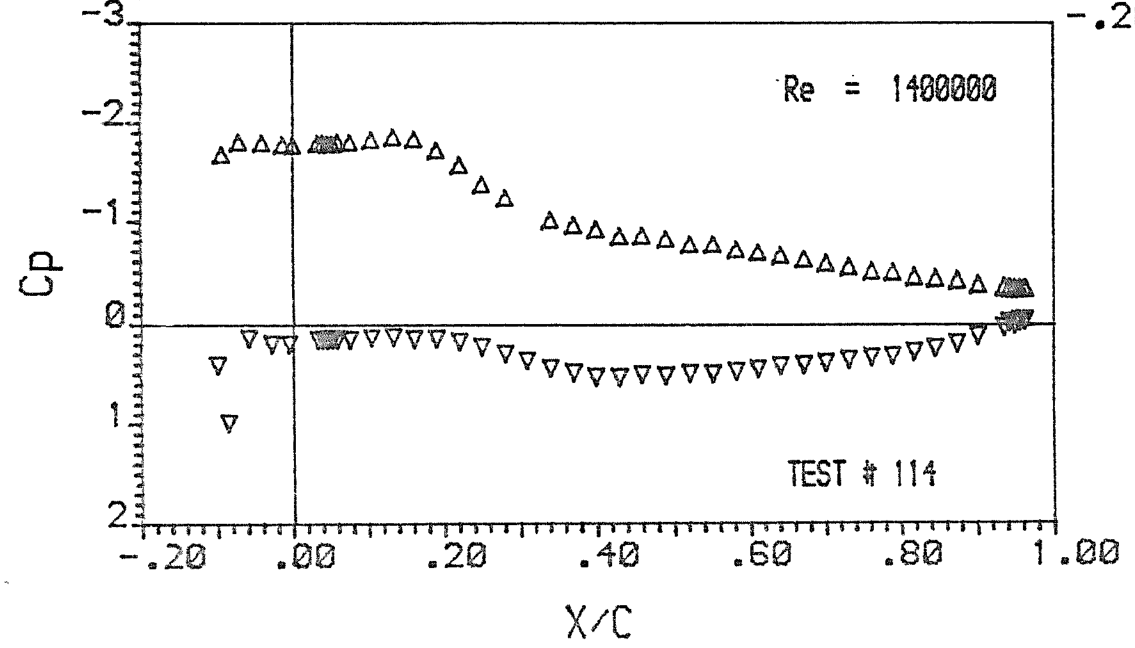

NACA 63

Incidence Angle = 5.00
Mast/Chord Ratio = .100
Mast Angle = 10.00
Camber Ratio = .100

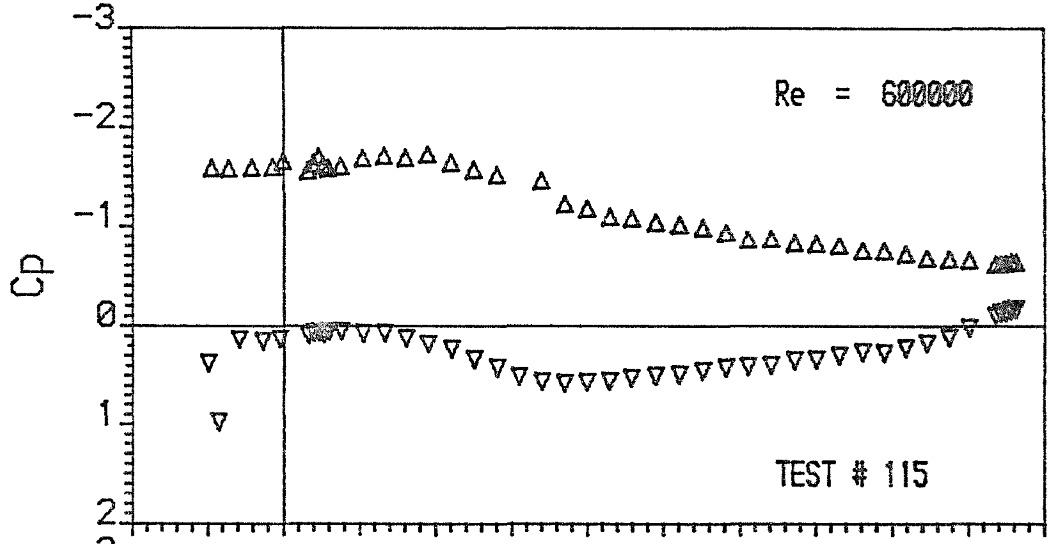

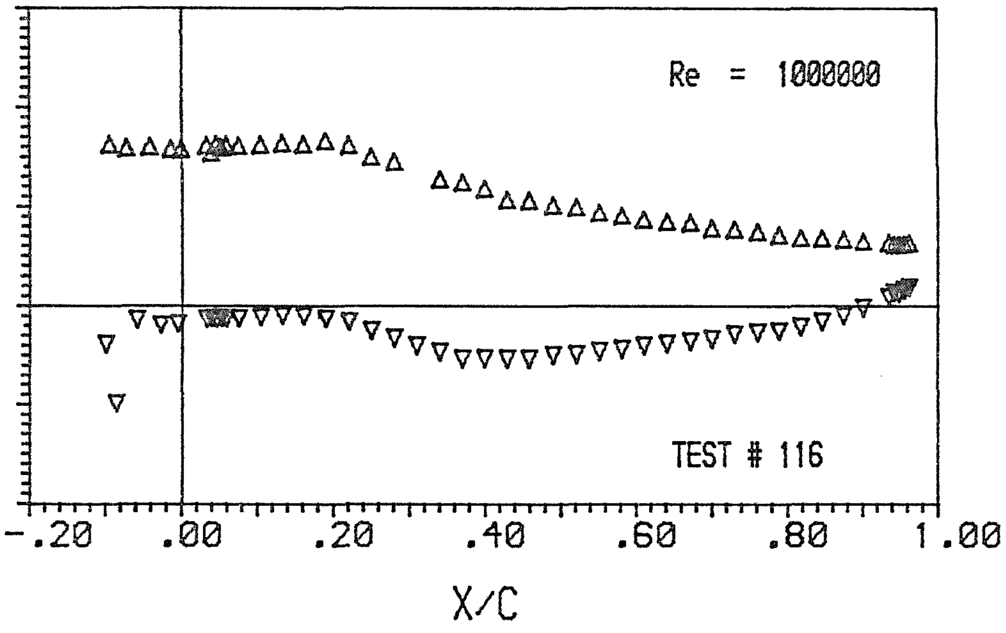

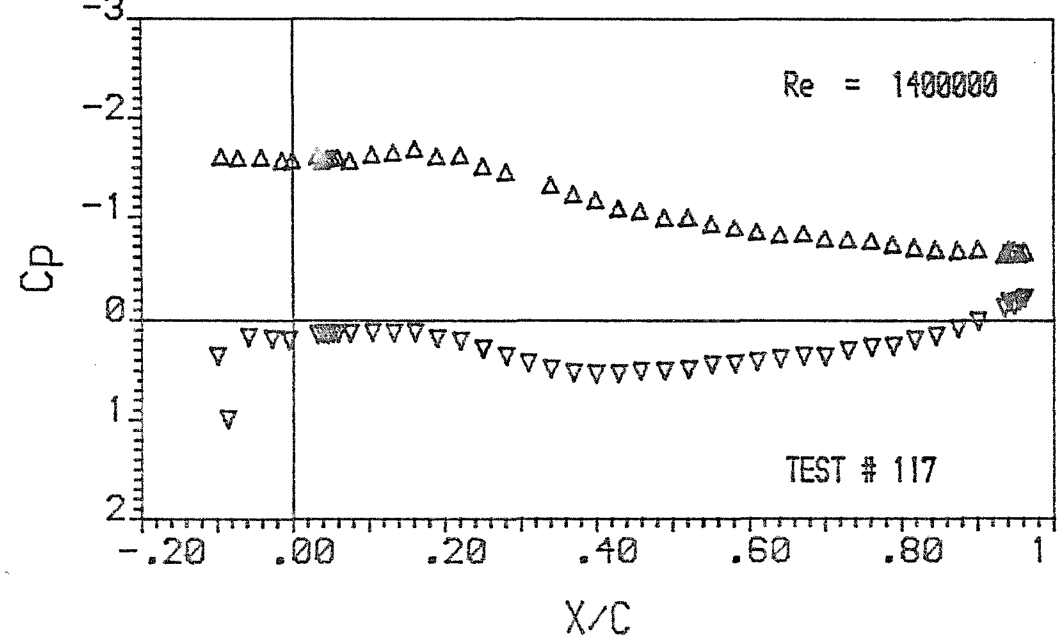

NACA 63

Incidence Angle = 7.50
Mast/Chord Ratio = .100
Mast Angle = 10.00
Camber Ratio = .100

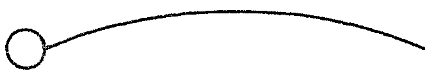

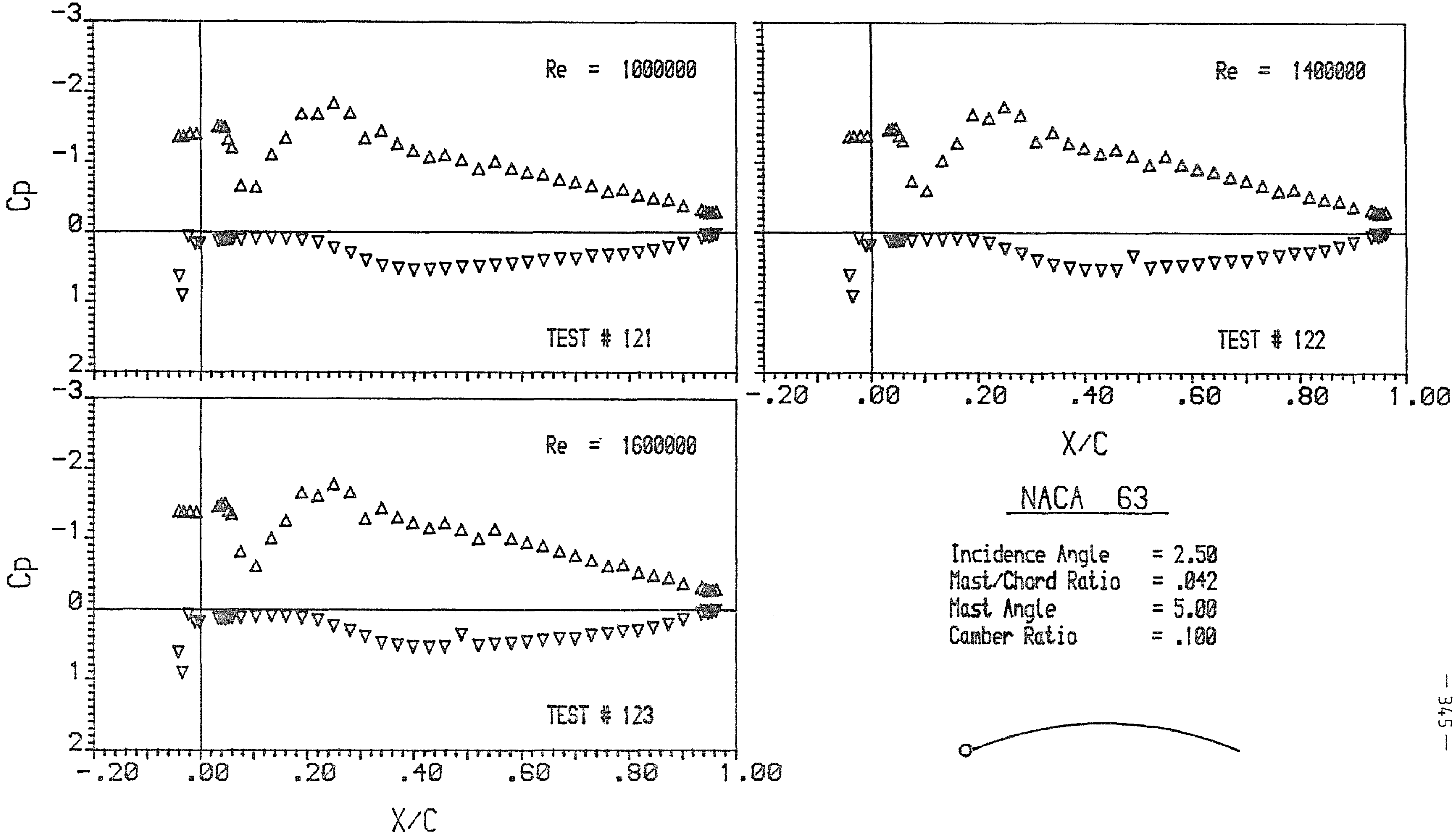

NACA 63

Incidence Angle = 2.50
Mast/Chord Ratio = .042
Mast Angle = 5.00
Camber Ratio = .100

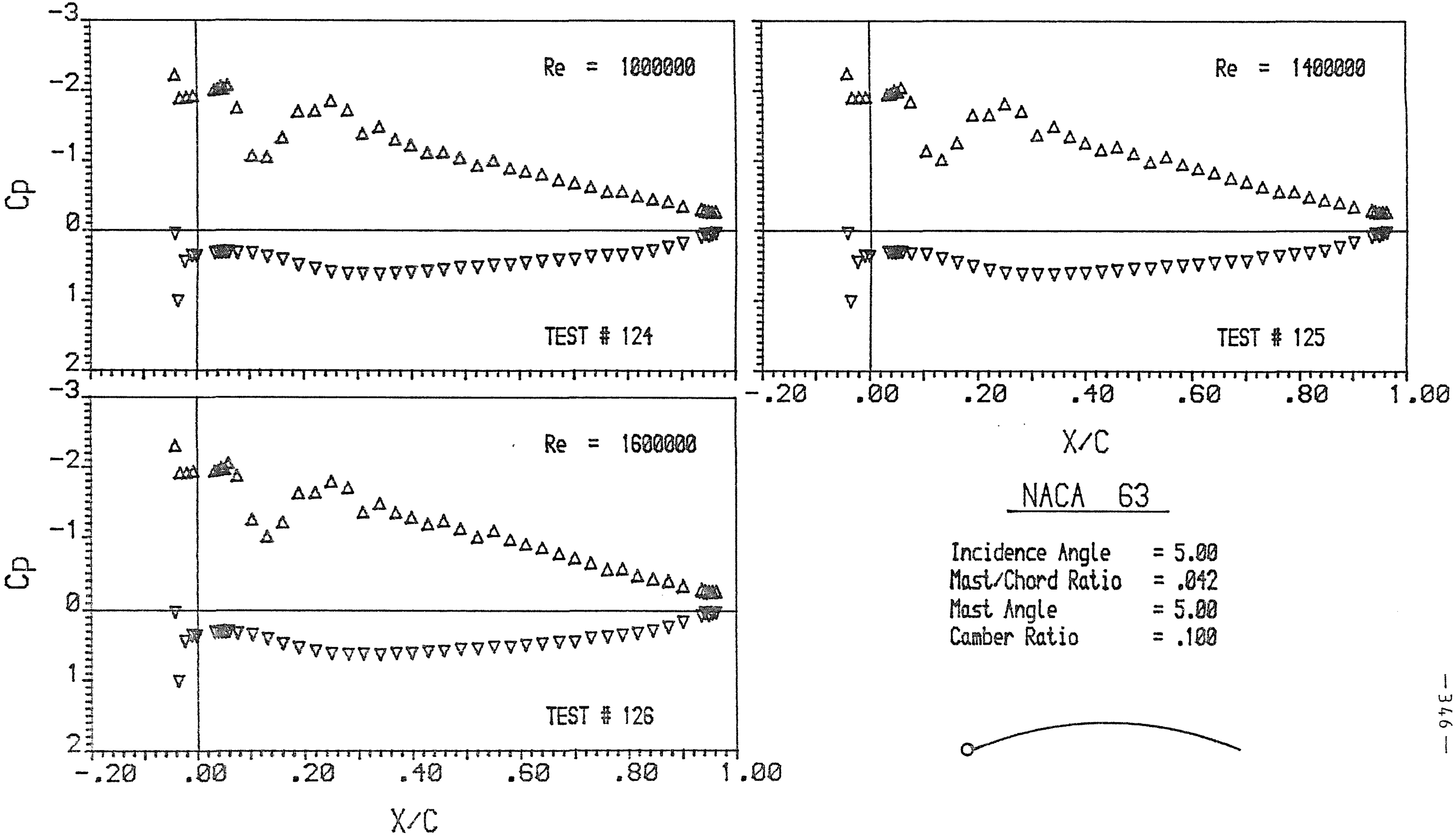

NACA 63

Incidence Angle = 5.00
Mast/Chord Ratio = .042
Mast Angle = 5.00
Camber Ratio = .100

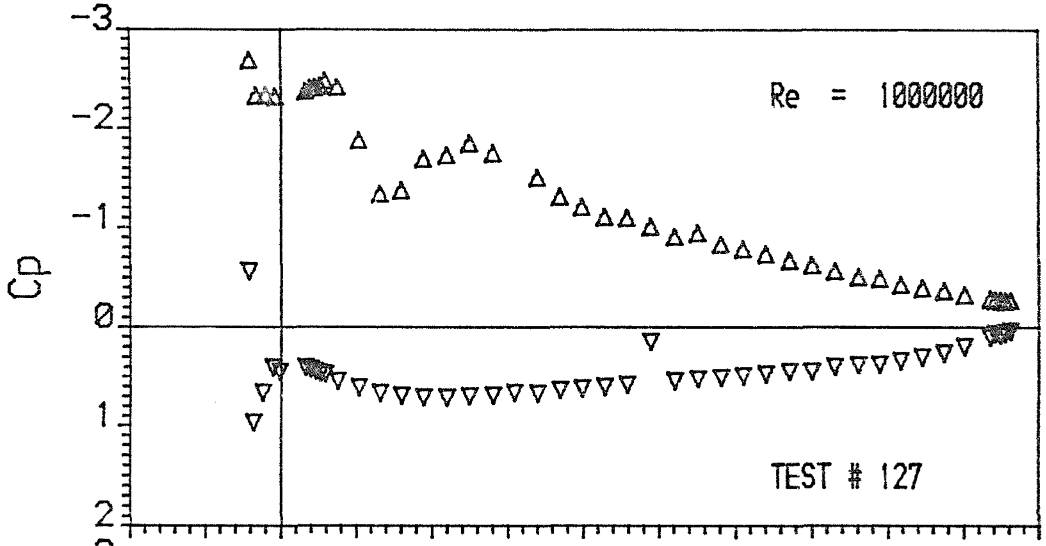

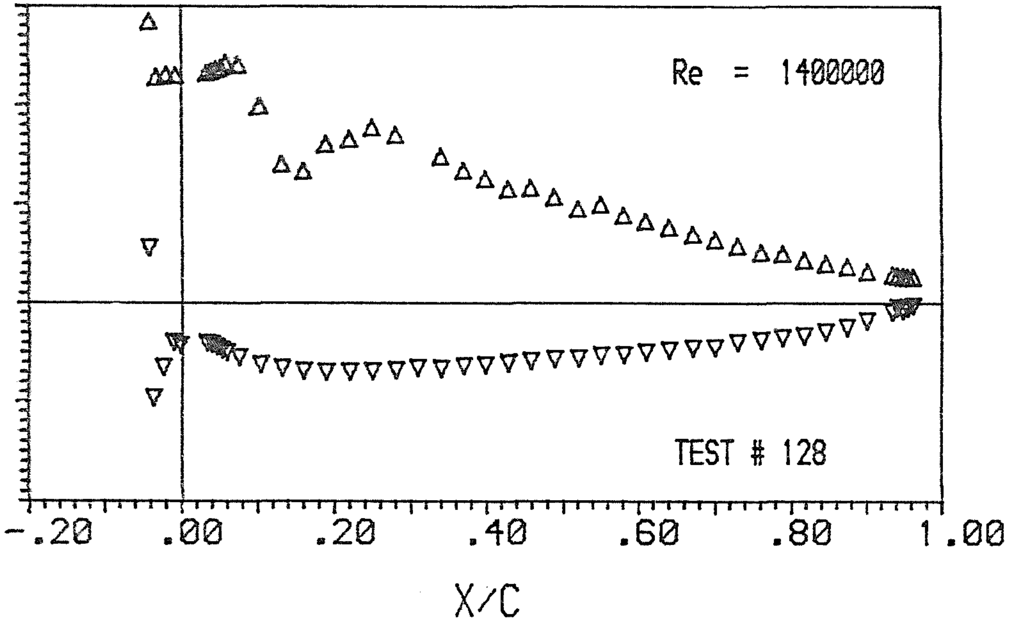

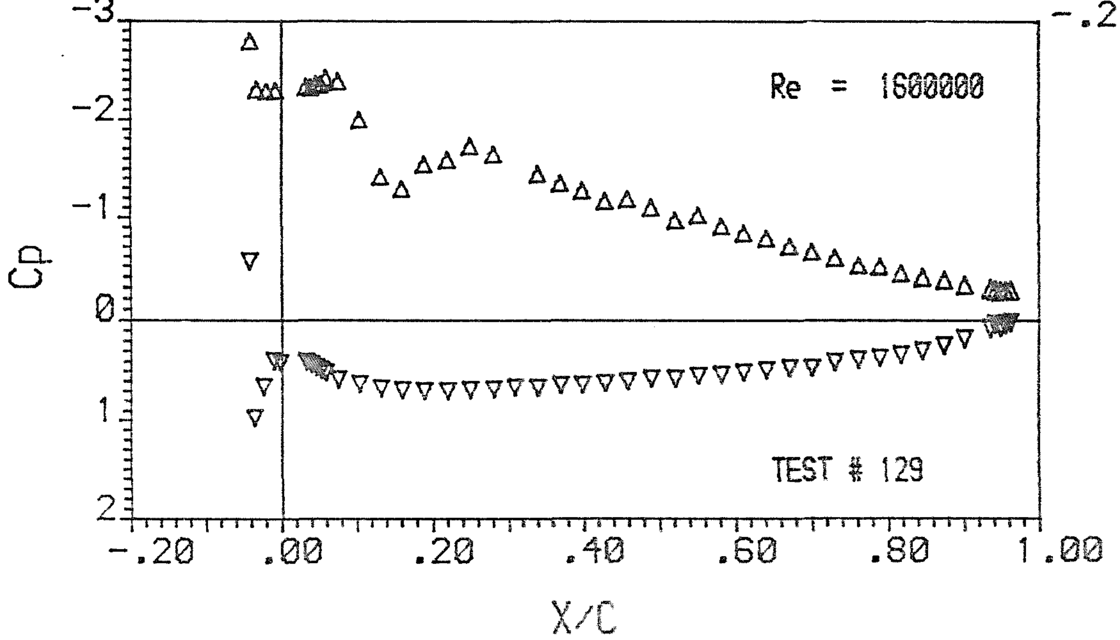

NACA 63

Incidence Angle = 7.50
Mast/Chord Ratio = .042
Mast Angle = 5.00
Camber Ratio = .100

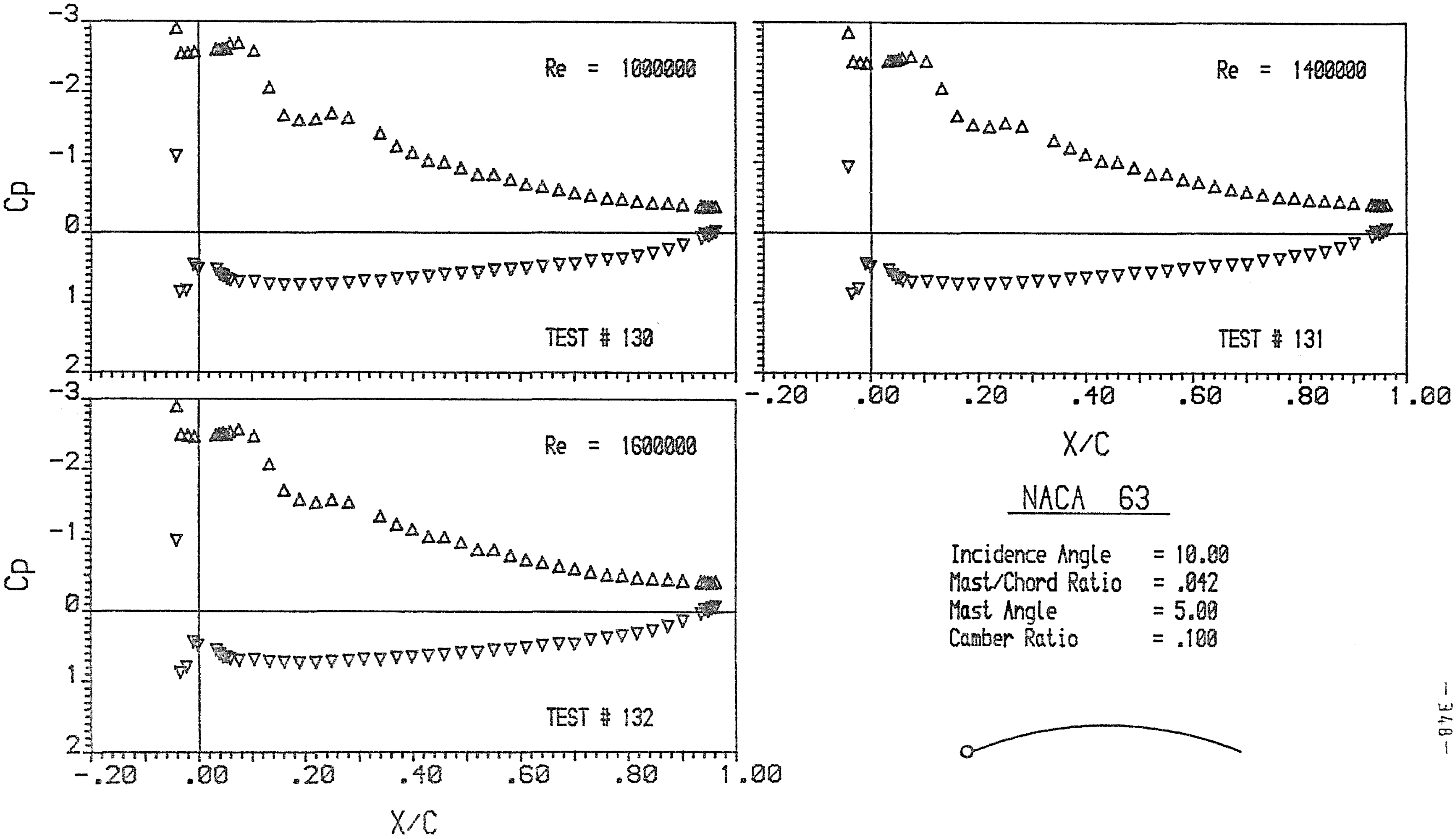

NACA 63

Incidence Angle = 10.00
Mast/Chord Ratio = .042
Mast Angle = 5.00
Camber Ratio = .100

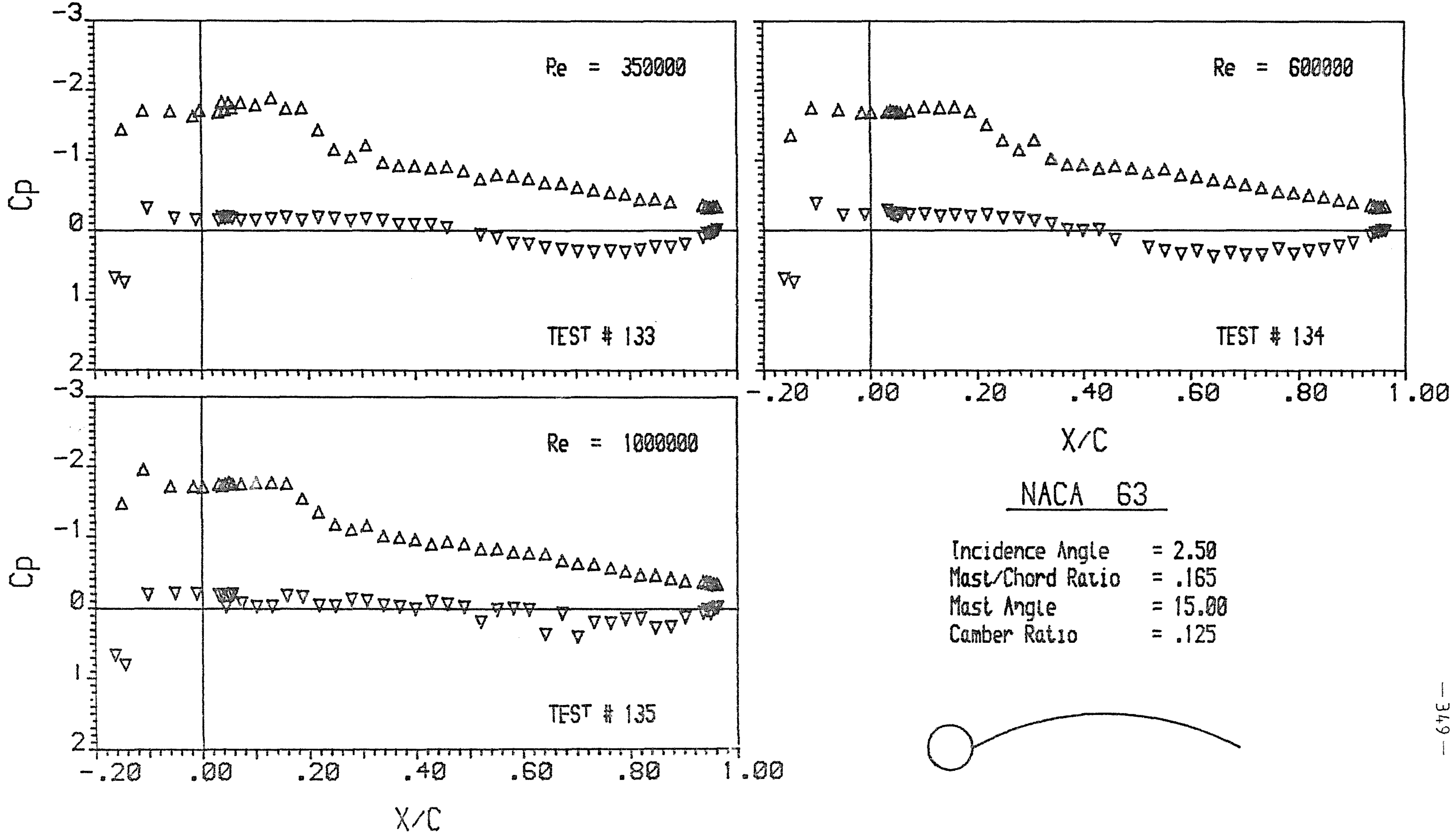

NACA 63

Incidence Angle = 2.50
Mast/Chord Ratio = .165
Mast Angle = 15.00
Camber Ratio = .125

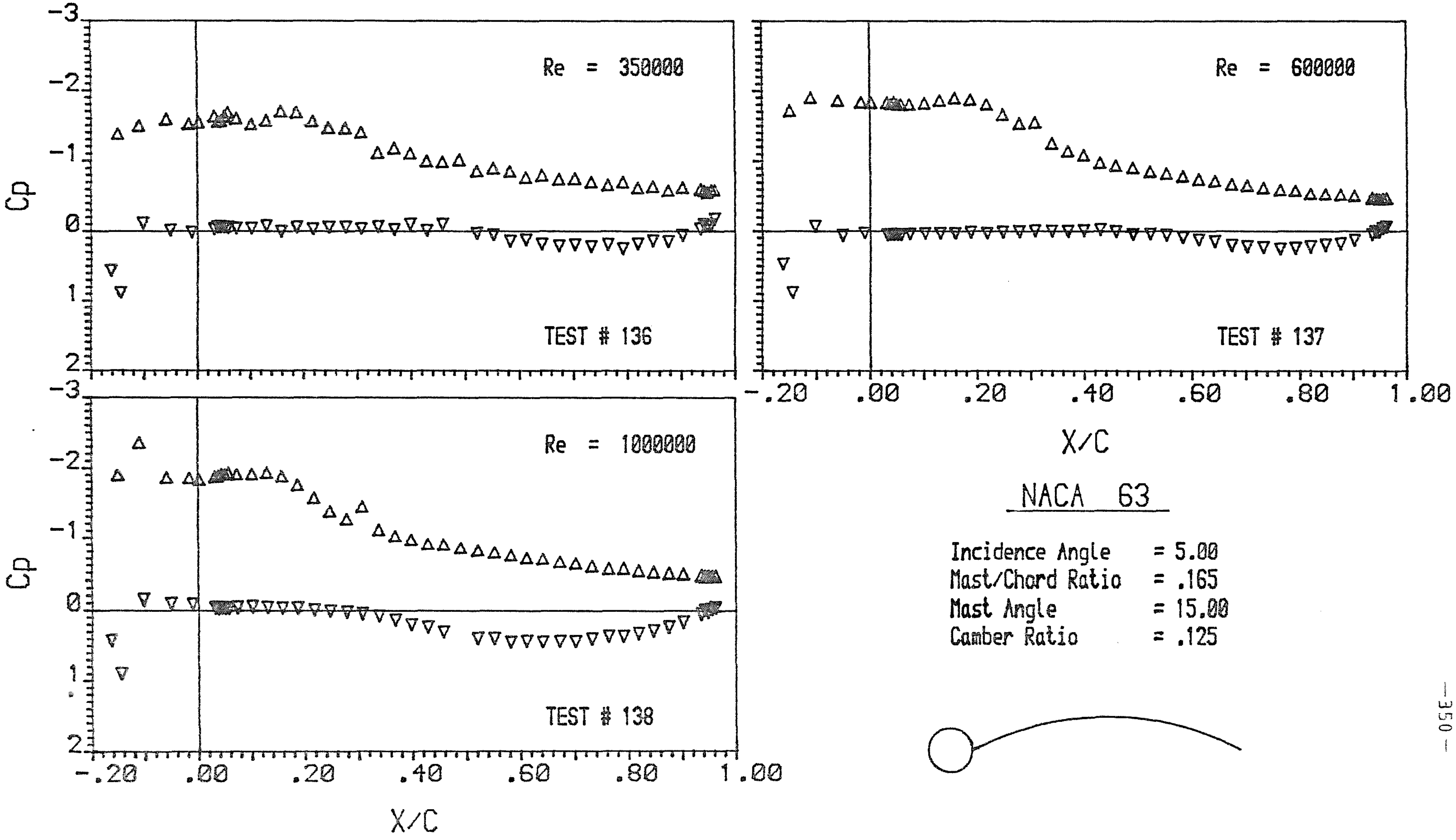

NACA 63

Incidence Angle = 5.00
Mast/Chord Ratio = .165
Mast Angle = 15.00
Camber Ratio = .125

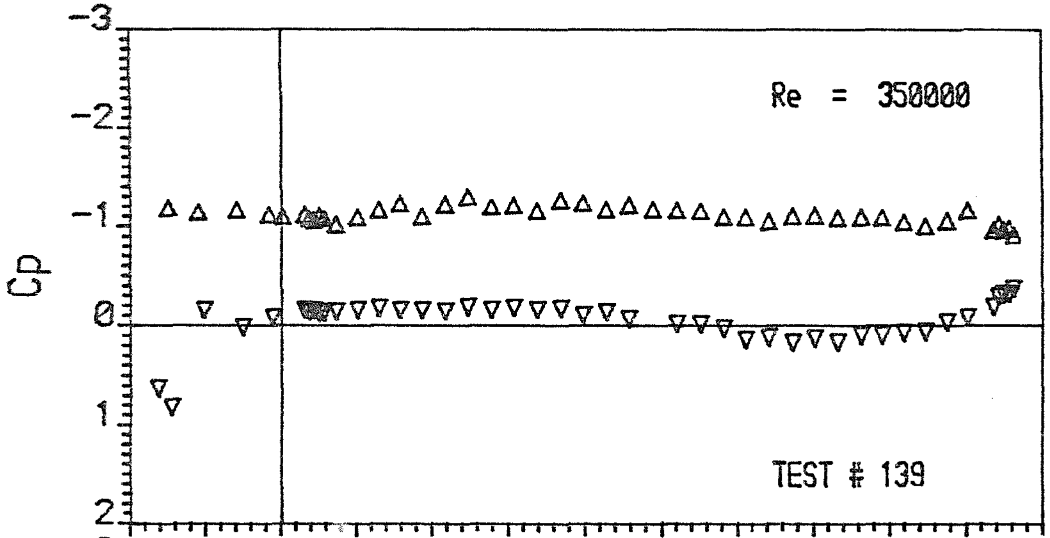

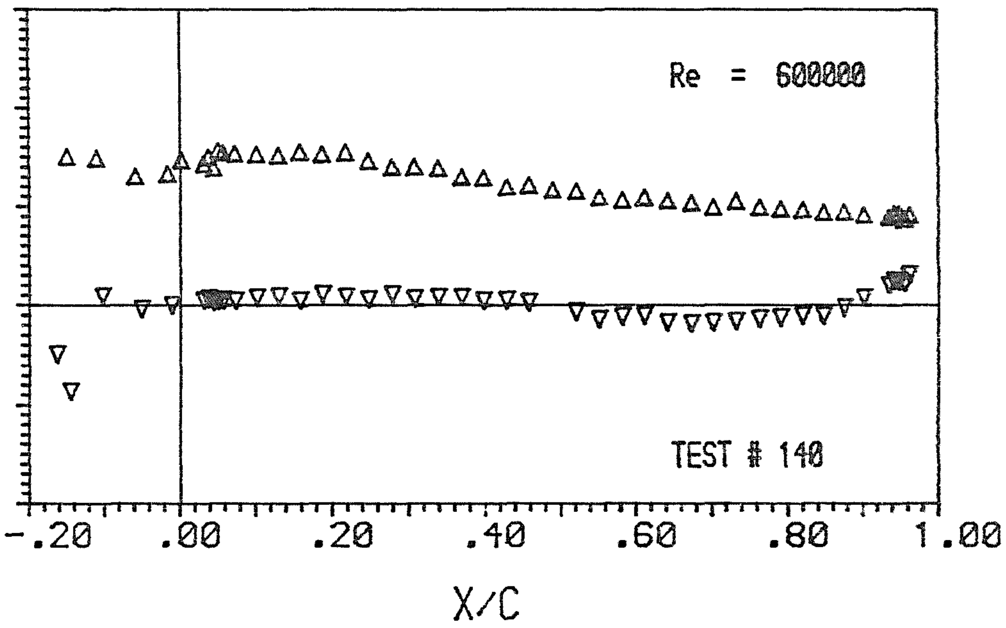

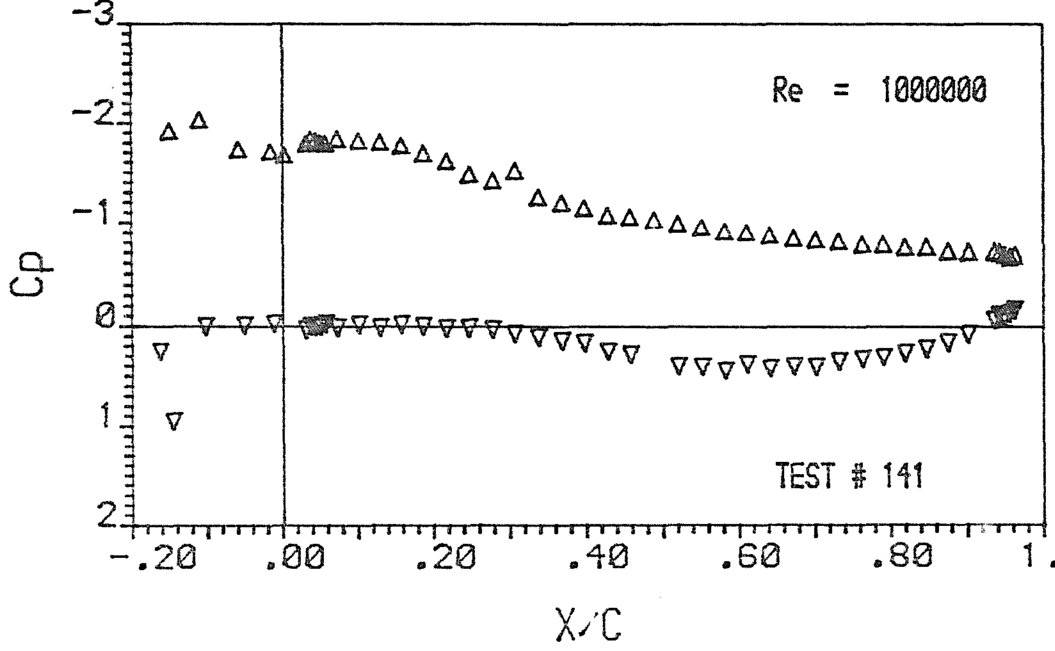

NACA 63

Incidence Angle = 7.50
Mast/Chord Ratio = .165
Mast Angle = 15.00
Camber Ratio = .125

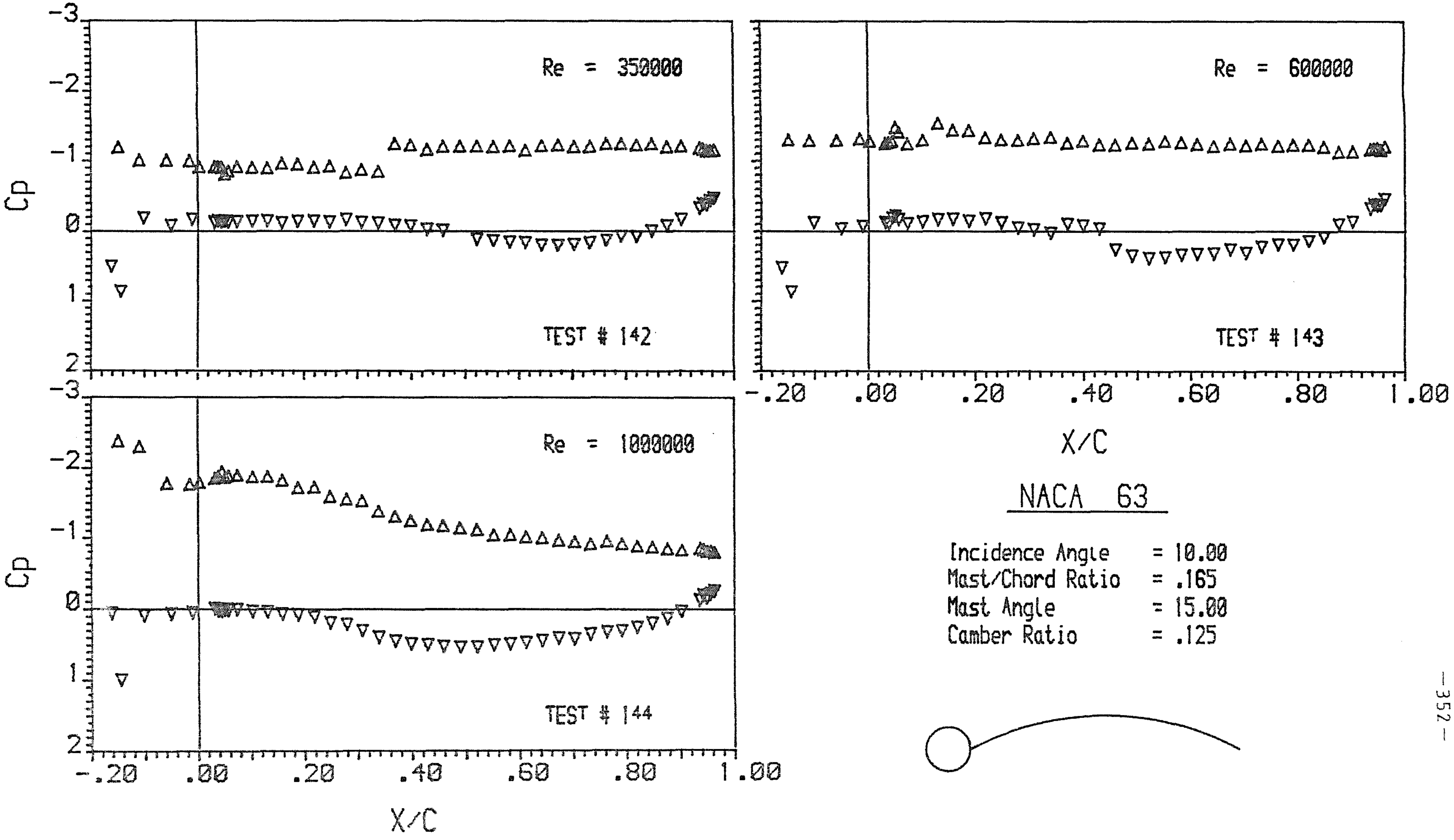

NACA 63

Incidence Angle = 10.00
Mast/Chord Ratio = .165
Mast Angle = 15.00
Camber Ratio = .125

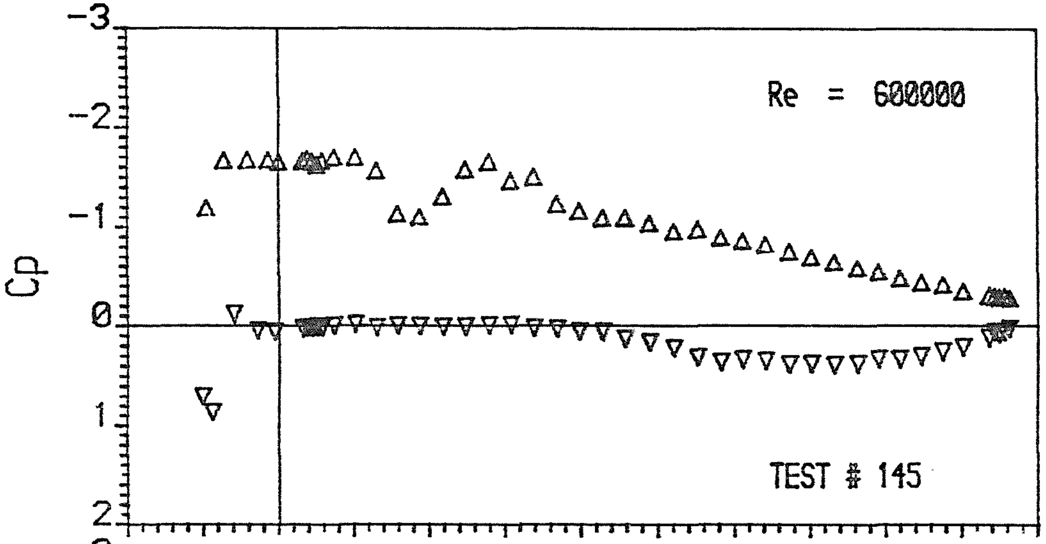

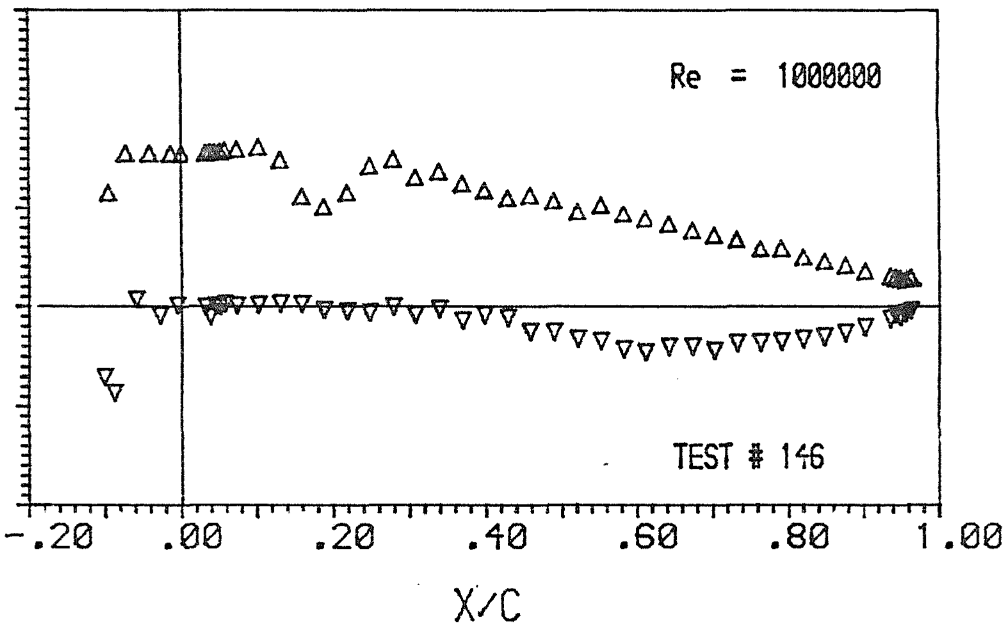

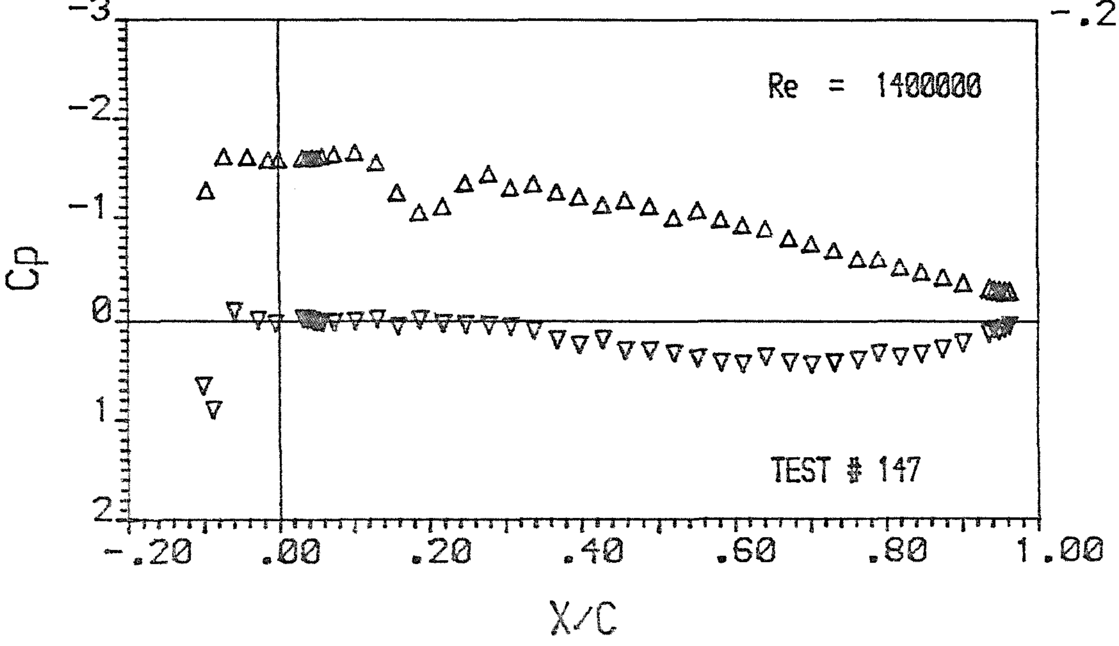

NACA 63

Incidence Angle = 2.50
Mast/Chord Ratio = .102
Mast Angle = 10.00
Camber Ratio = .125

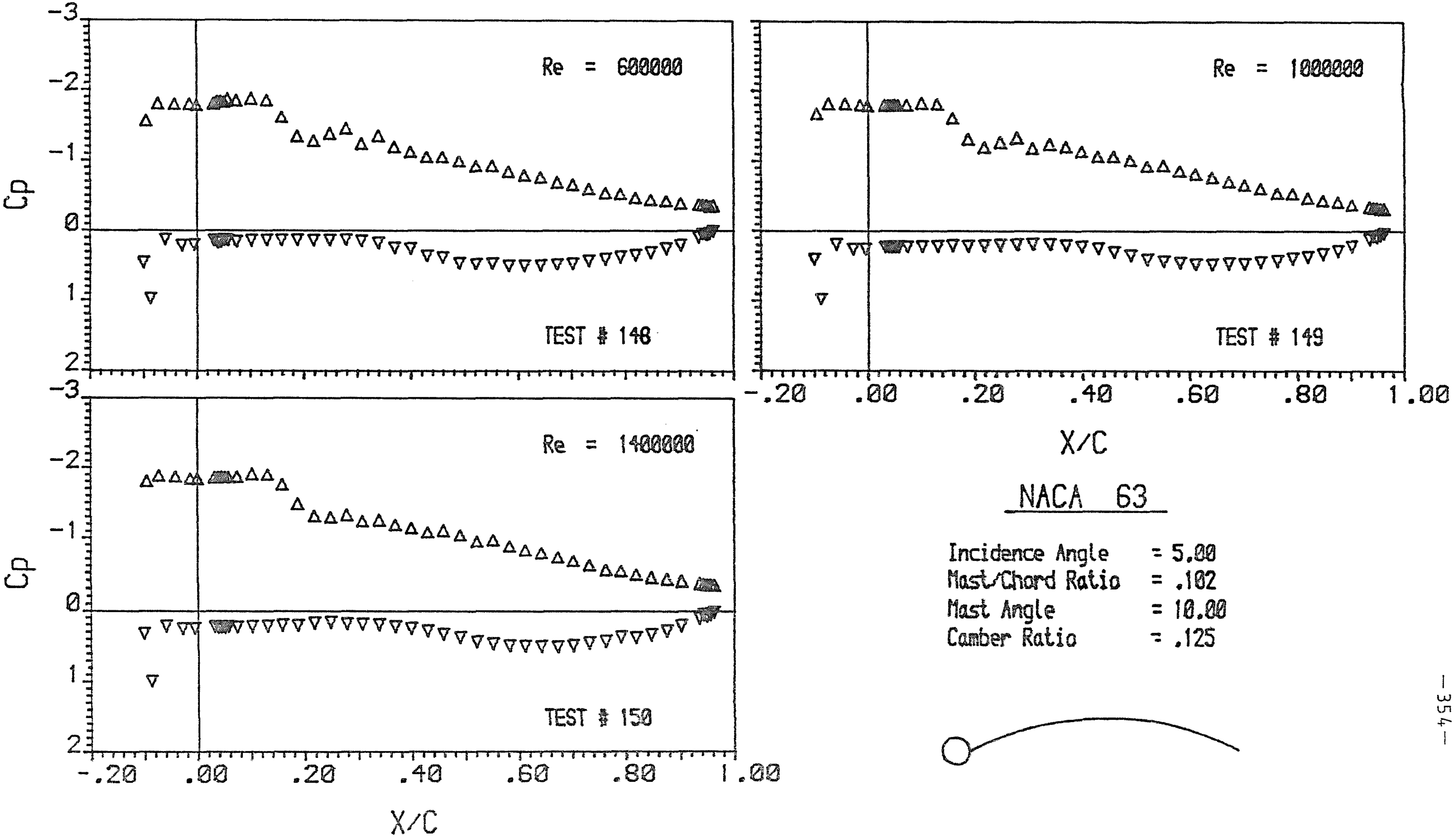

NACA 63

Incidence Angle = 5.00
Mast/Chord Ratio = .102
Mast Angle = 10.00
Camber Ratio = .125

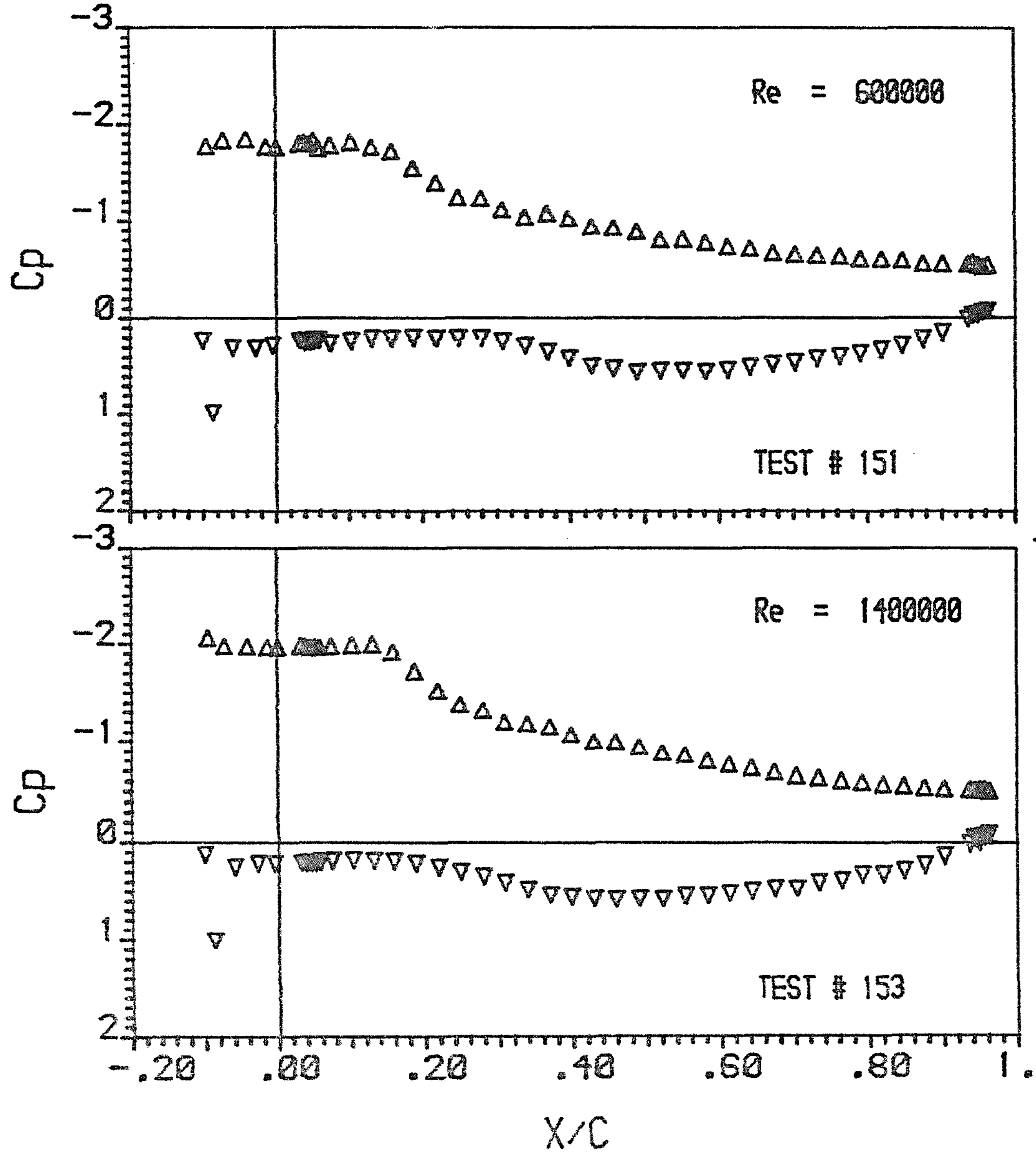
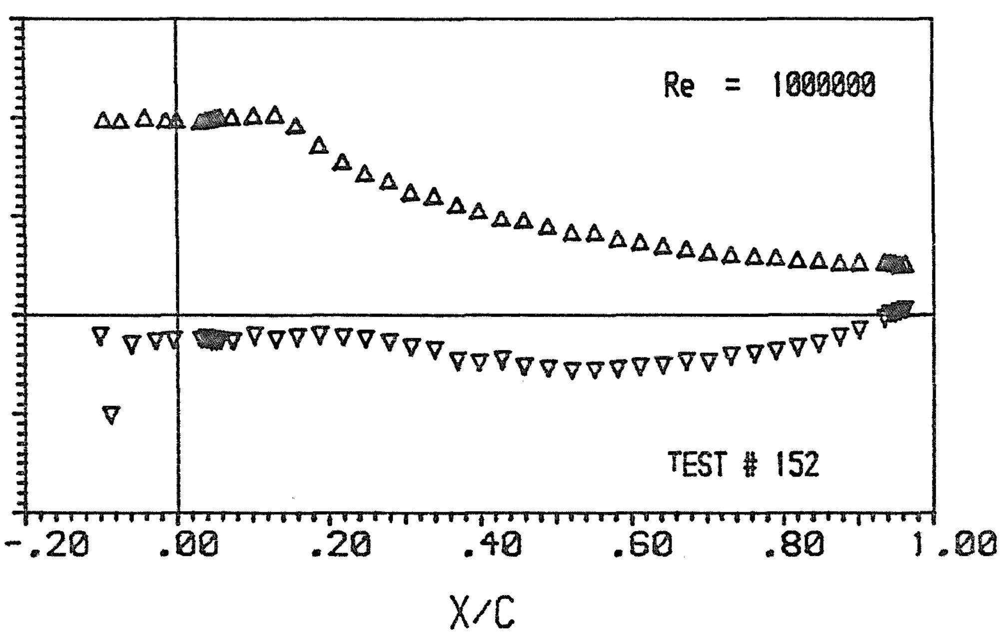

NACA 63

Incidence Angle = 7.50
Mast/Chord Ratio = .102
Mast Angle = 10.00
Camber Ratio = .125

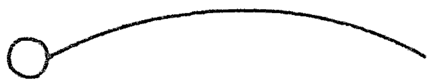

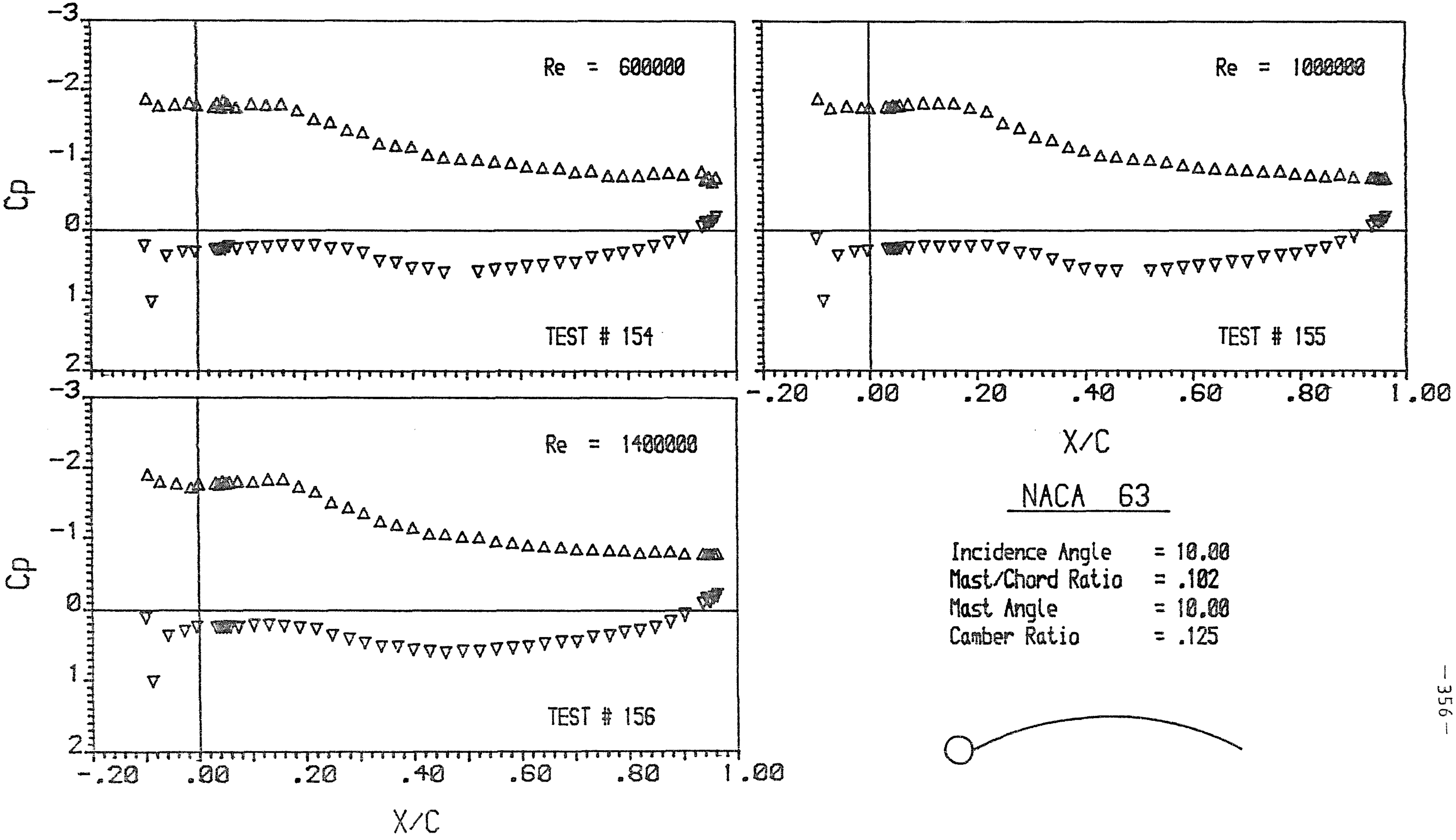

NACA 63

Incidence Angle = 10.00
Mast/Chord Ratio = .102
Mast Angle = 10.00
Camber Ratio = .125

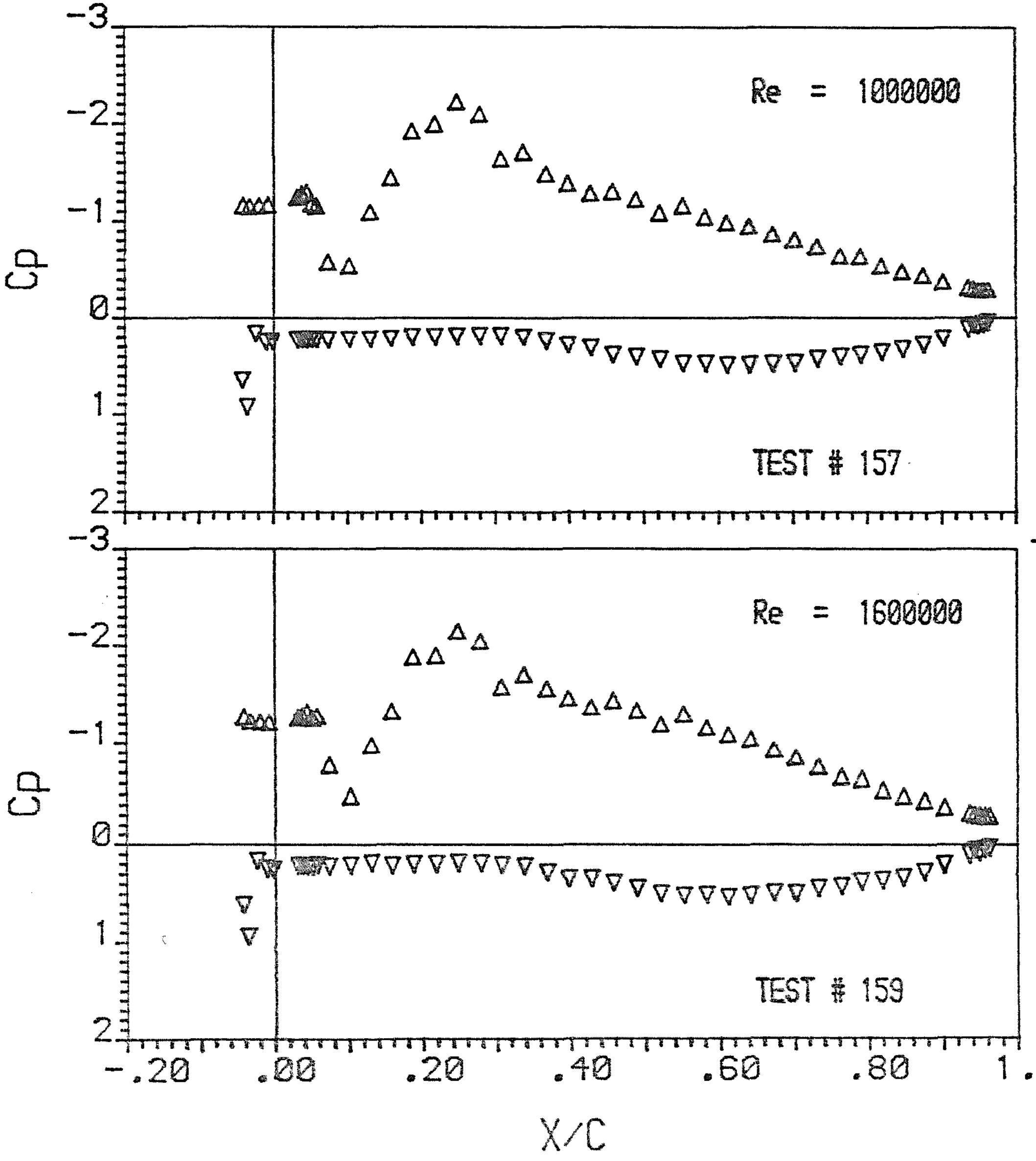

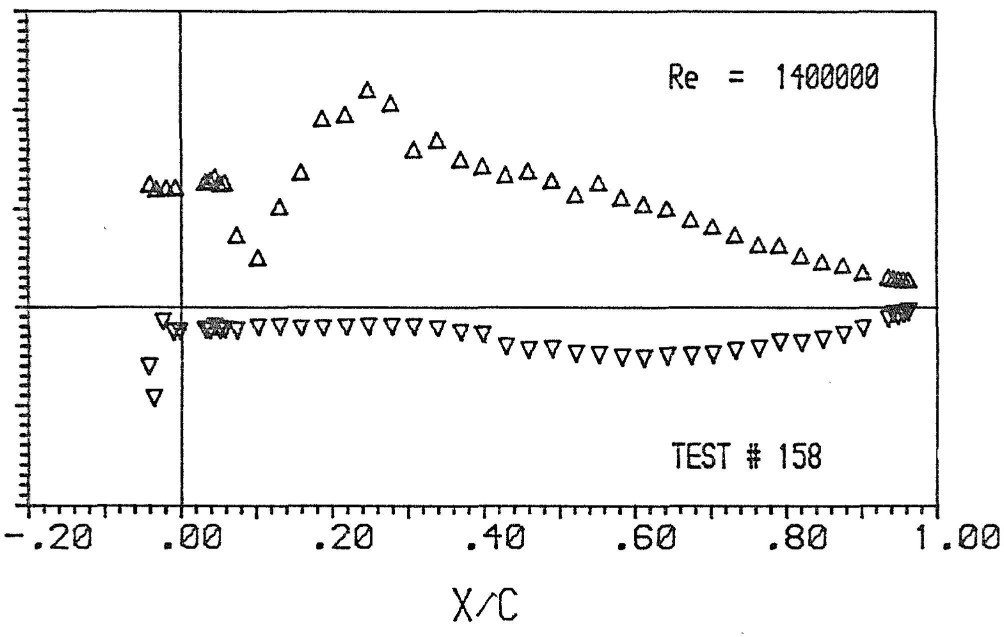

NACA 63

Incidence Angle = 2.50
Mast/Chord Ratio = .043
Mast Angle = 5.00
Camber Ratio = .125

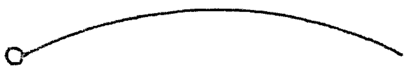

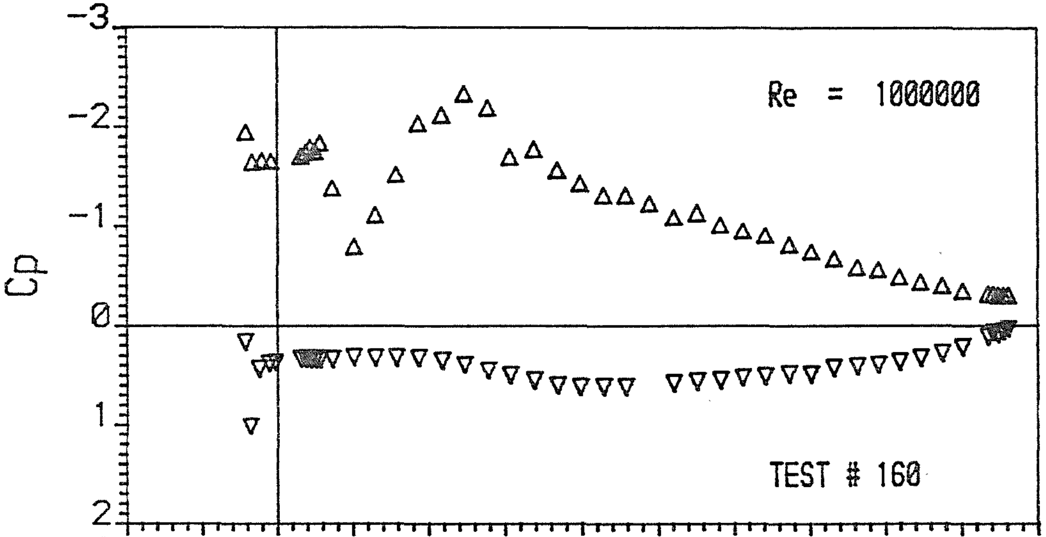

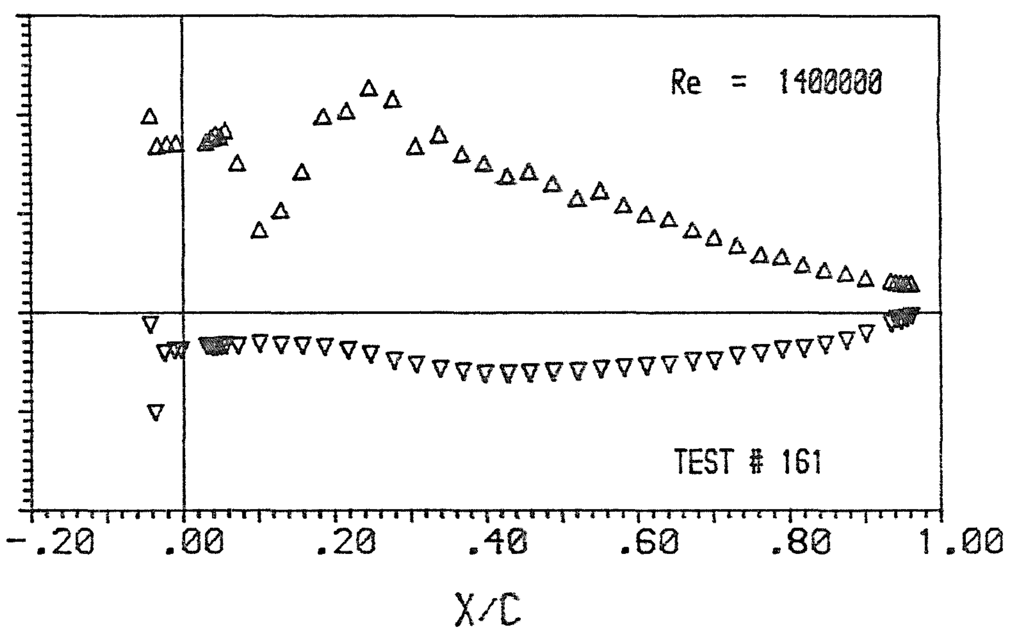

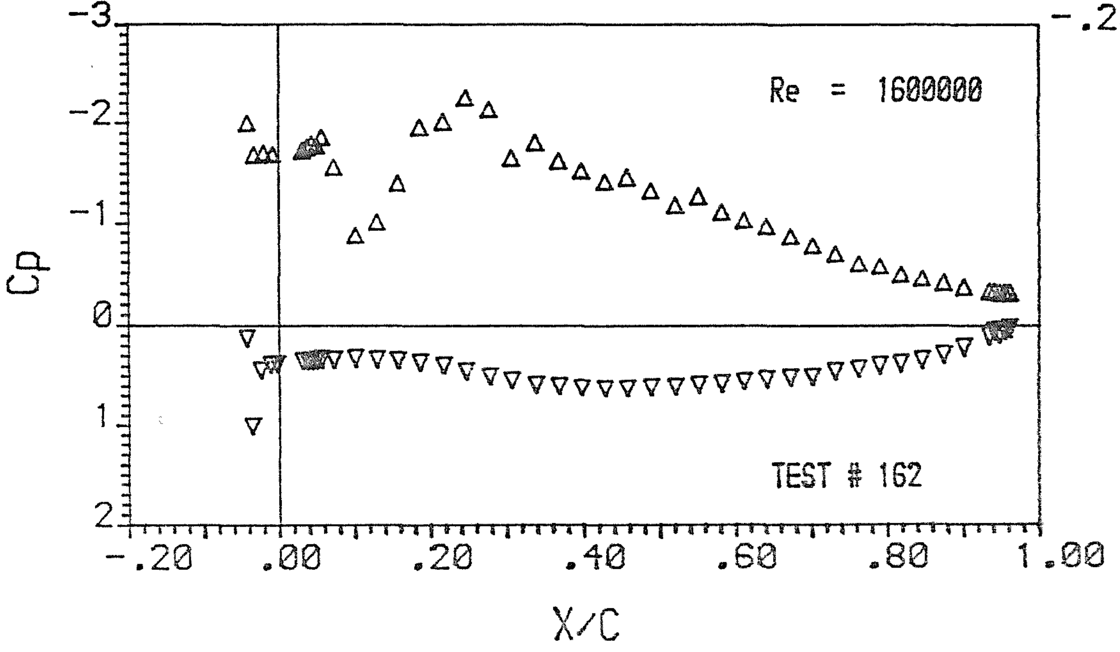

NACA 63

Incidence Angle = 5.00
Mast/Chord Ratio = .043
Mast Angle = 5.00
Camber Ratio = .125

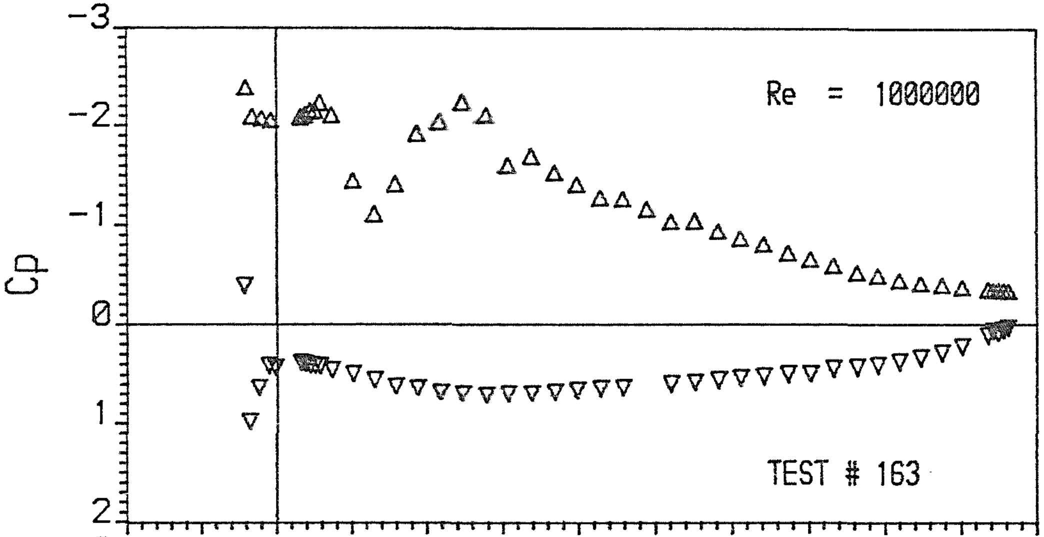

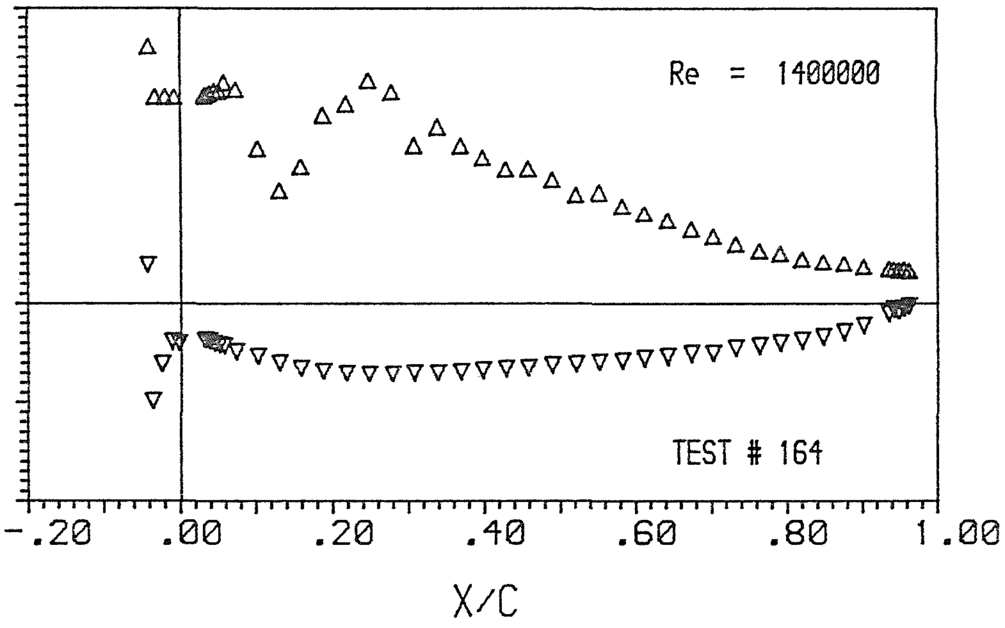

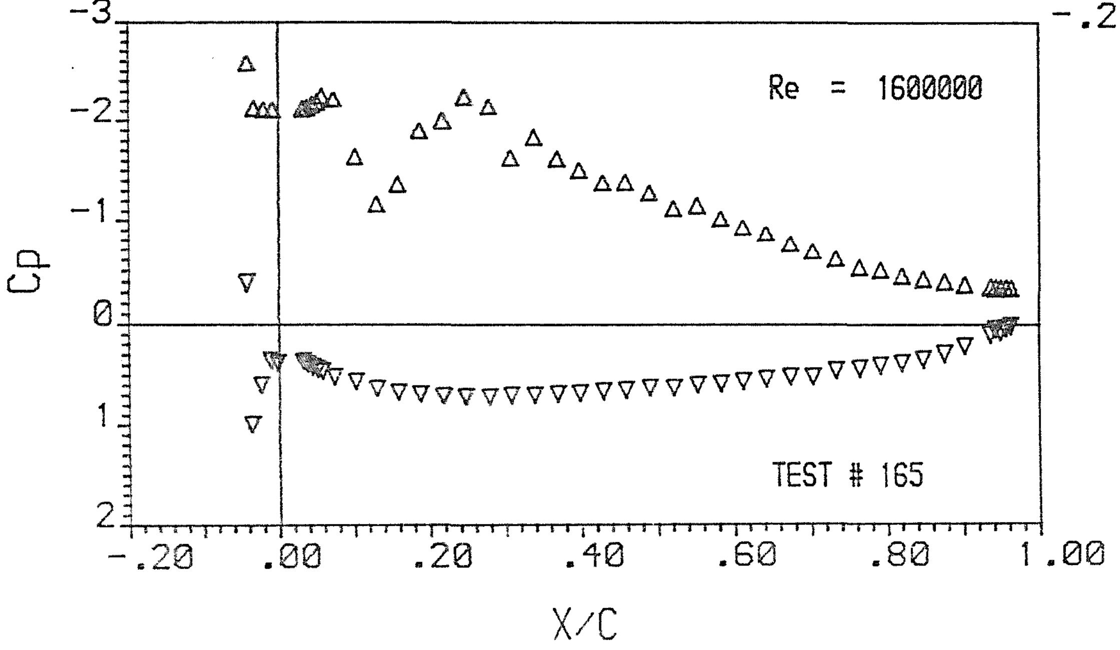

NACA 63

Incidence Angle = 7.50
Mast/Chord Ratio = .043
Mast Angle = 5.00
Camber Ratio = .125

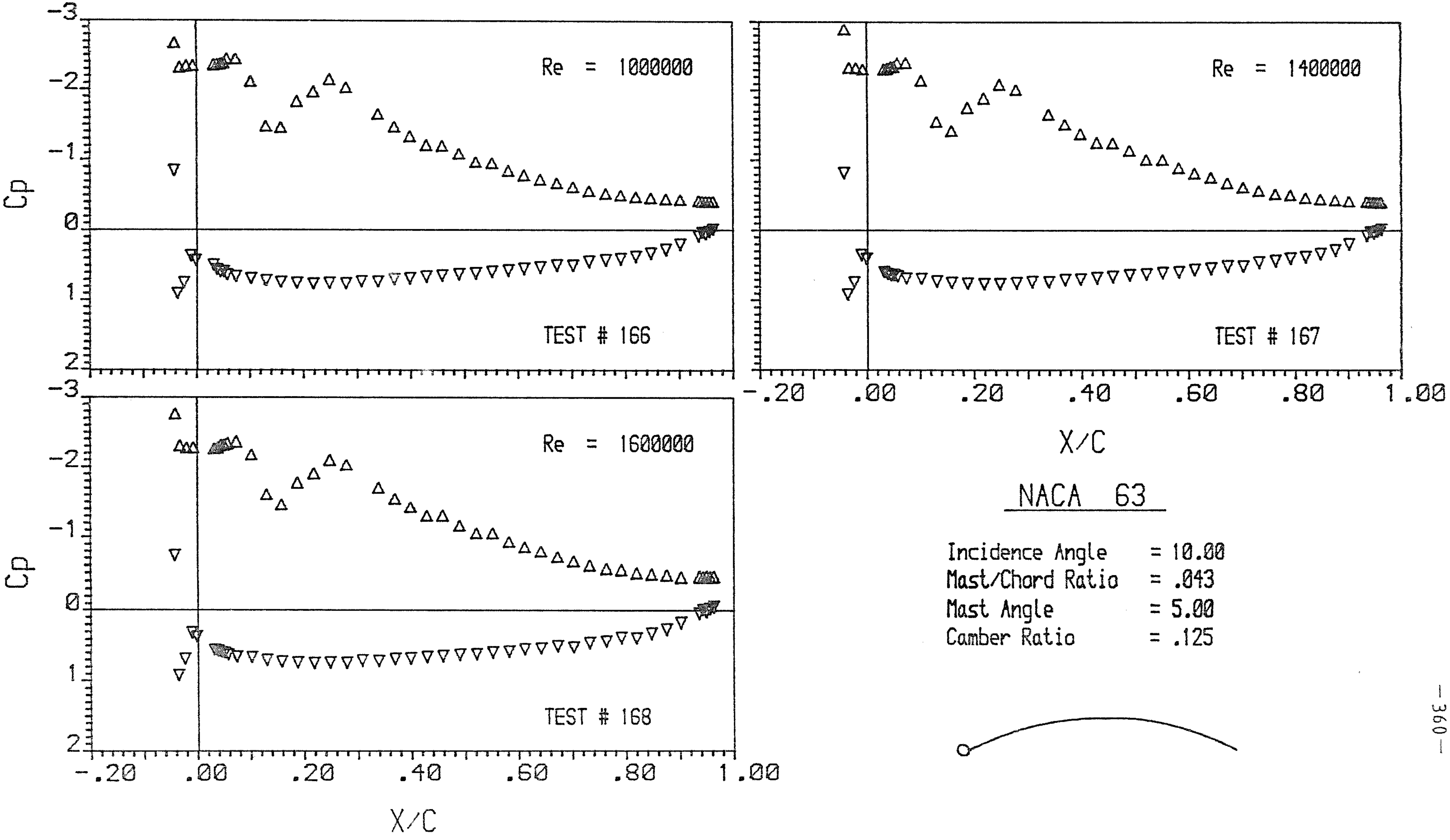

NACA 63

Incidence Angle = 10.00
Mast/Chord Ratio = .043
Mast Angle = 5.00
Camber Ratio = .125

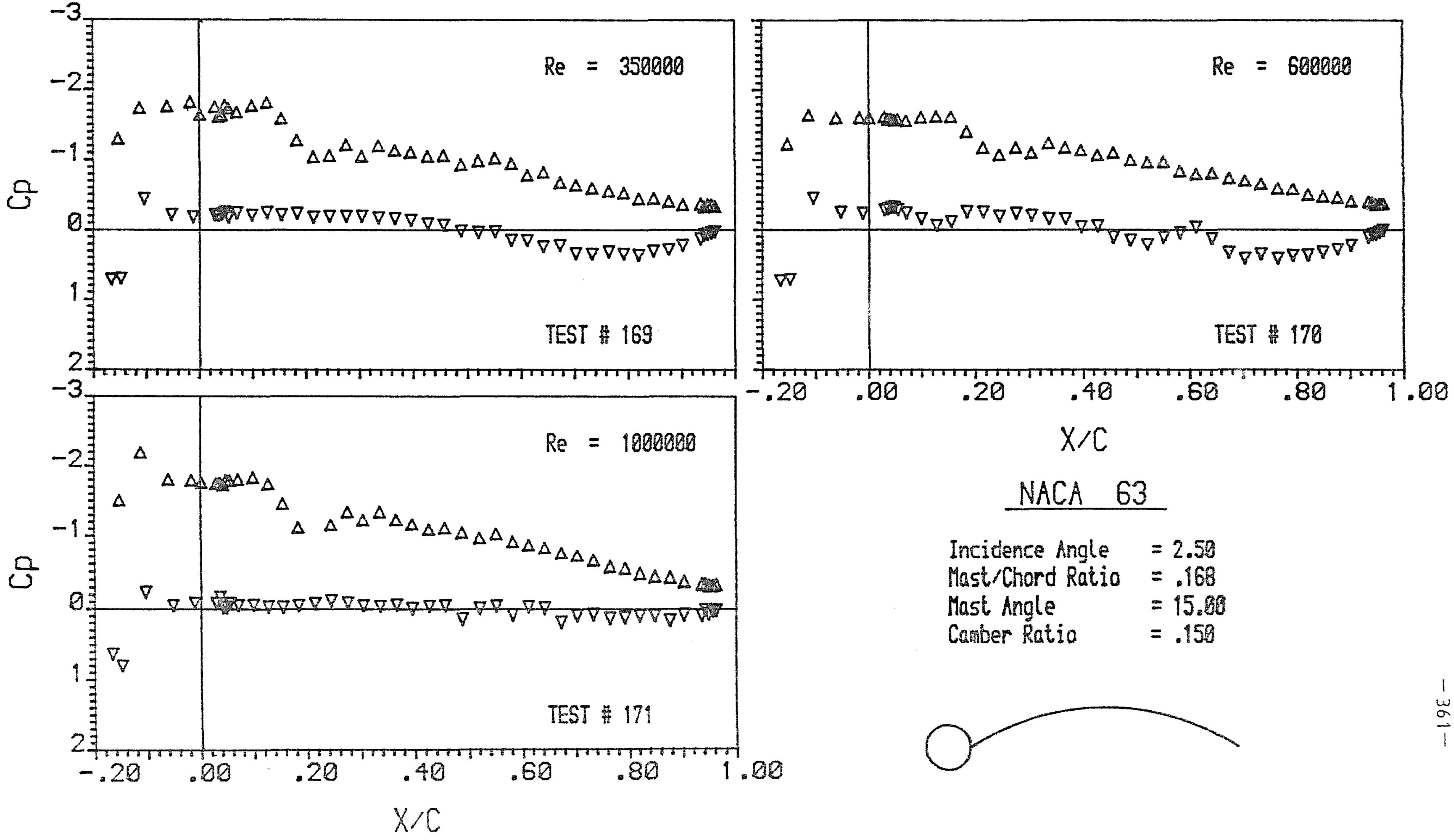

NACA 63

Incidence Angle = 2.50
Mast/Chord Ratio = .168
Mast Angle = 15.00
Camber Ratio = .150

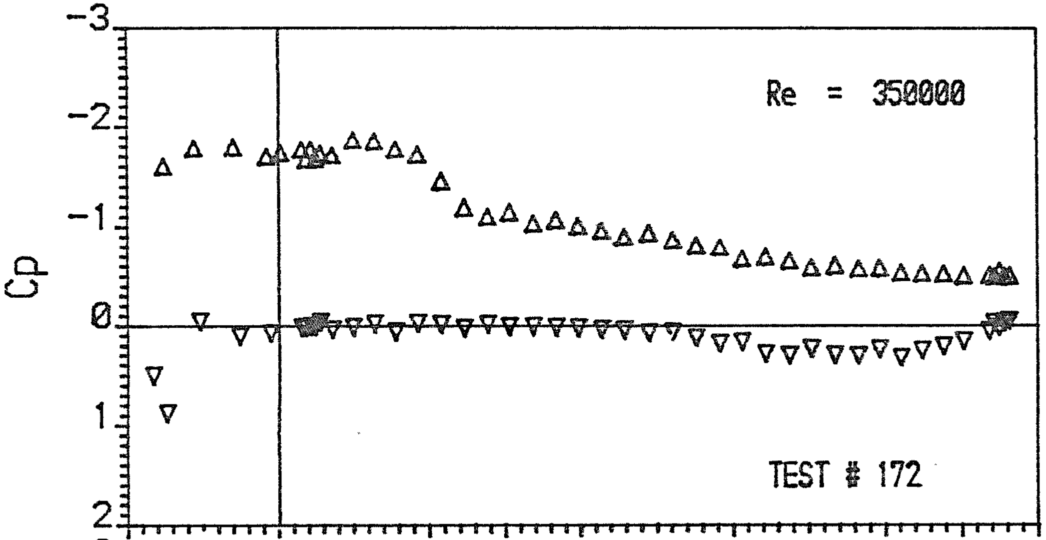

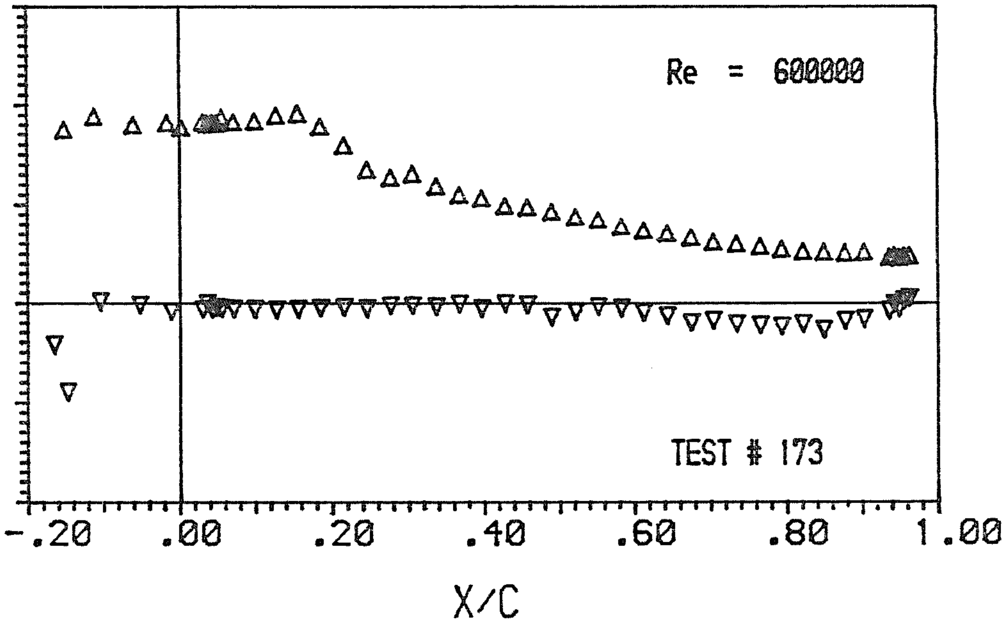

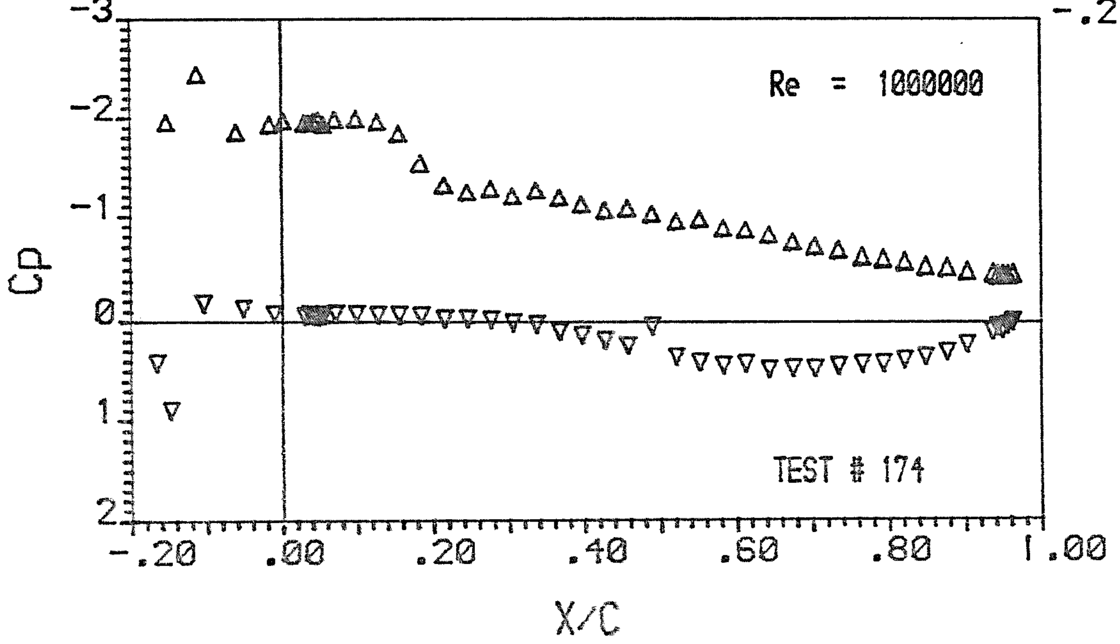

NACA 63

Incidence Angle = 5.00
Mast/Chord Ratio = .168
Mast Angle = 15.00
Camber Ratio = .150

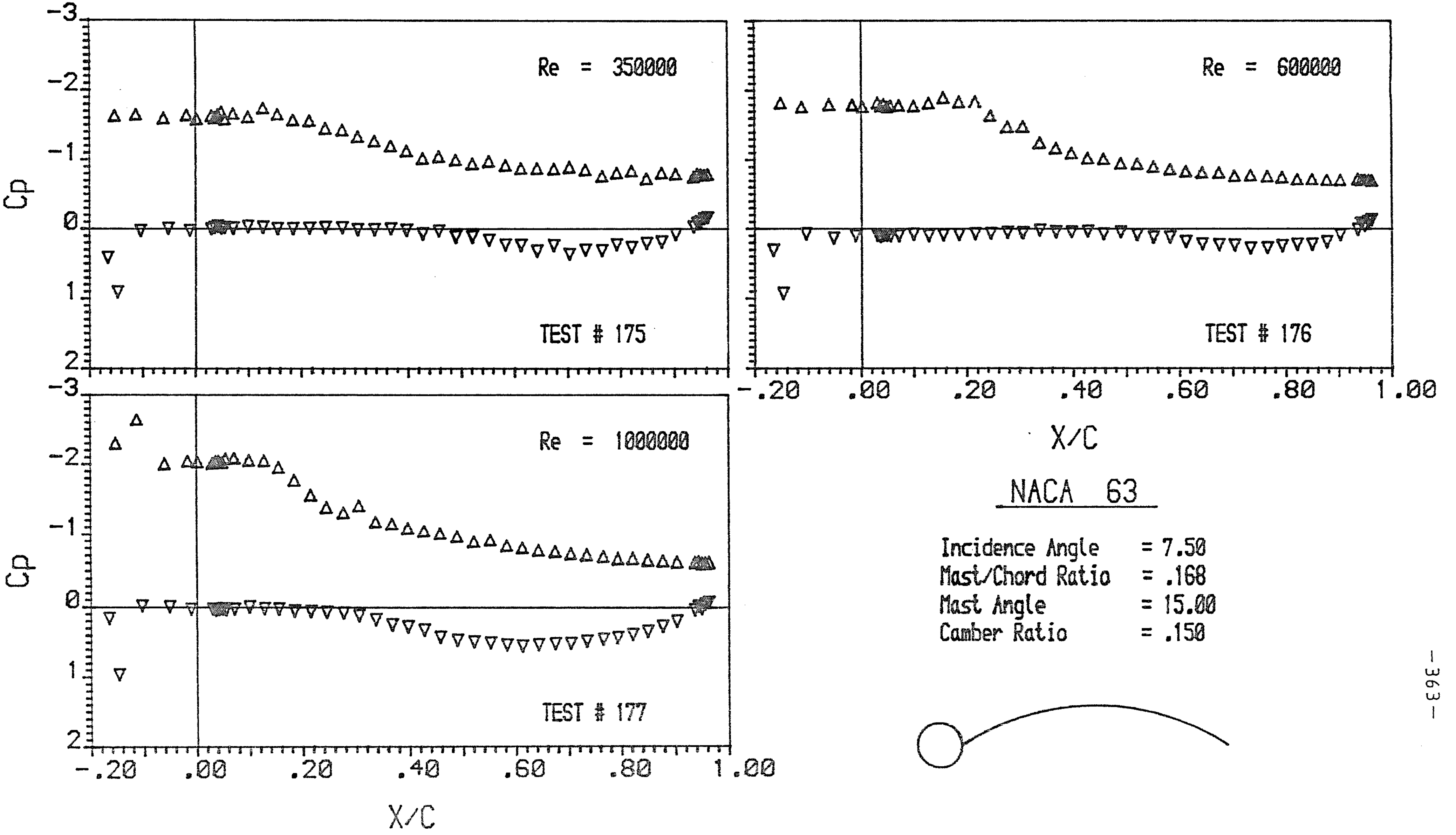

NACA 63

Incidence Angle = 7.50
Mast/Chord Ratio = .168
Mast Angle = 15.00
Camber Ratio = .150

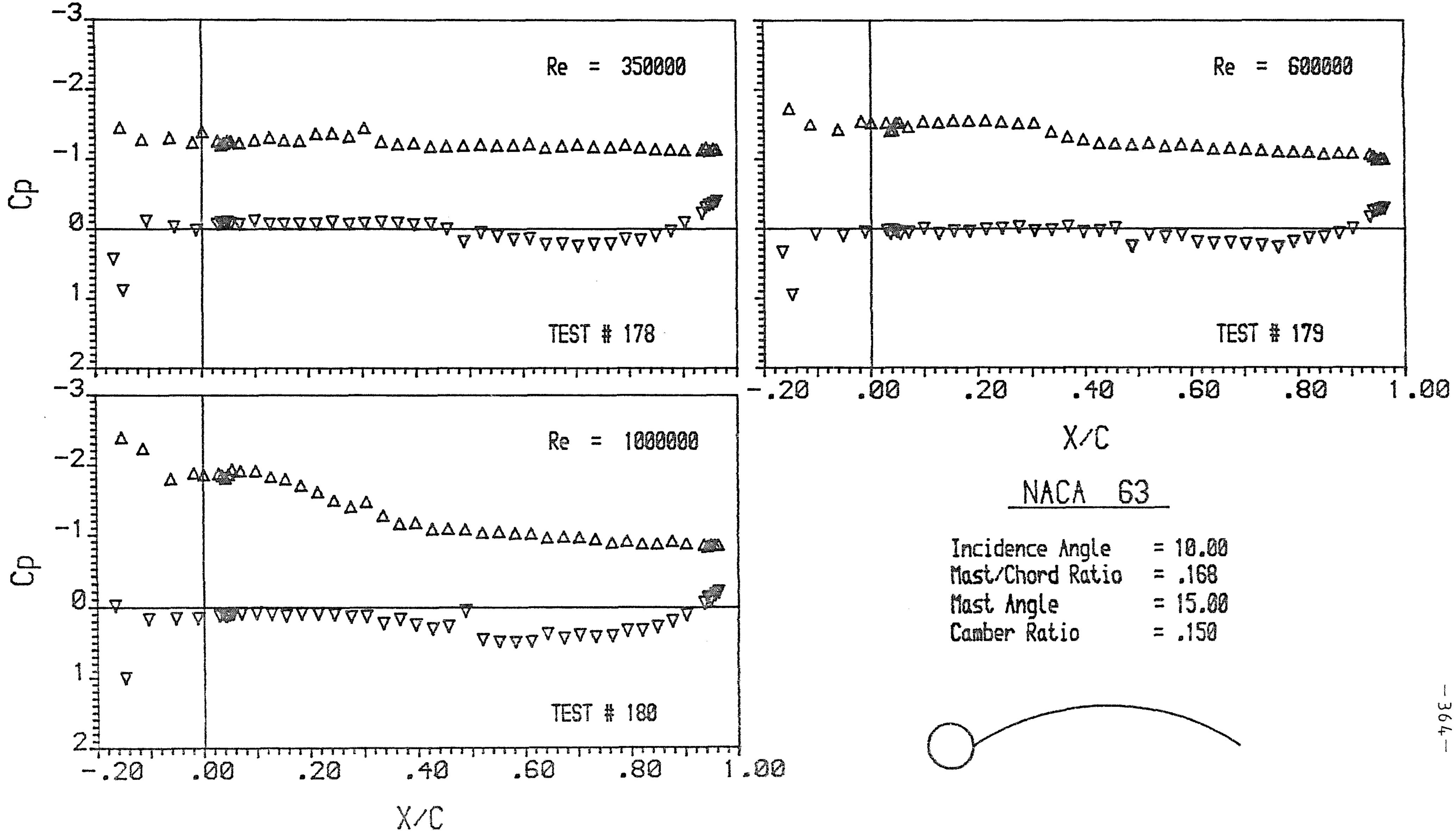

NACA 63

Incidence Angle = 10.00
Mast/Chord Ratio = .168
Mast Angle = 15.00
Camber Ratio = .150

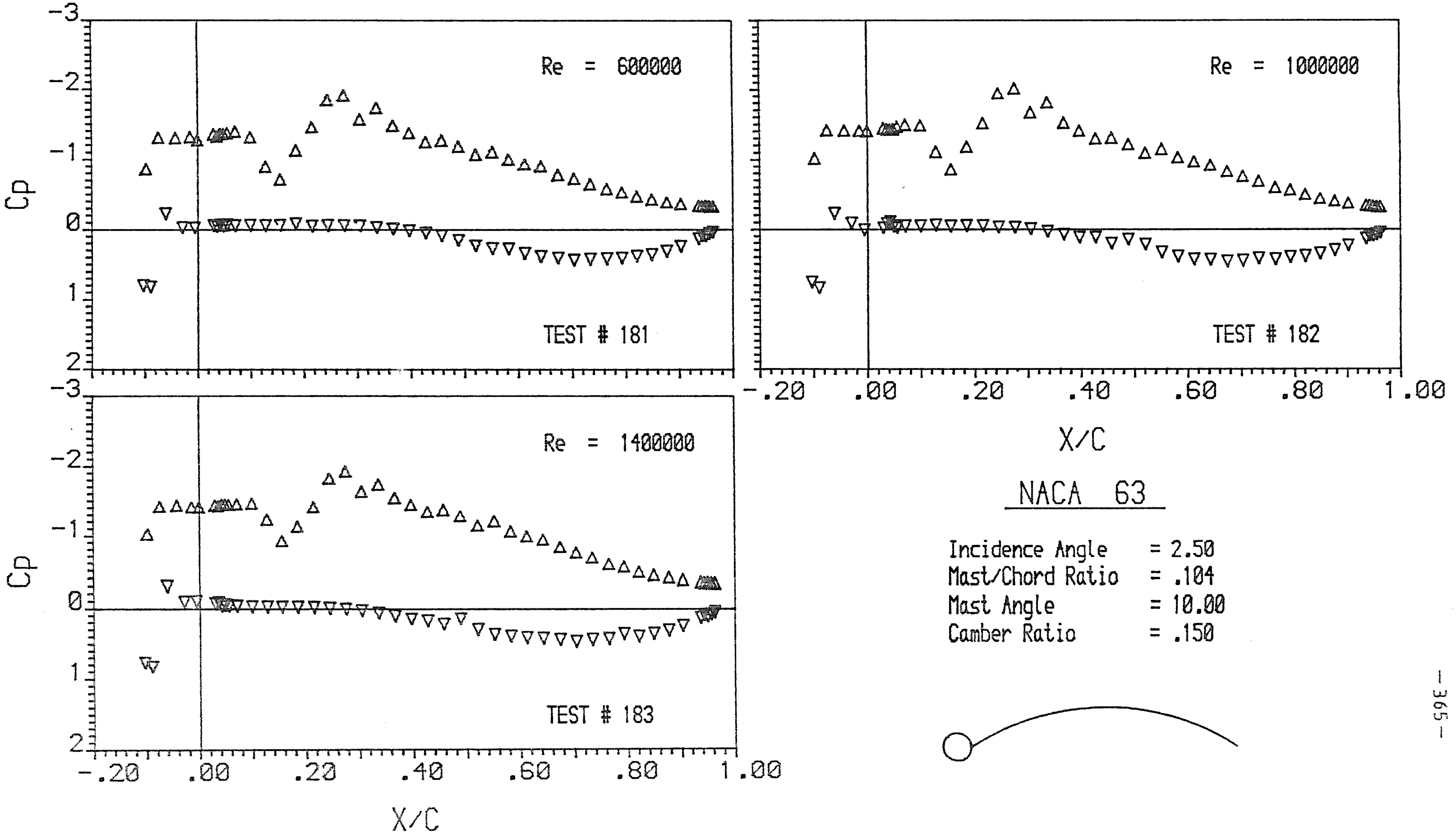

NACA 63

Incidence Angle = 2.50
Mast/Chord Ratio = .104
Mast Angle = 10.00
Camber Ratio = .150

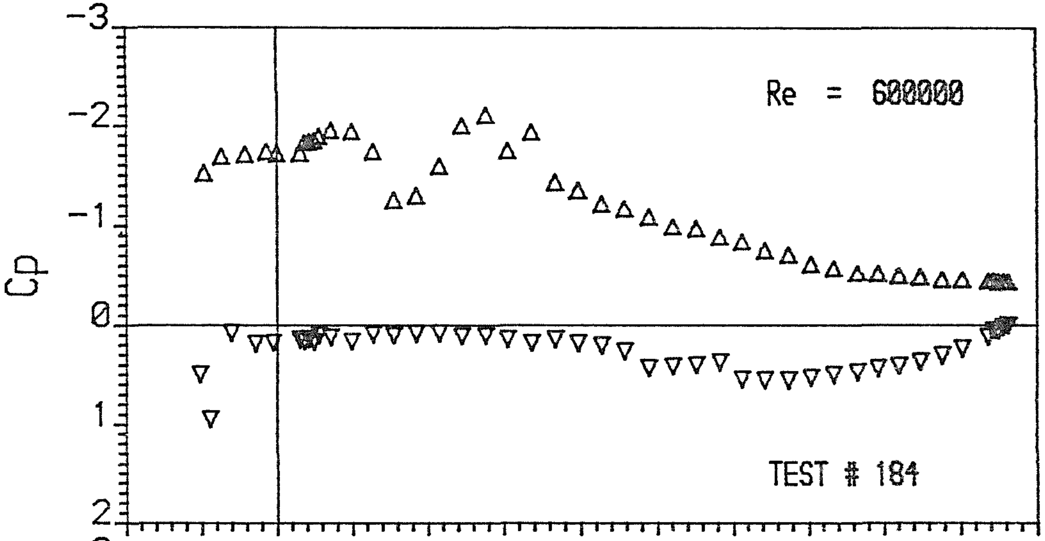

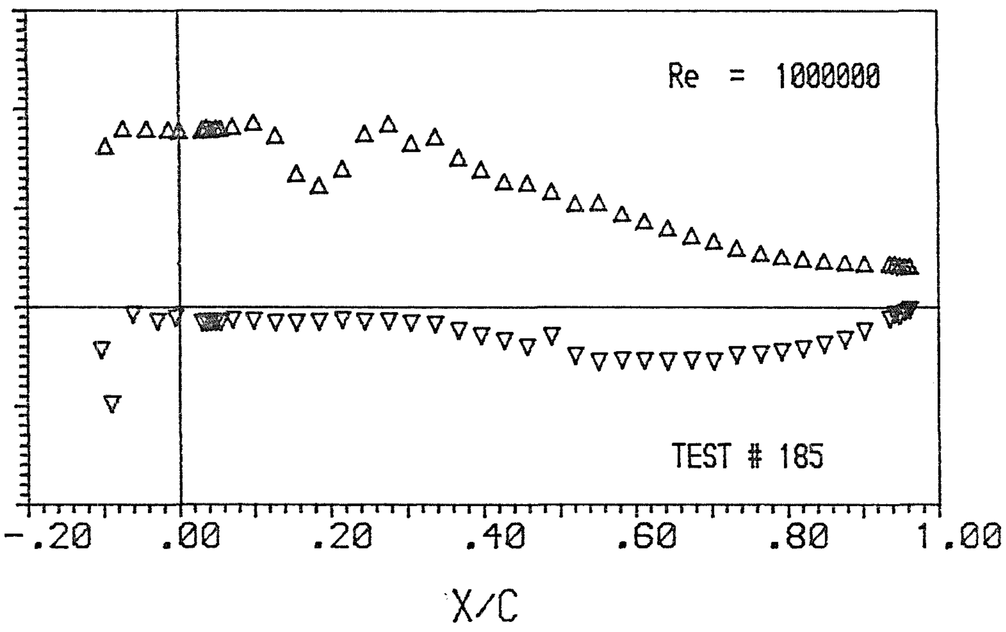

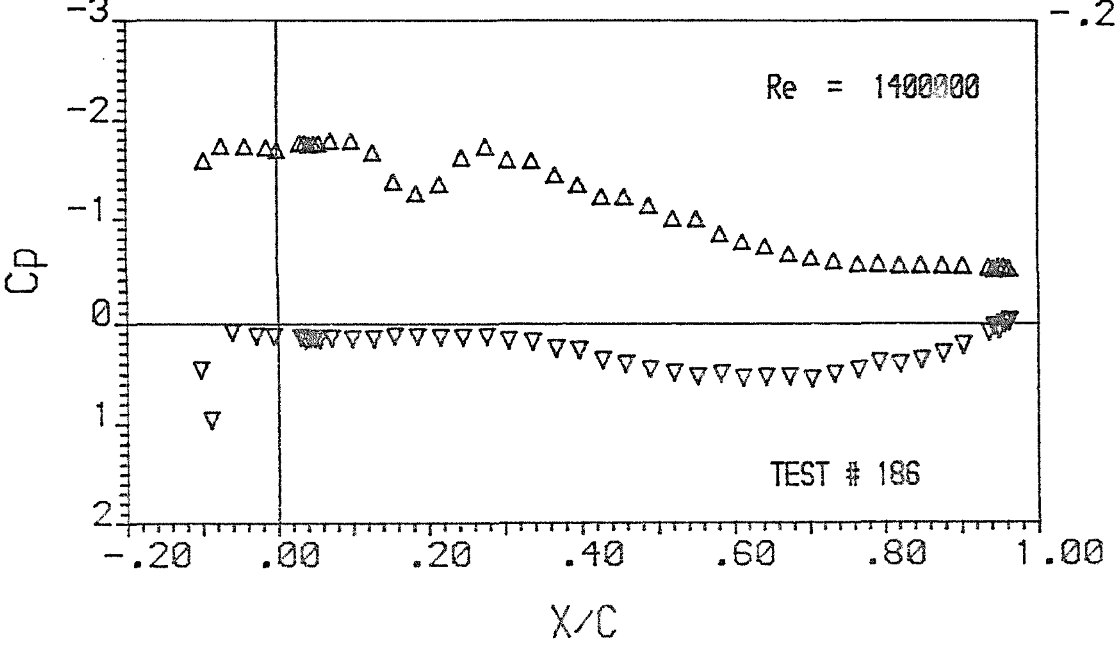

NACA 63

Incidence Angle = 5.00
Mast/Chord Ratio = .104
Mast Angle = 10.00
Camber Ratio = .150

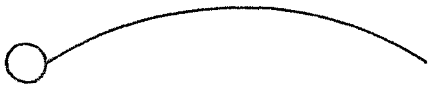

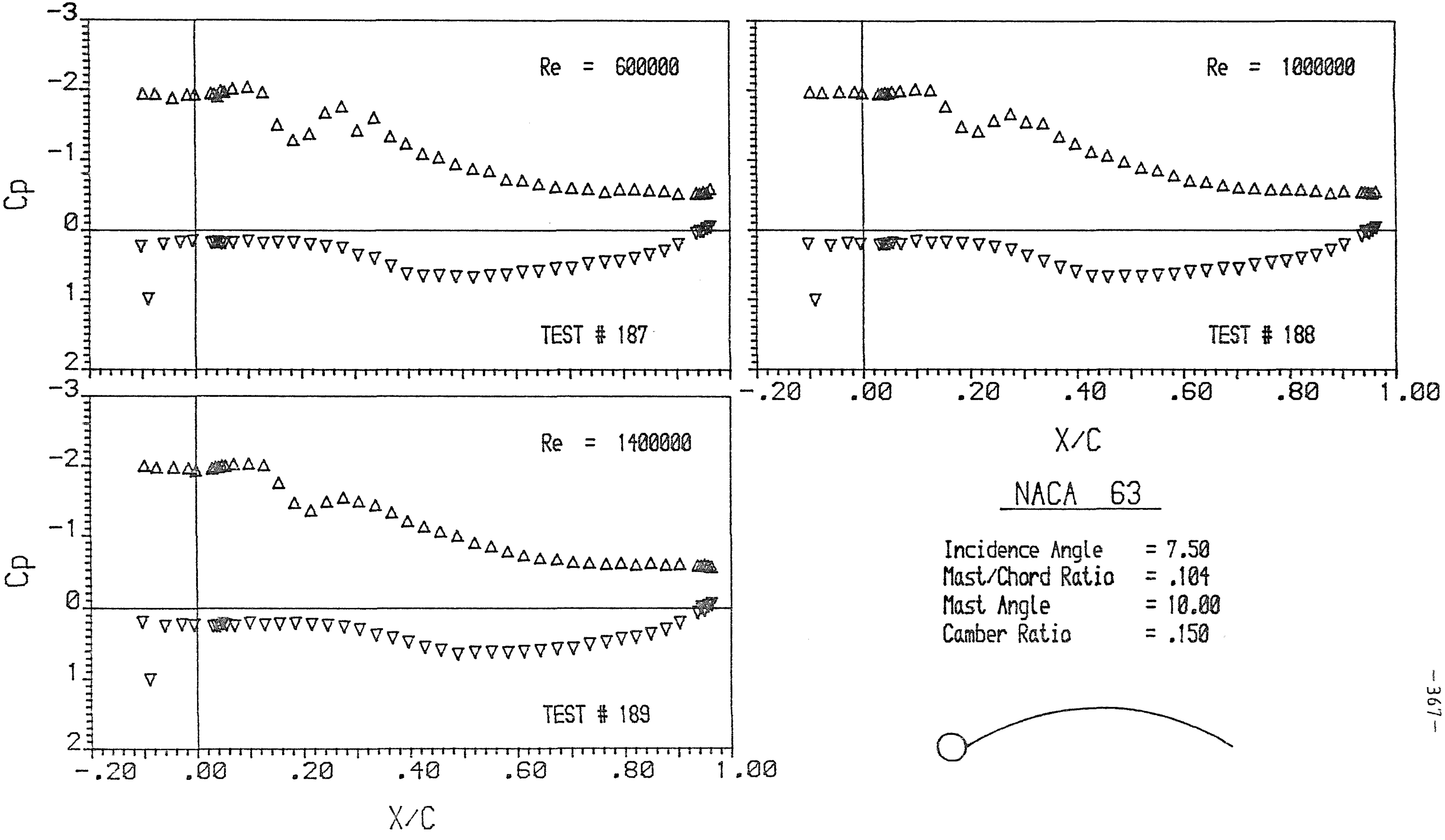

NACA 63

Incidence Angle = 7.50
Mast/Chord Ratio = .104
Mast Angle = 10.00
Camber Ratio = .150

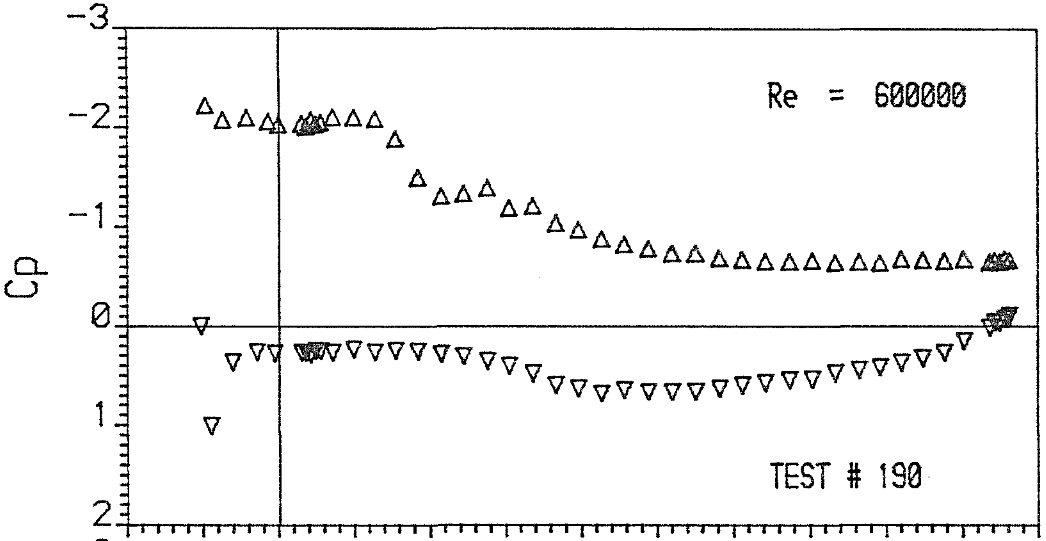

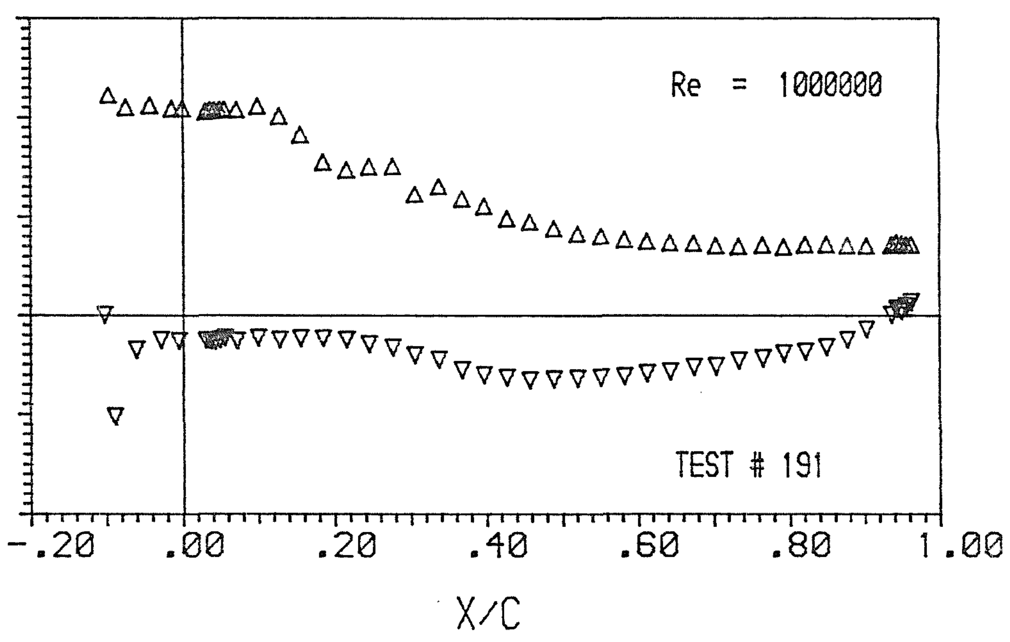

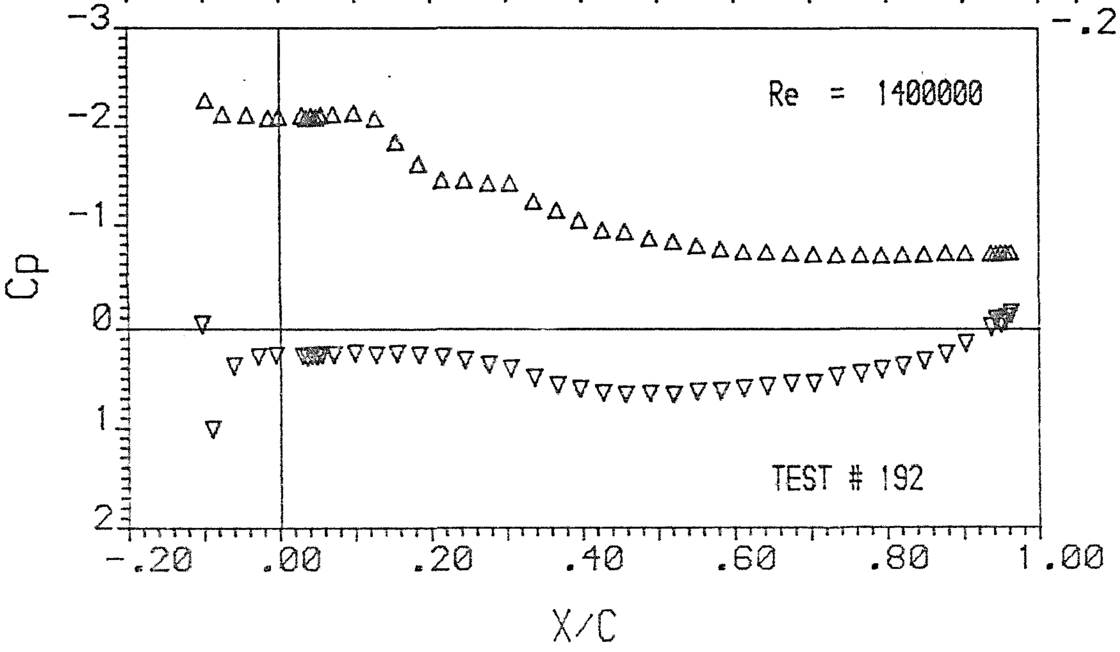

NACA 63

Incidence Angle = 10.00
Mast/Chord Ratio = .104
Mast Angle = 10.00
Camber Ratio = .150

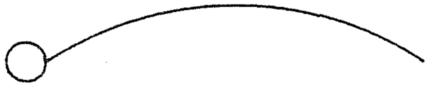

APPENDIX IV

SEPARATION AND REATTACHMENT RESULTS

NACA a=0·8						
Test #	Upper Bubble					Trailing Edge
	$\frac{X_T}{c}$	Cp_T	$\frac{X_R}{c}$	Cp_R	σ	$\frac{X_{Sep}}{c}$
1	0·16	-1·5	0·31	-0·9	0·24	0·79
4	0·21	-1·7	0·36	-1·0	0·26	0·76
7	0·24	-1·7	0·43	-1·1	0·22	0·72
10	0·26	-1·7	0·46	-1·3	0·15	0·66
14	0·18	-1·6	0·37	-0·9	0·27	0·81
17	0·21	-1·7	0·43	-0·9	0·30	0·80
20	0·24	-1·8	0·46	-1·0	0·29	0·79
23	0·30	-1·8	0·44	-1·2	0·21	0·76
25	0·13	-1·4	0·22	-0·8	0·25	0·80
28	0·16	-1·7	0·28	-1·1	0·22	0·77
31	0·14	-1·8	0·33	-1·1	0·25	0·76
34	0·22	-1·9	0·42	-1·1	0·28	0·71
37	0·24	-1·6	0·43	-0·8	0·31	0·86
40	0·28	-1·8	0·49	-1·1	0·25	0·80
45	0·19	-1·8	0·39	-1·1	0·25	0·74
48	0·19	-1·9	0·43	-1·2	0·24	0·76
49	0·13	-1·5	0·24	-0·8	0·28	0·84
52	0·16	-1·7	0·31	-0·9	0·31	0·82
55	0·22	-1·9	0·40	-1·0	0·31	0·80
58	0·25	-1·7	0·42	-1·2	0·19	0·69
61	0·06	-1·4	0·12	-0·5	0·38	0·82
64	0·08	-1·9	0·13	-0·9	0·34	0·80
67	0·08	-2·2	0·16	-1·2	0·31	0·79
70	0·13	-2·3	0·27	-1·3	0·30	0·78
73	0·16	-1·5	0·32	-0·9	0·24	0·90
76	0·21	-1·6	0·40	-0·9	0·27	0·82
79	0·30	-1·5	0·54	-0·9	0·24	0·76
82	0·34	-1·4	0·46	-1·2	0·08	0·76
85	0·08	-1·6	0·23	-0·7	0·35	0·92
88	0·10	-2·0	0·19	-1·0	0·33	0·91
91	0·14	-2·1	0·28	-1·2	0·29	0·84
94	0·20	-1·8	0·41	-1·1	0·25	0·72
97	0·08	-1·6	0·16	-0·8	0·31	0·92
100	0·11	-1·9	0·26	-1·0	0·31	0·90
103	0·22	-1·7	0·43	-1·0	0·26	0·79
106	0·28	-1·5	0·43	-1·1	0·16	0·72